AJNR

AMERICAN JOURNAL OF NEURORADIOLOGY

JULY 2014
VOLUME 35
NUMBER 7
WWW.AJNR.ORG

THE JOURNAL OF DIAGNOSTIC AND INTERVENTIONAL NEURORADIOLOGY

MRI surrogates for medulloblastoma

Natural course of vertebrobasilar dissecting aneurysms

MRI grading of Meniere disease

Official Journal ASNR • ASFNR • ASHNR • ASPNR • ASSR

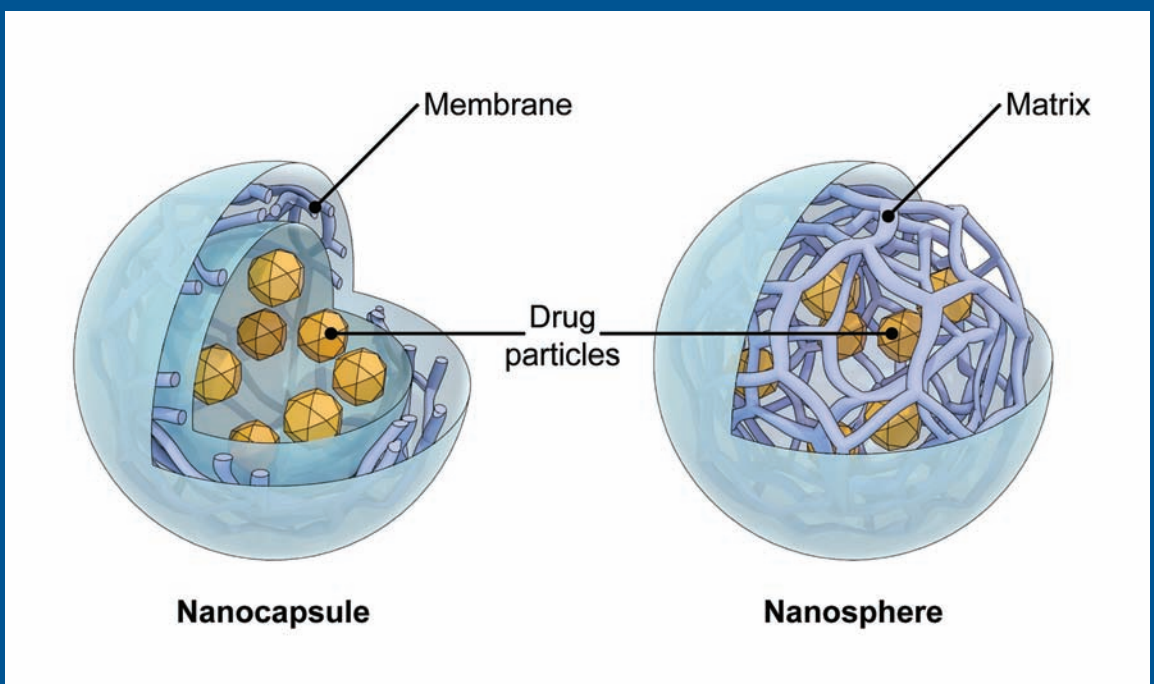

COIL PERFORMANCE AND

V-Trak® Advanced Coil System

Introducing the **V-Trak® Advanced Coil System**, the next generation to power the performance of our most technically advanced line of coils.

Best-in-class tactile feel	– Balanced design provides enhanced feel during coil delivery
Reengineered, anatomically designed pusher wire	– Superior control and 1:1 coil responsiveness even in tortuous anatomy – Smooth trackability and efficient pushability – Unmatched distal softness and minimal catheter kick-out
Streamlined detachment mechanism	– Best-in-class detachment reliability
Robust and tapered introducer sheath	– Smooth introduction of even the smallest coils – More secure seating inside microcatheter hub with smallest in-hub gap
Enhanced stretch resistance	– Precise coil repositioning and improved durability
Gapped coil hoop	– Easy flushing during coil preparation

Call your MicroVention representative to check availability and learn more about our new V-Trak® Advanced Coils including Cosmos®, HyperSoft®, HyperSoft® 3D, VFC®, HydroFrame®, HydroFill® and HydroSoft® coils.

microvention.com

CE 0297

CONTROL RE-IMAGINED

OPTIMAL COMBINATION OF SUPPORT AND FLEXIBILITY

ROBUST RELIABILITY

- **Streamlined detachment mechanism has best-in-class detachment reliability in bench testing**

SOFTNESS ZONE

- **Ultra soft coiled pusher wire for:**
  - Controlled, safe tracking through distal vasculature
  - Minimal catheter deflection and kick-out
  - Consistent pushability

TRANSITION ZONE

- Tapered transition from hypotube to coiled pusher wire
- Engineered polymer jacket for stability
- Optimized combination of support and softness

SUPPORT ZONE

- **Stable hypotube for:**
  - Excellent and smooth pushability
  - 1 : 1 coil responsiveness
- **Fluoro safe markers for ease of use, visualization and reduced fluoroscopy time**

MicroVention® TERUMO

MicroVention, Inc.
Worldwide Headquarters PH +1.714.247.8000
1311 Valencia Avenue
Tustin, CA 92780 USA
MicroVention UK Limited PH +44 (0) 191 258 6777
MicroVention Europe, S.A.R.L. PH +33 (1) 39 21 77 46
MicroVention Deutschland GmbH PH +49 211 210 798-0

BARRICADE™ COIL SYSTEM

PERFORMANCE AND VALUE DELIVERED

BLOCKADE MEDICAL

18 TECHNOLOGY DRIVE #169, IRVINE CA 92618 | **P** 949.788.1443
WWW.BLOCKADEMEDICAL.COM

MADE IN AMERICA

CE 0297

MKTG-020 REV. B

AJNR

AMERICAN JOURNAL OF NEURORADIOLOGY

JULY 2014
VOLUME 35
NUMBER 7
WWW.AJNR.ORG

Publication Preview at www.ajnr.org features articles released in advance of print. Visit www.ajnrblog.org to comment on AJNR content and chat with colleagues and AJNR's News Digest at http://ajnrdigest.org to read the stories behind the latest research in neuroimaging.

EDITORIAL

PERSPECTIVES

1243 **The Complicated Equation of Smell, Flavor, and Taste** *M. Castillo*

REVIEW ARTICLES

1246 **New Applications of Nanotechnology for Neuroimaging** *G. Suffredini, J.E. East, and L.M. Levy*

1254 **High WSS or Low WSS? Complex Interactions of Hemodynamics with Intracranial Aneurysm Initiation, Growth, and Rupture: Toward a Unifying Hypothesis** *H. Meng, V.M. Tutino, J. Xiang, and A. Siddiqui*

EXPEDITED PUBLICATION

1263 **MRI Surrogates for Molecular Subgroups of Medulloblastoma** *S. Perreault, V. Ramaswamy, A.S. Achrol, K. Chao, T.T. Liu, D. Shih, M. Remke, S. Schubert, E. Bouffet, P.G. Fisher, S. Partap, H. Vogel, M.D. Taylor, Y.J. Cho, and K.W. Yeom*

PATIENT PERSPECTIVES

1270 **Are We Effectively Informing Patients? A Quantitative Analysis of On-Line Patient Education Resources from the American Society of Neuroradiology** *D.R. Hansberry, N. Agarwal, S.F. Gonzales, and S.R. Baker*

PATIENT SAFETY

1276 **Brain Radiation Doses to Patients in an Interventional Neuroradiology Laboratory** *R.M. Sanchez, E. Vano, J.M. Fernández, M. Moreu, and L. Lopez-Ibor*

1281 **Repeated Head CT in the Neurosurgical Intensive Care Unit: Feasibility of Sinogram-Affirmed Iterative Reconstruction–Based Ultra-Low-Dose CT for Surveillance** *I. Corcuera-Solano, A.H. Doshi, A. Noor, and L.N. Tanenbaum*

1288 **Artifact Reduction of Different Metallic Implants in Flat Detector C-Arm CT** *S.-C. Hung, C.-C. Wu, C.-J. Lin, W.-Y. Guo, C.-B. Luo, F.-C. Chang, and C.-Y. Chang*

BRAIN

1293 **Diffusion-Weighted Imaging with Dual-Echo Echo-Planar Imaging for Better Sensitivity to Acute Stroke** *S.J. Holdsworth, K.W. Yeom, M.U. Antonucci, J.B. Andre, J. Rosenberg, M. Aksoy, M. Straka, N.J. Fischbein, R. Bammer, M.E. Moseley, G. Zaharchuk, and S. Skare*

1303 **Perfusion-Based Selection for Endovascular Reperfusion Therapy in Anterior Circulation Acute Ischemic Stroke** *S. Prabhakaran, M. Soltanolkotabi, A.R. Honarmand, R.A. Bernstein, V.H. Lee, J.J. Conners, F. Dehkordi-Vakil, A. Shaibani, M.C. Hurley, and S.A. Ansari*

Indicates Editor's Choices selection

Indicates Fellows' Journal Club selection

Indicates open access to non-subscribers at www.ajnr.org

Indicates article with supplemental on-line table

Indicates article with supplemental on-line photo

Indicates article with supplemental on-line video

Indicates Evidence-Based Medicine Level 1

Indicates Evidence-Based Medicine Level 2

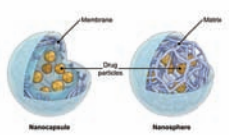

Schematic representations of a nanocapsule and a nanosphere.

Trevo® XP

PROVUE RETRIEVER

Take Control. Capture More.

The newly designed Trevo® XP ProVue Retriever takes proven Trevo Retriever performance to new levels for **easy delivery, easy placement,** and **easy visualization.**

When you're in control, it's amazing what you can capture.

stryker® Neurovascular

Stroke: *Our Only Focus. Our Ongoing Promise.*

1309 **Differentiation of Tumor Progression from Pseudoprogression in Patients with Posttreatment Glioblastoma Using Multiparametric Histogram Analysis** *J. Cha, S.T. Kim, H.-J. Kim, B.-j. Kim, Y.K. Kim, J.Y. Lee, P. Jeon, K.H. Kim, D.-s. Kong, and D.-H. Nam*

1318 **Cerebrovascular Collaterals Correlate with Disease Severity in Adult North American Patients with Moyamoya Disease** *M.K. Strother, M.D. Anderson, R.J. Singer, L. Du, R.D. Moore, Y. Shyr, T.R. Ladner, D. Arteaga, M.A. Day, P.F. Clemmons, and M.J. Donahue*

1325 **Low-Power Inversion Recovery MRI Preserves Brain Tissue Contrast for Patients with Parkinson Disease with Deep Brain Stimulators** *S.N. Sarkar, E. Papavassiliou, R. Rojas, D.L. Teich, D.B. Hackney, R.A. Bhadelia, J. Stormann, and R.L. Alterman*

1330 **Effects of Gadolinium Contrast Agent Administration on Automatic Brain Tissue Classification of Patients with Multiple Sclerosis** *J.B.M. Warntjes, A. Tisell, A.-M. Landtblom, and P. Lundberg*

INTERVENTIONAL *Published in collaboration with Interventional Neuroradiology*

1337 **Impact of Age and Baseline NIHSS Scores on Clinical Outcomes in the Mechanical Thrombectomy Using Solitaire FR in Acute Ischemic Stroke Study** *M.A. Almekhlafi, A. Davalos, A. Bonafe, R. Chapot, J. Gralla, V.M. Pereira, and M. Goyal, on behalf of the STAR Registry Investigators*

1341 **Flow Diversion versus Traditional Endovascular Coiling Therapy: Design of the Prospective LARGE Aneurysm Randomized Trial** *A.S. Turk III, R.H. Martin, D. Fiorella, J. Mocco, A. Siddiqui, and A. Bonafe*

1346 **Use of Flow-Diverting Devices in Fusiform Vertebrobasilar Giant Aneurysms: A Report on Periprocedural Course and Long-Term Follow-Up** *L. Ertl, M. Holtmannspötter, M. Patzig, H. Brückmann, and G. Fesl*

1353 **Role of C-Arm VasoCT in the Use of Endovascular WEB Flow Disruption in Intracranial Aneurysm Treatment** *J. Caroff, C. Mihalea, H. Neki, D. Ruijters, L. Ikka, N. Benachour, J. Moret, and L. Spelle*

1358 **Rupture-Associated Changes of Cerebral Aneurysm Geometry: High-Resolution 3D Imaging before and after Rupture** *J.J. Schneiders, H.A. Marquering, R. van den Berg, E. VanBavel, B. Velthuis, G.J.E. Rinkel, and C.B. Majoie*

1363 **Identification of the Inflow Zone of Unruptured Cerebral Aneurysms: Comparison of 4D Flow MRI and 3D TOF MRA Data** *K. Futami, H. Sano, K. Misaki, M. Nakada, F. Ueda, and J. Hamada*

1371 **Natural Course of Dissecting Vertebrobasilar Artery Aneurysms without Stroke** *N. Kobayashi, Y. Murayama, I. Yuki, T. Ishibashi, M. Ebara, H. Arakawa, K. Irie, H. Takao, I. Kajiwara, K. Nishimura, K. Karagiozov, and M. Urashima*

1376 **Influence of Patient Age on Angioarchitecture of Brain Arteriovenous Malformations** *S.W. Hetts, D.L. Cooke, J. Nelson, N. Gupta, H. Fullerton, M.R. Amans, J.A. Narvid, P. Moftakhar, H. McSwain, C.F. Dowd, R.T. Higashida, V.V. Halbach, M.T. Lawton, and H. Kim*

EXTRACRANIAL VASCULAR

1381 **A Sonographic Quantitative Cutoff Value of Cerebral Venous Outflow in Neurologic Diseases: A Blinded Study of 115 Subjects** *L. Monti, E. Menci, P. Piu, S. Leonini, U. Arrigucci, M. Bellini, A. Zandonella, P. Galluzzi, and A. Casasco*

HEAD & NECK

1387 **Detection and Grading of Endolymphatic Hydrops in Menière Disease Using MR Imaging** *K. Baráth, B. Schuknecht, A. Monge Naldi, T. Schrepfer, C.J. Bockisch, and S.C.A. Hegemann*

ASNR 53rd Annual Meeting & The Foundation of the ASNR Symposium 2015

Getting Personal • Getting Personal • Getting Personal

ASNR

CHICAGO ★ 2015

ASFNR ASHNR ASPNR ASSR SNIS

THE FOUNDATION OF THE ASNR

April 25-30, 2015

Chicago, Illinois

Sheraton Chicago Hotel & Towers

www.asnr.org/2015

1393 **Immunoglobulin G4–Related Disease of the Orbit: Imaging Features in 27 Patients** *C.A. Tiegs-Heiden, L.J. Eckel, C.H. Hunt, F.E. Diehn, K.M. Schwartz, D.F. Kallmes, D.R. Salomão, T.E. Witzig, and J.A. Garrity*

1398 **Role of Mastoid Pneumatization in Temporal Bone Fractures** *A. Ilea, A. Butnaru, S.A. Sfrângeu, M. Hedeşiu, C.M. Dudescu, P. Berce, H. Chezan, L. Hurubeanu, V.E. Trombitaş, R.S. Câmpian, and S. Albu*

1405 **Osteoradionecrosis after Radiation Therapy for Head and Neck Cancer: Differentiation from Recurrent Disease with CT and PET/CT Imaging** *L. Alhilali, A.R. Reynolds, and S. Fakhran*

1412 **Comparison of the T2 Relaxation Time of the Temporomandibular Joint Articular Disk between Patients with Temporomandibular Disorders and Asymptomatic Volunteers** *N. Kakimoto, H. Shimamoto, J. Chindasombatjaroen, T. Tsujimoto, S. Tomita, Y. Hasegawa, S. Murakami, and S. Furukawa*

PEDIATRICS

1418 **Correlation of Prenatal and Postnatal MRI Findings in Schizencephaly** *S.A. Nabavizadeh, D. Zarnow, L.T. Bilaniuk, E.S. Schwartz, R.A. Zimmerman, and A. Vossough*

1425 **The Diagnostic Value of CT Myelography, MR Myelography, and Both in Neonatal Brachial Plexus Palsy** *R. Tse, J.N. Nixon, R.S. Iyer, K.A. Kuhlman-Wood, and G.E. Ishak*

1433 **Hydrocephalus Decreases Arterial Spin-Labeled Cerebral Perfusion** *K.W. Yeom, R.M. Lober, A. Alexander, S.H. Cheshier, and M.S.B. Edwards*

SPINE

1440 **Risk Factors of Hematomyelia Recurrence and Clinical Outcome in Children with Intradural Spinal Cord Arteriovenous Malformations** *G. Saliou, A. Tej, M. Theaudin, M. Tardieu, A. Ozanne, M. Sachet, D. Ducreux, and K. Deiva*

ONLINE FEATURES (www.ajnr.org)

ERRATA

E4

BOOK REVIEWS *R.M. Quencer, Section Editor*

Please visit www.ajnrblog.org to read and comment on Book Reviews.

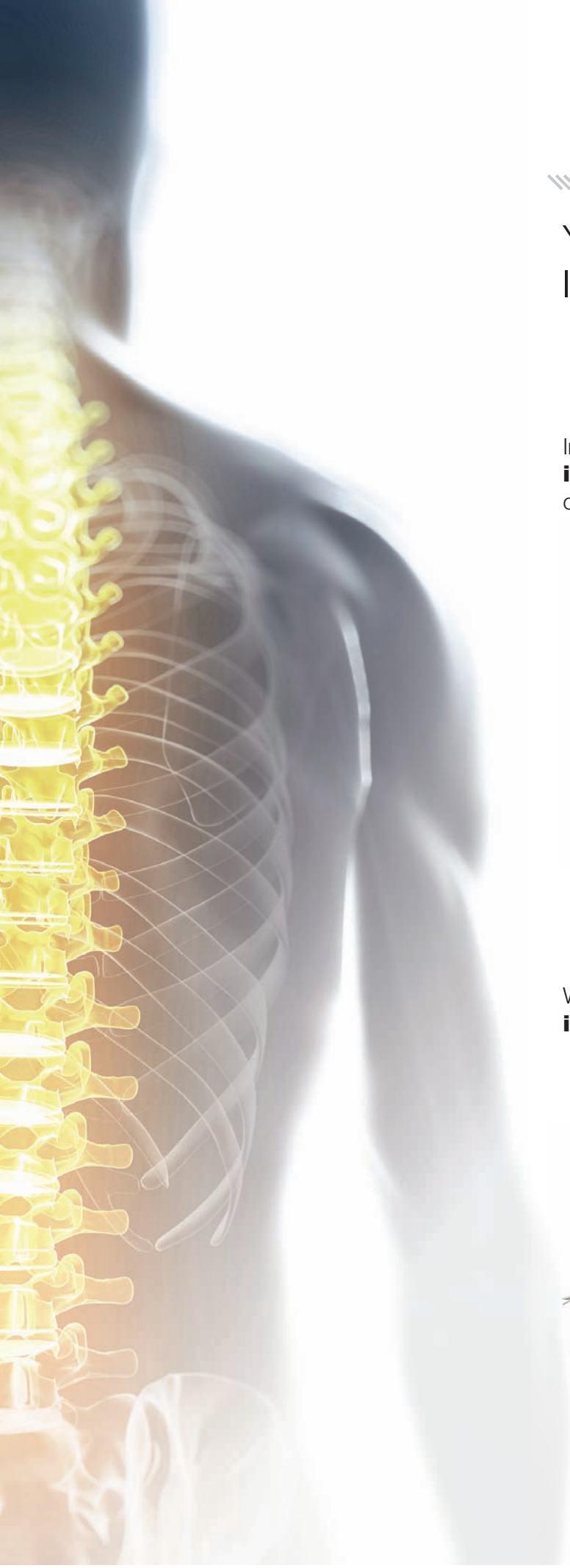

stryker®

Your **single source** for the latest in innovative **solutions.**

Introducing **the most complete and least invasive vertebral augmentation portfolios** on the market today.

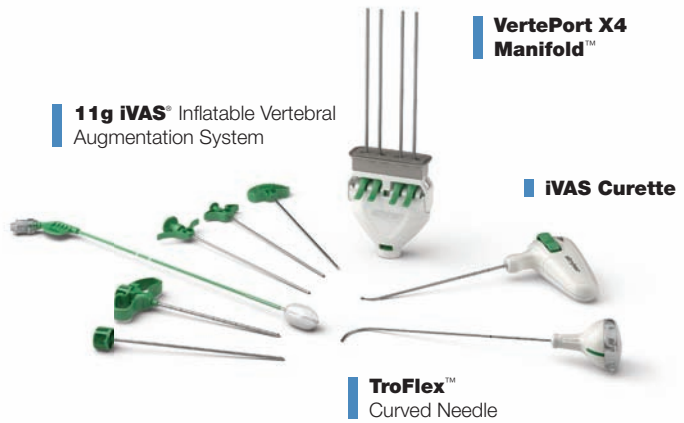

We are also proud to announce **a new paradigm in radiofrequency ablation**.

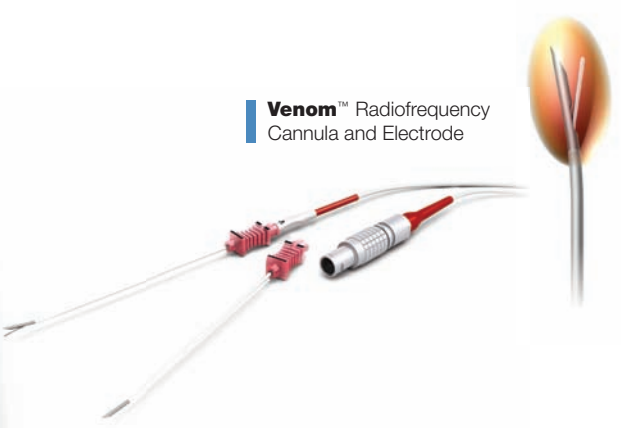

strykerIVS.com

1000-025-308 Rev B

AJNR

Letter from the President-Elect – Search for New *AJNR* Editor

In June, 2015, Mauricio Castillo, MD, FACR, will complete an eight-year term as the Editor-in-Chief of the *AJNR*. He follows a short list of illustrious neuroradiologists, from Dr. Juan Taveras to Dr. Michael Huckman to Dr. Robert Quencer to Dr. Robert Grossman.

One only has to pick up any random issue of the *AJNR* to realize what a tremendous mark Mauricio has made on the journal. His imprint starts on the first page of content with his column, Perspectives. Probing, erudite, at times very witty, and always brilliant, Mauricio turns out a monthly commentary on the state of neuroradiology, the state of our profession, and, at times, the state of the world. His references and quotations demonstrate a mind not only scientific and exacting but also knowledgeable in realms far beyond medicine.

Having worked with Mauricio very closely at the ASNR for the past two years, I can also attest to the fact that Mauricio is totally dedicated to the journal. At times, it seemed his reason for being. And the journal has benefitted immensely, in turn. From its look to its organization to the quality of the articles, Mauricio has brought the journal into the forefront of all radiology journals and it now ranks #2 in Impact Factor of all radiology journals. *AJNR* is the premier clinical neuroimaging journal with the highest circulation among all imaging-related subspecialty journals, publishing about 350 articles in 12 issues per year. It receives over 1400 original submissions annually and its Web site is accessed over 10 million times a year. In addition to the print version of the Journal, Mauricio also initiated its biannual Special Collections and monthly *AJNR* Digest. Other electronic activities which he began include its popular Case Collection (Case of the Week, Case of the Month, Classic Case, and Clinical Correlation), podcasts (editor's and fellows' journal club selections, travelling journal club, and Special Collections), and Fellows' Portal. With his international background, Mauricio has also been the ideal person to spread the word of the *AJNR* across the world. Finally, he has done all this and kept the journal in sound financial health through a period of difficult economic times.

Mauricio took over leadership of the journal at a time when the concept of the journal was beginning to enter a state of flux. One only has to look at your neighborhood newsstand to realize that this has been a time when many publications have been unable to adjust and have disappeared. In the past eight years, the demands on the journal have changed. Our current expectations are for instant gratification, not a lag time before publication. We require our information in more bite-size pieces, directed at us and easily accessible.

The new editor will face an even more rapidly evolving world. What is the future of radiology journals? We know that the *AJNR* will survive but in what form? What will be the best digital format? There will be an increased demand for electronic access and a further migration to tablets and smartphones. Preserving the brand of the *AJNR* will become more challenging. While in the past, publication was the end point, increasingly, publication today is the starting point, the beginning of an interactive discussion. How will this impact on the financial state of the journal, with decreasing print advertising? How will the *AJNR* respond to the demands of social media?

To assist the Executive Committee in the search for a new editor in these changing times, I will chair a search committee comprised, in part, of Tina Young-Poussaint, Chair of the Publications Committee, Laurie Loevner, Vice-President, Howard Rowley, Robert Quencer, Robert D. Zimmerman, James Barkovich, Tabbassum Kennedy, and some of the Senior Editors of the *AJNR*, Harry J. Cloft, Nancy Fischbein, Pamela W. Schaefer, Jody Tanabe, and Charles M. Strother, as well as James Gantenberg, Karen Halm, and Angelo Artemakis from the ASNR headquarters. The appointment of the new Editor-in-Chief will be announced in the spring of 2015.

All interested physicians are invited to send their curriculum vitae and an introductory letter of intent to Dr. Gordon Sze, American Society of Neuroradiology, 800 Enterprise Drive, Suite 205, Oak Brook, IL, 60523 and via email to gordon.sze@yale.edu and jgantenberg@asnr.org. In addition, we welcome nominations of candidates from the ASNR membership. The deadline for receipt of submissions is August 1, 2014 but earlier submissions are welcome. A position description for the *AJNR* Editor and basic qualifications are posted at: www.ajnr.org/site/misc/eic-search-2015.xhtml.

Gordon Sze, MD, FACR
Chair, Editor-in-Chief Search Committee
President-Elect
American Society of Neuroradiology

Simplify
the MOC Process

Manage
your CME Credits Online

CMEgateway.org

It's Easy and Free!

Log on to CME Gateway to:

- View or print reports of your CME credits from multiple societies from a single access point.
- Print an aggregated report or certificate from each participating organization.
- Link to SAMs and other tools to help with maintenance of certification.

American Board of Radiology (ABR) participation!

By activating ABR in your organizational profile, your MOC–fulfilling CME and SAM credits can be transferred to your own personalized database on the ABR Web site.

Sign Up Today!

go to CMEgateway.org

Available to Members of Participating Societies

American Board of Radiology (ABR)
American College of Radiology (ACR)
American Roentgen Ray Society (ARRS)
American Society of Neuroradiology (ASNR)
Commission on Accreditation of Medical Physics Educational Programs, Inc. (CAMPEP)
Radiological Society of North America (RSNA)
Society of Interventional Radiology (SIR)
SNM
The Society for Pediatric Radiology (SPR)

AJNR

AMERICAN JOURNAL OF NEURORADIOLOGY

Publication Preview at www.ajnr.org features articles released in advance of print. Visit www.ajnrblog.org to comment on AJNR content and chat with colleagues and AJNR's News Digest at http://ajnrdigest.org to read the stories behind the latest research in neuroimaging.

JULY 2014 • VOLUME 35 • NUMBER 7 • WWW.AJNR.ORG

AJNR (Am J Neuroradiol ISSN 0195–6108) is a journal published monthly, owned and published by the American Society of Neuroradiology (ASNR), 800 Enterprise Drive, Suite 205, Oak Brook, IL 60523. Annual dues for the ASNR include $170.00 for journal subscription. The journal is printed by Cadmus Journal Services, 5457 Twin Knolls Road, Suite 200, Columbia, MD 21045; Periodicals postage paid at Oak Brook, IL and additional mailing offices. Printed in the U.S.A. POSTMASTER: Please send address changes to American Journal of Neuroradiology, P.O. Box 3000, Denville, NJ 07834, U.S.A. Subscription rates: nonmember $370 ($440 foreign) print and online, $300 online only; institutions $430 ($495 foreign) print and basic online, $850 ($915 foreign) print and extended online, $355 online only (basic), extended online $770; single copies are $35 each ($40 foreign). Indexed by PubMed/Medline, BIOSIS Previews, Current Contents (Clinical Medicine and Life Sciences), EMBASE, Google Scholar, HighWire Press, Q-Sensei, RefSeek, Science Citation Index, and SCI Expanded.

AJNR

Go Green!

AJNR urges American Society of Neuroradiology members to reduce their environmental footprint by voluntarily suspending their print subscription.

The savings in paper, printing, transportation, and postage not only help members cut down on clutter, but go to fund new electronic enhancements and expanded content.

The digital edition of *AJNR* presents the print version in its entirety, along with extra features including:

- Publication Preview
- Case of the Week
- Podcasts
- Special Collections
- The *AJNR* Blog
- Weekly Poll

It also **reaches subscribers much faster than print**. An **electronic table of contents** will be sent directly to your mailbox to notify you as soon as it publishes.

Readers can **search, reference, and bookmark** current and archived content 24 hours a day on www.ajnr.org, rather than thumb through stacks of accumulated paper issues for articles and images they need.

http://www.ajnr.org/cgi/feedback

ASNR members who wish to opt out of print can do so by using the Feedback form on the *AJNR* Website (**http://www.ajnr.org/cgi/feedback**). Just type "Go Green" in the subject line to stop print and spare our ecosystem.

The Complicated Equation of Smell, Flavor, and Taste

M. Castillo, *Editor-in-Chief*

Our oldest senses are those related to chemogustatory capacities: smell and taste. Of these, smell is probably the oldest, and before we fully develop cerebral hemispheres, the olfactory apparatus already exists as extensions of the limbic system. The study of the senses of smell and taste is so complex that it encompasses armies of aromachologists, food scientists, physiologists, behavioral psychologists, cognitive neuroscientists, neuropharmacologists, biochemists, anthropologists, molecular biologists, and many more and is intimately related to the study of taste.

The olfactory system in vertebrates has a unique embryology. It forms from 1) paired placodes made of non-neural epithelium that have the capacity to give rise to sensory neurons and supporting cells in the olfactory epithelium, and 2) neural crest cells that give origin to the structural elements of the nose and its cavities.[1] Although one cannot form without the other, neural crest cells get to their destination first. The olfactory receptor neurons are in the nasal cavity, and their axons, arranged in fascicles, traverse the cribriform plates and dura to synapse with cells in the olfactory bulbs, which are extensions of the brain. The olfactory neurons and accompanying glial cells arise outside the central nervous system but have the capacity to regenerate throughout life; it seems that progenitor neural crest cells may be their origin.

The human sense of smell is bidirectional, and the way we perceive smells changes according to the direction of air flow. Orthonasal smell is perceived when breathing in, while retronasal smell occurs when odorized air arising from the mouth is forced into the nose. This last type of smell is much more complex than the first one because it recruits flavor, texture, hearing, and muscle activity. Animals with a great sense of smell like dogs are designed predominantly for orthonasal smell. Their long snouts concentrate, moisturize, and direct odorized air directly toward their olfactory epithelium, assuring that warmed molecules are easily detected. Dogs have over 220 million olfactory receptors (compared with 5–10 million in humans), a 40% greater area of the brain dedicated to smell, and the ability to smell 1000–10,000 times better than humans.[2] In addition, dogs have a large vomeronasal (Jacobson) organ, whose neurons extend to accessory olfactory bulbs and then to the hippocampi. This organ is predominantly involved in pheromone perception and does not play an important role in the human sense of smell. Pheromones have a "blind smell," meaning that they stimulate the brain (observed with fMRI) while having no odor that can be perceived. Females are sensitive to male pheromones, particularly during ovulation. Male pheromones are found in sweat, but only fresh sweat. After 20 minutes, sweat is oxidized and it just smells bad. Billing agencies will send out bills scented with androstenone (a pheromone) because they are then perceived as being more aggressive and increase their collection rates[3] (note: the report in this reference is wonderfully entertaining!).

Because humans mostly depend on vision that is stereoscopic, which in turn is contingent on a strict interocular distance, we do not have a long snout and our anterior nasal pathways are less complex, less efficient, and shorter than those of dogs. However, contrary to prior beliefs, there is no evolutionary competition between smell and taste and vision; our sight has improved but our sense of smell remains quite good and the blind do not have a better sense of smell than the sighted. Although most mammals depend on orthonasal smell, we humans mostly use retronasal smell. When we say something tastes good, in reality we mean that it smells good because most "flavor" is actually retronasal smell. While retronasal smell is essential for tasting, antegrade smelling is not.

Once odorized air enters the nose in antegrade or retrograde directions, it reaches the cilia of the olfactory neurons where about 1000 specific receptor proteins are present. Specific olfactory receptor genes encode each protein. The discoverers of these genes were awarded the 2004 Nobel Prize.[4] Because humans can see very well, we do not depend on smell too much. The development of tricolor vision led to many olfactory receptor genes disappearing.[5] Humans can still differentiate about 10,000 smells, but to name them all, you have to be an expert such as wine connoisseur Robert Parker. The molecules for each smell have individual chemical and physical configurations that allow them to bind with specific receptors (the so-called "lock and key" concept). Once the molecules bind, adenylate cyclase is stimulated, and the result is an electrical impulse carried to the mitral cells that reside in the olfactory bulbs and send axons to different parts of the brain as follows:

- The piriform cortex is formed by the amygdala, uncus, and parahippocampal gyrus and is involved in perception of smells.
- The entorhinal cortex is the anterior aspect of the parahippocampal gyrus. Its function is to pair specific odors to specific memories (remember that an abnormal sense of smell is typical of Alzheimer and Parkinson disease).[6,7]
- The olfactory tubercle is located close to the nucleus accumbens; it is not directly involved in the perception of smells but rather in reward behaviors associated with odors.
- The amygdala is involved in emotional and autonomic responses to odors.

A good sense of smell can make up for the loss of taste as seen in the case of Chef Grant Achatz. Mr Achatz's Chicago restaurant, Alinea, now ranks as the sixth best in the world (it also has been awarded 3 Michelin Stars). Mr Achatz developed and neglected an oral cancer until it became stage 4, and rather than losing his tongue, he decided to undergo chemotherapy, radiation, and surgery.[8] Although his cancer is in remission, he lost his sense of taste (but not his sense of smell). I have eaten at Alinea and can assure our readers that this handicap has not affected the taste of the wonderful food he there designs and prepares. The relationship between smell, taste, and the brain is studied by a discipline called "neurogastronomy."

Smells produce activation in specific olfactory bulb regions, depending on their specific chemical compounds and timing. It

http://dx.doi.org/10.3174/ajnr.A3739

seems that olfactory bulbs use mechanisms similar to our "visual pattern recognition" to identify discrete smells. "Odor images" refer to maps of olfactory bulb activity during olfaction. The SenseLab Web site contains many of these maps obtained with fMRI at 7T in animals (because the olfactory bulb contains neurons, their activation may be mapped by fMRI as we commonly do in the brain).[9] Curiously, smell perception may occur after all related brain areas are damaged, as long as the olfactory bulbs remain intact.

Similar to the olfactory system, taste depends on the specific recognition of different flavors by specific cells in the tongue. We Westerners recognize 4 stimuli (salt, acid, sweet, and bitter), while Asians can add Umami (savory or meatlike) to these. Unlike the olfactory cells, taste does not get to the brain directly but via the seventh, ninth, and tenth cranial nerves. It is unclear whether stimuli traveling through these nerves compete and complement each other, but the end of the road is the insular cortex, where taste becomes a conscious activity. Weak smells and taste are congruent with each other, and they add up to recognizable flavors. Molecular cuisine, like that practiced in Alinea, El Bulli, and other famous modernistic restaurants, is based on the combination of noncongruent ingredients that result in a new perception of flavors. For example, Adam Melonas, a disciple of El Bulli's Chef Ferran Adria, created the "Octopop," a lollipop made of sliced, orange-infused octopus.[10] In this dish, the strong retronasal smell of oranges mixed with the texture of the octopus leads to sensory fusion and a greater recruitment of brain regions needed to analyze what is in one's mouth, resulting in a totally new experience.

Chefs can only go so far because most tastes and smells have strong emotional (hedonic) components that may render some combinations repellent. Last year, my wife and I decided to eat at Corton's in New York and found ourselves disliking their utterly strange combination of flavors. Sensory fusion overload did us in, but what we disliked may have been pleasurable to others, particularly individuals (supertasters) who may be able to taste the individual components in a dish and enjoy them for what they are. When aiming for sensory fusion, one needs exact amounts of ingredients (that is why molecular cuisine is considered very close to chemistry). For example, add too much capsaicin and this irritant suppresses the taste of all else in a bite.

Although the title of this *Perspectives* refers to the equation "smell + taste = flavor," one must also add "mouth sense" to make it correct. Mouth sense is important to taste and refers to temperature, pain, touch, and pressure receptors inside the oral cavity. These sensations are transmitted to the somatosensory cortex via the trigeminal nerves. The cornerstones of molecular (also called modernistic) cuisine—foams, spheres, and powders—rely on producing a flavor with a totally different mouth sense to surprise us. Next, we must add vision to the equation. Vividly colored food tastes and smells more intense than bland colored food.[a] Conditioning also plays a role, and if, for example, white wines are colored red, many tasters will believe that they were given red wines. The last addition to the equation is hearing. If we buy a cracker said to be "crispy," it must produce a sound of more than 5 kHz in our mouth for us to perceive it as such. Carrots, which we expect to be "crunchy," produce a sound between 1 and 2 kHz.

In his book *Neurogastronomy,*[11] Gordon M. Shepherd, a professor of neurobiology at Yale University, refers to the "flavor perception system."[b] Professor Shepherd calls the other half of the equation (emotion + memory + decisions + plasticity + language + consciousness = flavor) the "flavor action system," and one system will not work without the other. Scientists who study addictions (particularly drug and food ones), as well as neuroeconomists, are very interested in these systems. On the basis of understanding both, the food industry has created the most addictive and universal food item: the French fry (buttery smell, salty taste, crunchy feel and sound, and a vivid yellow color). The industry also knows that children prefer sweet and salty over sour and bitter. Colors do strange things to flavor and our desire to eat. Orange and yellow are said to induce appetite and thus are used in the décor of many fast food restaurants. Green, brown, and red are the most used colors in the food industry because they are the naturally occurring ones and we associate them with nature and thus, health. Blue is linked to sweetness, but it is not a natural food color and we tend to avoid food of this color. Colors and taste have no relationship with nutritional value. Smells cause strange sensations; who would have imagined that the smell of pumpkin pie increases penile blood flow?

As we age; our senses of smell and taste deteriorate, a finding nearly universal after 60 years of age, and we are all familiar with the consequences of adding too much salt or sugar to our food. By 80 years of age, most individuals' sense of smell is significantly impaired (though women fare much better than men). Cuisine for the elderly attempts to compensate for decreasing senses by making food more palatable. Regardless of age, the flavor equation is complex, and I like to think of it as follows:

(smell + taste + mouth sense + sight + sound) × (emotion + memory + decisions + plasticity + language + consciousness) = flavor.

REFERENCES

1. Katoh H, Shibata S, Fukuda K, et al. **The dual origin of the peripheral olfactory system: placode and neural crest.** *Molecular Brain* 2011;4:34–50
2. The canine sense of smell. http://www.whole-dog-journal.com/issues/7_11/features/Canine-Sense-of-Smell_15668–1.html. Accessed August 14, 2013
3. The smell report. http://www.sirc.org/publik/smell.pdf. Accessed August 14, 2013
4. Buck L, Axel R. **A novel multigene family may encode odorant receptors: a molecular basis for odor recognition.** *Cell* 1991;65:175–87
5. Gilad Y, Przeworski M, Lancet D, et al. **Loss of olfactory receptor**

[a] "Synesthesia" refers to an ability to see color or hear sounds when smelling particular odors. Some individuals are gifted and have a broad sense of synesthesia (such as perfume makers); however, all of us have some synesthetic ability.

[b] Although this book can be found at your local Barnes and Noble, beware: It is an academic and serious work that requires some serious effort to read and understand.

genes coincides with the acquisition of full trichromatic vision in primates. *PLoS Biol* 2004;2:E5
6. Wesson DW, Levy E, Nixon RA, et al. **Olfactory dysfunction correlates with amyloid-beta burden in an Alzheimer's disease mouse model.** *J Neurosci* 2010;30:505–14
7. Haehner A, Hummel T, Hummel C, et al. **Olfactory loss may be a first sign of idiopathic Parkinson's disease.** *Mov Disord* 2007;22:839–42
8. Grant Achatz. Wikipedia. http://en.wikipedia.org/wiki/Grant_Achatz. Accessed August 14, 2013
9. Olfactory bulb odor map database. SenseLab. http://senselab.med.yale.edu/OdorMapDB. Accessed August 14, 2013
10. MADRID LAB. A progressive cuisine lab in Spain. http://www.madridlab.net/melonas. Accessed August 14, 2013
11. Shepherd GM. *Neurogastronomy*. New York: Columbia University Press; 2012

New Applications of Nanotechnology for Neuroimaging

G. Suffredini, J.E. East, and L.M. Levy

ABSTRACT

SUMMARY: Advances in nanotechnology have the potential to dramatically enhance the detection of neurologic diseases with targeted contrast agents and to facilitate the delivery of focused therapies to the central nervous system. We present the physicochemical rationale for their use, applications in animal models, and ongoing clinical trials using these approaches. We highlight advances in the use of nanoparticles applied to brain tumor imaging, tumor angiogenesis, neurodegeneration, grafted stem cells, and neuroprogenitor cells.

ABBREVIATIONS: amyloid beta = Aβ; NO = nitric oxide; NOS = nitric oxide synthase; PBCA = poly(*n*-butyl cyanoacrylate); QDots = quantum dots; SPIO = superparamagnetic iron oxide

Recent developments in nanotechnology have important implications for central nervous system imaging. These include pre- and intraoperative tumor imaging to facilitate accurate tumor characterization and resection, imaging of therapeutic stem cell delivery and viability in vivo, differentiation of pseudoprogression and pseudoresponse in antiangiogenic therapy for glioblastoma multiforme, detection of early stages of neurodegeneration, and advances in immunoimaging of the central nervous system. In this review, we will describe animal models, current and ongoing clinical trials, as well as future directions and implications for this exciting field.

GOLD NANOCAGES AND PHOTOACOUSTIC IMAGING

Gold nanocages are a novel class of optically tunable nanoparticles developed in the past decade.[1] These nanoparticles are highly porous, hollow, cube-shaped structures with edge length measurements between 30 and 200 nm.[2] Their surface plasmon resonance peaks can be tuned to have maximal optical absorption in the near-infrared spectrum. This spectrum is often referred to as the optical window of biologic tissues because in this spectrum, light attenuation by soft tissue and blood is low.[3] Gold nanoparticles have been actively investigated for their role as optical and photoacoustic imaging contrast agents.[4-7] The synthesis of gold nanocages and control of their surface plasmon resonance peaks has been reviewed.[8]

Photoacoustic tomography imaging is a hybrid technique that combines optical and sonographic imaging modalities and detects absorbed photons sonographically. This technique is based on the photoacoustic effect, in which energy absorption in the form of electromagnetic waves (optical and radio-frequency waves) can generate transient acoustic signals in a medium.[7] Optical and radio-frequency waves are the preferred waveforms used in photoacoustic imaging because they have more favorable properties, including deeper tissue penetration and higher absorption by contrast agents compared with other wave forms.[7] More important, photoacoustic tomography provides spatial-resolution imaging at depths 50 times greater than optical imaging alone.[2] Contrast agents such as gold nanocages can be tuned to have enhanced absorptive properties in the near-infrared region, which make them well-suited for photoacoustic imaging.[5,9]

Effective systemic delivery of nanoparticle contrast agents to interstitial tumor tissue relies on passive targeting through the enhanced permeability and retention effect.[10] Unique features of tumors that contribute to this passive targeting phenomenon are an increased microattenuation of vessels with widened gap junctions and deranged lymphatic drainage.[10] Intracellular delivery of nanoparticles can be achieved by linking to their surface antibodies or ligands (ie, albumin, transferrin, folate, lipoproteins, mannose, and others) to enable internalization by receptor-mediated endocytosis of the nanoparticle by specific targeted cells.[11]

Hollow gold nanospheres are effective photoacoustic contrast agents with the ability to depict brain blood vessels as small as 100 um in diameter.[5] Following a single dose in a mouse model, the nanospheres had distribution half-lives near

From the George Washington University School of Medicine and Health Sciences (G.S.), Washington, DC; Howard University School of Medicine (J.E.E.), Washington, DC; and Department of Radiology (L.M.L.), George Washington University Medical Center, Washington, DC.

Please address correspondence to Lucien M. Levy, MD, PhD, Professor of Radiology and Director of Neuroradiology, George Washington University Medical Center, 900 23rd St, NW, Washington, DC 20037; e-mail: llevy@mfa.gwu.edu

http://dx.doi.org/10.3174/ajnr.A3543

1.5 hours and elimination half-lives of nearly 71 hours and no evidence of systemic toxicity.

A novel application of photoacoustic imaging using gold nanocage contrast enhancement is accurate 3D imaging of brain tumors. Currently, a major limitation to gadolinium-based contrast imaging of brain tumors is the inaccurate margins encountered intraoperatively due to the disruption of the blood-brain barrier by surgery. Trimodal imaging by using MR imaging, Raman, and photoacoustic imaging by gold nanocage contrast enhancement provided highly accurate tumor description in a murine model, including delineation of the tumor parenchyma interface and microscopic tumor foci pre- and intraoperatively.[6]

These trimodal nanoparticles are composed of a 60-nm gold core, directly covered by a Raman active layer (trans-1.2[4-pyridyl]-ethylene). A 30-nm silica coating covers the Raman layer as a protective layer and maleimide–gadolinium-tetra-azacyclododecanetetra-acetic acid is linked to the silica layer. These nanoparticles accumulate in tumor via the enhanced permeability and retention effect preoperatively and are available as contrast for hours after the initial injection because of their long half-life. Because the contrast accumulates preferentially in tumor tissue and does not redistribute during surgical disruption of the blood-brain barrier, these contrast agents allow more precise tumor resection than resection with gadolinium-based contrast agents.[6]

EVALUATION AND VALIDATION OF ANTIANGIOGENIC THERAPY

Antiangiogenic therapy has broad applications in cancer therapy, and the angiogenesis inhibitor bevacizumab has been used in the treatment of recurrent glioblastoma.[12,13] Angiogenesis imaging is important to identify patients who would benefit from antiangiogenic therapies and to monitor treatment response. To date, there have been no well-validated radiologic markers to serve these purposes. Current assessment of tumor response via MR imaging is complicated by the "pseudoresponse" phenomenon, in which the treatment decreases the permeability of blood vessels giving the radiologic appearance of decreased enhancement on T1-weighted images, which may not reflect a true tumor response.[14,15]

Ferumoxytol is a superparamagnetic iron oxide (SPIO) nanoparticle that is approved for iron replacement therapy in patients with chronic kidney disease.[16] Ferumoxytol acts as a "blood pool" agent, indicating that it is confined to the vascular compartment for hours after administration and will not extravasate in the presence of a compromised blood-brain barrier. Ferumoxytol was recently investigated for its potential superiority to gadolinium to distinguish pseudoprogression from true tumor progression in patients with glioblastoma multiforme by comparing relative cerebral blood volume estimated from dynamic susceptibility-weighted contrast-enhanced MR imaging. Ferumoxytol was significantly more sensitive in detecting tumor progression and differentiating pseudoprogression compared with gadolinium (Fig 1).[17] There are several clinical trials currently evaluating the efficacy of ferumoxytol as an MR imaging contrast agent in evaluating brain malignancies (Table).

Other markers for targeted contrast agents include endothelial surface adhesion molecules whose over-expression is associated with vascular proliferation in tumor growth. The $\alpha_v\beta_3$ integrin is associated with neovascular proliferation and has been used as a target to monitor angiogenesis.[18-21] Optical imaging in the near-infrared window (650–900 nm) with a functionalized cyclic fluorophore was recently shown to target overexpressed integrin receptors, enabling near-infrared fluorescent imaging of tumor tissue and tumor margins in both murine and human glioblastoma models.[22] Because low-grade gliomas also express low levels of the $\alpha_v\beta_3$ integrin receptor, this functionalized cyclic fluorophore also has the potential to image low-grade gliomas.[23] Currently, a clinical trial in the recruitment phase is investigating the use of a functionalized cyclic fluorophore (IRDye800CW) conjugated to bevacizumab to determine its uptake and localization in breast tissue, surrounding healthy tissue, tumor margins, and lymph nodes.[24]

DETECTION OF NITRIC OXIDE

Nitric oxide is an inorganic gaseous molecule that is produced from L-arginine by nitric oxide (NO) synthase. NO has a number of physiologic functions related to neurotransmission and neovascularization and may contribute to neurotoxicity associated with tissue injury, apoptosis, and ischemia.[25,26] It is important in the generation of nitrotyrosine, which is implicated in the progression of Alzheimer disease and Parkinson disease.[27] As such, the detection of NO in biologic systems is an important area of research.

Classic methods used for detecting nitric oxide include spectroscopic and fluorescent dyes that rely on the reaction of NO with other molecules.[28] A central limitation of these detection methods is their inability to measure NO concentrations in 3D. Multidimensional in vivo NO monitoring has been achieved by using amperometric trimethylsilane conjugated platinum nanodisks.[29,30] This nanoscale sensor method was able to detect NO-producing neurons in a mouse model and was validated by immunohistochemistry (Fig 2). Although this method requires long acquisition times (~100 minutes) and is limited to surface scanning, it has the potential to correlate NO production and disease states for diagnostic purposes in humans.

Positron-emission tomography imaging of endotoxin-induced nitric oxide synthase activation in the lungs of healthy volunteers is currently under investigation.[31] In this investigation [^{18}F](±) nitric oxide synthase (NOS) is the radioactive drug that targets inducible nitric oxide synthase. Alternative investigations may seek to target the delivery of radioactive imaging agents such as [^{18}F](±)NOS to the CNS in patients who have Alzheimer disease, Parkinson disease, and other degenerative neurologic conditions in which nitric oxide is thought to play a central role in neural toxicity. Such an experiment could involve the delivery of agents such as [^{18}F](±)NOS in a vehicle such as poly(*n*-butyl cyanoacrylate) (PBCA) nanoparticles coated with the surfactant polysorbate 80 PBCA that would bypass the blood-brain barrier.

STEM CELL TRACKING WITH MR IMAGING

Regenerative therapy by using adult neuronal stem cells may have therapeutic potential in neurodegenerative,[32] ischemic,[33] and traumatic[34] brain injuries as well as systemic diseases such as diabetes.[35] Adult neurogenesis is restricted to the subgranular zone of the hippocampal dentate gyrus and to the subventricular zone

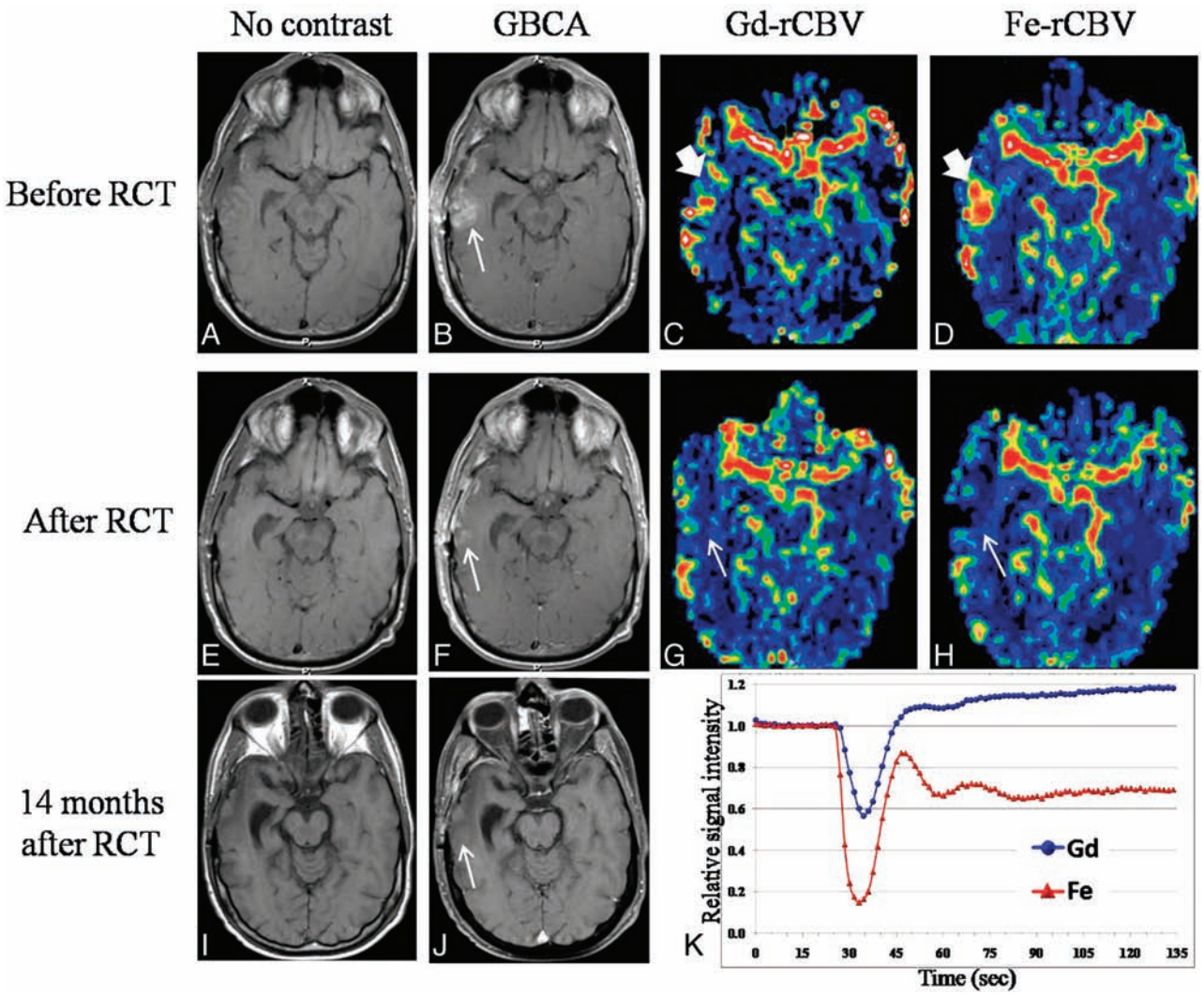

FIG 1. Dynamic susceptibility contrast MR imaging comparing gadoteridol and the iron oxide nanoparticle ferumoxytol in the evaluation of treatment response to standard radiochemotherapy for glioblastoma multiforme. RCT indicates regression after radiochemotherapy. T1-weighted MR imaging before (*A*, *E*, and *I*) and after (*B*, *F*, and *J*) gadoteridol (Gd) administration. *A* and *B*, MR imaging after surgery but before RCT demonstrates an area of enhancement in the right temporal lobe (*arrow*). Relative cerebral blood volume (rCBV) in the enhancing area was lower on the Gd-rCBV parametric map (*C*) compared with the ferumoxytol (Fe)-rCBV map (*D*) (*bold arrow*). *E* and *F*, MR imaging after completion of RCT revealed decreased enhancement (*F*, *arrow*) with low rCBV on Gd-rCBV (*G*) and Fe-rCBV parametric maps (*H*) (*arrow*). *I* and *J*, MR imaging 14 months after completion of RCT showed resolution of enhancement. *K*, First-pass time-intensity curves of the perfusions in *C* and *D* demonstrate postbolus increasing signal above the baseline when Gd was used, while ferumoxytol postbolus signal intensity is below the baseline and remains stable. Reprinted from *Intl Radiat Oncol Biol Phys*, Volume 79(2):514–23, Gahramanov S, Raslan AM, Muldoon LL. Potential for Differentiation of Pseudoprogression From True Tumor Progression With Dynamic Susceptibility-Weighted Contrast-Enhanced Magnetic Resonance Imaging Using Ferumoxytol vs. Gadoteridol: A Pilot Study. Copyright 2011, with permission from Elsevier.

adjacent to the lateral ventricles.[36] Current methods for neuronal regeneration include the use of scaffolds,[37] transcription factors,[38] or direct stem cell implantation.[39] Noninvasive in vivo imaging of these stem cell–based therapies is important to guide treatment as well as to evaluate the therapeutic effect in animal models and, eventually, patients.

MR imaging is well-suited for this goal and has been shown to be safe and effective in clinical trials tracking cells labeled with superparamagnetic iron oxide nanoparticles.[40] The SPIO nanoparticles are biocompatible and are degraded through the normal iron metabolism mechanisms in the body.[41] Clinical trials based on this approach include labeling and tracking of dendritic cells in immunotherapy of melanoma, autologous neural stem cells in traumatic head injury, bone marrow stem cells in chronic spinal cord injury, and cadaveric islet cells infused intraportally in the liver.[40]

The utility of SPIO nanoparticles for long-term in vivo cell tracking was investigated in allogeneic neural stem cell transplants performed in wild type (graft rejecting) BALb/c and immunodeficient (graft accepting) Rag2 mice.[42] SPIO-loaded neural stem cells were implanted in the corpus callosum of both sets of mice, and the progenitor cells were allowed to grow for 95 days while being monitored by MR imaging, immunohistochemistry, and bioluminescence.

The rate of MR signal decline defined 2 populations of cells. The early disappearance of the MR signal was associated with cell proliferation, thus diluting the amount of contrast per cell. The prolongation of the MR signal was associated with cell death and

Application of ferumoxytol as an MR imaging contrast agent in evaluating brain malignancies

Study Title	Phase	Clinical Trial Description
Imaging vascular properties of pediatric brain tumors using ferumoxytol and gadolinium in a single imaging session; an NCI-sponsored exploratory trial (code 7228) (NCT00978562)[73]	0	To assess the safety and effectiveness of ferumoxytol in improving the ability to image pediatric brain tumors
MRI using ferumoxytol in patients with primary brain cancer or brain metastases from lung or breast cancer; an NCI-sponsored multidisciplinary study (NCT00103038)[74]	2	Characterization of vascular properties of tumors in the CNS using ferumoxytol for dynamic-susceptibility contrast MRI to compare with those obtained using a gadolinium-based contrast agent for dynamic contrast-enhanced imaging in a single MR imaging session; imaging properties will be assessed longitudinally with up to 6 imaging sessions for 2 years
Magnetic resonance (MR) imaging study using ferumoxytol to assess early tumor response in patients with glioblastoma multiforme (code 7228) (NCT00660543)[75]	1	Evaluating the ability of ferumoxytol to assess effective early treatment response in glioblastoma multiforme using dynamic perfusion, BBB permeability measurement
Ferumoxytol and gadolinium magnetic resonance imaging (MRI) at 3T and 7T in patients with malignant brain tumors (NCT00659126)[76]	2	Comparing dynamic perfusion, BBB permeability measurement in 2 different magnetic fields (3T and 7T) in the evaluation of brain tumors; gadolinium and ferumoxytol will be used as contrast agents
Assessing dynamic magnetic resonance (MR) imaging in patients with recurrent high grade glioma receiving chemotherapy (code 7228) (NCT00769093)[77]	1	Evaluation of imaging changes induced by bevacizumab with dexamethasone in patients with high-grade glioma
MR, histologic and EM imaging of intravenous ferumoxytol in central nervous system (CNS) inflammation (NCT00659776)[78]	2	Evaluation of the safety and efficacy of ferumoxytol

phagocytic contrast retention. The authors of the study note that this finding was unexpected and may be related to the cell line used or the method of stem cell implantation (eg, direct implantation into the parenchyma or via the CSF). Thus, although short-term in vivo SPIO-labeled cell imaging is considered accurate, the long-term accuracy of SPIO-labeled cell imaging is complex and the authors of this study suggested that it be used only if the viability of the implanted cells is known.

A clinical trial pilot study is currently under investigation to assess the utility of MR imaging in tracking intravenously delivered SPIO-labeled stem cells in healthy human volunteers for periods of up to 1 week.[43]

NONINVASIVE DETECTION OF NEURAL PROGENITOR CELLS IN LIVING BRAINS BY MR IMAGING

Pericytes are a source of adult multipotent progenitor cells[44] located in the central nervous system between the inner and outer vascular basement membrane of CNS capillaries, and they function in the regulation of brain capillary blood flow, angiogenesis, and blood-brain barrier maintenance.[45-47] Recently, noninvasive imaging of neural progenitor cells during angiogenesis was demonstrated in a bilateral carotid artery occlusion murine model by using gene transcript–targeted MR imaging contrast agents. In this ischemic brain injury model, SPIO nanoparticles, modified with micro DNA targeting actin and nestin messenger ribonucleic acid (the latter uniquely expressed by pericytes), were administered to mice after bilateral carotid artery occlusion to image vessel formation by the detection of cerebral pericytes.[48] The dual gene transcript–targeted MR imaging successfully identified pericytes in living brains. Angiogenesis is dysregulated in several disease states including Alzheimer disease[49] and diabetes mellitus,[50] and the ability to image CNS pericyte activity in vivo may allow real-time longitudinal monitoring of angiogenesis in these disease states.

ENHANCED BRAIN DELIVERY OF BLOOD-BRAIN BARRIER IMPERMEABLE PROBES FOR OPTICAL AND MR IMAGING

Polymeric nanoparticles describe both nanospheres and nanocapsules. These are sphere-like structures composed of biodegradable polymers, and they contain a payload delivery confined to a central cavity[51] or dispersed within a matrix, respectively (Fig 3).[52] Nanoparticles composed of poly(*n*-butyl cyanoacrylate) coated with the surfactant polysorbate 80 can bypass the BBB by binding to *apolipoprotein E* followed by adhesion and receptor-mediated transcytosis via the low-attenuation lipoprotein receptor present on BBB endothelial cells.[53,54] This phenomenon has the potential to allow in vivo molecular imaging. Studies describing nanocarriers traversing the BBB have, in large part, relied on postmortem analysis; however, recently the delivery of BBB impermeable molecular imaging contrast agents for in vivo microscopy and MR imaging has been performed.[55] In this study, the delivery of a series of compounds known not to cross the BBB in their native state, including a DNA-binding dye bisBenzimide used to monitor neuronal nuclei; Texas red dextran, a targeted probe for imaging lesions characteristic of Alzheimer disease; and tryptan blue, a plaque-binding red fluorescing diazo dye, were delivered intravenously as 2 formulations: native species and encapsulated in polysorbate 80–coated PBCA nanoparticles. Each compound was found to traverse the BBB when encapsulated in polysorbate 80–coated PBCA nanoparticles and was found not to traverse the BBB when delivered in native form. Furthermore, the delivery of gadolinium-based MR imaging contrast agents

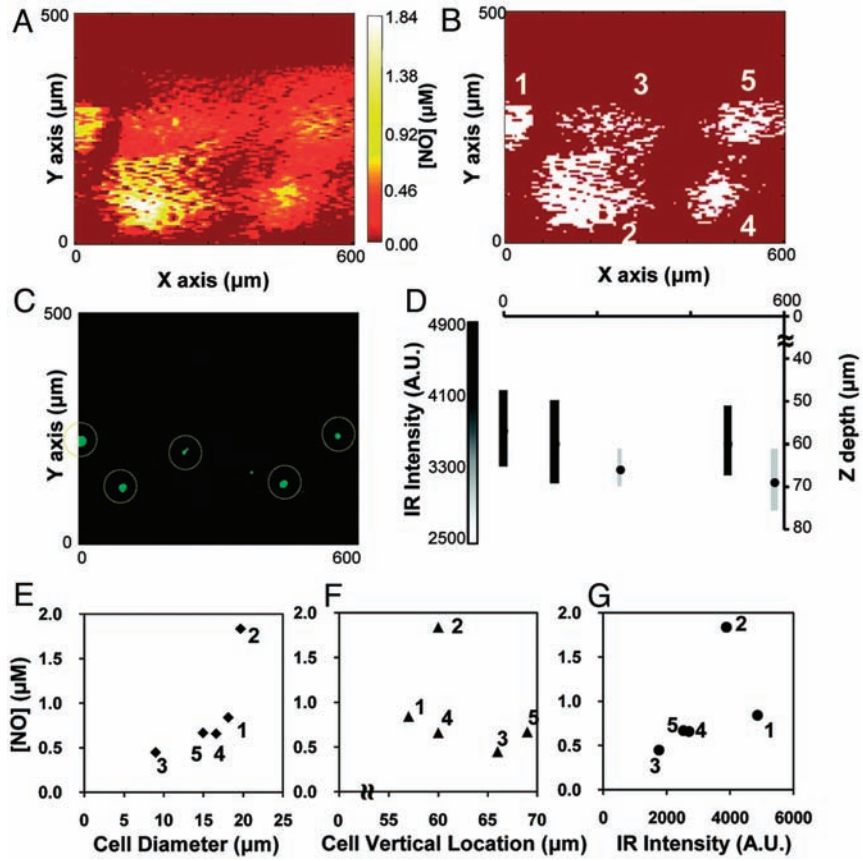

FIG 2. Real-time in vivo nitric oxide imaging with corresponding immunohistochemical analysis of neuronal NO synthase immunoreactive (nNOS-IR) cells. In vivo NO measurements and immunohistochemical analysis of nNOS-IR cells. *A*, A NO concentration image acquired over the cortical surface of a 600 × 500 μm^2 region. Higher NO concentrations are shown in lighter color, whereas lower NO concentrations are shown as a darker red. *B*, A thresholded image of *A*. The highest 10% NO concentrations of the entire concentration range are illustrated in white, whereas the other lower concentrations are in red. There are 5 distinct sections with high NO concentrations (labeled 1–5). *C*, A confocal microscopy image of nNOS-IR cells. The locations of yellow-circled cells are well-matched with the sites exhibiting relatively high NO concentrations in *A*. *D*, Five distinct nNOS-IR cells are plotted on the basis of the location information in the x- and z-axes. Each gray-scaled bar represents a corresponding single nNOS-IR cell. The color of each bar reflects the intensity of immunoreactivity (ie, darker color indicates strong immunoreactivity). The highest NO concentration measured in each section (labeled 1–5) is plotted as a function of *E*, the corresponding nNOS- IR cell size; the vertical cell location (depth) (*F*); and the immunoreactivity intensity of the cell (*G*) in the confocal image. *E–G*, The NO concentration means the highest NO level within each localized site. The NOS-IR cell size means the largest diameter of each cell observed in the confocal image. The cell location in depth means the vertical distance from the cortical upper surface to the cell center position. The inversion recovery intensity means the highest fluorescence intensity measured by confocal microscopy within each cell. Reprinted with permission from Jo A, Do H, Jhon GJ, et al. Electrochemical nanosensor for real-time direct imaging of nitric oxide in living brain. *Anal Chem* 83:8314-19. Copyright 2011, American Chemical Society.

encapsulated in polysorbate 80–coated PBCA nanoparticles enhanced brain delivery of the contrast agent several hundred-fold compared with delivery of free gadolinium, indicating the future possibility of targeted MR imaging contrast agents into the brain.

NANOBODIES

Nanobodies are a class of antibodies initially discovered in serum of the camel species *Camelus dromedarius*. They consist of heavy chains only and have desirable features such as small size, decreased immunogenicity, and high binding affinities.[56] Nanobodies have been designed for use in cancer therapy,[57,58] antivenoms,[59] inflammatory conditions,[60] and immunoimaging.[60-64] Nanobodies can detect vascular and parenchymal amyloid beta (Aβ) deposits in vivo to differentiate cerebral β-amyloid indicative of Alzheimer disease and vascular Aβ plaques associated with cerebral amyloid angiopathy.[65]

With the transgenic Alzheimer Disease Cerebral Amyloid Angiopathy (AD/CAA) mouse model, 2 distinct Aβ targeting nanobodies, ni3A and pa2H, were administered to evaluate their ability in vivo to differentially detect vascular or parenchymal amyloid-β deposits and their ability to cross the blood-brain barrier. In vivo specificity for Aβ was evaluated in this mouse model by direct topical application or intracarotid coinjection with mannitol with a fluorescently labeled nanobody. The in vivo murine models showed that both ni3A and pa2H had affinity for parenchymal and vascular deposits. However, in vitro topical applications to human brain tissue of patients with AD/CAA showed ni3A to specifically target only vascular Aβ.

Although there are specific active transport mechanisms known to be involved in the transport of nanobodies across the blood-brain barrier,[66] the nanobodies in this study were observed to have a limited ability to cross the BBB. Limited in vivo BBB passage was postulated by the authors to be due to low concentrations of nanobodies, low circulation time, or possibly a paucity of active transport receptors involved in BBB transport in this mouse model.[65] Future methods, such as nanobodies encapsulated in polysorbate 80–coated PBCA nanoparticles, could be used to increase in vivo BBB passage.

QUANTUM DOTS

Quantum dots (QDots) are 10- to 20-nm nanoparticles that consist of semiconductor material surrounded by a polymer shell. The polymer shell can then be functionalized; this process allows the linking of any number of biologically relevant molecules (oligopeptides, antibodies, and so forth) to the surface. These functionalized quantum dots have had applications in cellular imaging,[67,68] protein detection,[69] and cancer immunology.[70] Because of their unique charge-carrying abilities, QDots possess molar extinction coefficients 10–50 times greater than typical organic dyes and are also up to 20 times brighter.[71] Additionally QDots have decreased rates of photobleaching, which lends them to being well-suited for biologic imaging.

By varying the semiconductor material contained within quantum dot nanoparticles, one can manipulate the wavelength

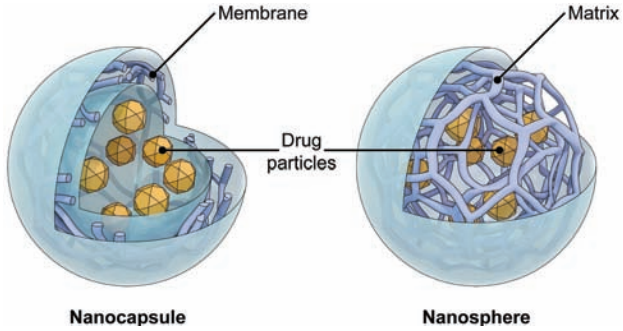

FIG 3. Schematic representation of the structure of a nanocapsule and a nanosphere. This research was supported by the Intramural Research Program of the National Institute of Neurologic Disorders and Stroke at the National Institutes of Health. The image is in the public domain and credited to the National Institutes of Health/Department of Health and Human Services.

that is emitted on excitation to skew emissions to the near-infrared portion of the electromagnetic spectrum. This region is optimal for deep-tissue imaging due to the optical characteristics of biologic tissue.[3]

Recently, a quantum dot fluorescent probe designed to target the epidermal growth factor receptor was evaluated for its ability to differentiate tumor cells from normal brain parenchyma in tumor biopsies of low-grade glioma.[72] In this study, quantum dots were conjugated to epidermal growth factor as well as monoclonal antibodies directed against the epidermal growth factor receptor and were evaluated for their ability to differentiate normal brain parenchyma from human glioma ex vivo (Fig 4). Tumor cells could be visualized from the macroscopic level, and this result indicated that quantum dot–targeted fluorescent probes could be used intraoperatively to assist in discerning tumor tissue from normal parenchyma in the resection of low-grade gliomas.

CONCLUSIONS

Nanotechnology is an exciting and burgeoning field that will greatly impact medical diagnostics and therapeutics across many medical specialties in the coming age of personalized and targeted medicine. These impacts will likely be seen in areas of stem cell therapy, immunoimaging and immunotherapy, enhanced pre- and intraoperative brain tumor characterization, and targeted payload delivery to the CNS.

The clinical development of neural stem cell therapies will require accurate tracking of their in vivo location and viability. SPIOs appear well-suited for this need. The delivery and monitoring of therapeutic stem cells is likely to play an important role for interventional and diagnostic radiologists in the treatment of autoimmune and degenerative diseases, including diabetes, multiple sclerosis, Parkinson disease, Alzheimer disease, amyotrophic lateral sclerosis, and spinal muscle atrophy.

Nanobodies are less immunogenic than monoclonal antibodies, are easy to produce, and can cross the BBB by their own unique mechanisms, opening up numerous opportunities for immunoimaging of the CNS and expanding the role of radiologists in molecular-based diagnostics of the CNS.

The pre- and intraoperative imaging of brain tumors with multifunctional nanoparticles combining photoacoustic, Raman, and MR imaging and/or QDots may facilitate more accurate tumor characterization and resection. Furthermore, ferumoxytol, a blood pool agent, has shown great potential in distinguishing pseudoprogression and pseudoresponse from true tumor progression and true treatment response in glioblastoma.

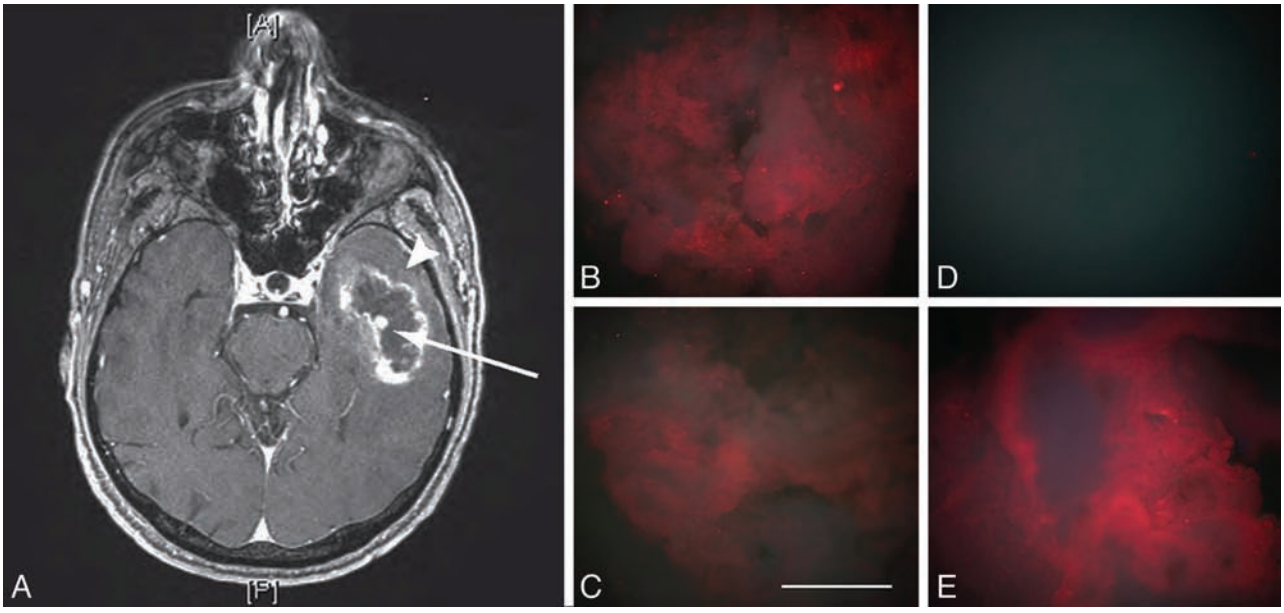

FIG 4. MR imaging and quantum dot (QD)-probe digital macroimages from glioblastoma multiforme, grade IV biopsy. Example of QD targeted to epidermal growth factor receptor (EGFR) to discriminate tumor tissue from normal parenchyma at the margin of a resected glioblastoma multiforme. *A*, T1-weighted MR axial image shows gadolinium-positive signal. *B–E*, Digital macrophotographic images of ex vivo stained biopsies from the resected tumor and adjacent brain tissue stained with targeted QD probes obtained with the same magnification and the same exposure times. *B*, Tumor tissue 625QDStAv-biotin-MAb528 EGFR staining. *C*, 625QDGAMIG-MAb 199.12 EGFR staining. *D*, Adjacent brain 625QDStAv-biotin-MAb528 EGFR staining. *E*, Invading tumor tissue, 625QDStAv-biotin-MAb528 EGFR staining. Excitation, 365 nm; emission, >450 mm; objective, 5X numeric aperture 0.15; bar 1 mm. Note that *D* serves as the control for *B* (ie, stained with the same probes under identical conditions). (Copyright © 2010 Kantelhardt al.[72])

The ability to accurately bypass the BBB with PBCA nanoparticles coated with polysorbate 80 and to deliver a payload such as a contrast agent or drug is no doubt an important and unique feature of nanobased applications that yields myriad possibilities for future treatment and imaging of the CNS.

REFERENCES

1. Sun Y, Xia Y. **Shape-controlled synthesis of gold and silver nanoparticles.** *Science* 2002;298:2176–79
2. Li W, Brown PK, Wang LV, et al. **Gold nanocages as contrast agents for photoacoustic imaging.** *Contrast Media Mol Imaging* 2011;6:370–77
3. Weissleder R. **A clearer vision for in vivo imaging.** *Nat Biotechnol* 2001;19:316–17
4. Chen J, Saeki F, Wiley BJ, et al. **Gold nanocages: bioconjugation and their potential use as optical imaging contrast agents.** *Nano Lett* 2005;5:473–77
5. Lu W, Huang Q, Ku G, et al. **Photoacoustic imaging of living mouse brain vasculature using hollow gold nanospheres.** *Biomaterials* 2010;31:2617–26
6. Kircher MF, de la Zerda A, Jokerst JV, et al. **A brain tumor molecular imaging strategy using a new triple-modality MRI-photoacoustic-Raman nanoparticle.** *Nat Med* 2012;18:829–34
7. Zhang Y, Hong H, Cai W. **Photoacoustic imaging.** *Cold Spring Harb Protoc* 2011:pbd.top065508
8. Hu M, Chen J, Li ZY, et al. **Gold nanostructures: engineering their plasmonic properties for biomedical applications.** *Chem Soc Rev* 2006;35:1084–94
9. Yang X, Skrabalak SE, Li ZY, et al. **Photoacoustic tomography of a rat cerebral cortex in vivo with au nanocages as an optical contrast agent.** *Nano Lett* 2007;7:3798–802
10. Maeda H, Fang J, Inutsuka T, et al. **Vascular permeability enhancement in solid tumor: various factors, mechanisms involved and its implications.** *Int Immunopharmacol* 2003;3:319–28
11. Peer DK, Hong S, Farokhzad OC, et al. **Nanocarriers as an emerging platform for cancer therapy.** *Nat Nanotechnol* 2007;2:751–60
12. Gerstner ER, Batchelor TT. **Antiangiogenic therapy for glioblastoma.** *Cancer J* 2012;18:45–50
13. Sorensen AG, Emblem KE, Polaskova P, et al. **Increased survival of glioblastoma patients who respond to antiangiogenic therapy with elevated blood perfusion.** *Cancer Res* 2012;72:402–07
14. Clarke JL, Chang S. **Pseudoprogression and pseudoresponse: challenges in brain tumor imaging.** *Curr Neurol Neurosci Rep* 2009;9:241–46
15. Pope WB, Young JR, Ellingson BM. **Advances in MRI assessment of gliomas and response to anti-VEGF therapy.** *Curr Neurol Neurosci Rep* 2011;11:336–44
16. Lu M, Cohen MH, Rieves D, et al. **FDA report: ferumoxytol for intravenous iron therapy in adult patients with chronic kidney disease.** *Am J Hematol* 2010;85:315–19
17. Gahramanov S, Raslan AM, Muldoon LL, et al. **Potential for differentiation of pseudoprogression from true tumor progression with dynamic susceptibility-weighted contrast-enhanced magnetic resonance imaging using ferumoxytol vs. gadoteridol: a pilot study.** *Int J Radiat Oncol Biol Phys* 2011;79:514–23
18. Shattil SJ. **Function and regulation of the beta 3 integrins in hemostasis and vascular biology.** *Thromb Haemost* 1995;74:149–55
19. De S, Razorenova O, McCabe NP, et al. **VEGF-integrin interplay controls tumor growth and vascularization.** *Proc Natl Acad Sci U S A* 2005;102:7589–94
20. Varner JA, Cheresh DA. **Tumor angiogenesis and the role of vascular cell integrin alphavbeta3.** *Important Adv Oncol* 1996;69–87
21. Folkman J. **Angiogenesis in cancer, vascular, rheumatoid and other diseases.** *Nat Med* 1995;1:27–31
22. Huang R, Vider J, Kovar JL, et al. **Integrin alphavbeta3-targeted IRDye 800CW near-infrared imaging of glioblastoma.** *Clin Cancer Res* 2012;18:5731–40
23. Schnell O, Krebs B, Wagner E, et al. **Expression of integrin alphavbeta3 in gliomas correlates with tumor grade and is not restricted to tumor vasculature.** *Brain Pathol* 2008;18:378–86
24. Groningen UMC. VEGF-targeted Fluorescent Tracer Imaging in Breast Cancer. http://clinicaltrials.gov/ct2/show/record/NCT01508572. Accessed November 8, 2012
25. Vincent SR. **Nitric oxide neurons and neurotransmission.** *Prog Neurobiol* 2010;90:246–55
26. Calabrese V, Mancuso C, Calvani M, et al. **Nitric oxide in the central nervous system: neuroprotection versus neurotoxicity.** *Nat Rev Neurosci* 2007;8:766–75
27. Garthwaite J, Boulton CL. **Nitric oxide signaling in the central nervous system.** *Annu Rev Physiol* 1995;57:683–706
28. Hong H, Sun J, Cai W. **Multimodality imaging of nitric oxide and nitric oxide synthases.** *Free Radic Biol Med* 2009;47:684–98
29. Jo A, Do H, Jhon GJ, et al. **Electrochemical nanosensor for real-time direct imaging of nitric oxide in living brain.** *Anal Chem* 2011;83:8314–19
30. Shim JH, Lee Y. **Amperometric nitric oxide microsensor based on nanopore-platinized platinum: the application for imaging NO concentrations.** *Anal Chem* 2009;81:8571–76
31. Medicine WUSo. PET imaging of endotoxin-induced iNOS activation. http://clinicaltrials.gov/ct2/show/NCT01407796. Accessed November 18, 2012
32. Borlongan CV. **Recent preclinical evidence advancing cell therapy for Alzheimer's disease.** *Exp Neurol* 2012;237:142–46
33. Song M, Mohamad O, Gu X, et al. **Restoration of intracortical and thalamocortical circuits after transplantation of bone marrow mesenchymal stem cells into the ischemic brain of mice.** *Cell Transplant* 2013;22:2001–15
34. Ugoya SO, Tu J. **Bench to bedside of neural stem cell in traumatic brain injury.** *Stem Cells Int* 2012;2012:141624
35. Kuwabara T, Asashima M. **Regenerative medicine using adult neural stem cells: the potential for diabetes therapy and other pharmaceutical applications.** *J Mol Cell Biol* 2012;4:133–39
36. Gage FH, Ray J, Fisher LJ. **Isolation, characterization, and use of stem cells from the CNS.** *Annu Rev Neurosci* 1995;18:159–92
37. Migliorini E, Grenci G, Ban J, et al. **Acceleration of neuronal precursors differentiation induced by substrate nanotopography.** *Biotechnol Bioeng* 2011;108:2736–46
38. Liu H, Zhang SC. **Specification of neuronal and glial subtypes from human pluripotent stem cells.** *Cell Mol Life Sci* 2011;68:3995–4008
39. Schwarz SC, Schwarz J. **Translation of stem cell therapy for neurological diseases.** *Transl Res* 2010;156:155–60
40. Bulte JW. **In vivo MRI cell tracking: clinical studies.** *AJR Am J Roentgenol* 2009;193:314–25
41. Ferrucci JT, Stark DD. **Iron oxide-enhanced MR imaging of the liver and spleen: review of the first 5 years.** *AJR Am J Roentgenol* 1990;155:943–50
42. Berman SC, Galpoththawela C, Gilad AA, et al. **Long-term MR cell tracking of neural stem cells grafted in immunocompetent versus immunodeficient mice reveals distinct differences in contrast between live and dead cells.** *Magn Reson Med* 2011;65:564–74
43. University of Edinburgh. Cell tracking using superparamagnetic particles of iron oxide (SPIO) and magnetic resonance imaging (MRI): a pilot study. http://www.clinicaltrials.gov/ct2/show/NCT00972946. Accessed November 18, 2012
44. Dore-Duffy P, Katychev A, Wang X, et al. **CNS microvascular pericytes exhibit multipotential stem cell activity.** *J Cereb Blood Flow Metab* 2006;26:613–24
45. Rodriguez-Baeza A, Reina-De La Torre F, Ortega-Sanchez M, et al. **Perivascular structures in corrosion casts of the human central nervous system: a confocal laser and scanning electron microscope study.** *Anat Rec* 1998;252:176–84
46. Itoh Y, Suzuki N. **Control of brain capillary blood flow.** *J Cereb Blood Flow Metab* 2012;32:1167–76
47. Bergers G, Song S. **The role of pericytes in blood-vessel formation and maintenance.** *Neuro Oncol* 2005;7:452–64

48. Liu CH, Ren JQ, You Z, et al. **Noninvasive detection of neural progenitor cells in living brains by MRI.** *FASEB J* 2012;26:1652–62
49. Kalaria RN, Cohen DL, Premkumar DR, et al. **Vascular endothelial growth factor in Alzheimer's disease and experimental cerebral ischemia.** *Brain Res Mol Brain Res* 1998;62:101–05
50. Zhu M, Bi X, Jia Q, et al. **The possible mechanism for impaired angiogenesis after transient focal ischemia in type 2 diabetic GK rats: different expressions of angiostatin and vascular endothelial growth factor.** *Biomed Pharmacother* 2010;64:208–13
51. Leary SP, Liu CY, Apuzzo ML. **Toward the emergence of nanoneurosurgery. Part III. Nanomedicine: targeted nanotherapy, nanosurgery, and progress toward the realization of nanoneurosurgery.** *Neurosurgery* 2006;58:1009–26, discussion 1026
52. Pinto Reis C, Neufeld RJ, Ribeiro AJ, et al. **Nanoencapsulation I. Methods for preparation of drug-loaded polymeric nanoparticles.** *Nanomedicine* 2006;2:8–21
53. Steiniger SC, Kreuter J, Khalansky AS, et al. **Chemotherapy of glioblastoma in rats using doxorubicin-loaded nanoparticles.** *Int J Cancer* 2004;109:759–67
54. Hasadsri L, Kreuter J, Hattori H, et al. **Functional protein delivery into neurons using polymeric nanoparticles.** *J Biol Chem* 2009;284:6972–81
55. Koffie RM, Farrar CT, Saidi LJ, et al. **Nanoparticles enhance brain delivery of blood-brain barrier-impermeable probes for in vivo optical and magnetic resonance imaging.** *Proc Natl Acad Sci U S A* 2011;108:18837–42
56. Hamers-Casterman C, Atarhouch T, Muyldermans S, et al. **Naturally occurring antibodies devoid of light chains.** *Nature* 1993;363:446–48
57. Tijink BM, Laeremans T, Budde M, et al. **Improved tumor targeting of anti-epidermal growth factor receptor nanobodies through albumin binding: taking advantage of modular nanobody technology.** *Mol Cancer Ther* 2008;7:2288–97
58. Roovers RC, Vosjan MJ, Laeremans T, et al. **A biparatopic anti-EGFR nanobody efficiently inhibits solid tumour growth.** *Int J Cancer* 2011;129:2013–24
59. Hmila I, Saerens D, Ben Abderrazek R, et al. **A bispecific nanobody to provide full protection against lethal scorpion envenoming.** *FASEB J* 2010;24:3479–89
60. Coppieters K, Dreier T, Silence K, et al. **Formatted anti-tumor necrosis factor alpha VHH proteins derived from camelids show superior potency and targeting to inflamed joints in a murine model of collagen-induced arthritis.** *Arthritis Rheum* 2006;54:1856–66
61. Devoogdt N, Xavier C, Hernot S, et al. **Molecular imaging using nanobodies: a case study.** *Methods Mol Biol* 2012;911:559–67
62. Vaneycken I, D'Huyvetter M, Hernot S, et al. **Immuno-imaging using nanobodies.** *Curr Opin Biotechnol* 2011;22:877–81
63. Vaneycken I, Devoogdt N, Van Gassen N, et al. **Preclinical screening of anti-HER2 nanobodies for molecular imaging of breast cancer.** *FASEB J* 2011;25:2433–46
64. Schoonooghe S, Laoui D, Van Ginderachter JA, et al. **Novel applications of nanobodies for in vivo bio-imaging of inflamed tissues in inflammatory diseases and cancer.** *Immunobiology* 2012;217:1266–72
65. Nabuurs RJ, Rutgers KS, Welling MM, et al. **In vivo detection of amyloid-beta deposits using heavy chain antibody fragments in a transgenic mouse model for Alzheimer's disease.** *PLoS One* 2012;7:e38284
66. Rutgers KS, Nabuurs RJ, van den Berg SA, et al. **Transmigration of beta amyloid specific heavy chain antibody fragments across the in vitro blood-brain barrier.** *Neuroscience* 2011;190:37–42
67. Pathak S, Choi SK, Arnheim N, et al. **Hydroxylated quantum dots as luminescent probes for in situ hybridization.** *J Am Chem Soc* 2001;123:4103–04
68. Bruchez M Jr, Moronne M, Gin P, et al. **Semiconductor nanocrystals as fluorescent biological labels.** *Science* 1998;281:2013–16
69. Sukhanova A, Devy J, Venteo L, et al. **Biocompatible fluorescent nanocrystals for immunolabeling of membrane proteins and cells.** *Anal Biochem* 2004;324:60–67
70. Sun W, Subrahmanyam PB, East JE, et al. **Connecting the dots: artificial antigen presenting cell-mediated modulation of natural killer T cells.** *J Interferon Cytokine Res* 2012;32:505–16
71. Smith AM, Dave S, Nie S, et al. **Multicolor quantum dots for molecular diagnostics of cancer.** *Expert Rev Mol Diagn* 2006;6:231–44
72. Kantelhardt SR, Caarls W, de Vries AH, et al. **Specific visualization of glioma cells in living low-grade tumor tissue.** *PLoS One* 2010;5:e11323
73. OHSU Knight Cancer Institute. Imaging vascular properties of pediatric brain tumors using ferumoxytol and gadolinium in a single imaging session. http://www.clinicaltrials.gov/ct2/show/NCT00978562, Accessed November 18, 2012
74. OHSU Knight Cancer Institute. MRI using ferumoxytol in patients with primary brain cancer or brain metastases from lung or breast cancer. http://clinicaltrials.gov/ct2/show/NCT00103038. Accessed November 18, 2012
75. OHSU Knight Cancer Institute. Magnetic resonance (MR) imaging study using ferumoxytol to assess early tumor response in patients with glioblastoma multiforme. http://clinicaltrials.gov/show/NCT00660543. Accessed November 18, 2012
76. OHSU Knight Cancer Institute. Ferumoxytol and gadolinium magnetic resonance imaging (MRI) at 3T and 7T in patients with malignant brain tumors. http://clinicaltrials.gov/ct2/show/NCT00659126. Accessed November 18, 2012
77. OHSU Knight Cancer Institute. Assessing dynamic magnetic resonance (MR) imaging in patients with recurrent high grade glioma receiving chemotherapy (code 7228). http://clinicaltrials.gov/ct2/show/NCT00769093. Accessed November 18, 2012
78. Oregon Health and Science University NIoNDaSN. MR, histologic and EM imaging of intravenous ferumoxytol in central nervous system (CNS) inflammation. http://clinicaltrials.gov/ct2/show/NCT00659776. Accessed November 18, 2012

High WSS or Low WSS? Complex Interactions of Hemodynamics with Intracranial Aneurysm Initiation, Growth, and Rupture: Toward a Unifying Hypothesis

H. Meng, V.M. Tutino, J. Xiang, and A. Siddiqui

ABSTRACT

SUMMARY: Increasing detection of unruptured intracranial aneurysms, catastrophic outcomes from subarachnoid hemorrhage, and risks and cost of treatment necessitate defining objective predictive parameters of aneurysm rupture risk. Image-based computational fluid dynamics models have suggested associations between hemodynamics and intracranial aneurysm rupture, albeit with conflicting findings regarding wall shear stress. We propose that the "high-versus-low wall shear stress" controversy is a manifestation of the complexity of aneurysm pathophysiology, and both high and low wall shear stress can drive intracranial aneurysm growth and rupture. Low wall shear stress and high oscillatory shear index trigger an inflammatory-cell-mediated pathway, which could be associated with the growth and rupture of large, atherosclerotic aneurysm phenotypes, while high wall shear stress combined with a positive wall shear stress gradient trigger a mural-cell-mediated pathway, which could be associated with the growth and rupture of small or secondary bleb aneurysm phenotypes. This hypothesis correlates disparate intracranial aneurysm pathophysiology with the results of computational fluid dynamics in search of more reliable risk predictors.

ABBREVIATIONS: CFD = computational fluid dynamics; ECM = extracellular matrix; WSS = wall shear stress

Intracranial aneurysms are pathologic outpouchings of the arterial walls. An estimated 5%–8% of the general population harbors intracranial aneurysms,[1] though the exact prevalence is unknown because most are asymptomatic. Aneurysm rupture is the most common cause of nontraumatic subarachnoid hemorrhage, a devastating event that carries high rates of mortality, morbidity, and disability, as well as high health care costs. Despite significant improvement in the clinical care of patients with subarachnoid hemorrhage, one-quarter still die, while roughly half of the survivors live with persistent neurologic deficits.[2] The estimated annual cost for hospitalized patients with unruptured intracranial aneurysms in the United States is $522,500,000, and $1,755,600,000 for patients with subarachnoid hemorrhage.[3] Recent advancements and increased use of neurovascular imaging have augmented detection of asymptomatic unruptured intracranial aneurysms, amplifying pressure on clinicians to decide which unruptured aneurysms to treat. This decision is not taken lightly because an overwhelming majority of intracranial aneurysms will not rupture,[1] while both endovascular and microsurgical treatments carry the risk of associated morbidity and mortality. Consequently, there is a real need for objective aneurysm rupture risk assessments that could reliably predict those at highest risk and subsequently select only them for intervention.

To this end, investigators have tried to identify aneurysmal characteristics that are associated with intracranial aneurysm growth and rupture. Hemodynamics is one of most widely accepted factors contributing to aneurysm pathophysiology, playing a fundamental role in the mechanisms of initiation, growth, and rupture.[4-9] Recent studies using image-based computational fluid dynamics (CFD) modeling and statistical analyses have identified connections between the hemodynamic properties of intracranial aneurysms and the likelihood of their growth and rupture.[5,9] Such findings have highlighted the exciting possibility that aneurysmal hemodynamics may provide objective metrics to improve rupture risk stratification.

The "High-versus-Low WSS" Controversy

A number of engineering and computational researchers have published CFD studies associating specific hemodynamic parameters with intracranial aneurysm growth and rupture.[5,7-14] While

From the Toshiba Stroke and Vascular Research Center (H.M., V.M.T., J.X., A.S.) and Departments of Mechanical and Aerospace Engineering (H.M.), Neurosurgery (H.M., J.X., A.S.), and Biomedical Engineering (H.M., V.M.T.), University at Buffalo, State University of New York, Buffalo, New York.

This work was supported by grants to H.M. from the National Institutes of Health (R01NS064592) and Toshiba Medical Systems.

Please address correspondence to Hui Meng, PhD, Toshiba Stroke and Vascular Research Center, University at Buffalo, Clinical and Translational Research Center, 875 Ellicott St, Buffalo, NY 14203; e-mail: huimeng@buffalo.edu

http://dx.doi.org/10.3174/ajnr.A3558

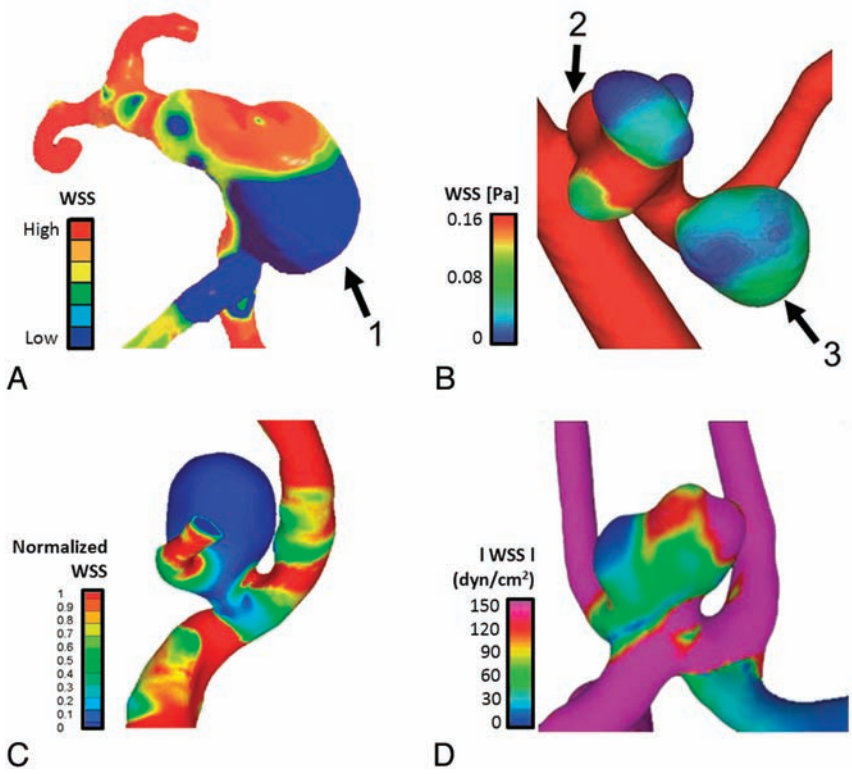

FIG 1. Examples of aneurysm growth (*A* and *B*) and rupture (*C* and *D*) correlated with high wall shear stress and low WSS. *A*, In a serial study consisting of a baseline and 4 follow-ups, Acevedo-Bolton et al[10] found that the maximal growth region (1) of a giant basilar fusiform intracranial aneurysm consistently had the lowest WSS. *B*, Sugiyama et al[13] reported 2 adjacent growing aneurysms, with different hemodynamic characteristics and growing patterns in 1 patient. The proximal growing aneurysm (2) was subjected to local high flow in the growing lobe, while the distal aneurysm (3) was associated with low and oscillatory WSS in the entire aneurysm sac. *C*, From multivariate statistical analysis of 119 aneurysms, Xiang et al[5] found that intracranial aneurysm rupture could be predicted by low WSS and high oscillatory shear index. *D*, Castro et al[11] found, from analysis of 26 aneurysms, that intracranial aneurysm rupture was correlated with high maximum WSS. Images were adapted with permission from the cited references.

clinicians welcome such effort, the growing number of proposed parameters remains inconsistent and confusing.[15-17] The most highlighted and controversial parameter has been wall shear stress (WSS), the frictional force exerted by the flowing blood tangentially on the vessel lumen. Both high and low aneurysmal WSS have been separately correlated with intracranial aneurysm growth and rupture.[16] This controversy is highlighted by findings presented in Fig 1.

Presently, it is unclear whether the "high-versus-low WSS" controversy stems purely from study limitations, such as skewness due to small sample sizes, inconsistent parameter definitions, flawed experimental design, variability in assumptions and compromises in CFD, or from the inherent complexity and heterogeneity of intracranial aneurysm growth and rupture mechanisms.[16,17] How high WSS and low WSS might be involved in aneurysm development remains unclear because the biologic mechanisms underlying growth and rupture and their interaction with hemodynamics have not been clearly elucidated. In this review, we provide a novel view of aneurysm development and a unified hypothesis regarding the mechanistic role of both high and low WSS in intracranial aneurysm growth and rupture.

Relationship between Hemodynamics and Aneurysm Development

Aneurysm Development Is a 3-Way Interactive Process Driven by Hemodynamics. In clinical practice, aneurysmal geometry (especially size and aspect ratio) has been the principal parameter used to gauge the rupture likelihood of intracranial aneurysms.[18] However, hemodynamics provides mechanical triggers that are transduced into biologic signals leading to this geometric evolution. Aneurysmal geometry and hemodynamics are mutually causal: Geometry instantaneously determines flow conditions, while flow drives aneurysm remodeling/growth through pathobiology, thereby determining future geometry (ie, enlargement and shape change). As this process continues, an intracranial aneurysm will either grow until homeostasis (stability) is reached or until its wall strength can no longer withstand the hemodynamic stress, in which case rupture occurs. This is best illuminated by a triangular relationship among geometry, flow, and pathobiology (Fig 2*A*).

As illustrated in Fig 2*A*, hemodynamics interacts with the aneurysm wall through blood flow (WSS and blood pressure). Pressure elicits tensile stresses in the wall, which are felt by vascular mural cells, namely smooth muscle cells and fibroblasts. Under unbalanced stresses, these mural cells can regulate collagen dynamics by cross-linking and synthesizing new collagen and degrading old collagen.[19] Meanwhile, endothelial cells lining the vessel lumen sense changes in WSS from blood flow and transduce these mechanical signals into biologic signals, activating pathways to maintain vascular homeostasis.[20] Through endothelial cell-mediated biology, WSS not only regulates vascular tone but also drives vascular remodeling under sustained deviations from physiologic baselines.[19] Pathologically high or low WSS and certain spatiotemporal patterns of its variation can potentiate endothelial cells to pathologic responses and aberrant functions. Presently, it is known that abnormal WSS drives endothelium-mediated proinflammatory responses,[21] matrix metalloproteinase activation,[22] cell death,[23] extracellular matrix (ECM) degradation, and vascular remodeling.[4,24,25]

Hemodynamics Plays a Critical Role in Intracranial Aneurysm Pathogenesis. A cerebral aneurysm is defined as a local outpouching of an intracranial artery exhibiting internal elastic lamina loss, tunica media thinning, and ECM degradation[23] and can either be saccular or fusiform. The pathogenesis of fusiform aneurysms, with some exceptions,[26] is closely related to atherosclerosis.[27] Because a

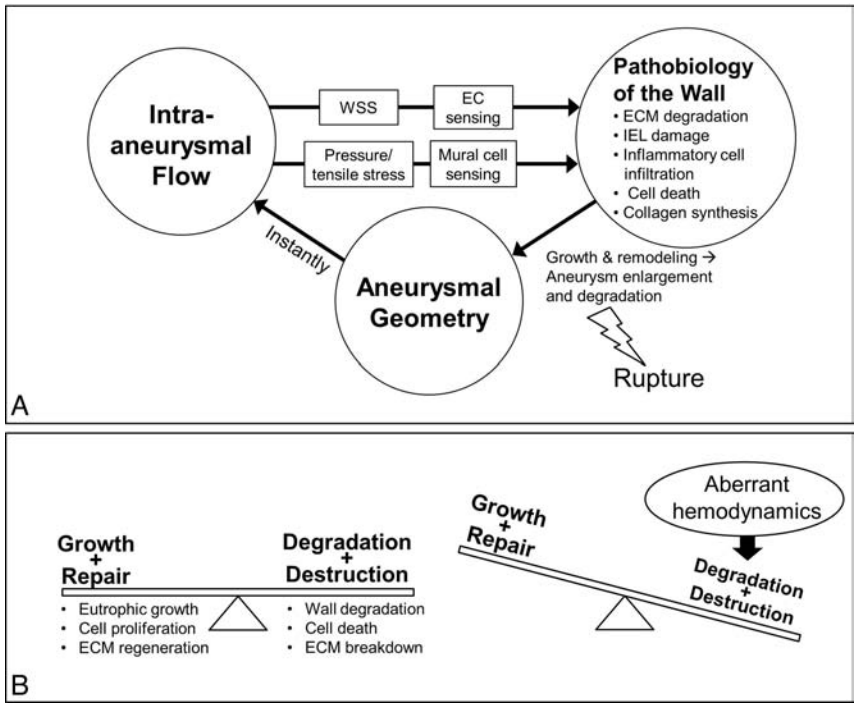

FIG 2. How hemodynamics plays into intracranial aneurysm dynamics. *A*, Three-way relationship of aneurysmal geometry, flow, and pathobiology. Flow exerts mechanical forces on the vessel wall, eliciting cell-mediated biologic pathways. Sustained changes in flow (thus WSS and pressure) lead to remodeling of the wall, resulting in aneurysm geometry change. In turn, geometry determines the flow, which could drive further biologic processes. *B*, The balance between growth/repair and degradation/destruction results in aneurysm stability. Aberrant hemodynamics disrupts the balance and amplifies degradation and destruction mechanisms, leading to enlargement and rupture of aneurysm.

vast majority (>80%) of intracranial aneurysms are saccular,[28] we will focus our discussion on this type of aneurysm.

The natural history of saccular intracranial aneurysms consists of 3 phases: initiation, growth, and either stabilization or rupture, with only a small minority of aneurysms ever progressing to rupture.[1] Intracranial aneurysm formation is the result of the interaction between the arterial wall and hemodynamic forces.[29] The cerebral vasculature is intrinsically prone to the effects of hemodynamic forces due to the lack of external elastic lamina, medial elastin, and supporting adventitial and perivascular tissues.[30,31] Moreover, cerebral arteries display structural irregularities at bifurcation apices, typical sites for saccular intracranial aneurysms.[32] These factors make such locations prone to insults by hemodynamic stresses and subsequent internal elastic lamina damage and aneurysm formation.[33]

Recent studies in animal models have elucidated the pivotal role of hemodynamics in intracranial aneurysm initiation.[25,34-38] Flow acceleration adjacent to impingement points at bifurcations produces a complex hemodynamic environment of high WSS and a positive WSS gradient along the flow,[4,37] which, through endothelium-mediated mechanotransduction, can initiate cascades of biochemical signals within the vessel wall and trigger aneurysm initiation.[4,25,39] In a hemodynamics-only model of intracranial aneurysm initiation, Metaxa et al[4] demonstrated that aneurysm initiation occurs when high WSS and positive WSS gradient exceed a certain threshold. This insult leads to local internal elastic lamina loss, media thinning, and bulge formation,[4,25,36] the earliest signs of intracranial aneurysm formation.

Prior to the initial aneurysmal damage triggered by hemodynamics, the cerebral vasculature may have already been weakened by various acquired (eg, cigarette smoking and hypertension)[40,41] or inherited risk factors (eg, polycystic kidney disease).[1] These factors compromise the ability of the cerebral vasculature to tolerate and properly adapt to hemodynamic insult,[39] most likely by lowering the threshold for the onset of pathologic responses.[42,43] Certainly, variations in hemodynamics and different risk factors among different individuals contribute to the heterogeneity of the disease.

Many studies have tried to incorporate various aneurysm risk factors such as hypertension, decreased collagen cross-linking, and estrogen deficiency into animal models.[34,44,45] In general, these studies have found that aneurysm progression starts with initial endothelial cell responses[45] and smooth muscle cell phenotypic modulation, after which an escalating inflammatory response may be provoked, accompanied by ECM remodeling and degradation and cell death.[46] These studies demonstrated that after intracranial aneurysm initiation, inflammation may play an important role in aneurysm progression (eg, inflammatory infiltrates produce matrix metalloproteinases, leading to wall degradation).[34] These animal models demonstrated aneurysm development only when a hemodynamic insult was also applied. This reaffirms the conclusion that hemodynamic insult is necessary for intracranial aneurysm genesis.

Aberrant Hemodynamics Can Disrupt Balance and Drive Intracranial Aneurysm Growth and Rupture. Aneurysm growth is dictated by the interplay between the local hemodynamic-biomechanical environment and aneurysm pathobiology. In the aneurysm wall, there are coincident and concurrent eutrophic changes (cell proliferation and ECM production) and destructive changes (cell death and ECM degradation) ongoing throughout the natural history of the intracranial aneurysm (Fig 2*B*).[23] When these 2 processes are balanced, the intracranial aneurysm remains stable; when the balance is disrupted, it may rupture. Clearly, aneurysm growth and rupture requires a disruptive agent. We believe that aberrant hemodynamics, chiefly through abnormal WSS, is a major disruptive agent. As illustrated in Fig 2*B*, intracranial aneurysm growth and rupture occur when aberrant hemodynamics cause destructive changes to outweigh eutrophic changes, making the aneurysm wall increasingly weaker and prone to rupture.[23]

Different Manifestations of Intracranial Aneurysms. Intracranial aneurysm lesion presentation is highly heterogeneous in almost every observable metric (Fig 3). Three principal aneurysm pheno-

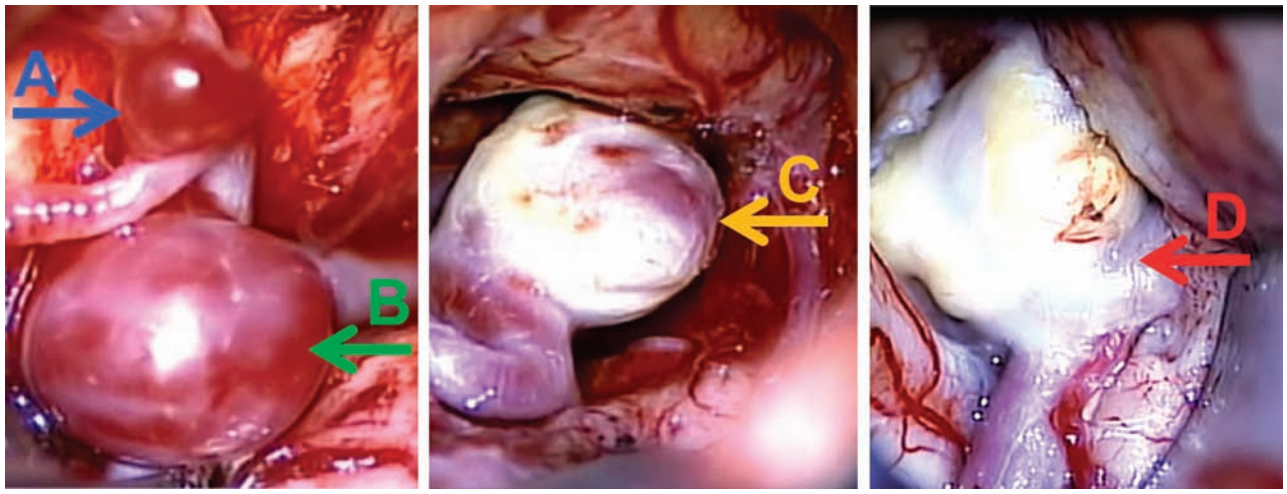

FIG 3. Heterogeneity of saccular aneurysms as a spectrum from type I (*A*) to type II (*D*) with various intermediate or combination types in between (*B* and *C*). *A*, A small thin-walled, entirely translucent aneurysm (type I). *B*, A mostly thin-walled aneurysm with some thicker-walled patches. *C*, A mostly thick-walled aneurysm with a few thin-walled patches. *D*, An aneurysm with an entirely thick, atherosclerotic wall (Type II). Images adapted with permission from Kadasi et al 2012.[50]

types have been reported from intraoperative observation of unruptured intracranial aneurysms.[47-49]

The first types are small aneurysms (<4 mm) with uniformly thin, smooth, hypocellular, translucent walls, through which reddish blood flow can be visualized at the time of surgical clipping. We refer to these as type I aneurysms (an example is seen in Fig 3*A*). The second types are entirely thick-walled large aneurysms (>10 mm), with an irregular surface on which whitish/yellowish atherosclerotic plaques obstruct the visualization of blood. We refer to these as type II aneurysms (an example is seen in Fig 3*D*). The third types are medium-sized aneurysms with a combination of thin- and thick-walled characteristics in different regions[47,49] or with intermediate wall thickness.[50] We refer to these as a combination type (examples are seen in Fig 3*B*, -*C*). According to Kadasi et al,[50] the distribution of these 3 phenotypes in unruptured aneurysms is 27%, 8%, and 65% for types I and II and the combination type, respectively.

Histologic analyses of both unruptured and ruptured aneurysm specimens from autopsy studies have mirrored such phenotypical classification:[50-54] Small intracranial aneurysms (<10 mm) have a higher rate (48%) of having thin, transparent, and hypocellular walls; absent smooth muscle cells, and inflammatory cells.[53,54] Large intracranial aneurysms (>10 mm) have a low rate (6%) of thin-walled regions but a high rate of thick walls with atherosclerotic changes, proliferation of smooth muscle cells, and inflammatory cells.[51-54]

These data suggest that intracranial aneurysm phenotypes exist on a spectrum: At one extreme is the small thin-walled phenotype (type I); at the other extreme is the large thick-walled phenotype (type II); and in between is a continuum representing an amalgamation of these 2 basic types. The recognition of different phenotypes in both incidentally discovered and ruptured aneurysms suggests that there may be a variety of nonconvergent hemodynamic-biologic pathways involved in the natural history of intracranial aneurysms.

Rupture Potential versus Rupture Event. Certainly, intracranial aneurysm rupture has been associated with intense physical activities and accompanying high blood pressure.[55] Large elevations in mean arterial blood pressure during such activities can increase aneurysm wall tension to a level that leads to rupture.[55] An increased heart rate during physical exertion and emotional excitement have also been suspected of contributing to rupture,[56] possibly through the increased frequency of cyclic stretching, which leads to hastened fatiguing of the wall.[57]

Why only some aneurysms are subjected to such catastrophe through routine activities is related to the vulnerable condition of their wall. Before rupture, the wall may have biologically remodeled and deteriorated with time,[33] decreasing the wall strength to such a level that normal physical exertion could generate enough pressure to push the wall tensile stress over the limit (ie, exceeding the wall strength),[33] rupturing the wall. Therefore, while the rupture episode itself is triggered by temporary pressure and/or frequency surge and wall failure, the predisposition of an intracranial aneurysm wall to rupture is due to biologic degradation, mediated by the interaction between hemodynamics and pathobiology with time.

A Unifying Hypothesis

Understanding the nature and origin of the high-versus-low WSS controversy is important in developing quantitative guidance for physicians to make better intracranial aneurysm treatment decisions.[15,16] Currently, the source of such heterogeneous findings remains elusive.[16,17] Here, we speculate that this heterogeneity may reflect the inherent complexity of natural history of intracranial aneurysms and the diversity of growth and rupture mechanisms. Understanding the biologic processes activated by different hemodynamic conditions, such as high and low WSS, may shed light on possible mechanisms that lead to intracranial aneurysm growth and rupture.

To address the conflicting CFD findings, we draw on the current understanding of hemodynamically induced pathobiologic

Vascular responses to aberrant WSS conditions reported in literature

Pathobiologic Responses to High WSS and Positive WSS Gradient[a]	Pathobiologic Responses to Low WSS and High OSI[b]
EC damage[24,45]	Proinflammatory ECs that are "leaky" and "sticky"[21,62]
EC turnover[25,72]	Increased ROS[62]
MMP production by mural cells[25]	Increased inflammatory cell infiltration[70]
ECM degradation[36]	MMP production by macrophages[61]
Medial thinning[36]	SMC proliferation and migration[63]
Mural cell apoptosis[25]	Thrombus formation[23,63]

Note:—EC indicates endothelial cell; ROS, reactive oxygen species; MMP, matrix metalloproteinase; OSI, oscillatory shear index; SMC, smooth muscle cell.
[a] From the literature on intracranial aneurysm genesis.
[b] From the literature on atherogenesis.

responses in better described vascular pathologies in the literature (the pathogenesis of atherosclerosis and intracranial aneurysm). Such knowledge, summarized in the Table, helps us conceptualize possible roles of similar responses in intracranial aneurysm pathophysiology.

High and Low WSS Can Drive Different Mechanistic Pathways of Intracranial Aneurysm Growth and Rupture. We submit that aberrant hemodynamics of both low and high WSS can drive intracranial aneurysm growth and rupture via different biologic mechanisms:

1) Low WSS and a high oscillatory shear index can trigger inflammatory-cell-mediated destructive remodeling.

2) High WSS and a positive WSS gradient can trigger mural-cell-mediated destructive remodeling.

By the pathobiologic effects in the Table, abnormal hemodynamic conditions of high and low WSS can disrupt the equilibrium between eutrophic and degradative processes in the intracranial aneurysm wall (Fig 2*B*).[23] Specifically, both high and low WSS can incite proteolytic and oxidative damage, which causes ECM degradation and cell death, thereby facilitating aneurysm growth and rupture. This hypothesis lays the foundation for a conceptual framework that helps us begin to dissect the complexity of the hemodynamics-aneurysm pathophysiologic interaction.

Figure 4 illustrates the unified role of hemodynamics throughout aneurysm development. Initiation of intracranial aneurysms is induced by a high WSS and a positive WSS gradient.[4,37] Through endothelial cell mechanotransduction, these hemodynamic stresses initiate biochemical cascades when they exceed certain thresholds, leading to local production and activation of proteases (most important, matrix metalloproteinase −2 and −9) by mural cells,[25] massive internal elastic lamina damage,[4] and apoptosis,[25] which are responsible for media thinning and bulge formation.[37] Most interesting, inflammatory cell infiltration was not observed in early-stage intracranial aneurysm initiation,[25] and macrophage depletion did not attenuate aneurysm formation, indicating that hemodynamic initiation of intracranial aneurysms is not mediated by infiltrating inflammatory cells. (M. Mandelbaum, J. Kolega, J.M. Dolan, A. Siddiqui, H. Meng, December 2012, unpublished data).

After initiation, aneurysmal bulge enlargement typically exposes the sac to increasingly lower WSS, leading to the biologic pathway shown by the right branch in Fig 4. After a recirculation zone forms in the sac, the flow environment is likely to be dominated by low and oscillating WSS. This condition is exacerbated if secondary vortices form and/or flow instability increases.[58] Low and oscillatory shear stress is known to elicit an inflammatory response in the endothelium. Endothelial cells produce reactive oxygen species, and upregulate surface adhesion molecules and cytokines in the vessel wall and increase luminal permeability.[59,60] A "sticky" and "leaky" endothelium, in combination with an increased blood residence time, facilitates leukocyte transmigration into the wall during aneurysm development. These inflammatory infiltrates can massively produce matrix metalloproteinases to degrade the ECM,[61] thus tipping the balance between eutrophic and degradative processes and driving intracranial aneurysm growth and rupture.[23] Furthermore, such "disturbed flow" environments also promote the formation of atherosclerotic plaques,[23,62] which exacerbate the effects of inflammatory cells. The inflammatory-cell-mediated degradation becomes even more pronounced upon the formation of a luminal thrombus, which can further trap macrophages and neutrophils, and harbor proteases, reactive oxygen species, and oxidized low-density lipoproteins.[63] Because wall degradation via this pathway relies on leukocyte infiltration, we term it "inflammatory-cell-mediated destructive remodeling."

On the other hand, impinging flow may persist after bulge formation in some aneurysms, so that high WSS and positive WSS gradient could remain prevalent in the aneurysmal sac. For example, in intracranial aneurysms with high-curvature parent vessels,[64] high aneurysm angle,[65] or high inflow angle,[66] inflow from the parent vessel can carry high inertia and impinge on the wall. This hemodynamic condition could lead to the pathway shown by the left branch in Fig 4. Contrary to the right branch, mural cells, instead of inflammatory cells, are most likely responsible for the destructive changes in the intracranial aneurysm wall in this pathway, just as in initiation.[25] Certainly, the high WSS environment is not conducive to leukocyte infiltration, which requires sufficient blood residence time and the endothelial cell responses commonly elicited under low WSS and oscillatory flow.[62,67] Systemic depletion of macrophages does not suppress aneurysm development induced by high WSS. Rather, in this pathway, phenotype-modulated smooth muscle cells are the source of proteolytic activities.[25] Therefore, we term it "mural-cell-mediated destructive remodeling."

Although leukocyte infiltration is not thought to be involved in the high-WSS-driven pathway, proinflammatory behavior could still be playing a critical role. Recently, it was found that in the internal elastic lamina damaged zones during intracranial aneurysm genesis, smooth muscle cells upregulated the proinflammatory proteins monocyte chemoattractant protein-1 and the transcription factor nuclear factor-κB, (M. Mandelbaum, J. Kolega, J.M. Dolan, A. Siddiqui, H. Meng, December 2012, unpublished data) and produced matrix metalloproteinase −2 and −9, which are required for aneurysmal degradation.[25] These "inflammatory" smooth muscle cells lose some of their contractile phenotype by decreasing smooth muscle actin expression. In some ways, smooth muscle cells under high WSS conditions could act like inflammatory cells to cause aneurysmal remodeling.

While some intracranial aneurysms may be dominated by one pathway, others could switch from one to another as the geometry

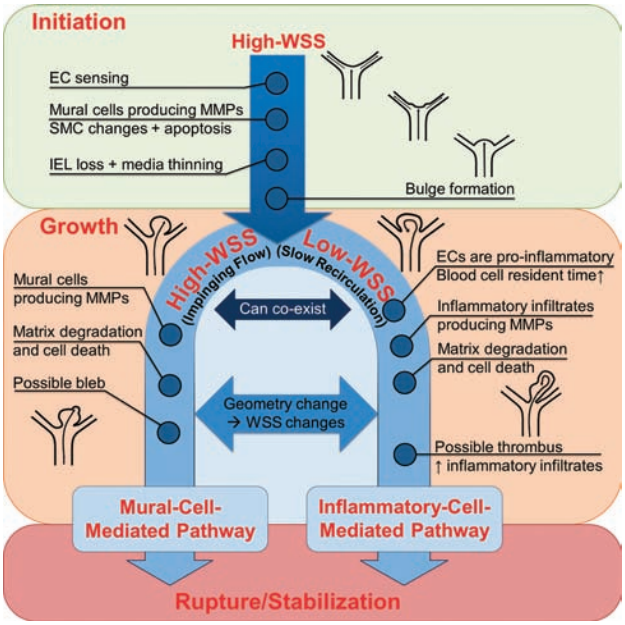

FIG 4. A unified role of high and low WSS in aneurysm initiation, growth, and rupture.

changes (eg, during the initiation of blebs), as illustrated by the double-headed arrows between the branches in Fig 4. In some aneurysms, both biologic mechanisms might dominate different parts of the sac, depending on the local hemodynamic condition. The 3-way relationship among flow, pathobiology, and geometry (Fig 2*A*) can lead to further complexities in intracranial aneurysm pathophysiology, both longitudinally (at different time points) and cross-sectionally (at different spatial regions of the aneurysm). As these conditions change, so does the balance between eutrophic and destructive processes, resulting in either stabilization or rupture of the intracranial aneurysm (Fig 2*B*).

Taken together, high WSS and low WSS are 2 aberrant hemodynamic conditions that could elicit pathologic remodeling pathways to drive intracranial aneurysm growth and rupture. Recognizing the heterogeneity of aneurysm phenotypes (see "Different Manifestations of Intracranial Aneurysms"), one cannot help but ask if these 2 pathways might be responsible for the 2 basic phenotypes (type I and type II) and if their interchange might account for the wide spectrum in between. We suspect that they do.

Emergence of Different Intracranial Aneurysm Phenotypes. We further hypothesize that the high-WSS-driven, mural-cell-mediated pathway is responsible for type I aneurysms, while the low-WSS-driven inflammatory-cell-mediated pathway is responsible for type II aneurysms. The interplay between these 2 pathways, both longitudinally and cross-sectionally, contributes to the wide spectrum of combined intracranial aneurysm phenotypes. This concept is illustrated in Fig 5.

Small and transparent type I aneurysms develop relatively quickly.[68] Their walls lack inflammatory cells and other cell types, as demonstrated by intraoperative[47-49] and postmortem studies.[52-54] It is possible that they are formed by impinging flow through the high-WSS-driven degradation mechanisms, as illustrated on the left side of Fig 5. The resident mural cells produce matrix maetalloproteinases under high WSS conditions, leading to significant ECM degradation and cell death by anoikis (apoptosis due to loss of ECM anchorage).[69] This degradative process may deplete the sac of resident cells and elastin fibers and reduce collagen fibers, forcing the remaining ECM to stretch, creating a stiff thin wall.[19,54]

On the other hand, the large, thick-walled, atherosclerotic type II aneurysms appear to have developed during a longer period of time through various attempts to heal the sac.[47-49] Indeed, most inflammatory cells found in aneurysm specimens came from this type of aneurysm.[52-54] We therefore conjecture that the natural history of type II aneurysms (after initiation) is dominated by the inflammatory-cell-mediated pathway, as illustrated on the right side of Fig 5. The destructive remodeling here is accompanied by increased inflammatory cell infiltration and smooth muscle cell proliferation, especially after atherosclerotic plaque and/or thrombus formation.[63,70] These processes lead to large, atherosclerotic, and thrombotic intracranial aneurysm phenotypes.

We expect that both pathways can dominate different phases of intracranial aneurysm natural history and/or different regions of the growing aneurysm, thereby contributing to the wide spectrum of the combined type aneurysms. As the aneurysm geometry changes, so does the dominant flow condition (jet or recirculation) and the pathway it espouses.

SUMMARY

Aneurysms occurring in different locations and perienvironments, with varied morphologies and flow dynamics, are associated with complex genetic and environmental contributing factors, which could modify the vascular response to hemodynamics. As such, studies containing a limited cohort of intracranial aneurysms are inevitably based on skewed samples. It is not surprising that their findings sometimes do not converge. Additionally, conflicting CFD results have been rationalized by inconsistent parameter definitions, flawed experimental design, or variability in assumptions and compromises adapted in CFD simulations.

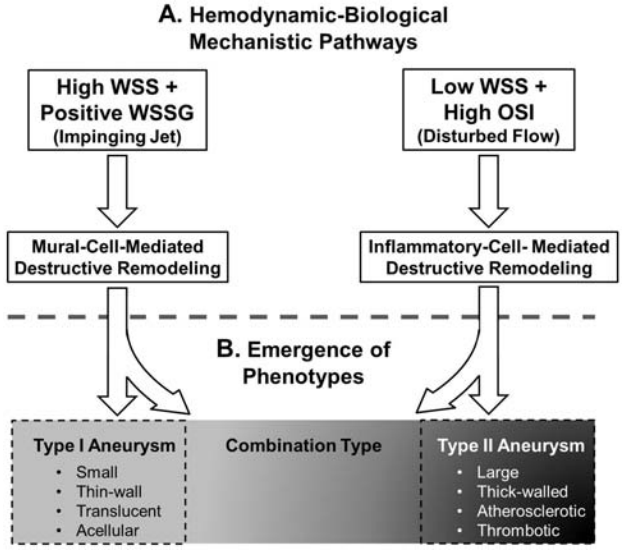

FIG 5. Two hypothesized, independent, hemodynamic-biologic pathways that drive intracranial aneurysm growth and rupture (*A*) and the proposed relationship between them and the spectrum of intracranial aneurysm phenotypes (*B*).

These factors aside, we believe there is intrinsic mechanistic complexity concerning intracranial aneurysms, which underlies the high-versus-low WSS controversy.

We submit that inconsistent findings about the role of WSS are principally a result of the inherent heterogeneity in intracranial aneurysm natural history and the diversity of hemodynamically driven growth and rupture mechanisms. A novel concept can help delineate such complexity: Aberrant hemodynamics including both high WSS and low WSS can tip the balance that maintains vascular homeostasis and can drive destructive remodeling to cause intracranial aneurysm progression and rupture. We propose that 2 independent hemodynamically driven biologic pathways could be associated with intracranial aneurysm growth and rupture: an inflammatory-cell-mediated pathway that is induced by low WSS and a high oscillatory shear index, and a mural-cell-mediated pathway that is induced by high WSS and a positive WSS gradient. Furthermore, these 2 hemodynamic-biologic pathways may be responsible for the 2 aneurysm phenotypes: large thick-walled atherosclerotic aneurysms (type II) and smaller thin-walled translucent aneurysms (type I), respectively. These processes reflect the variations in the tripartite interactions of geometry, flow, and pathobiology, which become apparent in the spectrum of intracranial aneurysm phenotypes. Each phenotype attempts to re-establish homeostasis between the eutrophic and destructive forces. If homeostasis is achieved, the aneurysm stabilizes; if not, it ruptures.

We argue that the high-versus-low WSS controversy is a manifestation of the heterogeneity in intracranial aneurysm pathophysiology and its intricate relationship with hemodynamics.

Future Directions

Going forward, we expect that large, multicenter, global studies will be needed to obtain a more comprehensive picture of intracranial aneurysm hemodynamic pathophysiology and to develop more reliable risk-prediction models. This effort will likely require better classification of aneurysms (eg, based on aneurysm size, location, phenotype, perienvironment, and patient population), rather than treating them as a conglomeration. Different predictive models could be extracted from different classes of datasets and applied to intracranial aneurysms that belong to specific categories. For example, statistical analyses of small aneurysms may produce a different set of predictive parameters (related to high WSS and a positive WSS gradient) from that of large aneurysms (related to low WSS and a high oscillatory shear index). We envision that intracranial aneurysm cases could be carefully classified and then subjected to the appropriate predictive models. The models should reflect the underlying mechanisms driving aneurysm growth and rupture. As such, intracranial aneurysm classification based on size alone may not be highly accurate. An alternative strategy would be to identify type I and II aneurysms from imaging and then to perform subgroup risk analyses and management.

There is a need to study the role of hemodynamic-biologic interactions in the natural history and rupture propensity of intracranial aneurysms in experimental models. Animal models commonly used for clinical studies are good for testing medical devices and investigating hemodynamics[71] but are generally biologically deficient. On the other hand, current endogenous models[34,37] capture some hemodynamic-biologic effects in the early stages of aneurysm formation but lack the ability to study growth and rupture. Therefore, improved animal models, aided by advancements in in vivo and molecular imaging, are needed to elucidate the hemodynamic-biologic mechanisms driving aneurysm growth, and models of aneurysm rupture must be developed to study the hemodynamic and biologic mechanisms involved in rupture.

Patient-specific CFD studies must be complemented by hemodynamic-biologic mechanistic studies because these 2 approaches are mutually informative and beneficial. Analysis of patient-specific CFD results may generate new questions concerning the pathophysiology of intracranial aneurysm (ie, which mechanistic studies should be investigated). Meanwhile, mechanistic studies based on animal models can help analyze and interpret the results of patient-specific CFD studies to facilitate the generation of future predictors.

The unifying hypothesis presented in this review may serve as a starting point to guide the design of these future endeavors. We anticipate that joint effort among clinicians, engineers, and basic scientists focused on better understanding aneurysm pathophysiology will lead to better risk prediction and management of intracranial aneurysms.

ACKNOWLEDGMENTS

We are grateful for stimulating discussions with Dr Charles Strother, and H.M. is grateful to Dr William L. Young for his mentorship.

Disclosures: Hui Meng—*RELATED*: *Grant*: National Institutes of Health/National Institute of Neurological Disorders and Stroke R01NS064592.* Adnan Siddiqui—*UNRELATED*: *Board Membership*: Codman & Shurtleff, *Comments*: Advisory Board; *Consultancy*: Codman & Shurtleff, Concentric Medical, ev3/Covidien Vascular Therapies, GuidePoint Global Consulting, Penumbra, Stryker Neurovascular, *Employment*: University at Buffalo, Kaleida Health, *Grants/Grants Pending*: National Institutes of Health, University at Buffalo, *Payment for Lectures (including service on Speakers Bureaus)*: Codman & Shurtleff, Genentech, *Stock/Stock Options*: Hotspur, Intratech Medical, StimSox, Valor Medical, *Travel/Accommodations/Meeting Expenses Unrelated to Activities Listed*: Covidien,* MicroVention,* *Other*: Penumbra, *Comments*: serve on National Steering Committee for Penumbra, Inc, 3D Separator Trial (no compensation received). * Money paid to the institution.

REFERENCES

1. Rinkel GJ, Djibuti M, Algra A, et al. **Prevalence and risk of rupture of intracranial aneurysms: a systematic review.** *Stroke* 1998;29:251–56
2. Connolly ES Jr, Rabinstein AA, Carhuapoma JR, et al. **Guidelines for the management of aneurysmal subarachnoid hemorrhage: a guideline for healthcare professionals from the American Heart Association/American Stroke Association.** *Stroke* 2012;43:1711–37
3. Wiebers DO, Torner JC, Meissner I. **Impact of unruptured intracranial aneurysms on public health in the United States.** *Stroke* 1992;23:1416–19
4. Metaxa E, Tremmel M, Natarajan SK, et al. **Characterization of critical hemodynamics contributing to aneurysmal remodeling at the basilar terminus in a rabbit model.** *Stroke* 2010;41:1774–82
5. Xiang J, Natarajan SK, Tremmel M, et al. **Hemodynamic-morphologic discriminants for intracranial aneurysm rupture.** *Stroke* 2011;42:144–52
6. Cebral JR, Mut F, Weir J, et al. **Quantitative characterization of the**

hemodynamic environment in ruptured and unruptured brain aneurysms. *AJNR Am J Neuroradiol* 2011;32:145–51
7. Jou LD, Lee DH, Morsi H, et al. **Wall shear stress on ruptured and unruptured intracranial aneurysms at the internal carotid artery.** *AJNR Am J Neuroradiol* 2008;29:1761–67
8. Shojima M, Oshima M, Takagi K, et al. **Magnitude and role of wall shear stress on cerebral aneurysm: computational fluid dynamic study of 20 middle cerebral artery aneurysms.** *Stroke* 2004;35:2500–05
9. Boussel L, Rayz V, McCulloch C, et al. **Aneurysm growth occurs at region of low wall shear stress: patient-specific correlation of hemodynamics and growth in a longitudinal study.** *Stroke* 2008;39:2997–3002
10. Acevedo-Bolton G, Jou LD, Dispensa BP, et al. **Estimating the hemodynamic impact of interventional treatments of aneurysms: numerical simulation with experimental validation: technical case report.** *Neurosurgery* 2006;59:E429–30, author reply E429–30
11. Castro MA, Putman CM, Sheridan MJ, et al. **Hemodynamic patterns of anterior communicating artery aneurysms: a possible association with rupture.** *AJNR Am J Neuroradiol* 2009;30:297–302
12. Qian Y, Takao H, Umezu M, et al. **Risk analysis of unruptured aneurysms using computational fluid dynamics technology: preliminary results.** *AJNR Am J Neuroradiol* 2011;32:1948–55
13. Sugiyama SI, Meng H, Funamoto K, et al. **Hemodynamic analysis of growing intracranial aneurysms arising from a posterior inferior cerebellar artery.** *World Neurosurg* 2012;78:462–68
14. Takao H, Murayama Y, Otsuka S, et al. **Hemodynamic differences between unruptured and ruptured intracranial aneurysms during observation.** *Stroke* 2012;43:1436–39
15. Kallmes DF. **Point: CFD—computational fluid dynamics or confounding factor dissemination.** *AJNR Am J Neuroradiol* 2012;33:395–96
16. Cebral JR, Meng H. **Counterpoint: realizing the clinical utility of computational fluid dynamics—closing the gap.** *AJNR Am J Neuroradiol* 2012;33:396–98
17. Robertson AM, Watton PN. **Computational fluid dynamics in aneurysm research: critical reflections, future directions.** *AJNR Am J Neuroradiol* 2012;33:992–95
18. Ujiie H, Tachibana H, Hiramatsu O, et al. **Effects of size and shape (aspect ratio) on the hemodynamics of saccular aneurysms: a possible index for surgical treatment of intracranial aneurysms.** *Neurosurgery* 1999;45:119–30, discussion 129–30
19. Humphrey JD, Taylor CA. **Intracranial and abdominal aortic aneurysms: similarities, differences, and need for a new class of computational models.** *Annu Rev Biomed Eng* 2008;10:221–46
20. Nixon AM, Gunel M, Sumpio BE. **The critical role of hemodynamics in the development of cerebral vascular disease.** *J Neurosurg* 2010;112:1240–53
21. Malek AM, Alper SL, Izumo S. **Hemodynamic shear stress and its role in atherosclerosis.** *JAMA* 1999;282:2035–42
22. Ota R, Kurihara C, Tsou TL, et al. **Roles of matrix metalloproteinases in flow-induced outward vascular remodeling.** *J Cereb Blood Flow Metab* 2009;29:1547–58
23. Frosen J, Tulamo R, Paetau A, et al. **Saccular intracranial aneurysm: pathology and mechanisms.** *Acta Neuropathol* 2012;123:773–86
24. Wang Z, Kolega J, Hoi Y, et al. **Molecular alterations associated with aneurysmal remodeling are localized in the high hemodynamic stress region of a created carotid bifurcation.** *Neurosurgery* 2009;65:169–77, discussion 177–78
25. Kolega J, Gao L, Mandelbaum M, et al. **Cellular and molecular responses of the basilar terminus to hemodynamics during intracranial aneurysm initiation in a rabbit model.** *J Vasc Res* 2011;48:429–42
26. Findlay JM, Hao C, Emery D. **Non-atherosclerotic fusiform cerebral aneurysms.** *Can J Neurol Sci* 2002;29:41–48
27. Park SH, Yim MB, Lee CY, et al. **Intracranial fusiform aneurysms: It's pathogenesis, clinical characteristics and managements.** *J Korean Neurosurg Soc* 2008;44:116–23
28. Yong-Zhong G, van Alphen HA. **Pathogenesis and histopathology of saccular aneurysms: review of the literature.** *Neurol Res* 1990;12:249–55
29. Hashimoto T, Meng H, Young WL. **Intracranial aneurysms: links among inflammation, hemodynamics and vascular remodeling.** *Neurol Res* 2006;28:372–80
30. Stehbens WE. **Pathology and pathogenesis of intracranial berry aneurysms.** *Neurol Res* 1990;12:29–34
31. Inci S, Spetzler RF. **Intracranial aneurysms and arterial hypertension: a review and hypothesis.** *Surg Neurol* 2000;53:530–40, discussion 540–42
32. Finlay HM, Whittaker P, Canham PB. **Collagen organization in the branching region of human brain arteries.** *Stroke* 1998;29:1595–601
33. Steiger HJ. **Pathophysiology of development and rupture of cerebral aneurysms.** *Acta Neurochir Suppl (Wien)* 1990;48:1–57
34. Aoki T, Kataoka H, Morimoto M, et al. **Macrophage-derived matrix metalloproteinase-2 and -9 promote the progression of cerebral aneurysms in rats.** *Stroke* 2007;38:162–69
35. Hashimoto N, Handa H, Nagata I, et al. **Animal model of cerebral aneurysms: pathology and pathogenesis of induced cerebral aneurysms in rats.** *Neurol Res* 1984;6:33–40
36. Meng H, Metaxa E, Gao L, et al. **Progressive aneurysm development following hemodynamic insult.** *J Neurosurg* 2011;114:1095–103
37. Meng H, Wang Z, Hoi Y, et al. **Complex hemodynamics at the apex of an arterial bifurcation induces vascular remodeling resembling cerebral aneurysm initiation.** *Stroke* 2007;38:1924–31
38. Cai J, He C, Yuan FL, et al. **A novel haemodynamic cerebral aneurysm model of rats with normal blood pressure.** *J Clin Neurosci* 2012;19:135–38
39. Meng H, Xiang J, Liaw N. **The role of hemodynamics in intracranial aneurysm initiation.** *Int Rev Thromb* 2012;7:40–57
40. Juvela S. **Natural history of unruptured intracranial aneurysms: risks for aneurysm formation, growth, and rupture.** *Acta Neurochir Suppl* 2002;82:27–30
41. Vega C, Kwoon JV, Lavine SD. **Intracranial aneurysms: current evidence and clinical practice.** *Am Fam Physician* 2002;66:601–08
42. Cebral JR, Raschi M. **Suggested connections between risk factors of intracranial aneurysms: a review.** *Ann Biomed Eng* 2013;41:1366–83
43. Dolan JM, Kolega J, Meng H. **High wall shear stress and spatial gradients in vascular pathology: a review.** *Ann Biomed Eng* 2013;41:1411–27
44. Aoki T, Kataoka H, Shimamura M, et al. **Nf-kappaB is a key mediator of cerebral aneurysm formation.** *Circulation* 2007;116:2830–40
45. Jamous MA, Nagahiro S, Kitazato KT, et al. **Vascular corrosion casts mirroring early morphological changes that lead to the formation of saccular cerebral aneurysm: an experimental study in rats.** *J Neurosurg* 2005;102:532–35
46. Chalouhi N, Ali MS, Jabbour PM, et al. **Biology of intracranial aneurysms: role of inflammation.** *J Cereb Blood Flow Metab* 2012;32:1659–76
47. Asari S, Ohmoto T. **Long-term outcome of surgically treated unruptured cerebral aneurysms.** *Clin Neurol Neurosurg* 1994;96:230–35
48. Inagawa T, Hirano A. **Autopsy study of unruptured incidental intracranial aneurysms.** *Surg Neurol* 1990;34:361–65
49. Mizoi K, Yoshimoto T, Nagamine Y. **Types of unruptured cerebral aneurysms reviewed from operation video-recordings.** *Acta Neurochir* 1996;138:965–69
50. Kadasi LM, Dent WC, Malek AM. **Cerebral aneurysm wall thickness analysis using intraoperative microscopy: effect of size and gender on thin translucent regions.** *J Neurointerv Surg* 2013;5:201–06
51. Chyatte D, Bruno G, Desai S, et al. **Inflammation and intracranial aneurysms.** *Neurosurgery* 1999;45:1137–46, discussion 1146–47
52. Frösen J, Piippo A, Paetau A, et al. **Remodeling of saccular cerebral artery aneurysm wall is associated with rupture: histological analysis of 24 unruptured and 42 ruptured cases.** *Stroke* 2004;35:2287–93
53. Kataoka K, Taneda M, Asai T, et al. **Structural fragility and inflammatory response of ruptured cerebral aneurysms: a comparative study between ruptured and unruptured cerebral aneurysms.** *Stroke* 1999;30:1396–401

54. Kataoka K, Taneda M, Asai T, et al. **Difference in nature of ruptured and unruptured cerebral aneurysms.** *Lancet* 2000;355:203–03
55. Reynolds MR, Willie JT, Zipfel GJ, et al. **Sexual intercourse and cerebral aneurysmal rupture: potential mechanisms and precipitants.** *J Neurosurg* 2011;114:969–77
56. Jiang J, Strother C. **Computational fluid dynamics simulations of intracranial aneurysms at varying heart rates: a "patient-specific" study.** *J Biomech Eng* 2009;131:091001
57. Foutrakis GN, Yonas H, Sclabassi RJ. **Saccular aneurysm formation in curved and bifurcating arteries.** *AJNR Am J Neuroradiol* 1999; 20:1309–17
58. Tremmel M, Dhar S, Levy EI, et al. **Influence of intracranial aneurysm-to-parent vessel size ratio on hemodynamics and implication for rupture: results from a virtual experimental study.** *Neurosurgery* 2009;64:622–30, discussion 630–31
59. Bian C, Xu G, Wang JA, et al. **Hypercholesterolaemic serum increases the permeability of endothelial cells through zonula occludens-1 with phosphatidylinositol 3-kinase signaling pathway.** *J Biomed Biotechnol* 2009;2009:814979
60. Ross R, Glomset JA. **The pathogenesis of atherosclerosis (first of two parts).** *N Engl J Med* 1976;295:369–77
61. Galis ZS, Sukhova GK, Lark MW, et al. **Increased expression of matrix metalloproteinases and matrix degrading activity in vulnerable regions of human atherosclerotic plaques.** *J Clin Invest* 1994;94: 2493–503
62. Chiu JJ, Chien S. **Effects of disturbed flow on vascular endothelium: pathophysiological basis and clinical perspectives.** *Physiol Rev* 2011;91:327–87
63. Ross R. **Mechanisms of disease: atherosclerosis—an inflammatory disease.** *N Engl J Med* 1999;340:115–26
64. Meng H, Wang Z, Kim M, et al. **Saccular aneurysms on straight and curved vessels are subject to different hemodynamics: implications of intravascular stenting.** *AJNR Am J Neuroradiol* 2006;27:1861–65
65. Dhar S, Tremmel M, Mocco J, et al. **Morphology parameters for intracranial aneurysm rupture risk assessment.** *Neurosurgery* 2008; 63:185–96, discussion 196–97
66. Baharoglu MI, Schirmer CM, Hoit DA, et al. **Aneurysm inflow-angle as a discriminant for rupture in sidewall cerebral aneurysms: morphometric and computational fluid dynamic analysis.** *Stroke* 2010;41:1423–30
67. Honda HM, Hsiai T, Wortham CM, et al. **A complex flow pattern of low shear stress and flow reversal promotes monocyte binding to endothelial cells.** *Atherosclerosis* 2001;158:385–90
68. Horie N, Morikawa M, Fukuda S, et al. **Detection of blood blister-like aneurysm and intramural hematoma with high-resolution magnetic resonance imaging.** *J Neurosurg* 2011;115:1206–09
69. Michel JB. **Anoikis in the cardiovascular system: known and unknown extracellular mediators.** *Arterioscler Thromb Vasc Biol* 2003;23:2146–54
70. Gui T, Shimokado A, Sun Y, et al. **Diverse roles of macrophages in atherosclerosis: from inflammatory biology to biomarker discovery.** *Mediators Inflamm* 2012;2012:693083
71. Zeng Z, Kallmes DF, Durka MJ, et al. **Sensitivity of CFD based hemodynamic results in rabbit aneurysm models to idealizations in surrounding vasculature.** *J Biomech Eng* 2010;132:091009
72. Dolan JM, Meng H, Sim FJ, et al. **Endothelial cells express a unique transcriptional profile under very high wall shear stress known to induce expansive arterial remodeling.** *Am J Physiol Cell Physiol* 2012; 302:C1109–18

MRI Surrogates for Molecular Subgroups of Medulloblastoma

S. Perreault, V. Ramaswamy, A.S. Achrol, K. Chao, T.T. Liu, D. Shih, M. Remke, S. Schubert, E. Bouffet, P.G. Fisher, S. Partap, H. Vogel, M.D. Taylor, Y.J. Cho, and K.W. Yeom

ABSTRACT

BACKGROUND AND PURPOSE: Recently identified molecular subgroups of medulloblastoma have shown potential for improved risk stratification. We hypothesized that distinct MR imaging features can predict these subgroups.

MATERIALS AND METHODS: All patients with a diagnosis of medulloblastoma at one institution, with both pretherapy MR imaging and surgical tissue, served as the discovery cohort ($n = 47$). MR imaging features were assessed by 3 blinded neuroradiologists. NanoString-based assay of tumor tissues was conducted to classify the tumors into the 4 established molecular subgroups (wingless, sonic hedgehog, group 3, and group 4). A second pediatric medulloblastoma cohort ($n = 52$) from an independent institution was used for validation of the MR imaging features predictive of the molecular subtypes.

RESULTS: Logistic regression analysis within the discovery cohort revealed tumor location ($P < .001$) and enhancement pattern ($P = .001$) to be significant predictors of medulloblastoma subgroups. Stereospecific computational analyses confirmed that group 3 and 4 tumors predominated within the midline fourth ventricle (100%, $P = .007$), wingless tumors were localized to the cerebellar peduncle/cerebellopontine angle cistern with a positive predictive value of 100% (95% CI, 30%–100%), and sonic hedgehog tumors arose in the cerebellar hemispheres with a positive predictive value of 100% (95% CI, 59%–100%). Midline group 4 tumors presented with minimal/no enhancement with a positive predictive value of 91% (95% CI, 59%–98%). When we used the MR imaging feature–based regression model, 66% of medulloblastomas were correctly predicted in the discovery cohort, and 65%, in the validation cohort.

CONCLUSIONS: Tumor location and enhancement pattern were predictive of molecular subgroups of pediatric medulloblastoma and may potentially serve as a surrogate for genomic testing.

ABBREVIATIONS: CP/CPA = cerebellar peduncle/cerebellopontine angle cistern; FSL = fMRI of the Brain Software Library; SHH = sonic hedgehog; WNT = wingless

Medulloblastoma is the most common malignant pediatric brain tumor, accounting for 40% of childhood tumors in the posterior fossa.[1] Genomic characterization of medulloblastoma has recently demonstrated that medulloblastomas can be subdivided into 4 distinct molecular subgroups: wingless (WNT), sonic hedgehog (SHH), group 3, and group 4.[2-4] These subgroups have shown different clinical behaviors and may benefit from subgroup-specific treatments. Despite the potential clinical utility of genomic analyses, their translation into clinical practice to improve treatment outcomes in children can be hampered by cost or lack of access to molecular-analysis tools when treatment is initiated. Immunohistochemistry markers have shown utility, but

Received February 17, 2014; accepted after revision March 20.

From the Department of Neurology (S. Perreault, S.S., P.G.F., S. Partap, Y.J.C.), Division of Child Neurology, Department of Neurosurgery (A.S.A., K.C.), and Department of Radiology (K.W.Y.), Lucile Packard Children's Hospital at Stanford University, Palo Alto, California; Division of Child Neurology (S. Perreault), Centre Hospitalier Universitaire Sainte-Justine, Montreal, Quebec, Canada; Division of Neurosurgery (V.R., D.S., M.R., M.D.T.), Labatt Brain Tumour Research Centre (V.R., D.S., M.R., E.B., M.D.T.), and Division of Pediatric Hematology/Oncology (E.B), Hospital for Sick Children, Toronto, Ontario, Canada; Department of Laboratory Medicine and Pathobiology (V.S., D.S., M.R., M.D.T.), University of Toronto, Toronto, Ontario, Canada; Department of Radiology (T.T.L.), Richard M. Lucas Center for Imaging, and Department of Pathology (H.V.), Stanford University, Stanford, California.

Yoon-Jae Cho and Kristen W. Yeom are co-senior authors.

Sébastien Perreault was a Beverly and Bernard Wolfe Pediatric Neuro-Oncology fellow at Lucile Packard Children's Hospital at Stanford University.

This work was supported by Fonds de Recherche en Santé du Québec (S. Perreault), Justine Lacoste Foundation (S. Perreault), St. Baldrick's Foundation (Y.J. Cho), and clinical fellowships from the Canadian Institutes of Health Research and Albert Innovates Health Solutions (V. Ramaswamy).

Previously presented in abstract form at: Annual Meeting of the Society for Neuro-Oncology, November 21–14, 2013; San Francisco, California.

Please address correspondence to Kristen W. Yeom, MD, Lucile Packard Children's Hospital, Stanford University, Department of Radiology, Pediatric MRI & CT, Room 0511, 725 Welch Rd, Palo Alto, CA 94304; e-mail: kyeom@stanford.edu

Indicates open access to non-subscribers at www.ajnr.org

Indicates article with supplemental on-line figures.

http://dx.doi.org/10.3174/ajnr.A3990

their use is still not widespread and interpretation can be challenging.[2,5]

MR imaging, on the other hand, is performed in all patients with brain tumor and remains the primary method for diagnosis, surgical guidance, and surveillance of these tumors. Therefore, MR imaging features specific to molecular subgroups of medulloblastoma could facilitate the real-time translation and integration of genomic-based studies into clinical practice. Prior studies have shown that medulloblastomas present with heterogeneous imaging features, including location and enhancement patterns.[6] These phenotypic radiologic features may reflect underlying differences in tumor biology.[7,8] In this study, we hypothesized that distinct MR imaging features predict molecular subgroups of pediatric medulloblastoma.

MATERIALS AND METHODS

Patient Cohorts

After institutional review board approval, we retrospectively identified a cohort of patients with medulloblastoma from January 1998 to January 2013 at Lucile Packard Children's Hospital (Stanford University, Palo Alto, California). Patients with both treatment-naive MR imaging and surgical tissue available for molecular analysis were included in the discovery cohort. An independent validation cohort of children with the same inclusion criteria was assembled from the Hospital for Sick Children (Toronto, Ontario, Canada).

Molecular Analysis

NanoString-based assay (http://www.nanostring.com) was performed to classify the medulloblastoma into the 4 main molecular subgroups (WNT, SHH, group 3, and group 4) on the basis of gene-expression profiling, as previously described.[9] For most of the patient cohort, molecular analysis was conducted on formalin-fixed paraffin-embedded tissue obtained at diagnosis. One patient underwent molecular subgrouping based on frozen tissue.

Imaging Technique

All patients from the discovery cohort underwent brain MR imaging at 1.5 or 3T (Signa or Discovery 750; GE Healthcare, Milwaukee, Wisconsin). We obtained the following sequences: axial and coronal T2 FSE (TR/TE, 2700/100 ms), axial FLAIR (TR/TE, 9000/120 ms; TI, 2200 ms), precontrast T1 spin-echo and contrast-enhanced T1 spoiled gradient-recalled echo (TR/TE, 8/3 ms; 1-mm section thickness, 0 skip), followed by 2 planes of contrast-enhanced T1 spin-echo (TR/TE, 600–700/20 ms; 5-mm section thickness, 0.5 skip). Many, but not all, patients underwent DWI (TR/TE, 8300/70 ms at 1.5T and 10,000/80 ms at 3T; b-value of 1000 s/mm^2; 3 directions; 4-mm thickness, 0 skip) and 2D gradient recalled-echo imaging (TR/TE, 570/30 ms at 1.5T; 700/25 ms at 3T). For the validation cohort, pre- and at least 2-plane postcontrast T1WI obtained at either 1.5T or 3T was used.

Imaging Analysis

Two board-certified radiologists (K.W.Y., J.A. [second-year neuroradiology fellow]) independently reviewed the MR images of the discovery cohort blinded to clinical, pathologic, and molecular data. Consensus for discordant readings was decided between the 2 attending neuroradiologists with Certificates of Added Qualification (K.W.Y. [7 years' experience] and P.B. [>30 years' experience]).

The MR imaging features assessed included the following: tumor location, enhancement pattern, cysts/cavities, hemorrhage/mineralization, intracranial or leptomeningeal seeding, tumor margin, necrosis as suggested by ring-enhancement, and region-of-interest-based ADC analysis, as previously described.[6] Specifically, "tumor location" was defined as midline vermian/fourth ventricle, cerebellar hemisphere, or cerebellar peduncle/cerebellopontine angle cistern (CP/CPA). "Tumor margin" was characterized as ill-defined if >50% of the margin could not be distinguished from the surrounding cerebellar parenchyma on the basis of all imaging sequences. "Enhancement pattern" was defined as minimal/none if <10% was estimated to enhance, solid if >90% of the tumor volume was estimated to enhance, and heterogeneous if varying degrees of enhancement were seen in 10%–90% of the tumor volume on the basis of radiologists' visual assessments. Low signal on 2D gradient recalled-echo was used to detect hemorrhage/mineralization.

For the validation cohort, only the MR imaging features found to be significant by the discovery cohort were used for tumor characterization. Two reviewers (S. Perreault and K.W.Y.) independently performed the imaging analysis blinded to clinical, histologic, and molecular information. Any discrepant reads were further weighed in by a third neuroradiologist (P.B.) for a final consensus read.

Stereospecific Computational Map ("Location Heat Maps")

ROIs outlining the tumor margin were manually drawn in every axial section by using OsiriX Imaging Software (http://www.osirix-viewer.com [A.S.A.]), and proper placement was confirmed by a neuroradiologist (K.W.Y.). All images for each patient were registered to a 1.0-mm isotropic brain atlas (Montreal Neurological Institute) by using a mutual-information algorithm and a transformation algorithm in 3D Slicer (www.slicer.org), followed by visual inspection and a consensus by 2 independent raters (A.S.A., T.T.L.) to ensure optimal alignment.[10] All lateralized medulloblastomas were projected to one side for analysis. After image registration, the resulting transformation matrix was used to map the ROI coordinates to the Montreal Neurological Institute atlas space followed by a second round of visual inspection and consensus by the raters. The frequency of tumor occurrence in each voxel of the Montreal Neurological Institute atlas space was then calculated to create a probabilistic radiographic atlas visualized as 3D heat maps in Slicer and by using FSLView (http://fsl.fmrib.ox.ac.uk/fsl/fslview/).

Neurosurgical Evaluation

Operative reports were independently reviewed by a blinded pediatric neurosurgeon (K.C.). Surgical examinations regarding primary tumor locations and areas of brain invasion were recorded and classified as midline vermian/fourth ventricle, cerebellar hemisphere, or CP/CPA.

Pathologic Evaluation

Hematoxylin-eosin–stained slides of formalin-fixed paraffin-embedded material were analyzed by an independent neuropathologist (H.V.) blinded to radiologic, clinical, or molecular information. Medulloblastomas were categorized according to the 2007 *WHO Classification of Tumors of the Central Nervous System*.[11]

Statistical Analysis

Statistical analyses were performed by using the Fisher exact test and χ^2 analysis for categoric data. A multivariable logistic regression model was developed to identify significant predictors of the medulloblastoma subgroup. We explored potential multicolinearity among the independent variables, examining changes in significance and exploring significant associations among independent variables. Pseudo R-squared goodness of fit ascertained by using the Cox and Snell method (Statistical Package for the Social Sciences Statistics, Version 20.0; IBM, Armonk, New York) was used for the above analyses. NanoString prediction and normalization of data were performed by using the R statistical environment (Version 2.5.1, http://www.r-project.org) as previously described.[9]

Statistical analysis to identify areas of differential involvement consisted of first constructing a contingency table comparing 2 differential phenotypes (eg, WNT versus groups 3 and 4, or SHH versus groups 3 and 4) and the presence of tumor versus no tumor involvement for each image voxel, with a 2-tailed Fisher exact test performed on a voxelwise basis (using the FSL tool Randomize [http://www.fmrib.ox.ac.uk/fsl/randomize/]). The resulting *P* value representing the contingency table (ie, tumor involvement of voxels in a particular phenotype) had <5% probability of occurring by chance. Permutations with the threshold-free cluster enhancement method previously described were applied to correct for multiple comparisons, and a family-wise error rate, to ensure a false discovery rate of <0.05.[12] A total of 3876 unique permutations were performed for an exhaustive test for WNT versus groups 3 and 4, and 10,000 permutations, for SHH versus groups 3 and 4. The resulting corrected *P* value representing tumor involvement of certain voxels in a particular phenotype had <5% false discovery rate, adjusted for multiple comparisons. These significant voxels were visualized by using FSLView.

RESULTS

Histology, Tumor Staging, and Molecular Subgroups

Forty-seven patients met the inclusion criteria and were included in the discovery cohort (Table 1). Median age at diagnosis was 8.2 years (range, 0.9–33.9 years). The 47 medulloblastomas consisted of 31 classic (66%), 10 large-cell/anaplastic (21%), 4 desmoplastic (9%), and 2 other medulloblastoma histologic features (4%).

NanoString assay demonstrated 4 WNT (9%), 13 SHH (28%), 13 group 3 (28%), and 17 group 4 (36%) medulloblastoma molecular subgroups (Table 1 and Fig 1).

MR Imaging Correlates of Molecular Features in the Discovery Cohort

Tumor location was highly predictive of the molecular subgroups (Figs 1 and 2 and On-line Figs 1 and 2). Seventy-five percent of WNT tumors occurred along the CP/CPA. This location was unique to this molecular subgroup ($P < .001$) and was associated with a positive predictive value of 100% (95% CI, 30%–100%). Cerebellar hemispheric location was characteristic of the SHH tumors and accounted for 54% of this molecular subgroup ($P \leq .001$, positive predictive value of 100% [95% CI, 59%–100%]). Groups 3 and 4 were primarily midline and occupied the fourth ventricle (100%, $P < .001$). Tumor location did not significantly differ on the basis of age.

Table 1: Cohort demographics

	Discovery Cohort Stanford (*n* = 47) (%)	Validation Cohort Toronto (*n* = 52) (%)
Sex		
Male	33 (70)	28 (54)
Female	14 (30)	24 (46)
Age (yr)		
Median (range)	8.2 (0.9–33.9)	7.9 (1–1–15.2)
0–3	5 (11)	5 (10)
>3–16	37 (78)	46 (88)
>16	5 (11)	1 (2)
Histology		
LCA	10 (21)	4 (8)
Classic	31 (66)	37 (71)
Desmoplastic	4 (9)	11 (21)
Other	2 (4)	0
Subgroup		
WNT	4 (8)	10 (19)
SHH	13 (28)	11 (21)
Group 3	13 (28)	12 (23)
Group 4	17 (36)	19 (37)

Note:—LCA indicates large-cell anaplastic.

Group 3 was characterized by an ill-defined tumor margin (63%), a feature not present in other subgroups (10%) ($P = .03$). Only 3 other tumors demonstrated ill-defined margins, all in the SHH subgroup. Minimal or no enhancement was characteristic of group 4 medulloblastoma, present in 10 patients (59%) compared with only 2 (7%) for the other subgroups ($P < .001$, positive predictive value of 83% [95% CI, 52%–97%]). Only 1 nonenhancing medulloblastoma belonged to group 3. This feature also distinguished group 4 from group 3 medulloblastomas with a positive predictive value of 91% (95% CI, 59%–98%).

The presence of hemorrhage/mineralization was assessed in 33 (70%) patients who had available 2D gradient recalled-echo sequences but was not found to correlate with specific molecular groups. The other MR imaging features (cysts, peritumoral edema, and tumoral necrosis) were not characteristic of specific molecular subgroups. Twenty-two (47%) patients had available DWI in the discovery cohort (WNT, 2/4; SHH, 8/13; group 3, 5/13; group 4, 7/17). Mean ADC did not significantly differ among the molecular subgroups: WNT, 740×10^{-6} mm^2/s (range, 684–796 mm^2/s); SHH, 714×10^{-6} mm^2/s (range, 655-947 mm^2/s); group 3, 733×10^{-6} mm^2/s (range, 650–847 mm^2/s); group 4, 767×10^{-6} mm^2/s (range, 661–813 mm^2/s).

Stereospecific Computational Map by Molecular Subgroup

Stereospecific computational analyses stratified by molecular subgroup identified group 3 and 4 medulloblastomas occurring predominantly in the midline/fourth ventricle (significant voxels,

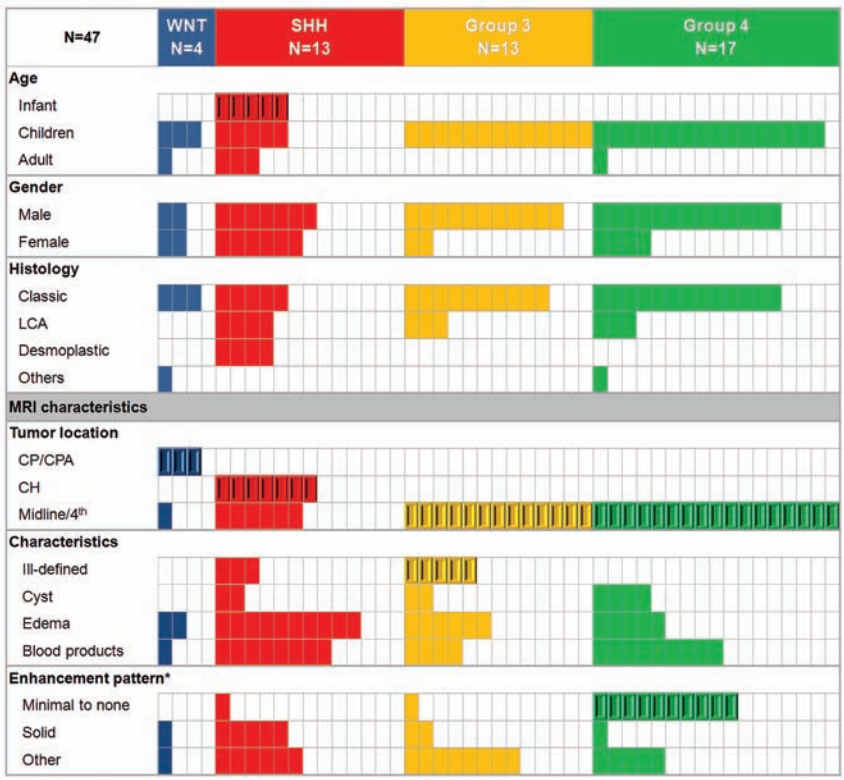

FIG 1. Patient characteristics of the discovery cohort according to the molecular subgroups and MR imaging features. CH indicates cerebellar hemisphere; LCA, large-cell anaplastic; enhancement pattern (*asterisk*), minimal to none, <10% tumor volume; solid, >90% tumor volume. Beveled rectangles represent statistical significance (Fisher exact test [$P < .005$], except for Ill-defined margins [$P = .03$]).

$P = .007$–$.05$; displayed as red in On-line Figs 1 and 2, third column), compared with WNT localization to the CP/CPA (significant voxels, $P = .003$–$.05$; displayed as green in On-line Fig 1, third column) and SHH tumors in the cerebellar hemispheres (significant voxels, $P = .02$–$.05$ after multiple-comparisons correction; blue in On-line Fig 2, third column).

Neurosurgical Findings

Surgical inspection regarding the primary tumor location was 100% concordant with the presurgical MR imaging assessment. The WNT tumors arose in the CP/CPA (75%); cerebellar SHH tumors occurred in the cerebellar hemispheres (23% versus 0% [$P = .02$]), and groups 3 and 4 commonly occurred in the midline/fourth ventricle compared with other subgroups (80% versus 40% [$P = .02$]). Tumor invasion of the brain stem floor/cerebellar peduncle differed among the groups: Adjacent brain invasion occurred in only 1 case of SHH tumor (9%), whereas invasion occurred in 77% for the other subgroups ($P = .001$).

A Model for Determining Tumor Molecular Subgroup Using the Discovery Cohort

Multivariable logistic regression showed that location (CP/CPA, cerebellar hemisphere, and midline/fourth ventricle, [$P < .001$]), pattern of enhancement ($P = .001$), and definition of tumor margin ($P = .01$) were predictors of medulloblastoma subgroups. With the logistic regression model based on location, pattern of enhancement, and tumor margins, 69% of tumors were appropriately classified. The multivariable model demonstrated a goodness of fit as assessed by the pseudo R-squared goodness of fit (Cox and Snell method) of 0.76.

Validation Cohort

There was no significant difference in terms of demographics, histology, and molecular subgroup proportions between the discovery (Stanford Lucile Packard Children's Hospital, $n = 47$ patients) and the validation (Toronto Hospital for Sick Children, $n = 52$ patients) cohorts ($P \geq .05$) (Table 1). T1WI pre- and postgadolinium images were used to address the significant imaging features of tumor location, margin, and enhancement pattern identified by the discovery cohort.

The only predictor from the discovery cohort that was not validated by the validation cohort was the tumor margin, with no significant difference between group 3 and other subgroups ($P = .7$). This variable was then removed from the multivariate model, and predictors, including location and pattern of enhancement, were used to develop a second model. This second multivariable model demonstrated a goodness of fit as assessed by the pseudo R-squared goodness of fit (Cox and Snell method) of 0.67 in the discovery cohort and 0.63 for the validation cohort. When we applied this model, 66% of medulloblastomas were correctly predicted in the discovery cohort, and 65%, in the validation cohort (Table 2 and On-line Fig 3).

DISCUSSION

Several studies have described heterogeneity of medulloblastomas and have related these features to histologic subgroups, age, or prognosis.[6,8] Recently, genomic studies have identified 4 unique molecular subgroups of medulloblastomas (WNT, SHH, group 3, group 4) that are more predictive of clinical behavior and outcome than either tumor histology (classic or "variants" [desmoplastic, large cell/anaplastic, extensive nodularity]) or clinical staging system.[2-4] For example, WNT tumors have shown good prognosis regardless of histology, whereas group 3 tumors have worse survival, independent of metastatic stage.[2,13]

The benefits of translating this information into the clinical arena are numerous, given the significant neurotoxic effects of current therapy.[14,15] For example, the low-risk molecular WNT medulloblastoma group could be stratified to surgery and chemotherapy only, without radiation that poses significant risk for cognitive impairment in children, while high-risk medulloblastoma molecular groups (groups 3 and 4) could require multimodal therapies and more frequent tumor monitoring; they would be ideal candidates for new targeted experimental therapies in clinical trials. As noted by Robinson[16] in a commentary letter, while

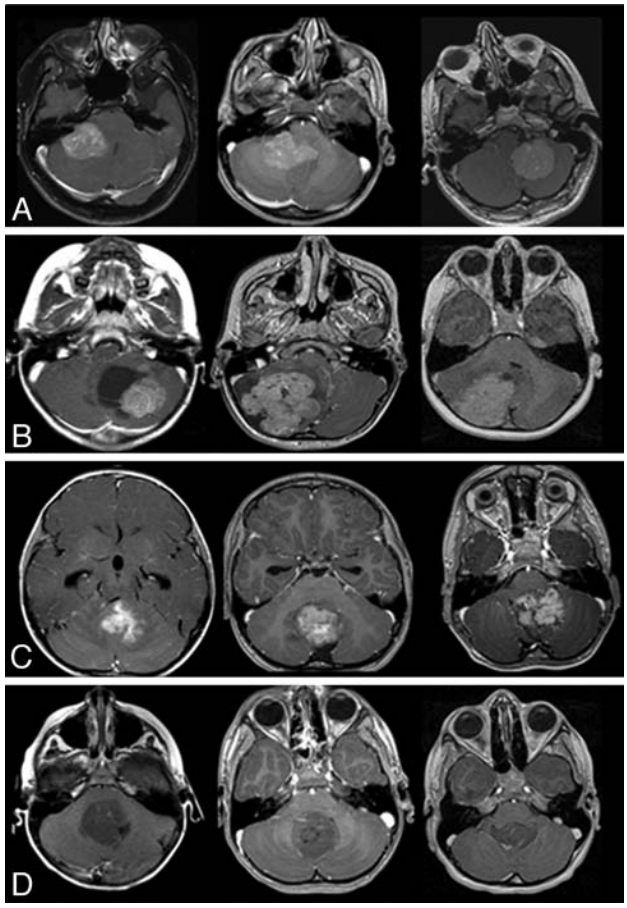

FIG 2. Characteristic MR imaging features according to medulloblastoma molecular subgroups. *A*, In the top row, characteristic location of WNT tumors in the CP/CPA region is shown. *B*, In the second row, SHH tumors are predominantly located in the cerebellar hemispheres. *C*, In the third row, group 3 tumors are located in the midline/fourth ventricle and show enhancement and ill-defined features against the adjacent brain parenchyma. *D*, In the fourth row, group 4 tumors are also located in the midline fourth ventricle but tend to show minimal or no enhancement.

no single tumor feature should be used alone to determine tumor subtype or tailor treatment, MR imaging can offer additional opportunities. Because MR imaging is already universally used in brain tumor diagnosis, identifying MR imaging correlates of molecular subgroups could further assist in this endeavor and play a key role when access to molecular analysis is limited.

This is the largest comprehensive study to investigate MR imaging correlates of molecular subgroups of medulloblastoma. Tumor location and pattern of gadolinium enhancement were found to be predictive; by using a regression model, most medulloblastoma molecular subgroups were accurately identified. Furthermore, our model was validated by an independent cohort from a second institution.

Using the NanoString assay, we were able to classify our medulloblastoma cohort into 4 recently established molecular subgroups.[2,4] Overall, our cohort recapitulated previously described distinct clinical features of each molecular group.[2,4] We observed that SHH tumors accounted for more infants, most adults, and females. Group 3 most commonly presented with metastases at diagnosis; and desmoplastic tumors exclusively belonged in the SHH subgroup.[17]

Table 2: Percentage correct with the model when applied to the discovery cohort and validation cohort

Medulloblastoma Subgroups	Percentage Correct in Discovery Cohort	Percentage Correct in Validation Cohort
Total	66%	65%
WNT	75%	50%
SHH	54%	73%
Group 3	92%	83%
Group 4	59%	58%

According to our model, location was a key feature predictive of molecular subgroup. Our MR imaging–based tumor location was also confirmed by surgical examination. Most WNT tumors arose in the CP/CPA, SHH most commonly involved the cerebellar hemispheres, and groups 3 and 4 were midline, filling the fourth ventricle.

Prior studies have shown that desmoplastic medulloblastomas frequently showed SHH molecular features and tended to involve the cerebellar hemispheres, especially in adults,[4,18,19] though figures have ranged from 17% to 100%, depending on the clinical inclusion criteria used in these various studies.[8,18-22] A cerebellar hemispheric location of SHH medulloblastomas is consistent with the results of the mouse models that have shown SHH tumor origin from committed granule neuron precursors of the cerebellum.[23,24] While studies have also suggested that SHH tumors could arise from the cochlear nucleus in the brain stem in younger patients,[25] we did not observe a difference in SHH tumor location between infants and older patients. Our results are also consistent with a study by Teo et al,[26] which reported cerebellar hemispheric involvement in 9 of 17 (53%) SHH medulloblastomas regardless of age at diagnosis. In our study, SHH rarely invaded the brain stem, consistent with a prior study that reported brain stem infiltration by WNT but not SHH tumors.[22]

However, our results of WNT tumors differ from those of Teo et al[26] in that while midline location was described for all 5/5 WNT tumors in that study, most of the WNT tumors in our study involved the CP/CPA (8/14). In another study, Gibson et al[22] reported 6/6 WNT tumors to be midline but infiltrating the dorsal brain stem. Discrepancies among these studies could be attributed to the small sample sizes. Alternatively, tumors that have cerebellar peduncle origin or involvement may have a "midline" appearance, particularly if they are protruding medially. Previously, Jaiwal et al[27] described CP/CPA tumor location in 14 of 140 (10%) medulloblastomas. While molecular analysis was not performed in that study, it would be interesting to test these tumors for the WNT pathway because this figure approximates overall prevalence of WNT tumors.[2] While we acknowledge that some WNT tumors are midline, we report that a significant percentage of these tumors involve the CP/CPA, which is a unique feature for this subtype.

A significant percentage of medulloblastomas present minimal or no enhancement.[6,8] Rare cases of hemispheric desmoplastic medulloblastoma have shown this feature as well.[18] In our study, nonenhancing tumors in the midline/fourth ventricle location were characteristic of group 4 medulloblastomas. This is an important observation because groups 3 and 4 are currently not well-differentiated by using immunohistochemistry markers.[2,5] The reason for the lack of enhancement in a significant subset of

group 4 tumors remains unknown, but molecular changes associated with vascular permeability might be involved.

We did not find a correlation between molecular subgroups and other MR imaging features in our discovery cohort. A prior study showed that ring enhancement/necrosis and higher mean ADC were more characteristic of large-cell/anaplastic medulloblastoma than classic medulloblastoma.[6] This finding could be explained by the fact that large-cell/anaplastic histology can be present in 3 different molecular subgroups (group 3, group 4, and SHH),[2,17] or even in WNT tumors.[13] Tumor margin against the brain parenchyma was a useful predictor in our discovery but not in the validation cohort. However, evaluation of tumor margins was significantly limited because only pre- and postcontrast T1WI were uniformly available in our validation cohort, without a complete MR imaging dataset inclusive of multiplanar T2WI (axial and coronal), FLAIR, and thin-section presurgical or spoiled gradient-recalled echo sequences in the discovery cohort. The definition of margins could have been either under- or overestimated, thereby potentially limiting its usefulness. Because this feature could not be used in our validation cohort, the first model could not be tested. A new model from our discovery cohort without this limiting feature was developed. Our final algorithm was, therefore, influenced by our discovery cohort but only because one of the features could not be tested.

This study was also limited by its retrospective nature. Some heterogeneity in imaging protocols reduced the sample size for some components of our analysis. For example, features such as mean ADC and hemorrhage/mineralization did not show a significant difference between subgroups in our exploratory cohort, but type II errors remain possible. To overcome such limitations, our plan includes a multicenter prospective study.

CONCLUSIONS

MR imaging features of tumor location and enhancement pattern were correlated with specific molecular subgroups of medulloblastoma and were validated by an independent cohort. This study represents an important step in using MR imaging as a surrogate to predict molecular subgroups of medulloblastoma. Future study that incorporates quantitative MR imaging signatures including perfusion, MR spectroscopy, high-order diffusion, and susceptibility metrics, could add insight into formulating a more robust radiogenomics model for medulloblastoma.

ACKNOWLEDGMENTS

We thank Drs Patrick D. Barnes, Jalal B. Andre, and Lex A. Mitchell for their work on tumor imaging annotations and DICOM data extraction, Amarjeet Grenwall and Dory Palacio for their help in tissue processing, and Dr Patryk Skowron for his involvement in NanoString-based assays.

Disclosures: Sébastien Perreault—*RELATED*: fellowship grants from Fonds de la Recherche en Santé du Québec and Irma-Levasseur. Vijay Ramaswamy—*RELATED*: clinical fellowships from the Canadian Institutes of Health and Alberta Innovates Health Solutions, providing salary support for work both related and unrelated to the current work. He also discloses the Canadian Cancer Society Research Institute travel award, to attend the International Society of Paediatric Oncology 2013 meeting in Hong Kong. Eric Bouffet—*RELATED*: grant support from the Medulloblastoma Advanced Genomics International Consortium (Principal Investigator: Dr Michael Taylor).* Paul Fisher—*UNRELATED*: payment for teaching lectures in general neurology for the American Academy of Pediatrics. He is also an associate editor on the *Journal of Pediatrics*, a paid position with Elsevier. Yoon-Jae Cho—*UNRELATED*: honoraria for grand rounds lectures at St. Jude, Memorial Sloan Kettering Cancer Center, and Texas Children's. *Money paid to the institution.

REFERENCES

1. Partap S, Curran EK, Propp JM, et al. **Medulloblastoma incidence has not changed over time: a CBTRUS study.** *J Pediatr Hematol Oncol* 2009;31:970–71
2. Northcott PA, Korshunov A, Witt H, et al. **Medulloblastoma comprises four distinct molecular variants.** *J Clin Oncol* 2011;29:1408–14
3. Taylor MD, Northcott PA, Korshunov A, et al. **Molecular subgroups of medulloblastoma: the current consensus.** *Acta Neuropathol* 2012;123:465–72
4. Cho YJ, Tsherniak A, Tamayo P, et al. **Integrative genomic analysis of medulloblastoma identifies a molecular subgroup that drives poor clinical outcome.** *J Clin Oncol* 2011;29:1424–30
5. Ellison DW, Dalton J, Kocak M, et al. **Medulloblastoma: clinicopathological correlates of SHH, WNT, and non-SHH/WNT molecular subgroups.** *Acta Neuropathol* 2011;121:381–96
6. Yeom KW, Mobley BC, Lober RM, et al. **Distinctive MRI features of pediatric medulloblastoma subtypes.** *AJR Am J Roentgenol* 2013;200:895–903
7. Koeller KK, Rushing EJ. **From the archives of the AFIP: medulloblastoma: a comprehensive review with radiologic-pathologic correlation.** *Radiographics* 2003;23:1613–37
8. Fruehwald-Pallamar J, Puchner SB, Rossi A, et al. **Magnetic resonance imaging spectrum of medulloblastoma.** *Neuroradiology* 2011;53:387–96
9. Northcott PA, Shih DJ, Remke M, et al. **Rapid, reliable, and reproducible molecular sub-grouping of clinical medulloblastoma samples.** *Acta Neuropathol* 2012;123:615–26
10. Johnson HJ, Harris G, Williams K. **BRAINSFit: mutual information registrations of whole-brain 3D images, using the insight toolkit.** *The Insight Journal* 2007, July-December
11. Louis DN, Ohgaki H, Wiestler CD, et al, eds. *WHO Classification of Tumours of the Central Nervous System.* Lyon: The International Agency for Research on Cancer; 2007
12. Smith SM, Nichols TE. **Threshold-free cluster enhancement: addressing problems of smoothing, threshold dependence and localisation in cluster inference.** *Neuroimage* 2009;44:83–98
13. Ellison DW, Onilude OE, Lindsey JC, et al. **beta-Catenin status predicts a favorable outcome in childhood medulloblastoma: the United Kingdom Children's Cancer Study Group Brain Tumour Committee.** *J Clin Oncol* 2005;23:7951–57
14. Crossen JR, Garwood D, Glatstein E, et al. **Neurobehavioral sequelae of cranial irradiation in adults: a review of radiation-induced encephalopathy.** *J Clin Oncol* 1994;12:627–42
15. Dennis M, Spiegler BJ, Hetherington CR, et al. **Neuropsychological sequelae of the treatment of children with medulloblastoma.** *J Neurooncol* 1996;29:91–101
16. Robinson GW. **Impact of tumor location on medulloblastoma subtyping and treatment.** *Pediatr Blood Cancer* 2013;60:1393–94
17. Northcott PA, Korshunov A, Pfister SM, et al. **The clinical implications of medulloblastoma subgroups.** *Nat Rev Neurol* 2012;8:340–51
18. Malheiros SM, Carrete H Jr, Stavale JN, et al. **MRI of medulloblastoma in adults.** *Neuroradiology* 2003;45:463–67
19. Menon G, Krishnakumar K, Nair S. **Adult medulloblastoma: clinical profile and treatment results of 18 patients.** *J Clin Neurosci* 2008;15:122–26
20. Bourgouin PM, Tampieri D, Grahovac SZ, et al. **CT and MR imaging findings in adults with cerebellar medulloblastoma: comparison with findings in children.** *AJR Am J Roentgenol* 1992;159:609–12
21. Bühring U, Strayle-Batra M, Freudenstein D, et al. **MRI features of primary, secondary and metastatic medulloblastoma.** *Eur Radiol* 2002;12:1342–48

22. Gibson P, Tong Y, Robinson G, et al. **Subtypes of medulloblastoma have distinct developmental origins.** *Nature* 2010;468:1095–99
23. Schüller U, Heine VM, Mao J, et al. **Acquisition of granule neuron precursor identity is a critical determinant of progenitor cell competence to form Shh-induced medulloblastoma.** *Cancer Cell* 2008;14:123–34
24. Yang ZJ, Ellis T, Markant SL, et al. **Medulloblastoma can be initiated by deletion of Patched in lineage-restricted progenitors or stem cells.** *Cancer Cell* 2008;14:135–45
25. Grammel D, Warmuth-Metz M, von Bueren AO, et al. **Sonic hedgehog-associated medulloblastoma arising from the cochlear nuclei of the brainstem.** *Acta Neuropathol* 2012;123:601–14
26. Teo WY, Shen J, Su JM, et al. **Implications of tumor location on subtypes of medulloblastoma.** *Pediatr Blood Cancer* 2013;60:1408–10
27. Jaiswal AK, Mahapatra AK, Sharma MC. **Cerebellopointine angle medulloblastoma.** *J Clin Neurosci* 2004;11:42–45

Are We Effectively Informing Patients? A Quantitative Analysis of On-Line Patient Education Resources from the American Society of Neuroradiology

D.R. Hansberry, N. Agarwal, S.F. Gonzales, and S.R. Baker

ABSTRACT

BACKGROUND AND PURPOSE: The ubiquitous use of the Internet by the public in an attempt to better understand their health care requires the on-line resources written at an appropriate level to maximize comprehension for the average user. The National Institutes of Health and the American Medical Association recommend on-line patient education resources written at a third-to-seventh grade level. We evaluated the readability of the patient education resources provided on the Web site of the American Society of Neuroradiology (http://www.asnr.org/patientinfo/).

MATERIALS AND METHODS: All patient education material from the ASNR Web site and the Society of Neurointerventional Surgery Web site were downloaded and evaluated with the computer software, Readability Studio Professional Edition, by using 10 quantitative readability scales: the Flesch Reading Ease, Flesch-Kincaid Grade Level, Simple Measure of Gobbledygook, Coleman-Liau Index, Gunning Fog Index, New Dale-Chall, FORCAST Formula, Fry Graph, Raygor Reading Estimate, and New Fog Count. An unpaired *t* test was used to compare the readability level of resources available on the American Society of Neuroradiology and the Society of Neurointerventional Surgery Web sites.

RESULTS: The 20 individual patient education articles were written at a 13.9 ± 1.4 grade level with only 5% written at <11th grade level. There was no statistical difference between the level of readability of the resources on the American Society of Neuroradiology and Society of Neurointerventional Surgery Web sites.

CONCLUSIONS: The patient education resources on these Web sites fail to meet the guidelines of the National Institutes of Health and American Medical Association. Members of the public may fail to fully understand these resources and would benefit from revisions that result in more comprehensible information cast in simpler language.

ABBREVIATIONS: AMA = American Medical Association; ASNR = American Society of Neuroradiology; CLI = Coleman-Liau Index; FKGL = Flesch-Kincaid Grade Level; FRE = Flesch Reading Ease; GFI = Gunning Fog Index; NDC = New Dale-Chall; NFC = New Fog Count; RRE = Raygor Reading Estimate; SMOG = Simple Measure of Gobbledygook; SNIS = Society of Neurointerventional Surgery

Easy accessibility and a seemingly unlimited supply of information on the Internet have made it a frequently accessed resource by the public. In fact, almost 80% of Americans are regularly on-line and up to 80% of them consult the Internet for information on health-related topics.[1,2] Patients and their families are most apt to seek Internet materials about a new diagnosis, the side effects of medications, a diagnostic or therapeutic procedure, or other treatment options.[3] The Internet is often accessed both before and after an initial visit to a health care provider. Perhaps not surprising, patients tend to value the Internet information. In one study, it was reported as the second most important resource, superseded in value only by consulting information coming directly from the physician.[4] As a result of the known importance of on-line health care information, many organizations have published Internet-based resources pitched specifically to patients.

However, by itself the delivery of health care–related information does not necessarily mean that the patient or his or her family will comprehend it. The American Medical Association has noted that the average American reads at only an eighth grade level, while those enrolled in Medicaid read at an even lower fifth grade level.[5] Limited health literacy, in particular, can be a barrier to

Received October 1, 2013; accepted after revision November 4.

From the Departments of Radiology (D.R.H., S.F.G., S.R.B.) and Neurological Surgery (N.A.), New Jersey Medical School, University of Medicine and Dentistry of New Jersey, Newark, New Jersey.

An abstract for this paper was accepted at: Annual Meeting of the American Society of Neuroradiology, May 17–22, 2014, Montreal, Canada, under the title "Online patient resources—the readability of neuroradiology-based education materials."

Please address correspondence to Stephen R. Baker, MD, Department of Radiology, New Jersey Medical School, Rutgers, The State University of New Jersey, 150 Bergen St, Room C320, Newark, NJ 07101-1709; e-mail: bakersr@njms.rutgers.edu

Indicates article with supplemental on-line table.

http://dx.doi.org/10.3174/ajnr.A3854

care, leaving patients with inadequate knowledge for making informed health care decisions.[6] Several studies have shown that limited health literacy has been associated with poor understanding of relatively simple instructions.[7-9] These studies found that of those with limited health literacy, 26% did not know when their next appointment was scheduled, 42% did not understand what it meant by "take medication on an empty stomach," and 86% did not understand the Medicaid application rights and responsibilities section.[7-9] A 2003 report from the American Medical Association (AMA) that evaluated the health literacy of adults found that those who did not graduate high school, those older than 65 years of age, Hispanic adults, black adults, those who did not speak English before starting school, those without medical insurance, those with disabilities, and prison inmates were more likely to have below-basic health literacy.[10] In an effort to broaden the reach of patient education materials, the AMA and the National Institutes of Health have recommended that they be written at a third-to-seventh grade level.[5,11]

Despite these guidelines, many of the Web sites of several national physician organizations, including medical, surgical, and subspecialty fields, have provided texts at a level too complex for most of the public to comprehend.[12-23] Recent reports that evaluate the readability of patient education resources on radiology Web sites, sponsored by major organizations such as the Radiological Society of North America, the American College of Radiology, the Society of Interventional Radiology, and the Cardiovascular and Interventional Radiologic Society of Europe, demonstrated that the material offered to the public is written at a level well above the AMA and the National Institutes of Health recommendations.[24,25]

In this study, we investigated the level of readability of all patient education resources on the American Society of Neuroradiology (ASNR) Web site by using a variety of quantitative readability-assessment scales. Additionally, we analyzed patient education resources from the Society of Neurointerventional Surgery (SNIS) Web site because the ASNR patient education Web site has links directly to the SNIS site.

MATERIALS AND METHODS

In September 2013, all patient education material available on the ASNR (http://www.asnr.org/patientinfo/) and SNIS (http://snisonline.org/patient-center) Web sites were downloaded into Microsoft Word (Microsoft Corporation, Redmond, Washington). Copyright information, references, and images were removed from the text. The ASNR Web site had 17 articles, which were subdivided into 3 categories: neuroradiology, procedures, and conditions. The patient education on the SNIS Web site was directly referenced from the ASNR Web site and included 3 additional articles. All 20 articles were individually analyzed for their level of readability, with 10 different quantitative readability scales by using the software program Readability Studio Professional Edition, Version 2012.1 (Oleander Software, Vandalia, Ohio). The readability scales included the Flesch Reading Ease (FRE),[26] Flesch-Kincaid Grade Level (FKGL),[27] Simple Measure of Gobbledygook (SMOG),[28] Coleman-Liau Index (CLI),[29] Gunning Fog Index (GFI),[30] New Dale-Chall (NDC),[31] FORCAST Formula,[32] Fry Graph,[33] Raygor Reading Estimate (RRE),[34] and the New Fog Count (NFC).[27] The FRE readability scale reports scores from 0 to 100, with higher scores indicating more readable text (Table 1). The 9 additional readability scores report a number that corresponds to an academic grade level (On-line Table).

Table 1: The FRE readability scale scoring system

FRE Score	Readability
0–30	Very difficult
30–50	Difficult
50–60	Fairly difficult
60–70	Standard
70–80	Fairly easy
80–90	Easy
90–100	Very easy

The 9 readability scales that report scores corresponding to an academic grade level were compared with a 1-way ANOVA test. A Tukey Honestly Statistically Different post hoc analysis was conducted for all ANOVA results with a $P < .05$. Additionally, the patient education material available on the ASNR and SNIS Web sites was compared by using an unpaired *t* test. Statistical analysis was performed by using OriginPro (OriginLab, Northampton, Massachusetts).

RESULTS

The FRE found that collectively, the 20 articles were written at a difficult (30–50) level, given its score of 34.9 ± 12.9 (Fig 1 and Table 2). The 9 other readability scales (CLI, NDC, FKGL, FORCAST Formula, Fry Graph, GFI, NFC, RRE, and SMOG) determined the readability of all 20 articles to be at the 13.9 ± 1.4 grade level. Individually, the 9 scales found the level of readability to range from the 11.4 (FORCAST Formula) grade level to the 15.5 (both the GFI and SMOG) grade level (Fig 1 and Table 2). Only one (5%) of the articles, which was on MRI, was written below the 11th grade level, and it was still difficult text to understand with a readability score at the 10.3 grade level (Fig 1 and Table 2). According to assessments using the NFC, CLI, NDC, and RRE scales, the material was written at the 12.4 ± 2.9, 13.2 ± 2.0, 13.8 ± 1.8, and 13.9 ± 2.5 grade levels, respectively (Fig 1 and Table 2). Analysis with the FKGL and Fry Graph revealed the patient education material to be even more difficult, with scores at the 14.1 ± 2.6 and 15.2 ± 2.0 grade levels, respectively (Fig 1 and Table 2). Only 3 articles (15%) were written at a level appropriate for viewers who had some level of high school education (10.3, 11.2, and 12.0 grade levels) (Table 2). Most of the articles, 65% (13/20), were written for a reader with some level of college education (12.3–15.0 grade levels), while 20% (4/20) were written for someone with a graduate level of education (16.2–16.9 grade levels) (Table 2). There was no statistical difference between the patient education materials found on the ASNR Web site and those provided by the SNIS Web site (Fig 2).

There was no statistical difference ($P = .69$) between the level of difficulty of the patient education material when comparing the ASNR and SNIS Web sites as assessed by the FRE readability scale. Furthermore, there was no difference ($P = .27$) between these Web sites as assessed by the 9 other readability scales. The 1-way ANOVA demonstrated a statistical difference in the average readability reported among the 9 readability scales, $F(8,171) = 8.59$, $P = .0001$. The Tukey Honestly Statistically Different post hoc analysis

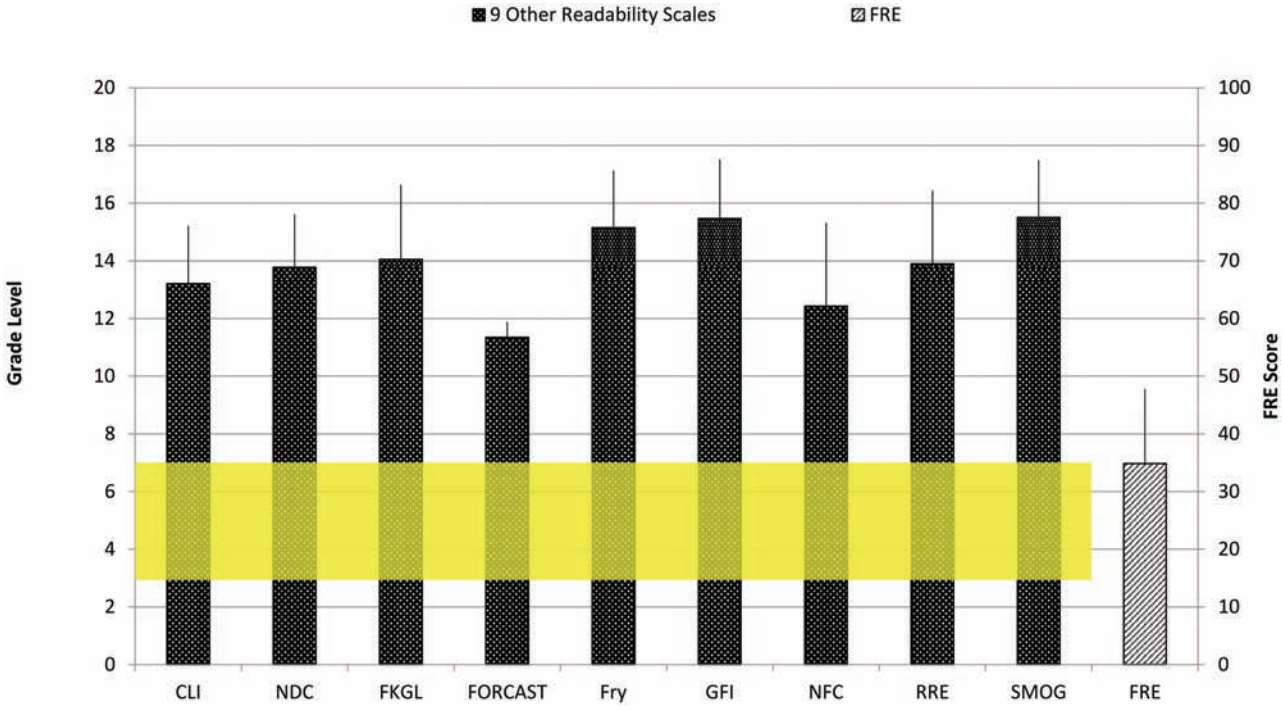

FIG 1. The readability of all the articles as measured individually by the 10 readability scales. The 9 other readability scales include the CLI, NDC, FKGL, FORCAST Formula, Fry Graph, GFI, NFC, RRE, and SMOG; and their grade level is measured on the left y-axis (Grade Level). The FRE score is measured on the right y-axis (FRE Score). The yellow area corresponds to the grade level recommendations from the National Institutes of Health and the AMA. FRE scores of 0–30 indicate the patient education resources are very difficult, 30–50 are difficult, 50–60 are fairly difficult, 60–70 are standard, 70–80 are fairly easy, 80–90 are easy, and 90–100 are very easy.

Table 2: The level of readability of each patient education article as measured by the 10 individual readability assessment scales

Document	Web Site	FRE	CLI	NDC	FKGL	FORCAST	Fry	GFI	NFC	RRE	SMOG	Avg	SD
About neurointerventions	SNIS	22	15.8	16	18.6	11.8	16	19	19	17	19	16.9	2.4
Acute stroke	SNIS	50	11.6	14	12.4	10.2	12	13.8	11.9	13	14.5	12.6	1.4
Aneurysms	SNIS	41	13.1	14	13	11.3	15	15.5	11.9	13	15.3	13.6	1.5
Alzheimer disease	ASNR	33	13.3	14	14.6	11.7	16	16.2	14.1	17	16	14.8	1.7
Brain tumor	ASNR	39	12.2	14	14	11.1	14	15.2	13.3	12	15.1	13.4	1.4
CT	ASNR	44	11.3	11.5	11.7	11.2	14	13.9	10.1	11	13.7	12.0	1.4
Headache	ASNR	29	14.2	14	14.9	11.8	17	15.7	11.6	17	15.6	14.6	2.0
Hearing loss	ASNR	51	10.8	11.5	11.3	10.3	11	12.5	9.7	11	13.1	11.2	1.0
Is CT safe for my child?	ASNR	25	12.9	16	18	11.3	17	14	11.4	13	18.1	14.6	2.7
MR angiography	ASNR	43	12.3	11.5	11.1	11.2	16	14.2	9.1	12	13.5	12.3	2.0
MRI	ASNR	54	10.2	9.5	9.8	10.8	11	11.7	8.5	9	12	10.3	1.2
Multiple sclerosis	ASNR	29	13.5	16	16.9	11.4	16	19	18.9	17	17.6	16.3	2.5
Myelography	ASNR	40	12.4	14	13.7	11.3	14	16.1	14.4	13	15.1	13.8	1.4
Percutaneous vertebroplasty	ASNR	41	13.5	14	11.7	11.6	17	13.4	8.9	13	13.2	12.9	2.2
Should I be concerned about radiation?	ASNR	16	15.1	16	16.1	12.2	17	19	15.4	17	17.9	16.2	1.9
Sinusitis	ASNR	36	12.1	14	13.9	11.3	16	15.7	13.3	13	15.6	13.9	1.6
Stroke	ASNR	42	12.8	11.5	12.4	11	14	14.5	11.2	13	14.3	12.7	1.3
Traumatic brain injury and concussion	ASNR	37	12.6	14	13.2	11.4	16	16.2	12.3	13	15.3	13.8	1.7
What is neuroradiology?	ASNR	0	19	16	19	12.3	17	16.6	11.6	17	19	16.4	2.8
Why subspecialty medicine?	ASNR	25	15.6	14	14.7	11.8	17	17.1	11.9	17	16.1	15.0	2.1

Note:—Avg indicates average; FORCAST, FORCAST Formula; Fry, Fry Graph.

found real differences with the CLI (13.2 ± 2.0 grade level) and the GFI (15.5 ± 2.1 grade level) and SMOG (15.5 ± 2.0 grade level) scales. It also found differences among the FORCAST Formula (11.4 ± 0.5 grade level) and the Fry Graph (15.2 ± 2.0 grade level), GFI (15.5 ± 2.1 grade level), NDC (13.8 ± 1.8 grade level), RRE (13.9 ± 2.5 grade level), SMOG (15.5 ± 2.0 grade level), and FKGL(14.1 ± 2.6 grade level). Last, it found differences between the NFC (12.4 ± 2.9 grade level) and the GFI (15.5 ± 2.1 grade level) and SMOG (15.5 ± 2.0 grade level) and Fry Graph (15.2 ± 2.0 grade level) scales. Despite these statistical differences among some of the readability scales, all patient education resources available on the ASNR and SNIS sites were still written at advanced levels above the National Institutes of Health and AMA recommendations.

DISCUSSION

Each of the patient education resources from the ASNR and SNIS Web sites failed to meet the AMA and the National Institutes of Health guidelines recommending a seventh grade level of read-

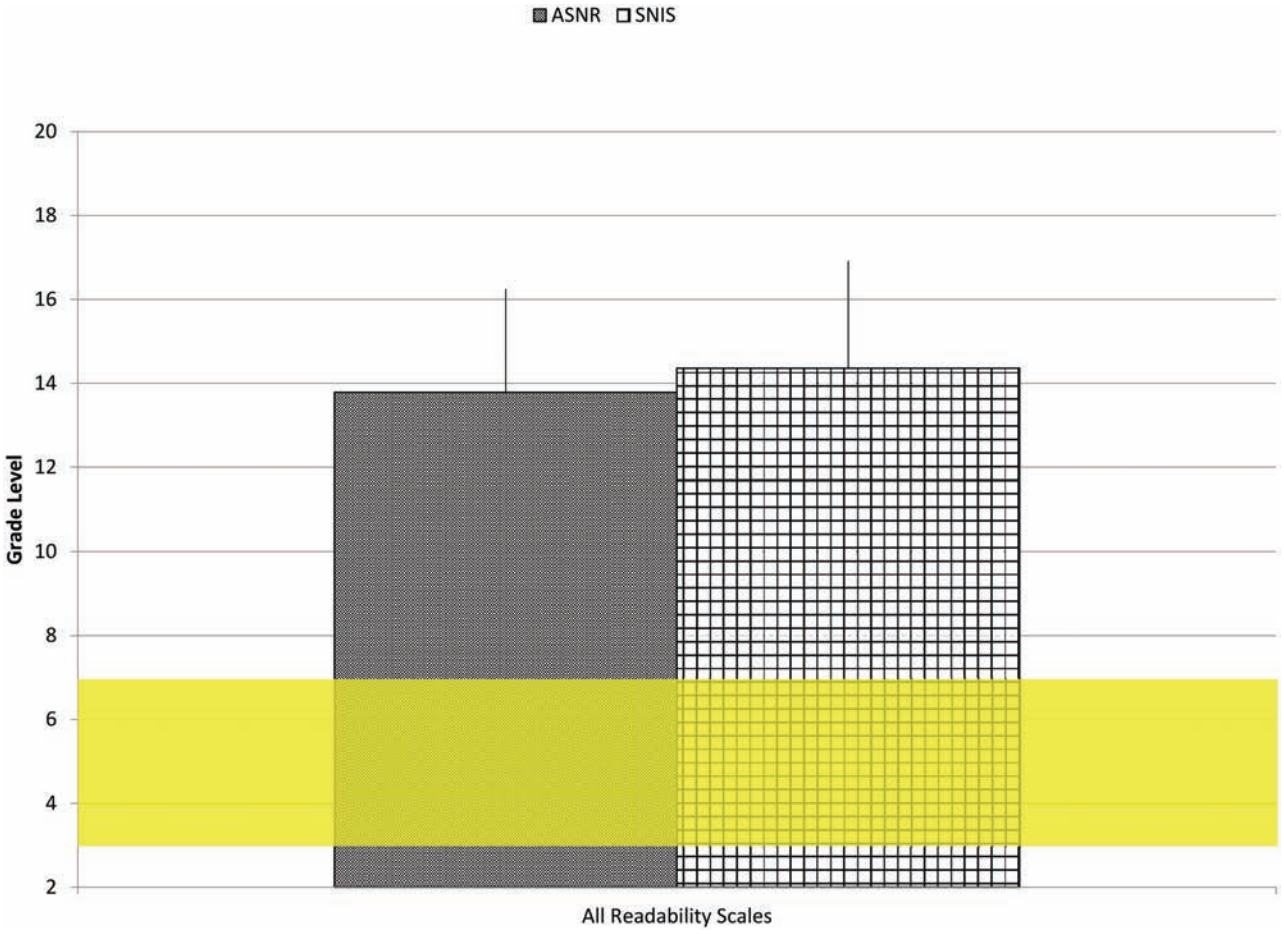

FIG 2. The readability of all articles from both the ASNR and SNIS patient education Web sites as measured by the 9 readability scales that correspond to academic grade level (CLI, NDC, FKGL, FORCAST Formula, Fry Graph, GFI, NFC, RRE, and SMOG). The yellow area corresponds to the grade level recommendations from the National Institutes of Health and the AMA.

ability. This finding held true regardless of the readability scale used. Furthermore, the readability assessment scales determined that the overwhelming majority, 85%, of the material was written at the college level or higher. The complex nature of the textual narratives provided by the ASNR and SNIS will likely hinder widespread understanding of the material by the public. Their narrative complexity may prevent effective transmission of health care information. These discrepancies in content versus intent are not a new phenomenon inasmuch as other Web sites have been shown to have a disjunction between the level of complexity of their patient education materials and the ability of the average reader to understand them.[13-15,20,23-25] A recent article from *JAMA Internal Medicine* revealed that 16 major national physician organizations had Web sites that presented patient education materials above the AMA and National Institutes of Health guidelines.[22] That study did note that one organization had marginally acceptable levels of readability of their resources (American Academy of Family Physicians), meeting the AMA and the National Institutes of Health guidelines on some but not all readability scales.[22]

Approximately 70% of patients have said that the on-line information they review has impacted their health care decisions.[35] In an effort to better help these patients make informed health care decisions, it is critical to revise current on-line resources so they are in accord with the capabilities of the consumers of the material. The AMA, National Institutes of Health, and Centers for Disease Control and Prevention have developed instructional guidelines on various ways to compose patient education narratives at or below a seventh grade level.[5,11,36] Web site developers may also benefit from consulting organizations such as the Institute for Healthcare Improvement (www.ihi.org) when developing patient education resources for the Internet.

Specific suggestions for improvement include the following: 1) Simple identifying methods, such as using bold type to emphasize major terms and categories, can facilitate patient comprehension.[37] 2) Using a font size between 12 and 14 points and avoiding all capital letters, italics, and nontraditional fonts can augment patient use of the Web site material.[38] 3) Avoiding the use of medical terminology, unless absolutely necessary, could improve patient comprehension as well.[39] 4) A major tool is the use of videos. A study on the implementation of videos for patients with breast cancer undergoing surgery showed that those who viewed educational videos, despite low education levels, lack of insurance, unemployment, and cultural diversity, were still able to score >80% on questionnaires.[40] When constructing these videos, one should also tailor the message to patients by including an introduction addressing the purpose of the video and how it can personally assist in their decision-making processes.[41] 5) Further-

more, the use of stories and pictures, which are often more memorable than statistics and recommendations, can help alleviate patient fears and address their emotional states.[42] Recent studies have demonstrated that pictorial aids enhance a patient's recall, comprehension, and adherence to treatments.[43] For individuals who perhaps understand the basic information and desire more advanced resources, links to scientific information could be provided.[44]

While the textual materials on the ASNR and SNIS Web sites demonstrate a high level of readability, there are likely other factors that contribute to understanding of patient education materials. Perhaps most important, as mentioned above, the use of images and videos can enhance the material and likely improve the reader's comprehension.[40-42] The impact of multimedia needs to be further studied to determine its impact on patients. Additionally, terminology related to neuroradiology is often complex. This may lead to unavoidably high readability scores. There are important limitations of this study. It is still imperative to address the complexity of the current text to improve its potential for patient appreciation. Goals for future work include evaluation of real patients to determine their understanding and comprehension of such resources.

CONCLUSIONS

Patient education resources available on the ASNR and SNIS Web sites are written well above the AMA and National Institutes of Health guidelines. Such information should be revised to the third-to-seventh grade reading levels. To achieve greater comprehension by the average Internet viewer, modification of this material into a simpler, easier-to-read format, would expand the population who could benefit from the information related to neuroradiology, its diagnostic procedures, and common conditions in which neuroradiology plays a vital role.

REFERENCES

1. Fox S. The Social Life of Health Information, 2011. http://www.pewinternet.org/~/media/Files/Reports/2011/PIP_Social_Life_of_Health_Info.pdf. Accessed September 1, 2013
2. Internet & American Life Project. Demographics of internet users. Pew Research Center; 2011. http://pewinternet.org/~/media/Files/Reports/2012/PIP_Digital_differences_041312.pdf. Accessed September 1, 2013
3. Fox S, Rainie L. Vital Decisions. Pew Internet & American Life Project; 2002. http://www.pewinternet.org/Reports/2002/Vital-Decisions-A-Pew-Internet-Health-Report.aspx. Accessed September 1, 2013
4. Diaz JA, Griffith RA, Ng JJ, et al. **Patients' use of the Internet for medical information.** *J Gen Intern Med* 2002;17:180–85
5. Weis BD. *Health Literacy: A Manual for Clinicians.* Chicago: American Medical Association, American Medical Foundation; 2003
6. Kutner M, Greenberg E, Jin Y, et al. *The Health Literacy of America's Adults: Results From the 2003 National Assessment of Adult Literacy (NCES 2006-483).* Washington, DC: National Center for Education Statistics; 2006
7. Williams MV, Parker RM, Baker DW, et al. **Inadequate functional health literacy among patients at two public hospitals.** *JAMA* 1995;274:1677–82
8. Baker D, Parker R, Williams MV, et al. **The health care experience of patients with low literacy.** *Arch Fam Med* 1996;5:329–34
9. Potter L, Martin C. Health Literacy Fact Sheets. Lawrenceville, New Jersey: Center for Health Care Strategies, 2013. http://www.chcs.org/usr_doc/CHCS_Health_Literacy_Fact_Sheets_2013.pdf. Accessed August 18, 2013
10. White S. *Assessing the Nation's Health Literacy: Key Concepts and Findings of the National Assessment of Adult Literacy (NAAL).* Chicago: AMA Foundation; 2008
11. National Institutes of Health. How to Write Easy-to-Read Health Materials. http://www.nlm.nih.gov/medlineplus/etr.html. Accessed July 1, 2013
12. Colaco M, Svider PF, Agarwal N, et al. **Readability assessment of online urology patient education materials.** *J Urol* 2013;189:1048–52
13. Eloy JA, Li S, Kasabwala K, et al. **Readability assessment of patient education materials on major otolaryngology association Websites.** *Otolaryngol Head Neck Surg* 2012;147:848–54
14. Kasabwala K, Agarwal N, Hansberry DR, et al. **Readability assessment of patient education materials from the American Academy of Otolaryngology-Head and Neck Surgery Foundation.** *Otolaryngol Head Neck Surg* 2012;147:466–71
15. Misra P, Agarwal N, Kasabwala K, et al. **Readability analysis of healthcare-oriented education resources from the American Academy of Facial Plastic and Reconstructive Surgery (AAFPRS).** *Laryngoscope* 2013;123:90–96
16. Misra P, Kasabwala K, Agarwal N, et al. **Readability analysis of internet-based patient information regarding skull base tumors.** *J Neurooncol* 2012;109:573–80
17. Svider PF, Agarwal N, Choudhry OJ, et al. **Readability assessment of online patient education materials from academic otolaryngology-head and neck surgery departments.** *Am J Otolaryngol* 2013;34:31–35
18. Kasabwala K, Misra P, Hansberry DR, et al. **Readability assessment of the American Rhinologic Society patient education materials.** *Int Forum Allergy Rhinol* 2013;3:325–33
19. Agarwal N, Sarris C, Hansberry DR, et al. **Quality of patient education materials for rehabilitation after neurological surgery.** *NeuroRehabilitation* 2013;32:817–21
20. Agarwal N, Chaudhari A, Hansberry DR, et al. **A comparative analysis of neurosurgical online education materials to assess patient comprehension.** *J Clin Neurosci* 2013;20:1357–61
21. Hansberry DR, Suresh R, Agarwal N, et al. **Quality assessment of online patient education resources for peripheral neuropathy.** *J Peripher Nerv Syst* 2013;18:44–47
22. Agarwal N, Hansberry DR, Sabourin V, et al. **A comparative analysis of the quality of patient education materials from medical specialties.** *JAMA Intern Med* 2013;173:1257–59
23. Hansberry DR, Agarwal N, Shah R, et al. **Analysis of the readability of patient education materials from surgical subspecialties.** *Laryngoscope* 2014;124:405–12
24. Hansberry DR, John A, John E, et al. **A critical review of the readability of online patient education resources from RadiologyInfo.org.** *AJR Am J Roentgenol* 2014;202:566–75
25. Hansberry DR, Kraus C, Agarwal N, et al. **Health literacy in vascular and interventional radiology: a comparative analysis of online patient education resources.** *Cardiovasc Intervent Radiol* 2014 Jan 31. [Epub ahead of print]
26. Flesch R. **A new readability yardstick.** *J Appl Psychol* 1948;32:221–33
27. Kincaid EH. **The Medicare program: exploring federal health care policy.** *N C Med J* 1992;53:596–601
28. McLaughlin GH. **SMOG grading: a new readability formula.** *Journal of Reading* 1969;12:639–46
29. Coleman M, Liau TL. **A computer readability formula designed for machine scoring.** *J Appl Psychol* 1975;60:283–84
30. Gunning R. *The Technique of Clear Writing.* New York: McGraw-Hill; 1952
31. Chall JS. *Readability Revisited: The new Dale-Chall Readability Formula.* Cambridge, Massachusetts: Brookline Books; 1995
32. Caylor JS, Sticht TG, Fox LC, et al. *Methodologies for Determining Reading Requirements of Military Occupational Specialties: Tech Report*

No. 73–5. Human Resources Research Organization. Defense Technical Information Center: Alexandria, Virginia; 1973
33. Fry E. **A readability formula that saves time.** *Journal of Reading* 1968; 11:513–16, 575–78
34. Raygor AL. **The Raygor Readability Estimate: a quick and easy way to determine difficulty.** In: Pearson PD, ed. *Reading: Theory Research and Practice*. Clemson, South Carolina: National Reading Conference; 1977:259–63
35. Penson RT, Benson RC, Parles K, et al. **Virtual connections: internet health care.** *Oncologist* 2002;7:555–68
36. US Department of Health and Human Services. *Simply Put: A Guide for Creating Easy-to-Understand Materials*. 3rd ed. Atlanta: Centers for Disease Control and Prevention; 2009
37. Aliu O, Chung KC. **Readability of ASPS and ASAPS educational web sites: an analysis of consumer impact.** *Plast Reconstr Surg* 2010;125:1271–78
38. Badarudeen S, Sabharwal S. **Assessing readability of patient education materials: current role in orthopaedics.** *Clin Orthop Relat Res* 2010;468:2572–80
39. Greywoode J, Bluman E, Spiegel J, et al. **Readability analysis of patient information on the American Academy of Otolaryngology-Head and Neck Surgery website.** *Otolaryngol Head Neck Surg* 2009;141:555–58
40. Bouton ME, Shirah GR, Nodora J, et al. **Implementation of educational video improves patient understanding of basic breast cancer concepts in an undereducated county hospital population.** *J Surg Oncol* 2012;105:48–54
41. Doak CC, Doak LG, Friedell GH, et al. **Improving comprehension for cancer patients with low literacy skills: strategies for clinicians.** *CA Cancer J Clin* 1998;48:151–62
42. Davis TC, Williams MV, Marin E, et al. **Health literacy and cancer communication.** *CA Cancer J Clin* 2002;52:134–49
43. Katz MG, Kripalani S, Weiss BD. **Use of pictorial aids in medication instructions: a review of the literature.** *Am J Health Syst Pharm* 2006;63:2391–97
44. Friedman DB, Hoffman-Goetz L. **A systematic review of readability and comprehension instruments used for print and web-based cancer information.** *Health Educ Behav* 2006;33:352–73

Brain Radiation Doses to Patients in an Interventional Neuroradiology Laboratory

R.M. Sanchez, E. Vano, J.M. Fernández, M. Moreu, and L. Lopez-Ibor

ABSTRACT

BACKGROUND AND PURPOSE: In 2011, the International Commission on Radiologic Protection established an absorbed-dose threshold to the brain of 0.5 Gy as likely to produce cerebrovascular disease. In this paper, the authors investigated the brain doses delivered to patients during clinical neuroradiology procedures in a university hospital.

MATERIALS AND METHODS: The radiation dose delivered to the brain was investigated in 99 diagnostic and therapeutic interventional neuroradiology procedures. Brain doses were calculated in a mathematic model of an adult standard anthropomorphic phantom by using the technical and radiation dose data of an x-ray biplane system submitted to regular quality controls and calibration programs.

RESULTS: For cerebral embolizations, brain doses resulted in a maximum value of 1.7 Gy, with an average value of 500 mGy. Median and third quartile resulted in 400 and 856 mGy, respectively. For cerebral angiography, the average dose in the brain was 100 mGy.

CONCLUSIONS: This work supports the International Commission on Radiologic Protection recommendation on enhancing optimization when doses to the brain could be higher than 0.5 Gy. Radiation doses should be recorded for all patients and kept as low as reasonably achievable. For pediatric patients and young adults, an individual evaluation of brain doses could be appropriate.

ABBREVIATIONS: AK = air kerma; CBCT = conebeam CT; DAP = dose-area product; ICRP = International Commission on Radiologic Protection; INR = interventional neuroradiology

Interventional neuroradiology (INR) provides important benefits to public health, but the use of ionizing radiation has inherent risks that must be evaluated and minimized. The new technology available has the potential to manage radiation risks properly but also allows more complex procedures to be undertaken that may require higher radiation doses for patients and staff. For instance, the inclusion of conebeam CT (CBCT) in modern INR laboratories offers advantages to patients in clinics but may also contribute to increased radiation doses.[1,2] The brain had traditionally been considered a highly radioresistant organ, but Shimizu et al[3] have recently reported a 9% excess relative risk per Gray for stroke death with brain doses above 0.5 Gy. The International Commission on Radiologic Protection (ICRP) has reviewed recent epidemiologic evidence suggesting that there are some tissue-reaction (deterministic) effects, particularly those with very late manifestation, in which threshold doses are or might be lower than previously considered. Although uncertainty remains, medical practitioners should be made aware that the absorbed-dose threshold for circulatory disease may be as low as 0.5 Gy to the brain.[4] Doses of such magnitude to patients could be reached during some complex interventional procedures; therefore, particular emphasis should be placed on optimization in these circumstances. The ICRP has also stated that in the case of pediatric patients, low-dose irradiation (1–2 Gy) to the developing brain of children can cause long-term cognitive and behavioral defects, and infants treated before 18 months[4] of age are even more susceptible to cognitive impairment in adult life after exposures to doses of >0.1 Gy.

Therefore, although these procedures have clear net clinical benefits for patients, it is necessary to know the range of radiation doses delivered to help INR specialists manage radiation risks so that they can provide appropriate information and counseling to their patients. There are few research articles on the topic of patient doses in INR, and the existing articles focus most often on the dose to the skin, the effective dose, or other dose indicators,[5-10] but they rarely deal with brain doses.

Received October 7, 2013; accepted after revision December 12.

From the Medical Physics Service (R.M.S., E.V., J.M.F.) and Interventional Neuroradiology Department (M.M., L.L.-I.). Instituto de Investigación Sanitaria del Hospital Clínico San Carlos, Madrid, Spain; and Radiology Department (R.M.S., E.V., J.M.F.), Universidad Complutense de Madrid, Medicine Faculty, Madrid, Spain.

Please address correspondence to Roberto Mariano Sanchez, MSc, Hospital Clinico San Carlos, Medical Physics, Madrid 28040, Spain; e-mail: robertomariano.sanchez@salud.madrid.org

http://dx.doi.org/10.3174/ajnr.A3884

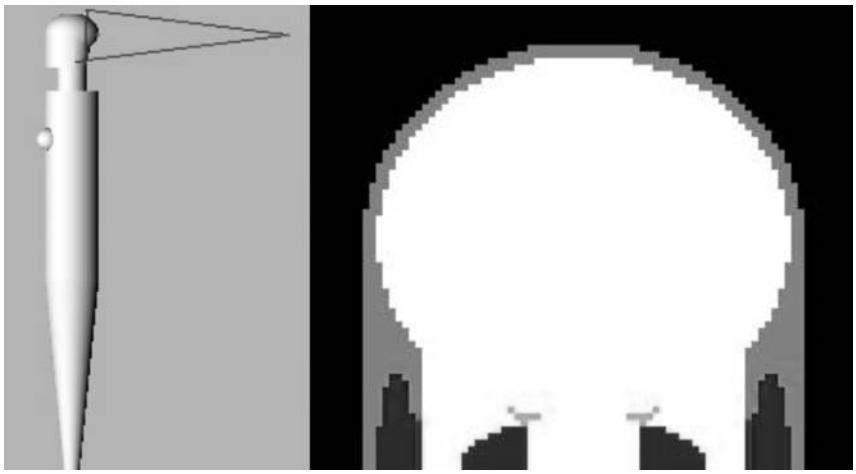

FIG 1. Anthropomorphic phantom used for brain-dose calculation. On the left, a posterior beam projection on the phantom head is shown. On the right, details of the phantom cranium and brain.

Regulations in some countries of the European Union require recording the radiation dose delivered to patients who undergo interventional procedures. In the new Council Directive on protection against ionizing radiation,[11] the European Commission has stated that "information relating to patient exposure forms part of the report of the medical radiological procedure." Modern INR units do not currently provide radiation doses delivered to patient organs. Instead, they can supply patient dose indicators like kerma area product, also used as dose-area product (DAP),[12] and air kerma (AK) at the patient entrance reference point,[13] provided they are suitably validated by a specialist. Because these dose indicators are not generally related directly to patient organ doses, which are the dosimetric quantities relevant to evaluate the biologic effects, the estimation of such doses requires individual calculation by a medical physicist.

In this work, brain doses delivered during INR procedures are reported for a sample of patients at a university hospital. The calculation was performed by using a mathematic model of an anthropomorphic phantom and detailed irradiation parameters recorded from clinical procedures (ie, all fluoroscopy runs and acquisition series). The influence of other variables in brain doses such as the DAP, AK, and beam collimation were also analyzed.

MATERIALS AND METHODS

Cases of diagnostic cerebral angiography and intracranial embolization were recorded sequentially during a 3-month period. Interventions at carotid and cervical levels were excluded. All procedures were performed in a neuroradiology room equipped with an Allura FD 10/20 (Philips Healthcare, Best, the Netherlands) biplane x-ray unit. The frontal C-arm has a flat detector with a 48-cm diagonal, and the lateral C-arm has a flat detector with a 25-cm diagonal. When locating the patient's head at isocenter, with the image detectors 10 cm from the patient's head and with no collimation, the frontal detector covers approximately 27×27 cm^2 and the lateral detector, 14×14 cm^2. Both C-arms have transmission ionization chambers installed at the x-ray tube exit to monitor the DAP delivered to patients, which is included in the patient dose reports. In most procedures, digital subtraction angiography series are acquired at 2 images per second during the first 10 seconds and at 1 image per second during the rest of the time. The system has the ability to perform 2 types of CT volumetric image acquisitions (conebeam CT) depending on the CT mode selected, either 313 images (low-dose CT mode) or 622 images (high-dose CT) over a 240° arc rotation with the largest possible beam size. Whatever the CT mode, the system always works with the same technique: 120 kV, 250 mA, 5 ms, and 0.4-mm Cu +2 mm Al of added filtration. At the end of all therapeutic procedures at our center, at least 1 CT series, approximately equivalent (in DAP) to 2.7 DSA series or 38 DSA images (cerebral protocol at our center), was acquired in the high-dose mode. For some procedures, a 3D reconstruction series obtained with rotational acquisition was performed.

The program PCXMC 2.0 Rotation (http://www.stuk.fi/sateilyn-hyodyntaminen/ohjelmat/PCXMC/en_GB/pcxmc/)[14] was used to calculate brain doses. This program calculates organ-equivalent doses and effective dose in a mathematic model of an anthropomorphic phantom of different ages and sizes. The program performs Monte Carlo simulations throughout the anthropomorphic phantom by using patient dose indicators (DAP, incident air kerma, and so forth) and geometric and physical parameters of the different x-ray projections (kilovolt, added filtration, C-arm angulation, and so forth). All calculations were performed on the standard phantom (Fig 1) corresponding to an adult measuring 179 cm and weighing 73 kg and containing the anatomic data based on the mathematic model of Cristy and Eckerman.[15]

Detailed information of the geometric and physical parameters was recorded for each beam projection at series level on the x-ray system and extracted with the help of Philips support engineers. This information, now directly available from the DICOM Radiation Dose Structured Reports, provided the x-ray system has been upgraded to allow this functionality, includes generator and x-ray tube setting potential (kilovolt), tube current (milliampere), pulse duration (milliseconds), added filtration, beam collimation, and C-arm angulations per projection for all fluoroscopy runs and DSA acquisition series. DAP and AK were also provided for each projection, then verified and corrected by a medical physicist, taking into account the couch and mattress attenuation in the frontal C-arm and the calibration of the DAP meter.

For the calculation of brain doses, DAP was used. The Philips Allura FD 20/10 has distances from the focus to rotation axis of 81 and 76.5 cm for the frontal and lateral C-arms, respectively. All data used to calculate patient doses were obtained from the data recorded at the radiation unit during clinical procedures, with the exception of the positioning of the patient whose brain is to be centered at the C-arm isocenter (a precondition of the conebeam CT acquisitions). The x-ray beam characteristics were introduced in the software by using the kilovolt and added filtration used on each beam projection. A fixed inherent filtration of 2.5 mm Al and anodic angles of 11° and 9° for the frontal and lateral x-ray tubes,

respectively, were also used. Wedge compensation filters were not used in our center for these procedures.

The brain doses calculated were compared with patient dose indicators (DAP and AK) and beam collimation.

RESULTS

Of 99 procedures recorded, 61 were cerebral angiographies and 38 were cerebral embolizations. On average, the diagnostic cases have lower DAP (64.5 Gy · cm^2) than the therapeutic ones (230 Gy · cm^2). The average number of projections (fluoroscopy runs and DSA acquisitions) was 49 for cerebral angiographies and 159 for therapeutics. A total of 9031 beam projections were processed for the brain-dose calculations. The main statistical parameters for brain doses are presented in Table 1. Figure 2 shows the frequency histograms. Thirty-four percent of therapeutic procedures had brain doses of ≥500 mGy. The total number of procedures (n = 99) corresponds to 81 patients because 14 patients underwent >1 procedure in the 3 months. If one takes into account the repetition of procedures, of the 38 patients with at least 1 therapeutic procedure, the fraction of patients with brain doses of >500 mGy is 40%, and with doses of >1000 mGy, 19%. Ten of 15 patients with brain doses greater than 500 mGy underwent >1 procedure.

Table 1: Main statistics for brain doses (in mGy) for cerebral angiography and embolization

	Cerebral Angiography	Cerebral Embolization
No.	61	38
Minimum	26	155
Maximum	568	1678
Mean	100	500
SD	92	346
1st Quartile	45	250
Median	73	397
3rd Quartile	123	645

Figure 3 presents brain doses versus DAP and AK. Lines show Pearson correlation coefficients of >0.9 for both variables. Figure 4 shows the brain dose relative to the AK ratio represented versus the weighted average field size for each procedure. The average field size for each patient is weighted by the DAP of each projection. An average difference of a factor of 2 can be observed in brain doses between the greatest and smallest field sizes.

The dose delivered during a CBCT series was 23.5 Gy · cm^2 in terms of DAP for the high-dose CBCT, which yielded a calculated 32 mGy to the brain and 1.65 mSv of effective dose (ICRP-103).[16] In the case of the low-dose CBCT, which uses half the projections with the same settings, brain and effective doses were also halved.

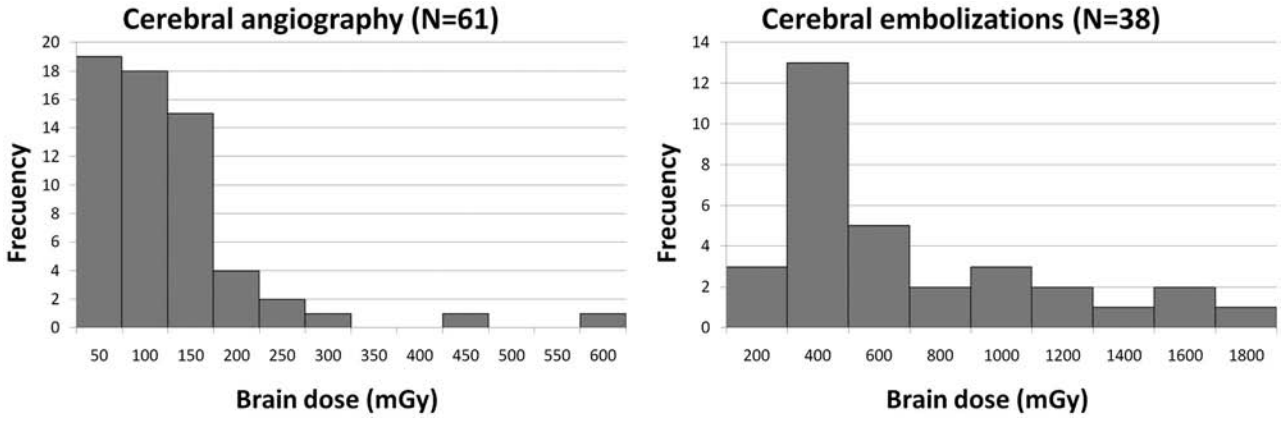

FIG 2. Frequency histogram with brain doses for cerebral angiography and embolization. Average brain dose resulted in 100 mGy for cerebral angiography and 500 mGy for embolizations.

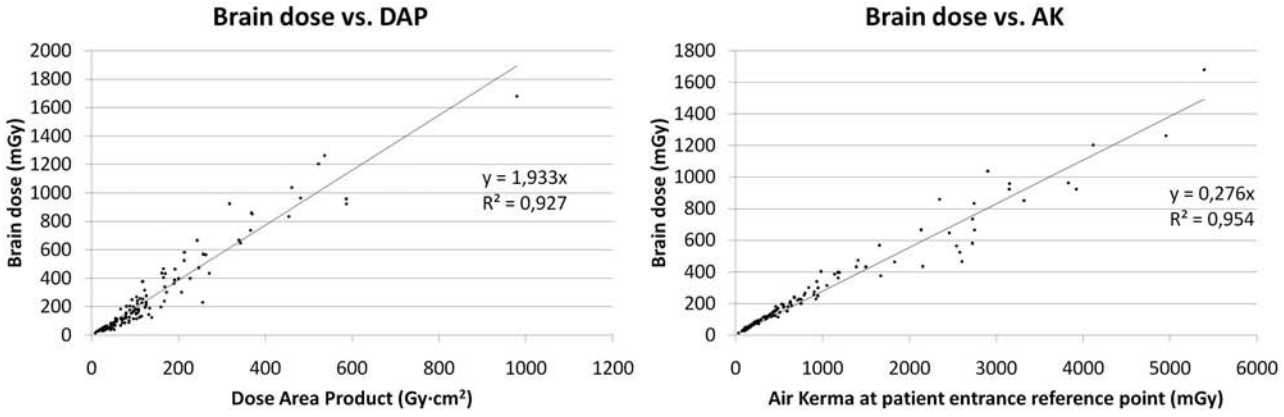

FIG 3. The brain dose for the 99 procedures is represented versus the 2 main dose indicators provided by modern interventional x-ray units, DAP and AK. Linear regression presents good correlation.

DISCUSSION

Doses as high as 1.7 Gy have been delivered to the brain during a therapeutic procedure in the sample of procedures included in this work. In 34% of these procedures in our institution, the dose exceeded 500 mGy (ie, the new dose threshold set by the ICRP). Given that, in some cases, several procedures are performed on the same patient, 40% of the patients in the sample investigated received >500 mGy in the brain. In diagnostic procedures, exceeding this threshold dose is unlikely. The ICRP has fixed the dose threshold when the probability of radiation injury is >1%. In the case of death from stroke, the excess of relative risk reported by Shimizu et al[3] is 3% between 0 and 0.5 Gy and approximately 11% for 1.5 Gy. Most of these therapeutic procedures are clearly justified for clinical reasons (they are life-saving), more particularly when they are expected to prevent stroke death, but the radiation doses to the brain reported in this article show that optimization, as recommended by the ICRP, is essential, especially in young patients with long life expectancies after interventions.

Figure 5 shows age histograms for the sample of patients investigated. Values for mean, median, and first quartile are quite similar for angiographies and embolizations. The average age of patients was 56 years, with a median of 60 years and a 25th percentile of 47 years; in both types of procedures, there was 1 patient younger than 15 years. Therefore, in such procedures, radiation risks must be taken into account, especially with pediatric patients and young adults.

When we compared scientific articles already published, we found that most publications reported patient dose indicators like DAP, AK, or skin dose. Miller et al[5] reported DAP in a multicenter survey in the United States, with an average DAP of 320 Gy · cm^2 for embolizations, 39% higher than in this work (230 Gy · cm^2). Sandborg et al[8] investigated skin doses to the head during INR cases and reported an average DAP for embolization of 189 Gy · cm^2. Thierry-Chef et al[7] investigated brain doses in a sample of 49 pediatric patients undergoing intracranial embolizations. Depending on the beam collimation (not reported in the article), the average brain dose could range from 68 to 490 mGy for the high and low levels of collimation, respectively. In this survey, mainly focused on adult patients, the average brain dose was 500 mGy.

A good correlation was shown between DAP and AK in the sample investigated, probably because of the simple irradiation geometry of the cranial procedures and the level of collimation. These findings make it possible to estimate brain doses with reasonable accuracy if the dose indicators (DAP and KA), available in most modern interventional x-ray units, are properly calibrated. The variability found in the literature on DAP values and brain doses indicates that a diligent mode of operation is essential to optimize radiation doses. Figure 3 shows that if one uses a beam size as small as possible, important dose reductions can be achieved and that when one uses x-ray beams with high filtration, brain doses can be reduced drastically during fluoroscopy runs and DSA acquisitions.

The dose delivered to the brain during a high-dose CBCT resulted in 32 mGy, 32% of the mean brain dose for a diagnostic procedure. In embolizations, with a higher mean dose (500 mGy), 1 high-dose CBCT represented 6% of the total brain dose. Other studies[17,18] have reported lower values of CBCT doses in the head as shown in Table 2. These lower values are mainly consequences of the use of automated exposure controls to adjust the dose required to a minimum for each projection and, in some cases, of a lower number of projections. However, the ratio effective dose over the DAP is of the same order of magnitude (Table 2). Koyama et al,[19] who measured doses in a phantom with a protocol but without automated exposure control and similar kilovolt and milliampere-second settings, reported brain doses similar to those in this study.

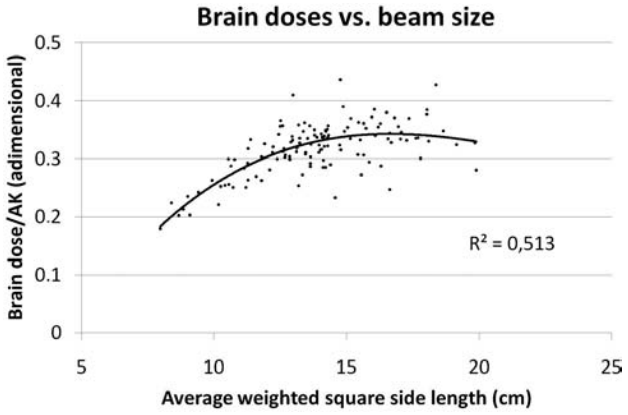

FIG 4. For the 99 procedures, the brain dose is related to the average weighted field size. In both images, one can appreciate how brain doses are almost doubled when the field size rises from 8 to 15 cm or more.

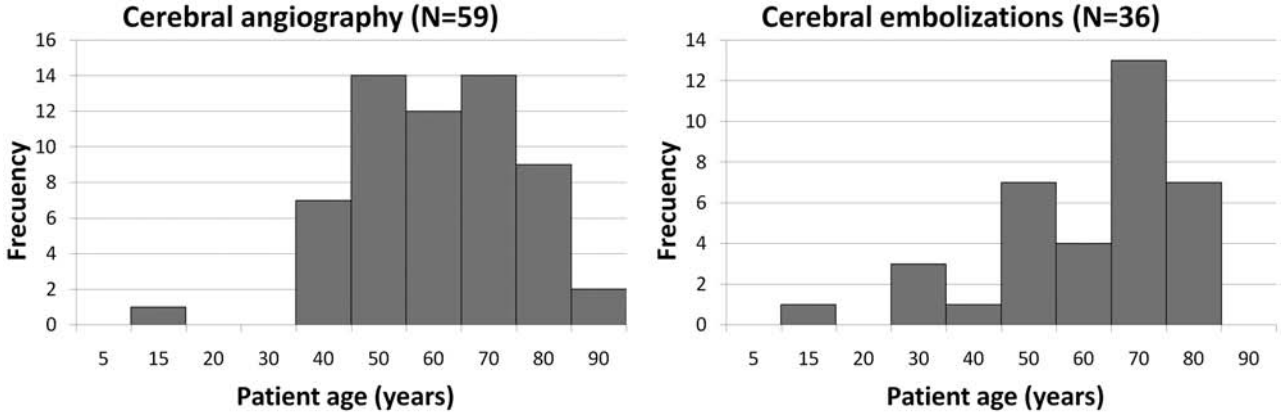

FIG 5. Age histograms for the sample of patients in this survey.

Table 2: Comparison of dose parameters in CBCT with other authors[a]

	DAP ($Gy \cdot cm^2$)	Brain Equivalent Dose (mGy)	ED ICRP-103[16] (mSv)	ED/DAP ($mSv/[Gy \cdot cm^2]$)
Koyama et al (2010)[19]	—	14–37	0.47–1.2	—
Kim et al (2012)[17]	5.99–9.61	5–6	0.38–0.87	0.06–0.09
Bai et al (2013)[18]	9.4 ± 2	6	0.30 ± 0.08	0.03–0.035
This study	11.75–23.5	16–32	0.83–1.6	0.09

Note:—ED indicates effective dose estimated with the parameters from the document ICRP-103.

[a] Kim et al and Koyama et al provide a range of dose estimations for several situations (kilovolt, collimation, or gantry tilt). Bai et al provide mean values ± SD for a sample of patients, except for the brain dose, for which they provide a phantom estimation.

The approach and process for calculating brain doses have some limitations. It was assumed that all fluoroscopic series were delivered to the brain, when, in fact, most procedures start at the femoral artery and a small part of the initial fluoroscopy could be made in the abdomen. Another source of inaccuracies could result from taking for granted that the patient brain is always centered at the C-arm isocenter, which happens not to be the case in some parts of the procedure. Therefore, in some cases with a large fluoroscopy time at leg or aortic levels and in cases in which the lesion is located at the brain peripheral region, a small overestimation of brain doses may be observed. Our approach could, therefore, be considered as a conservative estimation of brain doses in INR procedures.

CONCLUSIONS

The dose delivered to the brain of patients undergoing interventional neuroradiology procedures may be relevant enough to produce radiation side effects and must be minimized as much as possible. The radiation dose to patients should be monitored for all interventional procedures by using the standardized dose indicators DAP and AK and should be included in the patient clinical report. For interventions of high complexity and high radiation doses, an individual dose calculation to some sensitive organs/tissues like the brain, eye lenses, or skin may be needed, especially for pediatric patients and young adults and patients likely to undergo repeat procedures. To optimize the procedures and minimize patient doses, one must reduce the number of series, the number of frames per series, and the frame rates to the minimum necessary; collimate the radiation beam to the region of interest; reduce the detector-to-patient distance; and use x-ray beams with high-added filtration. It is also important to have a quality-assurance program to ensure that the x-ray dose rate remains within acceptable values.

ACKNOWLEDGMENTS

The authors thank Philips Medical Systems for their assistance in recording all the physical parameters of the x-ray system.

Disclosures: Manuel Moreu—*UNRELATED*: *Grants/Grants Pending*: Fundación para la Investigación Biomédica del Hospital Clínico San Carlos.

REFERENCES

1. Berris T, Gupta R, Rehani MM. **Radiation dose from cone-beam CT in neuroradiology applications.** *AJR Am J Roentgenol* 2013;200:755–61
2. Kyriakou Y, Richter G, Dölfler A, et al. **Neuroradiologic applications with routine C-arm flat panel detector CT: evaluation of patient dose measurements.** *AJNR Am J Neuroradiol* 2008;29:1930–36
3. Shimizu Y, Kodama K, Nishi N, et al. **Radiation exposure and circulatory disease risk: Hiroshima and Nagasaki atomic bomb survivor data, 1950–2003.** *BMJ* 2010;340:b5349
4. ICRP Statement on Tissue Reactions/Early and Late Effects of Radiation in Normal Tissues and Organs—Threshold Doses for Tissue Reactions in a Radiation Protection Context. ICRP Publication 118. Ann. ICRP 41(1/2) 2012
5. Miller DL, Balter S, Cole P, et al. **Radiation Doses In Interventional Radiology procedures: the RAD-IR Study.** *J Vasc Interv Radiol* 2003;14:977–90
6. Struelens L, Vanhavere F, Bosmans H, et al. **Skin dose measurement on patients for diagnostic and interventional neuroradiology: a multicentre study.** *Radiat Prot Dosimetry* 2005;114:143–46
7. Thierry-Chef I, Simon SL, Land CE, et al. **Radiation dose to the brain and subsequent risk of developing brain tumors in pediatric patients undergoing interventional neuroradiology procedures.** *Radiat Res* 2008;170:553–65
8. Sandborg M, Rossitti R, Pettersson H. **Local skin and eye lens equivalent doses in interventional neuroradiology.** *Eur Radiol* 2010;20:725–33
9. Kien N, Rehel JL, Étard C, et al. **Patient dose during interventional neuroradiology procedures: results from a multi-center study** [in French]. *J Radiol* 2011;92:1101–12
10. Vano E, Fernandez JM, Sanchez RM, et al. **Patient radiation dose management in the follow-up of potential skin injures in neuroradiology.** *AJNR Am J Neuroradiol* 2013;34:277–82
11. European Commission. COUNCIL DIRECTIVE 2013/59/EURATOM of 5 December 2013 laying down basic safety standards for protection against the dangers arising from exposure to ionising radiation, and repealing Directives 89/618/Euratom, 90/641/Euratom, 96/29/Euratom, 97/43/Euratom and 2003/122/Euratom. Available at http://eur-lex.europa.eu/JOHtml.do?uri=OJ:L:2014:013:SOM:EN:HTML. Accessed February 5, 2014.
12. International Commission on Radiation Units and Measurements. **ICRU report 74: patient dosimetry for X rays used in medical imaging.** *Journal of the International Commission on Radiation Units and Measurements* 2005:5
13. International Electrotechnical Commission. Medical electrical equipment. Part 2–43. Particular requirements for the safety of X-ray equipment for interventional procedures. Report IEC 60601-2-43 2010. Geneva, Switzerland.
14. Tapiovaara M, Siiskonen T. *PCXMC, A Monte Carlo program for calculating patient doses in medical x-ray examinations.* 2nd ed. Helsinki: STUK-Radiation and Nuclear Safety Authority of Finland; 2008
15. Cristy M, Eckerman KF. *Specific absorbed fractions of energy at various ages from internal photon sources. I. Methods. Report ORNL/TM-8381/V1.* Oak Ridge, Tennessee: Oak Ridge National Laboratory; 1987
16. ICRP 2007. The 2007 Recommendations of the International Commission on Radiological Protection. Ann. ICRP Publication 103. ICRP 37 (2–4)
17. Kim S, Sopko D, Toncheva G, et al. **Radiation dose from 3D rotational X-ray imaging: organ and effective dose with conversion factors.** *Radiat Prot Dosimetry* 2012;150:50–54
18. Bai M, Liu X, Liu B.. **Effective patient dose during neuroradiological C-arm CT procedures.** *Diagn Interv Radiol* 2013;19:29–32
19. Koyama S, Aoyama T, Oda N, et al. **Radiation dose evaluation in tomosynthesis and C-arm cone-beam CT examination with an anthropomorphic phantom.** *Med Phys* 2010;37:4298–306

Repeated Head CT in the Neurosurgical Intensive Care Unit: Feasibility of Sinogram-Affirmed Iterative Reconstruction–Based Ultra-Low-Dose CT for Surveillance

I. Corcuera-Solano, A.H. Doshi, A. Noor, and L.N. Tanenbaum

ABSTRACT

BACKGROUND AND PURPOSE: Patients in the neurosurgical intensive care unit undergo multiple head CT scans, resulting in high cumulative radiation exposures. Our aim was to assess the acceptability of a dedicated, special-purpose sinogram-affirmed iterative reconstruction–based ultra-low-dose CT protocol for neurosurgical intensive care unit surveillance head CT examinations, comparing image quality with studies performed with our standard-of-care sinogram-affirmed iterative reconstruction low-dose CT and legacy filtered back-projection standard-dose CT protocols.

MATERIAL AND METHODS: A retrospective analysis was performed of 54 head CT examinations: ultra-low-dose CT ($n = 22$), low-dose CT ($n = 12$), and standard-dose CT ($n = 20$) in 22 patients in the neurosurgical intensive care unit. Standard-dose CT was reconstructed by using filtered back-projection on a Somatom Sensation 64 scanner. Ultra-low-dose CT and ultra-low-dose CT examinations were performed on a Siemens AS+128 scanner with commercially available sinogram-affirmed iterative reconstruction. Qualitative and quantitative parameters, including image quality and dose, were evaluated.

RESULTS: Sinogram-affirmed iterative reconstruction ultra-low-dose CT represented a 68% lower dose index volume compared with filtered back-projection standard-dose CT techniques in the same patients while maintaining similar quality and SNR levels. Sinogram-affirmed iterative reconstruction low-dose CT offered higher image quality than filtered back-projection standard-dose CT ($P < .05$) with no differences in SNR at a 24% lower dose index volume. Compared with low-dose CT, ultra-low-dose CT had significantly lower SNR ($P = .001$) but demonstrated clinically satisfactory measures of image quality.

CONCLUSIONS: In this cohort of patients in the neurosurgical intensive care unit, dedicated ultra-low-dose CT for surveillance head CT imaging led to a significant dose reduction while maintaining adequate image quality.

ABBREVIATIONS: $CTDI_{vol}$ = dose index volume; FBP = filtered back-projection; IR = iterative reconstruction; LDCT = low-dose CT; NICU = neurosurgical intensive care unit; SAFIRE = sinogram-affirmed iterative reconstruction; SDCT = standard-dose CT; ULDCT = ultra-low-dose CT

CT by using iterative reconstruction (IR), an alternative to legacy filtered back-projection (FBP), is now ubiquitously available. IR methods loop iteratively through the image reconstruction, reducing noise, with each pass permitting the use of lower levels of ionizing radiation while preserving acceptable image quality.[1,2] IR methods have been successfully applied in cardiovascular,[3,4] thoracic,[5-8] abdominal,[9,10] and head CT applications.[11-14] This study used a commercially available advanced IR technique, sinogram-affirmed iterative reconstruction. Sinogram-Affirmed Iterative Reconstruction (SAFIRE) is a raw data and image domain–based[15] noise-modeling technique with 5 user-selectable strength levels. Previous work established the feasibility of SAFIRE for the study of body regions[15-20] and more recently in head CT[21] applications.

Patients in the neurosurgical intensive care unit (NICU) typically undergo multiple head CT examinations, resulting in high cumulative radiation exposures. In this study, we evaluated radiation dose and image quality of head CTs obtained with a NICU-designated ultra-low-dose (ULDCT) protocol (120 dose-modulated effective milliampere-second), with a dose index volume ($CTDI_{vol}$) approximately 80% below the recommended reference level in the current American College of Radiology guidelines.[22] We compared these studies with our standard-of-care low-dose

Received November 1, 2013; accepted after revision December 5.

From the Department of Neuroradiology, The Mount Sinai Medical Center, New York, New York.

Idoia Corcuera-Solano was supported by a grant from the Spanish foundation: Fundación Alfonso Martín Escudero.

Paper previously presented in part at: 37th Annual Meeting of the European Society of Neuroradiology, September 28-October 1, 2013; Frankfurt, Germany.

Please address correspondence to Lawrence N. Tanenbaum, MD, Mount Sinai Medical Center Department of Radiology, B1234, One Gustave L. Levy Place New York, NY 10029; e-mail: nuromri@gmail.com

Indicates open access to non-subscribers at www.ajnr.org

http://dx.doi.org/10.3174/ajnr.A3861

Table 1: CT protocols[a]

	FBP	SAFIRE	
	SDCT	LDCT	ULDCT
Scanner type	Siemens Somaton Sensation 64 scanner	Siemens Definition AS+128	Siemens Definition AS+128
kV(peak)	120	100	100
mAs	350	290	120
Section thickness	4.8	5	5
Reconstruction kernel	J40	J40f	J40f
Pitch	0.6	0.6	0.6
Rotation time (sec)	0.5	0.5	0.5

[a] In-plane, through-plane, and lens protective dose-modulation (X-CARE; Siemens) were used.

(LDCT) IR protocol (290 dose-modulated effective mAs), also SAFIRE-based, and with our legacy standard-dose (SDCT) FBP protocol (350 fixed milliampere-second). To our knowledge, the use of SAFIRE to support ultra-low-dose head CT for the repeated, approximately daily surveillance examinations in the vulnerable NICU population has not been reported.

MATERIALS AND METHODS

Patients

The institutional review board approved this retrospective single-center study, with a waiver of informed consent. Our institutional radiology data base was queried to identify NICU patients who underwent head CT by using ULDCT from December 2012 through February 2013. Sixty head CT examinations of 28 consecutive NICU patients were reviewed. We selected patients who underwent head CT using ULDCT, having at least 1 LDCT and/or SDCT for comparison. Six patients were excluded from the image analysis, 4 due to the lack of LDCT or SDCT available for comparison and 2 due to metallic artifacts caused by surgical material. Fifty-four head CT examinations, ULDCT ($n = 22$), LDCT ($n = 12$), and SDCT ($n = 20$), from 22 patients were included for analysis.

CT Protocol Selection

Scanner selection was based on availability. If the patient was scanned on the non-IR-equipped machine, a FBP-based SDCT was performed. If the IR-equipped scanner was available, our standard clinical LDCT was used for the initial evaluation. If the patient was seen subsequently, the surveillance ULDCT protocol was used whenever the IR-capable scanner was available. Because NICU patients underwent multiple examinations, many had SDCT and LDCT along with ULDCT examinations on sequential days, affording the opportunity to assess quality and dose across the examination types in individual patients.

CT Data Acquisition

SDCT was performed with FBP on a variety of clinical scanners unequipped with IR capability, most on a Somatom Sensation 64 scanner (Siemens, Erlangen, Germany). LDCT and ULDCT were performed on a Definition AS+128 scanner (Siemens). CT data parameters are summarized in Table 1.

Radiation Dose Assessment

The CT dose index volume in milligrays and the dose-length product were extracted from the scan-dose page. Effective dose in millisieverts was estimated by multiplying the dose-length product with a constant region-specific conversion coefficient of 0.0023 mSv/(mGy × cm).[23] Minimum, mean, and maximum doses of $CTDI_{vol}$, dose-length product and effective dose in the 3 subgroups were compared.

The difference in doses was calculated by subtracting the mean $CTDI_{vol}$ used in examinations with ULDCT from the mean $CTDI_{vol}$ of SDCT. The mean $CTDI_{vol}$ obtained from LDCT was subtracted from the SDCT values; and ULDCT, from LDCT. A percentage difference was also calculated. The same analysis was performed with the dose-length product and effective dose.

Image Quality Analysis

Quantitative Analysis. A board-certified radiologist with 1 year of neuroradiology experience (A.N.), not involved in the subjective analysis, performed the quantitative measurements. ROIs were placed in the white matter by using an analysis and viewing workstation (Advantage Workstation 4.6; GE Healthcare, Milwaukee, Wisconsin). We drew identical circular 10-mm^2 ROIs in the corona radiata, avoiding volume-averaging with sulci, cisterns, and gray matter. The following quantitative parameters were acquired for each set of images:

1) Signal (S), defined as the mean CT attenuation values in Hounsfield units.

2) Image noise (IN), defined as the SD of CT attenuation values.

3) SNR = (Mean WM Region of Interest)/(SD WM Region of Interest) or (S)/(IN).

Qualitative Analysis. Two board-certified neuroradiologists, with 10 and ≥25 years of experience (A.H.D., L.N.T.) independently analyzed the 3 sets of images. Readers were blinded to reconstruction methods and radiation dose. Readers were asked to evaluate image granularity, defined as the overall graininess or mottle; gray matter–white matter differentiation, defined as the perceived contrast between the gray and white matter; and overall image quality of each CT image on a 5-point scale (Table 2).

Direct pair-wise blinded comparison was performed within each of the ULDCT-SDCT, LDCT-SDCT, and ULDCT-LDCT image sets for each patient. Window and level settings were standardized for initial review, but each reader was also allowed to vary the settings. Image quality scores were averaged across both readers for analysis and are presented as mean value and SD.

Statistical Analysis

Statistical analyses were performed by using the commercially available IBM Statistical Package for the Social Sciences software (Version 20; IBM, Armonk, New York). Radiation variables were

Table 2: Grading system for the qualitative assessment

Score	Granularity	GM-WM Differentiation	Overall Quality
1	Much more than expected	Much worse than expected	Much worse than expected
2	More than expected	Worse than expected	Worse than expected
3	Normal, as expected	Normal, as expected	Equal, as expected
4	Less than expected	Better than expected	Better than expected
5	Much less than expected	Much better than expected	Much better than expected

Table 3: Radiation dose for the ULDCT, LDCT, and SDCT

	ULDCT (n = 22)	LDCT (n = 12)	SDCT (n = 20)
$CTDI_{vol}$ (mGy)			
Max	20.46	54.71	60.69
Min	11.77	26.79	33.80
Mean	15.55	36.47	48.38
DLP (mGy · cm)			
Max	375.00	958.00	1128.20
Min	188.00	471.00	574.65
Mean	273.39	668.58	843.30
ED (mSv)			
Max	0.86	2.20	2.59
Min	0.43	1.08	1.32
Mean	0.62	1.53	1.93

Note:—Max indicates maximum; Min, minimum; DLP, dose-length product; ED, effective dose.

compared by using the Student t test for paired samples. A nonparametric paired Wilcoxon test was used to perform inter-CT protocol comparisons between the image quality parameters. Numeric data were expressed as mean ± SD. Image quality scores, signal, image noise, and SNR for each set of CT images were analyzed. Difference was considered statistically significant at $P < .05$. Interobserver agreement for assessment of image quality was quantified by weighted κ statistics.[24]

RESULTS

Patient Groups

Scans of 22 patients (12 men, 10 women; mean age, 59 ± 0.81 years; range, 21–87 years) were analyzed. Ten patients had scans with ULDCT, LDCT, and SDCT techniques; 10 had scans with ULDCT and SDCT; and 2, with ULDCT and LDCT. The mean time interval between initial imaging with SDCT and ULDCT follow-up was 2.3 days; between SDCT and LDCT, it was 6.5 days; and between LDCT and ULDCT, 8.3 days.

All patients underwent CT examinations only for clinical assessment or follow-up. The reasons for scanning included ischemic stroke ($n = 7$), external ventricular drain placement ($n = 5$), hemorrhagic stroke ($n = 4$), subdural hematoma ($n = 1$), aneurysmal subarachnoid hemorrhage ($n = 3$), deep brain stimulation placement ($n = 1$), and brain tumor ($n = 1$).

Radiation Exposure

Differences in mean $CTDI_{vol}$, dose-length product, and effective dose between groups were statistically significant (all, $P < .01$).

A 68% reduction of the mean $CTDI_{vol}$ (15.55 mGy) was found with ULDCT compared with 48.38 mGy in the SDCT group. A 67% reduction of the mean dose-length product (273.39 mGy · cm) and 68% of the mean effective dose (0.62 mSv) were found when using ULDCT compared with the 843.30 mGy · cm and 1.93 mSv of SDCT, respectively.

When we used LDCT compared with the SDCT, a 24% reduction of the mean $CTDI_{vol}$ and a 21% reduction of the mean dose-length product and the mean effective dose was found.

A 57% reduction of the mean $CTDI_{vol}$ and a 59% reduction of the mean dose-length product and the mean effective dose were found when using ULDCT compared with the LDCT scans (Tables 3 and 4).

Quantitative Analysis

ULDCT was comparable with SDCT with respect to SNR, albeit with a significant increase of image noise ($P = .001$). The signal was significantly higher in ULDCT scans ($P = .007$). LDCT was comparable in terms of signal, image noise, and SNR with SDCT. ULDCT, performed with a 58% lower tube current setting than LDCT, had an expected relatively higher image noise ($P = .003$) and lower SNR ($P = .001$). No significant differences were found in the signal (Table 5 and Fig 1).

Qualitative Analysis

The interobserver agreement in the assessment of image quality parameters was good ($\kappa = 0.64$). No significant difference in overall quality was found between ULDCT and SDCT. The scores for ULDCT were significantly higher than those for SDCT for GM-WM differentiation ($P = .004$), while ULDCT was associated with significantly more granularity ($P = .023$). LDCT was associated with significantly less granularity ($P = .032$) and better overall quality ($P = .022$) compared with SDCT and resulted in a significant improvement of GM-WM differentiation ($P = .034$). Scores of the ULDCT and LDCT protocols for GM-WM differentiation were comparable, while LDCT was associated with significantly less granularity and better overall quality ($P = .003$) (Table 6 and Fig 2). Image examples are provided in Figs 3 and 4.

DISCUSSION

Concern over the potential dangers of high radiation exposures from CT scans has been growing in recent years.[25] We were particularly interested in reducing the cumulative exposure for the vulnerable NICU patient population—subjects who typically undergo multiple, often daily, head CT examinations for days to weeks; thus, we adopted a specific ultra-low-dose clinical protocol for these surveillance studies.

IR techniques reduce image noise, allowing the use of lower CT doses while preserving image quality.[26] Recently, a second-generation variation of iterative reconstruction for CT, SAFIRE, has become available for clinical use. To the best of our knowledge, this is the first study to evaluate the efficacy and adequacy of an extremely low-dose, special-purpose head CT protocol ($CTDI_{vol}$, 15.55 mGy) by using SAFIRE, against standard-of-care examinations by using IR and FBP in the same patient. We com-

pared 3 clinical CT protocols: 350 fixed milliampere-second SDCT with FBP, 290 effective milliampere-second LDCT, and 120 effective milliampere-second ULDCT (both LDCT and SDCT reconstructed with SAFIRE), performed on a consecutive group of NICU patients.

When the ULDCT studies were compared with SDCT, image overall quality was equivalent despite a 66% relative dose reduction. At a relative dose reduction of 17%, SAFIRE-based LDCT scored significantly higher for subjective image quality, with no differences in noise compared with SDCT images reconstructed with FBP. When the 2 SAFIRE techniques were compared, ULDCT had significantly higher image noise and lower image quality than LDCT. This finding was consistent with expectations that image quality will be proportional to the dose level used when all other parameters are fixed. Our findings are concordant with previous studies using SAFIRE-based CT. Kalra et al[18] compared the use of abdominal CT reconstructed with SAFIRE with CT reconstructed with FBP and demonstrated a 50% reduced dose and, in some patients, a 75% reduced dose when using SAFIRE without a loss of diagnostic value. Similarly, Winklehner et al[19] showed the potential to reduce the radiation dose by >50% in body CTA studies by using SAFIRE without a deterioration in image quality. In a chest CT study, Pontana et al[16] demonstrated a 50% lower dose while image quality was preserved. SAFIRE has also been recently applied in the study of cervical spine CT, providing better image quality for intervertebral disks, the neural foramina, and ligaments compared with FBP, while reducing the radiation dose by approximately 40%.[20] Korn et al[21] recently published the first study of the use of SAFIRE in head CT and demonstrated that at 20% dose reduction, image quality was better with SAFIRE than with standard-dose FBP.

In the literature, there is a wide variation of dose-reduction results by using SAFIRE,[15-21] which makes it difficult to compare results. Differences might be partially explained by the inconsistency

Table 4: Radiation dose for the ULDCT, LDCT, and SDCT

SDCT-ULDCT (100% - [ULDCT/SDCT] · 100)	SDCT-LDCT (100% - [LDCT/SDCT] · 100)	LDCT-ULDCT (100% - [ULDCT/LDCT] · 100)
Percentage reduction		
Difference $CTDI_{vol}$		
66%	10%	62%
65%	20%	56%
68%	24%	57%
Difference DLP		
67%	15%	61%
67%	18%	61%
67%	21%	59%
Difference ED		
67%	15%	61%
67%	17%	60%
68%	21%	59%

Note:—DLP indicates dose-length product; ED, effective dose.

Table 5: Quantitative analysis: signal, image noise, and SNR in ULDCT, LDCT, and SDCT[a]

	ULDCT	SDCT	*P*	LDCT	SDCT	*P*	ULDCT	LDCT	*P*
S (HU)	32.94 ± 4.16	29.59 ± 4.97	.007	31.67 ± 4.27	29.59 ± 4.97	.359	32.94 ± 4.16	31.67 ± 4.27	.320
IN (HU)	5.05 ± 0.92	4.40 ± 0.89	.001	3.81 ± 0.40	4.40 ± 0.89	.154	5.05 ± 0.92	3.81 ± 0.40	.003
SNR	6.71 ± 1.38	6.91 ± 1.45	.251	8.35 ± 1.2	6.91 ± 1.45	.164	6.71 ± 1.38	8.35 ± 1.2	.001

Note:—S indicates signal; IN, image noise.
[a] Data are presented as mean and SD.

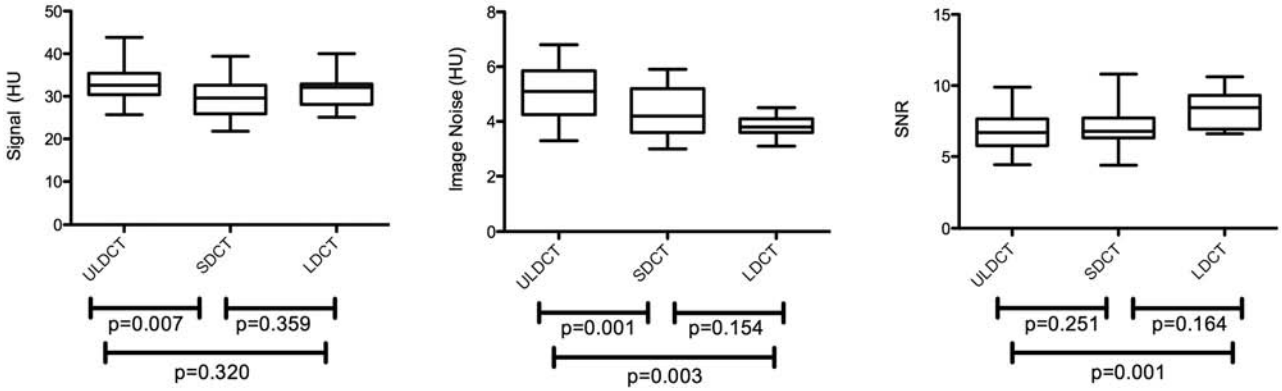

FIG 1. Boxplot diagrams. Signal, image noise, and SNR for SDCT, LDCT, and ULDCT are depicted. The line across the middle of the box identifies the mean sample value; boxes extend from the 25th to the 75th quartile, and whiskers, down to the minimum (min) and maximum (max) values.

Table 6: Qualitative analysis of granularity: GM-WM differentiation and overall quality in ULDCT, LDCT, and SDCT[a]

	ULDCT	SDCT	*P*	LDCT	SDCT	*P*	ULDCT	LDCT	*P*
Granularity	2.82 ± 0.47	3.38 ± 0.58	.023	4 ± 0.42	3.38 ± 0.58	.032	2.82 ± 0.47	4 ± 0.42	.003
GM-WM diff	3.50 ± 0.67	2.90 ± 0.59	.004	3.79 ± 0.49	2.90 ± 0.59	.034	3.50 ± 0.67	3.79 ± 0.49	.277
Overall quality	3.25 ± 0.45	3.25 ± 0.52	.908	4.08 ± 0.51	3.25 ± 0.52	.022	3.25 ± 0.45	4.08 ± 0.51	.003

Note:—GM-WM diff indicates gray matter–white matter differentiation.
[a] Data are presented as mean and SD.

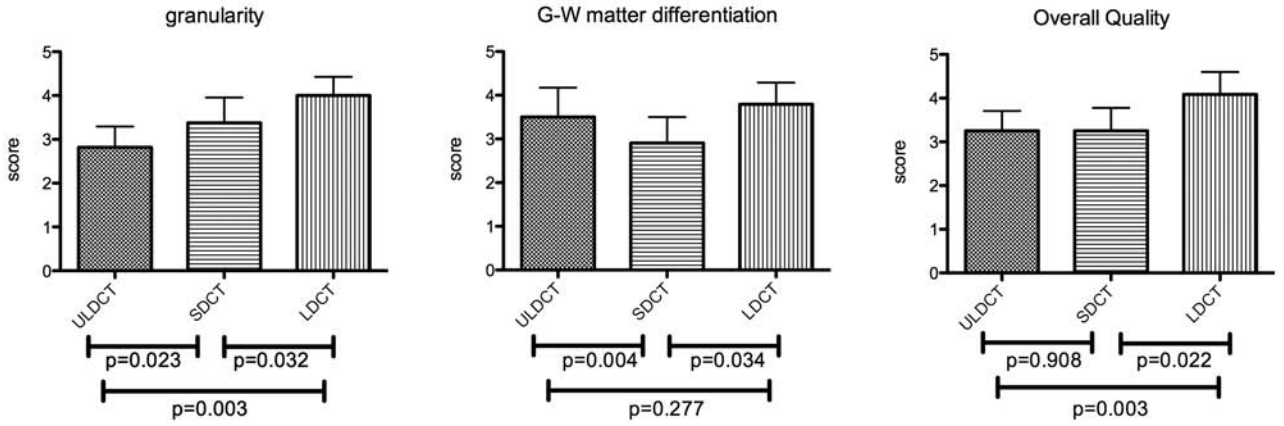

FIG 2. Qualitative analysis of granularity, GM-WM differentiation, and overall quality in ULDCT, LDCT, and SDCT. Data are presented as mean and SD.

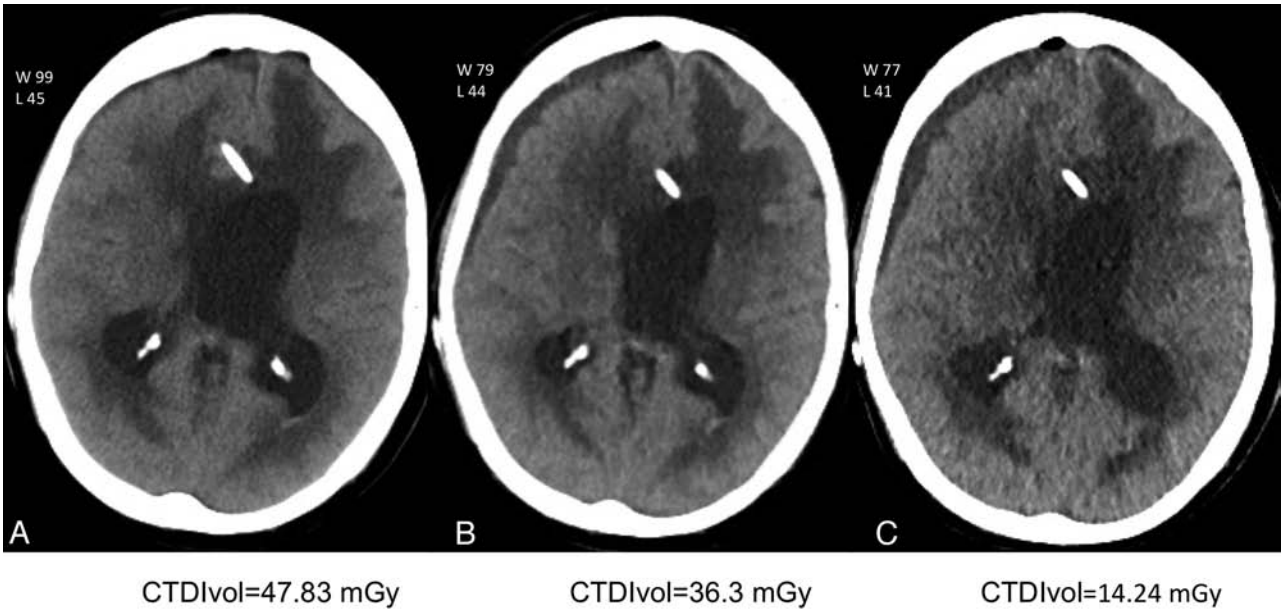

FIG 3. Comparison of SDCT-reconstructed FBP, LDCT, and ULDCT with SAFIRE obtained during 1 week in a 66-year-old NICU patient. Initial scan performed as an FBP SDCT (*A*) shows the reference image quality. Follow-up SAFIRE LDCT 24 hours later (*B*) and ULDCT SAFIRE (*C*) performed 72 hours after the initial examination, at approximately the same level as *A*.

in the method used to calculate dose reductions[26] and by the use of different scanners in those studies.

There are several aspects of our study that complement the published material to date. The ULDCT, LDCT, and SDCT scans were all obtained in the same patient cohort so that a more accurate intrapatient comparison could be performed. Additionally, we focused exclusively on the acceptability of a special-purpose, dedicated protocol for NICU patients—a vulnerable population subset in whom the frequent, repeated use of the head CT is of particular concern. Our approach used a significantly dose-reduced SAFIRE protocol, 58% lower than our routine clinical IR protocol and 53% lower than the low-dose protocol used in the Korn et al study.[21] While they reported a $CTDI_{vol}$ of 47.8 mGy in their low-dose CT protocol,[21] similar to the dose in our clinical standard LDCT, our ULDCT had a mean $CTDI_{vol}$ of 15.55 mGy, representing a 67% reduction in comparison, and it was 79% lower than the 75-mGy limit recommended by the American College of Radiology guidelines.[22]

An optimal CT protocol uses the lowest dose and provides the appropriate image quality for the clinical circumstances for which it is intended. Head CT is a critical tool for the surveillance of the NICU population, typically used serially to monitor and guide treatment. We presumed that a protocol with drastically reduced doses would be adequate for these surveillance examinations used primarily to follow known abnormalities such as hematoma size, catheter position, and ventricular caliber and that they would be clinically acceptable at a somewhat reduced level of quality and low contrast detectability than a routine CT. This retrospective study confirmed that this ULDCT approach provided acceptable quality for these surveillance examinations in the NICU population.

An important question concerns the level of dose reduction obtained before diagnostic accuracy is impaired. An optimal combination of SAFIRE and dose reduction has not yet been established. This study demonstrated the ability of reducing the

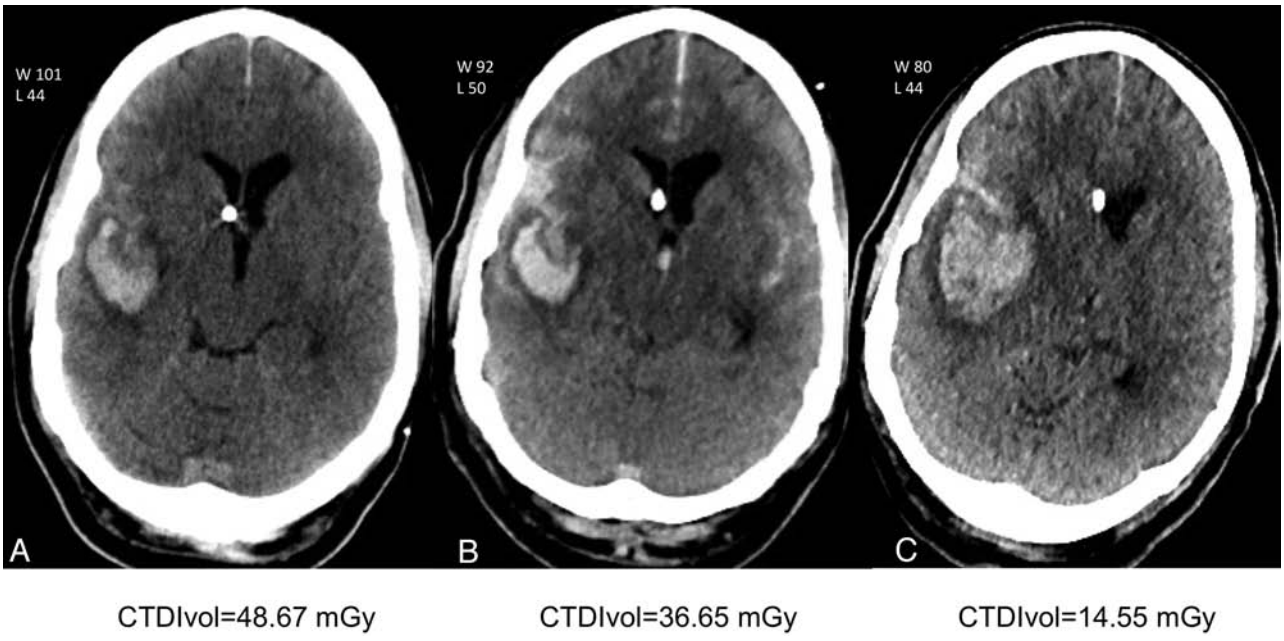

FIG 4. Comparison of FBP SDCT, SAFIRE LDCT, and ULDCT obtained over the course of 1 week in a 55-year-old NICU patient after Onyx (ev3, Irvine, California) embolization of a right parietotemporal AVM. SDCT image (*A*) obtained shortly after treatment shows the reference image quality. Follow-up LDCT 5 days later (*B*) and ULDCT SAFIRE (*C*) images obtained 7 days after the initial examination at approximately the same level as *A*. Note that the right parietotemporal hemorrhage is well-seen with both the LDCT and ULDCT studies.

dose up to 69% and maintaining diagnostic quality for this special purpose.

We acknowledge several study limitations. First, the retrospective design and the small sample size, with only 12 cases with dedicated ULDCT and LDCT for comparison, requires a confirmation of our findings in a prospective trial and a larger population. Second, while reviewers were blinded to protocol and reconstruction technique, blinding was not perfect because the varied use of scanner and reconstruction methods left subtle but recognizable differences in the appearance of the datasets. Third, different scanners were used for the SAFIRE and FBP groups; hence, we are unable to exclude the possible influence of different detector efficiency, image thickness, and reconstruction kernels on image quality and radiation dose. Finally, these results apply only to the specified protocols and CT scanners and will not translate exactly to other protocols and scanners, though the fundamentals with respect to a radiation-vulnerable population should apply in a vendor and IR agnostic fashion.

CONCLUSIONS

This study suggests that ULDCT with SAFIRE is a viable technique to significantly decrease radiation exposure while preserving image quality for the surveillance of the NICU population who are undergoing repeated head scanning. ULDCT could replace conventional CT for follow-up evaluations of the brain whenever serial examinations are performed or anticipated.

ACKNOWLEDGMENTS

We acknowledge John Doucette, PhD, for his statistical assistance during the development of this manuscript and Mark Smith, LRT (R), for his assistance at the CT scanners.

Disclosures: Idoia Corcuera-Solano—*RELATED*: supported by a grant from the Spanish foundation: Fundación Alfonso Martín Escudero. Lawrence N. Tanenbaum—*RELATED*: a speaker for Siemens.

REFERENCES

1. Nuyts J, De Man B, Dupont P, et al. **Iterative reconstruction for helical CT: a simulation study.** *Phys Med Biol* 1998;43:729–37
2. Thibault JB, Sauer KD, Bouman CA, et al. **A three-dimensional statistical approach to improved image quality for multislice helical CT.** *Med Phys* 2007;34:4526–44
3. Tumur O, Soon K, Brown F, et al. **New scanning technique using Adaptive Statistical Iterative Reconstruction (ASIR) significantly reduced the radiation dose of cardiac CT.** *J Med Imaging Radiat Oncol* 2013;57:292–96
4. Gosling O, Loader R, Venables P, et al. **A comparison of radiation doses between state-of-the-art multislice CT coronary angiography with iterative reconstruction, multislice CT coronary angiography with standard filtered back-projection and invasive diagnostic coronary angiography.** *Heart* 2010;96:922–26
5. Leipsic J, Nguyen G, Brown J, et al. **A prospective evaluation of dose reduction and image quality in chest CT using adaptive statistical iterative reconstruction.** *AJR Am J Roentgenol* 2010;195:1095–99
6. Pontana F, Pagniez J, Flohr T, et al. **Chest computed tomography using iterative reconstruction vs filtered back projection. Part 1. Evaluation of image noise reduction in 32 patients.** *Eur Radiol* 2011;21:627–35
7. Pontana F, Duhamel A, Pagniez J, et al. **Chest computed tomography using iterative reconstruction vs filtered back projection. Part 2. Image quality of low-dose CT examinations in 80 patients.** *Eur Radiol* 2011;21:636–43
8. Xu Y, He W, Chen H, et al. **Impact of the adaptive statistical iterative reconstruction technique on image quality in ultra-low-dose CT.** *Clin Radiol* 2013;68:902–08
9. Singh S, Kalra MK, Hsieh J, et al. **Abdominal CT: comparison of adaptive statistical iterative and filtered back projection reconstruction techniques.** *Radiology* 2010;257:373–83

10. Sagara Y, Hara AK, Pavlicek W, et al. **Abdominal CT: comparison of low-dose CT with adaptive statistical iterative reconstruction and routine-dose CT with filtered back projection in 53 patients.** *AJR Am J Roentgenol* 2010;195:713–19
11. Kilic K, Erbas G, Guryildirim M, et al. **Lowering the dose in head CT using adaptive statistical iterative reconstruction.** *AJNR Am J Neuroradiol* 2011;32:1578–82
12. Korn A, Fenchel M, Bender B, et al. **Iterative reconstruction in head CT: image quality of routine and low-dose protocols in comparison with standard filtered back-projection.** *AJNR Am J Neuroradiol* 2012;33:218–24
13. Rapalino O, Kamalian S, Kamalian S, et al. **Cranial CT with adaptive statistical iterative reconstruction: improved image quality with concomitant radiation dose reduction.** *AJNR Am J Neuroradiol* 2012;33:609–15
14. Vorona GA, Zuccoli G, Sutcavage T, et al. **The use of adaptive statistical iterative reconstruction in pediatric head CT: a feasibility study.** *AJNR Am J Neuroradiol* 2013;34:205–11
15. Moscariello A, Takx RA, Schoepf UJ, et al. **Coronary CT angiography: image quality, diagnostic accuracy, and potential for radiation dose reduction using a novel iterative image reconstruction technique-comparison with traditional filtered back projection.** *Eur Radiol* 2011;21:2130–38
16. Pontana F, Pagniez J, Duhamel A, et al. **Reduced-dose low-voltage chest CT angiography with sinogram-affirmed iterative reconstruction versus standard-dose filtered back projection.** *Radiology* 2013;267:609–18
17. Baumueller S, Winklehner A, Karlo C, et al. **Low-dose CT of the lung: potential value of iterative reconstructions.** *Eur Radiol* 2012;22:2597–606
18. Kalra MK, Woisetschlager M, Dahlstrom N, et al. **Radiation dose reduction with sinogram affirmed iterative reconstruction technique for abdominal computed tomography.** *J Comput Assist Tomogr* 2012;36:339–46
19. Winklehner A, Karlo C, Puippe G, et al. **Raw data-based iterative reconstruction in body CTA: evaluation of radiation dose saving potential.** *Eur Radiol* 2011;21:2521–26
20. Becce F, Ben Salah Y, Verdun FR, et al. **Computed tomography of the cervical spine: comparison of image quality between a standard-dose and a low-dose protocol using filtered back-projection and iterative reconstruction.** *Skeletal Radiol* 2013;42:937–45
21. Korn A, Bender B, Fenchel M, et al. **Sinogram affirmed iterative reconstruction in head CT: improvement of objective and subjective image quality with concomitant radiation dose reduction.** *Eur Radiol* 2013;82:1431–35
22. McCollough C, Branham T, Herlihy V, et al. **Diagnostic reference levels from the ACR CT Accreditation Program.** *J Am Coll Radiol* 2011;8:795–803
23. Bongartz G, Golding SJ, Jurik AG, et al. European Guidelines on Quality Criteria for Computed Tomography. 1999. http://www.drs.dk/guidelines/ct/quality. Accessed October 1, 2013
24. Landis JR, Koch GG. **The measurement of observer agreement for categorical data.** *Biometrics* 1977;33:159–74
25. Brenner DJ. **Slowing the increase in the population dose resulting from CT scans.** *Radiat Res* 2010;174:809–15
26. Willemink MJ, Leiner T, de Jong PA, et al. **Iterative reconstruction techniques for computed tomography. Part 2. Initial results in dose reduction and image quality.** *Eur Radiol* 2013;23:1632–42

Artifact Reduction of Different Metallic Implants in Flat Detector C-Arm CT

S.-C. Hung, C.-C. Wu, C.-J. Lin, W.-Y. Guo, C.-B. Luo, F.-C. Chang, and C.-Y. Chang

ABSTRACT

BACKGROUND AND PURPOSE: Flat detector CT has been increasingly used as a follow-up examination after endovascular intervention. Metal artifact reduction has been successfully demonstrated in coil mass cases, but only in a small series. We attempted to objectively and subjectively evaluate the feasibility of metal artifact reduction with various metallic objects and coil lengths.

MATERIALS AND METHODS: We retrospectively reprocessed the flat detector CT data of 28 patients (15 men, 13 women; mean age, 55.6 years) after they underwent endovascular treatment (20 coiling ± stent placement, 6 liquid embolizers) or shunt drainage ($n = 2$) between January 2009 and November 2011 by using a metal artifact reduction correction algorithm. We measured CT value ranges and noise by using region-of-interest methods, and 2 experienced neuroradiologists rated the degrees of improved imaging quality and artifact reduction by comparing uncorrected and corrected images.

RESULTS: After we applied the metal artifact reduction algorithm, the CT value ranges and the noise were substantially reduced (1815.3 ± 793.7 versus 231.7 ± 95.9 and 319.9 ± 136.6 versus 45.9 ± 14.0; both $P < .001$) regardless of the types of metallic objects and various sizes of coil masses. The rater study achieved an overall improvement of imaging quality and artifact reduction (85.7% and 78.6% of cases by 2 raters, respectively), with the greatest improvement in the coiling group, moderate improvement in the liquid embolizers, and the smallest improvement in ventricular shunting (overall agreement, 0.857).

CONCLUSIONS: The metal artifact reduction algorithm substantially reduced artifacts and improved the objective image quality in every studied case. It also allowed improved diagnostic confidence in most cases.

ABBREVIATIONS: CCF = carotid cavernous fistula; FDCT = flat detector CT; MAR = metal artifact reduction; HU = Hounsfield unit

Flat panel detectors have been used in radiography and fluoroscopy with the advantages of offering a higher dynamic range, dose reduction, direct digital readout, and a higher frame rate of dynamic image acquisition.[1] Earlier reports about projection data by C-arm-based flat detector–equipped angiography were published in the 2000s.[2,3] With the advances of flat detector technology, the angiographic suites equipped with C-arm flat detectors can generate 3D angiography and high-resolution volume images with soft-tissue contrast resolution. Today, the term "flat detector CT" (FDCT) refers to CT images with a series of projection data using a C-arm-based flat detector system, known as angiographic CT.[4] This technology has gained popularity and provided a number of important clinical applications.[5]

As a crucial tool for follow-up examinations in the angiographic suite, FDCT detects most intraparenchymal hemorrhages in emergency situations[6,7] and can recognize intracranial complications early during endovascular surgery, such as coiling of an intracranial aneurysm, stent placement, or other interventional procedures.[7] However, severe artifacts stemming from metallic objects remarkably degrade the image quality of FDCT and prevent visualization of the adjacent brain parenchyma or hemorrhage. Prell et al[8] described a metal artifact reduction (MAR) algorithm that significantly improved imaging quality in the FDCT of 7 patients. Further studies based on a previous MAR

Received September 17, 2013; accepted after revision November 18.

From the Department of Radiology (S.-C.H., C.-C.W., C.-J.L., W.-Y.G., C.-B.L., F.-C.C., C.-Y.C.), Taipei Veterans General Hospital, Taipei, Taiwan; and Department of Biomedical Imaging and Radiological Sciences (S.-C.H.) and School of Medicine (S.-C.H., C.-C.W., C.-J.L., W.-Y.G., C.-B.L., F.-C.C., C.-Y.C.), National Yang-Ming University, Taipei, Taiwan.

This work was supported, in part, by a collaborative project (T1100200) of Taipei Veterans General Hospital and Siemens. The MAR prototype was provided by Siemens.

Paper previously presented in part at: Annual Meeting of the Japanese Society of Neuroradiology, February 15–16, 2013; Kitakyushu, Japan.

Please address correspondence to WanYuo Guo, MD, PhD, No. 201, Sec 2, Shipai Rd, Beitou District, Taipei, Taiwan 11217; e-mail: wyguo@vghtpe.gov.tw


Indicates article with supplemental on-line figures.

http://dx.doi.org/10.3174/ajnr.A3851

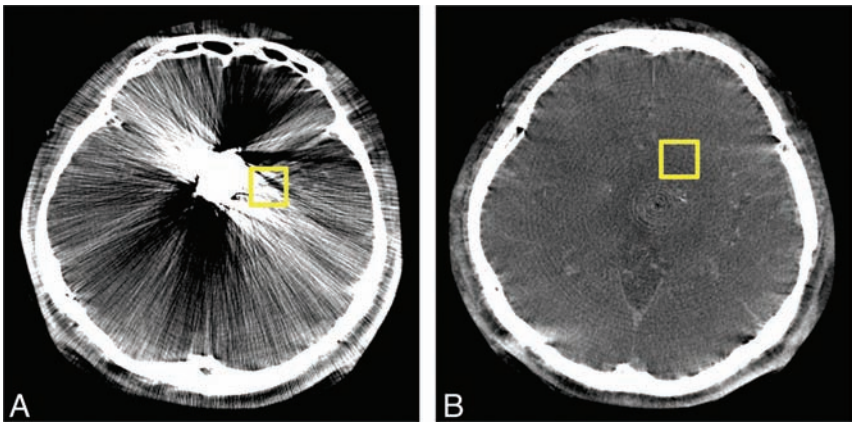

FIG 1. Hounsfield unit value range and noise were measured by two 1.5 × 1.5 cm^2 square ROIs. The first region of interest (ROI1) is placed in the region with most severe artifacts in the vicinity of the metal implant (*A*). The second region of interest (ROI0) is placed in the section just above the target metal object, which is degraded by metallic artifacts (*B*).

algorithm[8] have demonstrated the success in coiling and stent-assisted coiling FDCT and CT angiography.[9,10] However, the comparison of the efficacy of artifact reduction for various sizes and types of metal objects was seldom discussed. In this study, we investigated whether a MAR prototype software could reduce artifacts stemming from different high-attenuation implants and improve the diagnostic confidence of radiologists.

MATERIALS AND METHODS

Our institutional review board approved this study. We retrospectively reprocessed consecutive postinterventional FDCT images of 28 patients (15 men, 13 women; mean age, 55.6 years; range, 13–85 years) between January 2009 and November 2011. Twenty patients had aneurysms or carotid cavernous fistulas (CCFs) and were treated with endovascular coiling and stent placement. One patient had a left CCF, treated with 35% *n*-BCA. Five patients had cerebral AVMs or dural arteriovenous fistulas and were treated with Onyx (Covidien, Irvine, California). Two had hydrocephalus and were treated with ventricular shunt drainage.

All images were obtained from a flat panel angiographic C-arm system (Axiom Artis; Siemens, Erlangen, Germany) with the same FDCT protocol. The high-quality FDCT scan protocol included an acquisition range of 200° (20 seconds for acquisition, 1240 × 960 projection matrix, 0.4° angular increment) and 496 projections. The uncorrected FDCT images were reconstructed by using the dedicated software syngo InSpace 3D (Siemens).

All images were then postprocessed by using an MAR prototype software on an off-line workstation (MAR_VB21, Version 10; Siemens). The MAR algorithm investigated in this work is a modification and, additionally, an extension of a recently published MAR algorithm.[8] The algorithm consists of several steps. Initially, an uncorrected volume image is reconstructed from the measured data. By segmenting the metal objects in this volume, one can obtain a binary metal volume image. For each projection, this binary volume is forward-projected to yield a binary projection image of metal regions on the detector in the respective position. The projection data contained in these metal regions are generated by rays through metal objects, and thus these data are responsible for the artifacts. The data along the metal region boundaries are used to replace these data by a nonlinear interpolation procedure. The so-far corrected volume is used for a second normalized MAR correction step.[11] This step includes, additionally, iterative improvements of the metal region boundaries to enhance the consistency of the corrected data as a whole. Finally, a procedure minimizing the total variation is applied to reduce residual streaks.

The uncorrected and corrected image volumes were reformatted to stacks of transverse images with section thicknesses of 2.5 mm for the following analysis.

Image Analysis and Statistical Analysis

Objective Assessment. An experienced neuroradiologist (S.-C.H.) placed the first region of interest (ROI1) of 1.5 × 1.5 cm^2 in exactly the same location of the brain parenchyma closest to the metal objects in both uncorrected and corrected images. A second same-size region of interest (ROI0) was placed in the parenchyma in the section above or below the metal artifacts, which was used for the brain parenchyma reference without metal artifact interference (Fig 1).

The range of Hounsfield unit (HU) values in the region of interest was defined as the difference of maximal (max) and minimal (min) values,

$$\text{HU range} = \text{HU}_{\text{max}} - \text{HU}_{\text{min}},$$

and the noise was defined as the SD of HU values in the region of interest.

Subjective Assessment. Two neuroradiologists (S.-C.H. and C.-C.W.) evaluated each examination independently on the commercialized PACS viewer of our hospital. All images were anonymized; the raters were blinded to patient information and types of metal objects. The raters compared uncorrected and corrected images according to the artifacts around the metal objects and rated improved diagnostic confidence by using a 5-score system: (−1 = worse metal artifacts, 0 = no substantial change of metal artifacts, 1 = mild reduction of artifacts but not helpful for the diagnosis, 2 = marked reduction of metal artifacts and improved diagnostic confidence, 3 = no residual artifacts).

Statistical Analysis

We divided the patients into 3 groups according to the metal objects, including coiling ± stent placement, liquid embolizers (*n*-BCA or Onyx), and shunts. The coiling group was further divided into 3 subgroups according to the coil lengths (<25 cm, ≧25 cm but <100 cm, ≧100 cm). We used paired *t* tests to compare the range and noise of ROI1 between uncorrected and corrected images and between ROI0 and ROI1 in the corrected images. We calculated the overall interrater agreement by raw statistics and analyzed the reliability of the agreement by using κ statistics. We used the χ^2 and Fisher exact

Table 1: Quantitative assessment of metal artifacts before and after reduction

Objects	HU Range				Noise			
	Before	After	% Change	*P* Value	Before	After	% Change	*P* Value
ROI0 ($n = 28$)	247.2 ± 37.5	247.3 ± 37.3	0.04	NS	36.3 ± 4.8	36.2 ± 4.7	0.2	NS
Coiling ± stenting ($n = 20$)	2005.6 ± 804.0	282.6 ± 55.8	85.9	<.001	251.7 ± 94.4	42.9 ± 10.3	82.9	<.001
<25 cm ($n = 6$)	1613.7 ± 709.7	296 ± 44.7	81.7	.006	198.4 ± 83.8	42.8 ± 7.3	78.4	.007
25–100 cm ($n = 7$)	1954.9 ± 634.2	257.6 ± 23.5	86.8	<.001	238.6 ± 49.3	38.9 ± 5.6	83.7	<.001
>100 cm ($n = 7$)	2392.3 ± 945.6	296 ± 80.7	87.6	.001	310.3 ± 113.5	46.9 ± 15.0	84.9	.001
Liquid embolizer ($n = 6$)	1377.3 ± 646.6	428.5 ± 259.0	68.9	.019	206.0 ± 86.3	56.9 ± 21.6	72.3	.007
Shunt ($n = 2$)	1226.5 ± 259.5	368.0 ± 76.4	70.9	NS	109.8 ± 2.6	44.0 ± 0.7	60	.013
Overall (ROI1) ($n = 28$)	1815.3 ± 793.7	319.9 ± 136.6	82.3	<.001	231.7 ± 95.9	45.9 ± 14.0	80.2	<.001

Note:—NS indicates no significance.

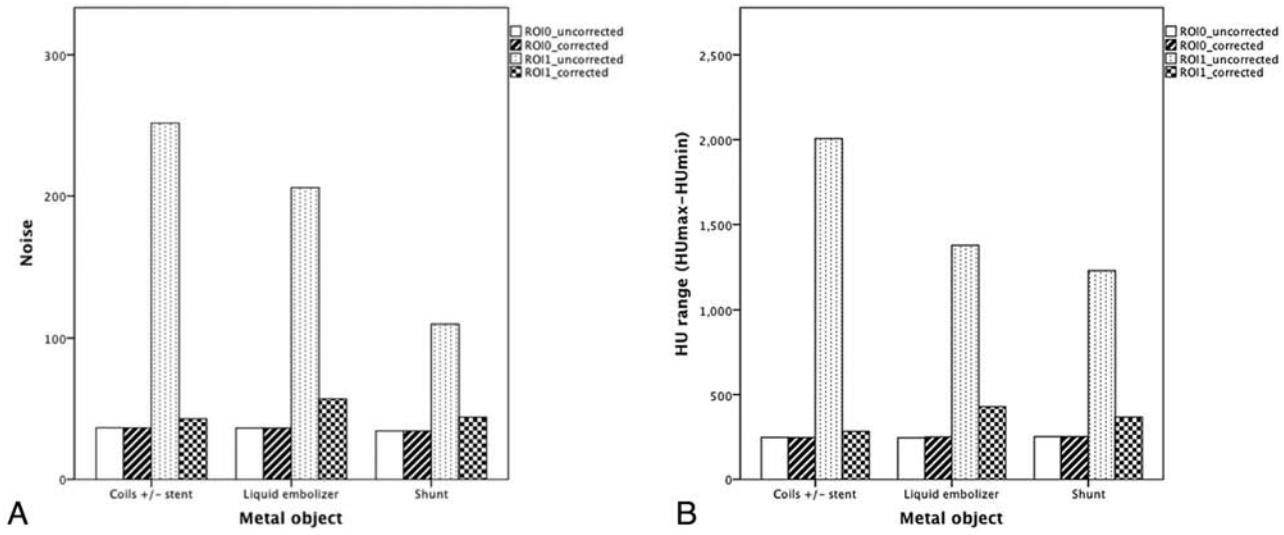

FIG 2. *A*, Comparison of Hounsfield unit range among different objects. *B*, Comparison of noise among different metal objects.

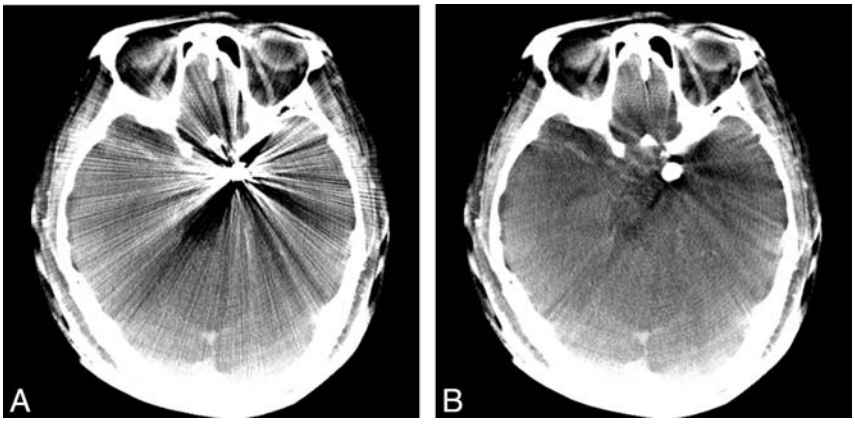

FIG 3. Illustrative case 1. FDCT without MAR (*A*) and with MAR (*B*) of a left-side ICA aneurysm post–coil embolization. The metal artifacts are significantly reduced, and the postcorrected images enable clearer evaluation of adjacent parenchyma.

tests to calculate the significance of the results. A 2-tailed level of $P < .05$ was considered significant.

RESULTS

The images of all patients demonstrated streak artifacts and were processed by the MAR algorithm successfully. The results are summarized in Table 1.

Comparison among Metal Objects

The application of the MAR algorithm did not compromise the image quality in the section without metal artifact contamination (ROI0) in all cases. The Hounsfield unit range and noise of ROI1 were higher in the coiling group compared with the liquid embolizer group (*n*-BCA or Onyx) or the ventricular shunt group in the uncorrected images, but no significant difference existed (Fig 2). A significant reduction of metal artifacts was achieved in all volume images of various metal objects, which showed a lower Hounsfield unit range and noise ($P <$ .001) (Fig 3). The Hounsfield unit range and noise of ROI1 in the corrected images remained significantly higher than those of ROI0 in the coiling group, but no significant difference existed in the other groups (Fig 2).

Comparison among Various Coil Lengths

In the coiling group, the Hounsfield unit range and noise of ROI1 were related to the coil length before the MAR algorithm correction; however, no significant difference existed (Fig 4). A significant reduction of metal artifacts was achieved in all patients with different metal objects ($P < .05$). Except for the noise in the subgroup length between 25 and 100 cm, the Hounsfield unit range and noise of ROI1 in the corrected images showed no significant difference compared with those of ROI0 in the other subgroups (Fig 3).

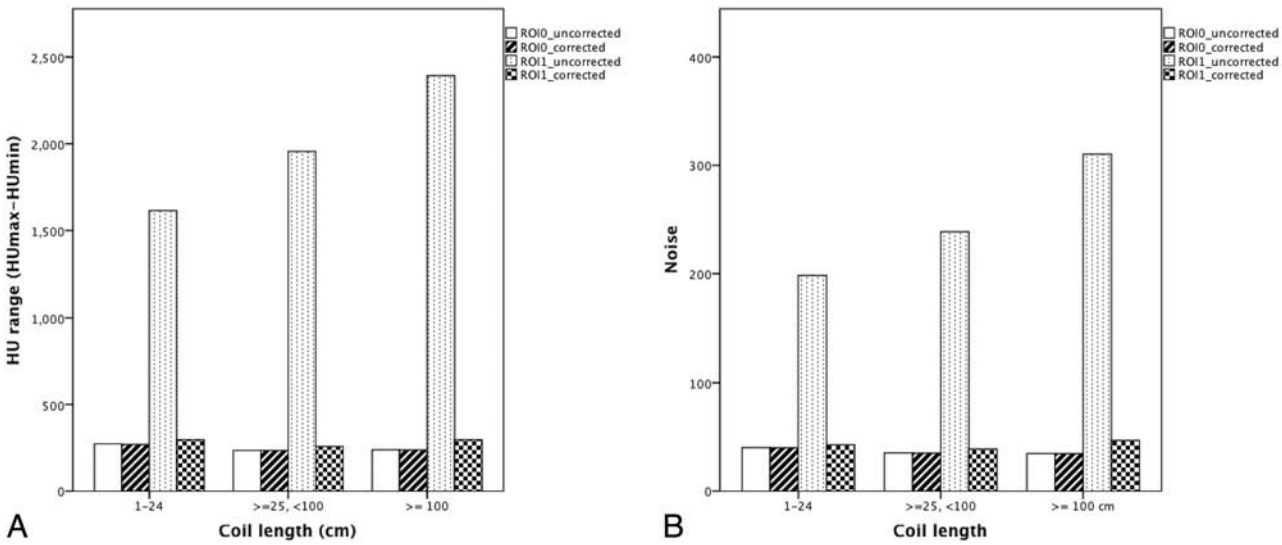

FIG 4. *A*, Comparison of Hounsfield unit range among different coil lengths. *B*, Comparison of noise among different coil lengths.

Table 2: Results of the observer study rating the imaging quality with MAR

	Rater 1 Score						Rater 2 Score					
Objects	−1	0	1	2	3	*P* Value	−1	0	1	2	3	*P* Value
Coiling ± stenting	0	0	0	18	2		0	0	1	13	6	
Liquid embolizer	0	0	2	4	0		0	0	3	3	0	
Shunt	0	0	2	0	0		0	2	0	0	0	
Overall	0	0	4	22	2	.002	0	2	4	16	6	<.001

Table 3: Inter-rater agreement of the observer study

	Overall Agreement	Rater 1, Score ≤ 2 (%)	Rater 2, Score ≤ 2 (%)	κ
Overall imaging quality	0.857	85.7	78.6	.517

Subjective Assessment of Image-Quality Improvement

The results of the observer study are summarized in Tables 2 and 3. The overall agreement of the 2 raters was 85.7% ($\kappa = 0.517$). No case had more severe artifacts or worse imaging quality after MAR correction. The number of cases in which the raters agreed on significant artifact reduction and improved image quality (score of ≥2) was >95% in the coiling group, 50% in the liquid embolizer group, and none in the shunt group.

DISCUSSION

An angiographic suite equipped with flat panel detectors can provide in-room CT-like images before or after neurointerventional procedures without transferring patients to another conventional CT scanner. These images can identify the relationship of the metal implants and provide early recognition of rebleeding or intracranial procedure-related complications, such as incomplete stent deployment, stent migration, stent fracture, or coil dislocation.[12-14] However, the metallic artifacts stemming from metal objects hinder clear visualization of a hematoma or parenchyma surrounding metal objects.[14]

Prell et al[15] demonstrated successfully reducing metal artifacts by using their version of a MAR algorithm in a small series of 7 patients who had cerebral aneurysms and were treated with coiling or clipping. Other studies, based on their own versions of a MAR algorithm, have further demonstrated the visualization usefulness of the stent strut and parent vessels in stent-assisted coiling.[9,10] However, the efficacy of the MAR algorithm, as described above in managing different metal objects, has not been reported, to our knowledge.

The patients in our study did not undergo FDCT before the operation. Therefore, we chose the brain parenchyma in a higher or lower section, which was free of metallic artifacts, as the internal reference of imaging quality. We demonstrated that the Siemens MAR software remarkably reduces artifacts and corrects image quality to a level close to the imaging quality of the native image by using adjacent parenchyma as the internal reference. Although the Hounsfield unit range and noise of the corrected images remained slightly higher than those of native images, no significant differences existed. We noticed that in most cases, certain darker areas surrounding the implants remained after MAR correction. These artifacts may be the secondary artifacts introduced by the correction scheme and may be the reason the imaging quality remained inferior to that of native images.[15,16] In our results, the types of metal objects and the coil lengths did not affect the results of the investigated MAR algorithm.

In assessing subjective image quality, we demonstrated that the MAR software substantially improved the visibility of the metal object vicinity, in which image qualities were most severely degraded before correction. Consequently, the overall imaging quality of surrounding regions improved in >78% of the cases following MAR. Nearly all coiling cases had increased diagnostic confidence following MAR. In contrast, the rater score was lower in the liquid embolizer group, though the Hounsfield unit range and noise in the corrected images showed no difference from

those of the coiling group. Our explanation is that liquid embolizer shape and distribution were typically irregular and scattered in these cases. Despite significant artifacts reduction, the blurred regions and the secondary artifacts introduced by the replaced imaging content of the original x-ray data accumulated in the central regions and significantly hindered the image interpretation (Online Fig 1). Therefore, only half of the cases achieved higher diagnostic confidence following MAR. None of the ventricular shunting group provided additional diagnostic information following MAR because the shunt artifacts were typically limited to the tip of the shunt and were minor, which explains why most cases could be interpreted easily without requiring MAR correction (Online Fig 2).

The main limitation of our study was the relatively small number of cases. We only analyzed 6 patients receiving liquid embolizers and 2 patients undergoing ventricular drainage. Although the sample size was small, the MAR application resulted in promising results for correcting metal artifacts and improving image quality, indicating the need for further research. In the coiling group, we chose coil length rather than aneurysm packing attenuation as the coil attenuation parameter. Because the coil masses are irregular and bilateral in CCF cases, it is difficult to apply the formula of the aneurysm packing attenuation in these cases. Our results indicate the correlation of coil length with artifact severity and achieving reduced metal artifacts in all subgroups of different coil lengths. These findings may provide indirect evidence that the MAR software successfully reduces metal artifacts, regardless of various coiling densities.

CONCLUSIONS

We demonstrated using the MAR prototype to reduce streak artifacts substantially around different metallic implants on FDCT and to improve objective and subjective imaging quality.

Disclosures: Sheng-Che Hung—*RELATED*: *Provision of Writing Assistance, Medicines, Equipment, or Administrative Support*: MAR prototype software,* *Comments*: collaborative project (T1100200) of the Taipei Veterans General Hospital and Siemens, the MAR. Wan-You Guo—*RELATED*: *Other*: supported in part by a collaboration research contract between Taipei Veterans General Hospital and Siemens. *Money paid to the institution.

REFERENCES

1. Kalender WA, Kyriakou Y. **Flat-detector computed tomography (FD-CT).** *Eur Radiol* 2007;17:2767–79
2. Akpek S, Brunner T, Benndorf G, et al. **Three-dimensional imaging and cone beam volume CT in C-arm angiography with flat panel detector.** *Diagn Interv Radiol* 2005;11:10–13
3. Kalender WA. **The use of flat-panel detectors for CT imaging** [in German]. *Radiologe* 2003;43:379–87
4. Gupta R, Cheung AC, Bartling SH, et al. **Flat-panel volume CT: fundamental principles, technology, and applications.** *Radiographics* 2008;28:2009–22
5. Hung SC, Lin CJ, Guo WY, et al. **Toward the era of a one-stop imaging service using an angiography suite for neurovascular disorders.** *Biomed Res Int* 2013;2013:873614
6. Struffert T, Richter G, Engelhorn T, et al. **Visualisation of intracerebral haemorrhage with flat-detector CT compared to multislice CT: results in 44 cases.** *Eur Radiol* 2009;19:619–25
7. Dörfler A, Struffert T, Engelhorn T, et al. **Rotational flat-panel computed tomography in diagnostic and interventional neuroradiology.** *Rofo* 2008;180:891–98
8. Prell D, Kalender WA, Kyriakou Y. **Development, implementation and evaluation of a dedicated metal artefact reduction method for interventional flat-detector CT.** *Br J Radiol* 2010;83:1052–62
9. van der Bom IM, Hou SY, Puri AS, et al. **Reduction of coil mass artifacts in high-resolution flat detector conebeam CT of cerebral stent-assisted coiling.** *AJNR Am J Neuroradiol* 2013;34:2163–70
10. Psychogios MN, Scholz B, Rohkohl C, et al. **Impact of a new metal artefact reduction algorithm in the noninvasive follow-up of intracranial clips, coils, and stents with flat-panel angiographic CTA: initial results.** *Neuroradiology* 2013;55:813–18
11. Meyer E, Raupach R, Lell M, et al. **Normalized metal artifact reduction (NMAR) in computed tomography.** *Med Phys* 2010;37:5482–93
12. Mordasini P, Al-Senani F, Gralla J, et al. **The use of flat panel angioCT (DynaCT) for navigation through a deformed and fractured carotid stent.** *Neuroradiology* 2010;52:629–32
13. Buhk JH, Kallenberg K, Mohr A, et al. **Evaluation of angiographic computed tomography in the follow-up after endovascular treatment of cerebral aneurysms–a comparative study with DSA and TOF-MRA.** *Eur Radiol* 2009;19:430–36
14. Clarençon F, Piotin M, Pistocchi S, et al. **Evaluation of stent visibility by flat panel detector CT in patients treated for intracranial aneurysms.** *Neuroradiology* 2012;54:1121–25
15. Prell D, Kyriakou Y, Struffert T, et al. **Metal artifact reduction for clipping and coiling in interventional C-arm CT.** *AJNR Am J Neuroradiol* 2010;31:634–39
16. Prell D, Kyriakou Y, Beister M, et al. **A novel forward projection-based metal artifact reduction method for flat-detector computed tomography.** *Phys Med Biol* 2009;54:6575–91

Diffusion-Weighted Imaging with Dual-Echo Echo-Planar Imaging for Better Sensitivity to Acute Stroke

S.J. Holdsworth, K.W. Yeom, M.U. Antonucci, J.B. Andre, J. Rosenberg, M. Aksoy, M. Straka, N.J. Fischbein, R. Bammer, M.E. Moseley, G. Zaharchuk, and S. Skare

ABSTRACT

BACKGROUND AND PURPOSE: Parallel imaging facilitates the acquisition of echo-planar images with a reduced TE, enabling the incorporation of an additional image at a later TE. Here we investigated the use of a parallel imaging–enhanced dual-echo EPI sequence to improve lesion conspicuity in diffusion-weighted imaging.

MATERIALS AND METHODS: Parallel imaging–enhanced dual-echo DWI data were acquired in 50 consecutive patients suspected of stroke at 1.5T. The dual-echo acquisition included 2 EPI for 1 diffusion-preparation period (echo 1 [TE = 48 ms] and echo 2 [TE = 105 ms]). Three neuroradiologists independently reviewed the 2 echoes by using the routine DWI of our institution as a reference. Images were graded on lesion conspicuity, diagnostic confidence, and image quality. The apparent diffusion coefficient map from echo 1 was used to validate the presence of acute infarction. Relaxivity maps calculated from the 2 echoes were evaluated for potential complementary information.

RESULTS: Echo 1 and 2 DWIs were rated as better than the reference DWI. While echo 1 had better image quality overall, echo 2 was unanimously favored over both echo 1 and the reference DWI for its high sensitivity in detecting acute infarcts.

CONCLUSIONS: Parallel imaging–enhanced dual-echo diffusion-weighted EPI is a useful method for evaluating lesions with reduced diffusivity. The long TE of echo 2 produced DWIs that exhibited superior lesion conspicuity compared with images acquired at a shorter TE. Echo 1 provided higher SNR ADC maps for specificity to acute infarction. The relaxivity maps may serve to complement information regarding blood products and mineralization.

ABBREVIATIONS: DW = diffusion-weighted; GRAPPA = generalized autocalibrating partially parallel acquisition; GRE = gradiant-recalled echo; PI = parallel imaging; R_2 = relaxivity map

Diffusion-weighted imaging plays a key role in evaluating multiple neurologic diseases, including stroke.[1-7] In DWI, the image intensity reflects the rate of water diffusion at a given location, but DWI also remains sensitive to T1 and T2 relaxation (and proton attenuation). T1 relaxation effects can be mitigated by using a long TR to allow longitudinal relaxation. Due to the insertion of the diffusion gradients and the associated TE prolongation, however, T2 effects cannot be mitigated during image acquisition. Thus, T2 and diffusion effects are entangled on DWI, though it is often clinically important to differentiate their relative contribution to the final image. Therefore, the quantitative ADC images are produced, which remove the T2 weighting effect.[8,9]

The most efficient, reliable, and thereby conventional method for DWI acquisition is with the EPI technique. A significant limitation of diffusion-weighted (DW)-EPI is the presence of susceptibility artifacts, which manifest as geometric distortion, signal drop-out, and image blurring. To reduce such artifacts in DW-EPI, parallel imaging (PI)[10,11] can be used to accelerate EPI.[12,13] In PI-enhanced EPI, the echo train is shortened, thereby reducing TE. A short TE in DWI is typically considered as advantageous because it results in a higher SNR and reduces the T2 contrast. However, because many lesions with reduced diffusivity also have prolonged T2 values compared with the surrounding tissue,[14] a short TE may reduce the conspicuity of ischemic lesions.

With the hypothesis that improved conspicuity of lesions with reduced diffusivity can be achieved by longer TEs than in conven-

Received August 9, 2013; accepted after revision December 5.

From the Department of Radiology (S.J.H., K.W.Y., M.U.A., J.R., M.A., M.S., N.J.F., R.B., M.E.M., G.Z.), Stanford University, Stanford, California; Department of Radiology (J.B.A.), University of Washington, Seattle, Washington; and Clinical Neuroscience (S.S.), Karolinska Institute, Stockholm, Sweden.

This work was supported by the National Institutes of Health (2R01 NS047607-06, 2R01 EB00271108-A1, 5RO1 EB008706, 5R01 EB01165402–02), the Center of Advanced MR Technology at Stanford (P41 EB015891), and the Lucas Foundation.

Please address correspondence to Samantha Holdsworth, PhD, Department of Radiology, Stanford University, Lucas Center, 1201 Welch Rd, Stanford, CA 94305-5488; e-mail: sholdsworth@stanford.edu

http://dx.doi.org/10.3174/ajnr.A3921

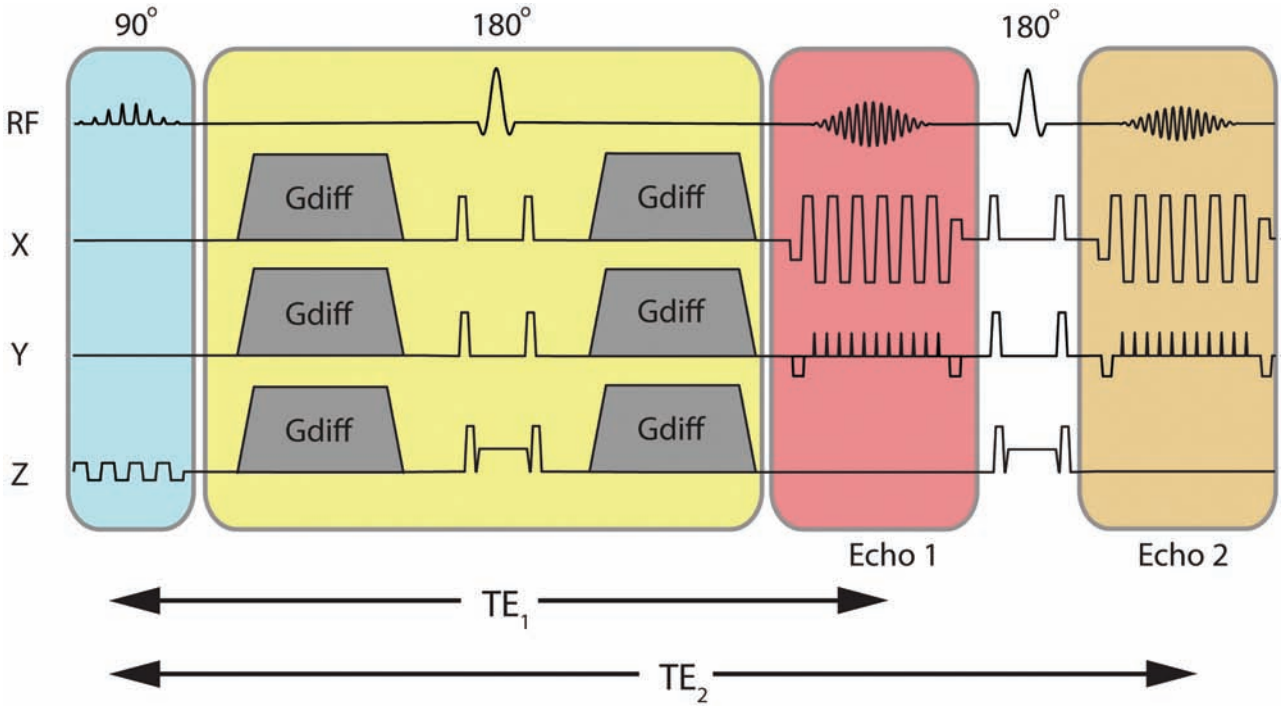

FIG 1. Dual-echo DWI pulse sequence showing the section-select module (blue); diffusion preparation period (yellow); and the first and second imaging echoes (echoes 1 and 2 acquired at 2 different TEs, TE_1 and TE_2) separated by a 180° refocusing pulse.

tional practice, 1 option is to simply increase the TE (within reasonable limits) of a DWI acquisition. Another option is to increase the b-value (which also increases the contribution of reduced diffusion in the signal). Unfortunately, both approaches reduce the SNR of the ADC image (computed from the $b=0$ and the DWI), which is used for diagnostic specificity. Another option is to add a second DW echo within the same TR[15,16]—an approach that does not significantly impact the overall scanning time. Figure 1 depicts this dual-echo DWI approach, with 2 EPI trajectories acquired for 1 diffusion-preparation period (echo 1 and echo 2, respectively). Here, echo 2 is used to increase the sensitivity to lesions, and echo 1 provides a higher SNR image used to calculate the ADC. Furthermore, relaxivity (R_2) maps can be calculated from the 2 $b=0$ images to potentially reveal an additional source of image contrast without additional scanning time.

In this work, we imaged patients clinically suspected of acute or subacute stroke by using a PI-enhanced dual-echo DW-EPI sequence on a 1.5T clinical scanner to explore the impact that a longer TE might have on clinical management and patient outcome. Our aim was to evaluate the 2 diffusion-weighted echoes (echo 1 and echo 2) obtained from the dual-echo sequence on image quality, lesion quality, and diagnostic quality metrics, and to evaluate relaxivity maps calculated from the 2 echo images as a potential additional source of image contrast.

MATERIALS AND METHODS

Patient Studies

All data were acquired on an inpatient 1.5T MR imaging system (Signa HD; GE Healthcare, Milwaukee, Wisconsin) equipped with an 8-channel head coil. With institutional review board approval, 50 consecutive adult patients who were clinically suspected of stroke were scanned with the dual-echo DWI sequence between January 13, 2011, and April 6, 2011. The product DWI sequence used as part of standard of care at our institution was used as the criterion standard comparison DWI sequence for this study. We also acquired additional routine MR images relevant to the clinical scenario: T2-weighted FLAIR, T2-weighted gradient-recalled echo (GRE), fast spin-echo, MRA of the circle of Willis, and bolus perfusion imaging. The final clinical diagnosis was based on the imaging findings that were correlated with appropriate clinical symptoms (Table 1).

Table 1: Clinical history of the 50 patients who were suspected of stroke and scanned for this study[a]

Clinical History	No. of Patients	No. of Patients with Lesions with Reduced Diffusivity
Moyamoya disease	5	5
Transient ischemic attack	16	5
Stroke	14	14
Cavernous malformation	3	2
Hemorrhage	5	5
Vasospasm post-subarachnoid hemorrhage	3	3
Metabolic disease	1	0
Brain tumor	2	1
Headache	1	1
Total No. of patients	50	36

[a] The number of patients with lesions with reduced diffusivity present on ≥1 of the scanned DWI sequences is also shown.

Imaging Sequence and Reconstruction

Our generalized autocalibrating partially parallel acquisition (GRAPPA)-accelerated DWI sequence was modified to include a second-echo EPI trajectory succeeding a second 180° refocusing pulse (Fig 1). Patient data were acquired by using the following imaging parameters: GRAPPA acceleration factor of R = 3, FOV =

Table 2: Agreement among readers on specific ratings using a weighted κ statistic ($N = 50$)[a]

	Echo 1			Echo 2		
	Diag Conf	Conspicuity	Quality	Diag Conf	Conspicuity	Quality
A vs B	−0.05	0.10	0.00	0.07	−0.00	−0.09
A vs C	0.10	0.13	0.31	0.16	0.13	−0.09
B vs C	0.02	−0.02	0.00	0.09	0.14	0.31

Note:—Diag Conf indicates diagnostic confidence.
[a] All ratings are with $P > .14$.

Table 3: Preference for the second echo over the first echo

Reader	Fraction	Percentage	95% CI	*P* Value (1-tailed)
Reader A	35/50	70%	(55%–82%)	.003
Reader B	38/50	76%	(62%–87%)	<.001
Reader C	34/50	68%	(53%–80%)	.008

Table 4: Percentage of cases rated greater than the product DWI ($N = 50$)

	Echo 1			Echo 2		
	Diag Conf	Conspicuity	Quality	Diag Conf	Conspicuity	Quality
A vs B	92%	84%	100%	96%	98%	100%
A vs C	78%	66%	100%	96%	98%	92%
B vs C	96%	92%	100%	96%	94%	94%

Note:—Diag Conf indicates diagnostic confidence.

Table 5: Mean (SD) of ratings ($N = 50$)

	Diagnostic Confidence		Conspicuity		Quality	
	Echo 1	Echo 2	Echo 1	Echo 2	Echo 1	Echo 2
Reader A	5.7 (0.9)	6.4 (0.7)	5.1 (1.0)	6.3 (0.9)	6.3 (0.5)	5.5 (0.6)
Reader B	4.8 (0.7)	5.6 (0.6)	4.4 (0.9)	6.0 (0.7)	5.8 (0.4)	4.5 (1.0)[a]
Reader C	5.8 (0.6)	6.4 (0.8)	5.2 (0.7)	6.1 (0.9)	6.1 (0.3)	4.8 (0.7)[b]

[a] $P = .004$.
[b] $P = .002$; all others, $P < .0001$.

24 cm, acquisition matrix = 192 × 192, 5-mm/0-mm section thickness/gap, partial Fourier encoding with 24 overscans, TE_1/TE_2 = 48/105 ms, Stejskal-Tanner diffusion preparation,[17] tetrahedral encoding (4 diffusion directions) with $b = 1000$ s/mm^2, and 1 T2-weighted ($b = 0$) image. Each volume was acquired by using 3 interleaves. The fully sampled $b = 0$ image was formed after combining the 3 interleaves and was used to enable the estimation of GRAPPA weights. These estimated GRAPPA weights were applied to all interleaves of all acquired volumes separately, including the $b = 0$ volume itself.[13] A TR of 3 seconds was used to keep T1 saturation effects small in the brain parenchyma (resulting in 95.8% and 99.3% T1 recovery at 1.5T, assuming a T1 = 950 ms/600 ms for gray and white matter, respectively[18]). A maximum of 23 sections was permitted in a TR of 3 seconds, and the total scanning time was 2 minutes 15 seconds. The product DWI sequence scanned routinely at our institution was used as the criterion standard DWI sequence for this study, which used a PI-enhanced (sensitivity encoding–type) EPI sequence with the following parameters: matrix size = 128 × 128, acceleration factor R = 2, partial Fourier encoding, TR/TE = 8 seconds/70 ms, twice-refocused[19,20] diffusion preparation, 23 sections with a 5-mm/0-mm section thickness/gap, partial Fourier encoding with 16 overscans, 3 diffusion directions with $b = 1000$ s/mm^2, one T2-weighted ($b = 0$) image, and a scanning time of 50 seconds.

The postprocessing of the dual-echo DWI data was performed

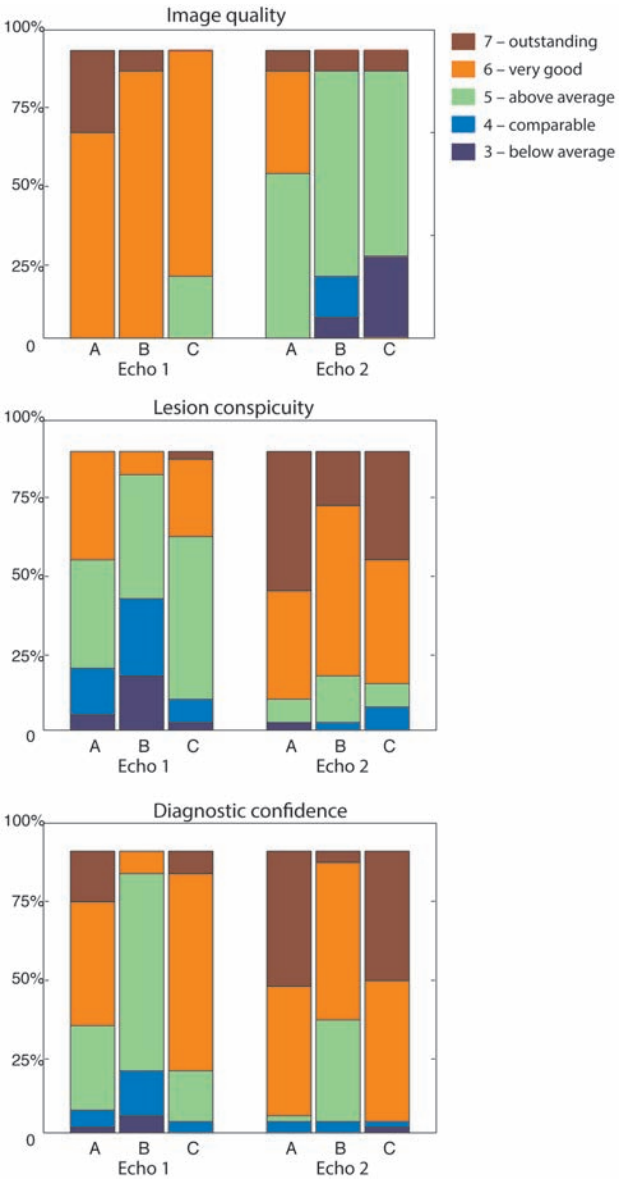

FIG 2. Assessment of readers A, B, and C of image quality, lesion conspicuity, and diagnostic confidence. Nominal values of 3–7 represent reader grading compared with the product DW-EPI (assigned as 4), represented by the percentage of total assigned values. Note that values of 1–2 (corresponding to "nondiagnostic" and "poor") are not shown because these values were not assigned in this study.

by using a compiled and multithreaded Matlab code (Version 7.8.0; MathWorks, Natick, Massachusetts). Both echoes (echo 1 and echo 2) were reconstructed and sent to our hospital image data base (PACS). These DWI datasets included the isotropic DWI from the 2 echoes (E_1 and E_2); the isotropic ADC calculated from the $b = 0$ and $b = 1000$ s/mm^2 from echo 1; and the relaxivity maps, R_2, calculated from the average of the $b = 0$ and $b = 1000$ s/mm^2 relaxivity maps as follows:

$$R2 = \frac{1}{2}(R_{E1} + R_{E2}) = \frac{1}{2}\left(\frac{\log(B0_2 / B0_1)}{TE_2 - TE_1} + \frac{\log(DW_2 / DW_1)}{TE_2 - TE_1}\right),$$

where *B0* represents the $b = 0$ s/mm^2 image, and *DW*, the $b = 1000$ s/mm^2 image at 2 TEs.

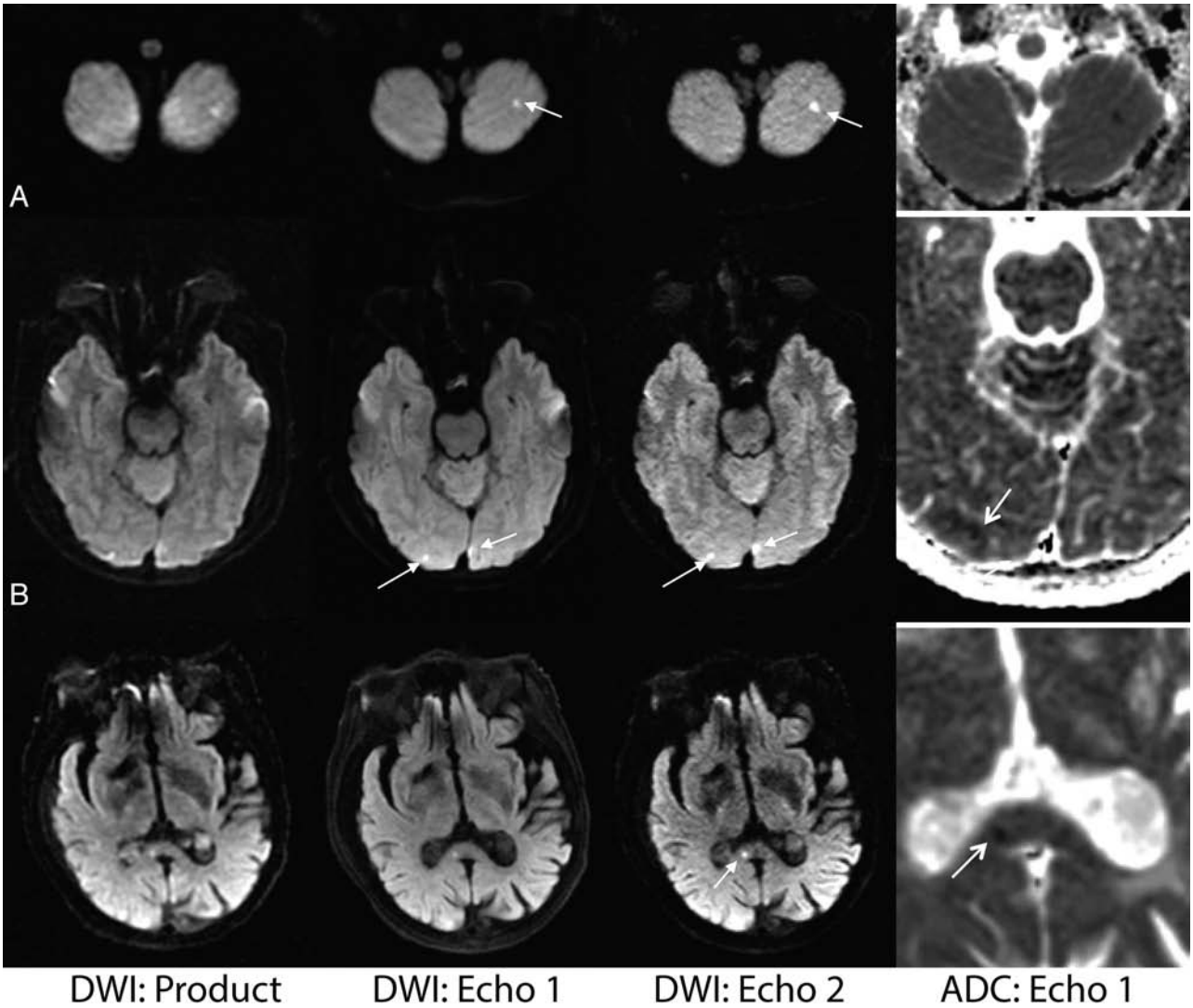

FIG 3. Comparison of the vendor-supplied (product) DWI, echo 1, and echo 2 DWI acquired from the dual-echo sequence on 3 patients (from left to right). The ADC (calculated from echo 1) shows the presence of reduced diffusivity in each lesion (far right column). *A*, A 62-year-old female patient with stroke. *B*, A 49-year-old male patient with vasospasm and infarction post-aneurysm clipping. *C*, An 88-year-old woman presenting with strokelike symptoms. Note that the small infarct in the splenium of the corpus callosum present on the dual-echo DWIs was initially missed on the product DWI.

Imaging Evaluation

Three blinded board-certified neuroradiologists (readers A–C) with 7 years', 5 years', and 1 year experience, respectively, independently evaluated the DWIs of echo 1 and echo 2 for lesions with reduced diffusivity in 50 patients admitted for possible stroke. Each reader, blinded to the clinical symptoms and final diagnosis, first viewed the DWI from echo 1, followed by the DWI from echo 2, by using the reference product DWI as the criterion standard. The neuroradiologists made following evaluations:

1) Presence/absence of DWI-hyperintense lesions on echoes 1 and 2 (yes/no)
2) Diagnostic confidence for each echo DWI (echo 1 and 2) relative to the reference image
3) For cases with DWI-hyperintense lesions, the lesion conspicuity of each echo image relative to the reference image
4) For cases without DWI-hyperintense lesions, the image quality of each echo image relative to the reference image
5) Overall preference for the DWI from echo 1 or echo 2 (binary forced choice).

Diagnostic confidence, lesion conspicuity, and image quality for the DWI echo images were scored on the following 7-point Likert scale: 1, nondiagnostic; 2, poor; 3, acceptable; 4, comparable with product DWI (the criterion standard); 5, above average; 6, very good; and 7, outstanding.

Reader B made the following additional evaluations:

1) The number of new lesions seen on the DWI of echo 2 compared with that of echo 1
2) The presence of something new on the DWI of echo 2 compared with that of echo 1 (yes/no)
3) Clinical impact: if additional information was garnered from the DWI of echo 2, would this alter clinical management, such as therapy or clinical referral? (0, no; 1, possible; 2, yes).

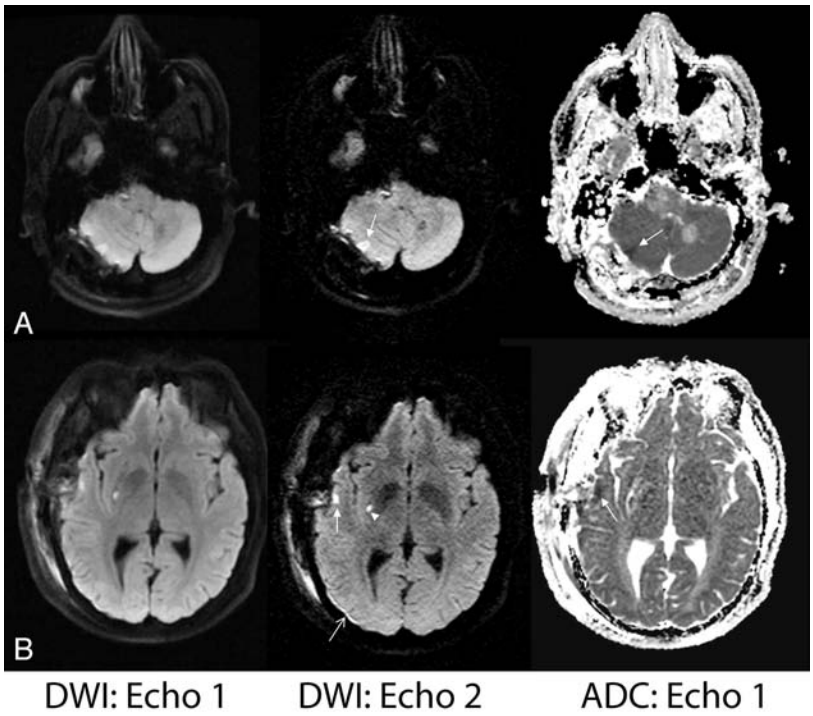

FIG 4. Examples of improved lesion detection of echo 2. *A*, A 56-year-old man status post posterior fossa tumor resection. Right cerebellar injury is more conspicuous on echo 2 and was confirmed to have reduced diffusion based on ADC. *B*, A 39-year-old man with known Moyamoya disease status post right superficial temporal artery to middle cerebral artery anastomosis presented with acute strokelike symptoms. Superficial temporal cortical lesion (*closed arrow*) and a punctate putaminal lesion (*arrowhead*) are confirmed with reduced diffusivity based on the ADC map. Also note improved delineation of a small subdural hematoma on echo 2 (*open arrow*).

For this last scenario, a representative case might be one in which echo 2 identified additional focal lesions in the same vascular territory. In such a case, clinical management would likely not be altered (score 0). However, if other lesions were seen in new vascular distribution, a more detailed clinical investigation may ensue for a potential embolic source (score 1). Alternatively, if echo 2 identified a new lesion in a case previously interpreted as having negative findings, management may alter in terms of patient risk stratification for future stroke or initiating therapies for the current lesion or for future stroke prevention (score 2).

Lesion conspicuity and diagnostic confidence took into account the readers' ability to readily observe lesions against the background tissue, as well as lesion delineation. Diagnostic confidence, clinical impression, and clinical impact were assessed in the context of other imaging data (ADC, FLAIR, GRE). Small lesions on echo 2 that were difficult to confirm on ADC were given independent assessments from the readers as to whether their presence increased or decreased diagnostic confidence. Final clinical diagnosis was made by using all clinical and imaging material (including previous examinations, if available) and served as ground truth for the study.

Lesions detected by echo 2 were validated for the presence of acute infarction by using the ADC from echo 1. If these lesions did not have reduced diffusivity, FLAIR images were used to identify possible associated parenchymal T2 hyperintensity. Extra-axial hemorrhage was excluded from this assessment.

Relaxivity Maps

The relaxivity maps were viewed and weighed against all other imaging data for potential complementary diagnostic information.

Statistical Analysis

All statistical analyses were performed with STATA, Release 11.1 (StataCorp, College Station, Texas). Agreement among readers was assessed by a linearly weighted κ statistic. Preference for echo 1 or echo 2 was tested with an exact binomial test with a null value of 0.5. Tests for superiority compared with standard imaging were performed with 2-tailed Wilcoxon signed rank tests with a null median of 4 on the Likert scale (comparable with product DWI). Tests for differences in ratings between echo 1 and echo 2 were performed by using 2-tailed Wilcoxon signed rank tests. There was no correction for multiple comparisons.

RESULTS

Table 1 shows the clinical diagnoses of all the patients who were referred for diagnostic work-up for stroke-like symptoms. Lesions with reduced diffusivity were found in 36 of the 50 patients. Readers B and C were in perfect agreement in assessing the presence of lesions with reduced diffusivity, and both differed from reader A in 4 cases (2 patients with lesions that had reduced diffusivity, and 2 lesions without reduced diffusivity; $\kappa = 0.80$; 95% CI, 0.58–0.95).

There was little agreement among readers for specific ratings (Table 2), yet all 3 readers preferred the DWI of echo 2 over echo 1 for patients with lesions with reduced diffusivity (Table 3). Echo 1 and echo 2 images were consistently preferred over the product DWI (reference) image (Table 4). For all readers, echo 1 had better image quality than echo 2 because echo 1 was subjectively a more aesthetically pleasing and higher SNR image. However, echo 2 was rated higher than echo 1 for lesion conspicuity and diagnostic confidence (Table 5). Figure 2 depicts individual reader assessment of image quality, lesion conspicuity, and diagnostic confidence for echoes 1 and 2, respectively, as a percentage of the total assigned values per reader. The median values for echo 1 and 2 assessments for all patients were the following: 6 and 5, respectively, for image quality; and 5 and 6, respectively, for lesion conspicuity and diagnostic confidence.

Seventy-two new lesions were identified on echo 2 DWI (that were not seen on echo 1) in 46% of evaluated patients. Of these, 67 were confirmed as lesions with reduced diffusivity based on the ADC generated from echo 1. Three lesions were too small to assess; 2 were deemed to represent edema associated with T2 prolongation based on ADC. The 72 newly identified lesions with reduced diffusivity on echo 2 were seen in 18 patients with acute

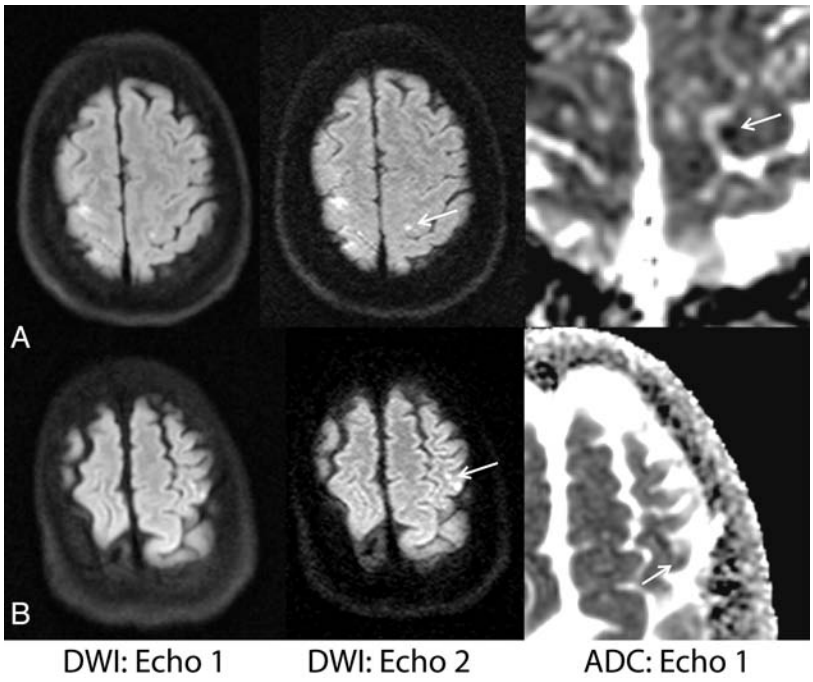

FIG 5. Examples in which additional lesions identified by echo 2 suggested a potential underlying mechanism of stroke and potentially altered diagnostic impression and clinical management. *A*, A 60-year-old woman with vasospasm after subarachnoid hemorrhage. *B*, A 65-year-old woman with embolic infarcts who also had lesions in the right cerebral hemisphere more inferiorly (not shown). On both patients, echo 2 showed missed sites of reduced diffusivity on the contralateral hemisphere (*arrows*), suggesting multiple vascular distribution involvement (vasospasm in multiple vascular territories or embolic source). Note that the lesions were retrospectively observed on echo 1 (but not on the product DWI).

infarction and 3 patients with intracranial hemorrhage. Of the 18 patients with acute infarction, 2 had embolic infarcts from cardiac causes, 4 had infarcts related to underlying Moyamoya disease, 4 had ischemic lesions related to vasospasm and prior aneurysm coiling/clipping, 1 had ischemic changes adjacent to operative site, and 7 patients had infarcts that were not otherwise specified clinically. Due to its added sensitivity to diffusion lesions, it was predicted that echo 2 would have impacted stroke work-up in 16% of cases (8 patients) and potentially influenced 32% of cases (16 patients).

Figure 3 is representative of a case in which the routine product DWI sequence demonstrated lower diagnostic confidence compared with echoes 1 and 2.

Figure 4 depicts 2 cases in which echo 2 demonstrates improved lesion conspicuity compared with echo 1. These patients had recently undergone surgery, and the findings on echo 2—while not likely to alter clinical management as determined during the radiologists' readings—better defined the nature of the postoperative changes (such as local isch-

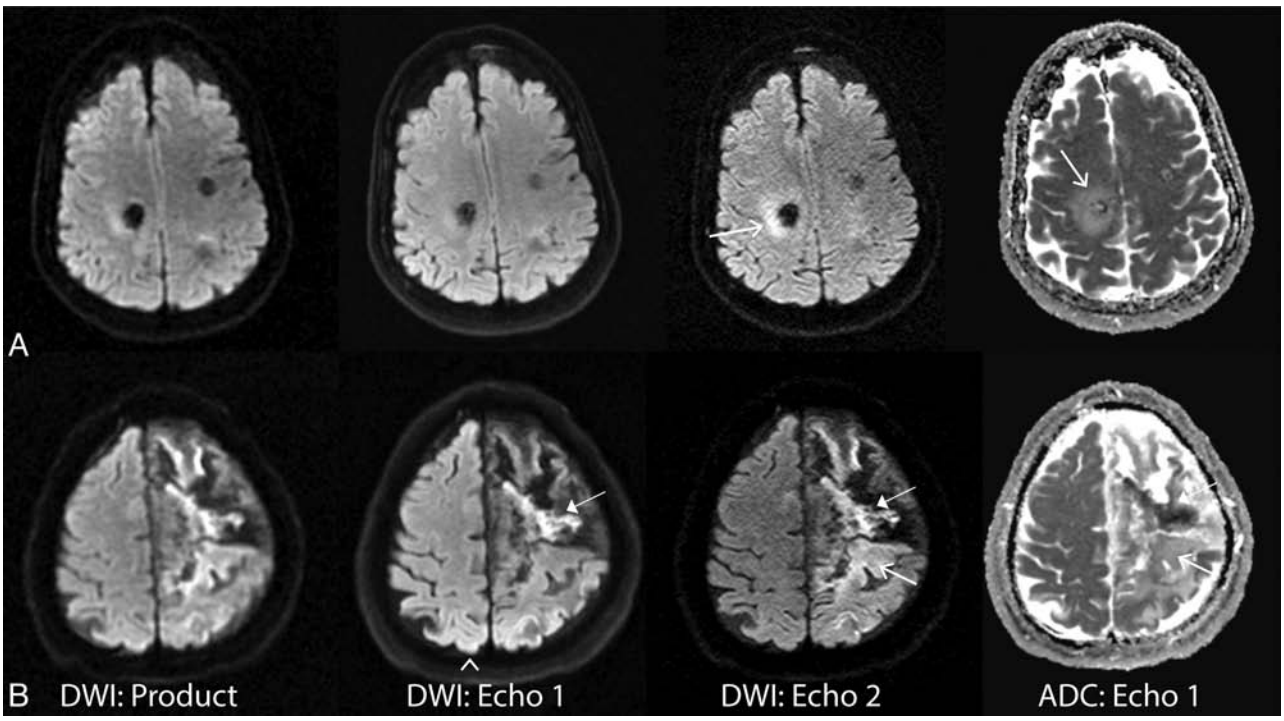

FIG 6. Examples in which the heightened sensitivity of echo 2 prompted further assessment by using ADC. *A*, A 61-year-old woman with hemorrhage from a cavernous malformation. Bright signal around the lesion was seen on echo 2 (and product) DWI and was confirmed as edema around a hemorrhage site (*open arrows*). *B*, A 69-year-old man with strokelike symptoms. Example of acute and subacute (*closed arrows*)/chronic stroke (*open arrows*) on echo 2 DWI, also present on the product DWI. Also note the arrowhead on echo 1 showing unwanted heightened coil sensitivity in the posterior brain region.

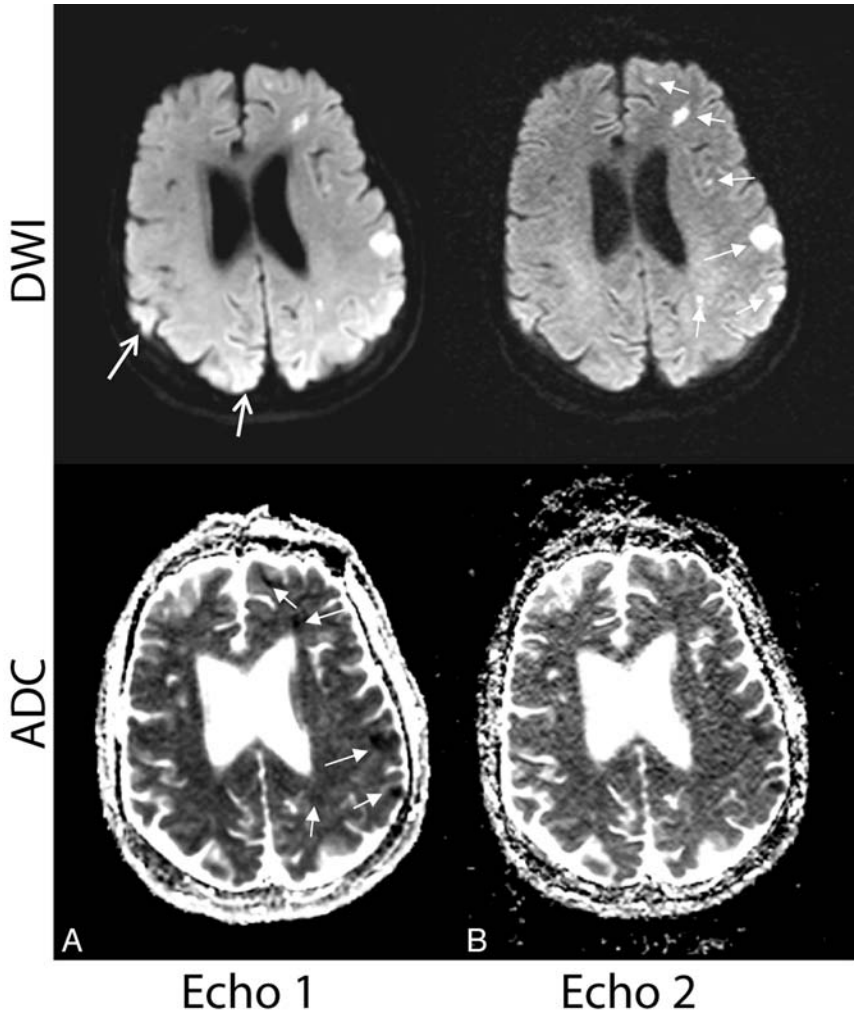

FIG 7. Case illustrating why echo 1 is more useful than echo 2 for calculating ADC maps used for the validation of acute infarct. Select images of a 66-year-old woman with embolic infarcts. DWI and ADC maps for echo 1 (*A*) and echo 2 (*B*) are shown. The DWI of echo 2 was found to have much higher sensitivity to acute lesions (confirmed on the ADC of echo 1) than echo 1. However, because the ADC of echo 2 is plagued by noise, echo 1 is considerably more useful for calculating ADC maps used for the validation of acute stroke (*closed white arrows*). The open white arrows represent areas where it can be difficult to rule out stroke from heightened coil sensitivity in (particularly posterior) regions of the brain.

emia and/or hemorrhage), potentially revealing etiologies for perioperative symptoms.

Figure 5 depicts examples in which echo 2 identified lesions with reduced diffusivity that were missed on echo 1. Here, a site of reduced diffusivity (confirmed on ADC, formerly missed by both echo 1 and the reference DWI) in the contralateral cerebral hemisphere was identified, raising the possibility of an embolic source of infarction.

In 2 cases, echo 2 revealed lesions that would not have been deemed acute (hyperintense lesions on echo 2 DWI but not confirmed by ADC and associated with high signal on FLAIR). In 1 such case, echo 2 revealed a halo of hyperintense signal resembling edema (Fig 6*A*), prompting the readers to review the ADC map. In another case, echo 2 identified both acute (low signal on ADC) and subacute (isointense to slightly bright signal on ADC) evolving areas of infarction (Fig 6*B*) as hyperintense foci. Without the aid of ADC, echo 2 thus overestimated regions of acute ischemia in this case.

Figure 7 shows both echo 1 and echo 2 DWI and ADC of a patient with multiple embolic infarcts. Fourteen new lesions were found on the DWI of echo 2 in this patient, all of which were confirmed as lesions with decreased diffusivity on ADC of echo 1.

Relaxivity Maps

The R_2 maps were deemed useful in several regards. Both acute and chronic infarcts demonstrated low R_2 values that were readily apparent. Even small areas of ischemia were identified on the R_2 maps. For instance, R_2 maps frequently identified lesions presumed to represent chronic small-vessel ischemic disease in the periventricular and subcortical white matter, a finding typically identified on FLAIR and T2-weighted images. The R_2 maps identified areas of subarachnoid, old cerebellar, and intraventricular hemorrhage (including some foci that were difficult to visualize on the GRE scan). Mineralization was depicted as regions of high R_2 and was particularly notable in the basal ganglia (Fig 8).

DISCUSSION

This work investigated an alternative-approach DWI with the use of a PI-enhanced dual-echo sequence. Typically, DWI sequences use the shortest TE available by the vendor to avoid significant T2-weighting. The primary underlying concern is that a longer TE will result in a lower SNR, and a higher rate of false-positive lesions (that is, lesions that do not have reduced diffusivity) on DWI from increased T2-weighting. However, many lesions with reduced diffusivity also have a prolonged T2 value compared with the surrounding tissue[6,8]; thus, DWI studies may benefit from a longer TE. Improved conspicuity of ischemic lesions bought by long TEs has also incidentally been observed in a comparison among DWI acquired with different imaging parameters.[9]

The findings in this work support the use of a DWI approach that achieves both a high effective resolution through the use of PI and a long TE to draw the radiologist's attention to acute ischemic lesions. However, because PI effectively shortens the TE, one approach is to "waste" sequence time and use a longer TE, and the other is to incorporate a more sensitive second echo at a reasonable TE, as done in this work, and thereby use the information from both echoes. With the acquisition of 2 echoes acquired at different TEs within 1 diffusion-preparation period, we found that one can use echo 2 for improved sensitivity to ischemic lesions with reduced diffusivity.

Radiologist Ratings

This study found that the DWI from echo 2 was useful for lesion delineation and improved detection compared with the DWI

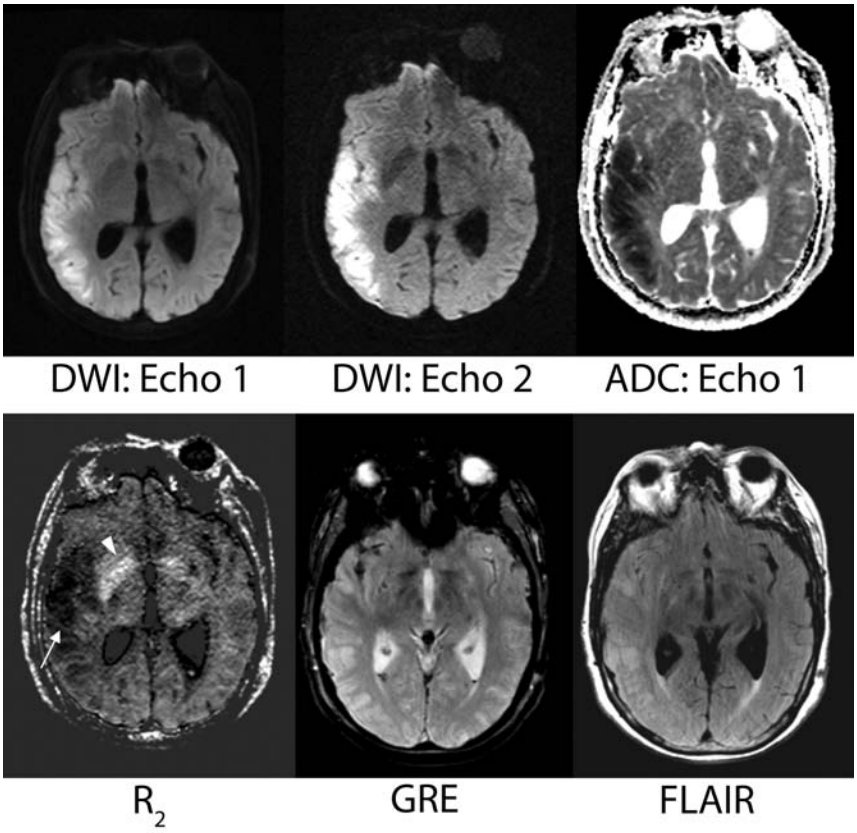

FIG 8. A sample case showing the potential contribution of the R_2 map. A 69-year-old female patient with vasospasm after subarachnoid hemorrhage. The low-R_2 lesion is more conspicuous than the corresponding T2 hyperintensity on the FLAIR image. On the basis of DWI/ADC, this area represents acute right MCA territory infarction. The potential contribution of the R_2 map with regard to timing of stroke and its evolution is unknown but prompts future investigation. The R_2 map also shows more conspicuous mineralization in the basal ganglia than the gradient-recalled echo image (*arrowhead*).

from echo 1 and the product DWI. Echo 2 was rated higher than both echo 1 and the reference product DWI for lesion conspicuity and diagnostic confidence (Fig 2). Echo 1 was rated as better than the product DWI sequence. While several lesions showed higher signal intensity on the product DWI than on echo 1 (related to the intermediate TE of the product DWI [70 ms] between that of echo 1 [48 ms] and that of echo 2 [105 ms]), echo 1 was preferred for its ability to resolve lesions.

Seventy-two additional lesions were identified on echo 2 (that were not seen on echo 1 in the initial reading) in 23 patients diagnosed with acute infarct. Of these, 93% were deemed lesions with "reduced diffusion" on ADC, 4% were too small to assess, and the remaining 3% were chronic lesions. As a result, of the 50 patients scanned for this study, the findings on echo 2 were predicted to have impacted stroke work-up in 16% of cases (8 patients) and potentially influenced 32% of cases (16 patients).

Echo 2 was rated lower than echo 1 for image quality—presumably on the basis of its reduced SNR. However, our data suggest that the benefit of heightened lesion conspicuity and diagnostic quality of echo 2 far outweighs the resultant decrease in image quality during clinical image interpretation. This benefit becomes particularly evident in the scoring of the 14 studies with negative findings. Despite consistently scoring echo 2 as having lower image quality, the clinical confidence in a negative study remained high. We speculate that this reflects the high sensitivity associated with echo 2. In addition, the more uniform background signal associated with echo 2 allowed greater reliability in radiologic interpretation and in distinguishing infarct from heightened coil sensitivity at the periphery of the image. This observation, coupled with improved sensitivity to lesions with reduced diffusivity, likely increased confidence in interpreting examinations as having negative findings when correlated with subsequent studies.

Representative Cases

Figure 3 is representative of a case in which the routine product DWI sequence demonstrated lower diagnostic confidence, due to inferior image quality, compared with echoes 1 and 2. In this case, a small infarct present on the dual-echo DWI on Fig 3*C* was initially missed on the product DWI, a finding that could have prompted further clinical investigation for the source or altered risk for future stroke. Figures 4 and 5 show cases in which echo 2 demonstrated improved lesion conspicuity and diagnostic confidence compared with echo 1. Figure 5 also shows an example of a missed contralateral lesion that would have changed the clinical management of the patient because it raised the possibility of an embolic source of infarction. Note that many lesions detected on echo 2 could be seen retrospectively, either by a side-by-side comparison with echo 1 or the product DWI, or simply by scrolling through the images at a considerably slower rate than is performed in a typical clinical practice.

Of the lesions that were either too small to assess or deemed chronic, we would argue that an image with heightened sensitivity to lesions with a relatively small false-positive rate is preferred over a less sensitive technique where one may miss lesions. Figure 6 shows 2 examples in which the heightened sensitivity of echo 2 to both acute and chronic lesions prompted radiologists to probe other imaging sequences to render the final imaging impression. In these instances, the radiologists still preferred echo 2 because combining the information obtained in echo 2 with the ADC generated from echo 1 improved specificity and guided their diagnostic process. Nevertheless, for any TE, DWI contains mixed contributions from diffusion, proton attenuation, and T2 effects.[9] Even by using a single-shot EPI technique, T2 contrast on DWI is never completely eliminated because the TE is too long (mainly due to the presence of the diffusion-preparation time). Thus, interpreting echo 2 in isolation can yield false-positive results. DWI should be used to screen for lesions and then should be

interpreted with reference to images obtained with other sequences, such as FSE, FLAIR, and the ADC map.[21]

Practical Considerations

While the DWI of echo 2 was considered superior to that of echo 1 in all measures apart from image quality, one must acquire a higher SNR echo 1 image to produce an ADC map to aid diagnostic specificity. Figure 7 shows echo 1 and echo 2 DWI and ADC maps of a patient with multiple embolic infarcts—illustrating the difficulty of decoupling noise from the infarct on the ADC of echo 2. Figure 7 also demonstrates that echo 2 can be more reliable in distinguishing infarct from heightened coil sensitivity present at the periphery of the image (particularly the posterior brain regions) on echo 1.

Relaxivity Maps

Another advantage of the dual-echo approach is that R_2 maps can be computed from the $b=0$ and $b=1000$ images acquired from the first and second echo, to reveal a potentially useful, additional image contrast typically acquired with a separate scan (Fig 8). Although not thoroughly studied, R_2 maps were particularly useful for visualizing hemorrhagic material and hemorrhagic transformation within a stroke, areas of mineralization, and new and old areas of infarction. In this capacity, relaxivity maps generated from the dual-echo process might provide complementary information otherwise obtainable only by requisite sequences such as FLAIR or GRE, though further research will be needed to fully explore this observation.

Limitations

With a PI factor of 3 to shorten the EPI readout coupled with the clinical DWI parameters used in this work, it was possible to acquire echo 2 with no increase in overall scanning time compared with its single-echo alternative, because its incorporation exploited the dead time of the sequence (ie, for 23 sections, the second echo fit within the TR of 3 seconds that we typically use clinically at our institution). However, a caveat of the dual-echo approach is that the scanning time will increase if one desires thinner sections or a higher spatial resolution than used in this work. For example, a section thickness of 3 mm coupled with 38 sections to maintain the same brain coverage as used here will result in an ~25% increase in scanning time compared with the single-echo alternative (for the same in-plane resolution and TR used in this study).

Another limitation of this study is our use of the Stejskal-Tanner diffusion preparation, rather than the twice-refocused[19,20] diffusion preparation sequence that minimizes eddy current effects. We purposely chose the Stejskal-Tanner approach to help minimize the TE of echo 2—to increase the SNR and avoid excessive T2 contrast; however, this resulted in eddy current–induced artifacts that manifested as blurring in the final DWI of both echoes. These artifacts can be reduced with the use of eddy current–correction methodology.[22,23]

Future Work

There are additional ways one may be able exploit a dual-echo sequence to reveal useful information. Because both echoes share the same coil sensitivity profile, one can "flatten" the DWI by removing the coil sensitivity.[24] While one cannot decouple proton attenuation from coil sensitivity by using this approach, the resulting image contrast may be an interesting one to explore and will be the subject of further investigation.

CONCLUSIONS

The PI-enhanced dual-echo DWI approach is a useful method for evaluating DWI lesions. Echo 2 can be used for added sensitivity in detecting lesions with reduced diffusivity; echo 1, for higher SNR ADC maps, while R_2 maps calculated from both echoes may provide a potential source of complementary information. We also demonstrated that many new lesions became apparent on echo 2 that predominantly reflected acute ischemia or brain injury, and we maintain that the TE in DWI can be exploited to draw the radiologist's attention to such lesions.

ACKNOWLEDGMENTS

We would like to thank Patrick D. Barnes for his generous support and assistance with this study.

Disclosures: Murat Aksoy—*RELATED*: *Grant*: National Institutes of Health. Matus Straka—*UNRELATED*: *Employment*: Kantonsspital Winterthur, Winterthur Switzerland, *OTHER RELATIONSHIPS*: Director of Research, iSchemaView Inc. Roland Bammer—*RELATED*: *Grant*: National Institute of Biomedical Imaging and Bioengineering,* *UNRELATED*: *Board Membership*: iSchemaView Inc, *Comment*: member, Board of Directors (no payment), *Stock/Stock Options*: iSchemaView Inc, founder. Michael E. Moseley—*UNRELATED*: *Grants/Grants Pending*: National Institutes of Health,* National Institute of Neurological Disorders and Stroke.* Greg Zaharchuk—*UNRELATED*: *Grants/Grants Pending*: GE Healthcare.* *Money paid to the institution.

REFERENCES

1. Le Bihan D, Douek P, Argyropoulou M, et al. **Diffusion and perfusion magnetic resonance imaging in brain tumors.** *Top Magn Reson Imaging* 1993;5:25–31
2. Hajnal JV, Doran M, Hall AS, et al. **MR imaging of anisotropically restricted diffusion of water in the nervous system: technical, anatomic, and pathologic considerations.** *J Comput Assist Tomogr* 1991;15:1–18
3. Sorensen AG, Buonanno FS, Gonzalez RG, et al. **Hyperacute stroke: evaluation with combined multisection diffusion-weighted and hemodynamically weighted echo-planar MR imaging.** *Radiology* 1996;199:391–401
4. Henkelman R. **Diffusion-weighted MR imaging: a useful adjunct to clinical diagnosis or a scientific curiosity?** *AJNR Am J Neuroradiol* 1990;11:932–34
5. Patterson DM, Padhani AR, Collins DJ. **Technology insight: water diffusion MRI—a potential new biomarker of response to cancer therapy.** *Nat Clin Pract Oncol* 2008;5:220–33
6. Sugahara T, Korogi Y, Kochi M, et al. **Usefulness of diffusion-weighted MRI with echo-planar technique in the evaluation of cellularity in gliomas.** *J Magn Reson Imaging* 1999;9:53–60
7. Sumi M, Sakihama N, Sumi T, et al. **Discrimination of metastatic cervical lymph nodes with diffusion-weighted MR imaging in patients with head and neck cancer.** *AJNR Am J Neuroradiol* 2003;24:1627–34
8. Le Bihan D, Breton E, Lallemand D, et al. **MR imaging of intravoxel incoherent motions: application to diffusion and perfusion in neurologic disorders.** *Radiology* 1986;161:401–07
9. Burdette JH, Elster AD, Ricci PE. **Acute cerebral infarction: quantification of spin-density and T2 shine-through phenomena on diffusion-weighted MR images.** *Radiology* 1999;212:333–39
10. Pruessmann KP, Weiger M, Scheidegger MB, et al. **SENSE: sensitivity encoding for fast MRI.** *Magn Reson Med* 1999;42:952–62
11. Griswold MA, Jakob PM, Heidemann RM, et al. **Generalized autocalibrating partially parallel acquisitions (GRAPPA).** *Magn Reson Med* 2002;47:1202–10

12. Bammer R, Auer M, Keeling SL, et al. **Diffusion tensor imaging using single-shot SENSE-EPI.** *Magn Reson Med* 2002;48:128–36
13. Skare S, Newbould RD, Clayton DB, et al. **Clinical multishot DW-EPI through parallel imaging with considerations of susceptibility, motion, and noise.** *Magn Reson Med* 2007;57:881–90
14. Geijer B, Sundgren PC, Lindgren A, et al. **The value of b required to avoid T2 shine-through from old lacunar infarcts in diffusion-weighted imaging.** *Neuroradiology* 2001;43:511–17
15. Feinberg DA, Kiefer B, Litt AW. **Dual contrast GRASE (gradient-spin echo) imaging using mixed bandwidth.** *Magn Reson Med* 1994;31:461–64
16. Gallichan D, Andersson JL, Jenkinson M, et al. **Reducing distortions in diffusion-weighted echo planar imaging with a dual-echo blip-reversed sequence.** *Magn Reson Med* 2010;64:382–90
17. Stejskal EO, Tanner JE. **Spin diffusion measurements: spin echoes in the presence of a time-dependent field gradient.** *J Chem Phys* 1965;42:288–92
18. Bernstein MA, King KF, Zhou XJ. *Handbook of MRI Pulse Sequences.* Burlington, Massachusetts: Elsevier Academic Press; 2004
19. Feinberg DA, Jakob PD. **Tissue perfusion in humans studied by Fourier velocity distribution, line scan, and echo-planar imaging.** *Magn Reson Med* 1990;16:280–93
20. Reese TG, Heid O, Weisskoff RM, et al. **Reduction of eddy-current-induced distortion in diffusion MRI using a twice-refocused spin echo.** *Magn Reson Med* 2003;49:177–82
21. Beauchamp NJ Jr, Bryan RN. **Acute cerebral ischemic infarction: a pathophysiologic review and radiologic perspective.** *AJR Am J Roentgenol* 1978;171:73–84
22. Andersson JL, Skare S, Ashburner J, et al. **How to correct susceptibility distortions in spin-echo echo-planar images: application to diffusion tensor imaging.** *Neuroimage* 2003;20:870–88
23. Zeineh MM, Holdsworth S, Skare S, et al. **Ultra-high resolution diffusion tensor imaging of the microscopic pathways of the medial temporal lobe.** *Neuroimage* 2012;62:2065–82
24. Holdsworth SJ, Skare S, Straka M, et al. **GRAPPA-accelerated dual-echo diffusion-weighted EPI with intensity correction.** In: *Proceedings of the 20th Annual Meeting of the International Society of Magnetic Resonance in Medicine*, Melbourne, Australia. May 5–11, 2012:20

Perfusion-Based Selection for Endovascular Reperfusion Therapy in Anterior Circulation Acute Ischemic Stroke

S. Prabhakaran, M. Soltanolkotabi, A.R. Honarmand, R.A. Bernstein, V.H. Lee, J.J. Conners, F. Dehkordi-Vakil, A. Shaibani, M.C. Hurley, and S.A. Ansari

ABSTRACT

BACKGROUND AND PURPOSE: Controversy exists about the role of perfusion imaging in patient selection for endovascular reperfusion therapy in acute ischemic stroke. We hypothesized that perfusion imaging versus noncontrast CT- based selection would be associated with improved functional outcomes at 3 months.

MATERIALS AND METHODS: We reviewed consecutive patients with anterior circulation strokes treated with endovascular reperfusion therapy within 8 hours and with baseline NIHSS score of ≥8. Baseline clinical data, selection mode (perfusion versus NCCT), angiographic data, complications, and modified Rankin Scale score at 3 months were collected. Using multivariable logistic regression, we assessed whether the mode of selection for endovascular reperfusion therapy (perfusion-based versus NCCT-based) was independently associated with good outcome.

RESULTS: Two-hundred fourteen patients (mean age, 67.2 years; median NIHSS score, 18; MCA occlusion 74% and ICA occlusion 26%) were included. Perfusion imaging was used in 76 (35.5%) patients (39 CT and 37 MR imaging). Perfusion imaging–selected patients were more likely to have good outcomes compared with NCCT-selected patients (55.3 versus 33.3%, $P = .002$); perfusion selection by CT was associated with similar outcomes as that by MR imaging (CTP, 56.; MR perfusion, 54.1%; $P = .836$). In multivariable analysis, CT or MR perfusion imaging selection remained strongly associated with good outcome (adjusted OR, 2.34; 95% CI, 1.22–4.47), independent of baseline severity and reperfusion.

CONCLUSIONS: In this multicenter study, patients with acute ischemic stroke who underwent perfusion imaging were more than 2-fold more likely to have good outcomes following endovascular reperfusion therapy. Randomized studies should compare perfusion imaging with NCCT imaging for patient selection for endovascular reperfusion therapy.

ABBREVIATIONS: DEFUSE-2 = Diffusion and Perfusion Imaging Evaluation for Understanding Stroke Evolution Study 2; ERT = endovascular reperfusion therapy; MRP = MR perfusion; THRIVE = Totaled Health Risks in Vascular Events

Endovascular reperfusion therapy (ERT) for acute ischemic stroke has been associated with mixed results. In trials of carefully selected patients with middle cerebral artery occlusion, a benefit of intra-arterial thrombolysis over placebo was seen when patients were treated within 6 hours.[1,2] However, subsequent single-arm studies of mechanical embolectomy have observed less impressive results[3,4] and suggest that outcomes are related to several key factors, including patient characteristics (age, co-morbidities, and stroke severity) and treatment factors (time to reperfusion).[5-10] Radiographic features, including pretreatment tissue status by NCCT of the head, brain MR imaging, and perfusion imaging (CTP or MR perfusion [MRP]), may improve patient selection.[5,8,9,11] Few studies have compared NCCT-based selection with perfusion imaging–based selection of patients for ERT following acute ischemic stroke.[12,13] We, therefore, sought to compare NCCT selection with perfusion imaging selection as a predictor of good outcome following ERT. We hypothesized that perfusion imaging–based selection would be associated with better functional outcomes at 3 months compared with NCCT-based selection alone.

MATERIALS AND METHODS

Data Sources

We analyzed a retrospective registry of consecutive patients treated with endovascular therapy at 4 tertiary stroke centers from January 2007 to December 2012. Participating hospitals submit-

Received October 9, 2013; accepted after revision November 25.

From the Departments of Neurology (S.P., R.A.B.) and Radiology (M.S., A.R.H., A.S., M.C.H., S.A.A.), Northwestern University, Chicago, Illinois; and Department of Neurology (V.H.L., J.J.C.), Rush University Medical Center, Chicago, Illinois; and Department of Economics and Decision Sciences (F.D.-V.), Western Illinois University, Macomb, Illinois.

Please address correspondence to Shyam Prabhakaran, MD, MS, Northwestern University-Feinberg School of Medicine, 710 N Lake Shore Dr, Room 1417, Chicago, IL 60611; e-mail: shyam.prabhakaran@northwestern.edu

Indicates article with supplemental on-line appendix

http://dx.doi.org/10.3174/ajnr.A3889

ted information on consecutive patients with ischemic stroke treated with ERT, de-identified for compliance with the Health Insurance Portability and Accountability Act. Institutional review board approval was granted from each participating center.

Inclusion criteria for this study were patients with acute ischemic stroke who presented within 8 hours of symptom onset with anterior circulation large-vessel occlusions and pretreatment National Institutes of Health Stroke Scale score of ≥8. Data were analyzed regarding demographics, previous medical history, pretreatment stroke severity by NIHSS score, time of symptom onset, treatment with intravenous tissue plasminogen activator, mode of selection for ERT (NCCT versus CTP or MRP), time of groin puncture, location of arterial occlusion on angiography, reperfusion status, radiographic interpretation of hemorrhages, and clinical outcomes. The site of occlusion was determined angiographically as the most proximal ipsilateral lesion with a TICI 0 or 1 perfusion grade. Successful reperfusion was defined as TICI 2b or higher on the final angiographic image.[14] Symptomatic hemorrhage was defined as a parenchymal hematoma type 1 or 2 by using the European Cooperative Acute Stroke Study definition[15] associated with an increase of >4 in the NIHSS score and any wire perforation resulting in subarachnoid hemorrhage. Patients with an mRS score of ≤2 at 90 days were considered to have good clinical outcomes. Pretreatment Totaled Health Risks in Vascular Events (THRIVE) scores were calculated on the basis of published criteria.[6] The THRIVE score has been validated as a simple pretreatment scoring tool to predict clinical outcome, mortality, and symptomatic hemorrhage after ERT and is calculated on the basis of age, NIHSS score, and history of atrial fibrillation, diabetes, and hypertension.

Imaging Acquisition and Interpretation

Site-specific imaging acquisition and software application details are included in the On-line Appendix. Imaging-based patient selection for ERT was dependent on local site determination of CT, CTP, or MRP eligibility criteria. Both qualitative visual inspection and volumetric measurements were used at sites. General imaging inclusion criteria were based on published or consensus guidelines: 1) NCCT with less than one-third hypoattenuation in the MCA territory; or 2) core infarct volume with less than one-third of the MCA territory or <70 mL, and perfusion abnormality to core infarct mismatch ratio of >1.2, which was increased to 1.8 after 2009, consistent with the Diffusion and Perfusion Imaging Evaluation for Understanding Stroke Evolution Study 2 (DEFUSE-2) trial.[16] Sites used similar relative and absolute thresholds for the definition of core infarct (cerebral blood volume of <2 mL/100 g on CTP or DWI hyperintensity with decreased ADC on MR imaging) and abnormal perfusion to estimate the ischemic penumbra (MTT > 6 seconds on CTP or time-to-maximum of the tissue residue function > 6 seconds on MRP). However, these guidelines were used by neurointerventional physicians at each site without central adjudication.

In a post hoc analysis of perfusion-based selected cases, we calculated mismatch ratios of abnormal perfusion volume to core infarct volume. Determinations of the core infarct and penumbra volumes were performed by using the ABC/2 method on postprocessing software (On-line Appendix) at each site.[17] Two independent raters also performed measurements in a sample of 10 de-identified CTP and MRP scans, respectively, and demonstrated high reproducibility (CTP: Kendall $\tau = 0.822$, $P = .002$; MRP: Kendall $\tau = 0.810$, $P = .016$).

Endovascular Reperfusion Therapy

Following transfemoral arterial access and modest (2000–4000 U) anticoagulation with heparin, Merci (14X or 18 L; Concentric Medical, Mountain View, California) or Penumbra reperfusion (041/054; Penumbra, Alameda, California) catheters were advanced coaxially over 021/032-inch microcatheters and/or 0.014/.016-inch microwires to the thromboembolic occlusion per published methods for clot retrieval or aspiration[3,4]; stent retrievers were used in a minority of cases because these were available only after 2011.[18,19] Intra-arterial thrombolysis with tPA (Genentech, San Francisco, California) was performed as an adjunct with mechanical thrombectomy by embedding the microcatheter in the clot and by using a pulse-spray technique. Major indications for intra-arterial tPA use were partial ineffectiveness of retrieval/aspiration, intraprocedural clot fragmentation with distal migration, or concomitant distal thromboemboli.

Statistical Analysis

Using univariable tests, we compared demographic, clinical, and outcome data among NCCT- and perfusion-selected patients by using χ^2 (or the Fisher exact if appropriate) tests for categoric variables and t tests (or Mann-Whitney if appropriate) for continuous variables. We then assessed univariable associations between these factors and good clinical outcome after ERT (defined as an mRS score of 0–2 at 90 days). A multivariable logistic regression analysis was performed to identify independent predictors of good outcome. Candidate variables were selected on the basis of statistically significant univariable relationships with good outcome. The fitness of the model was tested by using the Hosmer-Lemeshow test. All P values are 2-sided, with $P < .05$ considered statistically significant. Analyses were performed by using the Statistical Package for the Social Sciences software (Version 21; IBM, Armonk, New York).

RESULTS

Among 262 patients treated with ERT at 4 tertiary hospitals in the Chicago region, 48 were excluded due to vertebrobasilar artery occlusion ($n = 32$), isolated anterior cerebral artery occlusion ($n = 3$), isolated posterior cerebral artery occlusion ($n = 1$), initial NIHSS < 8 ($n = 5$), treatment >8 hours from symptom onset ($n = 4$), and missing outcome data ($n = 3$). Among the 214 patients who met our inclusion criteria (mean age, 67.2 ± 16.0 years; male, 40.7%), the median NIHSS score was 18 with 74.3% presenting with MCA occlusions, while 25.7% had occlusions involving the ICA and MCA.

Seventy-six (35.5%) patients were selected by using perfusion imaging (CTP: 39, 18.2%; MRP: 37, 17.3%). Selection mode varied by hospital with sites contributing 10.5%–34.2% of perfusion-selected cases ($P < .001$). During the study period, the use of perfusion imaging selection increased from 21.1% in year 1 to 56.5% in year 6 ($P = .215$). Median onset to groin puncture was 311 (interquartile range, 242–380) minutes but improved during

Table 1: Univariable analysis of characteristics associated with perfusion imaging selection

	Perfusion Selection (n = 76)	NCCT Selection (n = 138)	P Value
Age (yr)			<.001
Mean (SD)	72.4 (14.1)	64.4 (16.3)	
Male, No. (%)	26 (34.2)	61 (44.2)	.154
Onset to arrival time (min)			.520
Median (IQR)	245 (123.5–300.0)	241.5 (180.0–320.0)	
Initial NIHSS score			.018
Median (IQR)	18 (13–20)	19 (16–22)	
Initial THRIVE score			.529
Median (IQR)	4 (3–5)	4.5 (3–6)	
IV tPA prior to ERT, No. (%)	31 (40.8)	67 (48.6)	.275
Location of occlusion, No. (%)			<.001
Middle cerebral artery	68 (89.5)	91 (65.9)	
Internal carotid artery	8 (10.5)	47 (34.1)	
Mode of IA therapy			.028
Lytic only	3 (3.8)	0	
Mechanical only	44 (57.9)	95 (68.8)	
Lytic + mechanical	29 (38.2)	43 (31.2)	
Onset-to-GP time in minutes			.366
Median (IQR)	348 (225.75–399.75)	309 (245.5–375.0)	
Symptomatic hemorrhage, No. (%)	4 (5.3)	17 (12.3)	.148
TICI 2b/3 reperfusion, No. (%)	46 (62.5)	65 (47.1)	.036
Year			.215
2007	4 (5.3)	15 (10.9)	
2008	9 (11.8)	22 (15.9)	
2009	18 (23.7)	29 (21.0)	
2010	17 (22.4)	35 (25.4)	
2011	15 (19.7)	27 (19.6)	
2012	13 (17.1)	10 (7.2)	

Note:—IQR indicates interquartile range; IA, intra-arterial; GP, groin puncture.

the study period (year 1: 350 minutes to year 6: 228 minutes; P = .060). Mechanical thrombectomy devices were commonly used and often in combination: Merci (n = 106), Penumbra (n = 160), and stent retrievers (n = 15). TICI 2b or 3 reperfusion was achieved in 52.4% and did not vary by site (range, 45.9%–69.8%; P = .081) or with time (P = .280). Symptomatic hemorrhage occurred in 9.8% of patients and did not vary by site (range, 3.0%–13.3%; P = .349). Good outcome was observed in 41.1% of patients at 3 months. The mortality rate at 3 months was 16.4%.

When we compared those patients selected by perfusion imaging with those selected by NCCT alone, perfusion imaging–selected patients were older, had slightly lower NIHSS scores, more frequently had MCA occlusions and received multimodal (lytic plus mechanical) intra-arterial therapies, and had higher rates of TICI 2b or 3 reperfusion after treatment (Table 1). Other factors such as receipt of IV tPA before ERT, onset-to-arrival and onset-to-groin puncture times, THRIVE score, and symptomatic hemorrhage rates were similar between groups.

Perfusion-selected patients were more likely to have good outcomes at 3 months compared with NCCT-selected patients (any perfusion: 55.3% [CTP: 56.4% and MRP 54.1%] versus NCCT: 33.3%, P = .002). Good outcome among perfusion-selected patients ranged from 42.3% to 70.8% across the 4 sites (P = .213). Perfusion-selection patients also had lower 3-month mortality rates (7.9% versus 21.0%, P = .012). In post hoc analyses of patients selected by perfusion imaging, the median core infarct volume was 15.7 mL (interquartile range, 5.6–41.7 mL), and ischemic penumbra volume was 103.8 mL (interquartile range, 64.7–154.0 mL). The median mismatch ratio was 5.8 (interquartile range, 2.5–17.6). Only 9 (11.8%) of the perfusion-selected patients had mismatch ratios of <1.8.

Those achieving good outcome also had lower NIHSS and THRIVE scores, were more likely to have received IV tPA before ERT, had TICI 2b or 3 reperfusion after treatment, and were less likely to have symptomatic hemorrhages (Table 2). Other factors, including the location of arterial occlusion and mode of therapy, were similarly distributed by outcome.

In multivariable analysis (Table 3) to identify predictors of good outcome (mRS 0–2) and adjusting for factors significantly associated with the mode of selection or with outcome (age, calendar year, initial NIHSS score, IV tPA use, location of occlusion, mode of therapy, final TICI, symptomatic hemorrhage), perfusion selection remained independently associated with good outcome (adjusted OR, 2.3; 95%, CI 1.23%–4.47%).

DISCUSSION

In a multicenter study, we observed that patients selected for ERT by perfusion imaging were more than 2-fold more likely to have good functional outcomes compared with NCCT-selected patients, despite an older age and modest delays in time to treatment. These results were independent of other known predictors of good outcome, including stroke severity, comorbidities, IV tPA utilization, and TICI reperfusion score.

Our data are consistent with some previously published work that observed higher rates of good outcome ranging from 41% to 67% by using perfusion selection for ERT compared with historic controls.[20] Others have noted that perfusion selection attenuates or negates the influence of time so that good outcomes can be achieved in similar proportions after 8 hours compared with <8 hours by using perfusion imaging.[21,22] However, 2 retrospective prior studies comparing perfusion selection with NCCT selection have failed to show a benefit of one approach over the other.[12,13] Hassan et al[13] demonstrated equivalent discharge outcomes, symptomatic hemorrhage rates, and mortality rates in a retrospective analysis comparing NCCT- versus CTP-based patient selection. The methodology for qualitative and quantitative penumbral assessment was MTT ≥ 20% of the affected region or a presumed mismatch ratio of >1.2. Sheth et al[12] also performed a multicenter retrospective analysis and found no difference in clinical outcomes with NCCT, CTP, or MR imaging–based selection. However, this study provided no specific parameters used for advanced imaging selection and likely lacked standardized patient-selection approaches in each subgroup. Neither study performed post hoc core infarct/penumbra analyses. Lack of standardized and/or less stringent perfusion imaging criteria may explain their

Table 2: Univariable analysis of characteristics associated with good outcome (mRS 0–2) at 3 months

	Good Outcome (*n* = 88)	Poor Outcome (*n* = 126)	*P* Value
Age (yr)			.891
Mean (SD)	67.0 (15.6)	67.4 (16.3)	
Male, No. (%)	36 (40.5)	51 (40.9)	.949
Onset-to-arrival time in minutes			.627
Median (IQR)	240 (139.0–304.5)	250 (178.5–366.0)	
Initial NIHSS score			.009
Median (IQR)	18 (12.25–21.0)	19 (16–22)	
Initial THRIVE score			.004
Median (IQR)	4 (3–5)	5 (4–6)	
IV tPA prior to ERT, No. (%)	49 (55.7)	49 (38.9)	.015
Location of occlusion, No. (%)			.607
Middle cerebral artery	67 (76.1)	92 (73.0)	
Internal carotid artery	21 (23.9)	34 (27.0)	
Mode of ERT			.488
Lytic only	2 (2.3)	1 (0.8)	
Mechanical only	54 (61.4)	85 (67.5)	
Lytic + mechanical	32 (44.4)	40 (31.7)	
Onset to GP time in minutes			.790
Median (IQR)	306.5 (240.0–385.0)	315 (242.75–379.75)	
Symptomatic hemorrhage, No. (%)	3 (3.4)	18 (14.3)	.009
TICI 2b/3 reperfusion, No. (%)	64 (72.7)	47 (37.9)	<.001
Year			.147
2007	7 (8.0)	12 (9.5)	
2008	10 (11.4)	21 (9.8)	
2009	21 (23.9)	26 (20.6)	
2010	29 (33.0)	23 (18.3)	
2011	13 (14.0)	29 (23.0)	
2012	8 (9.1)	15 (11.9)	

Note:—IQR indicates interquartile range; GP, groin puncture.

Table 3: Multivariable model for good outcome (mRS 0–2 at 3 months) with the following dependent variables: age, calendar year, initial NIHSS score, IV tPA use, selection mode, location of occlusion, mode of therapy, final TICI score, and symptomatic hemorrhage[a]

	Adjusted OR	95% CI	*P* Value
Selection mode			.010
NCCT only (reference)	–	–	
Perfusion imaging	2.34	1.23–4.47	
Initial NIHSS score (per point)	0.92	0.87–0.98	.006
IV tPA prior to IAT	2.12	1.13–3.96	.019
TICI score			<.001
TICI <2b (reference)	–	–	
TICI 2b or 3	4.26	2.27–8.03	

Note:—IQR indicates interquartile range; IAT, intra-arterial therapy.
[a] Hosmer-Lemeshow test for goodness of fit: $P = .229$.

null results compared with our findings. Additionally, Sheth et al[12] noted that CT perfusion or MR imaging selection added approximately a 60-minute delay to treatment. Although we also observed a 40-minute delay with perfusion selection, the potential improved selection and association with better outcomes may justify this approach. It should be acknowledged that perfusion-based selection may result in higher proportions of treated patients with good outcomes, though fewer patients overall may actually receive ERT compared with NCCT-based selection.

Studies of imaging-based selection in acute ischemic stroke have produced mixed results, at least partly due to the variability of techniques, postprocessing software algorithms, and definitions of core infarct and penumbra that parse oligemia from true ischemia.[23] Critics of perfusion-based patient-selection strategies for acute stroke intervention cite the limited MR imaging accessibility; additional time required for imaging, resulting in endovascular treatment delays; the lack of standardized postprocessing perfusion software; failure to quantitatively model the dynamic properties of in vivo cerebral perfusion (ie, contrast delay-dispersion correction and retrograde pial collateral supply); and an inability to differentiate a true penumbra (ischemic tissue destined to infarct without reperfusion) versus false penumbra (oligemic tissue that will survive). Furthermore, a measurement made 1 or 2 hours before reperfusion may not be a reliable indicator of tissue fate; real-time measurement of tissue perfusion at the time of reperfusion therapy is preferred.

Prior clinical trials of perfusion-based selection for intravenous and intra-arterial reperfusion therapies have produced mixed results. In the desmoteplase studies, the phase 3 trial showed no benefit of delayed thrombolysis based on perfusion imaging selection, defined as a mismatch (penumbra-to-infarct) ratio of >1.2, despite promising phase 2 study results.[24-26] However, post hoc analyses suggested that a minimal mismatch volume of 60 mL would have led to a benefit in favor of desmoteplase.[27] Other intravenous thrombolytic phase 2 trials confirmed potential benefit in delayed treatment by using MR diffusion–perfusion imaging–based patient selection.[28,29] In the DEFUSE-2 trial, endovascular reperfusion was associated with a 5-fold increase in favorable clinical outcomes among patients with target mismatch (defined as ratio of >1.8), while no benefit was seen among patients without target mismatch. The trial used standardized MR imaging postprocessing software (RAPID; iSchemaView Inc, Palo Alto, California), which allowed uniform definitions of core infarct, severe perfusion abnormalities, and hence possibly a more accurate measurement of penumbra.[16] Our data are consistent with the DEFUSE-2 study, in which large mismatch ratios (median, 5.8 in our study) were also observed. These data suggest that perfusion imaging selection, if optimized with standardized parameters that best define mismatch and true penumbra, may identify patients most likely to benefit while excluding those who may incur harm from reperfusion therapy.

In contrast, the recently reported Mechanical Retrieval and Recanalization of Stroke Clots Using Embolectomy trial found no benefit of ERT over medical treatment, irrespective of a favorable perfusion imaging profile ("penumbral" versus "nonpenumbral" pattern).[30] Most interesting, patients with a penumbral pattern were found to have better outcomes and smaller infarct growth, suggesting a protective effect. It is therefore possible that penumbral selection, as in our study, identifies those patients destined for better outcomes irrespective of treatment. The Mechanical Retrieval and Recanalization of Stroke Clots Using Embolectomy

trial identified significant delays in randomization, ranging from 5 to 6 hours, suggesting relatively late CTP/MRP acquisitions. Penumbral patterns noted at various time points after stroke onset (early versus late) may also be indicative of differing risk profiles so that early imaging may mark those with a high risk of infarct growth and deterioration, while late imaging may identify those with good collateral flow that protects against infarct growth and deterioration.[31,32] Further work related to imaging techniques with respect to reproducibility, standardized definitions of optimal parameters, and postprocessing methodologies for distinguishing penumbra from infarct core are clearly needed.

Our study has several limitations. First, we did not prospectively adjudicate NCCT or perfusion imaging selection for ERT. While ASPECTS and mismatch criteria have been developed and may have been used at our sites,[11,16] decisions regarding eligibility were determined by the local treating physicians by using differing modalities and software platforms. In addition, CTP and MRP may have differing accuracies for predicting infarct core and penumbra and differing spatial coverage so that CTP may provide only limited coverage[23]; however, outcomes among those selected by CT versus MR perfusion were not different in our study. Second, our results are not generalizable to posterior circulation strokes. Besides different natural histories compared with anterior circulation stroke, posterior circulation stroke has challenges in perfusion imaging selection. Only small studies using MRP have been conducted in posterior circulation stroke, and none has clearly demonstrated its utility in selection for ERT.[33] Third, outcomes following ERT are also dependent on time to reperfusion.[10] Capturing reperfusion times is often challenging in clinical practice due to infrequent sequential angiographic runs and the possibility of slow and steady reperfusion or partial followed by complete reperfusion. Fourth, the type of mechanical thrombectomy device was not controlled for in the study, though a minority (15 patients) was treated with the new generation of stent retrievers. Recent advances in retrievable-stent technology may lead to earlier and higher rates of reperfusion with minimal symptomatic hemorrhage.[18,19]

Fifth, all data in the registry were entered by local sites without central adjudication and were aggregated post hoc in a de-identified manner. We do not know how many patients were excluded from ERT on the basis of NCCT or perfusion imaging results; therefore, we cannot comment on outcomes in those who did not receive ERT. Grading TICI scores, in particular, can demonstrate significant interobserver variability, depending on whether the primary arterial occlusion was completely or partially recanalized, the presence of distal emboli, and the role of pial collaterals. Grading final reperfusion can also demonstrate site-reported bias in favor of better scores, compared with central adjudication, as demonstrated in the solitaire flow restoration device versus the Merci retriever in patients with acute ischaemic stroke (SWIFT) trial.[19] However, our hospitals have participated in large endovascular clinical trials, and consensus definitions were used to define key variables such as TICI grade and symptomatic hemorrhage. Angiographic collateral grade was also not systematically documented or available on post hoc review. Sixth, bias from the treating physicians may have resulted in use of perfusion selection for specific subgroups of patients, which could account for the difference in outcomes. Seventh, we also did not adjust for site characteristics such as volume of cases per year or operator experience, which may influence outcomes.[34] However, site performance as measured by rates of TICI 2b or 3 reperfusion and symptomatic hemorrhage were not different by site. Last, residual or unmeasured confounding could account for some or all of our results.

CONCLUSIONS

In a multicenter study, we observed nearly double the rates of good outcome following ERT for acute ischemic stroke among patients selected by perfusion imaging compared with NCCT alone. Nevertheless, the added "costs" in terms of time delays, imaging acquisition and interpretation, and health care resource use need to be carefully considered. Quality improvement efforts in light of the recent endovascular stroke trials should focus on strategies to reduce throughput delays in onset-to-treatment times, especially with perfusion-based selection.

Disclosures: Shyam Prabhakaran—*UNRELATED*: *Consultancy*: American Heart Association as medical director of Quality Enhancement for Speedy Thrombolysis in Stroke initiative, *Grants/Grants Pending*: National Institute of Neurological Disorders and Stroke, *Royalties*: Up-To-Date Inc.

REFERENCES

1. Furlan A, Higashida R, Wechsler L, et al. **Intra-arterial prourokinase for acute ischemic stroke. The PROACT II study: a randomized controlled trial. Prolyse in Acute Cerebral Thromboembolism.** *JAMA* 1999;282:2003–11
2. Ogawa A, Mori E, Minematsu K, et al. **Randomized trial of intraarterial infusion of urokinase within 6 hours of middle cerebral artery stroke: the Middle Cerebral Artery Embolism Local Fibrinolytic Intervention Trial (MELT) Japan.** *Stroke* 2007;38:2633–39
3. Smith WS, Sung G, Starkman S, et al. **Safety and efficacy of mechanical embolectomy in acute ischemic stroke: results of the MERCI trial.** *Stroke* 2005;36:1432–38
4. Penumbra Pivotal Stroke Trial Investigators. **The Penumbra Pivotal Stroke Trial: safety and effectiveness of a new generation of mechanical devices for clot removal in intracranial large vessel occlusive disease.** *Stroke* 2009;40:2761–68
5. Fargen KM, Chaudry I, Turner RD, et al. **A novel clinical and imaging based score for predicting outcome prior to endovascular treatment of acute ischemic stroke.** *J Neurointerv Surg* 2013;5(suppl 1):i38–43
6. Flint AC, Cullen SP, Faigeles BS, et al. **Predicting long-term outcome after endovascular stroke treatment: the Totaled Health Risks in Vascular Events score.** *AJNR Am J Neuroradiol* 2010;31:1192–96
7. Hallevi H, Barreto AD, Liebeskind DS, et al. **Identifying patients at high risk for poor outcome after intra-arterial therapy for acute ischemic stroke.** *Stroke* 2009;40:1780–85
8. Vora NA, Shook SJ, Schumacher HC, et al. **A 5-item scale to predict stroke outcome after cortical middle cerebral artery territory infarction: validation from results of the Diffusion and Perfusion Imaging Evaluation for Understanding Stroke Evolution (DEFUSE) Study.** *Stroke* 2011;42:645–49
9. Yoo AJ, Verduzco LA, Schaefer PW, et al. **MRI-based selection for intra-arterial stroke therapy: value of pretreatment diffusion-weighted imaging lesion volume in selecting patients with acute stroke who will benefit from early recanalization.** *Stroke* 2009;40:2046–54
10. Khatri P, Abruzzo T, Yeatts SD, et al. **Good clinical outcome after ischemic stroke with successful revascularization is time-dependent.** *Neurology* 2009;73:1066–72
11. Hill MD, Rowley HA, Adler F, et al. **Selection of acute ischemic stroke patients for intra-arterial thrombolysis with pro-urokinase by using ASPECTS.** *Stroke* 2003;34:1925–31
12. Sheth KN, Terry JB, Nogueira RG, et al. **Advanced modality imaging evaluation in acute ischemic stroke may lead to delayed endovascu-**

lar reperfusion therapy without improvement in clinical outcomes. *J Neurointerv Surg* 2013;5(suppl 1):i62–65
13. Hassan AE, Zacharatos H, Rodriguez GJ, et al. **A comparison of computed tomography perfusion-guided and time-guided endovascular treatments for patients with acute ischemic stroke.** *Stroke* 2010;41:1673–78
14. Higashida RT, Furlan AJ, Roberts H, et al. **Trial design and reporting standards for intra-arterial cerebral thrombolysis for acute ischemic stroke.** *Stroke* 2003;34:e109–137
15. Hacke W, Kaste M, Bluhmki E, et al. **Thrombolysis with alteplase 3 to 4.5 hours after acute ischemic stroke.** *N Engl J Med* 2008;359:1317–29
16. Lansberg MG, Straka M, Kemp S, et al. **MRI profile and response to endovascular reperfusion after stroke (DEFUSE 2): a prospective cohort study.** *Lancet Neurol* 2012;11:860–67
17. Sims JR, Gharai LR, Schaefer PW, et al. **ABC/2 for rapid clinical estimate of infarct, perfusion, and mismatch volumes.** *Neurology* 2009;72:2104–10
18. Nogueira RG, Lutsep HL, Gupta R, et al. **Trevo versus Merci retrievers for thrombectomy revascularisation of large vessel occlusions in acute ischaemic stroke (TREVO 2): a randomised trial.** *Lancet* 2012;380:1231–40
19. Saver JL, Jahan R, Levy EI, et al. **Solitaire flow restoration device versus the Merci retriever in patients with acute ischaemic stroke (SWIFT): a randomised, parallel-group, non-inferiority trial.** *Lancet* 2012;380:1241–49
20. Rai AT, Raghuram K, Domico J, et al. **Pre-intervention triage incorporating perfusion imaging improves outcomes in patients undergoing endovascular stroke therapy: a comparison with the device trials.** *J Neurointerv Surg* 2013;5:121–27
21. Abou-Chebl A. **Endovascular treatment of acute ischemic stroke may be safely performed with no time window limit in appropriately selected patients.** *Stroke* 2010;41:1996–2000
22. Jovin TG, Liebeskind DS, Gupta R, et al. **Imaging-based endovascular therapy for acute ischemic stroke due to proximal intracranial anterior circulation occlusion treated beyond 8 hours from time last seen well: retrospective multicenter analysis of 237 consecutive patients.** *Stroke* 2011;42:2206–11
23. Goyal M, Menon BK, Derdeyn CP. **Perfusion imaging in acute ischemic stroke: let us improve the science before changing clinical practice.** *Radiology* 2013;266:16–21
24. Furlan AJ, Eyding D, Albers GW, et al. **Dose Escalation of Desmoteplase for Acute Ischemic Stroke (DEDAS): evidence of safety and efficacy 3 to 9 hours after stroke onset.** *Stroke* 2006;37:1227–31
25. Hacke W, Albers G, Al-Rawi Y, et al. **The Desmoteplase in Acute Ischemic Stroke Trial (DIAS): a phase II MRI-based 9-hour window acute stroke thrombolysis trial with intravenous desmoteplase.** *Stroke* 2005;36:66–73
26. Hacke W, Furlan AJ, Al-Rawi Y, et al. **Intravenous desmoteplase in patients with acute ischaemic stroke selected by MRI perfusion-diffusion weighted imaging or perfusion CT (DIAS-2): a prospective, randomised, double-blind, placebo-controlled study.** *Lancet Neurol* 2009;8:141–50
27. Warach S, Al-Rawi Y, Furlan AJ, et al. **Refinement of the magnetic resonance diffusion-perfusion mismatch concept for thrombolytic patient selection: insights from the desmoteplase in acute stroke trials.** *Stroke* 2012;43:2313–18
28. Albers GW, Thijs VN, Wechsler L, et al. **Magnetic resonance imaging profiles predict clinical response to early reperfusion: the diffusion and perfusion imaging evaluation for understanding stroke evolution (DEFUSE) study.** *Ann Neurol* 2006;60:508–17
29. Davis SM, Donnan GA, Parsons MW, et al. **Effects of alteplase beyond 3 h after stroke in the Echoplanar Imaging Thrombolytic Evaluation Trial (EPITHET): a placebo-controlled randomised trial.** *Lancet Neurol* 2008;7:299–309
30. Kidwell CS, Jahan R, Gornbein J, et al. **A trial of imaging selection and endovascular treatment for ischemic stroke.** *N Engl J Med* 2013;368:914–23
31. Bang OY, Saver JL, Kim SJ, et al. **Collateral flow predicts response to endovascular therapy for acute ischemic stroke.** *Stroke* 2011;42:693–99
32. Bang OY, Saver JL, Kim SJ, et al. **Collateral flow averts hemorrhagic transformation after endovascular therapy for acute ischemic stroke.** *Stroke* 2011;42:2235–39
33. Ostrem JL, Saver JL, Alger JR, et al. **Acute basilar artery occlusion: diffusion-perfusion MRI characterization of tissue salvage in patients receiving intra-arterial stroke therapies.** *Stroke* 2004;35:e30–04
34. Gupta R, Horev A, Nguyen T, et al. **Higher volume endovascular stroke centers have faster times to treatment, higher reperfusion rates and higher rates of good clinical outcomes.** *J Neurointerv Surg* 2013;5:294–97

Differentiation of Tumor Progression from Pseudoprogression in Patients with Posttreatment Glioblastoma Using Multiparametric Histogram Analysis

J. Cha, S.T. Kim, H.-J. Kim, B.-j. Kim, Y.K. Kim, J.Y. Lee, P. Jeon, K.H. Kim, D.-s. Kong, and D.-H. Nam

ABSTRACT

BACKGROUND AND PURPOSE: The multiparametric imaging can show us different aspects of tumor behavior and may help differentiation of tumor recurrence from treatment related change. Our aim was to differentiate tumor progression from pseudoprogression in patients with glioblastoma by using multiparametric histogram analysis of 2 consecutive MR imaging studies with relative cerebral blood volume and ADC values.

MATERIALS AND METHODS: Thirty-five consecutive patients with glioblastoma with new or increased size of enhancing lesions after concomitant chemoradiation therapy following surgical resection were included. Combined histograms were made by using the relative cerebral blood volume and ADC values of enhancing areas for initial and follow-up MR imaging, and subtracted histograms were also prepared. The histogram parameters between groups were compared. The diagnostic accuracy of tumor progression based on the histogram parameters of initial and follow-up MR imaging and subtracted histograms was compared and correlated with overall survival.

RESULTS: Twenty-four pseudoprogressions and 11 tumor progressions were determined. Diagnosis based on the subtracted histogram mode with a multiparametric approach was more accurate than the diagnosis based on the uniparametric approach (area under the receiver operating characteristic curve of 0.877 versus 0.801), with 81.8% sensitivity and 100% specificity. A high mode of relative cerebral blood volume on the subtracted histogram by using a multiparametric approach (relative cerebral blood volume $\times$ADC) was the best predictor of true tumor progression ($P < .001$) and worse survival ($P = .003$).

CONCLUSIONS: Multiparametric histogram analysis of posttreatment glioblastoma was useful to predict true tumor progression and worse survival.

ABBREVIATIONS: CCRT = concurrent chemoradiotherapy; RANO = Response Assessment in Neuro-Oncology; rCBV = relative cerebral blood volume

The current standard treatment protocol for glioblastomas is surgical resection followed by 6 weeks of radiation therapy plus concomitant temozolomide chemotherapy (CCRT) and 6 cycles of adjuvant temozolomide chemotherapy. This protocol increases median survival from 12 to 15 months.[1]

However, during the treatment, subacute treatment-related reactions called pseudoprogression frequently occur as edema and contrast enhancement on MR imaging.[2-5] Pseudoprogression is most commonly seen on the first MR imaging performed within 2 months after CCRT. Tumors with hypermethylation of the O^6-methylguanine-DNA methyltransferase promoter gene show pseudoprogression more frequently.[6]

As shown in previous studies, enlarged enhancing lesions on conventional MR images may actually represent pseudoprogression in up to 46.8%–64% of cases.[7,8] The Response Assessment in Neuro-Oncology (RANO) Working Group[9] proposed that within the first 12 weeks of completion of radiation therapy, when pseudoprogression is most prevalent, tumor progression can only be determined if most of the new enhancement is outside the radiation field or if there is pathologic confirmation of progressive disease.

There has been much effort to differentiate progression from pseudoprogression by using advanced MR imaging techniques such as DWI and dynamic susceptibility contrast PWI. On DWI, ADC values are higher in necrotic tissue than in recurrent tumor tissue because of the high cellularity of tumor tissue.[10] However, the use of DWI is limited due to the heterogeneity of tumor

Received August 16, 2013; accepted after revision November 28.

From the Departments of Radiology and Center for Imaging Science (J.C., S.T.K., H.-J.K., B.-j.K., Y.K.K., J.Y.L., P.J., K.H.K.) and Neurosurgery (D.-s.K., D.-H.N.), Sungkyunkwan University School of Medicine, Samsung Medical Center, Seoul, Korea.

Please address correspondence to Sung Tae Kim, MD, Department of Radiology and Center for Imaging Science, Samsung Medical Center, Sungkyunkwan University School of Medicine, 50, Irwon-dong, Gangnam-gu, Seoul 135-710, Republic of Korea; e-mail: st7.kim@samsung.com

http://dx.doi.org/10.3174/ajnr.A3876

content. Reduced diffusion represents not only highly cellular tumor areas but also inflammatory processes.[11]

On PWI, high relative cerebral blood volume (rCBV) is considered active neovascularization and viable tumor.[11,12] Kong et al[6] reported that rCBV > 1.47 had 81.5% sensitivity and 77.8% specificity for differentiating pseudoprogression from tumor progression. Kim et al[13] reported a histogram analysis of rCBV, in which a peak height position of >1.7 showed 90.2% sensitivity and 91.1% specificity for differentiating tumor recurrence from mixed and treatment change groups. However, rCBV analysis has limitations because most lesions have variable tumor fractions; therefore, mean rCBV and histogram-based metrics may be influenced by the rCBV from both tumoral and nontumoral components.[14]

To overcome these limitations, Mangla et al[12] evaluated 2 consecutive MR imaging studies after treatment and showed that in patients with pseudoprogression, there was a 41% mean decrease in rCBV, while in tumor progression, there was a 12% increase in rCBV from pretreatment to posttreatment. Baek et al[8] performed histogram analysis on 2 consecutive MR imaging studies of posttreatment glioblastomas and revealed that the percentage change of skewness and kurtosis of normalized CBV can differentiate pseudoprogression from true tumor progression with a sensitivity of 85.7% and a specificity of 89.2%.

In this study, in addition to the evaluation of 2 consecutive MR imaging studies, we tried a multiparametric approach—that is, the combined use of DWI and PWI. We hypothesized that a multiparametric approach may overcome the limitations of each imaging technique. DWI and PWI have characteristic functional or physiologic parameters such as ADC/cellularity and CBV/tumor angiogenesis. If we use these multiple parameters simultaneously, these multiparametric analyses can reveal different aspects of tumor behavior and may have added value for differentiating tumor progression from pseudoprogression.

The aims of this study were to compare the change of combined rCBV × ADC histograms in 2 consecutive MR imaging studies between true tumor progression and pseudoprogression and to compare the diagnostic efficacy of a uniparametric-versus-multiparametric approach.

MATERIALS AND METHODS

Study Population

Between April 2008 and July 2010, one hundred sixty consecutive patients underwent surgical treatment for glioblastoma in our institution. Of the 160 patients, 35 met the following criteria: 1) standard treatment for glioblastoma; 2) new or increased size of a measurable enhancing lesion (>1 cm) within the radiation field within 180 days after CCRT; 3) 2 consecutive MRIs with dynamic susceptibility contrast perfusion and DWI at the time of increased lesion size and within 3 months after the initial MR imaging; 4) >2 follow-up MRIs or pathologic diagnosis; and 5) MRIs without significant artifacts that prevented dynamic susceptibility contrast perfusion analysis. This retrospective study was approved by the institutional review board in the hospital, and the requirement for informed consent was waived.

There were 18 men and 17 women (age range, 24–70 years; mean, 49 years). The interval between the operation and initial MR imaging (at the time of increased lesion size) was 123.5 ± 34.7 days (range, 79~204 days), the interval between initial MR imaging and first follow-up MR imaging was 53.7 ± 36.0 days (range, 19~142 days), and the interval between the first and second follow-up MR imaging was 59.3 ± 17.5 days (range, 29~95 days). In 3 patients, craniotomy and tumor removal were performed for pathologic diagnosis.

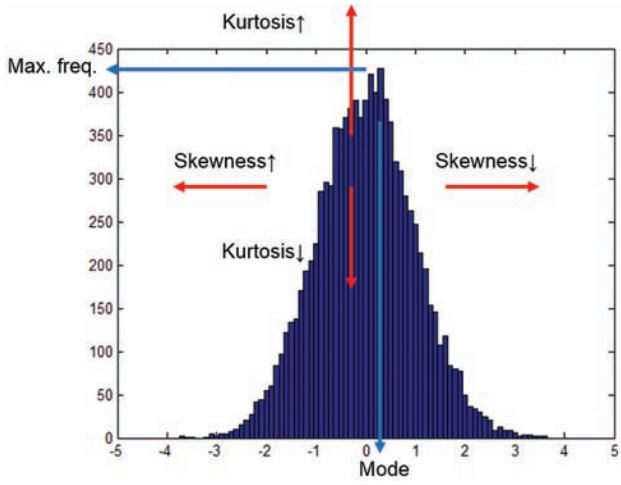

FIG 1. Histogram parameters. Mode is the value with the maximum frequency on the histogram. Median is the middle value. Kurtosis is a measure of whether the data are peaked (high kurtosis) or flat (low kurtosis) relative to a normal distribution. Skewness is a measure of asymmetry. Negative skew means that the left tail is longer; positive skew means that the right tail is longer.

True tumor progression and pseudoprogression were confirmed after adjuvant temozolomide according to the RANO criteria.[9] More specifically, pseudoprogression was defined as stable or decreased size of an enhancing lesion at ≥2 consecutive follow-up MR imaging studies compared with the initial MR imaging. Tumor progression was defined as increased size of the enhancing lesion at ≥2 consecutive follow-up MR imaging studies compared with the initial MR imaging or pathologically revealed recurrent tumor. Group categorization was performed with a qualitative method by consensus of 2 neuroradiologists (J.C., S.T.K.).

MR Imaging Protocol

MR imaging was performed at 3T (Achieva; Philips Healthcare, Best, the Netherlands) with an 8-channel sensitivity encoding head coil.

Contrast-enhanced axial spin-echo T1-weighted imaging was acquired after intravenous injection of contrast material (gadoterate meglumine, Dotarem; Guerbet, Aulnay-sous-Bois, France), 0.1 mmol/kg of body weight by power injector, with the following parameters: TR/TE = 500/10 ms, section thickness = 5 mm, acquisition matrix = 256 × 226.

Spin-echo EPI DWI (TR/TE = 3000/76 ms, section thickness = 5 mm, acquisition matrix = 128 × 128, b-value = 0, 1000 s/mm^2) and dynamic susceptibility contrast PWI (TR/TE = 1720/35 ms, flip angle = 40°, section thickness = 5 mm, acquisition matrix = 128 × 128, fifty volumes, acquisition time = 1 minute 30 seconds) were performed. All MR images were acquired with the same FOV (240 × 240 mm).

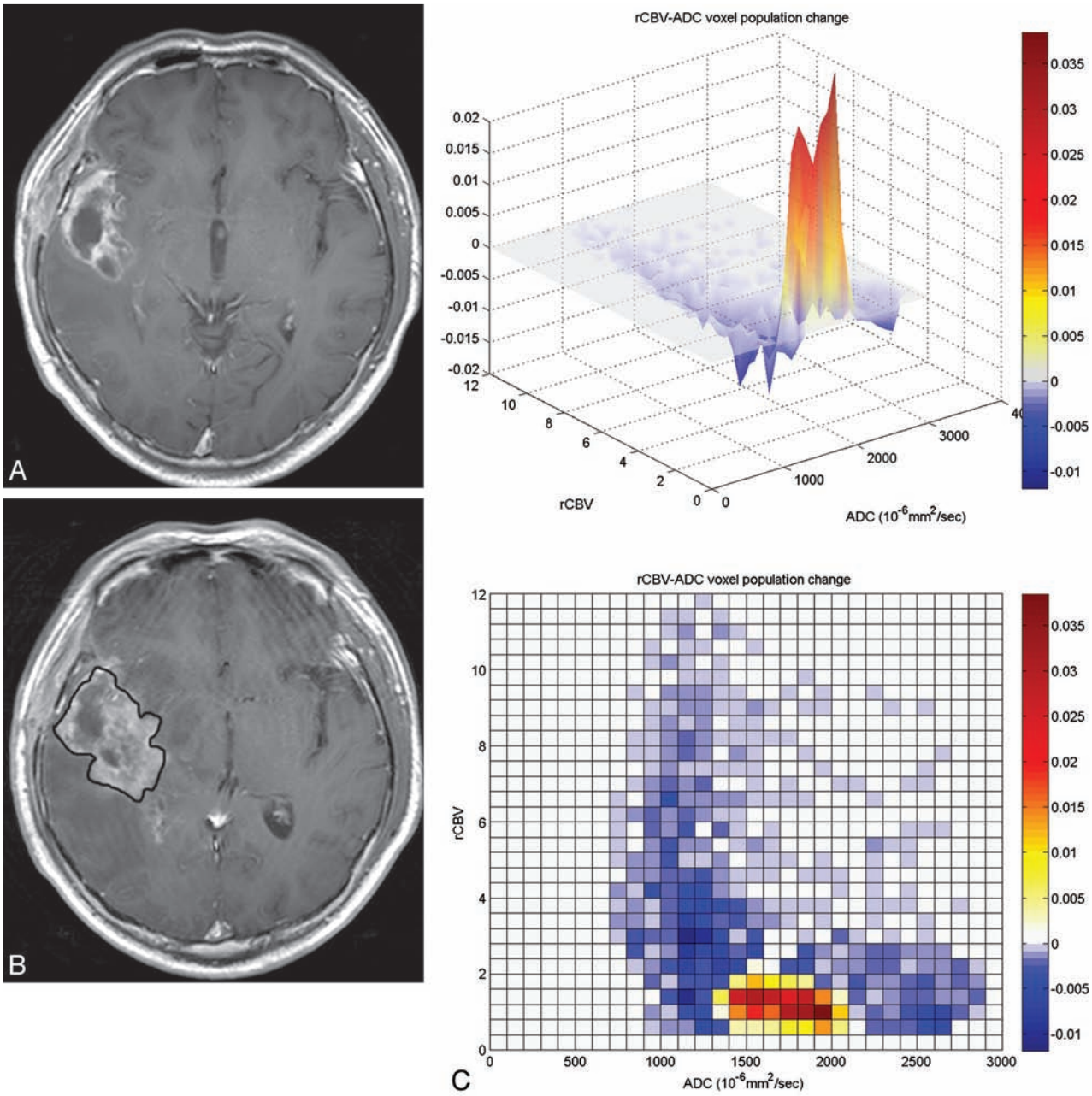

FIG 2. A 54-year-old man with glioblastoma who underwent tumor removal followed by CCRT. Sixty-eight days after CCRT, the enhancing lesion developed around the surgical cavity (*A*). On follow-up MR imaging performed 52 days after CCRT (*B*), the size of enhancing lesion was increased, suggestive of tumor progression. However, a subtracted 3D histogram shows a decreased population (blue) of high rCBV voxels (*C*), and an increased population (red) of low rCBV/high ADC components. Craniotomy and tumor removal were performed, and pathologic findings showed radiation necrosis, suggestive of pseudoprogression.

rCBV Map Analysis

Dynamic susceptibility contrast perfusion images were processed by using a dedicated software package (nordicICE; NordicNeuroLab, Bergen, Norway). An rCBV map was generated by using an established tracer kinetic model applied to the first-pass data.[15] Gamma variate fitting was applied to avoid a recirculation effect. As described previously, the dynamic curves were corrected mathematically to reduce contrast agent leakage effects.[16,17] The rCBV maps were normalized by dividing the rCBV value in the region of interest by the rCBV value of normal-appearing white matter defined by a neuroradiologist (J.C.).

Histogram Analysis

For each tumor, a region of interest was drawn on the contrast-enhanced T1-weighted images, including whole enhancing lesions, on each section by using MRIcro software (http://www.mccauslandcenter.sc.edu/mricro/mricro.html) from the initial (MR imaging obtained at the time of increased lesion size) and follow-up MR imaging (first follow-up MR imaging obtained within 3 months after the initial MR imaging) by a neuroradiologist (J.C.). The cerebral cortex was avoided when drawing the region of interest. Before data analysis, rCBV and ADC maps were coregistered to the contrast-enhanced T1-weighted

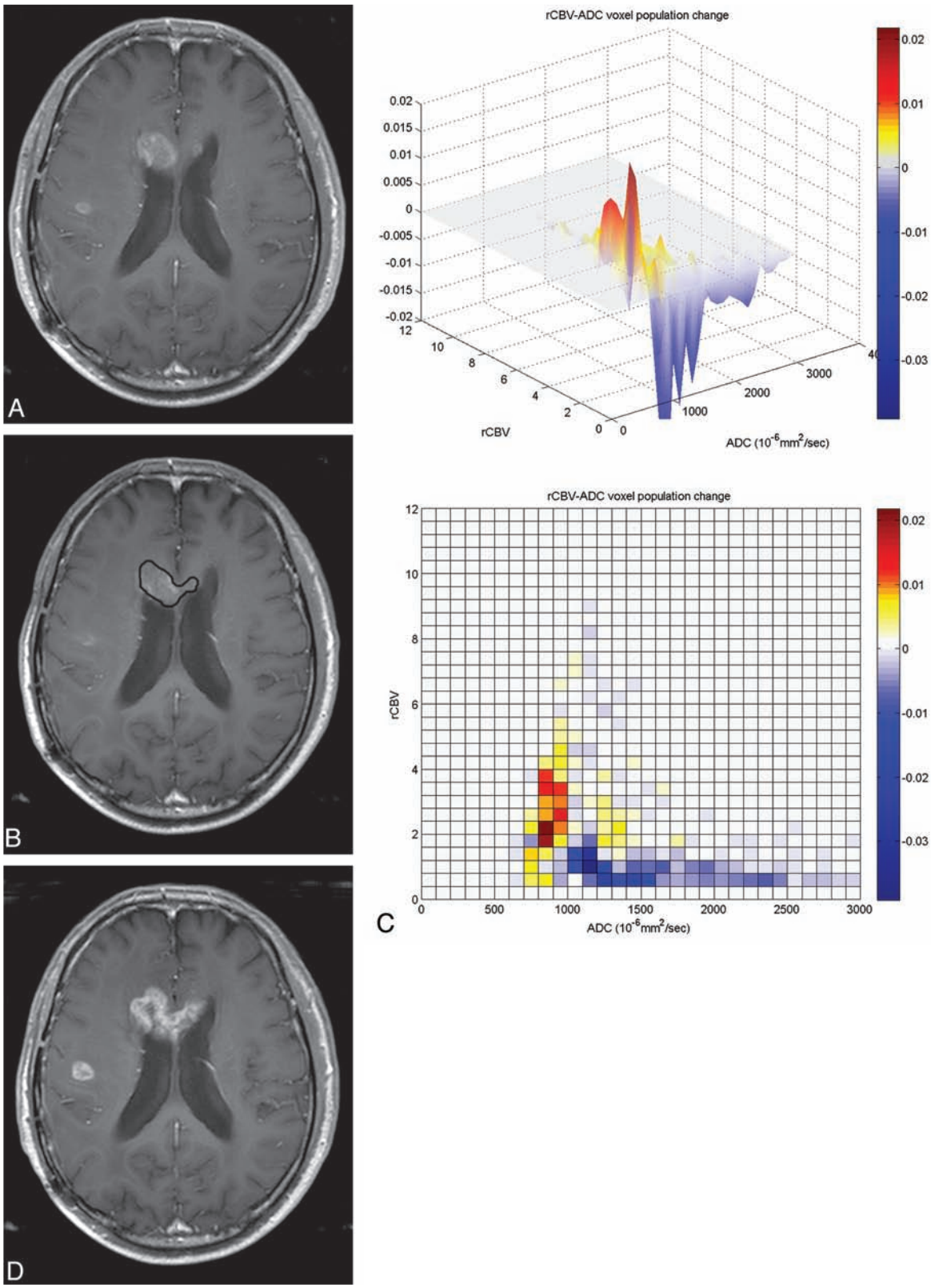

FIG 3. A 70-year-old man with glioblastoma who underwent tumor removal followed by CCRT. One hundred forty-two days after CCRT, the enhancing lesion developed in the genu of corpus callosum (*A*). On follow-up MR imaging performed 54 days after CCRT (*B*), the enhancing lesion was stable or somewhat decreased in size, suggestive of pseudoprogression. However, the 3D histogram shows a markedly increased population (coded as red) of high rCBV voxels with relatively low ADC values (*C*). Eventually, the enhancing lesion increased in size on follow-up MR imaging (*D*) performed after 67 days from first follow-up MR imaging (*B*), and tumor progression was diagnosed.

images by using affine transformation with normalized mutual information[18] as a cost function.

For histogram analysis, rCBV and ADC values within the region of interest were extracted by using Matlab software (MathWorks, Natick, Massachusetts). Only ADC values of 5~3000 and rCBV of 0.3~12 were considered meaningful, because beyond these ranges, the values may be from noise, cystic or necrotic areas, or CSF. Combined 3D histograms were made by using acquired rCBV and ADC values of each voxel (ADC range, 0~3000; interval, 100; rCBV range, 0~12, interval, 0.4; total, 900 bins). From the histogram, mean, SD, maximum frequency, mode, kurtosis, and skewness of ADC values and rCBV on the initial and follow-up MR imaging were calculated (Fig 1).

To evaluate the change in the histogram between initial and follow-up MR imaging, we subtracted the histograms of initial MR imaging from the histograms of follow-up MR imaging. The histogram subtraction was performed with a uniparametric approach (subtraction of ADC and rCBV histograms independently) and multiparametric approach (the combined ADC × rCBV 3D histogram of the initial MR imaging was subtracted from the combined 3D histogram of the follow-up MR imaging). Then, the mode of the ADC value and rCBV of the subtracted histogram were calculated.

Statistical Analysis

Statistical analyses were performed by using the IBM SPSS Statistics, Version 20 (IBM, Armonk, New York). The mean, SD, maximum frequency, mode, kurtosis, and skewness of ADC values and rCBV between the progression group and the pseudoprogression group were compared by using the Mann-Whitney test for initial and follow-up MR imaging. The mode of the ADC values and the rCBV of the subtracted histogram with uniparametric and multiparametric approaches were compared between the 2 groups by using the Mann-Whitney test. The diagnostic performance (sensitivity, specificity, accuracy) of tumor progression based on the increased size of the enhancing lesion, histogram parameters of the initial and follow-up MR imaging, and the subtracted histogram were compared by using a receiver operating characteristic curve analysis. Subsequently, multivariable stepwise logistic regression analysis was used to determine the significant predictors for the differential diagnosis between true progression and pseudoprogression.

We used the date of surgical resection to determine overall survival, and survival curves were calculated by using the Kaplan-Meier method. We compared overall survival between tumor progression and pseudoprogression using the log-rank test, and we correlated the parameters of histogram and mode of the subtracted histogram with overall survival.

RESULTS

Histogram Analysis

Twenty-four cases of pseudoprogression (Fig 2) and 11 cases of tumor progression (Fig 3) were determined on the basis of stable or decreased size of the enhancing lesion on the consecutive follow-up study ($n = 32$) or pathologic diagnosis ($n = 3$).

On the histogram analysis (Tables 1 and 2), at initial MR imaging, all parameters of ADC values and rCBV did not show any significant difference between the 2 groups. At follow-up MR imaging, the mean ($P < .001$) and SD ($P = .001$) of the rCBV were larger in the progression group than in the pseudoprogression group. Maximum frequency ($P < .001$), kurtosis ($P = .030$), and skewness ($P = .039$) of rCBV were smaller in the progression group than in the pseudoprogression group. The parameters of ADC values did not differ significantly between the groups on follow-up MR imaging.

Table 1: Histogram parameters of the initial MRI[a]

	Pseudoprogression (n = 24)	Progression (n = 11)	*P* Value
ADC[b]			
Mean	1404.9 ± 195.4	1376.0 ± 145.0	.570
SD	468.0 ± 118.9	368.5 ± 117.3	.055
Max freq	0.15 ± 0.05	0.16 ± 0.05	.356
Mode	1154.2 ± 196.7	1240.9 ± 186.8	.320
Kurtosis	4.89 ± 3.27	4.54 ± 2.29	.972
Skewness	1.14 ± 0.65	0.91 ± 0.64	.434
rCBV			
Mean	1.72 ± 0.59	1.72 ± 0.55	.804
SD	1.25 ± 0.45	1.18 ± 0.52	.722
Max freq	0.24 ± 0.09	0.24 ± 0.09	.972
Mode	0.93 ± 0.48	0.93 ± 0.30	.562
Kurtosis	8.74 ± 4.84	8.71 ± 7.52	.434
Skewness	1.89 ± 0.69	1.72 ± 0.99	.570

Note:—Max freq indicates maximum relative frequency.
[a] Numbers represent means.
[b] Unit of ADC value = 10^{-6}mm^2/s.

Table 2: Histogram parameters of the follow-up MRI[a]

	Pseudoprogression (n = 24)	Progression (n = 11)	*P* Value
ADC[b]			
Mean	1402.4 ± 187.7	1345.5 ± 204.5	.546
SD	404.0 ± 85.3	402.1 ± 110.1	.804
Max freq	0.14 ± 0.05	0.16 ± 0.05	.241
Mode	1245.8 ± 178.1	1222.7 ± 331.9	.430
Kurtosis	4.96 ± 2.31	4.64 ± 2.00	.776
Skewness	1.09 ± 0.62	1.05 ± 0.69	.915
rCBV			
Mean	1.40 ± 0.42	2.15 ± 0.51	<.001
SD	1.01 ± 0.40	1.50 ± 0.38	.001
Max freq	0.30 ± 0.10	0.17 ± 0.05	<.001
Mode	0.80 ± 0.26	0.96 ± 0.52	.522
Kurtosis	9.68 ± 4.11	6.49 ± 3.02	.030
Skewness	2.05 ± 0.65	1.54 ± 0.63	.039

Note:—Max freq indicates maximum relative frequency.
[a] Numbers represent means.
[b] Unit of ADC value = 10^{-6}mm^2/s.

On the subtracted histogram (Fig 4, Table 3), the mode of rCBV was higher ($P = .003$) and the mode of ADC ($P = .008$) was lower in the progression group with a uniparametric approach. However, with a multiparametric approach, only the mode of rCBV was higher ($P < .001$) in the progression group than in the pseudoprogression group. On multivariable logistic regression analysis, the multiparametric mode of rCBV was the only independently differentiating parameter ($P = .005$).

Diagnostic Performance of Histogram Parameters

On the histogram analysis of the initial and follow-up MR imaging studies, the most significant parameter was the mean rCBV of the follow-up MR imaging. For the subtracted histogram, receiver operating characteristic curve analysis (Fig 5) showed that the

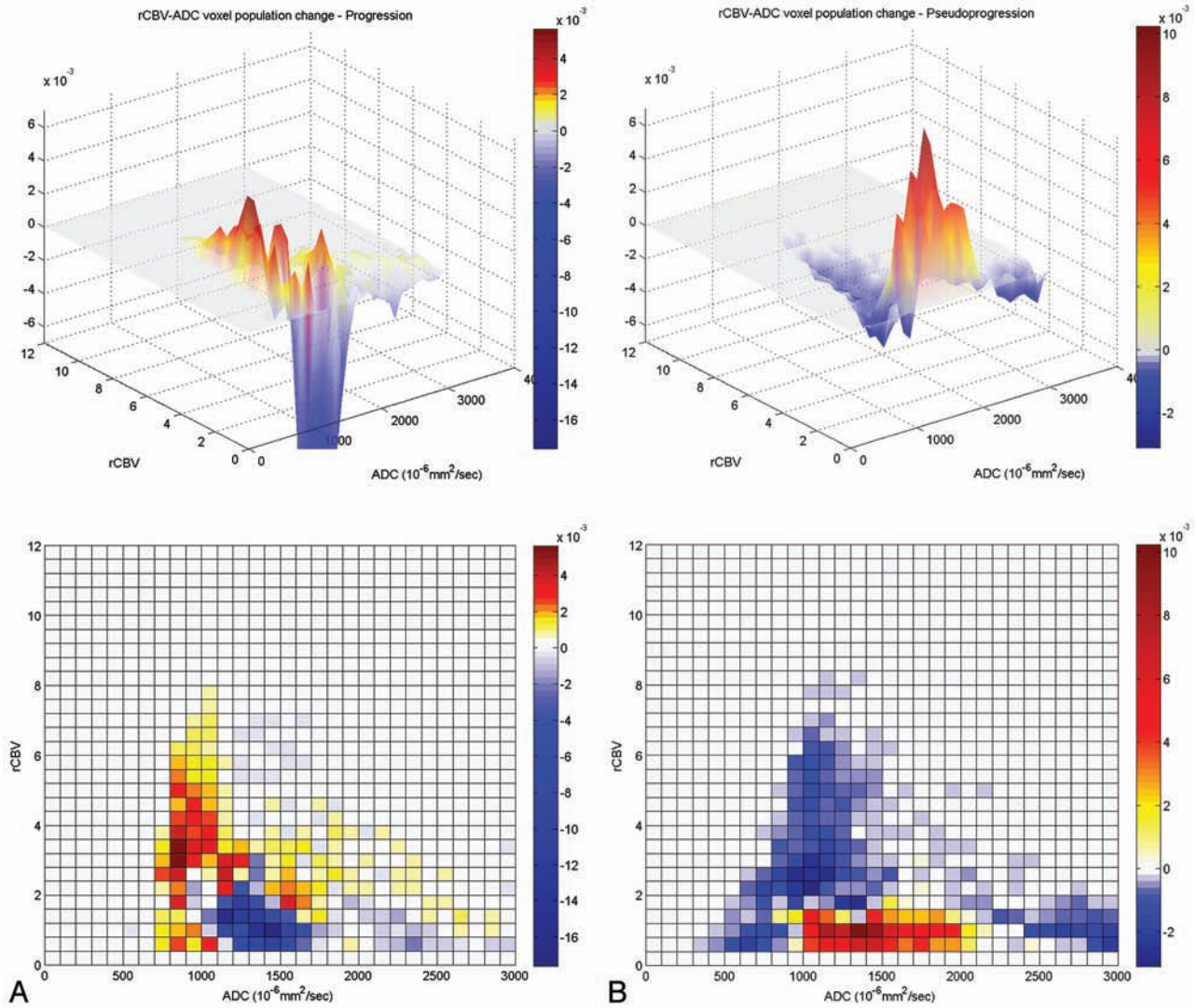

FIG 4. The subtracted 3D histogram of each group by using a multiparametric approach. *A*, The tumor progression group shows an increased voxel population with high rCBV and relatively low ADC values (800~1200 × 10^{-6}mm^2/s) and a decreased population with low rCBV with a wide range of ADC values. *B*, The pseudoprogression group shows a decreased voxel population with high rCBV and relatively low ADC, which shows increased population in the tumor progression group. In contrast, voxels with low rCBV with a wide range of ADCs (1000~2000 × 10^{-6}mm^2/s) show an increased population in the pseudoprogression group.

Table 3: The mode of rCBV and ADC values of the subtracted histogram using uniparametric and multiparametric approaches[a]

	Pseudoprogression (*n* = 24)	Progression (*n* = 11)	*P* Value
Uniparametric			
ADC mode[b]	1404.2 ± 407.5	1004.6 ± 317.4	.008
rCBV mode	1.0 ± 0.7	2.3 ± 1.2	.003
Multiparametric			
ADC mode[b]	1412.5 ± 365.7	1259.1 ± 320.8	.238
rCBV mode	1.0 ± 0.3	2.3 ± 1.1	<.001

[a] Numbers represent means.
[b] Unit of ADC value = 10^{-6}mm^2/s.

mode of rCBV by using a multiparametric approach had a larger area under the curve (0.877 versus 0.801) than when using the uniparametric approach for differentiating pseudoprogression from tumor progression. Therefore, we used the mean rCBV of the follow-up MR imaging and the mode of rCBV with the multiparametric approach as representative parameters to compare diagnostic performance.

The sensitivity, specificity, and accuracy of diagnosing tumor progression based on the size change of enhancing lesions were 72.7%, 83.3%, and 80.0%, respectively. The sensitivity, specificity, and accuracy of the diagnosis based on the mean rCBV > 1.8 of follow-up MR imaging were 81.8%, 83.3%, and 82.9%, respectively. The diagnosis based on the mode of rCBV > 1.6 on the subtracted histogram was most accurate, with 81.8% sensitivity, 100% specificity, and 94.3% accuracy.

Survival Analysis

Twenty-six (74%) of the 35 patients had died by the time of data analysis. The mean follow-up period was 556 ± 288 days. The overall median survival from the operation to death or last follow-up was 513 days. The median survival (Fig 6*A*) of the progression group (394 days) was significantly shorter than that of the pseudoprogression group (565 days) ($P = .037$). The median survival rate was not significantly different in terms of the mean rCBV of follow-up MR imaging with any threshold (rCBV

$> 1.5\sim 2.2$). The median survival (Fig 6*B*) was significantly different in terms of the mode of rCBV on the subtracted histogram with threshold rCBV > 1.8 (394 versus 561 days, $P = .003$), and it was statistically more significant than the survival difference of the progression and pseudoprogression groups.

DISCUSSION

In this study, we evaluated subtracted combined ADC × rCBV 3D histograms of 2 consecutive MR imaging studies; therefore, we could observe the changing trend of the histogram pattern between the 2 studies. The diagnostic performance of the subtracted histogram was better than that of a single MR imaging study; especially, the mode of the subtracted histogram, which was the best predictor. In addition, the mode acquired from the multiparametric approach showed better diagnostic performance than that of the uniparametric approach.

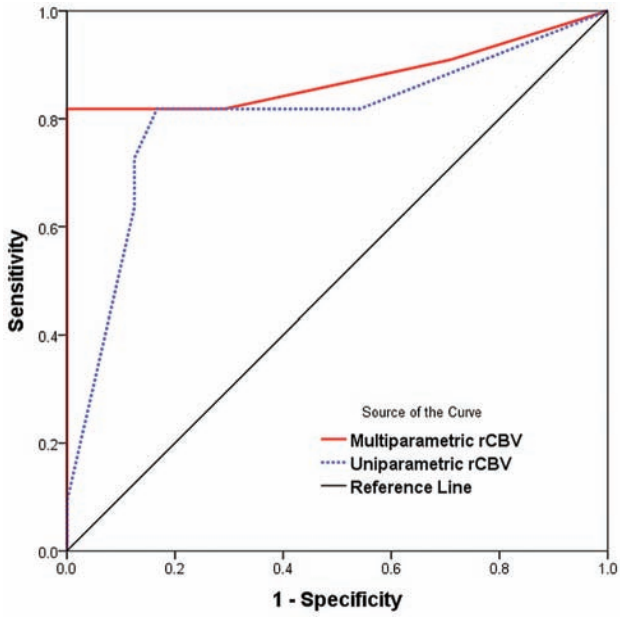

FIG 5. Receiver operating characteristic curve analysis for the mode of rCBV on the subtracted histogram by using uniparamteric and multiparametric approaches for differentiating tumor progression from pseudoprogression. Diagonal line = 50% of the area under the receiver operating characteristic curve analysis.

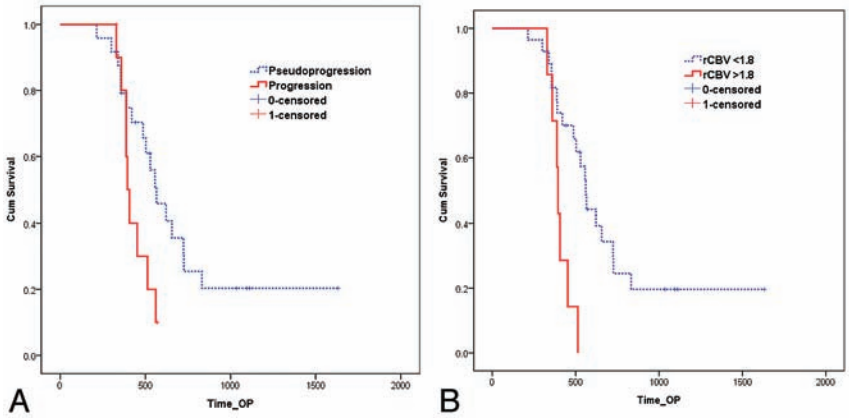

FIG 6. Graph data indicate that overall cumulative (Cum) survival is significantly better for patients with pseudoprogression (*A*) and mode of rCBV < 1.8 on the subtracted histogram with a multiparametric approach (*B*) after CCRT.

A major limitation of rCBV for posttreatment evaluation is that the treatment-related inflammation also causes increased rCBV. In cases of radiation necrosis of the brain[19] around the liquefied center, there are areas of active inflammatory responses with lymphocytes and macrophages, resulting in some degree of increased rCBV. On DWI, radiation necrosis may show diffusion restriction, probably due to intracellular edema and viscous pus-like material with abundant polymorphonuclear leukocytes in the transition zone.[10,20,21] Therefore, increased rCBV does not always mean viable tumor angiogenesis, and decreased ADC values do not always mean high cellularity. Using multiparametric analysis with rCBV and ADC values, we may exclude the effects of radiation necrosis when evaluating ADC values because radiation necrosis shows low rCBV on its diffusion-restriction area. In addition, we may exclude the effect of inflammation when evaluating rCBV because inflammation with edema shows increased ADC values. In this study, with a uniparametric approach, both rCBV and ADC were significantly different between the progression and pseudoprogression groups, but with the multiparametric approach, only rCBV was significantly different between the groups—that is, in terms of rCBV, the statistical significance was increased when the rCBV was stratified by ADC values; however, in terms of the ADC value, the statistical significance was decreased with stratification.

Another limitation of rCBV analysis is related to contrast material leakage. Because the rCBV calculation of dynamic susceptibility contrast perfusion MR imaging is based on the absence of contrast material leakage to the extravascular space, leakage of contrast material can cause underestimation of rCBV.[16] Contrast preload and mathematic correction can be used to overcome these effects. We used mathematic correction, which is known to be equivalent to preload for the correction of contrast material leakage effect.[17]

Emblem et al[22] suggested that tumor malignancy was related to CBV heterogeneity, and Law et al[23] also suggested that the histogram parameter that had the highest correlation with glioma grade was SD. This was because an increase of the SD and a decrease of the maximum frequency for high-grade gliomas could reflect heterogeneous tumor angiogenesis. High-grade gliomas that initially had heterogeneous vascularity may have reduced heterogeneity after radiation therapy. Tumor progression/recurrence may increase in heterogeneity due to heterogeneous angiogenesis of the viable tumor component. In this study, the tumor progression group showed increased voxel population with high rCBV and low ADC values (Fig 4*A*). In contrast, in the pseudoprogression group, the voxel population with high rCBV was decreased and the ADC was more elevated and dispersed (Fig 4*B*). In the tumor progression group, the SD of rCBV was increased, and the maximum frequency and kurtosis were decreased on follow-up MR imaging. These results suggest increased heterogeneity of the tumor.

Hu et al[14] proposed the perfusion MR imaging–fractional tumor burden method

for evaluation of post-treatment glioblastoma. The perfusion MR imaging (pMRI)–fractional tumor burden describes the population of the risk voxels with values of more than threshold rCBV (rCBV = 1). The perfusion MR imaging (pMRI)–fractional tumor burden metric reliably estimated the histologic tumor fraction and correlated with overall survival. However, the mean rCBV and histogram mode of rCBV less strongly correlated with the histologic tumor fraction and did not correlate with overall survival. This result is probably because most lesions are histologically admixed and broadly variable in tumor fractions; therefore, the mean rCBV (similar to other histogram-based metrics) is influenced by the rCBV from both tumoral and nontumoral components.[14] In our study, rCBV histogram parameters of initial MR imaging did not show any significant difference. Because of the heterogeneity of the lesion, posttreatment tumor evaluation by using the mean values of the overall lesion on a single MR imaging study is an intrinsically limited effort.

In this study, the proportion of pseudoprogression in patients with new or enlarged enhancing lesions was 69%. In previous studies, enlarged lesions on conventional MR images may actually have represented pseudoprogression in up to 46.8%–64% of cases, compatible with our results.[8,24] Because pseudoprogression is so common, the RANO Working Group recommended a second MR imaging at 4 weeks to confirm the presence of response or stable disease.[9] However, pseudoprogression can be sustained or aggravated for >4 weeks; therefore, it can mimic tumor progression.[25] Therefore, the diagnosis of tumor progression based on the size of the enhancing lesion may cause false-positive (Fig 2) or false-negative results (Fig 3). Mangla et al[12] showed that increased rCBV after treatment was a stronger predictor of poor survival (area under the receiver operating characteristic curve = 0.806). However, change in tumor size did not correlate with overall survival (area under the receiver operating characteristic curve = 0.566). If increased rCBV on follow-up MR imaging was used to differentiate true disease progression and pseudoprogression, the sensitivity was 76.9% and the specificity was 85.7%. In our study, if one considered the mode of rCBV on the subtracted histogram, the diagnostic accuracy was increased from 80% to 94.3%, compared with the diagnosis based on the tumor size change.

Another problem is the ambiguous nature of the reference standard of pseudoprogression. The criterion standard for diagnosing pseudoprogression is histopathology; however, biopsy may have sampling errors, and even a specimen obtained with second-look surgery may have residual infiltrated tumor cells, which can be erroneously interpreted by the pathologist.[26,27] Therefore, there is an innate limitation in differentiating pseudoprogression from tumor progression. In this study, we also correlated imaging biomarkers with overall survival. The high mode of rCBV on the subtracted histogram by using a multiparametric approach (rCBV × ADC) was a good predictor of worse survival as well as tumor progression.

Our study has several limitations. First is the retrospective nature of the study. Second, due to the small number of cases, especially progression relative to pseudoprogression, generalizability and statistical power are limited. Third, tumor progression and pseudoprogression were determined mainly by follow-up MR imaging, and pathologic confirmation was performed in only a few patients. Finally, the region of interest was drawn only on the enhancing portion of the lesion; therefore, the effect of the nonenhancing infiltrative portion was not evaluated. However, this study focused on the particular clinical situation—that is, a newly developed or increased size of the enhancing lesion mimicking tumor progression; therefore, only the nature or change of the enhancing lesion was considered.

CONCLUSIONS

Multiparametric 3D histogram analysis with ADC values and rCBV was useful to evaluate posttreatment glioblastomas. Tumor progression showed increased rCBV and increased heterogeneity on follow-up studies; however, pseudoprogression did not. A high mode of rCBV on the subtracted histogram by using a multiparametric approach (rCBV × ADC) was the best predictor of true tumor progression and worse survival.

REFERENCES

1. Stupp R, Mason WP, van den Bent MJ, et al. **Radiotherapy plus concomitant and adjuvant temozolomide for glioblastoma.** *N Engl J Med* 2005;352:987–96
2. Caroline I, Rosenthal MA. **Imaging modalities in high-grade gliomas: pseudoprogression, recurrence, or necrosis?** *J Clin Neurosci* 2012;19:633–37
3. Yang I, Aghi MK. **New advances that enable identification of glioblastoma recurrence.** *Nat Rev Clin Oncol* 2009;6:648–57
4. Brandsma D, Stalpers L, Taal W, et al. **Clinical features, mechanisms, and management of pseudoprogression in malignant gliomas.** *Lancet Oncol* 2008;9:453–61
5. Chaskis C, Neyns B, Michotte A, et al. **Pseudoprogression after radiotherapy with concurrent temozolomide for high-grade glioma: clinical observations and working recommendations.** *Surg Neurol* 2009;72:423–28
6. Kong DS, Kim ST, Kim EH, et al. **Diagnostic dilemma of pseudoprogression in the treatment of newly diagnosed glioblastomas: the role of assessing relative cerebral blood flow volume and oxygen-6-methylguanine-DNA methyltransferase promoter methylation status.** *AJNR Am J Neuroradiol* 2011;32:382–87
7. Husby JA, Espeland A, Kalyanpur A, et al. **Double reading of radiological examinations in Norway.** *Acta Radiol* 2011;52:516–21
8. Baek HJ, Kim HS, Kim N, et al. **Percent change of perfusion skewness and kurtosis: a potential imaging biomarker for early treatment response in patients with newly diagnosed glioblastomas.** *Radiology* 2012;264:834–43
9. Wen PY, Macdonald DR, Reardon DA, et al. **Updated response assessment criteria for high-grade gliomas: Response Assessment in Neuro-Oncology Working Group.** *J Clin Oncol* 2010;28:1963–72
10. Asao C, Korogi Y, Kitajima M, et al. **Diffusion-weighted imaging of radiation-induced brain injury for differentiation from tumor recurrence.** *AJNR Am J Neuroradiol* 2005;26:1455–60
11. Hygino da Cruz LC Jr, Rodriguez I, Domingues RC, et al. **Pseudoprogression and pseudoresponse: imaging challenges in the assessment of posttreatment glioma.** *AJNR Am J Neuroradiol* 2011;32:1978–85
12. Mangla R, Singh G, Ziegelitz D, et al. **Changes in relative cerebral blood volume 1 month after radiation-temozolomide therapy can help predict overall survival in patients with glioblastoma.** *Radiology* 2010;256:575–84
13. Kim HS, Kim JH, Kim SH, et al. **Posttreatment high-grade glioma: usefulness of peak height position with semiquantitative MR perfusion histogram analysis in an entire contrast-en-**

hanced lesion for predicting volume fraction of recurrence. *Radiology* 2010;256:906–15
14. Hu LS, Eschbacher JM, Heiserman JE, et al. **Reevaluating the imaging definition of tumor progression: perfusion MRI quantifies recurrent glioblastoma tumor fraction, pseudoprogression, and radiation necrosis to predict survival.** *Neuro Oncol* 2012;14:919–30
15. Ostergaard L, Weisskoff RM, Chesler DA, et al. **High resolution measurement of cerebral blood flow using intravascular tracer bolus passages. Part I. Mathematical approach and statistical analysis.** *Magn Reson Med* 1996;36:715–25
16. Boxerman JL, Schmainda KM, Weisskoff RM. **Relative cerebral blood volume maps corrected for contrast agent extravasation significantly correlate with glioma tumor grade, whereas uncorrected maps do not.** *AJNR Am J Neuroradiol* 2006;27:859–67
17. Boxerman JL, Prah DE, Paulson ES, et al. **The role of preload and leakage correction in gadolinium-based cerebral blood volume estimation determined by comparison with MION as a criterion standard.** *AJNR Am J Neuroradiol* 2012;33:1081–87
18. Maes F, Collignon A, Vandermeulen D, et al. **Multimodality image registration by maximization of mutual information.** *IEEE Trans Med Imaging* 1997;16:187–98
19. Yoshii Y. **Pathological review of late cerebral radionecrosis.** *Brain Tumor Pathol* 2008;25:51–58
20. Tung GA, Evangelista P, Rogg JM, et al. **Diffusion-weighted MR imaging of rim-enhancing brain masses: is markedly decreased water diffusion specific for brain abscess?** *AJR Am J Roentgenol* 2001; 177:709–12
21. Cha J, Kim ST, Kim HJ, et al. **Analysis of the layering pattern of the apparent diffusion coefficient (ADC) for differentiation of radiation necrosis from tumour progression.** *Eur Radiol* 2013; 23:879–86
22. Emblem KE, Nedregaard B, Nome T, et al. **Glioma grading by using histogram analysis of blood volume heterogeneity from MR-derived cerebral blood volume maps.** *Radiology* 2008;247: 808–17
23. Law M, Young R, Babb J, et al. **Histogram analysis versus region of interest analysis of dynamic susceptibility contrast perfusion MR imaging data in the grading of cerebral gliomas.** *AJNR Am J Neuroradiol* 2007;28:761–66
24. Brandes AA, Franceschi E, Tosoni A, et al. **MGMT promoter methylation status can predict the incidence and outcome of pseudoprogression after concomitant radiochemotherapy in newly diagnosed glioblastoma patients.** *J Clin Oncol* 2008;26:2192–97
25. Taal W, Brandsma D, de Bruin HG, et al. **Incidence of early pseudoprogression in a cohort of malignant glioma patients treated with chemoirradiation with temozolomide.** *Cancer* 2008;113:405–10
26. Chamberlain MC. **Pseudoprogression in glioblastoma.** *J Clin Oncol* 2008;26:4359, author reply 4359–60
27. Chamberlain MC, Glantz MJ, Chalmers L, et al. **Early necrosis following concurrent Temodar and radiotherapy in patients with glioblastoma.** *J Neurooncol* 2007;82:81–83

Cerebrovascular Collaterals Correlate with Disease Severity in Adult North American Patients with Moyamoya Disease

M.K. Strother, M.D. Anderson, R.J. Singer, L. Du, R.D. Moore, Y. Shyr, T.R. Ladner, D. Arteaga, M.A. Day, P.F. Clemmons, and M.J. Donahue

ABSTRACT

BACKGROUND AND PURPOSE: Cerebrovascular collaterals have been increasingly recognized as predictive of clinical outcomes in Moyamoya disease in Asia. The aim of this study was to characterize collaterals in North American adult patients with Moyamoya disease and to assess whether similar correlations are valid.

MATERIALS AND METHODS: Patients with Moyamoya disease ($n = 39$; mean age, 43.5 ±10.6 years) and age- and sex-matched control subjects ($n = 33$; mean age, 44.3 ± 12.0 years) were graded via angiography. Clinical symptoms of stroke or hemorrhage were graded separately by imaging. Correlations between collateralization and disease severity, measured by the modified Suzuki score, were evaluated in patients with Moyamoya disease by fitting a regression model with clustered ordinal multinomial responses.

RESULTS: The presence of leptomeningeal collaterals ($P = .008$), dilation of the anterior choroidal artery ($P = .01$), and the posterior communicating artery/ICA ratio ($P = .004$) all correlated significantly with disease severity. The presence of infarct or hemorrhage and posterior steno-occlusive disease did not correlate significantly with the modified Suzuki score ($P = .1$). Anterior choroidal artery changes were not specific for hemorrhage. Patients with Moyamoya disease were statistically more likely than controls to have higher posterior communicating artery/ICA ratios and a greater incidence of leptomeningeal collaterals.

CONCLUSIONS: As with Moyamoya disease in Asian patients, the presence of cerebrovascular collaterals correlated with the modified Suzuki score for disease severity in North American patients with Moyamoya disease. However, anterior choroidal artery changes, which correlated with increased rates of hemorrhage in Asian studies, were not specific to hemorrhage in North Americans.

ABBREVIATIONS: AchoA = anterior choroidal artery; LMC = leptomeningeal collaterals; MMD = Moyamoya disease; mSS = modified Suzuki score; P1= proximal segment of the posterior cerebral artery; PCA = posterior cerebral artery; PcomA = posterior communicating artery

Moyamoya disease (MMD) has been largely described by the Asian experience, yet varying epidemiologic and clinical features in North Americans with MMD suggest that pathophysiologic differences exist. MMD in North Americans and Europeans most commonly affects young women in the third-to-fourth decades of life, whereas MMD in Asians typically begins in childhood.[1-3] North American and European patients present with ischemic stroke or TIA as the most frequent manifestation,[1,4-9] whereas hemorrhage is more frequent in Asian cohorts.[3] Additionally, gene associations found in Asian cohorts have not been replicated by European investigators.[10]

Shared features for all MMD include predominantly anterior circulation involvement with progressive arteriopathy involving the ICA and proliferation of distinctive basal vessels—changes that have been well-correlated with disease severity.[11-13] Other collaterals, including dilated anterior choroidal arteries (AchoAs) and posterior communicating arteries (PcomAs), are less well-studied, particularly in North Americans. Histologic analysis of these collaterals has demonstrated evidence of stress related to increased flow, which may predispose patients to hemorrhage.[14] Dilated anterior choroidal and posterior communicating arteries have been shown to be strongly predictive of hemorrhage in Asian MMD.[15] The purpose of this study was to assess correlations between disease severity with less well-characterized collaterals, in-

Received August 29, 2013; accepted after revision November 28.

From the Departments of Radiology and Radiological Sciences (M.K.S., M.D.A., R.D.M., T.R.L., D.A., M.A.D., P.F.C., M.J.D.), Neurology (M.J.D.), Psychiatry (M.J.D), and Physics and Astronomy (M.J.D.), and Vanderbilt Center for Quantitative Sciences (L.D., Y.S.); Vanderbilt University School of Medicine, Nashville, Tennessee; and Section of Neurosurgery (R.J.S.), Dartmouth-Hitchcock Medical Center, Lebanon, New Hampshire.

This work was supported by the National Institutes of Health/National Institute of Neurological Disorders and Stroke (5R01NS078828–02) and the American Association of Neurological Surgeons Medical Student Summer Research Fellowship Program.

Please address correspondence to Megan K. Strother, MD, Vanderbilt University School of Medicine, 1161 21st Ave South, Nashville, TN 37232-2675; e-mail: Megan.strother@vanderbilt.edu

http://dx.doi.org/10.3174/ajnr.A3883

Table 1: Modified Suzuki scoring

Score	Description of classification
0	No evidence of disease
I	Mild-to-moderate stenosis around ICA bifurcation with absent or slightly developed ICA MMD[a]
II	Severe stenosis around the ICA bifurcation or occlusion of either proximal anterior or MCA branches with well-developed ICA MMD
III	Occlusion of both anterior and MCA branches with well-developed ICA MMD (only a few of anterior or MCA branches or both are faintly opacified in antegrade fashion through meshwork of ICA MMD)
IV	Complete occlusion of both anterior and MCA branches with absent or small amount of ICA MMD (without opacification of either anterior or MCA branches in antegrade fashion)

[a] ICA Moyamoya disease indicates perforating collateral vessels at or around the terminal ICA.

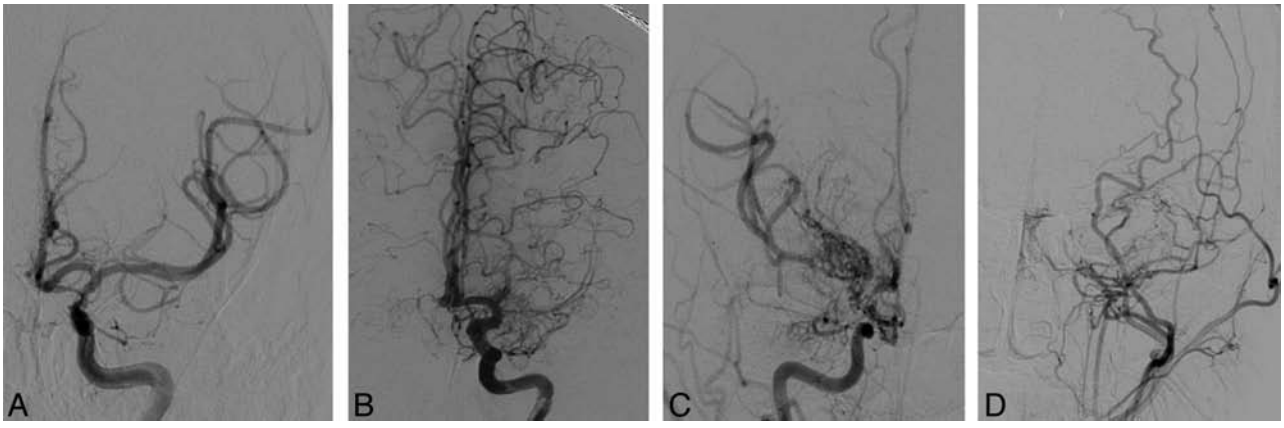

FIG 1. Modified Suzuki scoring. Anteroposterior projections from DSA demonstrate a moderately stenosed left ICA without anterior cerebral artery or MCA involvement or Moyamoya perforators (mSS I) (*A*); an occluded left M1 with well-developed ICA Moyamoya perforators (mSS II) (*B*); an occluded right ICA, A1 and M1 with extensive Moyamoya perforators (mSS III) (*C*); and an occluded left ICA, M1 and A1 with absent Moyamoya perforators (mSS IV)—external carotid collaterals are visualized from a common carotid injection (*D*).

cluding the PcomA/ICA ratio, leptomeningeal collaterals (LMC), and AchoA changes, in a cohort of adult North Americans with MMD. Our primary hypothesis is that these collaterals correlate variably with disease severity, as measured by the modified Suzuki score (mSS) and clinical findings of stroke or hemorrhage. Our secondary hypothesis is that these collaterals correlate with disease compared with control subjects.

MATERIALS AND METHODS

This retrospective review was approved by the local institutional review board. Subjects were identified by an electronic medical record search for all adult patients with MMD who underwent DSA from 2002 to 2012 at our institution. Idiopathic MMD was defined as mSS I–IV in at least 1 cerebral hemisphere without associated predisposing disease. Control subjects were selected sequentially from angiograms obtained for any non-Moyamoya indication. Two certified neuroradiologists, blinded to clinical and imaging findings, graded disease severity separately and resolved disagreement by consensus. Modifications have been made to the Suzuki classification so that the score can be applied to individual cases, rather than longitudinally.[16,17] The mSS used for this study (Table 1) includes 5 stages of disease severity,[18] examples of which are shown in Fig 1. In separate sessions divided by >2 weeks, the following were graded from DSA:

1) LMC circulation to the anterior circulation was classified into 2 stages: Stage 1, leptomeningeal cortical branches were found coursing from the posterior cerebral artery (PCA) to the frontal, temporal, or parietal Lobes; Stage 2, there was no leptomeningeal collateral circulation.[19,20]

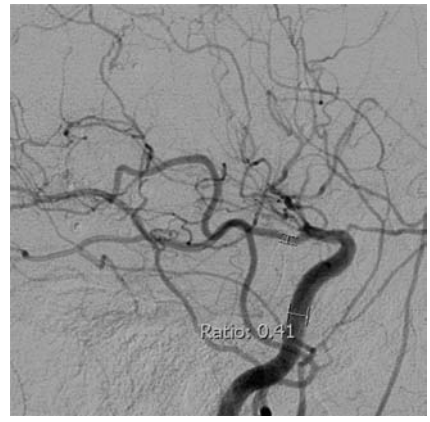

FIG 2. PcomA/ICA ratio method. Lateral projection from DSA with the PcomA/ICA ratio in a patient with MMD with distal ICA occlusion beyond the PcomA origin.

2) Ratio of the PcomA lumen diameter to the ipsilateral precavernous ICA lumen diameter[21] is shown in Fig 2. Because the distal ICA is stenosed in MMD, the ICA measurement was performed at the precavernous portion with the widest, parallel lumen. If a PcomA infundibulum was present, the diameter was measured distal to infundibulum.

3) Proximal segment of the posterior cerebral artery (P1) steno-occlusive changes were noted (1, no stenosis or occlusion; 2, stenosis or occlusion).[2,22]

An endovascular neurosurgeon (with 21 years of experience), blinded to clinical and imaging findings, separately graded the AchoA (zero, normal; 1, dilated with distal branching; and 2, di-

Table 2: Collateral and clinical characteristics by modified Suzuki score in subjects with Moyamoya disease[a]

Metric (*P* Value)	N	0 (*n* = 6)	I (*n* = 7)	II (*n* = 30)	III (*n* = 20)	IV (*n* = 15)
PcomA/ICA[b] (.024)	64	0.125	0.205	0.295	0.330	0.520
LMC (.001)	78					
1		17% (1)	29% (2)	63% (19)	80% (16)	93% (14)
2		83% (5)	71% (5)	37% (11)	20% (4)	7% (1)
CT/MR (.06)[c]	78					
1		83% (5)	57% (4)	37% (11)	15% (3)	33% (5)
2		17% (1)	42% (3)	60% (18)	70% (14)	67% (10)
3		0% (0)	0% (0)	3% (1)	15% (3)	0% (0)
AchoA (<.001)	78					
0		83% (5)	43% (3)	13% (4)	5% (1)	7% (1)
1		17% (1)	43% (3)	37% (11)	10% (2)	0% (0)
2		0% (0)	14% (1)	50% (15)	85% (17)	33% (5)
NV		0% (0)	0% (0)	0% (0)	0% (0)	60% (9)
P1 (.14)	78					
1		100% (6)	86% (6)	90% (27)	95% (19)	67% (10)
2		0% (0)	14% (1)	10% (3)	5% (1)	33% (5)

Note:—N indicates the number of nonmissing values; NV, not visualized.
[a] Numbers after percentages are frequencies.
[b] PcomA/ICA ratio provided is median.
[c] CT/MR 1—no infarct or hemorrhage, 2—infarct, 3—hemorrhage.

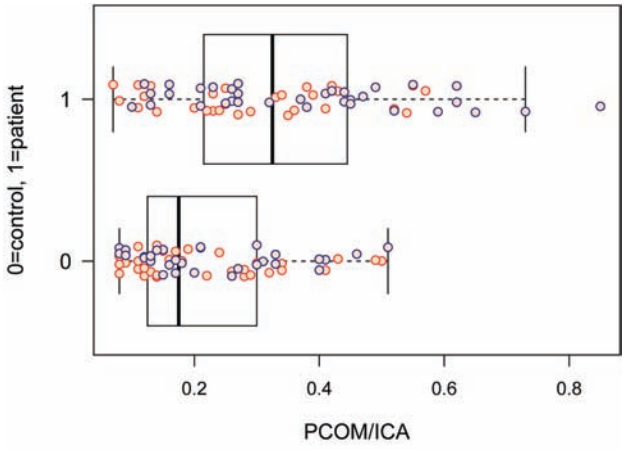

FIG 3. PcomA/ICA ratio in subjects with MMD versus control subjects by hemisphere. The PcomA/ICA ratio in a patient with MMD ($n = 1$) was significantly higher ($P < .001$) compared with control subjects ($n = 0$). Orange dots are observations for the left cerebral hemisphere, and blue dots are for the right cerebral hemisphere. The dark band represents the median in this boxplot.

lated with abnormal branches serving as collaterals to other regions).[15] The site of ICA occlusion was identified in subjects when the AchoA was not visualized. Hemorrhage or infarct or both were graded on CT or MR imaging performed within 30 days of DSA, and the location of the infarct was classified by territory. Exclusion criteria were the following: 1) For PcomA/ICA ratios, the hemisphere was excluded if the PcomA was not visualized on DSA; 2) both hemispheres were excluded for surgical revascularization before DSA; and 3) for AchoA grading, the hemisphere was excluded if the AchoA was not visualized.

Statistical Analysis

For univariate analysis for the association of the disease severity (mSS) with other collateral and clinical characteristics, the Kruskal-Wallis or Fisher exact test (2-sided) was used. For the comparison of the PcomA/ICA ratio between subjects with MMD and controls, the Wilcoxon rank sum test was used. Because hemispheres were considered separately, a multivariate regression model based on generalized estimating equations[23] for clustered ordinal responses with uniform local odds ratio structure was fit to evaluate the correlations between collateralization and disease severity among subjects with MMD. Hemispheres with an mSS of zero were included in the analysis because the typical progression of MMD is bilateral involvement.[24] Due to the small number of observations for mSS stages zero and I (6 and 7, respectively), we combined them as stage 1 in the regression model. Asian and African American races were also combined as nonwhite. For multivariate analysis, the CT/MR imaging findings of infarct and hemorrhage were combined. The Fisher exact test was used to correlate the incidence of hemorrhage in patients of Asian descent with non-Asian patients. All MMD statistics were adjusted by age, sex, race (white or nonwhite), LMC, the presence of infarct or hemorrhage, P1 and AchoA classification, and PcomA/ICA ratio.

RESULTS

We examined angiograms from 39 subjects with MMD (78 cerebral hemispheres). The mean age was 43.5 ± 10.6 years (range, 26–64 years). The median age was 44 years. Twenty-eight patients were women. Age- and sex-matched controls ($n = 33$; mean age, 44.3 ± 12.0 years) were included. Subjects with MMD were white ($n = 28$), African American ($n = 7$), and Asian ($n = 4$); control subjects were white ($n = 27$), African American ($n = 5$), and Hispanic ($n = 1$).

Fourteen hemispheres (9 left, 5 right) were excluded from measurement of the PcomA/ICA ratio secondary to lack of ipsilateral PcomA ($n = 2$), lack of DSA lateral projection ($n = 1$), prior aneurysm coiling ($n = 1$), and ipsilateral ICA occlusion ($n = 10$). All hemispheres excluded due to ICA occlusion had mSS grades of IV. Six subjects with MMD (15%) had unilateral involvement. Collateral characteristics by mSS are summarized in Table 2. Interobserver agreement for mSS rating meets acceptable statistical criteria with a Fleiss-Cohen κ statistic of 0.845 (95% CI, 0.785–0.904).

Figure 3 demonstrates PcomA/ICA ratios for subjects compared with controls. The mean PcomA/ICA ratio for subjects was 0.34, compared with 0.22 for controls. After we adjusted for age, sex, race, and LMC, a linear mixed-effects model estimate mean PcomA/ICA ratio difference between subjects and controls was significant at .115 ($P = .0002$, 95% CI, 0.058–0.172). PcomA/ICA ratios for subjects increased with increasing mSS (Fig 4). The multivariate regression model for correlated ordinal responses showed that for every 0.1-U increase in the PcomA/ICA ratio, the OR of having a more severe mSS classification (eg, mSS of II increases to mSS of III) was 1.61 ($P = .004$; 95% CI, 1.17–2.21).

The regression model also demonstrated a significant associa-

tion between mSS and the presence of LMC ($P = .008$) for subjects. The OR of having a more severe mSS classification was 4.79 times higher (95% CI, 1.51–15.21) for MMD hemispheres with LMC, compared with those without LMC. Only 2 of 66 hemispheres in control subjects had LMC (1 with a history of seizures and 1 with previously coiled aneurysms, but neither with vascular stenosis). Figure 5 demonstrates the appearance of LMC in 1 subject with MMD. All hemispheres with P1 steno-occlusive involvement had LMC. However, P1 steno-occlusive change was not significantly associated with mSS ($P = .485$).

AchoA grades are shown in Fig 6. Table 3 shows the distribution of AchoA grades by imaging findings. There was a significant association between the AchoA classification and mSS ($P = .02$). The OR of having a more severe mSS classification was 2.76 times higher (95% CI, 0.57–13.24) for hemispheres with grade I AchoA versus control subjects ($P = .21$), and the OR increased to 17.2 (95% CI, 2.26–131.1) when comparing grade II AchoA with control subjects ($P = .01$). In 9 hemispheres, the AchoA was occluded due to ICA occlusion proximal to the AchoA origin and lack of collateral AchoA filling via posterior collaterals. All such hemispheres were mSS IV; none had hemorrhage and 5 of 9 had infarcts. All hemispheres with hemorrhage (4 of 78) had AchoA grade 2, and none had P1 steno-occlusive findings.

There was no statistically significant association between mSS and imaging findings of infarct or hemorrhage ($P = .11$). Forty-six of 78 MMD hemispheres (59%) had infarcts. Of 15 mSS hemispheres, 5—including the only mSS IV hemisphere without LMC—had no infarcts, 2 had infarcts involving the ipsilateral basal ganglia, and all remaining mSS hemispheres had a watershed pattern of infarcts. No patient with mSS IV had posterior circulation or cortical MCA territory infarcts.

Two of 4 subjects with MMD with hemorrhage were of Asian descent. The Fisher exact test gave a 2-sided $P = .045$ for the correlation between the incidence of hemorrhage in patients of Asian descent with non-Asian patients, though findings were limited by the low number of hemispheres with hemorrhage. Only 1/78 MMD hemispheres had both hemorrhage and infarct on imaging. This hemisphere had no P1 steno-occlusive changes or LMC and had grade 2 AchoA changes.

Median follow-up time for subjects with angiography (19 of 39 subjects with MMD) was 463 days (minimum, 105 days; maximum, 1740 days).

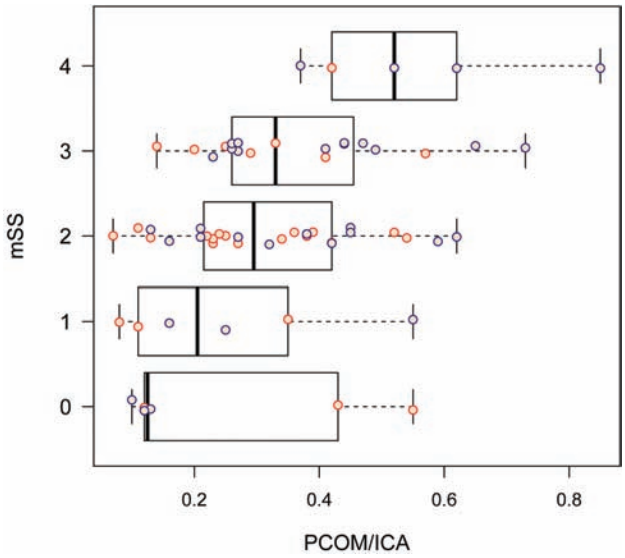

FIG 4. PcomA/ICA ratio in patients with MMD by mSS and hemisphere. The PcomA/ICA ratio increased with increasing mSS ($P = .024$). Orange dots are observations for the left cerebral hemisphere, and blue dots are for the right cerebral hemisphere.

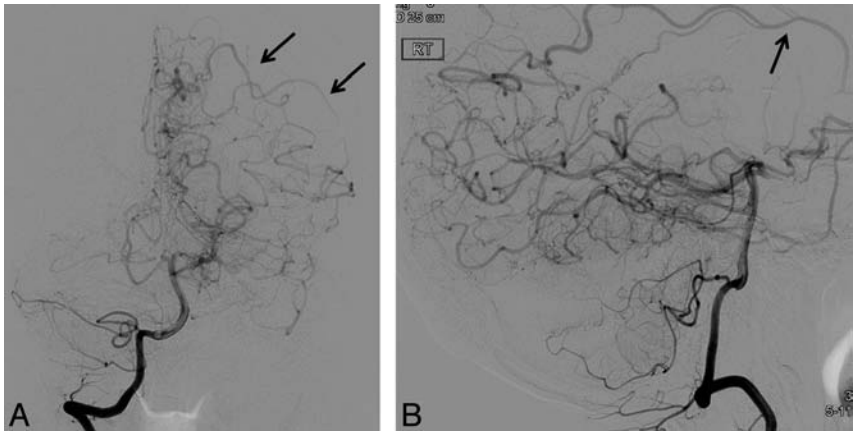

FIG 5. Anteroposterior (*A*) and lateral (*B*) projections from DSA with right vertebral injection in patient with MMD demonstrate leptomeningeal cortical branches (*arrows*) from the PCA to the left parietal and temporal lobes.

DISCUSSION

The primary findings of this work are the following: 1) As with prior studies on adult MMD, we observed a strong correlation between vascular collaterals, including the presence of LMC, dilated AchoAs, and larger PcomA/ICA ratios, and mSS in adult MMD. Despite these collateral networks, most subjects with MMD in our study had infarcts, and the presence of infarct and/or hemorrhage did not correlate with disease severity, as reflected by the mSS, due to the high frequency of infarcts in subjects with MMD with less severe mSSs (eg, 60% of mSSs II subjects). 2). In contrast to Asian studies, AchoA changes were sensitive but not specific for intracranial hemorrhage, and P1 steno-occlusive involvement did not appear to correlate with disease severity. Taken together, these findings suggest that mSS may not provide a comprehensive predictive model for the complex hemodynamic stress, which causes infarcts and hemorrhages in subjects with MMD. Additionally, as more nuanced predictive models arise, such as AchoA changes, our findings suggest the models may not generalize across ethnic cohorts.

The ischemic stress in MMD is imparted by progressive anterior circulation stenosis, which may include vascular constrictive changes, which narrows the terminal ICA and, in patients with mSS III–IV, occludes both the anterior and middle cerebral arteries.[21] When ICA stenosis occurs distal to the AchoA, both the AchoA and PcomA may be subjected to increased collateral flow and

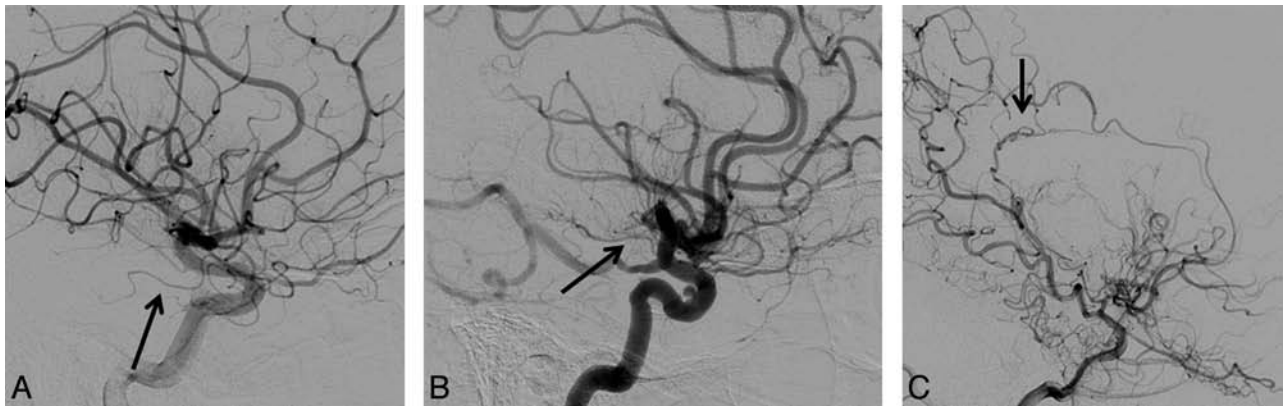

FIG 6. Lateral projections from DSA in 3 patients with Moyamoya disease, with the AchoA identified by the arrow. *A*, The AchoA appears normal without proliferative vessels (stage zero). *B*, The AchoA is thickened with distal branching (stage I). *C*, The AchoA is dilated, and abnormal branches serve as collaterals (stage II).

Table 3: Distribution of anterior choroidal artery grades by imaging findings[a]

		AchoA Grade		
Symptom of Hemisphere	*N*	0 (No.)	1 (No.)	2 (No.)
No symptom	24	29% (7)	33% (8)	38% (9)
Infarct	41	17% (7)	22% (9)	61% (25)
Hemorrhage	4	0% (0)	0% (0)	100% (4)

Note:—*N* indicates the number of nonmissing values.
[a] $P = .18$.

stress.[14] The correlation of the PcomA:ICA ratio in our study with disease severity may reflect a compensation mechanism for the hemodynamic stress imposed by progressive ICA arteriopathy.[25-27] PcomA collateral flow has been shown to be protective against watershed infarcts in patients with atherosclerotic ICA occlusion.[28] Although ICA stenosis in MMD can occlude the PcomA, stenosis typically occurred distal to the PcomA origin in our cohort (87%). The high rate of mSS IV in subjects with MMD in our study with a watershed pattern of infarcts (85% of mSS IV hemispheres with infarcts) suggests inadequate flow despite increased collaterals.

As in other North American studies, our cohort was much more likely to present with ischemia (59%) than hemorrhage (5%).[1,6-8,29,30] In contrast, Asian studies reported higher rates of hemorrhage, ranging from 25% to 62% (Japan, China, and Korea) compared with 10%–29% (Iowa and Hawaii).[3,15,29,31,32] Hemorrhage has been shown to be the most significant factor affecting poor outcome in Asian cohorts, and ruptured thin-walled basal perforators have been cited as the source of high rates of hemorrhage.[3,33] However, studies have not shown a correlation between the reduction in perforators following surgery and rates of hemorrhage.[34,35] More recently, Asian studies have implicated abnormal branching of the AchoA and dilation of the PcomA as a hemorrhagic source, particularly in subjects with intraventricular hemorrhage.[15,31,36,37]

Grade 1 or 2 AchoA changes were found in 89% of hemispheres with hemorrhage compared with only 44% of ischemic hemispheres in Asian MMD.[15] However, grade 1 or 2 AchoA changes were present in most (80%) subjects with MMD in our study and did not differentiate hemorrhage and infarct. Despite this high rate of AchoA changes, only 4 hemispheres presented with hemorrhage, compared with 27% in the Japanese cohort.[15] These findings suggest that AchoA changes in North Americans may not correlate with increased risk of hemorrhage to the extent that has been found in Asian cohorts. The impact of AchoA occlusion on future hemorrhage and ischemia risk is not clear from our study due to the small sample size and relatively short median follow-up. Only 1 MMD hemisphere had both hemorrhage and infarct, which is in line with published studies, suggesting the etiology for infarct and hemorrhage may be distinct.[3,22] The incidence of P1 steno-occlusive changes in our cohort (12%) was lower than that reported in Asian studies (20%–43%).[20,38]

It is unclear whether findings from intracranial atherosclerotic disease studies translate to MMD.[27,39] In the Warfarin Aspirin Symptomatic Intracranial Disease trial, very few cases of severe stenosis with good collaterals resulted in stroke, suggesting a protective role for LMC.[26] However, in moderately stenosed patients (50%–69% stenosis), the presence of LMC was associated with an increased risk of stroke.[26] LMC have been shown to be independent predictors of an increased oxygen extraction fraction in patients with atherosclerotic ICA occlusion.[40]

In our study, LMC correlated significantly with disease severity. The hemodynamic importance of LMC to the anterior circulation in MMD has recently been suggested in a Japanese cohort with P1 disease, in which P1 lesions led to MCA territory infarcts much more frequently than posterior infarcts.[22] P1 stenosis in patients with MMD following revascularization was associated with decreased LMC, which may increase ischemic symptoms.[28,38,41] P1 disease in our cohort did not correlate with disease severity, though it was most frequent in mSS IV hemispheres. Postrevascularization studies showing decreased steal phenomenon following revascularization suggest a dynamic component to MMD.[9,13,42]

Certainly, we could have used other published grading scales. Togao et al[20] described a 4-stage system in their study, building a multivariate model for the angiographic findings in subjects with MMD, ranging from no PCA occlusive change in stage 1 to PCA occlusion with almost no visualization of distal branches in stage 4. Using this system, Togao et al found 32 stage 1 PCA arteries, 1 stage 2 artery, 5 stage 3 arteries, and 2 stage 4 arteries. Our study had an even larger percentage of subjects with MMD (87%) without PCA steno-occlusive disease. Because only 10 hemispheres

had PCA steno-occlusive disease, subcategorization of PCA by stenosis degree was not thought to be statistically robust.

The findings of this work should be considered in the context of 4 limitations. First, as with most MMD studies, this study was limited by sample size ($n = 39$), owing to the relatively small prevalence of MMD in the general population (3 cases per 100,000).[43] This led to a relatively small number of hemispheres with hemorrhage. However, this is one of the larger studies of North American MMD; therefore, we believe the results presented should be used as an exemplar for motivating larger studies. Second, constraints are imposed by the retrospective design, which precluded direct PcomA luminal diameter measurement due to differences in magnification on DSA. The PcomA/ICA ratio was, therefore, used as a surrogate. The distal ICA diameter has been shown to decrease in patients with MMD, either due to vascular constrictive changes or as a flow-related phenomenon due to more distal disease; thus, the precavernous ICA was measured.[21] Third, our controls included subjects with intracranial pathology, including aneurysms and vascular stenosis, a limitation imposed by the standard for use of DSA at our institution, where DSA is reserved for subjects with suspected intracranial pathology, due to its invasive nature. Finally, our study represents a static view of what is known to be a dynamic disease. The 20 subjects with MMD without follow-up data, and the relatively short follow-up for several other subjects with MMD preclude drawing conclusions on whether the variables measured have prognostic implications. Longitudinal studies of these collateral pathways are necessary to understand the interplay between ischemic and hemorrhage risks.[9,13,42]

CONCLUSIONS

MMD in North Americans remains poorly characterized: The etiology is unknown; the natural history, unclear; and optimal treatment, untested. The varied clinical course for MMD may reflect the effectiveness of collaterals in compensating for the hemodynamic stress imposed by progressive ICA arteriopathy without imparting increased risk of hemorrhage. In our analysis, the presence of LMC, dilation of the AchoA, and the PcomA/ICA ratio were independent predictors of mSS severity for North Americans with MMD. However, AchoA changes did not correlate with increased risk of hemorrhage to the extent that has been found in Asian cohorts.

Disclosures: Megan K. Strother—*RELATED*: *Grant*: National Institute of Neurological Disorders and Stroke (5R01NS078828–02).* Morgan D. Anderson—*RELATED*: *Grant*: National Institute of Neurological Disorders and Stroke (5R01NS078828–02).* Yu Shyr—*UNRELATED*: *Consultancy*: GlaxoSmithKline, Aduro BioTech, Immunogen, *Grants/Grants Pending*: National Institutes of Health.* Travis R. Ladner—*UNRELATED*: *Grants/Grants Pending*: American Association of Neurological Surgeons Medical Student Summer Research Fellowship Program, *Comments*: The American Association of Neurological Surgeons through the Neurosurgery Research and Education Foundation is offering the American Association of Neurological Surgeons Medical Student Summer Research Fellowship program. Twenty Fellowships in the amount of $2500 will be awarded to medical students in the United States or Canada who have completed 1 or 2 years of medical school and wish to spend a summer working in a neurosurgical laboratory, mentored by a neurosurgical investigator who is a member of the American Association of Neurological Surgeons and will sponsor the student. Manus J. Donahue—*RELATED*: *Grant*: National Institutes of Health/National Institute of Neurological Disorders and Stroke (5 R01 NS078828 02).* *UNRELATED*: *Consultancy*: McLean Hospital (Boston, Massachusetts), *Comments*: I am a paid consultant on 2 National Institutes of Health–funded grants to McLean Hospital. *Money paid to the institution.

REFERENCES

1. Khan N, Achrol AS, Guzman R, et al. **Sex differences in clinical presentation and treatment outcomes in moyamoya disease.** *Neurosurgery* 2012;71:587–93, discussion 593
2. Bao XY, Duan L, Li DS, et al. **Clinical features, surgical treatment and long-term outcome in adult patients with moyamoya disease in China.** *Cerebrovasc Dis* 2012;34:305–13
3. Han DH, Kwon OK, Byun BJ, et al, for the Korean Society for Cerebrovascular Disease. **A co-operative study: clinical characteristics of 334 Korean patients with moyamoya disease treated at neurosurgical institutes (1976–1994): the Korean Society for Cerebrovascular Disease.** *Acta Neurochir (Wien)* 2000;142:1263–74, discussion 1273–74
4. Duan L, Bao XY, Yang WZ, et al. **Moyamoya disease in China: its clinical features and outcomes.** *Stroke* 2012;43:56–60
5. Zipfel GJ, Sagar J, Miller JP, et al. **Cerebral hemodynamics as a predictor of stroke in adult patients with moyamoya disease: a prospective observational study.** *Neurosurg Focus* 2009;26:E6
6. Chiu D, Shedden P, Bratina P, et al. **Clinical features of moyamoya disease in the U.S.** *Stroke* 1998;29:1347–51
7. Lee DJ, Liebeskind DS. **Characterization of inpatient moyamoya in the U.S.: 1988–2004.** *Front Neurol* 2011;2:43
8. Kainth D, Chaudhry SA, Kainth H, et al. **Epidemiological and clinical features of moyamoya disease in the USA.** *Neuroepidemiology* 2013;40:282–87
9. Hallemeier CL, Rich KM, Grubb RL, et al. **Clinical features and outcome in North American adults with moyamoya phenomenon.** *Stroke* 2006;37:1490–96
10. Krischek B, Kasuya H, Khan N, et al. **Genetic and clinical characteristics of moyamoya disease in Europeans.** *Acta Neurochir Suppl* 2011;112:31–34
11. Suzuki J, Kodama N. **Moyamoya disease: a review.** *Stroke* 1983; 14:104–09
12. Kuroda S, Hashimoto N, Yoshimoto T, et al. **Radiological findings, clinical course, and outcome in asymptomatic moyamoya disease: results of multicenter survey in Japan.** *Stroke* 2007;38:1430–35
13. Nariai T, Matsushima Y, Imae S, et al. **Severe haemodynamic stress in selected subtypes of patients with moyamoya disease: a positron emission tomography study.** *J Neurol Neurosurg Psychiatry* 2005; 76:663–69
14. Scott RM, Smith ER. **Moyamoya disease and moyamoya syndrome.** *N Engl J Med* 2009;360:1226–37
15. Morioka M, Hamada JI, Kawano T, et al. **Angiographic dilatation and branch extension of the anterior choroidal and posterior communicating arteries are predictors of hemorrhage in adult moyamoya patients.** *Stroke* 2003;34:90–95
16. Suzuki J, Takaku A. **Cerebrovascular "moyamoya" disease. Disease showing abnormal net-like vessels in base of brain.** *Arch Neurol* 1969;20:288–99
17. Mugikura S, Takahashi S, Higano S, et al. **Predominant involvement of ipsilateral anterior and posterior circulations in moyamoya disease.** *Stroke* 2002;33:1497–500
18. Donahue MJ, Ayad M, Moore R, et al. **Relationships between hypercarbic reactivity, cerebral blood flow, and arterial circulation times in patients with moyamoya disease.** *J Magn Reson Imaging* 2013; 38:1129–39
19. Bokkers RP, van Laar PJ, van de Ven KC, et al. **Arterial spin-labeling MR imaging measurements of timing parameters in patients with a carotid artery occlusion.** *AJNR Am J Neuroradiol* 2008;29:1698–703
20. Togao O, Mihara F, Yoshiura T, et al. **Cerebral hemodynamics in moyamoya disease: correlation between perfusion-weighted MRI and cerebral angiography.** *AJNR Am J Neuroradiol* 2006;27:391–97
21. Kaku Y, Morioka M, Ohmori Y, et al. **Outer-diameter narrowing of the ICA and MCA in moyamoya disease detected on 3D constructive interference in steady-state MR image: is arterial constrictive remodeling a major pathogenesis?** *Acta Neurochir (Wien)* 2012; 154:2151–57
22. Hishikawa T, Tokunaga K, Sugiu K, et al. **Clinical and radiographic**

features of moyamoya disease in patients with both cerebral ischemia and hemorrhage. *Br J Neurosurg* 2013;27:198–201
23. Touloumis A. multgee: GEE solver for Correlated Nomiinal or Ordianal Multinomial Responses, Version 1.3. http://cran.r-project.org/package=multgee
24. Czabanka M, Pena-Tapia P, Schubert GA, et al. **Proposal for a new grading of moyamoya disease in adult patients.** *Cerebrovasc Dis* 2011;32(1):41–50
25. Liebeskind DS, Cotsonis GA, Saver JL, et al. **Collaterals dramatically alter stroke risk in intracranial atherosclerosis.** *Ann Neurol* 2011;69:963–74
26. Liebeskind DS, Cotsonis GA, Saver JL, et al. **Collateral circulation in symptomatic intracranial atherosclerosis.** *J Cereb Blood Flow Metab* 2011;31:1293–301
27. Huang AP, Liu HM, Lai DM, et al. **Clinical significance of posterior circulation changes after revascularization in patients with moyamoya disease.** *Cerebrovasc Dis* 2009;28:247–57
28. Hendrikse J, Hartkamp MJ, Hillen B, et al. **Collateral ability of the circle of Willis in patients with unilateral ICA occlusion.** *Stroke* 2001;32:2768–73
29. Kleinloog R, Regli L, Rinkel GJ, et al. **Regional differences in incidence and patient characteristics of moyamoya disease: a systematic review.** *J Neurol Neurosurg Psychiatry* 2012;83:531–36
30. Mesiwala AH, Sviri G, Fatemi N, et al. **Long-term outcome of superficial temporal artery-MCA bypass for patients with moyamoya disease in the US.** *Neurosurg Focus* 2008;24:E15
31. Liu W, Zhu S, Wang X, et al. **Evaluation of angiographic changes of the anterior choroidal and posterior communicating arteries for predicting cerebrovascular lesions in adult moyamoya disease.** *J Clin Neurosci* 2011;18:374–78
32. Wetjen NM, Garell PC, Stence NV, et al. **Moyamoya disease in the Midwestern United States.** *Neurosurg Focus* 1998;5:e1
33. Fukui M, Kono S, Sueishi K, et al. **Moyamoya disease**. *Neuropathology* 2000;20(suppl):S61–S64
34. Fukui M. **Guidelines for the diagnosis and treatment of spontaneous occlusion of the circle of Willis ('moyamoya' disease).** Research Committee on Spontaneous Occlusion of the Circle of Willis (Moyamoya Disease) of the Ministry of Health and Welfare, Japan. *Clin Neurol Neurosurg* 1997;99(suppl 2):S238–S240
35. Okada Y, Shima T, Nishida M, et al. **Effectiveness of superficial temporal artery-MCA in adult moyamoya disease: cerebral hemodynamics and clinical course in ischemic and hemorrhagic varieties.** *Stroke* 1998;29:625–30
36. Nah HW, Kwon SU, Kang DW, et al. **Moyamoya disease-related versus primary intracerebral hemorrhage.** *Stroke* 2012;7:1947–50
37. Dolati P, Sutherland G, Wong J, et al. **Distal anterior choroidal artery aneurysm following iatrogenic posterior cerebral artery occlusion: a case report and review of literature.** *Acta Neurochir (Wien)* 2012;154:53–57
38. Yamada I, Himeno Y, Suzuki S, et al. **Posterior circulation in moyamoya disease: angiographic study.** *Radiology* 1995;197:239–46
39. Bang OY, Saver JL, Kim SJ, et al. **Collateral flow averts hemorrhagic transformation after endovascular therapy for acute ischemic stroke.** *Stroke* 2011;42:2235–39
40. Yamauchi H, Kudoh T, Sugimoto K, et al. **Patterns of collaterals, type of infarcts, and hemodynamic impairment in carotid artery occlusion.** *J Neurol Neurosurg Psychiatry* 2004;75:1697–701
41. Vajkoczy P. **Moyamoya disease: collateralization is everything.** *Cerebrovasc Dis* 2009;28:258
42. Lim SM, Chae EJ, Kim MY, et al. **Steal phenomenon through the anterior communicating artery in moyamoya disease.** *Eur Radiol* 2007;17:61–66
43. Wakai K, Tamakoshi A, Ikezaki K, et al. **Epidemiological features of moyamoya disease in Japan: findings from a nationwide survey.** *Clin Neuro Neurosurg* 1997;99(suppl 2):S1–S5

Low-Power Inversion Recovery MRI Preserves Brain Tissue Contrast for Patients with Parkinson Disease with Deep Brain Stimulators

S.N. Sarkar, E. Papavassiliou, R. Rojas, D.L. Teich, D.B. Hackney, R.A. Bhadelia, J. Stormann, and R.L. Alterman

ABSTRACT

BACKGROUND AND PURPOSE: Fast spin-echo short τ inversion recovery sequences have been very useful for MR imaging–guided deep brain stimulation procedures in Parkinson disease. However, high-quality fast spin-echo imaging deposits significant heat, exceeding FDA-approved limits when patients already have undergone deep brain stimulation and need a second one or a routine brain MR imaging for neurologic indications. We have developed a STIR sequence with an ultra-low specific absorption rate that meets hardware limitations and produces adequate tissue contrast in cortical and subcortical brain tissues for deep brain stimulation recipients.

MATERIALS AND METHODS: Thirteen patients with medically refractory Parkinson disease who qualified for deep brain stimulation were imaged at 1.5T with a fast spin-echo short τ inversion recovery sequence modified to meet conditional MR imaging hardware and specific absorption rate restrictions. Tissue contrast-to-noise ratios and implant localization were objectively and subjectively compared by 2 neuroradiologists, and image quality for surgical planning was assessed by a neurosurgeon for high and low specific absorption rate images.

RESULTS: The mean contrast-to-noise ratio for cerebral tissues without including the contrast-to-noise ratio for ventricular fluid was 35 and 31 for high and low specific absorption rate images. Subjective ratings for low specific absorption rate tissue contrast in 77% of patients were identical to (and in a few cases higher than) those of high specific absorption rate contrast, while the neurosurgical coordinates for fusing the stereotactic atlas with low specific absorption rate MR imaging were equivalent to those of the high specific absorption rate for 69% of patients.

CONCLUSIONS: Patients with Parkinson disease who have already had a deep brain stimulation face a risk of neural injury if routine, high specific absorption rate MR imaging is performed. Our modified fast spin-echo short τ inversion recovery sequence conforms to very conservative radiofrequency safety limits, while it maintains high tissue contrast for presurgical planning, postsurgical assessment, and radiologic evaluations with greater confidence for radiofrequency safety.

ABBREVIATIONS: CNR = contrast-to-noise ratio; DBS = deep brain stimulator or stimulation; FSTIR = fast spin-echo short τ inversion recovery; SAR = specific absorption rate; PD = Parkinson disease; RF = radiofrequency; STN = subthalamic nucleus

The diagnostic quality and radiofrequency (RF) safety of MR imaging for visualizing the subthalamic nucleus (STN) and globus pallidus are not simultaneously achievable, though both are crucial for surgical accuracy and treatment efficacy of deep brain stimulation (DBS) procedures[1-3] in patients with drug-refractory Parkinson disease (PD). Kitajima et al[3] observed significantly better, though not perfect, mapping of the STN by using inversion recovery (fast spin-echo short τ inversion recovery [FSTIR]) sequences. Ben-Haim et al[4] reported improved STN targeting by combining FSTIR and contrast-enhanced spoiled gradient-recalled-echo acquisitions. Although not currently approved for DBS recipients, higher fields show clear delineation of the STN at 7T.[5-7]

The deposited RF power (specific absorption rate [SAR]) increases with field strength; and the effective sequences, including FSTIR or T2, pose significant RF heating risk,[8] which has been a potential deterrent for MR imaging of DBS recipients.[9] Although experiences of incident-free routine high-SAR brain MR imaging in large groups of DBS patients have been reported[2,10] and sentinel events, including serious brain injury or death, are very few,[11] some researchers observed[12] a greater incidence of neurologic deficits and tissue edema surrounding electrodes in DBS recipients after routine MR imaging that perhaps were not caused by the surgical procedure itself. Note that local SAR near the contact points at the DBS electrode base is unknown, and because DBS belongs to a class of critical-length implants, the SAR can be an

Received September 30, 2013; accepted after revision November 13.

From the Department of Radiology (S.N.S., R.R., D.L.T., D.B.H., R.A.B., J.S.) and Division of Neurosurgery (E.P., R.L.A.), Beth Israel Deaconess Medical Center, Harvard Medical School, Boston, Massachusetts.

Please address correspondence to Subhendra N. Sarkar, PhD, Department of Radiology, Beth Israel Deaconess Medical Center, Harvard Medical School, 330 Brookline Ave, Ansin E/245, Boston, MA 02215; e-mail: ssarkar@bidmc.harvard.edu

http://dx.doi.org/10.3174/ajnr.A3896

Table 1: High- and low-SAR FSTIR sequence parameters for presurgical planning or postsurgical MR imaging assessment of DBS recipients with Parkinson disease[a]

Pulse Sequence	TR/TE/TI/Matrix/Scan Time (min)	Section Thickness/ FOV/No. of Avg/ No. of Sections	Echo-Train/ BW (kHz)	Refocusing Pulse Width (Default Value)/ Refocusing Pulse Flip Angles in FSTIR	Whole-Head SAR (W/kg) (Estimated)
High-SAR 2D Ax FSTIR (PD+T1w)[b]	4s/12 ms/140 ms/256 × 192/5:30	3 mm/24 cm/2/30	8/ ± 15.8	1.6 ms (1.6 ms)/180°	1.5
Low-SAR 2D Ax FSTIR (PD+T1w)[b]	10–13 s/11–13 ms/130 ms/256 × 192/7:10–8:30	3 mm/24 cm/1/24–32 (Interleave)	10/ ± 15.8	2.6 ms (1.6)/first = 110°, second = 100°, rest of the refocusing angles = 110°	≤0.1

Note:—BW indicates bandwidth; T1w, T1-weighted; Avg, average; Ax, axial.

[a] Magnet strength, 1.5T; RF coil: transmit-receive 1-channel head coil.

[b] Short Tau FSTIR produces T1-weighted for short T1 tissues (fat, white matter darker, close to null) and proton density (PD) weighting for long T1 tissues (CSF, gray matter brighter, far away from null).

order of magnitude higher.[13] Concerns about local heating and the variability of SAR among MR imaging machines[14,15] have led to strict MR imaging conditional labeling.[16,17] This has limited the choice of MR sequences and hardware with consequent loss of image quality. Using low-refocusing flip angle[18,19] high-quality brain imaging on healthy controls at a low SAR has been possible,[20] though this approach cannot be directly applied to DBS recipients due to hardware restrictions.[16,17] High-quality FSE imaging seems to require use of high RF power and thus is restricted to planning the first DBS only. A repeat of the high SAR sequence for high-quality FSE is not recommended for implanting a second DBS or for revising prior ones due to excessive local SAR. We propose to minimize such risks, though without completely eliminating them, by an ultra-low SAR high-resolution sequence and to test its utility for diagnostic and presurgical use.

The primary cause of heating at the implant tips with FSE sequences is due to the fast application of multiple high flip angle refocusing RF pulses. We used a high-SAR FSTIR sequence (1.5 W/kg) on DBS surgical candidates (with no electrodes) for presurgical planning for the first DBS and compared the tissue contrast by performing an ultra-low SAR MR imaging (≤0.1 W/kg or 15 times lower) on the same patients for planning additional DBS or for revising the prior ones. The resulting images were assessed both subjectively and objectively for cerebral tissue contrast.

MATERIALS AND METHODS

We followed institutional ethics and research review committee guidelines for modifications of the FSTIR sequence, with RF coil and RF power restrictions following conditional DBS MR imaging guidelines. The routine high-SAR and the low-SAR versions of the FSTIR sequence were applied to DBS candidates in 2 different sessions, and tissue contrasts were compared by 3 readers.

Patient Selection and MR Imaging Scan Design

A group of 13 patients with medically refractory Parkinson disease (DBS candidates; mean disease duration, 11 years; age, 55–78 years; 5 men) were imaged (parameters in Table 1) for 2 or 3 sessions (depending on the number and type of DBS interventions) on the same day or within 7 months:

Session I: 2D high-SAR FSTIR, DBS candidates before the first DBS
Session II: 2D low-SAR FSTIR on the same patients for assessing the first DBS or for presurgical coordinate planning for a second DBS

The lead localization and assessment for complications (first or second) were performed as follows: The patients were taken immediately after implantation from the operating room to the MR imaging unit, with or without the Leksell Frame (Elekta Instruments, Stockholm, Sweden) in place, to assess lead positions and to rule out intracerebral hemorrhage. The external components of the implanted lead wires were looped around the burr-hole cover in the subgaleal space, creating a closed-circuit configuration. If the patient already had a pulse generator in place, vendor guidelines for safe MR imaging were followed. The head position often was slightly angled when the patient was imaged without the stereotactic frame, so the axial images were angled along the anterior/posterior commissure line to match the preoperative images.

Objective Contrast-to-Noise Ratio Assessment

Null Hypothesis. If one allows for the extra scanning time needed and also accepts a somewhat lower SNR that results from a low SAR, mean tissue contrast-to-noise ratios (CNRs) in low- (≤0.1 W/kg) and high-SAR (1.5 W/kg) methods are not significantly different in patients with PD.

Region-of-Interest Placement and SNR, CNR, and Statistical Significance Computation

Eight different brain regions were bilaterally assessed for SNR computation. These were the following: temporal lobe gray matter, caudate head, body of the hippocampus, putamen, globus pallidus, thalamus, subthalamic nucleus, and ventricular fluid. Corresponding white matter ROIs were drawn in an insular region, anterior and posterior limbs of the internal capsule, substantia nigra, and corpus callosum to provide adjacent tissue signal intensities. The noise ROIs were drawn along the frequency-encoding direction to compute the CNR for the tissue pairs as

$$\mathrm{CNR} = [\mathrm{SI}(\mathrm{tissue1}) - \mathrm{SI}(\mathrm{tissue2})]/\mathrm{SD}(\mathrm{air}).$$

A nonparametric statistical test (Wilcoxon signed rank test for dependent samples) was applied to evaluate the significance of the mean CNR differences between the high- and low-SAR images (Fig 1).

Subjective Assessments

High- and low-SAR FSTIR images were compared by 3 neuroradiologists for radiologic evaluation (D.L.T. and R.R., with >15

years of experience) and a neurosurgeon (R.L.A., with >25 years of experience) for surgical planning.

The scores were divided into 3 categories as follows (category fractions are reported in Tables 2 and 3):

Low-SAR images that produced higher tissue conspicuity than images from high SAR (L > H)

Low-SAR images that produced lower tissue conspicuity than images from high SAR (L < H)

Low-SAR images that produced tissue contrast almost equal to that of high-SAR images (L = H).

RESULTS

Objective Assessments

Tissue CNR for all 8 tissue pairs are plotted in Fig 1, indicating comparable but somewhat lower CNR for low-SAR images except for ventricular fluid. The mean CNRs of 7 tissue pairs, excluding ventricular fluid, were 26.6 ± 10.6 and 20.0 ± 8.7, while these were 35.4 ± 27.1 and 31 ± 31, after including ventricular fluid, for high and low SAR. The nonparametric Wilcoxon signed rank test revealed no significant difference in mean CNR for whole brain (W = 5, W_{crit} = 3 for n = 8 tissue pairs at $P \leq .05$). However, the contrast for ventricular fluid is not useful for radiologic diagnosis or surgical planning, and with ventricular fluid excluded, the mean CNRs from high- and low-SAR results were somewhat different (W = 0, W_{crit} = 2 for n = 7 tissue pairs at $P \leq .05$).

Subjective Assessments

All 3 readers concluded that FSTIR images do not differ substantially in terms of SNR or tissue contrasts between low and high SAR and that low-SAR images have adequate contrast to identify structures critical for DBS recipients (Fig 2). MR imaging–based estimations of nuclear coordinates for stereotactic planning of STN or globus pallidus targets were successful in 9/13 patients, while one or both nuclear margins less conspicuous in the remaining 4/13 patients at low SAR. The suboptimal visualization of the target (STN or globus pallidus) can force the surgeon to be more reliant on indirect targeting methods (ie, based on the anterior/posterior commissure line) and microelectrode recording to finalize the targets (Fig 3).

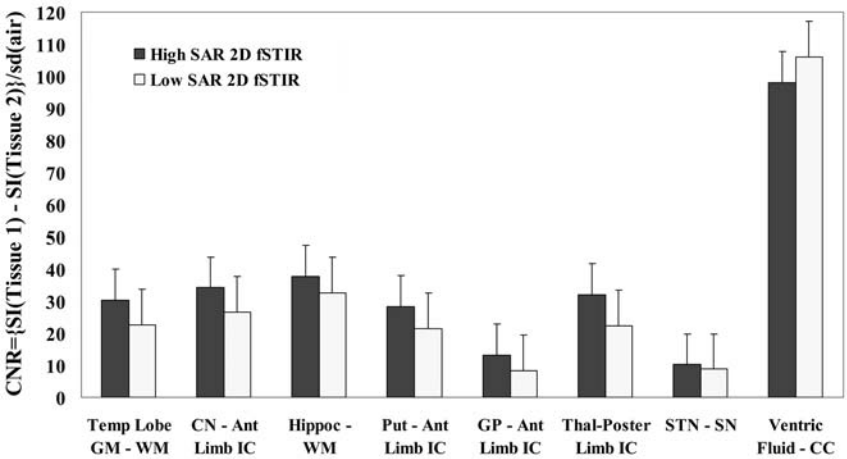

FIG 1. CNR of various tissue pairs from high- and low-SAR FSTIR sequences in 13 DBS recipients. Ant Limb or Poster Limb IC indicates anterior or posterior internal capsule; CC, corpus callosum; Put, putamen; Hippoc, body of the hippocampus; CN, caudate head; Thal, thalamus; Ventric Fluid, ventricular fluid; Temp Lobe, temporal lobe; SN, substantia nigra.

Table 2: Subjective assessment of high- and low-SAR FSTIR images of DBS candidates by various readers and percentage of patients rated for low-SAR images being higher (L > H), lower (L < H), or of equal utility (L = H) for radiologic assessments

Readers	STN and RN (Low vs High SAR)	GP (Low vs High SAR)	Temporal Cortical GM, CN, and Put (Low vs High SAR)	Ventricular Fluid Intensity and CSF/Tissue Margins
Neuroradiologist 1	L > H (31%)	L > H (23%)	L > H (23%)	L > H (85%)
	L < H (15%)	L < H (15%)	L < H (23%)	
	L = H (54%)	L = H (62%)	L = H (54%)	L = H (15%)
Neuroradiologist 2	L > H (23%)	L > H (15%)	L > H (31%)	L > H (85%)
	L < H (23%)		L < H (15%)	
	L = H (54%)	L = H (85%)	L = H (54%)	L = H (15%)

Note:—L indicates low; H, high; RN, red nucleus; CN, caudate head; Put, putamen; GP, globus pallidus.

DISCUSSION

Some of the features and SAR-lowering concepts used in this work are summarized below.

High fields, in general, are associated with high SAR. The scan averages (NEX) were reduced to perform low-SAR scans within clinically feasible scanning times, which likely have contributed to a somewhat lower, though acceptable, SNR. Alternatively one could reduce the number of sections for low SAR and maintain the original number of signal averaging or use compressed sensing and a parallel imaging algorithm to further lower the SAR. The factors that lead to increased SAR and therefore should be avoided are the following: short TR, long echo trains, short RF pulses, saturation bands, driven equilibrium pulses, 100% or similarly attenuated sampling of *k*-space, and high bandwidths. Note that SAR increases quadratically with a refocusing flip angle.[21] In the low-SAR version of the FSTIR sequence, we have applied the routine 180° inversion and 90° excitation pulses but used <180° for the train

Table 3: Subjective assessment of high- and low-SAR FSTIR images of DBS candidates by various readers and percentage of patients rated for low-SAR images being higher (L > H), lower (L < H), or of equal utility (L = H) for surgical planning

	STN/SN Contrast for New DBS Plan or for Prior DBS Assessment	Putamen and GP Contrast for New DBS Plan or Prior DBS Assessment	Temporal and Parietal Lobe Assessment of Postsurgical Complications	Ventricular Size, Shape, and Edge Detection for Planning DBS Lead Trajectories
Neurosurgeon 1	L = H (77%)	L = H (69%)	L = H (100%)	L = H (100%)
	L < H (23%)	L < H (31%)		

Note:—L indicates low; H, high; CN, caudate head; GP, globus pallidus; SN, substantia nigra.

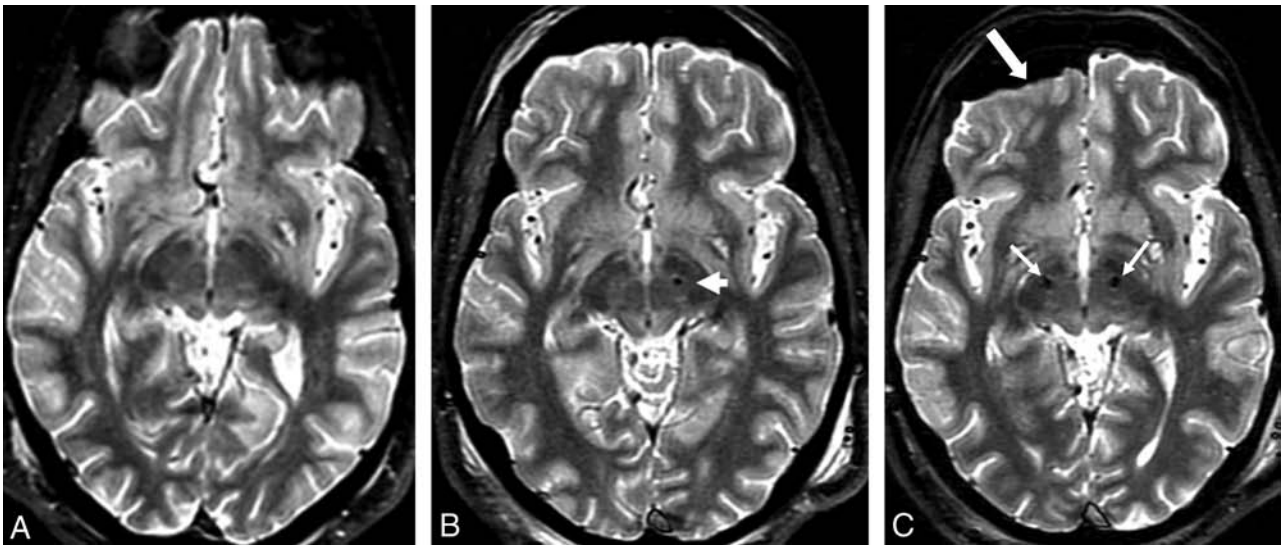

FIG 2. FSTIR 2D image sections for a typical patient scanned in 3 sessions. *A*, Presurgical high-SAR FSTIR image (1.5 W/kg) with interleaved 3-mm sections to plan for the first DBS implantation. *B*, Subsequent presurgical low-SAR FSTIR image (0.1 W/kg) to plan for the second DBS implantation. The arrow shows the first DBS tip at the desired location of the left STN. *C*, Low-SAR (0.1 W/kg) FSTIR image from the third session after a second lead implantation, to localize bilateral electrodes (*arrows*), visualize subcortical structures, and assess potential complications. Note the pneumocephalus (*thick arrow*), not uncommon during DBS implantation.

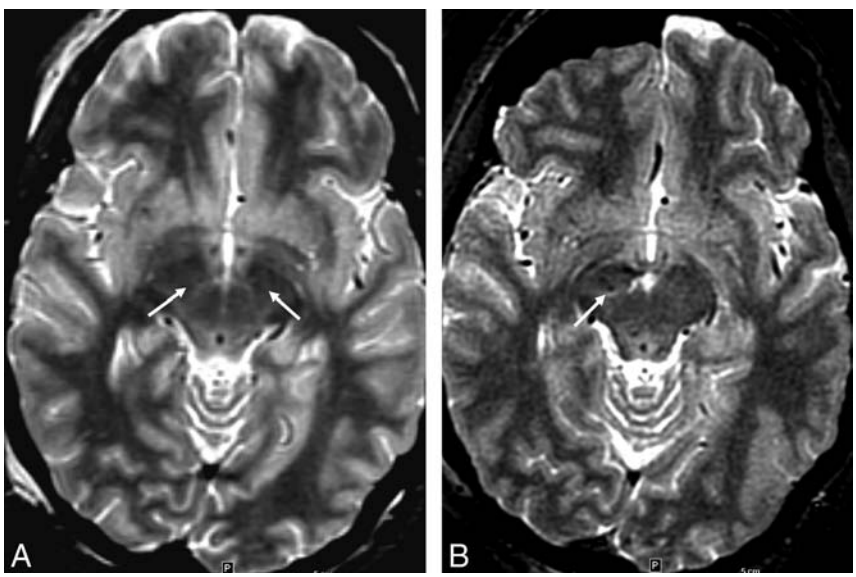

FIG 3. Example of lower STN conspicuity occasionally seen on low-SAR imaging, *A*, Presurgical image from high-SAR (1.5 W/kg) FSTIR MR imaging with adequate tissue contrast allowing MR imaging–based STN coordinate measurements (*arrows*). *B*, Subsequent postsurgical low-SAR FSTIR image (0.1 W/kg). Notice slightly lower STN contrast causing the coordinate estimation or assessment of the right lead position to be somewhat difficult (*arrow*) and requiring use of other landmarks and microelectrode recording.

of refocusing pulses (Table 1). This reduction in flip angle for each of the long echo trains produces a substantial reduction in energy deposition. Stretching the refocusing pulse widths (Table 1) additionally allows lower peak power and more time for heat dissipation for low echo trains. To the best of our knowledge, implementing these changes requires a research agreement. Of course, manufacturers could introduce such low-SAR sequences as product offerings.

There was a small amount of signal loss at the DBS leads in low SAR images, similar to that at high-SAR imaging reported in the literature,[2,10] and far less compared with gradient-echo sequences. Gradient echo-based susceptibility-weighted imaging with phase-correction software is a low-SAR sequence and offers high conspicuity for nuclei[22] and works well for preoperative MR imaging for the first DBS. However, during subsequent implantations or revisions, the metallic leads would generate significant artifacts, compromising image quality and coordinate measurements for surgical planning. Although useful, these SWIs do not reproduce the contrast characteristics of routine MR imaging, such as FSTIR.

As the use of DBS expands, there will be a greater need to use low-power MR imaging for surgical planning, evaluating implantation accuracy, and diagnosing neurologic disorders in patients with pre-existing DBS electrodes. Until fully MR imaging–compatible DBS systems are introduced and for some time after, low-SAR imaging techniques that can provide high-quality images while ensuring patient safety will be invaluable. High fields beyond 1.5T offer higher SNR, but these are not yet approved for DBS patients and create challenges for MR imaging safety and RF homogeneity.

This work was performed at 1.5T in full compliance with the very conservative regulatory guidelines.[16,17] The high-resolution ($0.9 \times 1.2 \times 3$ mm^3) low-SAR images are of diagnostic quality obtainable within clinically feasible scanning times. A moderate reduction in tissue SNR and consequently in tissue CNR at a low SAR is due to both hardware and sequence-specific limitations but provides adequate CNR for surgical planning and radiologic

assessments. Note that the longer scanning times needed at low SARs (7–8.5 minutes versus 5.5 minutes) may increase discomfort for some patients, though in practice, we have not observed any more motion artifacts by using the low-SAR method than with high SAR, which also can lead to the patients' subjective sensation of warmth and propensity for motion. The approximate equivalence between the 2 methods suggests that the low-SAR approach can be effectively used for radiologic assessments and stereotactic targeting in the DBS patient population that is currently either being denied MR imaging or is subjected to unknown, perhaps significant tissue heating from routine, high-SAR imaging.

CONCLUSIONS

This work reports the development and radiologic quality considerations of a modified FSTIR MR imaging sequence within very conservative hardware and RF exposure constraints in the presence of implanted DBS electrodes for patients with medically refractory Parkinson disease. The low-SAR sequence seems to offer tissue contrasts for stereotactic nuclear targeting and gray/white matter structures very similar to those obtainable by using the routine high-SAR sequence and hence can be applied with greater confidence toward RF safety when additional DBSs or evaluation of existing ones is needed or potential complications are suspected. Further improvements in imaging speed and CNR may be obtained with multichannel RF coils capable of parallel imaging.

ACKNOWLEDGMENTS

The authors acknowledge the assistance of Ines Cabral-Goncalves and Raymond Airhart for administrative planning and revision of departmental policies ensuring safety for DBS patients.

Disclosures: Ron L. Alterman—*UNRELATED: Consultancy*: Medtronic, *Comments*: I receive occasional consulting fees from Medtronic regarding their DBS technology. None of that work is related to the current work. Annual compensation is less than $10,000.

REFERENCES

1. Slavin KV, Thulborn KR, Wess C, et al. **Direct visualization of the human subthalamic nucleus with 3T MR imaging.** *AJNR Am J Neuroradiol* 2006;27:80–84
2. Larson P, Richardson R, Starr P, et al. **Magnetic resonance imaging of implanted deep brain stimulators: experience in a large series.** *Stereotact Funct Neurosurg* 2008;86:92–100
3. Kitajima M, Korogi Y, Kakeda S, et al. **Human subthalamic nucleus: evaluation with high-resolution MR imaging at 3.0 T.** *Neuroradiology* 2008;50:675–81
4. Ben-Haim S, Gologorsky Y, Monahan A, et al. **Fiducial registration with spoiled gradient-echo magnetic resonance imaging enhances the accuracy of subthalamic nucleus targeting.** *Neurosurgery* 2011;69:870–75
5. Abosch A, Yacoub E, Ugurbil K, et al. **An assessment of current brain targets for deep brain stimulation surgery with susceptibility-weighted imaging at 7 Tesla.** *Neurosurgery* 2010;67:1745–56
6. Cho Z-H, Min H-K, Oh S-H, et al. **Direct visualization of deep brain stimulation targets in Parkinson disease with the use of 7-Tesla magnetic resonance imaging.** *J Neurosurg* 2010;113:639–47
7. Eapen M, Zald DH, Gatenby JC, et al. **Using high-resolution MR imaging at 7T to evaluate the anatomy of the midbrain dopaminergic system.** *AJNR Am J Neuroradiol* 2011;32:688–94
8. Finelli DA, Rezai AR, Ruggieri P, et al. **MR-related heating of deep brain stimulation electrodes: an in vitro study of clinical imaging sequences.** *AJNR Am J Neuroradiol* 2002;23:1795–802
9. Tagliati M, Jankovi J, Pagan F, et al. **Safety of MRI in patients with implanted deep brain stimulation devices.** *Neuroimage* 2009; 47(suppl 2):T53–57
10. Zrinzo L, Yoshida F, Hariz M, et al. **Clinical safety of brain magnetic resonance imaging with implanted deep brain stimulation hardware: large case series and review of the literature.** *World Neurosurg* 2011;76:164–72
11. Henderson JM, Tkach J, Phillips M, et al. **Permanent neurological deficit related to magnetic resonance imaging in a patient with implanted deep brain stimulation electrodes for Parkinson's disease: case report**. *Neurosurgery* 2005:57:E1063, discussion E1063
12. Zekaj E, Saleh C, Menghetti C, et al. **Does magnetic resonance imaging induce tissue damage due to DBS lead heating?** *Acta Neurochir* 2013;155:1677–78
13. Kainz W. **MR heating tests of MR critical implants: editorial.** *J Magn Reson Imaging* 2007;26:450–51
14. Bottomley P. **Turning up the heat on MRI.** *J Am Coll Radiol* 2008;5:853–55
15. Baker K, Tkach J, Phillips M, et al. **Variability in RF-induced heating of a deep brain stimulation implant across MR systems.** *J Magn Reson Imaging* 2006;24:1236–42
16. Medtronic. *MRI Guidelines for Medtronic Deep Brain Stimulation Systems.* Minneapolis: Medtronic Inc; 2007
17. Guidance for Industry and FDA Staff. Center for Devices and Radiological Health. *Establishing Safety and Compatibility of Passive Implants in the Magnetic Resonance (MR) Environment*. Silver Spring, Maryland; FDA; August 21, 2008; http://www.fda.gov/cdrh/osel/guidance/1685.html
18. Busse R, Brau A, Vu A, et al. **Effects of refocusing flip angle modulation and view ordering in 3D fast spin echo.** *Magn Reson Med* 2008;60:640–49
19. Alsop DA. **The sensitivity of low flip angle rare imaging.** *Magn Reson Med* 1997;37:176–84
20. Sarkar SN, Alsop DA, Madhuranthakam AJ, et al. **Brain MRI at ultra-low SAR: a potential protocol for imaging of patients with contra-indicating implants.** *Radiology* 2011;259:550–57
21. Bernstein MA, King KF, Zhou XJ. *Handbook of MRI Pulse Sequences*. Amsterdam: Elsevier Academic Press; 2004;33
22. O'Gorman RL, Shmueli K, Ashkan K, et al. **Optimal MRI methods for direct stereotactic targeting of the subthalamic nucleus and globus pallidus.** *Eur Radiol* 2011;21:130–36

Effects of Gadolinium Contrast Agent Administration on Automatic Brain Tissue Classification of Patients with Multiple Sclerosis

J.B.M. Warntjes, A. Tisell, A.-M. Landtblom, and P. Lundberg

ABSTRACT

BACKGROUND AND PURPOSE: The administration of gadolinium contrast agent is a common part of MR imaging examinations in patients with MS. The presence of gadolinium may affect the outcome of automated tissue classification. The purpose of this study was to investigate the effects of the presence of gadolinium on the automatic segmentation in patients with MS by using the synthetic tissue-mapping method.

MATERIALS AND METHODS: A cohort of 20 patients with clinically definite multiple sclerosis were recruited, and the T1 and T2 relaxation times and proton density were simultaneously quantified before and after the administration of gadolinium. Synthetic tissue-mapping was used to measure white matter, gray matter, CSF, brain parenchymal, and intracranial volumes. For comparison, 20 matched controls were measured twice, without gadolinium.

RESULTS: No differences were observed for the control group between the 2 measurements. For the MS group, significant changes were observed pre- and post-gadolinium in intracranial volume (−13 mL, $P < .005$) and cerebrospinal fluid volume (−16 mL, $P < .005$) and the remaining, unclassified non-WM/GM/CSF tissue volume within the intracranial volume (+8 mL, $P < .05$). The changes in the patient group were much smaller than the differences, compared with the controls, which were −129 mL for WM volume, −22 mL for GM volume, +91 mL for CSF volume, 24 mL for the remaining, unclassified non-WM/GM/CSF tissue volume within the intracranial volume, and −126 mL for brain parenchymal volume. No significant differences were observed for linear regression values against age and Expanded Disability Status Scale.

CONCLUSIONS: The administration of gadolinium contrast agent had a significant effect on automatic brain-tissue classification in patients with MS by using synthetic tissue-mapping. The observed differences, however, were much smaller than the group differences between MS and controls.

ABBREVIATIONS: BPV = brain parenchymal volume; CSFV = cerebrospinal fluid volume; EDSS = Expanded Disability Status Scale; Gd = gadolinium; GMV = gray matter volume; ICV = intracranial volume; NV = the remaining, unclassified non-WM/GM/CSF tissue volume within the ICV, defined as ICV − (WMV + GMV + CSFV); PD = proton density; WMV = white matter volume

Multiple sclerosis is a chronic inflammatory disorder of the central nervous system. Typically, focal white matter lesions are regarded as a hallmark pathologic finding. These lesions, however, show a limited correlation with clinical findings.[1-3]

Instead, brain-tissue loss shows a stronger correlation with disease progression, especially in a later stage of the disease.[3-9] The key for the practical, clinical application of brain-tissue volume measurements is an automated, fast method that can be integrated into the clinical workflow. Numerous automated methods exist for this purpose, generally based on conventional T1-weighted, T2-weighted, and FLAIR images or a combination thereof. In these methods, tissue is classified on signal-intensity differences in the images where each pixel can be assigned to 1 specific tissue type[10-15] or multiple tissue types such that partial volume effects are accounted for.[16-19] The latter method is advantageous because it decreases the dependency on image resolution.

Despite the obvious benefits, brain volumetric measurements are not widely used in clinical practice. One of the main difficulties is that the image intensity of the input images can vary sub-

Received October 9, 2013; accepted after revision December 13.

From the Center for Medical Image Science and Visualization, (J.B.M.W., A.T., P.L.) and Clinical Physiology (J.B.M.W.) and Radiation Physics (P.L.), Department of Medical and Health Sciences, Linköping University, Linköping, Sweden; Departments of Clinical Physiology (J.B.M.W.), Clinical Neuroscience (A.-M.L.), and Radiation Physics (P.L.), UHL, County Council of Östergötland, Linköping, Sweden; Radiation Physics (A.T.), Department of Medical and Health Sciences, Faculty of Health Sciences, Linköping University, Linköping, Sweden; and Neurology, Department of Clinical and Experimental Medicine (A.-M.L.), Linköping University, Linköping, Sweden.

This work was supported in part by Grant No. VR/NT 2008-3368 from the National Research Council.

Please address correspondence to J.B.M. Warntjes, Center for Medical Image Science and Visualization, Linköping University Hospital, Linköping 58185, Sweden; e-mail: marcel.warntjes@cmiv.liu.se

Indicates open access to non-subscribers at www.ajnr.org

http://dx.doi.org/10.3174/ajnr.A3890

stantially due to scanner configuration and examination parameters[20] and age- or disease-related tissue changes,[21,22] leading to differences in classification. Second, extensive manual interaction of the postprocessing software or long processing times may be required, which may lead to hours or even days of lag time to retrieve the volumetric information.[23] A complicating factor for automatic segmentation methods is the use of contrast agents. Gadolinium (Gd) contrast agent is generally administered to patients with MS to highlight any damage to the blood-brain barrier, indicating inflammatory lesions and helping to stage disease evolution. Leakage of Gd into brain tissue strongly reduces the T1 relaxation, resulting in hyperintensity on T1-weighted images. Even in the absence of leakage, the presence of Gd in the capillary network of the brain parenchyma may slightly reduce T1 relaxation of the brain tissue, which could have a secondary effect on automated tissue-classification methods. This effect may even vary with the amount and timing of contrast administration.

In this work, the synthetic tissue-mapping (SyMap) method, which previously reported on measurements of the intracranial volume (ICV),[24] the brain parenchymal fraction,[25] and all tissue fractions,[16] was evaluated for brain-tissue measurements in patients with MS with and without the presence of a Gd contrast agent. The method is based on quantitative MR imaging to measure the longitudinal relaxation time, T1; the transverse relaxation time, T2; and proton density.[26] The procedure does not generate conventional MR images but maps of physical parameters that directly reflect tissue properties. Such a quantitative measurement removes a large number of dependencies of MR imaging scanner settings and imperfections.[27] The method includes a fully automatic postprocessing software, to calculate the white matter volume (WMV), gray matter volume (GMV), cerebrospinal fluid volume (CSFV), the remaining, unclassified non-WM/GM/CSF tissue volume within the ICV (NV), brain parenchymal volume (BPV), and ICV on the basis of the measured T1, T2, and PD maps. The total postprocessing time is <1 minute, which makes it appropriate for routine clinical purposes.

The aim of this study was to evaluate the use of synthetic tissue-mapping for the measurement of WMV, GMV, CSFV, NV, BPV, and ICV in patients with MS pre- and post-Gd. In addition, the brain-tissue fractions of WM, GM, CSF, remaining, unclassified non-WM/GM/CSF tissue, and brain parenchyma, normalized against the ICV, were evaluated. The repeatability of the automatic brain segmentation was assessed by measuring the controls twice.

MATERIALS AND METHODS

Subjects

The study included a group of 20 patients (5 men, 15 women; mean age, 47 ± 12 years) diagnosed with clinically definite MS based on clinical presentation and laboratory findings. All patients fulfilled the Poser criteria with at least 2 relapses, separated in space and time.[28,29] The mean Expanded Disability Status Scale (EDSS) score[30] for patients was 3.8 ± 2.3 (median, 3.5; range, 1.0–7.5). EDSS is a method of evaluating the degree of neurologic impairment in MS, scoring 8 functional systems, resulting in steps of 0.5 from 0 (healthy) to 10 (death due to MS). The mean disease duration was 15 ± 11 years. No differentiation was made between types of MS, and the group consisted of 12 patients with relapsing-remitting and 8 with secondary-progressive MS. One patient was excluded from the analysis due to severe MR imaging receive coil signal-intensity problems. The study was part of routine follow-up examinations. For comparison, a group of 20 age- and sex-matched healthy controls was included (5 men, 15 women; mean age, 48 ± 12 years). The mean age difference compared with the MS group was 0.7 ± 2.7 years. The study was approved by the Regional Ethics Committee (reference number Dnr M88–07), and written informed consent was obtained from all participants.

Scanning Protocol

The MR imaging quantification method QRAPMASTER (also known as Qmap)[26] was performed to simultaneously retrieve the T1 and T2 relaxation and proton density. The sequence was a multi-spin-echo saturation recovery sequence with 4 saturation delays and 5 echoes. Hence, the sequence produced a matrix of $4 \times 5 = 20$ images per slice with the combined effects of T1 and T2 relaxation in the image intensity. The saturation delay times were at 100, 400, 1380, and 2860 ms with a TR of 2950 ms. The TEs were 14, 28, 42, 56, and 70 ms. The in-plane resolution was 1×1 mm^2 over an FOV of 210 mm; 30 axial sections of 4 mm thickness (no gap) were acquired in a scan time of 8 minutes and 21 seconds. The MR imaging scanner was an Achieva 1.5T (Philips Healthcare, Best, the Netherlands). All subjects were scanned twice with 20 minutes between the scans. Only the patient group received a single dose of gadopentetate dimeglumine contrast agent (0.2 mL/kg, Magnevist 0.5 mmol/mL; Schering, Berlin, Germany) 10 minutes before the second acquisition.

Image Postprocessing

The raw data were analyzed with the SyMRI 7.0 software (Synthetic MR, Linköping, Sweden) to retrieve the T1, T2, and PD maps. These maps were used as input for the automatic brain segmentation in the same software. In summary, WM, GM, and CSF tissue clusters and mixtures thereof were recognized as specific combinations of T1, T2, and PD values, as previously reported.[16] The total ICV comprised all recognized WM, GM, and CSF, for which a region-growing algorithm ensured a contiguous volume. The border of the ICV was refined to set the threshold at PD = 50%, by using the definition of the tissue interface between CSF (with visible PD = 100%) and bone (with visible PD = 0%). The ICV was automatically cut at the base of the skull. The sum of all WM, GM, and CSF partial volumes inside the ICV provided the WMV, GMV, and CSFV, respectively. The BPV was defined as the ICV minus the CSFV. The region-growing algorithm leads to the inclusion of volume that does not match the defined WM, GM, or CSF characteristics within the ICV. This remaining tissue was labeled the non-WM/GM/CSF volume, comprising unspecified tissue such as blood vessels, motion artifacts, or pathologic tissue. Normalization with the ICV resulted in the white matter fraction, gray matter fraction, CSF fraction, the non-WM/GM/CSF fraction, and the brain parenchymal fraction. The software did not have a standard brain or any atlas-driven models; tissue was segmented on T1-T2-PD characteristics only.

Loading all raw data from a PACS required 20–30 seconds, and calculating the T1, T2, and PD maps with subsequent seg-

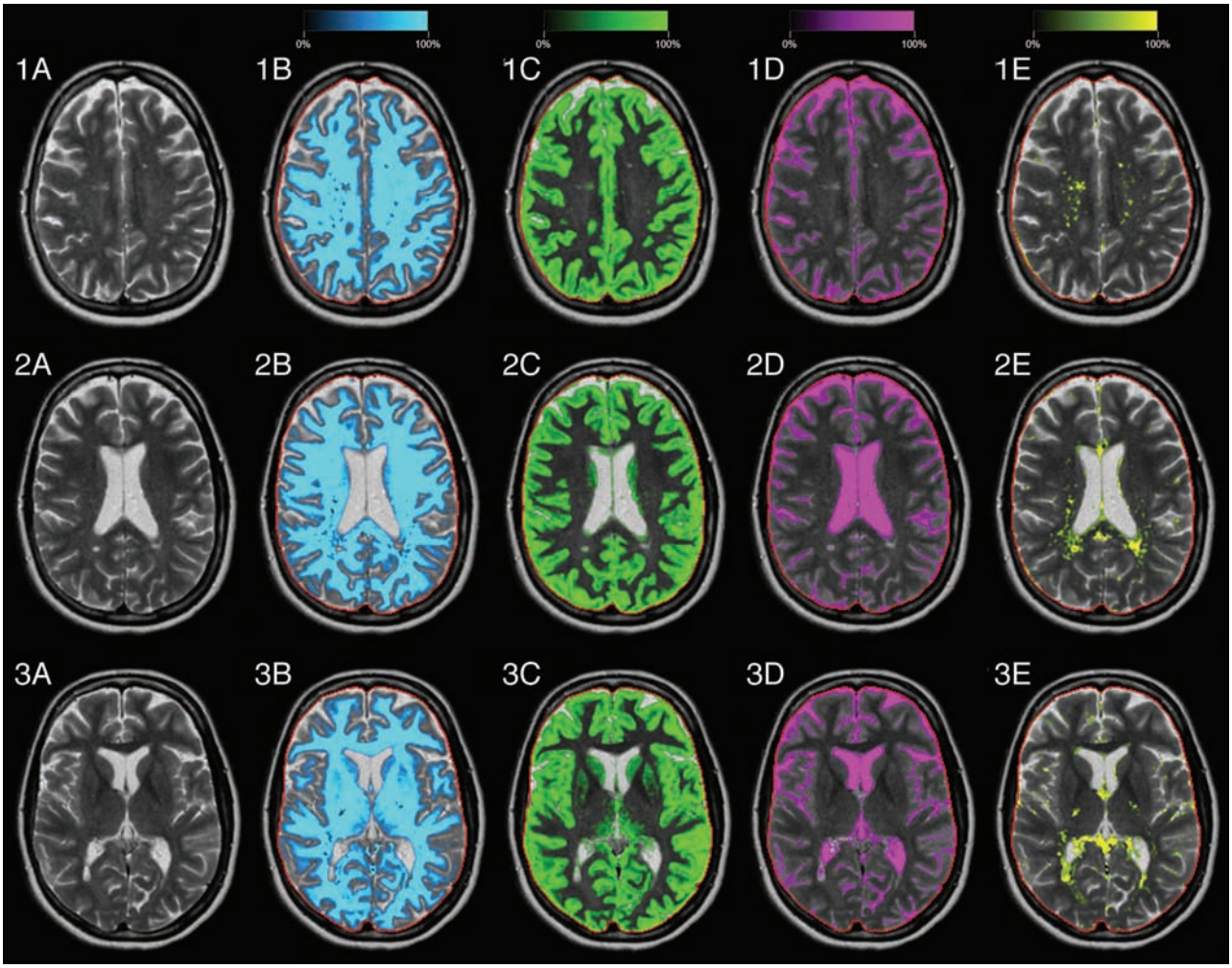

FIG 1. Typical images of the automatic segmentation software of a patient with MS (39-year-old woman, EDSS = 4.0). Three slices are shown, numbers 19, 16, and 13 of the 30 acquired slices. *A*, T2-weighted image. *B*, White matter segmentation, in which the intensity of the light-blue color overlay corresponds to the calculated white matter partial volume per voxel. The red line indicates the intracranial volume. Similar images are shown for gray matter in green (*C*), CSF in pink (*D*), and non-WM/GM/CSF in yellow (*E*).

mentation of the brain was performed within 10–20 seconds. A standard 64-bit PC with 6 gigabytes of RAM was used.

Statistics

For the WMV, GMV, CSFV, NV, BPV, and ICV and for WM fraction, GM fraction, CSF fraction, remaining, unclassified non-WM/GM/CSF tissue fraction, and brain parenchymal fraction, the mean value and SD were calculated for each measurement. Linear regression was used to analyze the relation of the volume and fraction values to age. The results from the regression analysis of the controls were used to correct the values of the patients with MS for age. Linear regression with EDSS was then performed as a separate step. A Shapiro-Wilk test was applied for normal distribution. A paired *t* test was performed to find the significance of the difference between measurement 1 and measurement 2. A 1-way ANOVA with post hoc Tukey analysis was used to assess group differences between controls and patients with MS.

RESULTS

Typical results of the segmentation software on 3 of the 30 acquired slices are shown in Fig 1. An axial slice of the head of one of the patients with MS (a 39-year-old woman; EDSS = 4.0) is displayed. In the left column, the T2-weighted images are shown for comparison. On the right, the calculated WM, GM, CSF, and non-WM/GM/CSF partial volume maps are displayed as a color overlay in which the color intensity corresponds to the partial volume in the range between 0% and 100% tissue. The red line indicates the border of the ICV. The mean ICV of all subjects at the first measurement was 1387 mL, with an SD of 110 mL (7.9%). White matter lesions mainly show up as the remaining non-WM/GM/CSF but are partly recognized as GM and CSF. Radiologic inspection showed that no patient had Gd-enhancing lesions.

In Table 1, the results of the fully automatic tissue volume measurements are shown for WMV, GMV, CSFV, NV, BPV, and ICV. No statistically significant difference was found between the 2 measurements for all volumes of the control group. The differences for the patient group were much larger; a significant reduction of the ICV of 13 mL and of the CSFV of 16 mL was observed as patients were exposed to Gd. The differences in BPV, WM, and GM were not significant, but the ratio of WMV and GMV changed toward higher WMV. Visual inspection did not result in locating a specific area in which differences in volumes were pro-

Table 1: Fully automatic measurements of the WMV, GMV, CSFV, NV, BPV, and ICV volumes of the control group and the MS group[a]

	WMV (mL)	GMV (mL)	CSFV (mL)	NV (mL)	BPV (mL)	ICV (mL)
Contr1	581 ± 67	639 ± 58	156 ± 45	28 ± 7	1247 ± 119	1404 ± 119
Contr2	581 ± 69	637 ± 53	156 ± 47	31 ± 12	1250 ± 119	1406 ± 120
MS1	452 ± 88	617 ± 48	247 ± 60	52 ± 22	1122 ± 99	1369 ± 99
MS2	464 ± 109	600 ± 47	231 ± 60	60 ± 21	1124 ± 98	1355 ± 97
Diff Contr1-Contr2	0 ± 11	−1 ± 13	0 ± 4	4 ± 12	2 ± 6	2 ± 7
Diff MS1-MS2	12 ± 37	−17 ± 40	−16 ± 7[c]	8 ± 11[b]	2 ± 9	−13 ± 8[c]
Diff Contr1-MS1	−129 ± 104[c]	−22 ± 68	91 ± 71[c]	24 ± 18[c]	−126 ± 133[c]	−35 ± 117
Diff Contr2-MS2	−117 ± 113[c]	−37 ± 67[b]	75 ± 70[c]	29 ± 17[c]	−126 ± 136[c]	−50 ± 116

Note:—Diff indicates difference; Contr, control group; MS, MS patient group; 1, measurement 1; 2, measurement 2.

[a] For each tissue volume, the mean value and SD are given. The mean difference and SD of the first measurement and the second measurement and between controls and patients with MS are also provided. The MS group received Gd in the second measurement.

[b] $P < .05$ (significant difference).

[c] $P < .005$ (significant difference).

Table 2: Fully automatic measurements of the normalized WMF, GMF, CSFF, NF, and BPF of the control group and the MS group[a]

	WMF (%)	GMF (%)	CSFF (%)	NF (%)	BPF (%)
Contr1	41.4 ± 2.6	45.5 ± 1.9	11.2 ± 3.1	2.0 ± 0.5	88.8 ± 3.1
Contr2	41.3 ± 2.4	45.4 ± 1.8	11.1 ± 3.1	2.2 ± 0.9	88.9 ± 3.1
MS1	32.9 ± 5.4	45.2 ± 3.0	18.0 ± 4.1	3.8 ± 1.7	82.0 ± 4.1
MS2	34.0 ± 6.8	44.5 ± 4.6	17.1 ± 4.2	4.4 ± 1.6	82.9 ± 4.2
Diff Contr1-Contr2	−0.1 ± 0.9	−0.1 ± 0.8	0.0 ± 0.3	0.2 ± 0.8	0.0 ± 0.3
Diff MS1-MS2	1.1 ± 2.9	−0.7 ± 3.2	−1.0 ± 0.5[c]	0.6 ± 0.8[b]	1.0 ± 0.5[c]
Diff Contr1-MS1	−8.4 ± 6.1[c]	−0.4 ± 3.4	6.9 ± 5.1[c]	1.9 ± 1.5[c]	−6.9 ± 5.1[c]
Diff Contr2-MS2	−7.3 ± 6.9[c]	−0.9 ± 4.3	6.0 ± 5.1[c]	2.2 ± 1.4[c]	−6.0 ± 5.1[c]

Note:—Diff indicates difference; Contr, control group; MS, MS patient group; 1, measurement 1; 2, measurement 2; WMF, WM fraction; GMF, GM fraction; CSFF, CSF fraction; NF, remaining, unclassified non-WM/GM/CSF tissue fraction; BPF, brain parenchymal fraction.

[a] Each tissue fraction corresponds to the tissue volume divided by the ICV. The mean value and SD are given as well as the mean difference and SD of the first measurement and the second measurement and between the controls and patients with MS.

[b] $P < .05$ (significant difference).

[c] $P < .005$ (significant difference).

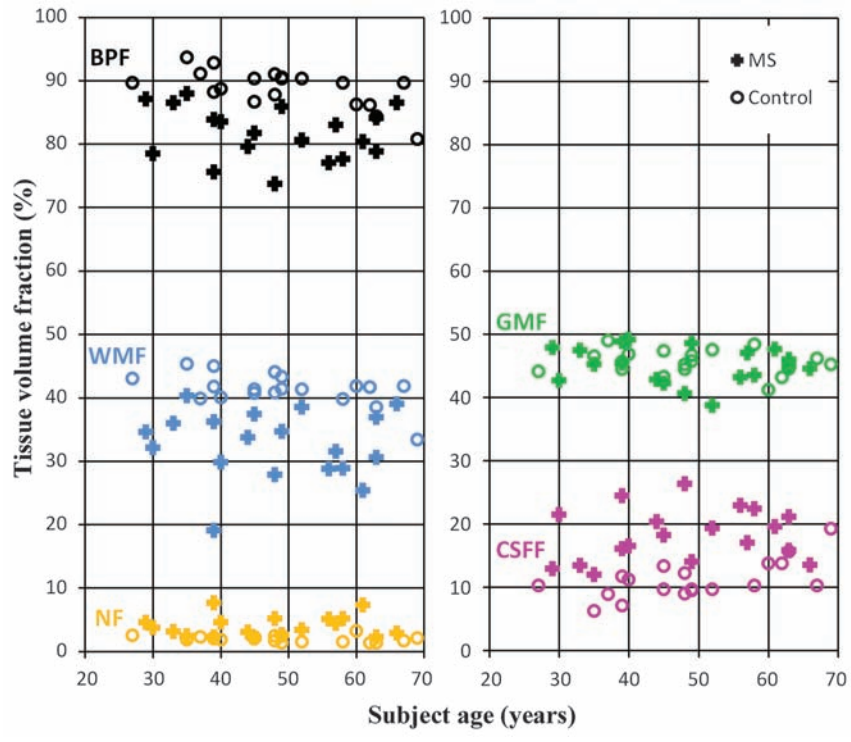

FIG 2. Brain-tissue fraction results of the first measurement: the brain parenchymal fraction, white matter fraction, gray matter fraction, CSF fraction, and the non-WM/GM/CSF fraction of the intracranial volume, as a function of subject age. Markers are zero for the control group and plus for the MS group. The colors are similar to the segmentation overlay colors of Fig 1.

nounced. The observed differences were distributed over all slices and ranged between 0 and 1 mL per section. Between the control and patient groups, large volume differences were observed. The mean BPV was 126 mL smaller for the MS group, similar to the total mean WMV difference (129 mL). The CSFV was significantly larger for patients, with a mean difference of 91 mL. In addition, the remaining NV was larger (24 mL).

In Table 2, the normalized tissue fractions of WM, GM, CSF, remaining, unclassified non-WM/GM/CSF tissue, and brain parenchyma are shown. Again only small differences were observed for the control group. For the MS group, on the other hand, the WM fraction, remaining, unclassified non-WM/GM/CSF tissue fraction, and brain parenchymal fraction increased, whereas the GM fraction and CSF fraction decreased after Gd administration. The changes in CSF fraction, remaining, unclassified non-WM/GM/CSF tissue fraction, and brain parenchymal fraction were significant. When one compared the 2 groups, a significant difference in WM fraction, CSF fraction, remaining, unclassified non-WM/GM/CSF tissue fraction, and brain parenchymal fraction between the controls and the patients with MS was observed. The differences between the 2 groups are visualized in Fig 2, where the normalized WM fraction, GM fraction, CSF fraction, remaining, unclassified non-WM/GM/CSF tissue fraction, and brain parenchymal fraction measurements are shown for all subjects as a function of age for the first measurement.

In Table 3, linear regression slopes and confidence intervals are shown for both groups. For the control group, a significant decrease of WM fraction and brain

Table 3: Linear regression of the normalized WMF, GMF, CSFF, NF, and BPF of the control and the MS groups as a function of age[a]

	WMF	GMF	CSFF	NF	BPF
Contr1-age (%/yr)	−0.12 (−0.21 to −0.03)[b]	−0.03 (−0.11–0.05)	0.17 (0.07–0.27)[c]	−0.01 (−0.03–0.01)	−0.17 (−0.27 to −0.07)[c]
Contr2-age (%/yr)	−0.10 (−0.19 to −0.01)[b]	−0.05 (−0.12–0.03)	0.17 (0.07–0.27)[c]	−0.02 (−0.05–0.02)	−0.17 (−0.2 to −0.07)[c]
MS1-age (%/yr)	−0.02 (−0.26–0.22)	−0.03 (−0.16–0.10)	0.05 (−0.13–0.23)	0.00 (−0.08–0.07)	−0.05 (−0.23, −0.13)
MS2-age (%/yr)	−0.01 (−0.31–0.30)	−0.05 (−0.25–0.15)	0.04 (−0.14–0.23)	0.02 (−0.06–0.09)	−0.04 (−0.23–0.14)
MS1-EDSS (%/unit)	−1.16 (−2.28 to −0.05)[b]	−0.17 (−0.87–0.54)	0.93 (−0.19–2.04)	0.23 (−0.14–0.62)	−1.08 (−1.90 to −0.26)[b]
MS2-EDSS (%/unit)	−1.34 (−2.81–0.13)	0.09 (−1.01–1.19)	0.93 (−0.19–2.06)	0.19 (−0.20–0.58)	−1.06 (−1.92 to −0.20)[b]

Note:—Contr indicates control group; MS, MS patient group; 1, measurement 1; 2, measurement 2; WMF, WM fraction; GMF, GM fraction; CSFF, CSF fraction; NF, remaining, unclassified non-WM/GM/CSF tissue fraction; BPF, brain parenchymal fraction.

[a] The 95% confidence interval is given between parentheses. For the MS group, the linear regression of the age-corrected fractions with EDSS is provided.

[b] $P < .05$ (significant difference).

[c] $P < .005$ (significant difference).

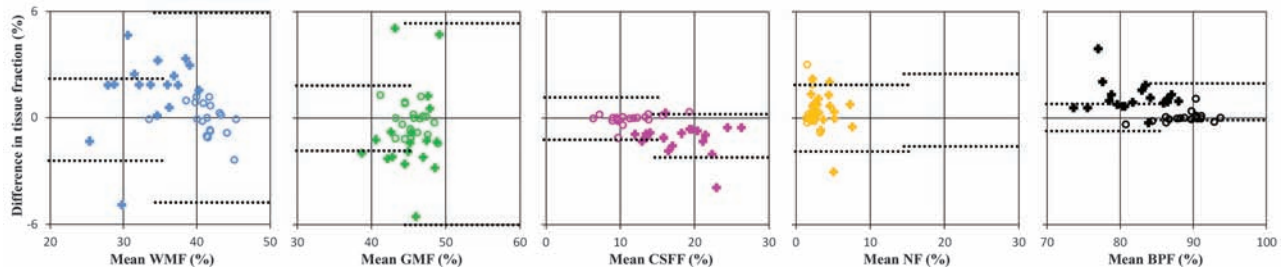

FIG 3. Bland-Altman plots for WM fraction, GM fraction, CSF fraction, remaining, unclassified non-WM/GM/CSF tissue fraction, and brain parenchymal fraction of all subjects with the mean tissue fraction against the difference in tissue fraction between measurements 1 and 2. The dotted lines indicate the mean difference ± 2 SDs, on the left for the controls and on the right for the MS group. The scaling on both axes is identical; the colors are identical to those in Fig 2.

parenchymal fraction and a significant increase of CSF fraction with age were observed. No significant correlation with age was found for the MS group. After age correction, the patients with MS showed a significant decrease of brain parenchymal fraction and of WM fraction. Between measurements 1 and 2, the regression values were very similar and no significant difference was observed for any slope for either group. In Fig 3, Bland-Altman plots are shown for WM fraction, GM fraction, CSF fraction, remaining, unclassified non-WM/GM/CSF tissue fraction, and brain parenchymal fraction for all subjects, in which the mean tissue fraction was plotted against the difference in tissue fraction between measurements 1 and 2. The 2 times SD areas are indicated by the dotted lines for both groups, on the left for the controls, and on the right for the MS group. For WM fraction and GM fraction, the SD of the patient group is much larger than that for the control group; for CSF fraction, remaining, unclassified non-WM/GM/CSF tissue fraction, and brain parenchymal fraction, it was similar.

DISCUSSION

In this work, a recently developed method of combining quantitative MR imaging with fully automatic tissue classification, synthetic tissue-mapping, was used to investigate brain-tissue volumes of patients with MS pre- and post-contrast agent administration. This method is both fast and objective because brain segmentation can be obtained in a total time of 10 minutes (acquisition plus postprocessing) and without user interaction for tissue classification.

In a clinical and research context, accurate measurement of the ICV is important because it is used to normalize brain-tissue volumes to reduce the effect of differences in subject head size.[31] The repeatability of the ICV segmentation was estimated by using the 2 measurements of the control group. The software reproduced values for the repeated measurements with a nonsignificant difference of 2 mL, which corresponds to only 0.14% of the ICV. The intrasubject SD in this cohort was 0.50%, which was somewhat lower than the 0.83%, found in a previous assessment by Ambarki et al.[24] The administration of Gd, however, had a significant effect on the measurement of the ICV; after contrast agent administration, the ICV was 13 mL smaller. Visual inspection did not result in locating a specific area where differences in ICV were pronounced, and ICV was measured slightly smaller on every slice. Our interpretation of these observations is that the slight reduction in the T1 relaxation of brain tissue due to the presence of Gd contrast agent in the capillary network resulted in a slight decrease of the measured PD, though PD should be invariant to T1. A lower PD will consequently shift the ICV border somewhat because the border was defined in the software at PD = 50%. A reduction of the ICV with a mean of 13 mL, however, is relatively small. If one considers a 1387-mL skull as a spheric object, the volume loss would correspond to a radial decrease of 0.2 mm. Such a reduction is well below the resolution of our acquisitions.

The BPV was identical for both measurements and for both groups. The reduction of the ICV, observed post-Gd in patients with MS, resulted in a reduction of the observed CSFV. This means that the ratio between BPV and ICV, the brain parenchymal fraction, changed, as shown in Table 2, with a significant increase of 1.0% in a paired test. The brain parenchymal fraction is considered a valid measure for brain atrophy,[32] and the effect of the presence of Gd is therefore important for follow-up. The apparent increase of brain parenchymal fraction of 1.0% was smaller than the observed variation of brain parenchymal fraction within the MS group (4.2%). Furthermore, it was much smaller than the difference between the MS group and the controls (6.9% for measurement 1 and 6.0% for measurement 2). Linear regression (Table 3) showed that the difference pre- and post-Gd appears to be

an offset, which was similar for all subjects; the measured slopes as a function of age and EDSS were very similar for both measurements. The results of this study suggest that a common practice, comparing images of patients with MS acquired post-Gd with those of healthy controls without Gd should still be considered a valid approach, despite the effects of Gd on the tissue-classification volumes. Further investigation is required to confirm this for patients with MS at earlier stages of the disease and patients with MS with enhancing lesions.

The results for brain parenchymal fraction in this work were very close to the values of Vågberg et al,[25] who reported a brain parenchymal fraction of 85.2% for the MS group on the basis of analysis using the same software. These patients had a median EDSS = 2.5, which was acquired post-Gd. In this work, the mean (post-Gd) brain parenchymal fraction was 82.9% for patients, who had a higher median EDSS = 3.5. For the control group, it was 89.0% (no Gd), compared with our 88.8%. The coefficients of variation of repeated BPF measurements were comparable.

The measured values for brain parenchymal fraction for the control group were higher than those in a large study by DeCarli et al,[33] in which a mean brain parenchymal fraction of 78% was found (mean subject age, 62 years). Differences in absolute brain parenchymal fraction values may have various causes: DeCarli et al, for example, used another definition of the ICV, in which the cerebellum was excluded. Furthermore, CSF was manually segmented in a binary fashion by using an image-intensity threshold. Because any method has a cascade of segmentation process details, they easily lead to differences in the final results. As shown in our work, the absence or presence of Gd contributes to these differences. It is, therefore, clinically more relevant to focus on the change of tissue classification values with time or over disease severity. As shown in Table 3, there was no significant difference in the correlation of the volume fractions with age and EDSS. In the study of DeCarli et al, a decrease of brain parenchymal fraction of 0.26% per year was reported, an observation that was within the 95% confidence interval of our measurements. The lower rate of 0.17% that was found could partly be explained by the fact that our subjects were on average 14 years younger.

Gd contrast agent is expected to decrease the T1 relaxation in brain tissue. Even though no enhancing lesions were observed for the included patients with MS, a nonzero Gd concentration must have been present in the capillary network. Because of this shift toward shorter T1 relaxation times, the segmentation results may show an apparent increase of the brain tissue with the shortest T1 relaxation time (ie, white matter). As seen in Tables 1 and 2, there was a trend that WM increased somewhat, at the expense of GM post-Gd, but this effect was not significant. The Gd concentration in nonlesional normal-appearing brain tissue must, therefore, be relatively low.

Within the ICV, some tissue was not recognized as either WMV, GMV, or CSFV, and was labeled NV. The advantage of the presence of a fourth class for the remaining, unclassified tissue fraction is that it avoids forcing tissue into the WMV, GMV, or CSFV classes. Therefore, it reduces the effect of the presence of white matter lesions, which can be a problem for automatic brain-tissue-classification algorithms.[34] As is shown in Fig 1, white matter lesions mainly show up in NV; therefore, it could serve as a basis for MS lesion-load estimation. An offset of the NV, corresponding to 28–31 mL (2.0%–2.2% of the ICV), was observed in healthy subjects, mainly consisting of blood vessels and small rims at the intracranial edge. For the MS group, the NV was significantly higher, at 52 mL pre-Gd and 60 mL post-Gd (3.8% and 4.4% of the ICV, respectively), suggesting that 24–29 mL might be assigned to MS lesion volume. Although these higher values suggests that the NV might be useful for MS lesion-load measurements, currently, extensive manual correction will be required, both to reduce false-positives of nonlesional areas and to correct false-negatives when MS lesions are recognized as partial volume GM or CSF instead. The effect of Gd was significant, apparently increasing the potential MS volume to 8 mL post-Gd, a 15% increase in comparison with the pre-Gd volume. Further investigation on, for example, the reproducibility and the influence of the rather thick sections (4 mm) is required to confirm this finding. It could be speculated that the introduction of a fifth class, blood vessels, could improve the specificity of the NV to segment MS lesions. Blood vessels typically have very low PD values because synthetic tissue-mapping uses a black-blood acquisition sequence.

A limitation of the study was the low number of included subjects and the combination of subjects diagnosed with relapsing-remitting MS and secondary-progressive MS in the group of patients with MS. The effects of Gd may, therefore, be different for the different MS groups. Furthermore, only single-dose Gd and a fixed time after administration were investigated. Although these 2 variables were carefully controlled, the absolute Gd concentration may still have varied over the patients due to, for example, weight, blood volume, and perfusion rate. As seen in Fig 3, the variation in segmentation results increased significantly for WM and GM, which may be a sign of different Gd concentrations. Administration of double-dose Gd, or choosing another delay time after administration of Gd, may further affect the automatic tissue classification. The results of the synthetic tissue-mapping method, however, are congruent with the results of other, larger studies on controls and patients with MS. A limitation for the repeated measurements was the lack of measurements for controls with Gd and patients with MS without Gd, which was beyond the scope of our ethical permission. Therefore, the observed effect of changes in the automatic segmentation after Gd administration may be specific for our groups. Especially, the effect of minor Gd leakage on the MS lesions can be of influence because the measured NV did increase to 8 mL post-Gd. It is more likely, however, that the increase of NV occurred simultaneously with a decrease of the sum of WMV and GMV (observed 12–17 = −5 mL) and therefore did not have an influence on BPV. The effects on automatic tissue classification of other patient populations, other Gd concentrations, and acquisitions on other scanner brands are subject to future investigations of the method.

A potential limitation could be the relatively low resolution of the method, which could decrease the variation between measurements. The method, however, is relatively insensitive to resolution, owing to the incorporation of a partial volume model, and it has been shown that the volume measurements are similar by using a variety of resolutions.[16] It is, therefore, not expected that the application of a higher spatial resolution would alter the differences pre- and post-Gd. The effect of choosing different geometries was not investigated.

CONCLUSIONS

The synthetic tissue-mapping method provides automatic measurements of WMV, GMV, CSFV, NV, BPV, and ICV, with a high degree of repeatability within a short time. The administration of Gd contrast agent in patients with MS had a significant effect on the tissue-classification results, and changes were observed for CSFV, NV, and ICV. For brain-tissue fractions, normalized with the ICV, changes were observed in CSF fraction, remaining, unclassified non-WM/GM/CSF tissue fraction, and brain parenchymal fraction. The observed changes in this study, however, were much smaller than the differences between the group of patients with MS and healthy controls. There were no significant differences between the correlations with age and EDSS pre- and post-Gd.

Disclosures: J.B.M. Warntjes—*UNRELATED: Employment*: Synthetic MR AB, *Comments*: I am employed part-time at Synthetic MR AB, a software company specializing in MR image analysis and the manufacturer of SyMRI 7.0, *Stock/Stock Options*: Synthetic MR AB, *Comments*: I own shares. P. Lundberg—*RELATED: Grant*: National Research Council/NT*, *UNRELATED: Board Membership*: Amra AB, *Comments*: not related to this work (no money paid), *Grants/Grants Pending*: National Medical Research Council,* VINNOVA,* *Comments*: funding for other research, *Patents (planned, pending or issued)*: Improvement in Magnetic Resonance Imaging Relating to Correction of Chemical Shift Artifact and Intensity Inhomogeneity, EP Patent 2,283,376; Improvement in Magnetic Resonance Imaging Relating to Correction of Chemical Shift Artifact and Intensity Inhomogeneity, US Patent 20, 110,091,090, Comments: held by Amra AB (no money received), *Stock/Stock Options*: Amra AB, *Comments*: no money paid, *Travel/Accommodations/Meeting Expenses Unrelated to Activities Listed*: paid by my employer (County Council University Hospital) for attending ISMRM. *Money paid to the institution.

REFERENCES

1. Barkhof F. **The clinico-radiological paradox in multiple sclerosis revisited.** *Curr Opin Neurol* 2002;15:239–45
2. Chard D, Miller D. **Is multiple sclerosis a generalized disease of the central nervous system? An MRI perspective.** *Curr Opin Neurol* 2009;22:214–18
3. Minneboo A, Uitdehaag BM, Jongen P, et al. **Association between MRI parameters and the MS severity scale: a 12 year follow-up study**. *Mult Scler* 2009;15:632–37
4. Zivadinov R, Cox JL. **Neuroimaging in multiple sclerosis.** *Int Rev Neurobiol* 2007;79:449–74
5. Filippi M, Tortorella C, Bozzali M. **Normal-appearing white matter changes in multiple sclerosis: the contribution of magnetic resonance techniques.** *Mult Scler* 1999;5:273–82
6. Miller DH, Barkhof F, Frank JA, et al. **Measurement of atrophy in multiple sclerosis: pathological basis, methodological aspects and clinical relevance.** *Brain* 2002;125:1676–95
7. Mortazavi D, Kouzani AZ, Soltanian-Zadeh H. **Segmentation of multiple sclerosis lesions in MR images: a review.** *Neuroradiology* 2012;54:299–320
8. Grassiot B, Desgranges B, Eustache F, et al. **Quantification and clinical relevance of brain atrophy in multiple sclerosis: a review.** *J Neurol* 2009;256:1397–412
9. Chard DT, Griffin CM, Parker GJ, et al. **Brain atrophy in clinically early relapsing-remitting multiple sclerosis.** *Brain* 2002;125:327–37
10. Andersen AH, Zhang Z, Avison MJ, et al. **Automated segmentation of multispectral brain MR images.** *J Neurosci Methods* 2002; 122:13–23
11. Alfano B, Brunetti A, Covelli EM, et al. **Unsupervised, automated segmentation of the normal brain using a multispectral relaxometric magnetic resonance approach.** *Magn Reson Med* 1997;37:84–93
12. Ishii K, Soma T, Kono AK, et al. **Automatic volumetric measurement of segmented brain structures on magnetic resonance imaging.** *Radiat Med* 2006;24:422–30
13. Ashburner J, Friston KJ. **Unified segmentation.** *Neuroimage* 2005; 26:839–51
14. Fischl B. **FreeSurfer.** *Neuroimage* 2012;62:774–81
15. Hasan KM, Walimuni IS, Abid H, et al. **Human brain atlas-based multimodal MRI analysis of volumetry, diffusimetry, relaxometry and lesion distribution in multiple sclerosis patients and healthy adult controls: implications for understanding the pathogenesis of multiple sclerosis and consolidation of quantitative MRI results in MS.** *J Neurol Sci* 2012;313:99–109
16. West J, Warntjes JB, Lundberg P. **Novel whole brain segmentation and volume estimation using quantitative MRI.** *Eur Radiol* 2012; 22:998–1007
17. Anbeek P, Vincken KL, van Bochove GS, et al. **Probabilistic segmentation of brain tissue in MR imaging.** *Neuroimage* 2005;27:795–804
18. Shattuck DW, Sandor-Leahy SR, Schaper KA, et al. **Magnetic resonance image tissue classification using a partial volume model.** *Neuroimage* 2001;13:856–76
19. Kovacevic N, Lobaugh NJ, Bronskill MJ, et al. **A robust method for extraction and automatic segmentation of brain images.** *Neuroimage* 2002;17:1087–100
20. Jovicich J, Czanner S, Han X, et al. **MRI-derived measurements of human subcortical, ventricular and intracranial brain volumes: reliability effects of scan sessions, acquisition sequences, data analyses, scanner upgrade, scanner vendors and field strengths.** *Neuroimage* 2009;46:177–92
21. MacKay A, Laule C, Vavasour I., et al. **Insights into brain microstructure from the T2 distribution.** *Magn Reson Imaging* 2006;24: 515–25
22. Larsson HB, Frederiksen J, Petersen, et al. **Assessment of demyelination, edema and gliosis by in-vivo determination of T1 and T2 in the brain of patients with acute attack of multiple sclerosis.** *J Magn Reson Med* 1989;11:337–38
23. Pengas G, Pereira JMS, Williams GB, et al. **Comparative reliability of total intracranial volume estimation methods and the influence of atrophy in a longitudinal semantic dementia cohort.** *J Neuroimaging* 2009;19:37–46
24. Ambarki K, Lindqvist T, Wåhlin A, et al. **Evaluation of automatic measurement of the intracranial volume based on quantitative MR imaging.** *AJNR Am J Neuroradiol* 2012;33:1951–56
25. Vågberg M, Lindqvist T, Ambarki K, et al. **Automated determination of brain parenchymal fraction in multiple sclerosis.** *AJNR Am J Neuroradiol* 2013;34:498–504
26. Warntjes JB, Dahlqvist Leinhard O, West J, et al. **Optimization for clinical usage of rapid magnetic resonance quantification on the brain.** *Magn Reson Med* 2008;60:320–29
27. Tofts P. *Quantitative MRI of the Brain.* Chichester, UK: Wiley; 2003
28. Poser CM, Paty DW, Scheinberg L, et al. **New diagnostic criteria for multiple sclerosis: guidelines for research protocols.** *Ann Neurol* 1983;13:227–31
29. McDonald WI, Compston A, Edan G, et al. **Recommended diagnostic criteria for multiple sclerosis: guidelines from the International Panel on the Diagnosis of Multiple Sclerosis.** *Ann Neurol* 2001;50: 121–27
30. Kurtzke JF. **Rating neurologic impairment in multiple sclerosis: an expanded disability status scale (EDSS).** *Neurology* 1983;33:1444–52
31. Whitwell JL, Crum WR, Watt HC, et al. **Normalization of cerebral volumes by use of intracranial volume: implications for longitudinal quantitative MR imaging.** *AJNR Am J Neuroradiol* 2001;22: 1483–89
32. Rudick RA, Fisher E, Lee JC, et al. **Use of brain parenchymal fraction to measure whole brain atrophy in relapsing-remitting MS: Multiple Sclerosis Collaborative Group.** *Neurology* 1999;53:1698–704
33. DeCarli C, Massaro J, Harvey D, et al. **Measures of brain morphology and infarction in the Framingham Heart Study: establishing what is normal.** *Neurobiol Aging* 2005;26:491–510
34. Battaglini M, Jenkinson M, De Stefano N. **Evaluating and reducing the impact of white matter lesions on brain volume measurements.** *Hum Brain Mapp* 2012;33:2062–71

Impact of Age and Baseline NIHSS Scores on Clinical Outcomes in the Mechanical Thrombectomy Using Solitaire FR in Acute Ischemic Stroke Study

M.A. Almekhlafi, A. Davalos, A. Bonafe, R. Chapot, J. Gralla, V.M. Pereira, and M. Goyal, on behalf of the STAR Registry Investigators

ABSTRACT

BACKGROUND AND PURPOSE: Age and stroke severity are inversely correlated with the odds of favorable outcome after ischemic stroke. A previously proposed score for Stroke Prognostication Using Age and NIHSS Stroke Scale (SPAN) indicated that SPAN-100-positive patients (ie, age + NIHSS score = 100 or more) do not benefit from IV-tPA. If this finding holds true for endovascular therapy, this score can impact patient selection for such interventions. This study investigated whether a score combining age and NIHSS score can improve patients' selection for endovascular stroke therapy.

MATERIALS AND METHODS: The SPAN index was calculated for patients in the prospective Solitaire FR Thrombectomy for Acute Revascularization study: an international single-arm multicenter cohort for anterior circulation stroke treatment by using the Solitaire FR. The proportion with favorable outcome (90-day mRS score ≤2) was compared between SPAN-100-positive versus-negative patients.

RESULTS: Of the 202 patients enrolled, 196 had baseline NIHSS scores. Fifteen (7.7%) patients were SPAN-100-positive. There was no difference in the rate of successful reperfusion (Thrombolysis In Cerebral Infarction 2b or 3) between SPAN-100-positive versus -negative groups (93.3% versus 82.8%, respectively; $P = .3$). Stroke SPAN-100-positive patients had a significantly lower proportion of favorable clinical outcomes (26.7% versus 60.8% in SPAN-100-negative, $P = .01$). In a multivariable analysis, SPAN-100-positive status was associated with lower odds of favorable outcome (OR, 0.3; 95% CI, 0.1–0.9; $P = .04$). A higher baseline Alberta Stroke Program Early CT Score and a short onset to revascularization time also predicted favorable outcome in the multivariable analysis.

CONCLUSIONS: A significantly lower proportion of patients with a positive SPAN-100 achieved favorable outcome in this cohort. SPAN-100 was an independent predictor of favorable outcome after adjusting for time to treatment and the extent of preintervention tissue damage according to the Alberta Stroke Program Early CT Score.

ABBREVIATIONS: SPAN = Stroke Prognostication Using Age and NIH Stroke Scale; STAR = Solitaire FR Thrombectomy for Acute Revascularization study

Stroke-related disability remains high at nearly 2 decades since the introduction of IV-tPA as an acute ischemic stroke therapy.[1] Three recent large randomized trials failed to demonstrate the efficacy of endovascular therapies in improving the 90-day functional outcomes over IV-tPA alone.[2-4] These trials are criticized for time delays in achieving reperfusion and for the use of dated devices in most patients. Stent retrievers have proved efficacy over the Merci retriever (Concentric Medical, Mountain View, California),[5,6] but they were used in <1% of patients in the recent neutral trials. Therefore, at least 4 multicenter randomized trials of acute stroke endovascular therapy by using stent retrievers are currently recruiting, and other trials are launching soon.

Received August 28, 2013; accepted after revision November 11.

From the Departments of Clinical Neurosciences (M.A.A.), and Radiology (M.A.A., M.G.), University of Calgary, Calgary, Alberta, Canada; Faculty of Medicine (M.A.A.), King Abdulaziz University, Jeddah, Saudi Arabia; Department of Neurology (A.D.), University Hospital Germans Trias i Pujol, Badalona, Barcelona, Spain; Department of Neuroradiology (A.B.), Centre Hospitalier Universitaire de Montpellie-Guy de Chauliac, Montpellier, France; Department of Neuroradiology (R.C.), Alfred Krupp Krankenhaus, Essen, Germany; Department of Diagnostic and Interventional Neuroradiology (J.G.), Inselspital, University of Bern, Bern, Switzerland; Department of Neuroradiology (V.M.P.), University Hospital of Geneva, Geneva, Switzerland; and Department for Radiology (M.G.), Hotchkiss Brain Institute, University of Calgary, Calgary, Alberta, Canada.

The STAR study was sponsored by Covidien Neurovascular. Two academic Principal Investigators (J.G., V.M.P.) and an academic Steering Committee supervised the STAR trial design and operations. The Principal Investigators and the Steering Committee interpreted the results and wrote the report. The Principal Investigators and the Steering Committee had full access to the study data and had the final decision to submit for publication. The sponsor of the study was responsible for site management, data management, and safety reporting. Statistical analyses were conducted by Jill Schafer, Senior Statistician, and NAMSA, a commercial medical research organization (www.namsa.com). This study is registered with ClinicalTrials.gov (http://www.clinicaltrials.gov), number NCT01327989.

Please address correspondence to Mayank Goyal, MD, FRCPC, Department of Radiology, Seaman Family MR Research Centre, Foothills Medical Centre, 140329th St NW, Calgary, Alberta T2N 2T9, Canada; e-mail: mgoyal@ucalgary.ca

Indicates article with supplemental on-line table.

EBM 2 Evidence-Based Medicine Level 2.

http://dx.doi.org/10.3174/ajnr.A3855

The importance of patient selection for endovascular therapy of acute ischemic stroke cannot be overemphasized. While controversy exists regarding the optimal imaging technique for patient selection for endovascular therapy, there are proved and readily-available clinical indicators. Among the factors associated with poor functional recovery, age and NIHSS score are most relevant.[7] This finding led to the derivation of the Stroke Prognostication Using Age and NIHSS Stroke Scale (SPAN) index by adding the patient age in years plus the baseline NIHSS score. Investigators reported that patients in the National Institute of Neurological Disorders and Stroke trial with a score of ≥100 (SPAN-100) did not benefit from IV-tPA therapy, with a higher rate of symptomatic intracranial hemorrhage and poor functional outcome compared with SPAN-100-negative patients.[8] However, these findings do not take into account the rate of successful recanalization that has been consistently shown to be one of the strongest predictors of favorable stroke outcome.[9] The National Institute of Neurological Disorders and Stroke trial,[10] conducted between 1991 and 1994, does not reflect contemporary stroke care; this feature limits its generalizability.

If the SPAN-100 index can identify patients who do not benefit from endovascular therapy, this simple and readily available index will have implications for patient eligibility for these interventions. We assessed the impact of the SPAN-100 index in the large multicenter prospective study for mechanical thrombectomy in acute ischemic stroke, Solitaire FR Thrombectomy for Acute Revascularization (STAR).[11]

MATERIALS AND METHODS

The STAR registry was a single-arm prospective one conducted in 12 centers in Europe, Canada, and Australia.[11] Patients were eligible for enrollment if they presented within 8 hours after onset of an acute ischemic stroke due to a proximal intracranial arterial occlusion in the anterior circulation. Key inclusion criteria were the following: age (18 years of age and older and younger than 85 years), NIHSS score of 8–30, mRS score of <2, and a documented occlusion of an intracranial artery on conventional angiography.

Treatment Protocol and Outcomes

Patients arriving at the hospital within 4.5 hours were treated with IV-tPA in the absence of contraindications, while the rest were referred for primary mechanical thrombectomy. The Solitaire FR (flow restoration) device (Covidien, Irvine, California) was the primary stent retrievers used in the study. Successful revascularization was defined as a TICI score of 2b or more of the target territory with a maximum of 3 passes of the study device per vessel. Rescue therapy was permitted if adequate revascularization (TICI > 2b) had not been achieved.

The primary end point of the STAR registry was the revascularization rate (TICI 2b or greater) of the occluded vessel after a maximum of 3 passes of the study device as determined by an independent core laboratory.

SPAN-100 Index

The SPAN index was calculated by adding age in years to the baseline NIHSS score, as described previously.[8] Scores were dichotomized as SPAN-100-positive if the index score was ≥100 and SPAN-100-negative if the index score was <100.

Statistical Analysis

Patients were stratified according to the SPAN-100 index and successful revascularization status. The proportion of patients with favorable clinical outcome (90-day mRS score ≤2) was compared between SPAN-100-positive versus -negative. In addition, the rates of symptomatic hemorrhage and procedure-related complications were compared between the 2 groups. A multivariable logistic regression model was fitted for favorable clinical outcome, adjusting for the SPAN-100 index, successful revascularization, baseline ASPECTS, IV-tPA treatment, and time from symptom onset to revascularization. Statistical analysis was performed in SAS, Version 9.3 (SAS Institute, Cary, North Carolina). All tests were 2-tailed with a prespecified P value of .05.

Role of the Funding Source

The STAR registry was designed by academic principal investigators and had an academic Steering Committee composed of experts in vascular neurology and interventional neuroradiology. An independent Clinical Events Committee was responsible for the review and validation of all complications. The principal investigators and the Steering Committee interpreted the results and wrote the final report of the study. Study management and funding were provided by Covidien Neurovascular. The STAR registry is registered with ClinicalTrials.gov, number NCT01327989.

The current report is a post hoc analysis that is investigator-driven.

RESULTS

Of the 202 patients enrolled, 196 had NIHSS scores at baseline. Fifteen patients (7.7%) had a SPAN index of ≥100. The On-line Table shows the baseline characteristics of the study groups.

As expected, the SPAN-100-positive group was relatively older, with 60% being 80 years of age or older. This group also had a higher prevalence of diabetes mellitus, hypertension, atrial fibrillation, and prior history of myocardial infarction compared with SPAN-100-negative patients. There was no difference in the median baseline ASPECTS or the location of arterial occlusions. There were delays (45 minutes on average) in the time from stroke-symptom onset to groin arterial access for the endovascular procedure in the SPAN-100-positive group.

Outcomes

Successful revascularization was achieved in 88% of patients in the STAR registry (Table 1). This rate was similar in the SPAN-100-positive versus -negative groups (93.3% versus 82.8%, respectively; $P = .3$). Procedure-related complications were not different between the 2 groups. A significantly lower proportion of patients in the SPAN-100-positive group achieved revascularization within 4.5 hours from stroke-symptom onset compared with the SPAN-100-negative group (20% versus 47%, respectively; $P = .043$). There was no difference in the time interval from CT to TICI 2b or 3 or final angiographic run (mean time of 165.7 versus 141.5 minutes in SPAN-100-positive and -negative, respectively; $P = .2$).

While there was a suggestion of a higher incidence of any intracranial hemorrhage in the SPAN-100-positive group (27% ver-

Table 1: Outcome measures

Outcome	Entire Cohort (*N* = 202)	SPAN-100-Positive (*n* = 15)	SPAN-100-Negative (*n* = 181)
Median time from stroke onset to groin puncture (min) (range)	238 (72–714)	280 (140–450)	235 (72–714)
Successful recanalization (after rescue therapy) as per core lab[a]	88% (171/194)	93% (14/15)	87% (151/173)
Median time from stroke onset to TICI 2b or 3 (or final DSA run) (min) (range)	282 (100–800)	322 (188–483)	282 (100–800)
Stroke onset to successful revascularization categories			
0–4.5 hr	46% (92/201)	20% (3/15)	47% (84/180)
4.5–8 hr	50% (101/201)	73% (11/15)	49% (89/180)
≥8 hr	4% (8/201)	7% (1/15)	4% (7/180)
Device- or procedure-related serious adverse events	7% (15/202)	7% (1/15)	8% (14/181)
Any intracranial hemorrhage	19% (38/202)	27% (4/15)	19% (34/181)
Symptomatic intracranial hemorrhage	1% (3/202)	0% (0/15)	2% (3/181)
90-Day clinical outcomes			
Death from any cause	7% (14/202)	27% (4/15)	6% (10/181)
Good functional recovery (modified Rankin Scale score 0–2)	58% (117/202)	27% (4/15)	61% (110/181)

[a] Core laboratory missed the primary end point data of 8 subjects.

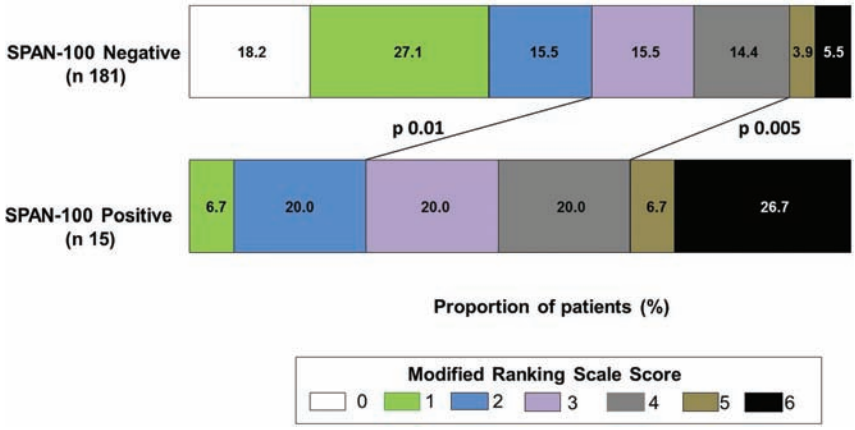

FIG 1. Ninety-day modified Rankin Scale scores. The distribution of 90-day modified Rankin Scale scores among patients according to the SPAN-100 index. The lines indicate the mRS category (mRS 0–2 and mRS 5–6) between SPAN-100 groups. *P* value refers to the significance level of the χ^2 test for proportion comparison.

sus 19% in the SPAN-100-negative group, $P = .5$), none of those patients were symptomatic compared with only 2% symptomatic intracranial hemorrhages in the SPAN-100-negative group.

None of the SPAN-100-positive patients achieved a 90-day mRS score of zero, and only 1 patient (6.7%) achieved an mRS score of 1 (Fig 1; $P = .004$ for the difference in the 90-day mRS of ≤1 between SPAN-100-positive versus -negative). Similarly, a significantly lower proportion of patients in the SPAN-100-positive group achieved a 90-day mRS score of ≤2 compared with the SPAN-100-negative group (26.7% versus 60.8%, respectively; $P = .01$).

In a univariable logistic regression for favorable clinical outcome at 90 days (Table 2), significant predictors were the SPAN-100-positive index (OR = 0.2; 95% CI, 0.1–0.8; $P = .02$), baseline ASPECTS (OR = 1.3; 95% CI, 1.1–1.6; $P = .003$), and time from stroke onset to successful revascularization (OR = 0.7; 95% CI, 0.6–0.8; $P < .001$). When these predictors were analyzed in a multivariable logistic regression model (Table 2), SPAN-100 remained a significant predictor of favorable outcome (OR 0.3; 95% CI, 0.1–0.9; $P = .04$). In addition, the baseline ASPECTS (OR = 1.3; 95% CI, 1.04–1.6; $P = .02$) and time from stroke onset to successful revascularization (OR = 0.7; 95% CI, 0.6–0.8; $P < .001$) were significant. There was no interaction between the SPAN-100 index and time from stroke onset to successful revascularization.

DISCUSSION

Patient selection for endovascular acute ischemic stroke therapy remains a challenge. The relatively high rates of successful revascularization are unable to improve the number of patients with favorable clinical outcomes.[12] This result might be explained, at least in part, by inappropriate patient selection for endovascular interventions. The SPAN-100 index is promising to provide a simple and readily available tool to enhance the patient-selection process. In the STAR registry, we found that patients with a SPAN-100-positive index do not benefit from endovascular therapy to the same extent as patients who are SPAN-100-negative. This effect remains significant even after adjusting for those with a limited extent of ischemic change on baseline CT and a short onset to successful revascularization time.

This is the first study to evaluate the SPAN-100 index in a cohort of patients with acute stroke treated with the most recent and effective endovascular devices, stent retrievers. This analysis may have implications for patient selection for future endovascular randomized trials. The findings highlight the importance of selecting appropriate patients for endovascular therapy and achieving successful revascularization quickly to improve the outcome of acute ischemic stroke. Although SPAN-100-positive patients may still achieve favorable outcome if revascularized quickly, the size of the effect in this patient population is expected to be smaller than that in SPAN-100-negative patients. While there was no difference in the baseline ASPECTS for patients in the SPAN-100-positive versus -negative groups, differences in the extent of collateral circulation in those patients might be relevant. The known association between poor collaterals and older age may account for the lack of efficacy of endovascular therapy in this patient population and indicates the importance of collateral assessment in selecting patients for this therapy. Finally, trials for endovascular therapy beyond 4.5 hours from stroke onset may consider ex-

Table 2: Univariable and multivariable logistic regressions of favorable clinical outcome (mRS ≤2)

Variable	Univariable			Multivariable		
	Odds Ratio	95% CI	*P* Value	Odds Ratio	95% CI	*P* Value
SPAN-100-positive	0.23	(0.07–0.77)	.02	0.25	(0.07–0.91)	.04
Baseline ASPECTS	1.32	(1.10–1.59)	.003	1.28	(1.04–1.58)	.02
Time from stroke onset to TICI 2b or 3 (or final DSA run, hr)	0.70	(0.58–0.84)	<.001	0.68	(0.55–0.84)	<.001
Primary end point success	1.81	(0.82–3.96)	.14	1.73	(0.74–4.03)	.21
IV-tPA administered (vs contraindicated or bridging)	1.05	(0.59–1.87)	.87	1.27	(0.64–2.52)	.49

cluding SPAN-100-positive patients on the basis of the results of this analysis.

The significant difference in functional outcome between the SPAN-100 groups has implications for the outcome measures in endovascular stroke trials. While patients in the SPAN-100-positive group were less likely to have mRS ≤2, the proportion of patients in the intermediate disability categories (mRS 3 or 4) was not different from that in the SPAN-100-negative group. In endovascular trials with no upper age limit for enrollment, patients with a SPAN-100-positive index are likely to be encountered and may dilute any efficacy in the endovascular arm if a dichotomous analysis of outcome is adopted. In these trials, alternative analytic approaches that take into account the entire distribution of the 90-day mRS (eg, shift analysis)[13] might help capture any treatment effect compared with the traditional dichotomous outcome analysis.

This study has limitations. It was based on the nonrandomized STAR prospective registry. Therefore, the effect of endovascular therapy compared with IV-tPA in SPAN-100-positive versus-negative patients could not be assessed. Approximately 8% of the STAR registry patients were SPAN-100-positive. This relatively small number may limit the generalizability of the results. While the multivariable logistic regression identified the SPAN-100 index as a predictor of favorable outcome, rapid revascularization of patients with limited early ischemic changes on baseline imaging may still be of benefit, even with SPAN-100-positive status.

CONCLUSIONS

A significantly lower proportion of patients with a positive SPAN-100 index achieved a favorable outcome at 90 days in this cohort. SPAN-100 was an independent predictor of favorable outcome after adjusting for time to treatment and the extent of preintervention tissue damage according to ASPECTS.

ACKNOWLEDGMENTS

We thank Jill Schafer for her assistance with the statistical analyses.

Disclosures: Antonio Davalos—*RELATED*: *Consulting Fee or Honorarium*: Covidien, *Comments*: moderate, as member of the Steering Committee of the STAR trial, *Support for Travel to Meetings for the Study or Other Purposes*: Covidien, *Comments*: moderate, as member of the Steering Committee of the STAR trial, *UNRELATED*: *Consultancy*: Lundbeck, *Comments*: member of the Steering Committee of the Desmoteplase in Acute Ischemic Stroke (DIAS)3 and DIAS4 trials, *Grants/Grants Pending*: Covidien,* *Comments*: The grant is unrestricted and given to a nonprofit private foundation (Fundació Ictus) in order to finance an academic trial, the Randomized Trial of Revascularization with Solitaire FR, *Payment for Lectures (including service on Speakers Bureaus)*: Lundbeck, *Comments*: member of the Steering Committee of the Desmoteplase in Acute Ischemic Stroke (DIAS)3 and DIAS4 trials. Alain Bonafe—*UNRELATED*: *Consultancy*: Covidien. Rene Chapot—*UNRELATED*: *Consultancy*: Covidien,* MicroVention,* *Travel/Accommodations/Meeting Expenses Unrelated to Activities Listed*: Balt,* MicroVention,* Covidien.* Jan Gralla—*RELATED*: *Consulting Fee or Honorarium*: Covidien,* *Comments*: Global Principal Investigator of the STAR study and consultant. Vitor Mendes Pereira—*RELATED*: *Grant*: Covidien,* *Comments*: Principal Investigator of STAR trial, *UNRELATED*: *Consultancy*: Covidien.* Mayank Goyal—*RELATED*: *Grant*: Covidien/ev3,* *Comments*: funding for the Endovascular Treatment for Small Core and Anterior Circulation Proximal Occlusion with Emphasis on Minimizing CT to Recanalization Times (ESCAPE) trial;, *Consulting Fee or Honorarium:* Covidien/ev3, *Comments*: for teaching engagements and trial design and execution. *Money paid to the institution.

REFERENCES

1. Mukherjee D, Patil CG. **Epidemiology and the global burden of stroke.** *World Neurosurg* 2011;76:S85–90
2. Kidwell CS, Jahan R, Gornbein J, et al. **A trial of imaging selection and endovascular treatment for ischemic stroke.** *N Engl J Med* 2013;368:914–23
3. Broderick JP, Palesch YY, Demchuk AM, et al. **Endovascular therapy after intravenous t-PA versus t-PA alone for stroke.** *N Engl J Med* 2013;368:893–903
4. Ciccone A, Valvassori L, Nichelatti M, et al. **Endovascular treatment for acute ischemic stroke.** *N Engl J Med* 2013;368:904–13
5. Saver JL, Jahan R, Levy EI, et al. **Solitaire flow restoration device versus the Merci retriever in patients with acute ischaemic stroke (SWIFT): a randomised, parallel-group, non-inferiority trial.** *Lancet* 2012;380:1241–49
6. Nogueira RG, Lutsep HL, Gupta R, et al. **Trevo versus Merci retrievers for thrombectomy revascularisation of large vessel occlusions in acute ischaemic stroke (TREVO 2): a randomised trial.** *Lancet* 2012;380:1231–40
7. Weimar C, Konig IR, Kraywinkel K, et al. **Age and National Institutes of Health Stroke Scale score within 6 hours after onset are accurate predictors of outcome after cerebral ischemia: development and external validation of prognostic models.** *Stroke* 2004;35:158–62
8. Saposnik G, Guzik AK, Reeves M, et al. **Stroke prognostication using age and NIH Stroke Scale: SPAN-100.** *Neurology* 2013;80:21–28
9. Rha JH, Saver JL. **The impact of recanalization on ischemic stroke outcome: a meta-analysis.** *Stroke* 2007;38:967–73
10. **Tissue plasminogen activator for acute ischemic stroke: the National Institute of Neurological Disorders and Stroke rt-PA Stroke Study Group.** *N Engl J Med* 1995;333:1581–87
11. Pereira VM, Gralla J, Davalos A, et al. **Prospective, multicenter, single-arm study of mechanical thrombectomy using Solitaire flow restoration in acute ischemic stroke.** *Stroke* 2013;44:2802–07
12. Almekhlafi MA, Menon BK, Freiheit EA, et al. **A meta-analysis of observational intra-arterial stroke therapy studies using the Merci device, Penumbra system, and retrievable stents.** *AJNR Am J Neuroradiol* 2013;34:140–45
13. Saver JL, Gornbein J. **Treatment effects for which shift or binary analyses are advantageous in acute stroke trials.** *Neurology* 2009;72:1310–15

Flow Diversion versus Traditional Endovascular Coiling Therapy: Design of the Prospective LARGE Aneurysm Randomized Trial

A.S. Turk III, R.H. Martin, D. Fiorella, J. Mocco, A. Siddiqui, and A. Bonafe

ABSTRACT

BACKGROUND AND PURPOSE: The goal of aneurysm treatment is occlusion of an aneurysm without morbidity or mortality. Using well-established, traditional endovascular techniques, this is generally achievable with a high level of safety and efficacy. These techniques involve either constructive treatment of the aneurysm (coils with or without an intravascular stent) or deconstruction (coil occlusion) of the aneurysm and the parent artery. While established as safe and efficacious, the constructive treatment of large and giant aneurysms with coils has typically been associated with relatively lower rates of complete occlusion and higher rates of recurrence. Parent artery deconstruction, though immediately efficacious in achieving complete and durable occlusion, does require occlusion of a major intracranial blood vessel and is associated with risk of stroke.

MATERIALS AND METHODS: Flow diversion represents a new technology that can be used to constructively treat large and giant aneurysms. Once excluded successfully, the vessel reconstruction and aneurysm occlusion appears durable. The ability to definitively reconstruct cerebral blood vessels is an attractive approach to these large and giant complex aneurysms and allows the treatment of some aneurysms which were previously not amenable to other therapies. By comparison, conventional coiling techniques have traditionally been used for endovascular treatment of large aneurysms. Large and giant aneurysms that are amenable to either flow diversion or traditional endovascular treatment will be randomized to either therapy with FDA (or appropriate regulatory body) approved devices.

RESULTS: The trial is currently enrolling and results of the data are pending the completion of enrollment and follow-up.

CONCLUSIONS: This paper details the trial design of the LARGE trial, a blinded, prospective randomized trial of large anterior circulation aneurysms amenable to either traditional endovascular treatments using coils or reconstruction with flow diverters.

ABBREVIATIONS: IA = intracranial aneurysms; LARGE = Large Aneurysm Randomized Trial: Flow Diversion Versus Traditional GDC Based Endovascular Therapy

Cerebral aneurysms (ie, intracranial aneurysms [IAs]) are a relatively common cerebrovascular abnormality that has been reported to occur in 0.8%–10.0% of the population.[1-4] The risk of IA rupture has been shown to increase with increasing size.[5,6] The most common presentation of IAs is subarachnoid hemorrhage, the annual incidence of which varies by geographic region from 10 to 20 per 100,000 with a case-fatality rate of 51%.[7,8] For these reasons, most physicians recommend treatment for large (>10 mm), intradural IAs.

Historically, the treatment of very large and giant aneurysms has focused on deconstructive approaches in which the parent artery bearing the aneurysm is occluded, or complex microsurgical procedures requiring flow arrest with clip reconstruction or entailing bypass strategies to distal-downstream cerebral circulation.[9-11] This requires that a patient has ample collateral channels to compensate for the occlusion of the artery supplying the aneurysm and typically this must be confirmed by a test balloon occlusion.[12,13] This method of aneurysm treatment yields an immediate and durable cure of the lesion treated and has been shown to have an acceptable safety profile with morbidity and mortality rates ranging from 0%–16%. These rates appear to be dependent upon rigorous physiologic assessment of collateral circulation reserve using intraprocedural hypotensive challenges and or postprocedural imaging with CBF assessment using SPECT or other modalities. When parent

Received August 29, 2013; accepted after revision November 4.

From the Department of Radiology (A.S.T., R.H.M.), Medical University of South Carolina, Charleston, South Carolina; Department of Neurological Surgery (D.F.), Stony Brook Medicine, Stony Brook, New York; Department of Neurological Surgery (J.M.), Vanderbilt University Medical Center, Nashville, Tennessee; Department of Neurosurgery (A.S.), University of Buffalo, Buffalo, New York; and Department of Neurosurgery (A.B.), Hospital Gui de Chauliac, Centre Hospitalier Universitaire de Montpellier, Montpellier, France.

This research was supported by Codman, Microvention, Penumbra, and Stryker.

Please address correspondence to Aquilla S. Turk, III, DO, Professor, Department of Radiology, Medical University of South Carolina, 96 Jonathan Lucas St, MSC 323, Charleston, SC 29425; e-mail: turk@musc.edu

Indicates article with supplemental on-line table.

http://dx.doi.org/10.3174/ajnr.A3968

vessel deconstruction is used for the treatment of symptomatic aneurysms, the presenting clinical symptoms have been reported to resolve in 75% of cases, improve in 10%, and remain unchanged in 15% of cases.[9] When feasible, deconstructive treatment remains a viable treatment strategy for these lesions.

Currently, the most common endovascular treatment approach to IAs has been constructive endosaccular coil embolization. Despite the popularity of coil embolization for the treatment of IAs, incomplete occlusion of the target IA is surprisingly common, approaching 65% in aneurysms larger than 10 mm.[14-16] Several factors are known to predict the likelihood of complete IA occlusion after constructive treatment with coil embolization. The most important factors predicting incomplete occlusion are overall lesion diameter and neck size. Large and giant IAs and those with wide necks are even less likely to have complete occlusion after coil embolization.[16,17] The presence of intraluminal thrombus is also highly associated with repeated incidences of recurrence and retreatment. Other accepted morphologic predictors of incomplete IA occlusion include aneurysm shape and location. Complete or near complete IA occlusion is the goal of endosaccular aneurysm treatment. Several studies have shown that incomplete occlusion of the target IA is a risk factor for subsequent IA regrowth and retreatment and it is believed that incompletely occluded aneurysms retain their risk for rupture and subarachnoid hemorrhage.[18] The evolution of coil technology and the advent of adjunctive devices such as stents and balloons have greatly facilitated the constructive treatment of large and giant, wide-neck IAs. With modern constructive techniques, peri-procedure morbidity rates for the treatment of these challenging aneurysms has declined from 25% to 2%–11%.[19] Moreover, there are some data to suggest that the application of these adjunctive devices, particularly endoluminal stents, may improve the rates of complete aneurysm occlusion and support the durability of treatment.[20]

Endoluminal aneurysm reconstruction using flow diverters represents a new endovascular approach to IA treatment. Emerging clinical data have shown that this approach may yield considerably higher rates of complete aneurysm occlusion in comparison with traditional endosaccular approaches.[21] The prospective, multicenter, Pipeline for Uncoilable or Failed Aneurysms (PUFS) study that trialed the treatment of large and giant wide-neck carotid aneurysms with the Pipeline embolization device (Covidien, Irvine, California) flow diverter reported complete angiographic occlusion rates approaching 90% at 1-year follow-up.[22]

The recent PUFS data reported a 15% major neurologic adverse event rate and 44% minor adverse event rate with flow diverters. Particularly of concern are unexplained incidences of catastrophic delayed spontaneous ipsilateral intracranial parenchymal hemorrhage and delayed aneurysmal ruptures that have been reported in up to 5% of cases after flow diversion and have not been typically associated with standard endosaccular coil embolization or parent artery deconstruction.[23-25]

To date, no study has directly compared the safety and efficacy of flow diverters with conventional endovascular coil-based techniques for the treatment of large and giant, wide-neck IAs that are amenable to either treatment approach. In this article, we describe the design and methods of a large, ongoing randomized clinical trial (NCT01762137) to assess efficacy and safety of traditional endovascular therapy using coils with or without adjunctive devices in a reconstructive or deconstructive manner versus approved flow-diversion technologies in the treatment of large anterior circulation intracranial aneurysms.

METHODS AND DESIGN

Design

LARGE is an international prospective multicenter trial to compare the safety and efficacy of flow diversion to traditional endovascular techniques for the treatment of anterior circulation large and giant aneurysms. Subjects will be randomized to either flow diversion or endovascular coiling (reconstructive coiling with or without adjunctive devices [stents, balloons] or deconstruction) cohorts in a 1:1 fashion and will be assessed for the primary outcome at 6 months with subsequent outcomes until 3 years from aneurysm repair. The primary objective is to show that flow diversion is noninferior to endovascular coiling at 180 days from aneurysm treatment on the primary end point by less than an absolute difference of 15%. The primary outcome is a combined efficacy and safety end point defined by greater than 90% angiographic occlusion with stable or decreased aneurysm size on cross-sectional imaging (CT or MR) at 180 days postprocedure and freedom from any major neurologic event (defined as change in NIHSS from baseline >4 points) or death at 180 days postprocedure.

Patient Population

The On-line Table shows patient eligibility criteria. Figure 1 shows the flow chart of patients through LARGE. The LARGE trial includes current flow-diversion on-label patients, with aneurysms larger than 1 cm located on the internal carotid artery below the level of the posterior communicating artery. The aneurysm must be amenable to either conventional endovascular therapy or flow diversion according to the operator's discretion. Many patients with large paraclinoid aneurysms present clinically with visual or ocular findings. If the patient's presentation includes any eye signs or symptoms, the patient will be referred for evaluation by a neuro-ophthalmologist preprocedurally.

Randomization

Randomization will occur in a 1:1 ratio to either flow diversion or endovascular coiling. The covariate adaptive randomization balances treatment assignment based on aneurysm location (intradural versus extradural), presence of intraluminal thrombus ("yes" versus "no"), aneurysm shape (saccular versus fusiform), prior balloon test occlusion ("yes" versus "no"), and current status of treatment groups within and across clinical sites. Once the patient is determined to meet all study eligibility criteria, covariate adaptive randomization takes place centrally via the LARGE Study Web site on the WebDCU (https://webdcu.musc.edu).

Treatment

Subjects assigned to coil embolization will undergo treatment of the target IA with endovascular coiling with FDA-approved technologies. Procedures will be performed according to the technology instructions for use. The goal of coil treatment is to completely occlude the IA. Other devices (eg, intravascular balloons ["balloon remodeling"], intravascular stents, dual catheters, etc) may be used adjunctively to deliver or direct coils into the target IA. Alternatively, deconstructive techniques with parent vessel occlusion utilizing en-

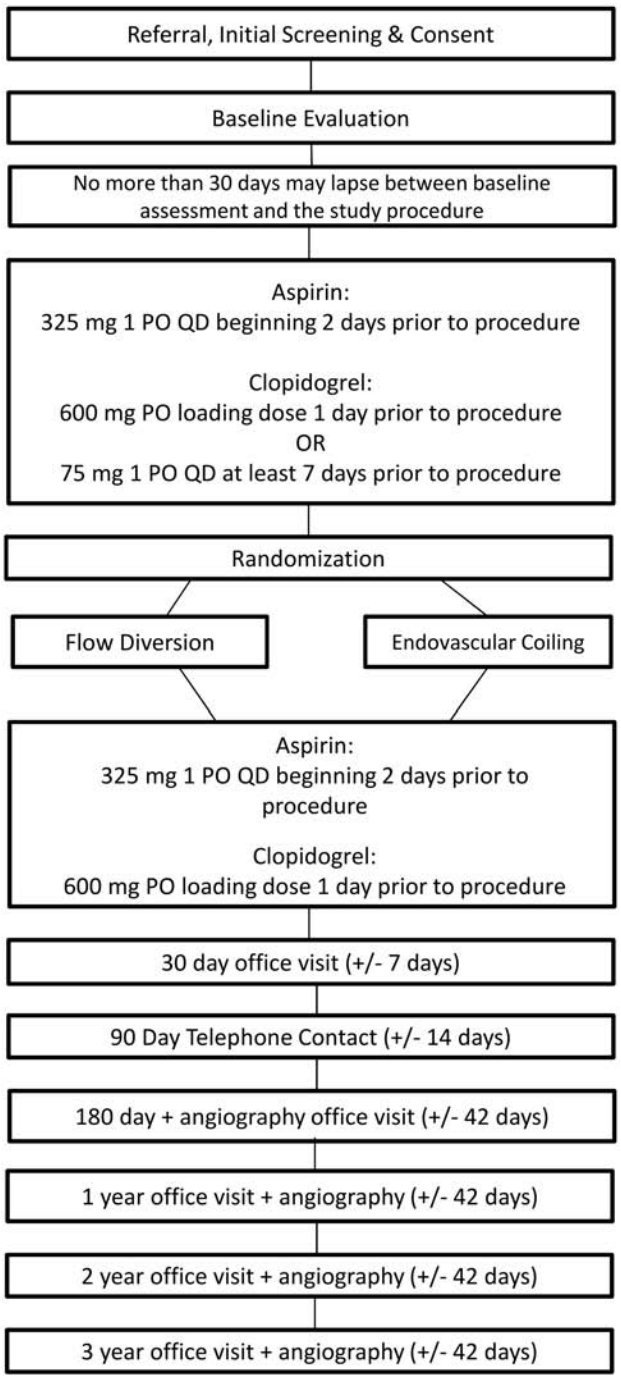

FIG 1. Study flow from referral through follow-up.

dovascular coiling are allowed if this option is felt to be the best treatment technique for the patient. The patient must first successfully pass a balloon test occlusion before vessel occlusion.

Subjects assigned to flow diversion will undergo placement of flow diverter(s) across the target IA. The placement procedure is described briefly in Fig 1 and in more detail in the device instructions for use document. One or more flow diverters may be placed as deemed necessary by the investigator.

Aspirin and clopidrogel are used before flow diverter placement or endovascular coiling embolization. Aspirin is used for at least 1 year after endovascular coiling or flow diverter placement. Clopidogrel is used for at least 3 months after endovascular coiling embolization or flow diverter placement. Aspirin and/or clopidogrel may be used beyond (or at higher doses) than the indicated regimen, if appropriate clinically (eg, patient previously taking aspirin for coronary artery disease prophylaxis).

Primary Outcome

The primary outcome is a dual end point of efficacy and safety. Efficacy is defined as >90% angiographic occlusion with stable (or decreased) aneurysm size on cross-sectional imaging (CT or MR) at 180 days postprocedure. Safety is defined as the patient being free of any major ipsilateral neurologic event (defined as change in NIHSS from baseline >4 points) including ipsilateral neurologic stroke or death at 180 days postprocedure.

Data Safety Monitoring Board

A data safety monitoring board will comprise 4 members not participating in the trial and will include a neuroradiologist, neurologist, neurosurgeon, and statistician. The data safety monitoring board will exercise review of the overall safety of the trial, periodically review all adverse events occurring in the trial, and make recommendations to adjustments in the study protocol, should any be considered necessary for safety or other related reasons.

Sample Size

The sample size of 316 randomized subjects was selected. Sample size was based on the noninferiority design whereby the proportion of success under the endovascular coiling arm (the active control arm) is considered to be 0.75, the noninferiority margin (Δ) is set at 0.15, the type I error is selected to be 0.025, there are 2 interim analyses for futility, a 15% inflation because of potential loss to follow-up, and 80% power.

Statistical Analyses

Statistical analyses are based on a noninferiority trial to test the hypothesis that the efficacy of flow diversion is not worse than that of endovascular coiling by more than a prespecified absolute amount $\delta = 15\%$ (ie, the noninferiority margin or prespecified clinically unimportant difference) for the treatment of large and giant aneurysms. Therefore, rejection of the null hypothesis indicates that the flow diversion is not inferior to the endovascular coiling by this prespecified amount. The primary analysis will be intent-to-treat and will assess efficacy with respect to the proportion of subjects with successful outcome at 180 days postrandomization using a generalized linear model adjusting for baseline aneurysm location (intradural versus extradural), presence of intraluminal thrombus ("yes" versus "no"), aneurysm shape (saccular versus fusiform), and undergoing balloon test occlusion ("yes" versus "no"). The primary approach to handling missing primary outcome data, ie, if a subject has a missing angiogram at the 180-day visit or does not attend the 180-day clinical follow-up visit, will be to consider the subject a treatment failure for the primary effectiveness end point.

Additional potentially confounding variables (ie, sex, race, ethnicity, baseline risk factors) will be considered as covariates in secondary analyses of the primary outcome. Univariate analyses

of these covariates will first be conducted to determine inclusion in the multivariate model.

As specified in the objectives, if noninferiority is demonstrated, then superiority of the safety end point will be assessed. Safety outcomes include the proportion of subjects who experience any treatment-related serious adverse events during the treatment phase and up to 180 days following completion of the treatment. The treatment-related serious adverse events will be considered along with the following:

1. Neurologic deterioration during the hospitalization phase.
2. All deaths by cause (broad categories) within 180 days of randomization.
3. Incidence of neurologic death by 180 days.

A number of secondary analyses will be conducted:

- Incidence of device or procedure related adverse events at 180 days, 1 year, and 3 years.
- Aneurysm rupture or retreatment of index aneurysm rates at 180 days, 1 year, and 3 years.
- Change in clinical functional outcome at 180 days, 1 year, and 3 years postendovascular treatment procedure, as measured by an increase in the modified Rankin Scale from baseline.
- Incidence of worsening of baseline neurologic signs/symptoms as measured by NIHSS or ophthalmologic examination related to target IA at 180 days.
- Number of inpatient hospital (and re-hospitalized) days (subgrouped >7 days) at 180 days, 1 year, and 3 years.
- Packing attenuation as measured by volumetric filling of the aneurysm if aneurysm is coiled.
- Device cost of therapy at treatment and any subsequent retreatment.
- Procedure time, as measured as the time from placement of the treating guide catheter for purposes of aneurysm treatment (not balloon test occlusion) until guide catheter removal.

Prespecified subgroup analyses will also be conducted on clinical and angiographic outcomes for the following:

- Subjects with aneurysms 10–20 mm and >2 cm.
- Intradural versus extradural location.
- Reconstructive versus deconstructive technique.
- Downstream flow-related ischemic stroke, parenchymal hemorrhage, subarachnoid hemorrhage.
- Complete aneurysm occlusion and no neurologic events at 6 months.
- IA neck size ≥4 mm versus <4 mm.
- Current/former smoker versus never smoker.

Technical success, defined as: for flow diversion, the proportion of patients in whom at least 1 attempt was made to pass the access catheter distal to the target IA in whom the final location of placed flow diverters covers the IA neck. For endovascular coiling, the proportion of patients in whom at least 1 attempt was made to pass the access catheter into the target IA fundus (for coil delivery) in whom at least 1 coil was left behind in the target IA. If the plan is for deconstructive treatment, then the parent vessel supplying the artery is occluded without residual flow.

All models will be assessed with and without covariates (age, aneurysm location, etc); this is in keeping with our randomization scheme and is not anticipated to negatively affect the power of the test.

Two protocol-specified interim analyses for futility are planned to be conducted when approximately one-third (n = 105) and two-thirds (n = 210) of the total required number of randomized subjects have been evaluated for the primary outcome. These interim analyses will use the error spending function method with O'Brien and Fleming–type stopping guidelines.[26-28] The error spending function distributes the type I and II error rates across the interim monitoring points giving the flexibility of changing the intervals of monitoring while still preserving the overall type I and II error rates. The O'Brien and Fleming–type boundary is considered conservative as its boundaries make it difficult to terminate a study early on by requiring extreme early evidence of futility. It spends smaller amounts of alpha at the first look and gradually increases the spending as more information is acquired. The trial may be stopped for futility at the planned interim analyses if the test statistic crosses the respective boundaries.

Study Organization and Funding

The trial was funded in November 2012 through a collaborative sponsorship with equal participation from Codman, Microvention-Terumo, Penumbra, and Stryker. Enrollment began in March 2013 and is currently enrolling patients. The trial is international with sites in the United States, Canada, France, Italy, Spain, and Turkey. The clinical and statistical and data coordination for the trial is being conducted at the Medical University of South Carolina in Charleston, SC.

CONCLUSIONS

The LARGE trial is an international prospective, randomized multicenter trial designed to compare the safety and efficacy of conventional endovascular techniques versus flow diversion for the treatment of large and giant aneurysms of the carotid siphon that are amenable to either treatment strategy. The primary outcome is a dual end point of efficacy and safety defined as >90% angiographic occlusion with stable (or decreased) aneurysm size on cross-sectional imaging (CT or MR) at 180 days postprocedure and freedom of any major ipsilateral neurologic event (defined as change in NIHSS from baseline >4 points) including ipsilateral neurologic stroke or death at 180 days postprocedure. Secondary aims follow the primary and secondary outcomes for 3 years. The prespecified subgroup analyses will be performed on aneurysms 10–20 mm and >2 cm, intradural versus extradural location, reconstructive versus deconstructive technique, downstream flow-related ischemic stroke, parenchymal hemorrhage, subarachnoid hemorrhage, complete aneurysm occlusion, no neurologic events at 6 months, and aneurysm neck size ≥4 mm versus <4 mm. Secondary outcomes will evaluate complications such as downstream flow-related ischemic stroke, parenchymal hemorrhage, subarachnoid hemorrhage, aneurysm rupture, or retreatment of index aneurysm rates; change in clinical functional outcome; incidence of worsening of baseline neurologic signs/symptoms as measured by NIHSS or ophthalmologic examination; number of inpatient hospital days; packing attenuation as measured by volumetric filling of the aneurysm if coiled; device

cost of therapy at treatment and any subsequent retreatment; and procedure time. The LARGE trial was designed to enroll 316 patients and have an 80% power to demonstrate that flow diversion is not inferior to conventional endovascular coiling techniques.

Disclosures: Aquilla Turk—*RELATED: Grant:* Penumbra,* Covidien,* MicroVention,* Stryker,* Siemens,* Codman*; *Consulting Fee or Honorarium:* Penumbra, Covidien, MicroVention, Stryker, Siemens, Codman; *Support for Travel to Meetings for the Study or Other Purposes:* Penumbra, MicroVention, Stryker; *Provision of Writing Assistance, Medicines, Equipment, or Administrative Support:* Penumbra,* Covidien,* MicroVention,* Stryker,* Siemens,* Codman*; *UNRELATED: Consultancy:* Penumbra, Covidien, MicroVention, Stryker, Siemens, Codman; *Grants/Grants Pending:* Penumbra,* Covidien,* MicroVention,* Stryker,* Siemens,* Codman*; *Payment for Lectures (including service on speakers bureaus):* Penumbra, Covidien, MicroVention, Stryker, Siemens, Codman; *Travel/Accommodations/Meeting Expenses Unrelated to Activities Listed:* Penumbra, Covidien, MicroVention, Stryker, Siemens, Codman. Renee Martin—*RELATED: Other:* Penumbra,* *Comments*: The Data Coordination Unit (DCU) at the Medical University of South Carolina is receiving funding to support the data management and statistical activities for the LARGE study. As part of the DCU, I am funded for a percentage of my time to participate as the Primary Statistician for the trial. David Fiorella—*RELATED: Grant:* LARGE Trial,* *Comments*: Grant from Medical University of South Carolina; *Consulting Fee or Honorarium:* Codman/JnJ, Covidien/ev3, *Comments*: Consulting/proctoring; *UNRELATED: Grants/Grants Pending:* Stenting versus Agressive Medical Therapy for Intracranial Arterial Stenosis (NIH),* LARGE,* Perfusion Imaging Selection of Ischemic Stroke Patients for Endovascular Therapy,* MicroVention,* Low-profile Visualized Intraluminal Support Post Market Approval,* Siemens*; *Patents (planned, pending or issued):* Codman/JnJ; *Royalties:* Codman/J&J. J Mocco—*UNRELATED: Consultancy:* NFocus, Lazarus Effect, Reverse Medical Pulsar. Adnan Siddiqui—*UNRELATED: Board Membership:* Codman and Shurtleff, Covidien; Comments: Advisory boards; *Consultancy:* Codman and Shurtleff, Concentric Medical, Covidien Vascular Therapies, Guidepoint Global Consulting, Penumbra, Stryker, Pulsar Vascular, Microvention; *Grants/Grants Pending:* The National Institutes of Health (co-investigator: National Institute of Neurological Disorders and Stroke 1R01NS064592-01A1; Hemodynamic Induction of Pathologic Remodeling Leading to Intracranial Aneurysms), University at Buffalo (Research Development Award), The National Institutes of Health (co-investigator: National Institutes of Neurosciences and Hospital 5 R01 EB002873-07, Micro-Radiographic Image for Neurovascular Interventions); *Payment for Lectures (including service on speakers bureaus):* Codman and Shurtleff; *Stock/Stock Options:* Hotspur, Intratech Medical, StimSox, Valor Medical, Blockade Medical; *Other:* Abbott Vascular, for training physicians in endovascular stenting for aneurysms; American Association of Neurological Surgeons' Courses; Penumbra, Comments: Honoraria; *OTHER RELATIONSHIPS:* Serve on National Steering Committees for: Penumbra. 3D Separator Trail and Covidien Solitaire FR as Primary Treatment for Acute Ischemic Stroke Trial. Alain Bonafe—*UNRELATED: Consultancy:* Stryker, MicroVention. **money paid to institution.*

REFERENCES

1. Caranci F, Briganti F, Cirillo L, et al. **Epidemiology and genetics of intracranial aneurysms.** *Eur J Radiol.* 2013;82:1598–605
2. Molyneux A, Kerr R, Stratton I, et al. **International subarachnoid aneurysm trial (ISAT) of neurosurgical clipping versus endovascular coiling in 2143 patients with ruptured intracranial aneurysms: a randomized trial.** *Lancet* 2002;360:1267–74
3. Molyneux AJ, Kerr RS, Yu LM, et al. **International subarachnoid aneurysm trial (ISAT) of neurosurgical clipping versus endovascular coiling in 2143 patients with ruptured intracranial aneurysms: a randomized comparison of effects on survival, dependency, seizures, rebleeding, subgroups, and aneurysm occlusion.** *Lancet* 2005;366:809–17
4. FDA. **Summary FE. P100018: Chestnut medical Pipeline embolization device.** In: Administration FaD, ed. FDA, Washington, DC: Executive Summary; 2011:72
5. International Study of Unruptured Intracranial Aneurysms Investigators. **Unruptured intracranial aneurysms—risk of rupture and risks of surgical intervention.** *N Engl J Med* 1998;339:1725–33
6. Gonzalez N, Sedrak M, Martin N, et al. **Impact of anatomic features in the endovascular embolization of 181 anterior communicating artery aneurysms.** *Stroke* 2008;39:2776–82
7. Byrne JV, Sohn MJ, Molyneux AJ, et al. **Five-year experience in using coil embolization for ruptured intracranial aneurysms: outcomes and incidence of late rebleeding.** *J Neurosurg* 1999;90:656–63
8. Hayakawa M, Murayama Y, Duckwiler GR, et al. **Natural history of the neck remnant of a cerebral aneurysm treated with the Guglielmi detachable coil system.** *J Neurosurg* 2000;93:561–68
9. Clarencon F, Bonneville F, Boch AL, et al. **Parent artery occlusion is not obsolete in giant aneurysms of the ICA. Experience with very-long-term follow-up.** *Neuroradiology* 2011;53:973–82
10. Higashida RT, Halbach VV, Dowd C, et al. **Endovascular detachable balloon embolization therapy of cavernous carotid artery aneurysms: results in 87 cases.** *J Neurosurg* 1990;72:857–63
11. Linskey ME, Sekhar LN, Hirsch W, Jr, et al. **Aneurysms of the intracavernous carotid artery: clinical presentation, radiographic features, and pathogenesis.** *Neurosurgery* 1990;26:71–79
12. Larson JJ, Tew JM, Jr, Tomsick TA, et al. **Treatment of aneurysms of the internal carotid artery by intravascular balloon occlusion: long-term follow-up of 58 patients.** *Neurosurgery* 1995;36:26–30
13. Wong GK, Poon WS, Chun H, et al. **Balloon test occlusion with hypotensive challenge for main trunk occlusion of internal carotid artery aneurysms and pseudoaneurysms.** *Br J Neurosurg* 2010;24:648–52
14. Gallas S, Pasco A, Cottier JP, et al. **A multicenter study of 705 ruptured intracranial aneurysms treated with Guglielmi detachable coils.** *AJNR Am J Neuroradiol* 2005;26:1723–31
15. Murayama Y, Nien YL, Duckwiler G, et al. **Guglielmi detachable coil embolization of cerebral aneurysms: 11 years' experience.** *J Neurosurg* 2003;98:959–66
16. Vinuela F, Duckwiler G, Mawad M. **Guglielmi detachable coil embolization of acute intracranial aneurysm: perioperative anatomical and clinical outcome in 403 patients.** *J Neurosurg* 1997;86:475–82
17. Fernandez Zubillaga A, Guglielmi G, Vinuela F, et al. **Endovascular occlusion of intracranial aneurysms with electrically detachable coils: correlation of aneurysm neck size and treatment results.** *AJNR Am J Neuroradiol* 1994;15:815–20
18. Raymond J, Guilbert F, Weill A, et al. **Long-term angiographic recurrences after selective endovascular treatment of aneurysms with detachable coils.** *Stroke* 2003;34:1398–403
19. Ortiz R, Song J, Niimi Y, et al. **Rate of recanalization and safety of endovascular embolization of intracranial saccular aneurysms framed with GDC 360 coils.** *Interv Neuroradiol* 2008;14:397–401
20. Fiorella D, Hsu D, Woo HH, et al. **Very late thrombosis of a Pipeline embolization device construct: case report.** *Neurosurgery* 2010; onsE313–314; discussion onsE314
21. Fiorella D, Lylyk P, Szikora I, et al. **Curative cerebrovascular reconstruction with the Pipeline embolization device: the emergence of definitive endovascular therapy for intracranial aneurysms.** *J Neurointerv Surg* 2009;1:56–65
22. Becske T, Kallmes DF, Saatci I, et al. **Pipeline for uncoilable or failed aneurysms: results from a multicenter clinical trial.** *Radiology* 2013;267:858–68
23. Kawanabe Y, Sadato A, Taki W, et al. **Endovascular occlusion of intracranial aneurysms with Guglielmi detachable coils: correlation between coil packing density and coil compaction.** *Acta Neurochir (Wien)* 2001;143:451–55
24. Reul J, Spetzger U, Weis J, et al. **Endovascular occlusion of experimental aneurysms with detachable coils: influence of packing density and perioperative anticoagulation.** *Neurosurgery* 1997;41:1160–65; discussion 1165–68
25. Tamatani S, Ito Y, Abe H, et al. **Evaluation of the stability of aneurysms after embolization using detachable coils: correlation between stability of aneurysms and embolized volume of aneurysms.** *AJNR Am J Neuroradiol* 2002;23:762–67
26. O'Brien PC, Fleming TR. **A multiple testing procedure for clinical trials.** *Biometrics* 1979;35:549–56
27. Pampallona STA, Kim KM. **Interim monitoring of group sequential trials using spending functions for the Type I and Type II error probabilities.** *Drug Inf J* 2001;35:1113–21
28. Pocock SJ. **Statistical and ethical issues in monitoring clinical trials.** *Stat Med* 1993;12:1459–69; discussion 1471–55

Use of Flow-Diverting Devices in Fusiform Vertebrobasilar Giant Aneurysms: A Report on Periprocedural Course and Long-Term Follow-Up

L. Ertl, M. Holtmannspötter, M. Patzig, H. Brückmann, and G. Fesl

ABSTRACT

BACKGROUND AND PURPOSE: Fusiform vertebrobasilar giant aneurysms are a rare (<1% of all intracranial aneurysms) but challenging aneurysm subtype. Little data are available on the natural history of this aneurysm subtype and the impact of the use of flow-diverting stents on the long-term clinical and imaging follow-up. In this article, we present our experience with the treatment of fusiform vertebrobasilar giant aneurysms by flow diverting stents. We aim to stimulate a discussion of the best management paradigm for this challenging aneurysm subtype.

MATERIALS AND METHODS: We retrospectively identified 6 patients with fusiform vertebrobasilar giant aneurysms who had been treated with flow-diverting stents between October 2009 and March 2012 in our center. The available data were re-evaluated. The modified Rankin Scale score was assessed before intervention, during the stay in hospital, and at discharge.

RESULTS: Six patients were identified (all male; age range, 49–71 years; median age, 60 years). Handling of material was successful in all cases. No primary periprocedural complications occurred. The mean follow-up was 13 months (15 days to 29 months). During follow-up, 3 of 6 patients had recurrent cerebral infarctions, but no patient experienced SAH. Two patients presented with acute thrombotic stent occlusion. The modified Rankin Scale score was not higher than 3 in any of the cases before intervention, whereas the best mRS score at the last follow-up was 5. Four of 6 patients died during follow-up.

CONCLUSIONS: Endovascular treatment of fusiform vertebrobasilar giant aneurysms with flow-diverting devices is feasible from a technical point of view; however, changes in hemodynamics with secondary thrombosis are not predictable. We currently do not intend to treat fusiform vertebrobasilar giant aneurysms with flow-diverting devices until we have further understanding of the pathophysiology, natural history, and hemodynamic effects of flow diversion.

ABBREVIATIONS: ASA = acetylsalicylic acid; FVBGA = fusiform vertebrobasilar giant aneurysm

Fusiform vertebrobasilar giant aneurysms (FVBGAs) are a rare but important and challenging aneurysm subtype. The incidence of FVBGAs is estimated to be only <1% of all intracranial aneurysms.[1-12] Little is known about the natural history of FVBGAs, but the data available indicate poor outcome and continuous progression of aneurysm size and related symptoms (brain stem compression, brain stem ischemia, subarachnoid hemorrhage in particular).[13,14]

The treatment of FVBGAs presents enormous challenges. Complex treatment objectives include prevention of hemorrhage, control of thromboembolic complications, and relief of mass effect.[15] Anatomic predispositions limit therapeutic options to an endovascular approach with preservation of the parent artery and perforators.[15] Flow-diverting stents, a new option in endovascular therapy specifically designed for endovascular reconstruction of circumscript segments of the main brain-supplying arteries, seem to be a therapeutic option. However little is known about the potential limitations and threats in the application of these devices in the vertebrobasilar arterial system.[16-18]

It is, thus, extremely difficult to decide whether to treat FVBGAs with flow-diverting devices. In this article, we present our experience with the treatment of FVBGAs by flow-diverting stents and the long-term clinical and imaging follow-up. We aim to

Received August 29, 2013; accepted after revision November 4.

From the Department of Neuroradiology (L.E., M.P., H.B., G.F.), Institute of Clinical Radiology, Grosshadern Campus, University of Munich, Munich, Germany; and Center for Diagnostic Radiology (M.H.), Department of Neuroradiology, Rigshospitalet, University of Copenhagen, Copenhagen, Denmark.

Paper previously presented in part at: 47th Annual Meeting of the German Society of Neuroradiology, October 11–13, 2012; Cologne, Germany.

Please address correspondence to Lorenz Ertl, MD, Department of Neuroradiology, University of Munich, Grosshadern Campus, Marchioninistr 15, D-81377 Munich, Germany; e-mail: lorenz.ertl@med.uni-muenchen.de

http://dx.doi.org/10.3174/ajnr.A3859

Table 1: Treatment & primary periprocedural complications

No.	Material	Several Sessions	Additional Coiling	Primary Periprocedural Complications
1	6 × Pipeline	No	No	No
2	2 × Silk, 3 × LEO	No	No	No
3	2 × Silk, 7 × LEO+	Yes	No	No
4	2 × Silk, 3 × LEO	No	Yes	No
5	4 × Silk, 4 × LEO+	Yes	Yes	No
6	3 × Silk	No	No	No
Ratio		2/6	2/6	0/6

stimulate a discussion of the best management paradigm for this challenging aneurysm subtype.

MATERIALS AND METHODS

Patient Selection

We retrospectively reviewed the endovascular data base at the University of Munich Hospital, Großhadern Campus, and identified 6 patients with FVBGAs who had been treated between October 2009 and March 2012 with either Pipeline Embolization Devices (ev3, Irvine, California) or Silk flow-diverting stents (Balt Extrusion, Montmorency, France) (Table 1).

Data Collection and Interpretation

The available data, consisting of imaging and patient reports, were re-evaluated by 3 experienced neuroradiologists. Patient reports were reviewed to assess the preinterventional modified Rankin Scale scores[19,20] and the clinical course, including symptoms before intervention, during the hospital stay, and at discharge. Additionally, patients or relatives were interviewed in our outpatient clinic or contacted by telephone to determine clinical symptoms during follow-up, current modified Rankin Scale scores and/or cause of death.

Follow-up imaging reviewed consisted of digital subtraction angiography and MR imaging examinations performed on a 3T scanner (Signa HDxt; GE Healthcare, Milwaukee, Wisconsin), including gradient-echo, diffusion-weighted imaging, T2WI and T1WI (with or without gadolinium), T2-weighted fluid-attenuated inversion recovery, and MR vascular imaging (3D time-of-flight angiography and contrast-enhanced MR angiography). All images were re-evaluated with special regard to aneurysm size and location, intraluminal thrombus formation, stent patency, territorial ischemia, and/or intracranial hemorrhage.

Primary periprocedural complications were defined as any technical problems in the delivery of the device or as any clinical deterioration observed within the first 24 hours after the procedure. Due to the retrospective study design, institutional review board approval was not obtained.

Indications and Decision-Making Process

In all cases, the indication for an interventional approach was the result of an individual patient-based and interdisciplinary decision-making process. Endovascular therapy by flow diversion was considered in patients with acute or chronically deteriorating brain stem symptoms due to FVBGAs in combination with a high psychological strain on the patient. These patients were presented for discussion at a weekly case conference attended by neurosurgeons, neuroradiologists, vascular surgeons, neurologists, and radiotherapists.

An interdisciplinary decision in favor of an endovascular approach led to an honest, transparent, and open-outcome discussion with the patient and family, in which the current state of information was clearly presented. The discussion included the probably poor natural history of the disease and any complications associated with all methods of treatment. All patients were made aware that the use of flow-diverting stents in this aneurysm subtype was not a firmly accepted therapeutic paradigm but an individualized investigational therapeutic approach. During the observation period, all patients were put on acetylsalicylic acid (ASA), 100 mg/day. All patients received the best medical treatment to control other cardiovascular risk factors (hypertension and hypercholesterolemia in particular).

Periprocedural Management

All procedures were performed with the patient under intubation anesthesia conditions. Activated clotting time was continuously measured and elevated on a level of >200 seconds by heparin during the entire procedure. Adjunctive coiling to assist thrombosis of the aneurysm was performed when appropriate during the intervention. After the procedure, all patients were kept under surveillance, including continuous blood pressure monitoring, for at least 24 hours in a neurosurgical or neurologic intensive care unit.

All patients underwent a standardized closely monitored antiplatelet medication regimen. Tirofiban (Aggrastat) was intravenously administered with a loading dose of 0.4 μg/kg/min for 30 minutes followed by a maintenance dose with a continuous perfusion rate of 0.1 μg/kg/min. At 12:00 AM on the first postinterventional day, 300-mg clopidogrel and 100-mg ASA were given orally, whereas 4 hours later (04:00 AM), tirofiban infusion was stopped. Therapeutic responses to tirofiban, clopidogrel, and ASA were monitored by Multiplate (Roche Diagnostics International, Rotkreuz, Switzerland) testing performed 15 minutes after the beginning of the tirofiban infusion, at the end of the intervention, and at 10:00 AM on first postinterventional day. During follow-up, a combination of clopidogrel, 75 mg/day, and ASA, 100 mg/day, was given for a minimum of 6 months followed by a life-long therapy with ASA, 100 mg/day (Table 2).

Study Devices

Flow-diverting devices consist of a flexible, microcatheter-delivered, self-expanding, endovascular "stentlike" construct intended to create a laminar flow pattern in the parent artery and secondary thrombosis within the aneurysm, while keeping open the arterial perforators.[21] Patients in this case series were treated with either Pipeline or Silk devices, the latter partially in a "telescoping technique,"[22] combining LEO (Balt Extrusion) and Silk stents (Table 1).

Table 2: Antiplatelet regimen timeline

Observation Period	Intervention		Day 1 after intervention			Follow-Up Period
	Delivery of the First Stent	During Intervention	12:00 AM	4:00 AM	10:00 AM	
ASA 100 mg/day	Tirofiban (Aggrastat) i.v.,	Multiplate test	Clopidogrel 300 mg p.o.	Tirofiban (Aggrastat) i.v., stopped	Multiplate test	1) First 6 months clopidogrel 75 mg/day and ASA 100 mg/day
	1) loading dose, 0.4 μg/kg/min (30 min),	1) 15 min after tirofiban start,	ASA 100 mg p.o.		ASA response? clopidogrel response?	2) lifelong therapy ASA 100 mg/day
	2) maintenance dose, 0.1 μg/kg/min	2) end of the intervention, tirofiban response?				

Note:—p.o. indicates by mouth; i.v., intravenous.

Table 3: Clinical characteristics of the patients

No.	Sex	Age (yr)	Symptoms Leading to Intervention
1	M	64	Left-sided hemiplegia and facial nerve paresis, line-of-sight nystagmus to the left, dysarthria, dysphagia
2	M	71	Diplopia, insecure gait, progressive aneurysm size, fear of death
3	M	65	Progressive right-sided hemiparesis, increasingly insecure gait with recurrent falls, clumsiness, and sensory deficits in the right upper extremity
4	M	58	Recurrent episodes of dizziness, headache, tinnitus, sensory deficits in right arm and limb and acute prepontine SAH
5	M	54	Persistent central oculomotor disorder, progressive dysarthria, and latent monoparesis of the right limb
6	M	49	Diplopia due to abducens nerve paresis, dysphagia, hypesthesia of left face and hand, dysarthria, instable gait
Mean age (range)		60 (49–71)	

Table 4: Anatomical and clinical findings during observation period

No.	Aneurysm Location and Size (cm)		Time between Initial Diagnosis and Procedure (mo)	Territorial Infarct Prior to Procedure	SAH Prior to Procedure
1	BA/V4	2.2	8	Yes, pontomedullary	No
2	BA	2.8	48	No	No
3	BA/V4	2.0	13	Yes, pericallosal	No
4	BA/V4	1.3	4	No	Yes
5	BA	3.0	29	Yes, brain stem	No
6	BA/V4	2.1	3	Yes, brain stem	No
Mean (range, ratio)		2.23 (1.3–3)	17.5 (3–48)	4/6	1/6

Note:—BA indicates basilar artery.

RESULTS

Patient Collective

Six patients were identified. They were all male. Age at the time of the decision to intervene ranged from 49 to 71 years (median, 60 years). Patients presented with a heterogeneous set of symptoms, mostly consistent with progressive brain stem dysfunction and compatible with the specific anatomic shape, size, and position of the underlying aneurysm in all cases (Table 3). In 4 patients (patients 1, 3, 5, and 6), there was evidence of territorial infarction in preinterventional MR imaging. With the exception of patient 3, in whom the infarct was located in the vascular territory of the left posterior pericallosal artery (>10 years ago), all infarcts were either in a brain stem or pontomedullary location (Table 3).

Only 1 patient (patient 4) had a FVBGA-induced acute subarachnoid hemorrhage during the observation period. Most interesting, the patient presented with a Glasgow Coma Scale score of 14, when referred to our emergency department. In this case, the presence of an SAH was the determining factor in the decision to intervene (Tables 3 and 4). The wide range of observation periods (mean, 17.5 months; range, 3–48 months) was the result of the individualized decision-making process, mainly driven by individual clinical deterioration and changes in aneurysm shape and size (Table 4). All aneurysms were located in the basilar artery, 4 extending into the V4 segment of the left vertebral artery (patients 1, 3, 4, and 6). The maximum aneurysm diameter was 2.23 cm on average, ranging from 1.3 to 3.0 cm (Table 4).

Intervention and Primary Periprocedural Complications

The material and periprocedural course are summarized in Table 3. Four patients (patients 2, 3, 4, and 5) were treated with a combination of Silk and LEO or LEO+ stents in a "telescoping technique" to provide a scaffold of support. Patient 1 was treated with a series of overlapping Pipeline Embolization Devices, and patient 6 was treated solely with Silk stents (Table 1). In 2 patients (patients 4 and 5), the V4 segment of the right vertebral artery was occluded directly at the anatomic intersection to the basilar artery by coiling due to its contribution to the aneurysm supply. In 2 cases (patients 3 and 5), the procedure was split into 3 sessions on consecutive days to achieve optimum results of the flow-diversion effect (Table 1). The detachment of the stents and handling of material were successful in all cases. No primary periprocedural complications, according to our definition, were observed within the first 24 hours after the intervention (Table 1). No nonresponders on tirofiban, ASA, or clopidogrel were detected in Multiplate testing.

Secondary Complications and Follow-Up

Secondary complications and follow-up are summarized in Tables 5 and 6. Three of 6 patients (patients 3, 4, and 5) had recurrent cerebral infarctions in anatomic locations shown in Table 5. No patient experienced SAH during follow-up (Table 4). In all except 1 patient (patient 6), thrombotic occlusion of the aneurysm outside the stent was continuously progressive but incomplete during follow-up (Table 5).

Table 5: Secondary complications during follow-up

No.	Territorial Ischemia during FU	SAH during FU	Complete Aneurysmal Thrombotic Occlusion	Stent Occlusion during FU
1	No	No	No	No
2	No	No	No	No
3	Yes, brain stem	No	No	Stent occlusion (day 9) → successful recanalization
4	Yes, brain stem/cerebellum, thalamus/pontomedullary	No	No	Stent occlusion (day 32) → successful recanalization
5	Yes, brain stem/cerebellum	No	No	No
6	No	No	Yes	No
Ratio	3/6	0/6	1/6	2/6

Note:—FU indicates follow-up.

Table 6: Follow-up and clinical outcome

No.	Duration Follow-Up	mRS Prior to Procedure	mRS Last Follow-Up	Cause of Death
1	17 mo	3	6	Brain stem compression (due to secondary pneumonia)
2	5 mo	3	6	Cardiac
3	12 days	2	6	Locked-in syndrome, dismissal of therapy at the request of the patient and relatives
4	17 mo	1	5	–
5	29 mo	3	5	–
6	9 mo	3	6	Brain stem compression
Mean (range)	13 mo (0.5–29 mo)			

Note:—mRS indicates modified Rankin Scale score.

Stents remained patent in most cases; however, 2 patients (patients 3 and 4) presented with acute thrombotic stent occlusion on days 9 and 32, respectively. Immediate interventional recanalization procedures were performed successfully; however, residual neurologic deficits were persistent in both cases (Table 5). In particular, growing thrombus formation led to an in-stent thrombosis (~80%) at the upper part of the stent construct of patient 3. Neither local thrombolysis with 20-mg rtPA nor direct aspiration maneuvers showed significant effects. Partial recanalization of the stent construct could finally be achieved by using a 6 × 3 cm Solitaire stent-retriever system (Covidien, Irvine, California). However, the final result showed an entry/re-entry flow pattern, which bypassed persistent in-stent stenosis via the nonthrombosed superior aneurysm part. Patient 4 presented with thrombotic occlusion of the proximal stent construct ranging from the V4 segment of the left vertebral artery into the middle basilar artery. Local thrombolysis with a total of 25-mg rtPA for 30 minutes and a singular aspiration maneuver resulted in complete recanalization of the stent and all arteries.

Follow-up was 13 months on average, ranging from 15 days to 29 months (Table 6). The mRS score was not higher than 3 in any of the cases before intervention, whereas the best mRS score at the last follow-up was 5. As indicated in Table 6, four patients died during follow-up. In 2 cases, the clinical course and MR imaging indicated progressive brain stem compression leading to neurologic deficits. Related secondary pneumonia was the cause of death in patient 1. Patient 2 died during the follow-up period due to a malignant cardiac arrhythmia and myocardial failure. Patient 3 had an extremely poor course with recurrent ischemia and thrombotic stent occlusion on day 9 after primary intervention. Despite a successful recanalization procedure, bilateral pontomedullary infarcts remained, leading clinically to a locked-in-syndrome. The patient died on day 15 after the primary procedure (Tables 5 and 6).

DISCUSSION

FVBGAs still represent a worst case scenario for both patient and physician. Data available on the natural history of this disease suggest a progressive and fatal clinical course. The mortality rate is 23%–35% during 5 years.[14,23,24] Death is mainly caused by cerebral infarction and brain stem compression, with spontaneous ruptures and consecutive subarachnoid hemorrhage occurring rather infrequently (0.9%–2.3% a year).[14,24,25] The recent literature mentioned above represents the best available evidence to underpin therapeutic decisions. Mainly due to the rare occurrence of this type of fusiform aneurysm disease, the literature only consists of case series. Despite their important impact on clinical decision-making, the evidence level of these publications is thus limited.

The specific anatomic feature of the basilar artery with its multisegmental supply of the brain stem by numerous perforating branches rules out a vessel-occluding therapeutic approach. Previous treatment effort, surgical or endovascular, including proximal vessel occlusion with or without bypass could not resolve this problem. Despite aggressive surgical treatment, the long-term outcome remains poor for most patients.[26]

Flow-diverting stents, available since 2007, seemed to be a therapeutic option. Data available in the literature on the use of flow-diverting stents, mostly case series, gave rise to optimism. In a series by Phillips et al,[27] 32 aneurysms of the posterior circulation were treated with flow-diverting stents. Mean aneurysm size was 9.7 mm. Twenty aneurysms classified as fusiform, blister, sidewall, or dissecting were included. The authors reported a complete occlusion rate of 96% in a follow-up of >12 months. Fischer et al[28] reported complete occlusion rates of 74% in combination with 4.54% morbidity and 2.27% mortality in a cohort of 88 patients (mean aneurysm size, 3.8 mm; 22% posterior circulation). They included 63 (62%) saccular aneurysms, 33 (33%) fusiform aneurysms, and 5 (5%) dissections. Finally, McAuliffe et

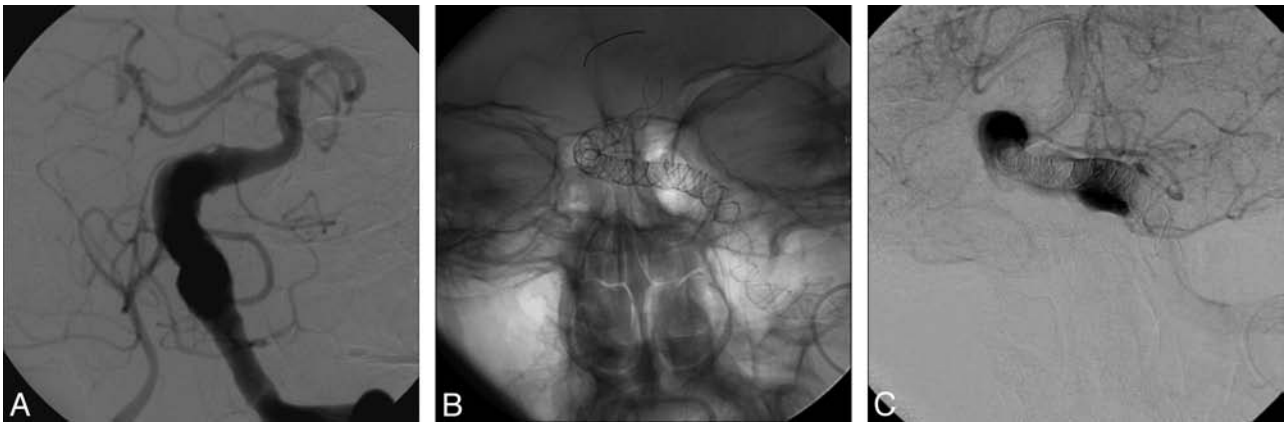

FIG 1. *A*, Patient 4, primary intervention. Anteroposterior view of a vertebral artery angiogram shows an FVBGA involving the distal V4 segment of the left vertebral artery. *B*, Patient 4, primary intervention. Anteroposterior view of a vertebral artery angiogram demonstrates the final stent position. *C*, Patient 4, primary intervention. Anteroposterior view of a vertebral artery angiogram shows patency of the stents with adjacent contrast agent pooling, indicating hemostasis inside the aneurysm.

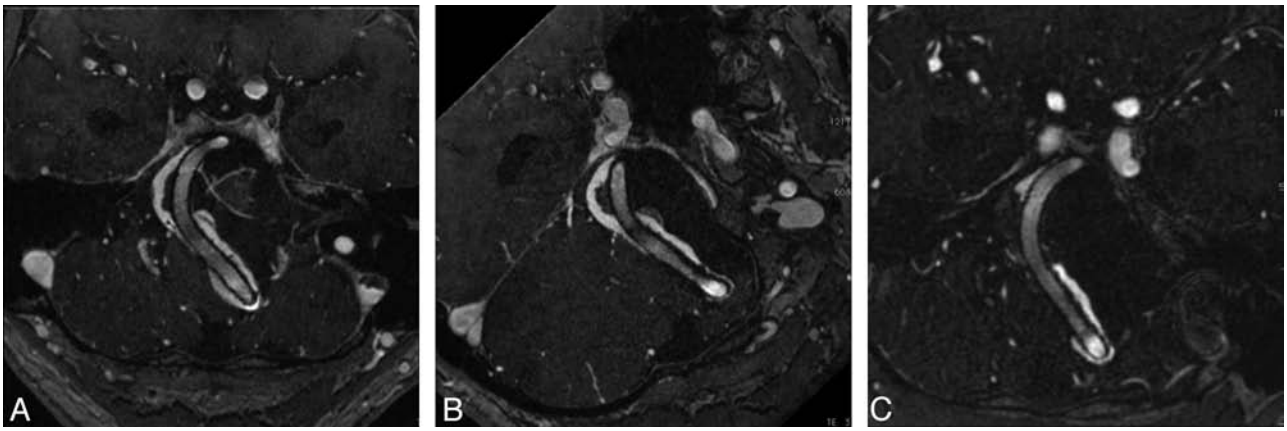

FIG 2. *A*, Patient 4, MR imaging during follow-up. Transverse contrast-enhanced MR angiography on day 3 after intervention shows patency of the stents with adjacent thrombus formation inside the aneurysm. *B*, Patient 4, MR imaging during follow-up. Transverse contrast-enhanced MR angiography on day 8 after the intervention shows patency of the stents with progressive-yet-incomplete thrombus formation inside the aneurysm. *C*, Patient 4, MR imaging during follow-up. Transverse contrast-enhanced MR angiography on day 39 after the intervention shows patency of the stents with progressive yet incomplete thrombus formation inside the aneurysm.

al[29]reported 54 cases (19% posterior circulation; mean aneurysm size, 13.1 mm) with a complete occlusion rate of 85.7% in a 6-month follow-up in combination with 0% morbidity and 0% mortality.

However, the problem with all these publications is that a statistically relevant extrapolation of data on the anatomic subtype of FVBGA is not feasible. Of the total of 32 aneurysms in the posterior circulation in the article by Phillips et al,[27] only 8 were located in the basilar trunk. No detailed information on aneurysm morphology or giant subtype was provided. Fischer et al[28] did not specifically address this aneurysm subtype. Furthermore, only 50% of their baseline collective had a 10-month follow-up. In the collective of McAuliffe et al,[29] no differentiated information on performance of flow diverters in FVBGAs was provided and the total follow-up of all cases was not longer than 6 months. To sum up, despite positive results on the use of flow-diverting stents in other aneurysm types and/or anatomic locations, little has been reported on the complication rate of flow-diverting stents in the FVBGA subtype.

Siddiqui et al[30] reported specifically on flow diversion in the treatment of large or giant fusiform vertebrobasilar aneurysms. The authors presented their initial results with this therapy approach, including significant morbidity and mortality encountered. Of the 7 patients treated with flow-diversion devices, 4 died. The authors "have opted to cease treating most large aneurysms of the entire basilar artery with flow-diversion techniques" until they "can gain further understanding of the hemodynamic effects on brain stem perforators."[30]

Meckel et al[31] also reported on 10 patients treated with flow-diverting stents in complex aneurysms at the vertebrobasilar junction. Six patients had a large or giant aneurysm of the fusiform subtype. Four of these 6 patients died during follow-up, and 1 of the remaining 2 patients was "lost to further follow-up after 6 months."

The preinterventional clinical course of our patients—some under observation for up to 4 years—continuously deteriorated and finally resulted in an interdisciplinary, patient-specific decision in favor of an experimental endovascular therapeutic approach. All patients were exposed to a high load of psychological strain and endured their chronically deteriorating disease with a poor history. Even if we cannot quantify this factor by means of a

scored survey, it is not negligible because it represents a human factor in the decision-making process.

Primary procedural success was remarkably good, and the procedural complication rate was very low. As shown in Table 1, no technical problems occurred during deployment of the stents. Stent implantation and periprocedural management were performed according to all principles of good clinical practice and in line with the recommendations of the manufacturer. As indicated in Fig 1*A–C*, flow diversion with deceleration of blood flow in the aneurysm outside the implanted devices was demonstrable in all cases (Fig 1*A–C*). In addition, no clinical complications were observed within the first 24 hours after the initial intervention (Table 1).

However, the clinical course in the further follow-up was extremely poor. In 2 cases, stent occlusion occurred on days 9 and 32 (patients 3 and 4, respectively), leading to an immediately life-threatening thrombotic occlusion of the basilar artery. Despite immediate medical and endovascular interventions, both patients had persistent grave neurologic deficits. Patient 3 was "locked-in" after this incident and died on day 15 after the primary intervention.

As shown in Fig 2*A–C*, thrombotic occlusion of the primary aneurysm was progressive but incomplete in 5 of 6 cases (Table 5 and Fig 2*A–C*). After a mean follow-up of 13 months, 4 of 6 patients had died. With an mRS score of 5 in the last follow–up, the remaining 2 patients also showed an extremely poor outcome compared with their preinterventional mRS values of 1 and 3, respectively (patients 4 and 5, Table 6).

Although we cannot prove this statement, the clinical course in all cases was presumably worse than the known evidence-based data would suggest for the spontaneous natural history of the disease. Two patients died because of progressive mass effect of their FVBGAs in long-term follow-up. Steroidal treatment and other antiedema therapy always should be considered, of course, but in our cases, unfortunately, they were unable to stop continuous aneurysm growth and aggravating brain stem compression. Treatment with anticoagulants may seem to be justified in light of the high risk of ischemic stroke. However, the increased risk of intracranial hemorrhage might cause complications as well. Hence, no definite statement on medical treatment can be given.[32]

An important limitation of our data needs to be discussed: The monocentric approach with 6 patients does not allow statistically valuable conclusions. However, because there are only a few publications on the use of flow-diverting stents in fusiform vertebrobasilar aneurysms in the literature, we consider our findings to be an important message to the neurointerventional community.

CONCLUSIONS

Endovascular treatment of FVBGAs with flow-diverting devices is feasible from a technical point of view and did not cause any immediate periprocedural complications. However, changes in hemodynamics with secondary thrombosis are not predictable. The patency of brain stem perforators intended to have continuing ability to draw blood through the flow-diversion devices cannot be guaranteed. Evidence on the natural history of this aneurysm subtype is poor; this knowledge hinders treatment decisions. Despite all limitations, we believe that out treatment effort worsened rather than positively affected the individual prognosis of our patients. In accordance with other authors, we currently do not intend to treat fusiform vertebrobasilar giant aneurysms with flow-diverting devices until we have gained further understanding of the pathophysiology, natural history, and hemodynamic effects of flow-diversion devices on FVBGAs. We strongly encourage the publication of the experiences of other centers of this challenging and yet not appropriately treatable aneurysm subtype.

Disclosures: Markus Holtmannspötter—*UNRELATED*: *Consultancy*: Covidien, MicroVention, Sequent Medical, *Comments*: proctor and consultant for Covidien/ev3 and Sequent Medical, consultant for MicroVention, *Payment for Lectures (including service on Speakers Bureaus)*: Covidien, MicroVention, Sequent Medical, *Travel/Accommodations/Meeting Expenses Unrelated to Activities Listed*: Codman, Stryker.

REFERENCES

1. Miller JD, Jawad K, Jennett B. **Safety of carotid ligation and its role in the management of intracranial aneurysms.** *J Neurol Neurosurg Psychiatry* 1977;40:64–72
2. Lawton MT, Spetzler RF. **Surgical strategies for giant intracranial aneurysms.** *Neurosurg Clin N Am* 1998;9:725–42
3. Sadik AR, Budzilovich GN, Shulman K. **Giant aneurysm of middle cerebral artery: a case report.** *J Neurosurg* 1965;22:177–81
4. McCormick WF, Acosta-Rua GJ. **The size of intracranial saccular aneurysms: an autopsy study.** *J Neurosurg.* 1970;33:422–27
5. Drake CG. **Giant intracranial aneurysms: experience with surgical treatment in 174 patients.** *Clin Neurosurg* 1979;26:12–95
6. Hosobuchi Y. **Direct surgical treatment of giant intracranial aneurysms.** *J Neurosurg* 1979;51:743–56
7. Locksley HB, Sahs AL, Sandler R. **Report on the cooperative study of intracranial aneurysms and subarachnoid hemorrhage. 3. Subarachnoid hemorrhage unrelated to intracranial aneurysm and A-V malformation—a study of associated diseases and prognosis.** *J Neurosurg* 1966;24:1034–56
8. Pia HW, Zierski J. **Giant cerebral aneurysms.** *Neurosurg Rev* 1982;5:117–48
9. Rinne J, Hernesniemi J, Niskanen M, et al. **Analysis of 561 patients with 690 middle cerebral artery aneurysms: anatomic and clinical features as correlated to management outcome.** *Neurosurgery* 1996;38:2–11
10. Drake CG, Peerless SJ. **Giant fusiform intracranial aneurysms: review of 120 patients treated surgically from 1965 to 1992.** *J Neurosurg* 1997;87:141–62
11. German WJ, Black SP. **Intra-aneurysmal hemodynamics-jet action.** *Circ Res* 1955;3:463–68
12. Choi IS, David C. **Giant intracranial aneurysms: development, clinical presentation and treatment.** *Eur J Radiol* 2003;46:178–94
13. Flemming KD, Wiebers DO, Brown RD Jr, et al. **Prospective risk of hemorrhage in patients with vertebrobasilar nonsaccular intracranial aneurysm.** *J Neurosurg* 2004;101:82–87
14. Flemming KD, Wiebers DO, Brown RD Jr, et al. **The natural history of radiographically defined vertebrobasilar nonsaccular intracranial aneurysms.** *Cerebrovasc Dis* 2005;20:270–79
15. Gonzalez NR, Duckwiler G, Jahan R, et al. **Challenges in the endovascular treatment of giant intracranial aneurysms.** *Neurosurgery* 2006;62(6 suppl 3):1324–35
16. Fiorella D, Kelly ME, Albuquerque FC, et al. **Curative reconstruction of a giant midbasilar trunk aneurysm with the Pipeline embolization device.** *Neurosurgery* 2009;64:212–17
17. Fiorella D, Woo HH, Albuquerque FC, et al. **Definitive reconstruction of circumferential, fusiform intracranial aneurysms with the Pipeline embolization device.** *Neurosurgery* 2008;62:1115–20, discussion 1120–21

18. Nelson PK, Lylyk P, Szikora I, et al. **The Pipeline embolization device for the intracranial treatment of aneurysms trial.** *AJNR Am J Neuroradiol* 2011;32:34–40
19. Rankin J. **Cerebral vascular accidents in patients over the age of 60. II. Prognosis.** *Scott Med J* 1957;2:200–15
20. Duncan PW, Jorgensen HS, Wade DT. **Outcome measures in acute stroke trials: a systematic review and some recommendations to improve practice.** *Stroke* 2000;31:1429–38
21. Wong GK, Lau JC, Poon WS. **Flow diverting stents for cerebral aneurysm treatment: time to replace coiling?** *J Clin Neurosci* 2011; 18:1143
22. Pumar JM, Blanco M, Vazquez F, et al. **Preliminary experience with Leo self-expanding stent for the treatment of intracranial aneurysms.** *AJNR Am J Neuroradiol* 2005;26:2573–77
23. Raphaeli G, Collignon L, De Witte O, et al. **Endovascular treatment of posterior circulation fusiform aneurysms: single-center experience in 31 patients.** *Neurosurgery* 2011;69:274–83
24. Echiverri HC, Rubino FA, Gupta SR, et al. **Fusiform aneurysm of the vertebrobasilar arterial system.** *Stroke* 1989;20:1741–47
25. Mizutani T, Miki Y, Kojima H, et al. **Proposed classification of nonatherosclerotic cerebral fusiform and dissecting aneurysms.** *Neurosurgery* 1999;45:253–59
26. Kalani MY, Zabramski JM, Nakaji P, et al. **Bypass and flow reduction for complex basilar and vertebrobasilar junction aneurysms.** *Neurosurgery* 2013;72:763–76, discussion 775–76
27. Phillips TJ, Wenderoth JD, Phatouros CC, et al. **Safety of the Pipeline embolization device in treatment of posterior circulation aneurysms.** *AJNR Am J Neuroradiol* 2012;33:1225–31
28. Fischer S, Vajda Z, Aguilar PM, et al. **Pipeline embolization device (PED) for neurovascular reconstruction: initial experience in the treatment of 101 intracranial aneurysms and dissections.** *Neuroradiology* 2012;54:369–82
29. McAuliffe W, Wycoco V, Rice H, et al. **Immediate and midterm results following treatment of unruptured intracranial aneurysms with the Pipeline embolization device.** *AJNR Am J Neuroradiol* 2012;33:164–70
30. Siddiqui AH, Abla AA, Kan P, et al. **Panacea or problem: flow diverters in the treatment of symptomatic large or giant fusiform vertebrobasilar aneurysms.** *J Neurosurg* 2012;116:1258–66
31. Meckel S, McAuliffe W, Fiorella D, et al. **Endovascular treatment of complex aneurysms at the vertebrobasilar junction with flow-diverting stents: initial experience.** *Neurosurgery* 2013;73: 386–94
32. Wolters FJ, Rinkel GJ, Vergouwen MD. **Clinical course and treatment of vertebrobasilar dolichoectasia: a systematic review of the literature.** *Neurol Res* 2013;35:131–37

Role of C-Arm VasoCT in the Use of Endovascular WEB Flow Disruption in Intracranial Aneurysm Treatment

J. Caroff, C. Mihalea, H. Neki, D. Ruijters, L. Ikka, N. Benachour, J. Moret, and L. Spelle

ABSTRACT

BACKGROUND AND PURPOSE: The WEB aneurysm embolization system is still under evaluation but seems to be a promising technique to treat wide-neck bifurcation aneurysms. However, this device is barely visible using conventional DSA; thus, high-resolution contrast-enhanced flat panel detector CT (VasoCT) may be useful before detachment to assess the sizing and positioning of the WEB. The purpose of this study was to evaluate the interest of VasoCT during WEB procedures.

MATERIALS AND METHODS: From March 2012 to July 2013, twelve patients (10 women and 2 men; age range, 44–55 years) were treated for 13 intracranial aneurysms with the WEB device. DSA and VasoCT were used and compared to depict any protrusion of the device in parent arteries before detachment. Two neuroradiologists reviewed each VasoCT scan, and the quality was graded on a subjective quality scale.

RESULTS: The mesh of the WEB was very well-depicted in all cases, allowing a very good assessment of its deployment. Device protrusion was clearly detected with VasoCT in 5 cases, leading to WEB repositioning or size substitution. During follow-up, VasoCT also allows good assessment of eventual residual blood flow inside the aneurysm or the WEB device.

CONCLUSIONS: Unlike DSA, VasoCT is an excellent tool to assess WEB deployment and positioning. In our experience, it allowed a precise evaluation of the WEB sizing and its relation to the parent vessel. Such information very likely enhances the ability to safely use this device, avoiding potential thromboembolic events in cases of protrusion in the parent arteries.

ABBREVIATIONS: WEB = Woven EndoBridge Embolization System

The Woven EndoBridge Embolization System (WEB; Sequent Medical, Aliso Viejo, California) is a 2-compartment intrasaccular flow disrupter, particularly dedicated to the treatment of intracranial wide-neck bifurcation aneurysms. This device has an attenuated microbraided mesh structure constructed from a large number of nitinol wires (ranging from 19 to 38 microns). This mesh is almost not visible with standard DSA because of the small diameter of nitinol wires, so 3 platinum markers represent the proximal, middle, and distal parts of inner and outer braids (Fig 1).[1,2] The first clinical results suggest a high feasibility of the treatment with acceptable morbidity and mortality.[3-5]

Flat panel detector CT has proved to be a very accurate tool to assess the structure and deployment of intracranial stents.[6,7] VasoCT (Philips Healthcare, Best, the Netherlands) provides simultaneous detailed visualization of neurovascular stents and parent arteries.[8,9]

We present here our experience using VasoCT as a systematic method to control WEB deployment before and after its detachment.

MATERIALS AND METHODS

Population

Between March 2012 and July 2013, twelve patients were treated for 13 intracranial aneurysms with the WEB device in our hospi-

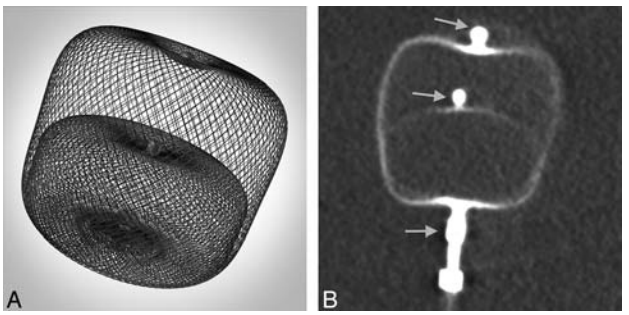

FIG 1. *A*, Photograph of the WEB device. *B*, Corresponding nonenhanced VasoCT clearly depicts the 2 different compartments and the 3 markers (*arrows*).

Received October 9, 2013; accepted after revision November 25.

From the Department of Interventional Neuroradiology (J.C., C.M., H.N., L.I., N.B., J.M., L.S.), Beaujon Medical Centre, Clichy, France; and Interventional X-Ray Innovation (D.R.), Philips Healthcare, Best, the Netherlands.

Please address correspondence to Jildaz Caroff, MD, Beaujon Medical Centre, 100, Boulevard Général Leclerc, 92110 Clichy, France; e-mail: Jildaz.caroff@gmail.com

http://dx.doi.org/10.3174/ajnr.A3860

tal. All subjects gave informed consent for the treatment. There were 10 women and 2 men with a mean age of 52 years (range, 44–55 years).

Treatment Technique

Endovascular treatment was performed by using a biplane flat panel angiographic system (Allura Xper 20/10; Philips Healthcare). Endovascular procedures were performed with the patient under general anesthesia and systemic heparinization.

A guiding catheter, FargoMax 6F (Balt, Montmorency, France) was advanced in the internal carotid or vertebral artery. To deliver the WEB, we used different microcatheters and placed them at the base of the aneurysmal sac: Rebar 27 (Covidien, Irvine, California), DAC 38 (Concentric Medical, Mountain View, California), Headway 27 (MicroVention, Tustin, California), and Via 27 or 33 (Sequent Medical). The microcatheter was chosen according to the WEB size. The WEB size choice was based on 3D rotational angiography performed during treatment.

Control DSA and VasoCT were performed before delivery. If the position was not satisfactory, the WEB was resheathed and repositioned. If the sizing was not adequate, the WEB was removed and another device was used. At the end of the procedure, both DSA and VasoCT were repeated after detachment of the WEB.

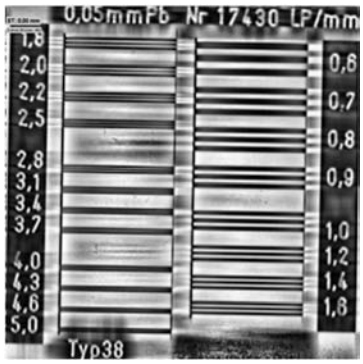

FIG 2. Central section of the VasoCT conebeam reconstruction of a line-pair phantom. The numbers at the left and right side indicate the line pairs per millimeter.

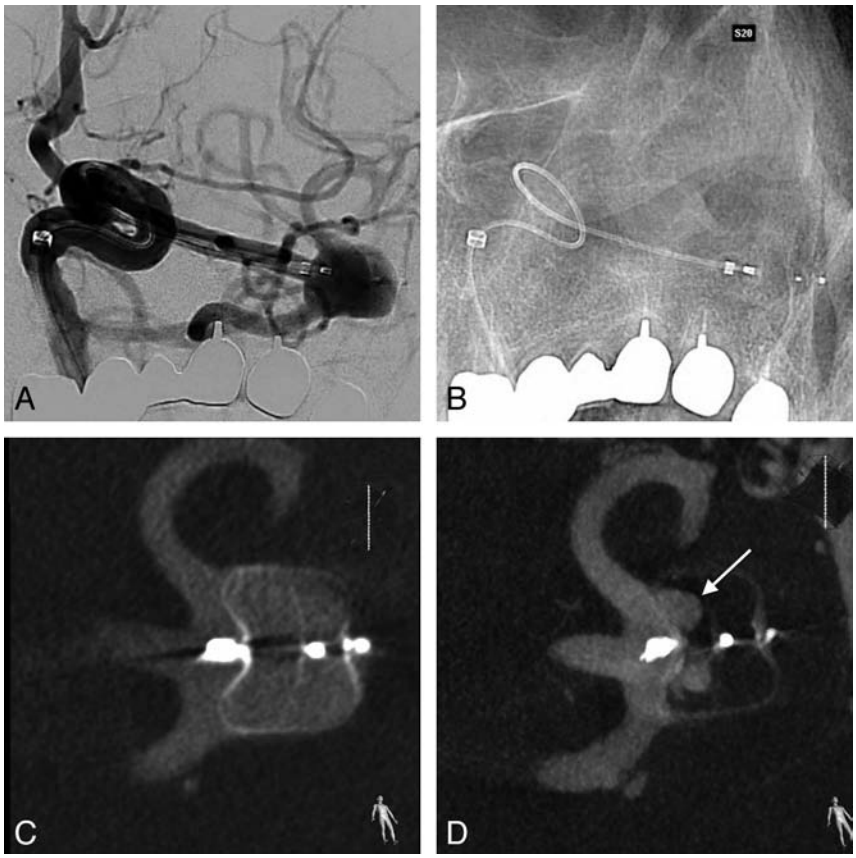

FIG 3. *A*, DSA before detachment of a WEB positioned in a left MCA bifurcation aneurysm. It is impossible to depict any protrusion of the device in the parent artery because only the 3 markers are seen and the mesh is almost not visible. *B*, Corresponding unsubstracted image. *C*, VasoCT confirms correct positioning of the WEB without any protrusion. *D*, Three-month control VasoCT shows residual flow in the proximal compartment (*arrow*).

High-Resolution Flat Panel Detector CT

For high-spatial-resolution imaging of intravascular devices and their parent vessel lumen, a dedicated iodine contrast-enhanced conebeam CT protocol was developed (VasoCT). It is acquired by using a neuroangiographic x-ray C-arm (Allura Xper FD20; Philips Healthcare) equipped with a cesium iodide–amorphous silicon flat panel detector. The sensor area of the flat detector measures approximately 30 × 40 cm and consists of 1920 × 2480 pixels. The conebeam acquisition consists of a rotational trajectory over a 200° arc while acquiring 620 projection images at a fixed source-to-detector distance of 1195 mm. The objects of interest should be positioned in the center of the rotation, 810 mm from the source. The x-ray tube voltage is set to 80 kV; the focal spot, to 0.4 mm, while no copper filter is used. The associated radiation dose ranges from 45 to 49 mGy CT dose index. The imaged detector area is fixed to a diameter of 22 cm, which enables an unbinned pixel size of 0.154 mm, allowing very high-spatial-resolution 3D reconstructions. The 3D reconstruction is obtained by using the Feldkamp-Davis-Kress method.[10] Preprocessing steps of the projection images include gain correction, scatter correction, water beam-hardening correction, and Parker weighting. The WEB VasoCT was reconstructed with a 512^3 matrix covering a cubic FOV of 34.44 mm in each dimension.

Figure 2 shows a VasoCT reconstruction of a line-pair phantom. As can be seen, up to 4.6 line pairs per millimeter (lp/mm) can be distinguished, which correspond to an intrinsic resolution of 0.109 mm according to the following formula: Resolution Intrinsic Millimeter = 0.5 [lp / mm].

The spatial resolution is substantially higher than the resolutions reported for

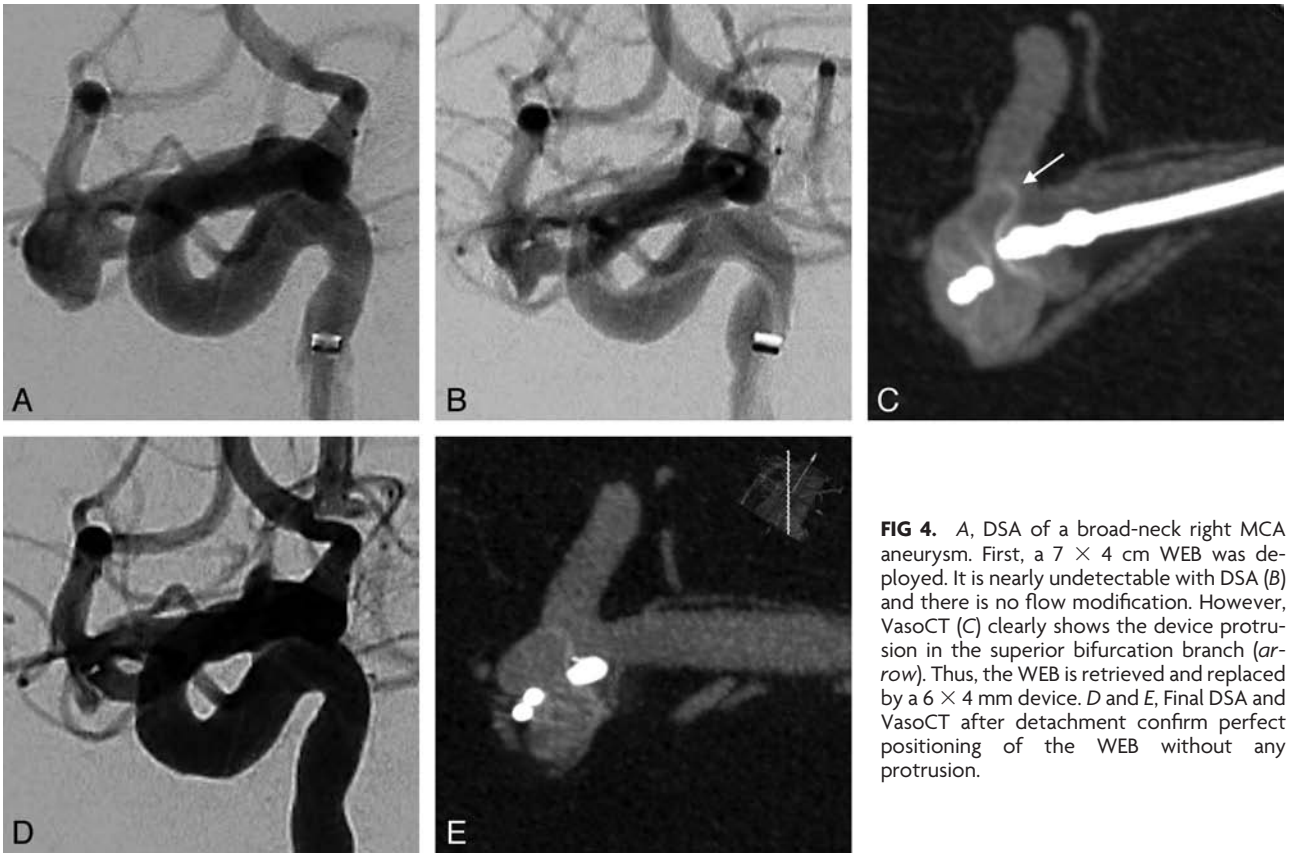

FIG 4. *A*, DSA of a broad-neck right MCA aneurysm. First, a 7 × 4 cm WEB was deployed. It is nearly undetectable with DSA (*B*) and there is no flow modification. However, VasoCT (*C*) clearly shows the device protrusion in the superior bifurcation branch (*arrow*). Thus, the WEB is retrieved and replaced by a 6 × 4 mm device. *D* and *E*, Final DSA and VasoCT after detachment confirm perfect positioning of the WEB without any protrusion.

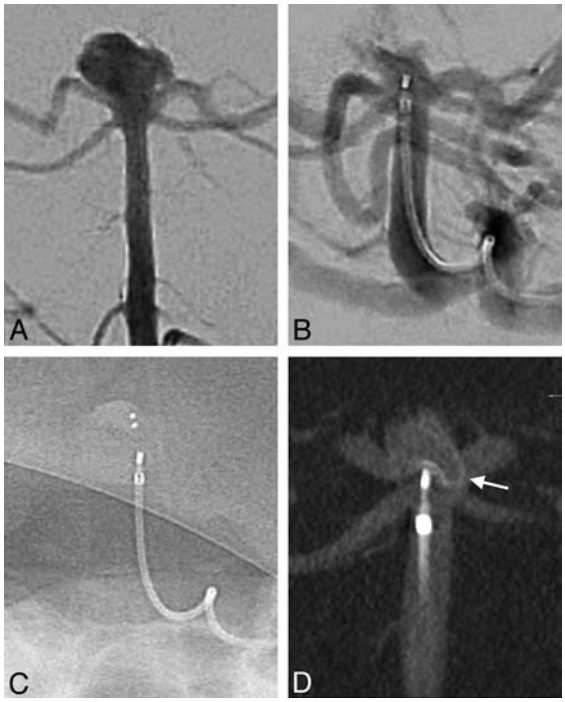

FIG 5. *A*, DSA anteroposterior view of a basilar tip aneurysm. *B*, Control angiogram and corresponding unsubtracted view (*C*) prior to detachment of the WEB. Some contrast agent stagnation is visible in the second layer. It is impossible to analyze the good positioning of the device; no flow abnormality is depicted in the left P1 segment. *D*, VasoCT clearly shows the protrusion in the left P1 segment. The WEB was then retrieved and replaced by a smaller one.

multisection CT. For 64-section CT, a resolution of approximately 1.5 lp/mm has been reported.[11] The high spatial resolution of VasoCT allows imaging the stent struts of intracranial nitinol stents.[9] To visualize the vessel lumen and the intravascular devices simultaneously, we used a diluted iodine contrast agent with 20% iodixanol (Visipaque 270; GE Healthcare, Mississauga, Ontario, Canada) and 80% saline solution. The total volume used was 90 mL at the injection rate of 3 mL/s. In case of streaking artifacts caused by nearby metal (eg, coils), the image quality can be improved by applying a metal-artifacts-reduction algorithm in a second-pass reconstruction.[12] Data were analyzed with MPR and MIP reconstructions.

Quality Assessment

VasoCT scans were reviewed in consensus by 2 interventional neuroradiologists. For every case, the quality of visualization of the WEB and the parent vessels was scored in ordered scales from 1 to 3. A score of 1 indicated that visualization was insufficient for evaluation; a score of 2 was given if the visualization was good; and a score of 3, if excellent. Metal artifacts from the WEB device and microcatheter, if present, were also evaluated. A score of 3 was given when no artifacts were depicted; a score of 2, if mild artifacts were observed. A score of 1 indicated severe artifacts, making evaluation of the WEB positioning impossible.

Those scores were added to obtain a global quality score on a 9-point subjective scale. Global VasoCT quality scores were compared with WEB dimensions by using the Pearson correlation coefficient.

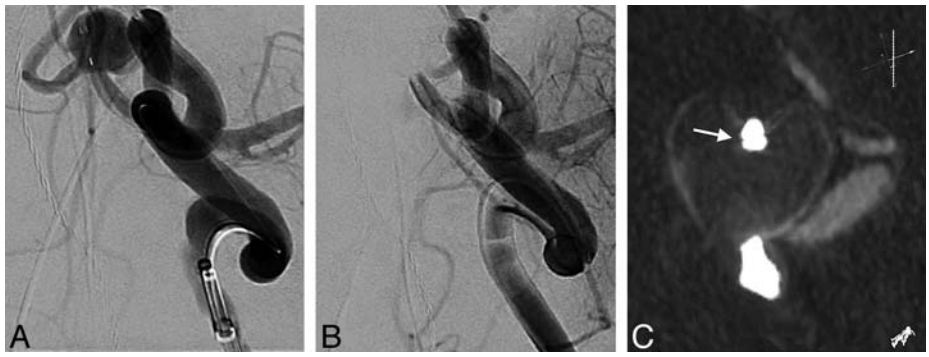

FIG 6. *A*, DSA working projection of a large-neck anterior communicating artery aneurysm. *B*, After placement of a 9 × 7 mm WEB, the control DSA shows the occlusion of the right A2 segment and a narrowing of the left A2. *C*, VasoCT confirms the occlusion and that the WEB is not properly deployed. It is in a heart-shaped configuration with a distal trough; the 2 distal markers are attached (*arrow*). This "heart sign" depicts an inappropriate width of the WEB regarding aneurysm dimensions. It was then replaced by a correctly deployed 7 × 6 cm WEB.

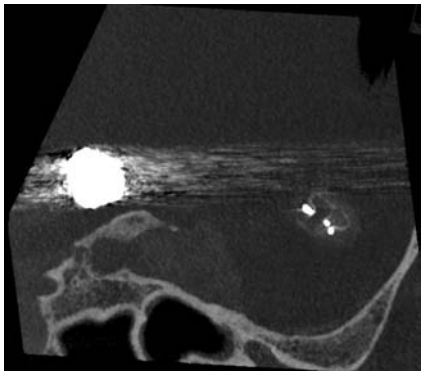

FIG 7. Nonenhanced VasoCT. It is very important to consider the acquisition plane to avoid the projection of any metal artifacts over the region of interest. Here, the angulation of the head of the patient was modified so that coil artifacts from a previously treated basilar tip aneurysm do not superimpose on the MCA bifurcation.

Additionally, reviewers had to evaluate whether any protrusion, clotting, vessel occlusion, or residual neck was present.

RESULTS

Most treated aneurysms were unruptured (3 ruptured cases), with an unfavorable wide-neck anatomy (mean dome/neck ratio = 1:1). The mean aneurysm size was 7.3 mm (range, 5–11 mm).

WEB placement was not possible in 1 case because of the unavailability of an appropriate-sized device. Device protrusion was clearly detected with VasoCT in 5 cases, leading to WEB repositioning or size substitution (Figs 3 and 4). The average number of WEBs used to obtain good sizing was 1.3 per procedure.

The total number of VasoCT scans reviewed was 31, with an average number of 2.4 VasoCT scans performed per procedure. The mean quality score was 6.6 ±1.4 (range, 4–9). Visualization of the WEB and/or the parent vessel was insufficient for evaluation in 3 cases of VasoCT (9%).

Quality score was significantly and inversely correlated to the WEB height ($r = 0.78$, $P < .0001$).

DISCUSSION

The visibility of the WEB is very poor with conventional angiography (Fig 5). Unlike DSA, VasoCT offers a very good visualization of the microbraided mesh structure and shape of the WEB device. It allows a precise study of its relationship with the parent arteries. This is fundamental before detachment of this completely retrievable device to avoid potential thromboembolic complications due to protrusion (Fig 6).

We have encountered some differences in VasoCT image quality. Some features seem to be significantly influencing the visibility of the WEB. The device should always be placed in the isocenter of the acquired volume. All movements of the patient have to be limited; therefore, apnea is required during acquisition. No geometric disturbances should occur; these can be seen when the C-arm hits the infusion stand or table. High-attenuating items need to be avoided in the reconstruction plane of the WEB by positioning the head of the patient so that coils or clip streak artifacts appear in another plane (Fig 7). Metal artifacts reduction may be useful in some cases, especially when WEB-marker artifacts are projected over the parent artery (ie, MCA bifurcation aneurysms) (Fig 8).

WEB markers made of iridium and platinum alloy generate significant metal artifacts (unlike nitinol mesh). We have noticed that distal markers of the delivery microcatheter, made with the same iridium and platinum alloy, also induce artifacts; they can be avoided by retrieving the catheter proximally in the parent artery.

The quality score was inversely correlated to the WEB height. This observation can be explained first because the diameter of nitinol wires is variable (ie, smaller for the smallest WEB). Thus, the largest WEB sizes are more radiodense and easily assessed. This feature should encourage manufacturers to increase the visibility of the smaller devices. Second, the distance between the markers is small for the small WEB, leading to overlapping metal streak artifacts that are summed, deteriorating the visualization of the parent arteries.

We advise a systematic calibration of the angiographic suite prior to each acquisition. When the system is used for a long time with a reduced FOV (as is usual during a procedure), then the pixels that have been irradiated within this image format have a different response than the ones that were not irradiated. The calibration corrects this phenomenon, allowing an optimal image quality.

Some authors report the use of 3D rotational angiography to control WEB positioning.[5] There are similarities and differences

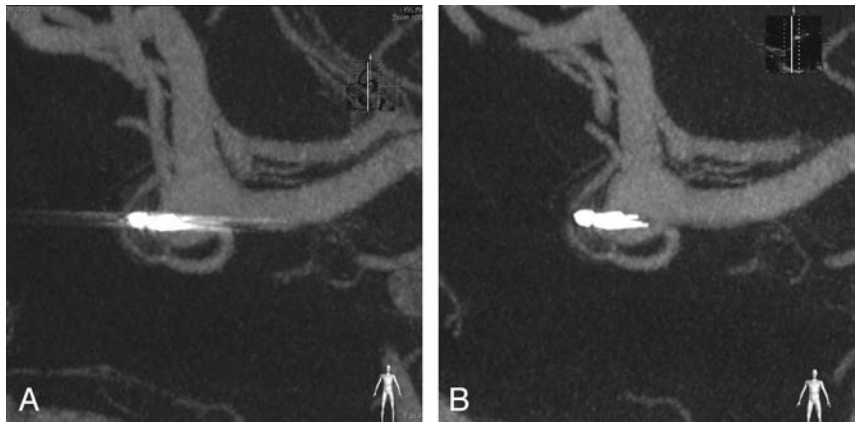

FIG 8. *A*, VasoCT of an MCA aneurysm treated with a WEB. Marker artifacts are projecting over the parent vessels. *B*, A new reconstruction with a metal-artifacts-reduction algorithm clearly improves the image quality and the visualization of the bifurcation.

between VasoCT and 3D rotational angiography. Both protocols are optimized for visualization of iodine contrast; hence, both use approximately 80 kV for the x-ray tube and both are optimized for high-resolution reconstructions (either volume-rendering or multiplanar mode). While VasoCT is meant for small contrast differences (with diluted contrast medium), 3D rotational angiography is meant for larger contrast differences (with pure contrast medium). To achieve the high contrast resolution, VasoCT acquires 620 images, whereas 3D rotational angiography records 120 images in the rotation. As a result, the VasoCT acquisition takes longer (20 versus 4 seconds); and because of the larger number of images, the reconstruction times for VasoCT are also longer (approximately 26 seconds versus 5 seconds for 256^3). Because of its superior contrast resolution, VasoCT is the most appropriate technique for use with the WEB device.

VasoCT x-ray skin dose calculated from simulations amounts to 0.89 mSv, and the effective dose is 0.51 mSv. For comparison, the standard brain CT effective dose average is 1.5 mSv.[13]

While VasoCT appears essential during endovascular treatment, it is also very useful during follow-up. It can be performed with the patient under local anesthesia, and it allows the assessment of any residual flow inside the 2 separate layers (Fig 3).

CONCLUSIONS

Unlike DSA, VasoCT is an excellent tool to assess WEB deployment and positioning. In our experience, it allows a precise evaluation of the WEB sizing and its relation to the parent vessel. Such information likely enhances the ability to use this device safely, avoiding a potential thromboembolic event in cases of protrusion in the parent arteries.

Disclosures: Daniel Ruijters—*UNRELATED*: *Employment*: I am a Philips Healthcare employee. Jacques Moret—*UNRELATED*: *Consultancy*: Covidien, MicroVention.

REFERENCES

1. Ding YH, Lewis DA, Kadirvel R, et al. **The Woven EndoBridge: a new aneurysm occlusion device.** *AJNR Am J Neuroradiol* 2011;32:607–11
2. Klisch J, Sychra V, Strasilla C, et al. **The Woven EndoBridge cerebral aneurysm embolization device (WEB II): initial clinical experience.** *Neuroradiology* 2011;53:599–607
3. Pierot L, Liebig T, Sychra V, et al. **Intrasaccular flow-disruption treatment of intracranial aneurysms: preliminary results of a multicenter clinical study.** *AJNR Am J Neuroradiol* 2012;33:1232–38
4. Lubicz B, Mine B, Collignon L, et al. **WEB device for endovascular treatment of wide-neck bifurcation aneurysms.** *AJNR Am J Neuroradiol* 2013;34:1209–14
5. Pierot L, Klisch J, Cognard C, et al. **Endovascular WEB flow disruption in middle cerebral artery aneurysms: preliminary feasibility, clinical, and anatomical results in a multicenter study.** *Neurosurgery* 2013;73:27–35, discussion 34–35
6. Richter G, Engelhorn T, Struffert T, et al. **Flat panel detector angiographic CT for stent-assisted coil embolization of broad-based cerebral aneurysms.** *AJNR Am J Neuroradiol* 2007;28:1902–08
7. Benndorf G, Strother CM, Claus B, et al. **Angiographic CT in cerebrovascular stenting.** *AJNR Am J Neuroradiol* 2005;26:1813–18
8. Patel NV, Gounis MJ, Wakhloo AK, et al. **Contrast-enhanced angiographic cone-beam CT of cerebrovascular stents: experimental optimization and clinical application.** *AJNR Am J Neuroradiol* 2011;32:137–44
9. Snoeren RM, Söderman M, Kroon JN, et al. **High-resolution 3D X-ray imaging of intracranial nitinol stents.** *Neuroradiology* 2012;54:155–62
10. Feldkamp L, Davis L, Kress J. **Practical cone-beam algorithm.** *J Opt Soc Am A Opt Image Sci Vis* 1984;1:612–19
11. Flohr T, Stierstorfer K, Raupach R, et al. **Performance evaluation of a 64-slice CT system with z-flying focal spot.** *Rofo* 2004;176:1803–10
12. van der Bom IM, Hou SY, Puri AS, et al. **Reduction of coil mass artifacts in high-resolution flat detector conebeam CT of cerebral stent-assisted coiling.** *AJNR Am J Neuroradiol* 2013;34:2163–70
13. van der Molen AJ, Schilham A, Stoop P, et al. **A national survey on radiation dose in CT in the Netherlands.** *Insights Imaging* 2013;4:383–90

Rupture-Associated Changes of Cerebral Aneurysm Geometry: High-Resolution 3D Imaging before and after Rupture

J.J. Schneiders, H.A. Marquering, R. van den Berg, E. VanBavel, B. Velthuis, G.J.E. Rinkel, and C.B. Majoie

ABSTRACT

BACKGROUND AND PURPOSE: Comparisons of geometric data of ruptured and unruptured aneurysms may yield risk factors for rupture. Data on changes of geometric measures associated with rupture are, however, sparse, because patients with ruptured aneurysms rarely have undergone previous imaging of the intracranial vasculature. We had the opportunity to assess 3D geometric differences of aneurysms before and after rupture. The purpose of this study was to evaluate possible differences between prerupture and postrupture imaging of a ruptured intracranial aneurysm.

MATERIALS AND METHODS: Using high-quality 3D image data, we generated 3D geometric models before and after rupture and compared these for changes in aneurysm volume and displacement. A neuroradiologist qualitatively assessed aneurysm shape change, the presence of perianeurysmal hematoma, and subsequent mass effect exerted on aneurysm and parent vessels.

RESULTS: Aneurysm volume was larger in the postrupture imaging in 7 of 9 aneurysms, with a median increase of 38% and an average increase of 137%. Three aneurysms had new lobulations on postrupture imaging; 2 other aneurysms were displaced up to 5 mm and had changed in geometry due to perianeurysmal hematoma.

CONCLUSIONS: Geometric comparisons of aneurysms before and after rupture show a large volume increase, origination of lobulations, and displacement due to perianeurysmal hematoma. Geometric and hemodynamic comparison of series of unruptured and ruptured aneurysms in the search for rupture-risk-related factors should be interpreted with caution.

Unruptured intracranial aneurysms are found in approximately 3% of the population.[1] Once they are detected, the decision for preventive treatment has to be weighed against the risk of rupture, with inherent high case fatality and morbidity.[2] Prediction of rupture of intracranial aneurysms remains poor, with size as the most important risk factor. However, not all large aneurysms would rupture if left untreated; whereas small aneurysms, which are often left untreated, do sometimes rupture during follow-up. Better predictors are, therefore, needed. Intra-aneurysmal hemodynamic characteristics may have predictive value.[3,4]

Computational fluid dynamics have been applied to simulate hemodynamic flow patterns in the aneurysm and surrounding vessels to relate hemodynamic characteristics with aneurysmal rupture risk.[4,5] Several studies indeed found differences in flow patterns between ruptured and unruptured aneurysms.[3,4,6] However, if one compares ruptured with unruptured aneurysms, the potential changes of the aneurysm geometry before, during, or after rupture itself are neglected.

The rupture of the aneurysm may result in shape changes of the aneurysm due to changes in the aneurysmal sac. These changes potentially alter the aneurysmal or perianeurysmal geometry and its related hemodynamic patterns. It is, therefore, pivotal to know whether changes before, during, or shortly after rupture of aneurysms in themselves affect aneurysm geometry and aneurysm hemodynamics; and if so, what these changes are. Such data are difficult to collect because high-quality images of intracranial aneurysms before and after rupture are rare. We had the opportunity to assess changes in aneurysm geometry associated with rupture in a series of 9 patients by using advanced image registration of high-quality 3D imaging data performed before and after rupture.

Received October 12, 2013; accepted after revision December 5.

From the Departments of Radiology (J.J.S., H.A.M., R.v.d.B., C.B.M.) and Biomedical Engineering and Physics (H.A.M., E.V.), Academic Medical Center, Amsterdam, the Netherlands; and Department of Neurology and Neurosurgery (G.J.E.R.), Brain Center Rudolf Magnus, and Department of Radiology (B.V.), University Medical Center Utrecht, Utrecht, the Netherlands.

J.J. Schneiders and H.A. Marquering have contributed equally to this article.

This work was supported by a grant from the Nuts-OHRA Foundation, Amsterdam, the Netherlands.

Please address correspondence to Joppe Schneiders, MD, Department of Radiology, C1, Academic Medical Center, University of Amsterdam, PO Box 22660, 1100 DD Amsterdam, the Netherlands: e-mail: j.j.schneiders@amc.uva.nl

Indicates article with supplemental on-line table.

http://dx.doi.org/10.3174/ajnr.A3866

Table 1: Imaging modalities used before and after rupture

No.	Imaging Modality before Rupture	Resolution (mm)	Imaging Modality after Rupture	Resolution (mm)
1	3D TOF MRA	0.49 × 0.49 × 1.2	3D RA	0.22 × 0.22 × 0.22
2	3D TOF MRA	0.31 × 0.31 × 1.0	CTA	0.31 × 0.31 × 0.45
3	CTA	0.33 × 0.33 × 1.0	CTA	0.35 × 0.35 × 0.33
4	3D PC MRA	0.78 × 0.78 × 1.0	3D RA	0.25 × 0.25 × 0.25
5	3D TOF MRA	0.45 × 0.45 × 1.0	3D RA	0.39 × 0.39 × 0.39
6	CTA	0.43 × 0.43 × 0.9	3D RA	0.22 × 0.22 × 0.22
7	3D TOF MRA	0.20 × 0.20 × 1.0	3D RA	0.17 × 0.17 × 0.17
8	3D TOF MRA	0.35 × 0.35 × 1.4	3D RA	0.17 × 0.17 × 0.17
9	CTA	0.33 × 0.33 × 1.3	3D RA	0.09 × 0.09 × 0.09

Note:—PC indicates phase-contrast; RA, rotational angiography.

MATERIALS AND METHODS

We searched the neurovascular data bases for patients presenting with aneurysmal subarachnoid hemorrhage who underwent 3D cerebral angiography (3D rotational angiography, MRA, or CTA) before the aneurysm rupture. We retrieved imaging of 9 patients from 2 institutions (Academic Medical Center [Amsterdam] and University Medical Center Utrecht) collected during a 6-year period. Approval of the medical ethics committee was given for this retrospective analysis of anonymized patient data. Informed consent was waived because no diagnostic tests other than routine clinical imaging were used in this study.

A number of geometric features of the intracranial aneurysms were quantitatively and qualitatively determined in both pre- and postrupture imaging. The quantitatively determined features were aneurysm volume and maximal aneurysm diameter. The maximal diameter was defined as the maximal distance between 2 locations on the aneurysm surface with their connecting line completely located in the aneurysm sac. Furthermore, we determined displacement and shape changes between the 2 image datasets. To better assess shape change, we registered the pre- and postrupture imaging data so that the aneurysm sac was optimally matched. To determine the displacement of the aneurysm, we registered a proximal segment of the parent artery of the pre- and postrupture imaging data.

Registration

The pre- and postrupture images were registered by a closed-source in-house developed software system for modality registration and visualization (WorldMatch).[7] The registration of the images was performed twice: First, the images were registered by using a volume of interest around the aneurysm sac to obtain an optimal match of the aneurysm itself. Second, the images were registered to obtain an optimal match of the feeding artery. A single observer (H.A.M.), who had no clinical information other than the location of the aneurysm, performed these registrations. The highest resolution of the 2 image datasets was used for the spatial grid of the registered images.

Segmentation

The aneurysms and adjacent arteries were segmented by using level set segmentation (Vascular Modeling ToolKit; http://www.vmtk.org).[8] An experienced neuroradiologist (C.B.M.) inspected all segmentations for accuracy by using all available image data. Segmentation inaccuracies were manually corrected by using ITK-SNAP, a software application for medical image segmentation and manual delineation (ITK-SNAP 2.2.0, http://www.itksnap.org),[9] until the neuroradiologist decided the segmentation was accurate. Subsequently, the aneurysm sac was separated from the arterial tree by using ITK-SNAP. These aneurysm sac models were used to calculate the volume of the aneurysms and aneurysm shape changes.

Surface models were generated from the matched segmentations. The registration was inspected by a second observer (R.v.d.B.) and adjusted if needed by using a combination of iterative closest point registration and manual transforms.

Quantitative Measurements

The volume of the aneurysms was defined as the number of segmented aneurysm voxels multiplied by the volume of a single voxel. Absolute and relative volume changes were determined. We defined the displacement of the aneurysm sac as the distance between the center of the pre- and postrupture aneurysm sacs, by using the images in which the parent arteries were registered. The center of the aneurysm was mathematically defined as the center of the mass of the segmented aneurysm volume.

The shape change was quantified by using the point-surface distances of the surface of the pre- and postrupture aneurysm segmentations in images in which the aneurysm domes were registered. A point-surface distance is the minimal distance of a location of one aneurysm surface to the surface of the other. The average and maximum point-surface distances are presented in the On-line Table. To avoid overestimations due to modality-driven variations in the definition of the aneurysm neck,[10] we ensured that this maximum distance was remote from the neck.

Qualitative Assessments

The neuroradiologist (C.B.M.) evaluated all the available pre- and postrupture imaging for the presence of intra-aneurysmal thrombus that could influence angiography-derived segmentations. The postrupture data were also examined for the presence of a perianeurysmal hematoma and new lobulations. In the presence of perianeurysmal hematoma, it was judged whether this mass had induced a displacement or shape change in the aneurysm.

The postrupture DSA examinations were also assessed for the presence of new lobulations and pseudoaneurysms (a contained extraluminal rupture within a reorganized clot). Pseudoaneurysms were differentiated from true lobulations by their appearance with delayed and incomplete opacification and delayed washout.[11]

RESULTS

3D angiographic imaging, before and after rupture, was available for 9 patients. The image modalities used and the resolution are shown in Table 1. The average time between prerupture imaging and rupture was 1 year 127 days, with an SD of 1 year 199 days. The On-line Table shows the geometric measures of the aneurysms pre- and postrupture. Seven aneurysms showed an increase

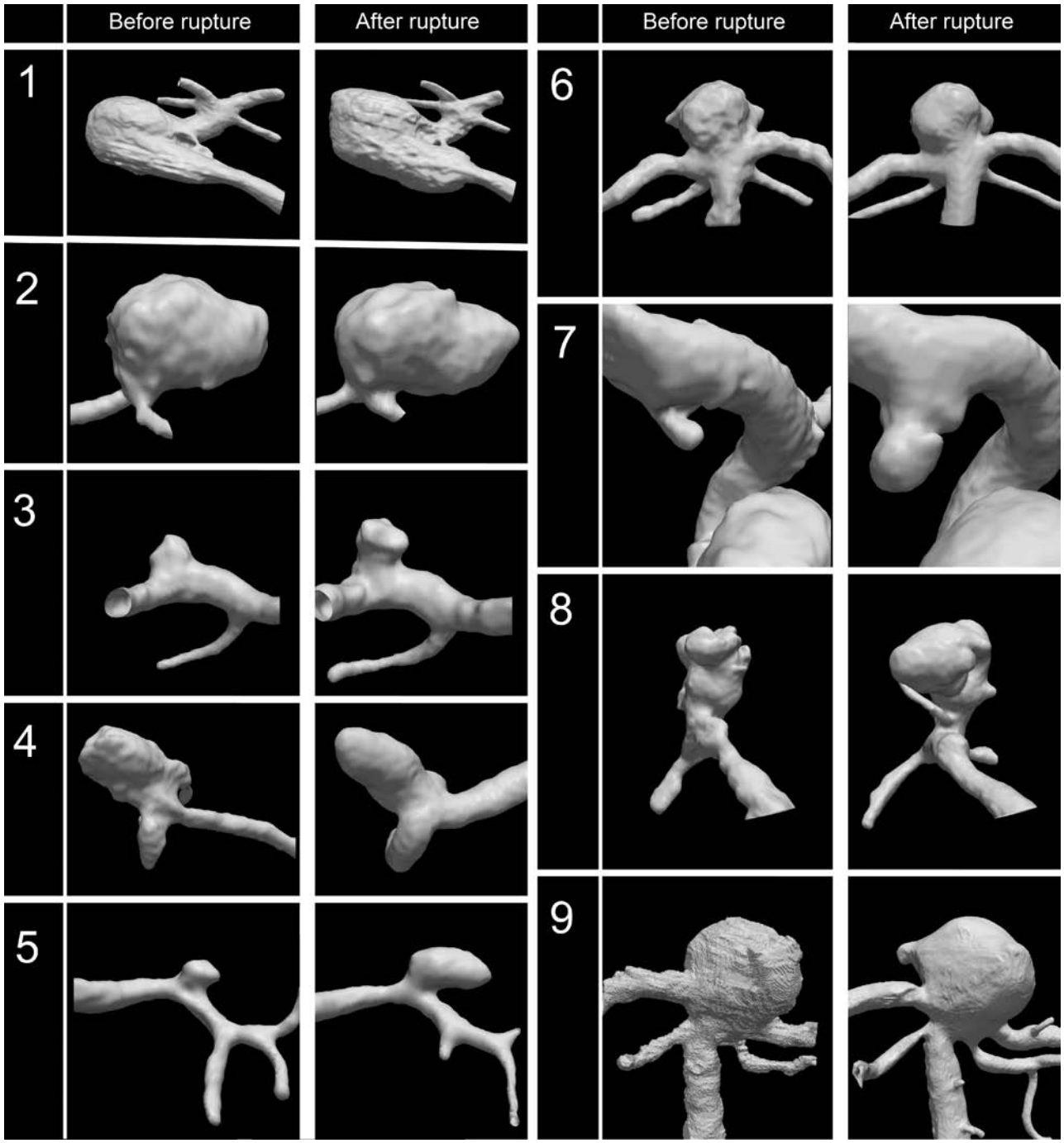

FIG 1. Volume rendering of angiographic imaging data before and after rupture for all cases. Cases 1 and 2 show the largest absolute increase in aneurysm volume (+433 and +613 mm^3, respectively); case 5 and 7, the largest relative increase in aneurysm volume (176% and 832%, respectively).

in volume with a median increase of 38% and an average increase of 137 ± 266%.

Two aneurysms (cases 1 and 2 in Fig 1) showed a large absolute volume increase of 433 and 613 mm^3, respectively, in the postrupture imaging. This increase had occurred in a relatively short time of 183 and 72 days, respectively. Furthermore, in case 7, a large relative volume increase of 832% had occurred within a time frame of no more than 14 days (Fig 2).

Table 2 shows the qualitative observations made by the neuroradiologist. Three aneurysms had new lobulations on postrupture imaging; no pseudoaneurysms and no intra-aneurysmal thrombus were found in any aneurysm. A perianeurysmal hematoma was present in 3 cases, 2 of which exerted mass effect on the aneurysm, thereby changing the aneurysm geometry (see Fig 3 for an example).

DISCUSSION

On the basis of pre- and postrupture 3D imaging of ruptured aneurysms, we found significant volume changes, new lobulations, and aneurysm displacement due to hematoma mass effect after rupture.

Most aneurysms showed an increase in volume in postrupture imaging. It has been shown that aneurysm growth is associated with an increased rupture risk.[12] Annual growth in untreated unruptured aneurysms is reported to be between 1.5% and 22.7%, corresponding to a diameter growth between 0.12 and 1.3 mm.[13-15] In the current study, the average growth rate was much larger (4.8 mm/year). Our findings are more in line with another study that included 13 ruptured aneurysms with pre- and postrupture 2D-DSA, which showed an average increase in maximal diameter of 3.2 mm/year.[16] A possible explanation of the difference in growth rate compared with previous imaging follow-up studies of unruptured aneurysms[13-15] is that the population of Rahman et al[16] and our study consisted of selected ruptured aneurysms, in which the rupture itself may be associated with larger growth.

We found no apparent examples of aneurysm shrinkage after rupture.[16,17] In 2 instances, we found a small volume decrease of 3% and 4%, but these changes fall within the margin of error of the volume measurement due to differences in the modalities used and/or processing methods.

Because of the relatively large time interval between prerupture and postrupture imaging, no conclusions on the causality or the timing of these changes can be drawn. The observed changes could have occurred before, during, or shortly after rupture. Hence, we can only conclude that they were associated with rupture. However, in case of a large hematoma formation, an obvious causal relation exists between rupture and consequent geometry change because large hematomas can displace and deform the aneurysm.

A few aneurysms were displaced due to hematoma mass effect, thereby changing the geometric relation with their supplying artery. The resulting displacement may have an effect on the relative position of the aneurysm parent vessel and location of inflow. In our cases, the displacement changed the angle of the parent vessel with regard to the aneurysm neck. The parent vessel angle has been described as a surrogate measure for the direction of the blood flow into the aneurysm and was proposed as a risk factor for aneurysm rupture.[18,19] The supplying artery is also an important determinant for intra-aneurysmal hemodynamics calculated by using computational fluid dynamics. The

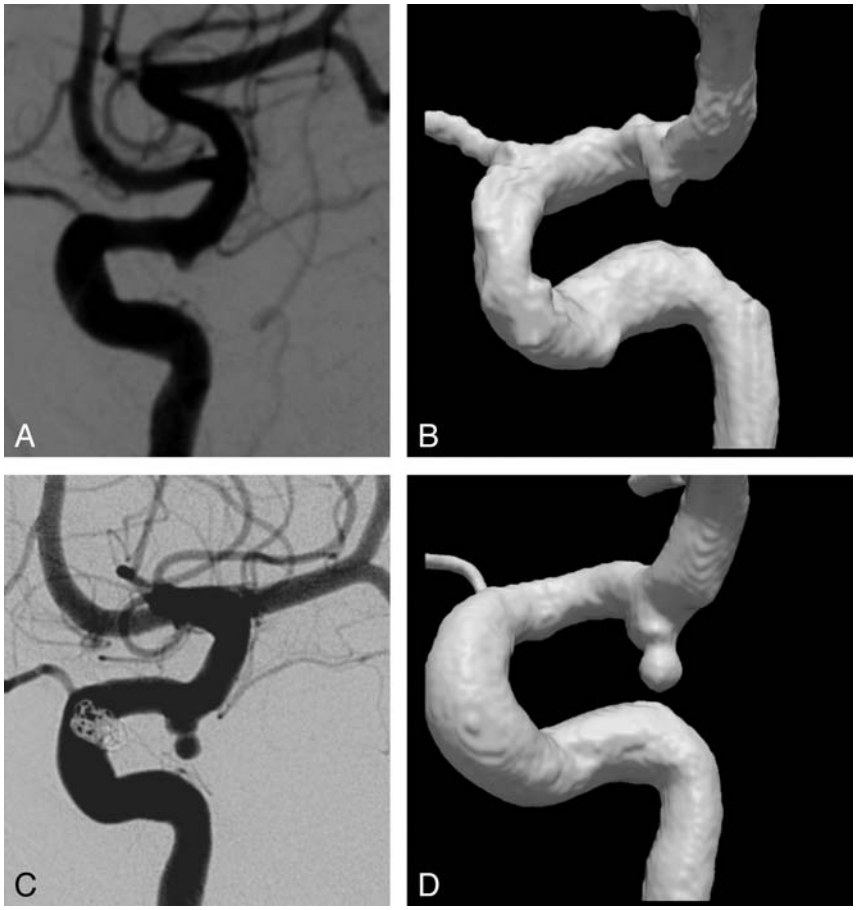

FIG 2. Case 7. Lateral view of 2D DSA (*A*) and 3DRA (*B*) before rupture shows a small aneurysm at the posterior communicating artery. Postrupture 2D DSA (*C*) and 3DRA (*D*) show a large increase of aneurysm volume and a new lobulation at the aneurysm dome.

Table 2: Qualitative assessment of pre- and postrupture imaging

Case	Postrupture Imaging[a]
1	Large amount of subarachnoid hemorrhage No hematoma, no mass effect; no intra-aneurysmal thrombus; no lobulations
2	SAH, large perianeurysmal hematoma (28 × 22 × 35 mm) with mass effect on the aneurysm (slightly flattened contour right side); no intra-aneurysmal thrombus; no lobulations
3	SAH, no hematoma; no intra-aneurysmal thrombus; 1 new lobulation
4	SAH, large perianeurysmal hematoma in Sylvian fissure (46 × 33 × 38 mm) with mass effect, anterior displacement of vessels and aneurysm; no intra-aneurysmal thrombus; no lobulations
5	Large amount of subarachnoid hemorrhage Hematoma (10 × 20 × 10 mm), no mass effect on the aneurysm; no intra-aneurysmal thrombus; no lobulations
6	SAH, no hematoma; no intra-aneurysmal thrombus; no lobulation
7	SAH, no hematoma; no intra-aneurysmal thrombus; 1 new lobulation
8	Diffusely spread SAH, no hematoma; no intra-aneurysmal thrombus; the 2 initial lobulations were merged into a single large lobulation
9	SAH, no hematoma; no intra-aneurysmal thrombus; 1 new lobulation

[a] None of the prerupture imaging showed an intra-aneurysmal thrombus. Only case 8 showed lobulations on the prerupture imaging (2 lobulations).

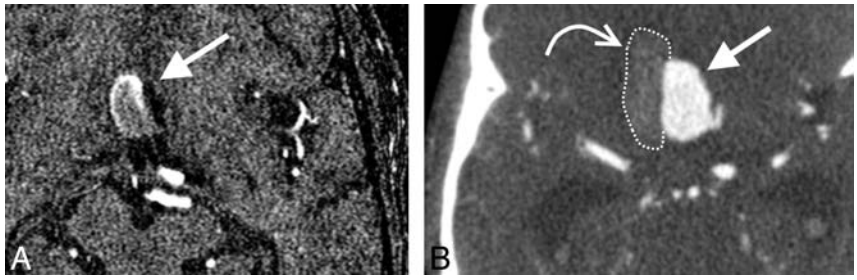

FIG 3. Case 2. *A*, Axial 3D TOF MRA source image shows an anterior communicating artery aneurysm (*arrow*). *B*, Axial CTA source image after rupture shows an increase of aneurysm volume and flattening of the right aneurysm border and displacement of the aneurysm to the left side due to a large perianeurysmal hematoma (*curved arrow*).

change in geometry of the parent artery and aneurysm sac may have important implications for measurements of intra-aneurysmal hemodynamics by using computational fluid dynamics. Computational fluid dynamics–based calculations are commonly used to estimate hemodynamic risk factors, whereas the postrupture geometry is assumed representative of the geometry before rupture. This assumption may not hold for the change in parent artery–aneurysm geometry shown here.

Some aneurysms showed a new focal bulging or lobulation that was not present on prerupture imaging Although lobulations may have been caused by the rupture itself, the high number of lobulations are in line with previous studies in which the presence of lobulations was associated with an increased rupture risk.[19,20] One may argue that some of these new lobulations could also be pseudoaneurysms (ie, a contained extraluminal rupture within a reorganized clot). We think this is unlikely because on postrupture DSA examinations, they did not demonstrate delayed opacification and washout.[11]

A limitation of this study is that we compared images and segmentations originating from different imaging modalities. Differences in the segmented volumes may be caused by differences in these modalities. Especially 3D TOF MRA is prone to introduce angiographic inaccuracies due to signal loss and may underestimate aneurysm volume. As a result, volume comparison of prerupture MRA with postrupture 3D rotational angiography or CTA could incorrectly be interpreted as aneurysm growth. Although this effect could produce incorrect conclusions on aneurysm growth, the increase in size in some cases in this study was much too large to be explained by this limitation of MRA imaging.

CONCLUSIONS

The geometric changes we found in aneurysms before and after rupture show that direct comparison of these geometric and hemodynamic features between series of ruptured and unruptured aneurysms for assessment of risk factors should be considered with caution.

Disclosures: Joppe J. Schneiders—*RELATED*: supported by the NUTS-OHRA Foundation (grant SNO-T-0702–92). Brigitta Velthuis—*UNRELATED*: *Payment for Lectures (including service on Speakers Bureaus)*: Philips Healthcare.* Charles B. Majoie—*RELATED*: *Grant*: NUTS-OHRA Foundation,* *UNRELATED*: *Grants/Grants Pending*: Dutch Heart Foundation.* *Money paid to the institution.

REFERENCES

1. Vlak MH, Algra A, Brandenburg R, et al. **Prevalence of unruptured intracranial aneurysms, with emphasis on sex, age, comorbidity, country, and time period: a systematic review and meta-analysis.** *Lancet Neurol* 2011;10:626–36
2. McDonald JS, McDonald RJ, Fan J, et al. **Comparative effectiveness of ruptured cerebral aneurysm therapies: propensity score analysis of clipping versus coiling**. *AJNR Am J Neuroradiol* 2014;35:164–69
3. Cebral JR, Mut F, Weir J, et al. **Association of hemodynamic characteristics and cerebral aneurysm rupture.** *AJNR Am J Neuroradiol* 2011;32:264–70
4. Xiang J, Natarajan SK, Tremmel M, et al. **Hemodynamic-morphologic discriminants for intracranial aneurysm rupture.** *Stroke* 2011;42:144–52
5. Cebral JR, Castro MA, Burgess JE, et al. **Characterization of cerebral aneurysms for assessing risk of rupture by using patient-specific computational hemodynamics models.** *AJNR Am J Neuroradiol* 2005; 26:2550–59
6. Jou LD, Lee DH, Morsi H, et al. **Wall shear stress on ruptured and unruptured intracranial aneurysms at the internal carotid artery.** *AJNR Am J Neuroradiol* 2008;29:1761–67
7. Wolthaus JW, van Herk M, Muller SH, et al. **Fusion of respiration-correlated PET and CT scans: correlated lung tumour motion in anatomical and functional scans.** *Phys Med Biol* 2005;50:1569–83
8. Antiga L, Piccinelli M, Botti L, et al. **An image-based modeling framework for patient-specific computational hemodynamics.** *Med Biol Eng Comput* 2008;46:1097–112
9. Yushkevich P, Piven J, Hazlett HC, et al. **User-guided 3D active contour segmentation of anatomical structures: significantly improved efficiency and reliability.** *Neuroimage* 2006;31:1116–28
10. Schneiders JJ, Marquering HA, Antiga L, et al. **Intracranial aneurysm neck size overestimation with 3D rotational angiography: the impact on intra-aneurysmal hemodynamics simulated with computational fluid dynamics.** *AJNR Am J Neuroradiol* 2013;34:121–28
11. D'Urso PI, Loumiotis I, Milligan BD, et al. **"Real time" angiographic evidence of "pseudoaneurysm" formation after aneurysm rebleeding.** *Neurocrit Care* 2011;14:459–62
12. Villablanca JP, Duckwiler GR, Jahan R, et al. **Natural history of asymptomatic unruptured cerebral aneurysms evaluated at CT angiography: growth and rupture incidence and correlation with epidemiologic risk factors.** *Radiology* 2013;269:258–65
13. Wermer MJ, van der Schaaf IC, Velthuis BK, et al. **Yield of short-term follow-up CT/MR angiography for small aneurysms detected at screening.** *Stroke* 2006;37:414–18
14. Juvela S, Porras M, Poussa K. **Natural history of unruptured intracranial aneurysms: probability of and risk factors for aneurysm rupture.** *J Neurosurg* 2008;108:1052–60
15. Ferns SP, Sprengers ME, van Rooij WJ, et al. **De novo aneurysm formation and growth of untreated aneurysms: a 5-year MRA follow-up in a large cohort of patients with coiled aneurysms and review of the literature.** *Stroke* 2011;42:313–18
16. Rahman M, Ogilvy CS, Zipfel GJ, et al. **Unruptured cerebral aneurysms do not shrink when they rupture: multicenter collaborative aneurysm study group.** *Neurosurgery* 2011;68:155–60, discussion 160–61
17. Kataoka K, Taneda M, Asai T, et al. **Difference in nature of ruptured and unruptured cerebral aneurysms.** *Lancet* 2000;355:203
18. Baharoglu MI, Schirmer CM, Hoit DA, et al. **Aneurysm inflow-angle as a discriminant for rupture in sidewall cerebral aneurysms: morphometric and computational fluid dynamic analysis.** *Stroke* 2010;41:1423–30
19. de Rooij NK, Velthuis BK, Algra A, et al. **Configuration of the circle of Willis, direction of flow, and shape of the aneurysm as risk factors for rupture of intracranial aneurysms.** *J Neurol* 2009;256:45–50
20. Beck J, Rohde S, el Beltagy M, et al. **Difference in configuration of ruptured and unruptured intracranial aneurysms determined by biplanar digital subtraction angiography.** *Acta Neurochir (Wien)* 2003;145:861–65, discussion 865

Identification of the Inflow Zone of Unruptured Cerebral Aneurysms: Comparison of 4D Flow MRI and 3D TOF MRA Data

K. Futami, H. Sano, K. Misaki, M. Nakada, F. Ueda, and J. Hamada

ABSTRACT

BACKGROUND AND PURPOSE: The hemodynamics of the inflow zone of cerebral aneurysms may be a key factor in coil compaction and recanalization after endovascular coil embolization. We performed 4D flow MR imaging in conjunction with 3D TOF MRA and compared their ability to identify the inflow zone of unruptured cerebral aneurysms.

MATERIALS AND METHODS: This series comprised 50 unruptured saccular cerebral aneurysms in 44 patients. Transluminal color-coded 3D MRA images were created by selecting the signal-intensity ranges on 3D TOF MRA images that corresponded with both the luminal margin and the putative inflow.

RESULTS: 4D flow MR imaging demonstrated the inflow zone and yielded inflow velocity profiles for all 50 aneurysms. In 18 of 24 lateral-projection aneurysms (75%), the inflow zone was located distally on the aneurysmal neck. The maximum inflow velocity ranged from 285 to 922 mm/s. On 4D flow MR imaging and transluminal color-coded 3D MRA studies, the inflow zone of 32 aneurysms (64%) was at a similar location. In 91% of aneurysms whose neck section plane angle was $<30°$ with respect to the imaging section direction on 3D TOF MRA, depiction of the inflow zone was similar on transluminal color-coded 3D MRA and 4D flow MR images.

CONCLUSIONS: 4D flow MR imaging can demonstrate the inflow zone and provide inflow velocity profiles. In aneurysms whose angle of the neck-section plane is obtuse vis-a-vis the imaging section on 3D TOF MRA scans, transluminal color-coded 3D MRA may depict the inflow zone reliably.

ABBREVIATION: TC 3D MRA = transluminal color-coded 3D MRA

Although endovascular coil embolization has become a major tactic to address cerebral aneurysms, recanalization or recurrence, which may result in rebleeding, are important problems. Recanalization was reported in 6.1%–39.8% of patients who had undergone endovascular treatment,[1-6] and a meta-analysis found that 20.8% of treated aneurysms recurred.[3] The rate of rerupture after endovascular treatment for ruptured aneurysms has ranged from 0.11% to 5.3%,[1,4,6] and the rupture rate in the first year after coil embolization was reported as 2.5%[7] and 2.2%.[8] Because hemodynamics acting on the aneurysmal inflow zone may play a key role in the development of coil compaction or recanalization after endovascular coil embolization, the aneurysmal inflow zone must be packed densely to preserve the durability of aneurysm obliteration and to prevent rerupture.[9-15]

The inflow through the aneurysmal neck into the dome can be seen on 3D TOF MRA images.[13,16,17] Satoh et al,[16,17] who used conventional 3D TOF MRA techniques to select threshold ranges based on the signal intensity of the volume-rendering data, determined the spatial signal-intensity distribution in aneurysms. They developed transluminal color-coded 3D MRA (TC 3D MRA) to improve visualization of the aneurysmal inflow. More recently, 4D flow MR imaging based on time-resolved 3D cine phase-contrast MR imaging techniques was used to evaluate the hemodynamics of cerebral aneurysms.[18-27] However, 4D flow MR imaging requires additional time for data acquisition, and TC 3D MRA may be a convenient alternative to 4D flow MR imaging for identifying the aneurysmal inflow zone.

Here, we compared the ability of 4D flow MR imaging and TC 3D MRA to identify the inflow zone of cerebral aneurysms.

MATERIALS AND METHODS

The institutional review board of Mattoh-Ishikawa Central Hospital approved this study; prior informed consent was obtained from all patients.

Received August 27, 2013; accepted after revision December 16.

From the Department of Neurosurgery (K.F.), Mattoh-Ishikawa Central Hospital, Ishikawa, Japan; and Departments of Neurosurgery (H.S., K.M., M.N., J.H.) and Radiology (F.U.), Kanazawa University School of Medicine, Ishikawa, Japan.

Please address correspondence to Kazuya Futami, MD, Department of Neurosurgery, Mattoh-Ishikawa Central Hospital, 3-8 Kuramitsu, Hakusan, 920-8588 Ishikawa, Japan; e-mail: kfutami@mattohp.com

http://dx.doi.org/10.3174/ajnr.A3877

Table 1: Aneurysm location and consistency of findings

Location	Total	Accordant (Group 1)	*P* Value	Contralateral (Group 2)	*P* Value	Undefined (Group 3)	*P* Value
ICA							
Cavernous	2	1	1.0 (NS)	0	1.0 (NS)	1	.329 (NS)
Paraclinoid	11	6	.494 (NS)	5	.004 (S)	0	.093 (NS)
ICA-PcomA	8	6	.694 (NS)	1	1.0 (NS)	1	.666 (NS)
Bifurcation	1	0	.36 (NS)	0	1.0 (NS)	1	.220 (NS)
AcomA	8	7	.231 (NS)	0	.580 (NS)	1	.666 (NS)
MCA	16	10	1.0 (NS)	1	.406 (NS)	5	.297 (NS)
BA	4	2	.612 (NS)	0	1.0 (NS)	2	.206 (NS)
Total	50	32		7		11	

Note:—S indicates significant; NS, not significant by the Fisher exact test adjusted for the *P* value threshold for each location; BA, basilar artery; AcomA, anterior communicating artery; PcomA, posterior communicating artery.

Table 2: Aneurysm parameters: correlation of group 1 and group 2 and 3 aneurysms[a]

Parameters	Total	Accordant (Group 1)	Contralateral (Group 2)	*P* Value	Undefined (Group 3)	*P* Value
MD	5.2 ± 2.4	5.3 ± 2.1	5.6 ± 2.5	.570 (NS)	4.6 ± 1.4	.823 (NS)
ND	4.1 ± 1.7	4.2 ± 1.7	4.3 ± 1.7	.891 (NS)	3.7 ± 1.7	.372 (NS)
MD/ND ratio	1.3 ± 0.5	1.3 ± 0.4	1.3 ± 0.3	.608 (NS)	1.4 ± 0.8	.616 (NS)
Maximum perpendicular height	4.1 ± 1.3	4.0 ± 1.4	4.2 ± 1.2	.583 (NS)	4.1 ± 1.3	.911 (NS)
Aspect ratio	1.1 ± 0.5	1.0 ± 0.3	1.0 ± 0.4	.91 (NS)	1.3 ± 0.7	.344 (NS)
Maximum height	4.3 ± 1.4	4.3 ± 1.4	4.4 ± 1.3	.826 (NS)	4.2 ± 1.4	.824 (NS)
Size ratio	1.6 ± 0.6	1.7 ± 0.7	1.4 ± 0.4	.360 (NS)	1.6 ± 0.5	.922 (NS)
Angle of neck section to imaging section	52.1 ± 21.8	47.8 ± 22.9	52.9 ± 10.0	.375 (NS)	64.0 ± 20.8	.045 (S)
Maximum inflow velocity	577 ± 164	604 ± 169	449 ± 159	.029 (S)	583 ± 136	.721 (NS)
MRA signal intensity	355 ± 69.0	356 ± 64.6	348 ± 56.8	.752 (NS)	356 ± 91.6	.955 (NS)

Note:—NS indicates not significant by the comparison test adjusted for the *P* value threshold for each parameter; MD, maximum diameter; ND, neck diameter.
[a] Data are means.

Materials

Our study included 50 unruptured saccular cerebral aneurysms (44 patients); 24 were lateral projection and 26 were terminal aneurysms. They were evaluated by 3D TOF MRA and 4D flow MR imaging techniques. Of the 50 aneurysms, 2 were located on the cavernous and 11 on the paraclinoid segment of the ICA; 8 were on the bifurcation of the ICA and the posterior communicating artery; 1 was on the ICA bifurcation; 8 were on the anterior communicating artery; 16, on the MCA bifurcation; and 4, on the basilar artery bifurcation. The maximum diameters of the aneurysms and the neck were 5.2 ± 2.4 mm (range, 2.5–15 mm) and 4.1 ± 1.7 mm (range, 1.5–11.3 mm), respectively.

MR Imaging

MR images were obtained on a 1.5T scanner (Magnetom Avanto; Siemens, Erlangen, Germany) with a slew rate of 125 T/m/s. We used an 8-channel head array coil. Volume datasets were acquired by using a 3D TOF sequence with flow compensation in all 3 orthogonal directions. The imaging parameters for 3D TOF MRA were the following: TR/TE/NEX, 35 ms/7.15 ms/average 1; flip angle, 22°; FOV, 150 × 123 mm; z-coverage, 45.6 mm; 0.6-mm thickness; 3 slabs; 30 sections per slab; slab interval, −4.2 mm; matrix, 256 × 168 (512 × 336 with zero-filling interpolation processing); voxel size, 0.59 × 0.73 × 0.6 mm (0.295 × 0.365 × 0.6 mm with zero-filling); bandwidth, 87 Hz/px; imaging time, 4 minutes 53 seconds; transaxial direction.

The details of 4D flow MR imaging are described elsewhere.[18-20] The imaging parameters were the following: TR/TE/NEX, 33.05 ms/5.63 ms/average 1; flip angle, 22°; FOV, 200 × 200 mm; 0.8-mm thickness; 1 slab; 24–26 sections per slab; z-coverage, 19.2 mm; matrix, 192 × 192; no interpolation processing; voxel size, 1.04 × 1.04 × 0.8 mm; velocity-encoding, 80 cm/s; bandwidth, 434 Hz/px; parallel imaging with reduction factor, 2; imaging time, 20–30 minutes depending on each patient's heart rate; transaxial direction; retrospective gating with electrocardiogram; 20 phases.

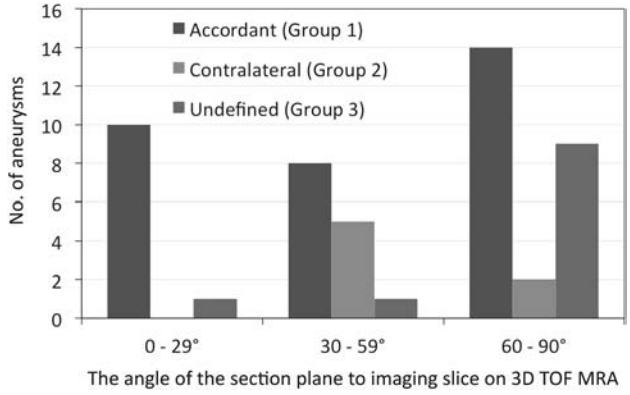

FIG 1. The distribution of group 1, 2, and 3 aneurysms and the 3 ranges (0°–29°, 30°–59°, 60°–90°) of the angle of the section plane that identified the aneurysm orifice with respect to the imaging section direction on 3D TOF MRA (group 1, the location of the inflow zone was in accord on 4D flow MR imaging and transluminal color-coded 3D MRA scans; group 2, the location of the inflow zone was on the contralateral side of the neck; group 3, the location of the inflow zone was undefined). There was a significant difference in the distribution among the angle ranges ($P = .018$). Of 11 aneurysms with the 0°–29° angle range, 10 (90.9%) were assigned to group 1; and the others, to group 3 ($P = .072$, compared with the other angle ranges).

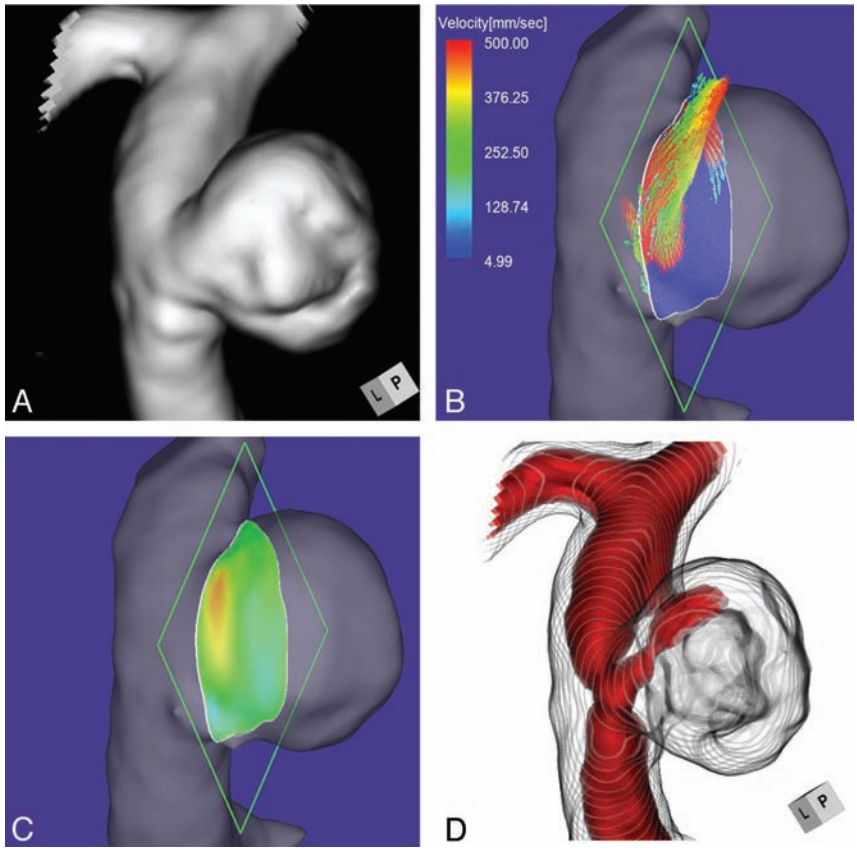

FIG 2. Case 1. A 75-year-old woman with an unruptured right ICA–posterior communicating artery bifurcation aneurysm. *A*, 3D TOF MRA image. *B*, 4D flow MR image demonstrates the inflow area (red) on the section plane and yields inflow velocity profiles. The angle of the section plane that determines the aneurysm orifice with respect to the imaging section direction on 3D TOF MRA is 73°. *C*, 4D flow MR image demonstrates the inflow zone (red). *D*, TC 3D MRA image depicts the putative inflow zone located on the distal neck. Red indicates the area where the MR signal intensity exceeded 375.

The 3D datasets obtained by 4D flow MR imaging were analyzed with commercially available software (Flova II, Version 2.8.6; R'tech Co, Hamamatsu, Japan). On the basis of the 3D TOF MRA datasets, the vascular structures were segmented by using the region-growing method.[28] Vascular shapes were created with the "marching cubes" method.[29] For visualization of 3D flow information, the 3D datasets obtained by 4D flow MR imaging were converted to pixel datasets at a spatial resolution of 0.5 × 0.5 × 0.5 mm by a function of the software. To evaluate the inflow area, we selected a section plane corresponding to the aneurysmal orifice. Cerebral aneurysms with a complicated neck configuration were excluded from this study. Three of the authors (K.F., M.N., and F.U.) determined the window width and level of all datasets and selected the section plane of the neck. Each had >15 years of experience; decisions were made by consensus. The inflow zone obtained by 4D flow MR imaging was defined as the orifice area where components vertical to the section plane of the inflow vectors exceeded 60% of the maximum inflow velocity at peak systole; automatic depiction was as an animation image.

Details on the reconstruction of TC 3D MRA images have been described elsewhere.[16,17] Briefly, volume data comprising 76 source axial images were transferred to a workstation with medical visualization software (Zio Station 2, Version 2.1; AMIN, Tokyo, Japan). Using a perspective volume-rendering algorithm, we created TC 3D MRA images by selecting a histogram of the signal intensity of volume-rendering 3D TOF MRA data that corresponded to the luminal margin (signal intensity; 145–160) and by determining the depiction range of the signal-intensity distribution in the aneurysmal lumen. On TC 3D MRA images, the luminal margin was visualized as a series of rings. The putative inflow zone on TC 3D MRA images was defined as the part of the orifice where the area of high MR signal intensity continued through the orifice into the aneurysmal lumen. The MR signal intensity used to identify the inflow zone ranged from 240 to 550 (mean; 355 ± 69.0).

Data Analysis

We compared the inflow zone of the cerebral aneurysms identified by TC 3D MRA and 4D flow MR imaging. We also compared data obtained by these methods with respect to the aneurysm location, morphologic parameters, maximum inflow velocity, MRA signal intensity of the inflow, and angle of the section plane that identified the aneurysm orifice with respect to the imaging section direction on 3D TOF MRA. The morphologic parameters included the maximum diameter of the aneurysm and its neck, the maximum perpendicular height, the maximum height, the aspect ratio, and the size ratio of the aneurysm.[30-32] Each numeric value of the various parameters was determined as the mean of the nearest 2 values independently estimated by the 3 readers.

Data are expressed as the mean ± SD. For statistical analysis, we used the Student *t* test or the Mann-Whitney *U* test for continuous variables and the Fisher exact test for categoric variables. A *P* value < .05 was considered significant.

RESULTS

4D flow MR imaging demonstrated the inflow zone and the inflow velocity profiles. In 18 of the 24 lateral-projection aneurysms, the inflow zone was in the distal neck; in 2, it was in the proximal neck; and in 4, it was on the other side of the neck. In these 24 aneurysms, there was no significant difference with respect to their location or morphologic parameters. In all 26 terminal aneurysms, the inflow zone encompassed a line extending from the central axis of the parent artery. Maximum inflow velocity ranged from 285 to 922 mm/s (mean, 577 ± 164 mm/s).

In 32 aneurysms (group 1, 64%), the location of the inflow zone was in accord on 4D flow MR imaging and TC 3D MRA scans; in 7 (group 2, 14%), it was on the contralateral side of the neck, and in 11 (group 3, 22%), its location was undefined. We looked for factors involved in the consistency of findings made by TC 3D MRA and 4D flow MR imaging with respect to the location of the

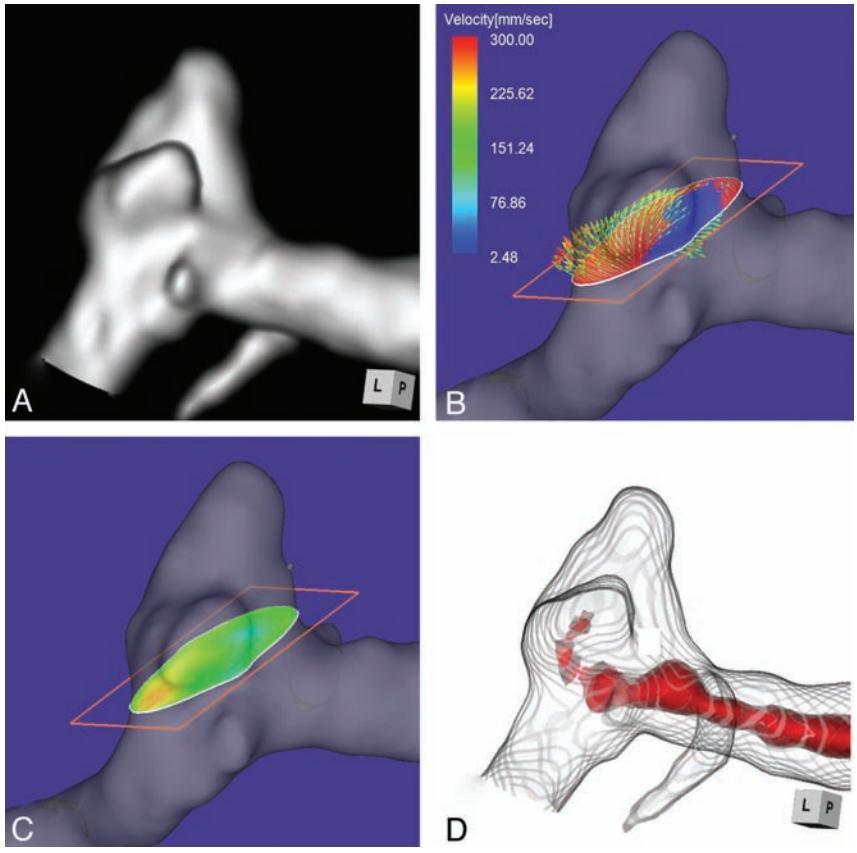

FIG 3. Case 2. A 58-year-old woman with an unruptured multilobulated aneurysm at the left MCA bifurcation. *A*, 3D TOF MRA. *B*, 4D flow MR imaging demonstrates inflow entering through the distal neck of the aneurysmal orifice. The angle of the section plane that identifies the aneurysmal orifice with respect to the imaging section direction on 3D TOF MRA is 25°. *C*, 4D flow MR imaging demonstrates the inflow zone (red). *D*, TC 3D MRA depicts the putative inflow zone located on the distal neck. Red indicates the area where the MR signal intensity exceeds 320.

inflow zone (Tables 1 and 2). In 11 aneurysms on the paraclinoid segment of the ICA, there was a significant correlation with findings that located the inflow zone on the contralateral side of the neck ($P = .004$). The maximum inflow velocity was significantly lower in group 2 than group 1 aneurysms (449 ± 159 versus 583 ± 136 mm/s, $P = .029$). There was no significant difference with respect to morphologic parameters and the MRA signal intensity.

The angle of the section plane of the neck with respect to the imaging section on 3D TOF MRA was significantly lower in group 1 than in group 3 (47.8 ± 22.8° versus 64.0 ± 20.8°, $P = .045$) (Table 2). Figure 1 shows the distribution of group 1, 2, and 3 aneurysms and the degree ranges (0°–29°, 30°–59°, 60°–90°) of the angle of the section plane with respect to the imaging section. The difference in the distribution among the 3 degree ranges was significant ($P = .018$). Ten of 11 aneurysms with an angle range of 0°–29°(90.9%) were in group 1; the other was a group 3 aneurysm ($P = .072$, compared with the other angle ranges).

Case Presentation

Case 1. Case 1 was a 75-year-old woman with an incidentally detected unruptured aneurysm at the right ICA–posterior communicating artery bifurcation. Its maximum diameter and neck diameter were 8.0 and 4.6 mm, respectively (Fig 2*A*). The angle of the section plane that identified the aneurysm orifice with respect to the imaging section direction on 3D TOF MRA was 73°. 4D flow MR imaging demonstrated that the flow entered through the distal neck of the aneurysmal orifice (Fig 2*B*). At peak systole, the maximum inflow velocity was 536 mm/s. 4D flow MR imaging placed the inflow zone on the distal side of the orifice (Fig 2*C*). We used red color coding to identify the area where the MR signal intensity exceeded 375 on TC 3D MRA images (Fig 2*D*). Consistent with the findings returned by 4D flow MR imaging, the inflow entered the aneurysmal lumen on the distal side of the neck. This aneurysm was placed in group 1.

Case 2. Case 2 was a 58-year-old woman with an unruptured multilobulated aneurysm at the left MCA bifurcation. The aneurysmal maximum diameter and neck measured 5.1 and 5.0 mm, respectively (Fig 3*A*). The angle of the section plane that identified the orifice with respect to the imaging section direction on 3D TOF MRA was 25°. 4D flow MR imaging showed that the inflow entered through the distal neck of the aneurysmal orifice (Fig 3*B*). The maximum inflow velocity was 301 mm/s. The inflow zone was located at the distal neck (Fig 3*C*). On TC 3D MRA images, the area with a signal intensity of >320 suggested that the inflow entered through the distal neck (Fig 3*D*). This aneurysm was recorded as a group 1 aneurysm.

Case 3. Case 3 was a 51-year-old woman who presented with a medially projecting unruptured aneurysm on the paraclinoid segment of the left ICA (Fig 4*A*). The maximum diameters of the aneurysm and the neck were 5.4 and 2.9 mm, respectively. The angle of the section plane that identified the aneurysmal orifice with respect to the imaging section direction on 3D TOF MRA was 56°. 4D flow MR imaging showed that the inflow entered through a small area on the distal neck (Fig 4*B*) where the inflow zone was located (Fig 4*C*); maximum inflow velocity was 285 mm/s. On TC 3D MRA images, color coding of the area with a signal intensity of >300 suggested that the inflow entered through the proximal neck and flowed along the aneurysm wall (Fig 4*D*). Because these findings suggested that the putative inflow zone was located on the proximal rather than the distal neck, this aneurysm was placed in group 2.

Case 4. Case 4 was a 70-year-old man who presented with a medially projecting, unruptured aneurysm on the paraclinoid segment of the right ICA (Fig 5*A*). The maximum diameters of the aneurysm and neck were 3.6 and 4.0 mm, respectively. The angle of the section plane that identified the aneurysm orifice with respect to the imaging section direction on 3D TOF MRA

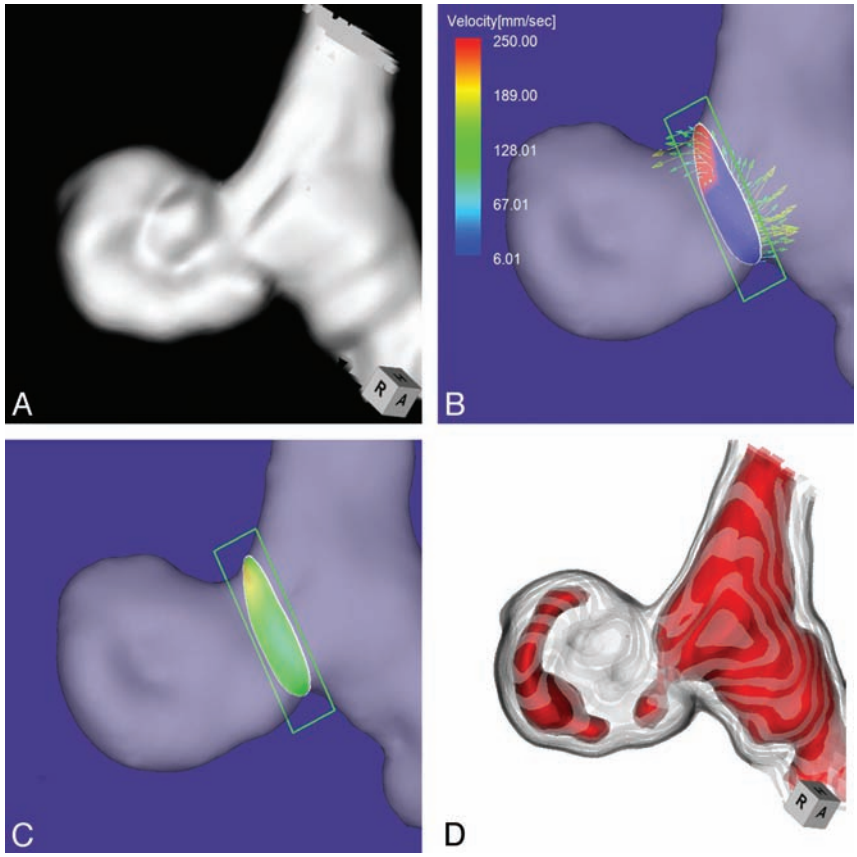

FIG 4. Case 3. A 51-year-old woman with a medially projecting unruptured aneurysm on the paraclinoid segment of the left ICA. *A*, 3D TOF MRA image. *B*, 4D flow MR imaging demonstrates flow entering through the distal neck. The angle of the section plane that identifies the aneurysm orifice with respect to the imaging section direction on 3D TOF MRA is 56°. *C*, 4D flow MR imaging shows the inflow zone (red). *D*, TC 3D MRA image depicts the putative inflow zone on the proximal neck. Red indicates the area where the MR signal intensity exceeds 300.

was 65°. 4D flow MR imaging showed that the flow entered the aneurysmal lumen through an area along the distal margin of the neck (Fig 5*B*). The inflow zone was located on the distal neck (Fig 5*C*). The maximum inflow velocity was 406 mm/s. On TC 3D MRA images, color coding of the area with a signal intensity of >395 suggested that inflow entered through the proximal neck (Fig 5*D*). We posited that the putative inflow zone was located on the proximal rather than the distal neck and placed this aneurysm in group 2.

Case 5. Case 5 was a 65-year-old man with an unruptured lateral-projection aneurysm on the cavernous segment of the left ICA. The maximum diameters of the aneurysm and the neck were 7.3 and 6.8 mm, respectively (Fig 6*A*). The angle of the section plane that identified the aneurysm orifice with respect to the imaging section direction on 3D TOF MRA was 86°. By 4D flow MR imaging, the inflow entered through the lateral half of the aneurysmal orifice (Fig 6*B*). The inflow zone was located on the side lateral to the neck (Fig 6*C*). The maximum inflow velocity was 647 mm/s. However, on TC 3D MRA images, identification of the area with a signal intensity of >410 suggested that the putative inflow zone was located on the distal neck (Fig 6*D*). This aneurysm was assigned to group 3.

DISCUSSION

Graves et al[9] studied a canine carotid aneurysm model and reported that aneurysms exhibited 3 distinct flow zones: an inflow zone, an outflow zone, and a central slow flow vortex. They stressed the importance of packing the inflow zone for successful aneurysm obliteration. Coils placed in the inflow zone block the impact exerted by the blood stream on the aneurysmal wall and induce thrombosis formation within the dome.[9,15] After endovascular treatment, the water hammer effect of the blood flow results in coil compaction in the inflow zone and recanalization.[10,15] Valencia et al[14] observed high wall shear stress and increased pressure in the inflow zone; both are related to the regrowth and rerupture of cerebral aneurysms. Therefore, to obtain good treatment outcomes, one must identify the exact location of the inflow zone and evaluate the hemodynamics in this area.

During the coil embolization procedure, DSA may yield information on the temporally resolved hemodynamics and may help to identify the inflow zone. However, the information provided by this conventional method is limited. It cannot be used for the acquisition of quantitative variables of various hemodynamic parameters or of data at arbitrary time points in the cardiac cycle, and it is not 3D. Furthermore, DSA information can be affected by the speed or direction of the injected contrast medium and even by the mass effect of an inserted catheter.

4D flow MR imaging facilitates the direct, noninvasive measurement of the in vivo 3D blood flow and its velocity in the vascular region of interest.[33-35] Technologic advances in MR imaging have made it possible to assay the flow condition in aneurysms by 4D flow MR imaging.[18,19] Both 4D flow MR imaging and computational fluid dynamics studies, used to evaluate the hemodynamics of cerebral aneurysms, returned similar results with respect to velocity distributions, inflow streamlines, and intraaneurysmal flow patterns in human cerebral[19,21,23] and experimental canine aneurysms.[36] In addition, 4D flow MR imaging results were validated by computational fluid dynamics studies performed on a life-size human aneurysm phantom.[37-39] Moreover, previous studies confirmed the feasibility of depicting the aneurysmal inflow.[18,20,23,26,27] Consequently, 4D flow MR imaging is the criterion standard for the identification of the inflow zone of cerebral aneurysms.

According to others,[11,13,40] the inflow zone of lateral-projection aneurysms was located on the distal neck. However, in 6 of our 24 lateral-projection aneurysms (25%), it was found on the other side of the neck. Because these 6 aneurysms did not differ in their location

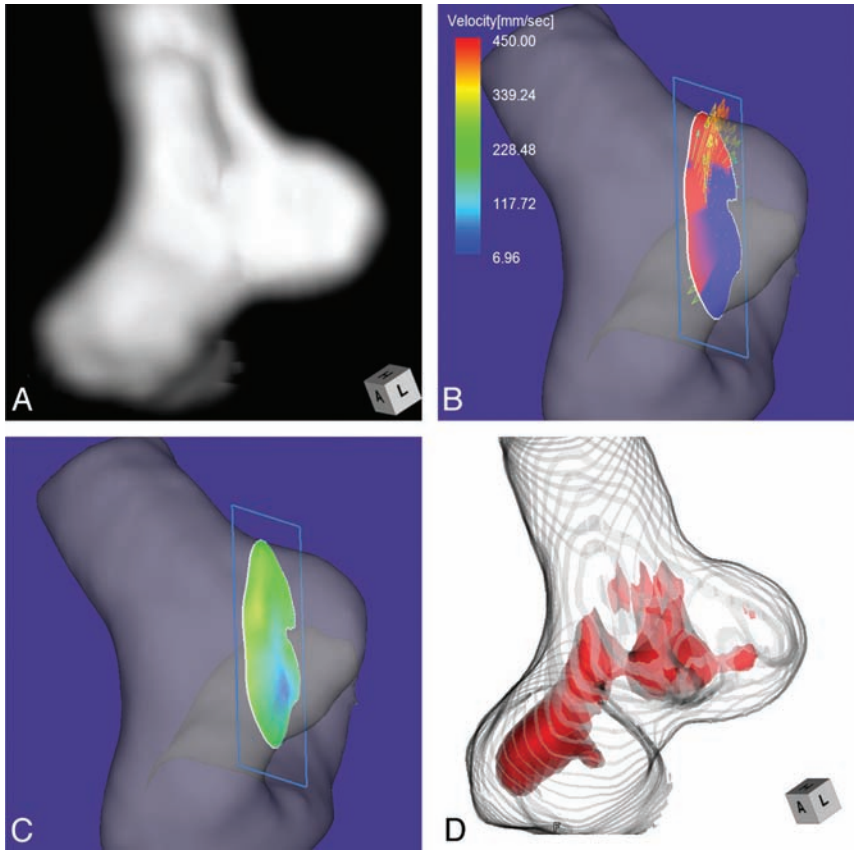

FIG 5. Case 4. A 70-year-old man with a medially projecting, unruptured aneurysm on the paraclinoid segment of the right ICA. *A*, 3D TOF MRA image. *B*, 4D flow MR image shows that the inflow enters through the area along the distal margin of the neck. The angle of the section plane that identifies the aneurysm orifice with respect to the imaging section direction on 3D TOF MRA is 65°. *C*, 4D flow MR imaging shows the inflow zone (yellow). *D*, TC 3D MRA image depicts the putative inflow zone on the proximal neck. Red indicates the area where the MR signal intensity exceeded 395.

and morphologic parameters from aneurysms whose inflow zone was on the distal neck, it is important to identify the exact location of the inflow zone even in lateral-projection aneurysms. The range of maximum inflow was very wide (285–922 mm/s). High inflow velocity might be a predisposing factor for coil compaction or recanalization after endovascular coil embolization.

We investigated whether TC 3D MRA represents a convenient alternative to 4D flow MR imaging for identifying the aneurysmal inflow zone. We found that in 64% of our aneurysms (group 1), the inflow zone identified on TC 3D MRA and 4D flow MR imaging coincided, while in 14%, especially in paraclinoid aneurysms, the 2 methods localized the inflow zone on opposite sides of the neck (group 2). To identify aneurysms whose inflow zone is reliably depicted on TC 3D MRA images without the aid of 4D flow MR imaging, we looked for factors that played a role in the consistency of findings made with TC 3D MRA and 4D flow MR imaging. Neither the aneurysm location, morphologic parameters, nor the MRA signal intensity of the inflow could predict the consistency.

The signal intensity of 3D TOF MRA is mainly affected by the flow velocity.[41-44] In this study, the maximum inflow velocity in our group 2 aneurysms was significantly lower than that in group 1 ($P = .029$). The sensitivity of 3D TOF MRA, on the other hand, is affected by the direction of the blood flow.[41-44] We measured the angle of the section plane that identified the aneurysm orifice with respect to the imaging section direction on 3D TOF images. This angle was significantly smaller in group 1 than in group 3 aneurysms ($P = .045$). In 10 of 11 aneurysms (91%) whose angle ranged from 0° to 29°, the inflow zone was at a similar location on 4D flow MR imaging and TC 3D MRA studies. In the remaining aneurysm, 3D TOF MRA failed to depict the putative inflow zone. Our findings suggest that if 3D TOF MRA can depict the putative inflow zone in aneurysms whose neck has a section plane angle below 30° with respect to the imaging section direction, the information it yields is very precise. Concentric flow conditions such as slow or turbulent flow may lead to a regional elimination of TOF signal intensities,[41-44] and this may result in misidentification of the inflow zone on 3D TOF MRA images. However, in this study, no aneurysms were excluded due to signal loss when estimating the inflow zone and measuring morphologic parameters. Moreover, in conjunction with interpolation methods for 3D TOF MRA, the voxel dimensions may affect TOF signal intensities.[42-44] Further studies are needed to improve the accuracy of 3D TOF MRA results,.

Our study has some limitations. First, because most of the aneurysms were part of a long-term follow-up study, many of the included small and wide-neck aneurysms were not candidates for endovascular coil embolization. Second, for 4D flow MR imaging to evaluate the inflow zone, we used a section plane that corresponded to the aneurysm orifice. This rendered difficult the 4D flow MR imaging of cerebral aneurysms whose neck configuration was complicated, and such aneurysms were excluded from the present study. Third, the spatial resolution of both 4D flow MR imaging and 3D TOF MRA is limited. Although we expected the visibility of the inflow zone of small aneurysms to be poor on both types of study, there was no significant difference in our ability to identify the inflow zone in groups categorized by the maximum diameter of the aneurysm (data not shown). On 4D flow MR images, the spatial averaging effect and the partial volume effect may result in incorrect flow estimation.[18] To evaluate the flow condition in aneurysms with a minimum diameter of 2.0 mm, a spatial resolution of 0.5 mm in the isotropic voxel dimensions may be desirable.[37] Because the number of aneurysms included in this study was relatively small, larger series are needed to identify the role of aneurysmal size.

CONCLUSIONS

We recommend that before endovascular coil embolization, the exact location of the inflow zone be identified, even in

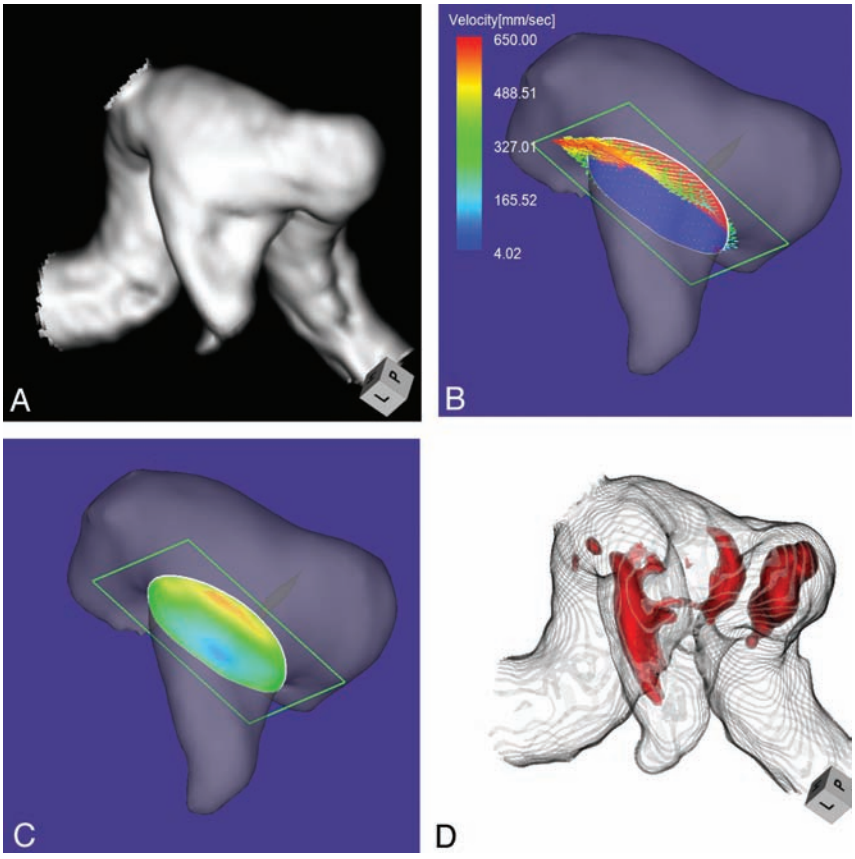

FIG 6. Case 5. A 65-year-old man with an unruptured aneurysm on the cavernous segment of the left ICA. *A,* 3D TOF MRA image. *B,* 4D flow MR image shows the inflow area (red) on the section plane and inflow velocity profiles. The angle of the section plane that identifies the aneurysm orifice with respect to the imaging section direction on 3D TOF MRA is 86°. *C,* 4D flow MR imaging shows the inflow zone (red). *D,* TC 3D MRA image depicts the putative inflow zone on the distal neck. Red indicates the area where the MR signal intensity exceeds 410.

lateral-projection aneurysms. 4D flow MR imaging can demonstrate the inflow zone and provide inflow velocity profiles. In aneurysms whose neck section plane angle is <30° with respect to the imaging section direction on 3D TOF MRA images, TC 3D MRA may depict the inflow zone reliably. Further studies on the hemodynamics of the inflow zone are needed to clarify the mechanisms of coil compaction or recanalization in patients with cerebral aneurysms treated by endovascular coil embolization.

ACKNOWLEDGMENTS

We are grateful to Professor Jun-ichiro Hamada for his encouragement and his dedication to our work. We mourn his untimely death. We thank Aki Watanabe, MR application specialist, Application Department, Siemens Japan, Tokyo, Japan, for technical advice, and Keiko Sumita, RT, and Takamitsu Matsuzaki, RT, of the Department of Radiation Technology, Mattoh-Ishikawa Central Hospital, Hakusan, Japan, for their dedicated support in performing this study.

REFERENCES

1. Choi DS, Kim MC, Lee SK, et al. **Clinical and angiographic long-term follow-up of completely coiled intracranial aneurysms using endovascular technique.** *J Neurosurg* 2010;112:575–81
2. Crobeddu E, Lanzino G, Kallmes DF, et al. **Review of 2 decades of aneurysm-recurrence literature. Part 2. Managing recurrence after endovascular coiling.** *AJNR Am J Neuroradiol* 2013;34:481–85
3. Ferns SP, Sprengers MES, van Rooji WJ, et al. **Coiling of intracranial aneurysms: a systematic review on initial occlusion and reopening and retreatment rates.** *Stroke* 2009;40:e523–29
4. Ries T, Siemonsen S, Thomalla G, et al. **Long-term follow-up of cerebral aneurysms after endovascular therapy: prediction and outcome of retreatment.** *AJNR Am J Neuroradiol* 2007;28:1755–61
5. Tso MK, Kochar P, Goyal M, et al. **Long-term angiographic and clinical outcomes in completely versus incompletely coiled ruptured intracranial aneurysms.** *Clin Neurosurg* 2011;58:143–48
6. Willinsky RA, Peltz J, da Costa L, et al. **Clinical and angiographic follow-up of ruptured intracranial aneurysms treated with endovascular embolization.** *AJNR Am J Neuroradiol* 2009;30:1035–40
7. Johnston SC, Dowd CF, Higashida RT, et al. **Predictors of rehemorrhage after treatment of ruptured intracranial aneurysms: the Cerebral Aneurysm Rerupture After Treatment (CARAT) study.** *Stroke* 2008;39:120–25
8. Molyneux A, Kerr R, Stratton I, et al, for the International Subarachnoid Aneurysm Trial (ISAT) Collaborative Group. **International Subarachnoid Aneurysm Trial (ISAT) of neurosurgical clipping versus endovascular coiling in 2143 patients with ruptured intracranial aneurysms: a randomised trial.** *Lancet* 2002;360:1267–74
9. Graves VB, Strother CM, Duf TA, et al. **Early treatment of ruptured aneurysms with Guglielmi detachable coils: effect on subsequent bleeding.** *Neurosurgery* 1995;37:640–48, discussion 647–48
10. Hayakawa M, Murayama Y, Duckwiler GR, et al. **Natural history of the neck remnant of a cerebral aneurysm treated with the Guglielmi detachable coil system.** *J Neurosurg* 2000;93:561–68
11. Hoh BL, Putman CM, Budzik RF, et al. **Combined surgical and endovascular techniques of flow alteration to treat fusiform and complex wide-necked intracranial aneurysms that are unsuitable for clipping or coil embolization.** *J Neurosurg* 2001;95:24–35
12. Imbesi SG, Kerber CW. **Analysis of slipstream flow in a wide-necked basilar artery aneurysm: evaluation of potential treatment regimens.** *AJNR Am J Neuroradiol* 2001;22:721–24
13. Kudo T, Satow T, Yamada N, et al. **Identification of inflow zone of cerebral aneurysms by MRA for effective coil embolization** [in Japanese with an English abstract]. *Surg Cerebral Stroke* (Jpn) 2008;36:459–63
14. Valencia AA, Guzmán AM, Finol EA, et al. **Blood flow dynamics in saccular aneurysm models of the basilar artery.** *J Biomech Eng* 2006;128:516–26
15. Viñuela F. **Comments for histological findings in coil-packed experimental aneurysms 3 months after embolization.** *Neurosurgery* 2002;50:384–85
16. Satoh T, Onoda K, Tsuchimoto S. **Visualization of intraaneurysmal flow patterns with transluminal flow images of 3D MR angiograms in conjunction with aneurysmal configurations.** *AJNR Am J Neuroradiol* 2003;24:1436–45
17. Satoh T, Ekino C, Ohsako C. **Transluminal color-coded three-di-**

mensional magnetic resonance angiography for visualization of signal intensity distribution pattern within an unruptured cerebral aneurysm: preliminarily assessment with anterior communicating aneurysms. *Neuroradiology* 2004;46:628–34
18. Meckel S, Stalder AF, Santini F, et al. **In vivo visualization and analysis of 3-D hemodynamics in cerebral aneurysms with flow-sensitized 4-D MR imaging at 3 T.** *Neuroradiology* 2008;50:473–84
19. Boussel L, Rayz V, Martin A, et al. **Phase-contrast magnetic resonance imaging measurements in intracranial aneurysms in vivo of flow patterns, velocity fields, and wall shear stress: comparisons with computational fluid dynamics.** *Magn Reson Med* 2009;61:409–17
20. Hope TA, Hope MD, Purcell DD, et al. **Evaluation of intracranial stenoses and aneurysms with accelerated 4D flow.** *Magn Reson Imaging* 2010;28:41–46
21. Isoda H, Ohkura Y, Kosugi T, et al. **Comparison of hemodynamics of intracranial aneurysms between MR fluid dynamics using 3D cine phase contrast MRI and MR-based computational fluid dynamics.** *Neuroradiology* 2010;52:913–20
22. Isoda H, Ohkura Y, Kosugi T, et al. **In vivo hemodynamic analysis of intracranial aneurysms obtained by magnetic resonance fluid dynamics (MRFD) based on time-resolved three-dimensional phase-contrast MRI.** *Neuroradiology* 2010;52:921–28
23. Naito T, Miyachi S, Matsubara N, et al. **Magnetic resonance fluid dynamics for intracranial aneurysms: comparison with computed fluid dynamics.** *Acta Neurochir (Wien)* 2012;154:993–1001
24. Kawaguchi T, Nshimura S, Kanamori M, et al. **Distinctive flow pattern of wall shear stress and oscillatory shear index: similarity and dissimilarity in ruptured and unruptured cerebral aneurysm blebs.** *J Neurosurg* 2012;117:774–80
25. Kecskemeti S, Johnson K, Wu Y, et al. **High resolution three-dimensional cine phase contrast MRI of small intracranial aneurysms using a stack of stars k-space trajectory.** *J Magn Reason Imaging* 2012;35:518–27
26. van Ooij P, Schneuders JJ, Marquering HA, et al. **3D cine phase-contrast MRI at 3T in intracranial aneurysms compared with patient-specific computational fluid dynamics.** *AJNR Am J Neuroradiol* 2013;34:1785–91
27. Schnell S, Ansari SA, Vakil P, et al. **Three-dimensional hemodynamics in intracranial aneurysms: influence of size and morphology.** *J Man Reason Imaging* 2014;39:120–31
28. Lorensen WE, Cline HE. **Marching cubes: a high resolution 3D surface construction algorithm.** *Comput Graph* 1987;21:163–69
29. Shimai H, Yokota H, Nakamura S, et al. **Extraction from biological volume data of a region of interest with nonuniform intensity.** In Sumi K, ed. *Optomechatronic Machine Vision. Proceedings of SPIE.* Bellingham: WA: SPIE; 2005;6051:605
30. Dhar S, Tremmel M, Mocco J, et al. **Morphological parameter for intracranial aneurysm rupture risk assessment.** *Neurosurgery* 2008; 63:185–96, discussion 196–97
31. Raghavan ML, Ma B, Harbaugh RE. **Quantified aneurysm shape and rupture risk.** *J Neurosurg* 2005;102:355–62
32. Ujiie H, Tamano Y, Sasaki K, et al. **Is the aspect ratio a reliable index for predicting the rupture of a saccular aneurysm?** *Neurosurgery* 2001;48:495–502, discussion 502–03
33. Pelc NJ, Herfkens RJ, Shimakawa A, et al. **Phase contrast cine magnetic resonance imaging.** *Magn Reson Q* 1991;4:229–54
34. Markl M, Chan FP, Alley MT, et al. **Time-resolved three-dimensional phase-contrast MRI.** *J Magn Reason Imaging* 2003;17:499–506
35. Bammer R, Hope TA, Aksoy M, et al. **Time-resolved 3D quantitative flow MRI of the major intracranial vessels: initial experience and comparative evaluation at 1.5T and 3.0T in combination with parallel imaging.** *Magn Reson Med* 2007;57:127–40
36. Jiang J, Johnson K, Valen-Sendstad K, et al. **Flow characteristics in a canine aneurysm model: a comparison of 4D accelerated phase contrast MR measurements and computational fluid dynamics simulations.** *Med Phys* 2011;38:6300–12
37. Hollnagel DI, Summers PE, Poulikakos D, et al. **Comparative velocity investigations in cerebral arteries and aneurysms: 3D phase-contrast MR angiography, laser Doppler velocimetry and computational fluid dynamics.** *NMR Biomed* 2009;22:795–808
38. van Ooij P, Guedon A, Poelma C, et al. **Complex flow patterns in a real-size intracranial aneurysm phantom: phase contrast MRI compared with particle image velocimetry and computational fluid dynamics.** *NMR Biomed* 2012;25:14–26
39. van Ooij P, Potters WV, Guédon A, et al. **Wall shear stress estimated with phase contrast MRI in an in vitro and in vivo intracranial aneurysm.** *J Magn Reson Imaging* 2013;38:876–84
40. Byun HS, Rhee K. **CFD modeling of blood flow following coil embolization of aneurysms.** *Med Eng Phys* 2004;26:755–61
41. Bradley WD, Walunch V. **Blood flow: magnetic resonance imaging.** *Radiology* 1985;154:443–50
42. Sevick RJ, Tsuruda JS, Schmalbrock P. **Three-dimensional time-of-flight MR angiography in the evaluation of cerebral aneurysms.** *J Comput Assist Tomogr* 1990;14:874–81
43. Schuierer G, Huk WJ, Laub G. **Magnetic resonance angiography of intracranial aneurysms: comparison with intra-arterial digital subtraction angiography.** *Neuroradiology* 1992;35:50–54
44. Kim SE, Parker DL. **Time-of-flight angiography.** In: Carr JC, Carroll TJ, eds. *Magnetic Resonance Angiography: Principles and Applications.* Vol 39. New York: Springer-Verlag Science+Business Media; 2012

Natural Course of Dissecting Vertebrobasilar Artery Aneurysms without Stroke

N. Kobayashi, Y. Murayama, I. Yuki, T. Ishibashi, M. Ebara, H. Arakawa, K. Irie, H. Takao, I. Kajiwara, K. Nishimura, K. Karagiozov, and M. Urashima

ABSTRACT

BACKGROUND AND PURPOSE: The natural history and therapeutic management of dissecting vertebrobasilar aneurysms without ischemic or hemorrhagic stroke (nonstroke dissecting vertebrobasilar aneurysms) are not well-established. We conservatively followed patients with nonstroke dissecting vertebrobasilar aneurysms and evaluated the factors related to clinical and morphologic deterioration.

MATERIALS AND METHODS: One hundred thirteen patients were enrolled and divided by clinical presentation at diagnosis: asymptomatic (group 1, $n = 52$), pain only (group 2, $n = 56$), and mass effect (group 3, $n = 5$). Patients were conservatively managed without intervention and antithrombotic therapy. Clinical outcomes and morphologic changes were analyzed.

RESULTS: A total of 113 patients who were diagnosed with nonstroke dissecting vertebrobasilar aneurysm had a mean follow-up of 2.9 years (range, 27 days to 8 years). Throughout that period, 1 patient in group 1 (1.9%) and 1 patient in group 2 (1.8%) showed clinical deterioration due to mass effect, and 1 patient in group 3 (20%) developed ischemic stroke followed by subarachnoid hemorrhage. Most patients (97.3%) were clinically unchanged. Three patients who had clinical deterioration showed aneurysm enlargement ($P < .001$). Aneurysms remained morphologically unchanged in 91 patients (80.5%). Aneurysm enlargement was seen in 5 patients (4.4%); risk of enlargement was significantly associated with either maximum diameter (hazard ratio = 1.30; 95% CI, 1.11–11.52; $P = .001$) or aneurysm ≥10 mm (hazard ratio = 18.0; 95% CI, 1.95–167; $P = .011$).

CONCLUSIONS: The natural course of these lesions suggests that acute intervention is not always required and close follow-up without antithrombotic therapy is reasonable. Patients with symptoms due to mass effect or aneurysms of >10 mm may require treatment.

ABBREVIATIONS: DVBA = dissecting vertebrobasilar aneurysm

The detection and diagnosis of dissecting vertebrobasilar aneurysms without ischemic or hemorrhagic stroke (nonstroke DVBAs) have increased due to recent advancements in noninvasive brain imaging screening techniques. At the same time, the natural history of nonstroke DVBA is unknown.[1,2] Furthermore, the risks and benefits of antiplatelet or anticoagulation therapy for nonstroke DVBA are unclear. The aim of this study was to evaluate the natural course of nonstroke DVBA by identifying the factors associated with clinical and morphologic deterioration and thus contributing to the optimal management strategy.

Received August 30, 2013; accepted after revision December 2.

From the Department of Neurosurgery (N.K., Y.M., I.Y., T.I., M.E., H.A., K.I., H.T., I.K., K.N., K.K.) and Division of Molecular Epidemiology (M.U.), The Jikei University School of Medicine, Tokyo, Japan.

Please address correspondence to Yuichi Murayama, MD, Department of Neurosurgery, The Jikei University School of Medicine, 3-25-8 Nishi-Shinbashi, Minato-ku, Tokyo, Japan; e-mail: ymurayama@jikei.ac.jp

http://dx.doi.org/10.3174/ajnr.A3873

MATERIALS AND METHODS

From October 2003 to April 2012, one hundred fifty-five patients at our institution were diagnosed with intracranial DVBA, defined as a nonsaccular aneurysm located at a nonbranching site of the vertebrobasilar artery system. Patients with subarachnoid hemorrhage ($n = 11$), ischemic stroke ($n = 8$), prior surgery ($n = 11$), and a single visit for a second opinion ($n = 12$) were excluded; thus, 113 patients were enrolled prospectively in this study. It was approved by the institutional review board of our university, and informed consent was obtained from all patients for inclusion.

The 113 patients were divided into 3 groups based on their clinical presentation at diagnosis. Group 1 included asymptomatic patients who were diagnosed incidentally on a prophylactic brain screening MRA study ($n = 52$), group 2 patients presented with pain only ($n = 56$), and group 3 patients presented with mass effect from the aneurysm ($n = 5$). A history of pain was considered relevant only when the patient had a sudden onset of neck or back pain and the date and timing were clearly indicated (Table 1). Patients were followed conservatively with noninvasive imag-

ing studies, without endovascular or surgical intervention. The existence of pre-existing conditions and risk factors, such as hypertension, hyperlipidemia, and current smoking, was evaluated; however, antiplatelet or anticoagulation therapy was not applied in addition to their pre-existing management.

Radiographic evaluation was performed by using 3D-CTA (Somatom Sensation 16; Siemens, Erlangen, Germany) according to our currently accepted protocol. The parameters include FOV = 180, 100 kV, 250 mA, 60-mL contrast at 4 mL/s. The data were transferred to a 3D workstation (TeraRecon, San Mateo, California) by using stretch view software, and the maximum diameter of each aneurysm was measured (including the parent artery, $n = 92$) (Fig 1). Patients who had contraindications or refused contrast-enhanced CTA ($n = 21$) were evaluated by MR angiography (Magnetom Symphony 1.5T; Siemens), and their aneurysms were measured by using axial source images from time-of-flight sequences. All 113 patients were observed with consecutive 3D-CTA and/or MRA TOF. Morphologic evaluation classified results as "unchanged," "improved," or "enlarged." "Improved" was defined as any reduction by ≥1 mm in aneurysm diameter or normalization of pearl-and-strings findings (ie, stenosis normalization).

Clinical outcomes were evaluated with the modified Rankin Scale, and "deteriorated" was defined as ≥1 point deterioration on the scale.

To find the factors related to clinical and morphologic changes, we also included the following criteria: sex, size (<10 mm versus >10 mm), initial presentation, pre-existing diseases, and smoking history.

Table 1: Patient characteristics stratified by clinical presentation at diagnosis

	Group 1: Asymptomatic (*n* = 52)	Group 2: Pain (*n* = 56)	Group 3: Mass Effects (*n* = 5)	*P* Value
Age (yr) (mean) (SD)[a]	59.3 (9.4)	51.1 (10.6)	54.0 (11.7)	.0002[a]
Male (No.) (%)	38 (73.1)	44 (78.6)	4 (80.0)	.78[b]
Hypertension (No.) (%)	35 (67.3)	19 (33.9)	2 (40.0)	.002[b]
Diabetes (No.) (%)	1 (1.9)	5 (8.9)	0 (0.0)	.23[b]
Hyperlipidemia (No.) (%)	7 (13.5)	14 (25.0)	2 (40.0)	.18[b]
Current smoker (No.) (%)	24 (46.2)	26 (46.4)	1 (20.0)	.51[b]
Initial size of aneurysm (mean) (SD)[a]	7.7 (3.3)	7.2 (3.2)	10.2 (3.5)	.12[a]
Aneurysm location (No.) (%)				.70[b]
Left VA	18 (34.6)	25 (44.6)	1 (20.0)	
Right VA	26 (50)	26 (46.4)	3 (60.0)	
Bilateral VA	5 (9.6)	5 (8.9)	1 (20.0)	
BA	2 (3.8)	0 (0.0)	0 (0.0)	
Both VA and BA	1 (1.9)	0 (0.0)	0 (0.0)	
Radiologic changes				<.001[b]
Improved (No.) (%)	1 (1.9)	15 (26.8)	1 (20.0)	<.001[c]
Unchanged (No.) (%)	50 (96.2)	38 (67.9)	3 (60.0)	<.001[d]
Enlarged (No.) (%)	1 (1.9)	3 (5.4)	1 (20.0)	.15[e]
Clinical course				.048[f]
Stable (No.) (%)	51 (98.1)	55 (98.2)	4 (80.0)	
Deteriorated (No.) (%)	1 (1.9)	1 (1.8)	1 (20.0)	

Note:—VA indicates vertebral artery; BA, basilar artery.
[a] *P* value was calculated by analysis of variance.
[b] *P* value was calculated by the χ^2 test.
[c] *P* value was calculated by the χ^2 test between improved or not improved.
[d] *P* value was calculated by the χ^2 test between unchanged or changed, either improved or enlarged.
[e] *P* value was calculated by the χ^2 test between enlarged or not enlarged.
[f] *P* value was calculated by the χ^2 test between clinically stable or deteriorated.

Statistical Analysis

Associations between clinical presentation at diagnosis (asymptomatic, pain, and mass effects) and patient characteristics were evaluated by using the χ^2 test and analysis of variance. Associations between reduction or enlargement in aneurysm size and clinical presentation at diagnosis and the size of aneurysms and other possible confounders (age, sex, hypertension, diabetes, hyperlipidemia, and smoking status) were evaluated by using the Cox proportional hazards model. Then, significant variables in the models were applied to a multivariate analysis. Two-sided *P* values < .05 were considered statistically significant. All statistical analyses were performed by using STATA 12.0 (StataCorp, College Station, Texas).

RESULTS

Patient Characteristics

The final cohort consisted of 113 patients, ranging from 31 to 78 years of age

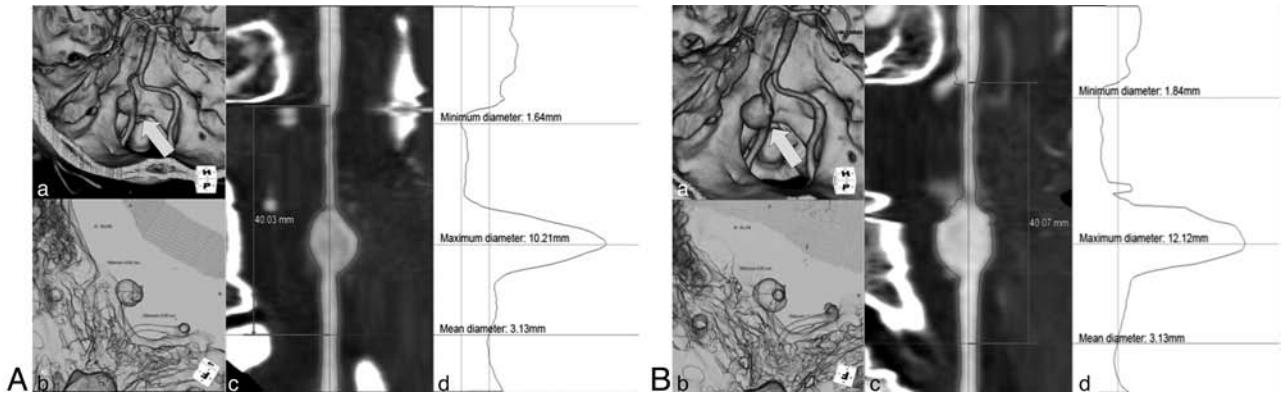

FIG 1. 3D-CTA reconstruction on the TeraRecon workstation and stretch view evaluating enlargement of the aneurysm diameter. Initial findings show a maximum diameter, 10.2 mm (*A*). Follow-up findings after 2 years show an increased maximum diameter, 12.2 mm (*B*). *a*, Volume rendering image (*arrow* indicates an aneurysm). *b*, Translucent image. *c*, MIP image of the stretch view. *d*, Calculated diameter.

Table 2: Cases with radiologic and clinical deterioration

Patient No. (age [yr])/sex)	Initial Size (mm)	Maximum Size (mm)	Follow-Up Period (mo)	Clinical Deterioration	Treatment
48/M	21.2	27.5	91.1	Cerebellar ataxia	Endovascular trapping
59/F	17.7	25.9	19.2	Cerebellar ataxia, dysphagia	Endovascular trapping
43/F	16.1	18.3	20.4	Wallenberg syndrome, SAH	Endovascular trapping
35/M	9.1	12.3	35.4	None	Stent-assisted coiling
48/M	10.1	12	8.3	None	Stent-assisted coiling

Table 3: Cox proportional hazards model to find factors associated with aneurysm reduction

	Single Cox Proportional Hazards Model			Multiple Cox Proportional Hazards Model[a]		
	Hazard Ratio	95% CI	*P* Value	Hazard Ratio	95% CI	*P* Value
Age (yr)	0.93	0.89–0.98	.003	0.99	0.93–1.05	.63
Male sex	0.68	0.25–1.86	.46			
Clinical presentation at diagnosis						
Asymptomatic	Reference	–	–	Reference	–	–
Pain	14.7	1.94–111	.009	3.63	0.38–34.8	.26
Mass effect	7.94	0.50–127	.14	13.3	0.59–299	.10
Size						
Maximum diameter (mm)	0.61	0.46–0.82	.001	0.58	0.41–0.84	.004
≥10 mm	0.29	0.04–2.26	.24			
Hypertension	0.08	0.02–0.35	.001	0.12	0.02–0.70	.018
Diabetes[b]						
Hyperlipidemia	0.47	0.11–2.08	.32			
Smoking	0.78	0.29–2.13	.63			
Location						
Left	1.39	0.16–12.5	.77			
Right	2.87	0.37–22.1	.31			
Bilateral	Reference					

Note:—CI indicates confidence interval.

[a] Variables that were statistically significant in single Cox proportional hazards models were used in the multiple Cox proportional hazards models. The cutoff point of the *P* value was set at <.05.

[b] All 6 patients with diabetes were excluded from this analysis because their aneurysms were unchanged.

(mean, 55 years) and 86 men (76%). The mean follow-up was 2.9 years (range, 27 days to 8 years). Fifty-six (49.6%) patients had a history of hypertension; 51 (45.1%), smoking history; and 23 (20.4%) a history of hyperlipidemia. Patients with hypertension and hyperlipidemia were on medication according to their physicians' prescriptions. Patients in group 1 were significantly older than those in group two: 59.3 years versus 51.1 years, respectively. Hypertension was more prevalent in group 1 than in the other 2 groups.

Clinical Findings

Of 113 patients, 3 deteriorated during the study period, and the incidence of clinical deterioration was significantly higher in group 3 ($P = .048$). One patient in group 3 (0.9%) developed an ischemic stroke (Wallenberg syndrome) and was admitted to another institution where the patient received anticoagulation therapy. Subsequently, the patient had SAH (Hunt and Hess grade 2) and was transferred back to our institution, where endovascular obliteration was performed. Two patients (1.8%), 1 in group 1 and 1 in group 2, experienced new clinical symptoms due to mass effect (Tables 1 and 2).

Radiologic Findings

Radiologic evaluation of aneurysm size revealed a statistically significant difference ($P < .001$) among the 3 groups: In most of the patients in group 1 (96.2%), aneurysm size remained unchanged, in contrast to 26.8% of patients in group 2% and 20% in group 3 in whom aneurysm size became smaller.

On the basis of proportional hazards models, pain as a clinical presentation at diagnosis significantly increased the chance for aneurysm reduction. In contrast, larger maximum aneurysm diameter and hypertension at diagnosis were associated with less possibility of aneurysm reduction. Using an adjustment with significant variables, a multiple regression analysis found that pain and aneurysm size at diagnosis were still significantly associated with aneurysm reduction (Table 3).

Next, similar to our analysis of the factors associated with aneurysm reduction, we analyzed the factors associated with aneurysm enlargement. The risk of aneurysm enlargement was significantly associated with either maximum diameter (hazard ratio = 1.30; 95% CI, 1.11–11.52; $P = .001$) or aneurysm of ≥10 mm (hazard ratio = 18.0; 95% CI, 1.95–167; $P = .011$) (Table 4). All 3 patients who clinically deteriorated showed enlarged aneurysms, and that association was statistically significant ($P < .001$), though the number was small.

DISCUSSION

Management Strategy and Clinical Findings

Reports of incidentally found DVBAs are rare, but the detection of DVBAs is rising due to increased and improved screening by brain imaging. Therapeutic management of patients with DVBA who are asymptomatic or present only with pain remains controversial and is not well-established.[2,3] DVBA with pain is considered a critical condition predictive of stroke, for which either a surgical or endovascular

Table 4: Cox proportional hazards model to find factors associated with aneurysm enlargement

	Single Cox Proportional Hazards Model		
	Hazard Ratio	95% CI	*P* Value
Age (yr)	0.93	0.85–1.01	.086
Male sex	0.54	0.09–3.22	.50
Clinical presentation at diagnosis			
Asymptomatic	Reference	–	–
Pain	2.83	0.29–27.3	.37
Mass effect	9.38	0.56–156	.12
Size			
Maximum diameter (mm)	1.30	1.11–1.52	.001
≥10 mm	18.0	1.95–167	.011
Hypertension	0.38	0.06–2.34	.30
Diabetes[a]			
Hyperlipidemia	0.88	0.10–7.92	.91
Smoking	0.85	0.14–5.10	.86
Location			
Left	0.13	0.01–1.65	.12
Right	0.19	0.02–1.57	.12
Bilateral	Reference		

Note:—CI indicates confidence interval.

[a] All 6 patients with diabetes were excluded from this analysis because their aneurysms were unchanged.

approach is the treatment of choice.[4-6] Rabinov et al[7] reported on 28 patients with DVBA who were treated surgically or endovascularly; 2 patients presented with pain only, of whom 1 was surgically treated and rated a score of 3 on the modified Rankin Scale. Ahn et al[5] reported their endovascular treatment of 14 patients with DVBA, of whom 5 presented with headache only. In our series, none of the patients who presented with pain only at diagnosis had a hemorrhagic or ischemic stroke during observation. On the basis of our results, aggressive interventional treatment may not be necessary for patients with DVBA presenting with pain only.

The establishment of optimal medical management is also controversial. Kim et al[8] reported their large series of 191 patients with unruptured vertebrobasilar artery dissections, including ischemic and nonischemic symptoms, in which 81 patients presented with headache only. All were treated either endovascularly ($n = 46$) or by medical therapy with anticoagulation ($n = 49$), antiplatelet therapy ($n = 48$), or analgesics ($n = 48$). The necessity for anticoagulation or antiplatelet therapy remains unclear; our results, at least, do not prove the necessity for anticoagulation or antiplatelet therapy for patients presenting with pain only.

We did not use any antiplatelet or anticoagulation therapy during observation. One patient who presented with mass effect at diagnosis had a brain stem infarction during observation and was admitted to another hospital. The patient received anticoagulation therapy and subsequently experienced SAH. Some similarities can be found with Tsutsumi et al,[9] who reported a vertebral artery dissection causing SAH in a similar patient who had initially presented with infarction and had received antiplatelet agent therapy. Thus, pain management and blood pressure control are recommended for patients presenting with pain only or ischemic symptoms.

Yasui et al[10] reported their histopathologic findings of incidentally detected fusiform vertebrobasilar aneurysms, which demonstrated intimal thickening, disruption of the internal elastic lamina, and degeneration of the media. They concluded that an incidental fusiform vertebrobasilar aneurysm has the potential to develop into a dissecting aneurysm. In our series, only 1 patient with an incidentally found DVBA experienced clinical deterioration and aneurysm growth during observation.

Morphologic Changes

Observation with serial radiologic examinations should be performed on patients with unruptured DVBAs. Most of the DVBAs in group 1 did not show morphologic findings in the vessel wall. Sato et al[11] showed that disrupted internal elastic lamina, covered with intimal thickening, is commonly found at postmortem examination in normal intracranial vertebral arteries of patients who died of causes other than intracranial lesions. Most of the incidentally detected lesions occurred silently or with minor headache and vessel wall healing occurred silently.

Ahn et al[12] reported the difference in the morphologic evolution of the lesion; 25 of 34 symptomatic intracranial vertebrobasilar dissections with dilation without stenosis had no change compared with their initial shape. Pozzati et al[13] described cases of spontaneous resolution of fusiform aneurysm in the vertebrobasilar system proved by angiography. Naito et al[1] reported that angiographic features of vertebral artery dissection changed for 12 of 20 patients (60%) and that deterioration of features was seen in 4 cases (20%). Nakagawa et al[14] reported serial angiographic changes in 88.2% of unruptured vertebral artery dissections. In our series, morphologic changes were observed in 22 of 113 patients (19.5%) and 5 (4.4%) had DVBAs that enlarged. As for DVBAs having the possibility of changing morphologically, we suggest serial radiologic follow-up for nonstroke DVBAs.

Mizutani[15] reported on 44 patients who presented with nonischemic unruptured dissections in the vertebrobasilar system, of which 10 DVBAs improved, 4 enlarged, and 1 ruptured during observation. Mangrum et al[16] reported that enlargement of nonsaccular intracranial aneurysms correlated significantly with median aneurysm diameter and symptomatic compression at diagnosis. Flemming et al[17] reported that the annual prospective risk of hemorrhage from a vertebrobasilar artery nonsaccular intracranial aneurysm is 0.9% and that an aneurysm diameter of at least 10 mm is strongly indicative of future rupture. In our series, aneurysms of <10 mm had a favorable clinical outcome, but aneurysms of >10 mm with symptoms due to mass effect had a risk of clinical deterioration and enlargement. In such cases, surgical or endovascular intervention should be considered.

Limitations of the Study

This study has several limitations. First, the radiologic examination findings were not the same for all patients. The diameter of the aneurysm was different between CTA and MRA. Nevertheless, the goal of this study was not to compare the differences in the devices but to evaluate the changes in findings with the same method. Each patient was evaluated with either CTA or MRA TOF only. Second, we defined "DVBA" as a nonsaccular aneurysm located at a nonbranching site of the vertebrobasilar artery; however, it is sometimes difficult to determine whether an incidental asymptomatic fusiform aneurysm may have resulted from spontaneously healed dissections or other underlying vascular abnormalities, especially with only CT. Third, intramural hema-

toma was significantly associated with a change of vertebrobasilar dissection on follow-up in a previous report.[12] In this study, most imaging was performed with CT angiography. CTA has limitations in detecting an intramural hematoma. Fourth, in this study, mean follow-up was 2.9 years. This time is relatively short to evaluate the natural history of these lesions. In this study group, 3 patients demonstrated relatively good clinical outcome, though these patients showed significant risk of enlargement. This discrepancy may be due to lack of long-term follow-up. Fifth, in some cases, follow-up was discontinued, and these patients might have experienced SAH or infarction and might have been admitted elsewhere. Finally, we have a small number of patients with nonstroke DVBA who were treated with endovascular therapy; they do not entirely reflect the results of the study, but this small number will have a negligible effect on the natural course of nonstroke DVBA for the whole group. Although the study has these limitations, the results may provide important information for the treatment and further investigation of nonstroke DVBA.

CONCLUSIONS

The natural course of nonstroke DVBA is favorable during a 2.9-year period. The short-term course of these lesions suggests that acute intervention is not always required and close follow-up is reasonable, unless patients develop symptoms associated with significant mass effect. Patients with symptoms due to mass effect or the size of the aneurysm (diameter of >10 mm) may deteriorate and eventually require intervention.

ACKNOWLEDGMENTS

The authors acknowledge the assistance of Naoya Kunikane, RT, Yukiko Abe, RT, and Hiroto Narita, PhD, with technical support for 3D-CTA.

Disclosures: Yuichi Murayama—*UNRELATED*: *Consultancy*: Asahi Intecc, Stryker, *Grants/Grants Pending*: Siemens,* Stryker,* Asahi Intecc,* Fujifilm,* *Patents (planned, pending, or issued)*: Stryker,* *Royalties*: Stryker.* Ichiro Yuki—*UNRELATED*: *Grants/Grants Pending*: Siemens.* Toshihiro Ishibashi—*UNRELATED*: *Consultancy*: Stryker Japan. Hiroyuki Takao—*UNRELATED*: *Grants/Grants Pending*: Fujifilm,* NTT DoCoMo.* Ikki Kajiwara—*UNRELATED: Grants/Grants Pending*: Siemens.* Mitsuyoshi Urashima—*UNRELATED*: *Grants/Grants Pending*: Ministry of Education, Culture, Sports, Science, and Technology in Japan, a supported program for the Strategic Research Foundation at private universities.* *Money paid to the institution.

REFERENCES

1. Naito I, Iwai T, Sasaki T. **Management of intracranial vertebral artery dissections initially presenting without subarachnoid hemorrhage.** *Neurosurgery* 2002;51:930–37, discussion 937–38
2. Kai Y, Nishi T, Watanabe M, et al. **Strategy for treating unruptured vertebral artery dissecting aneurysms.** *Neurosurgery* 2011;69:1085–91, discussion 1091–92
3. Santos-Franco JA, Zenteno M, Lee A. **Dissecting aneurysms of the vertebrobasilar system: a comprehensive review on natural history and treatment options.** *Neurosurg Rev* 2008;31:131–40, discussion 140
4. Jin SC, Kwon DH, Choi CG, et al. **Endovascular strategies for vertebrobasilar dissecting aneurysms.** *AJNR Am J Neuroradiol* 2009;30:1518–23
5. Ahn JY, Han IB, Kim TG, et al. **Endovascular treatment of intracranial vertebral artery dissections with stent placement or stent-assisted coiling.** *AJNR Am J Neuroradiol* 2006;27:1514–20
6. Shin YS, Kim HS, Kim SY. **Stenting for vertebrobasilar dissection: a possible treatment option for nonhemorrhagic vertebrobasilar dissection.** *Neuroradiology* 2007;49:149–56
7. Rabinov JD, Hellinger FR, Morris PP, et al. **Endovascular management of vertebrobasilar dissecting aneurysms.** *AJNR Am J Neuroradiol* 2003;24:1421–28
8. Kim BM, Kim SH, Kim DI, et al. **Outcomes and prognostic factors of intracranial unruptured vertebrobasilar artery dissection.** *Neurology* 2011;76:1735–41
9. Tsutsumi M, Kawano T, Kawaguchi T, et al. **Dissecting aneurysm of the vertebral artery causing subarachnoid hemorrhage after nonhemorrhagic infarction: case report.** *Neurol Med Chir (Tokyo)* 2000;40:628–31
10. Yasui T, Komiyama M, Iwai Y, et al. **Evolution of incidentally-discovered fusiform aneurysms of the vertebrobasilar arterial system: neuroimaging features suggesting progressive aneurysm growth.** *Neurol Med Chir (Tokyo)* 2001;41:523–27, discussion 528
11. Sato T, Sasaki T, Suzuki K, et al. **Histological study of the normal vertebral artery: etiology of dissecting aneurysms.** *Neurol Med Chir (Tokyo)* 2004;44:629–35, discussion 636
12. Ahn SS, Kim BS, Suh SH, et al. **Spontaneous symptomatic intracranial vertebrobasilar dissection: initial and follow-up imaging findings.** *Radiology* 2012;264:196–202
13. Pozzati E, Padovani R, Fabrizi A, et al. **Benign arterial dissections of the posterior circulation.** *J Neurosurg* 1991;75:69–72
14. Nakagawa K, Touho H, Morisako T, et al. **Long-term follow-up study of unruptured vertebral artery dissection: clinical outcomes and serial angiographic findings.** *J Neurosurg* 2000;93:19–25
15. Mizutani T. **Natural course of intracranial arterial dissections.** *J Neurosurg* 2011;114:1037–44
16. Mangrum WI, Huston J 3rd, Link MJ, et al. **Enlarging vertebrobasilar nonsaccular intracranial aneurysms: frequency, predictors, and clinical outcome of growth.** *J Neurosurg* 2005;102:72–79
17. Flemming KD, Wiebers DO, Brown RD Jr, et al. **Prospective risk of hemorrhage in patients with vertebrobasilar nonsaccular intracranial aneurysm.** *J Neurosurg* 2004;101:82–87

Influence of Patient Age on Angioarchitecture of Brain Arteriovenous Malformations

S.W. Hetts, D.L. Cooke, J. Nelson, N. Gupta, H. Fullerton, M.R. Amans, J.A. Narvid, P. Moftakhar, H. McSwain, C.F. Dowd, R.T. Higashida, V.V. Halbach, M.T. Lawton, and H. Kim

ABSTRACT

BACKGROUND AND PURPOSE: The imaging characteristics and modes of presentation of brain AVMs may vary with patient age. Our aim was to determine whether clinical and angioarchitectural features of brain AVMs differ between children and adults.

MATERIALS AND METHODS: A prospectively collected institutional data base of all patients diagnosed with brain AVMs since 2001 was queried. Demographic, clinical, and angioarchitecture information was summarized and analyzed with univariable and multivariable models.

RESULTS: Results often differed when age was treated as a continuous variable as opposed to dividing subjects into children (18 years or younger; $n = 203$) versus adults (older than 18 years; $n = 630$). Children were more likely to present with AVM hemorrhage than adults (59% versus 41%, $P < .001$). Although AVMs with a larger nidus presented at younger ages (mean of 26.8 years for >6 cm compared with 37.1 years for <3 cm), this feature was not significantly different between children and adults ($P = .069$). Exclusively deep venous drainage was more common in younger subjects when age was treated continuously ($P = .04$) or dichotomized ($P < .001$). Venous ectasia was more common with increasing age (mean, 39.4 years with ectasia compared with 31.1 years without ectasia) and when adults were compared with children (52% versus 35%, $P < .001$). Patients with feeding artery aneurysms presented at a later average age (44.1 years) than those without such aneurysms (31.6 years); this observation persisted when comparing children with adults (13% versus 29%, $P < .001$).

CONCLUSIONS: Although children with brain AVMs were more likely to come to clinical attention due to hemorrhage than adults, venous ectasia and feeding artery aneurysms were under-represented in children, suggesting that these particular high-risk features take time to develop.

ABBREVIATIONS: HR = hazard ratio; p50 = median (i.e., 50% proportion of sample)

An enormous diversity of brain vascular malformations occur in children. These include vein of Galen malformations, dural arteriovenous fistulas, non-Galenic pial arteriovenous fistulas, and nidal arteriovenous malformations.[1] AVMs are defined by a group of vessels with an abnormal low-resistance connection between arteries and veins occurring in a focal geographic area of the brain parenchyma—the nidus. Nidal AVMs in children have been described as being different from those in adults. In fact, a diffuse nidus with intervening brain tissue is sometimes termed "juvenile" AVM angioarchitecture.[1] A smaller nidus size, the presence of multiple large arteriovenous fistulas, preferential location deep within the brain, and more frequent deep venous drainage have also been described as occurring more commonly in children.[2-4]

Children with brain AVMs are more likely to present with hemorrhage than adults, particularly including intraventricular hemorrhage.[2] Several studies have identified specific angioarchitectural features that confer higher risk for hemorrhage in adults, children, or both.[3-7] Using data obtained from a large, prospectively collected patient cohort, we sought to determine whether the clinical and angioarchitectural features of brain AVMs differ by patient age. We conducted our analysis both by using the age at

Received September 1, 2013; accepted after revision November 25.

From the Division of Neurointerventional Radiology (S.W.H., D.L.C., M.R.A., J.A.N., P.M., H.M., C.F.D., R.T.H., V.V.H.), Department of Radiology and Biomedical Imaging; Center for Cerebrovascular Research (J.N., H.K.), Department of Anesthesia and Perioperative Care; Division of Pediatric Neurosurgery (N.G.) and Division of Cerebrovascular Neurosurgery (M.T.L.), Department of Neurological Surgery; Division of Child Neurology (H.F.), Department of Neurology; and Department of Pediatrics (N.G., H.F.), University of California, San Francisco, San Francisco, California.

This project was supported by National Institutes of Health grants R01 NS034949; and UL1 TR000004.

The content is solely the responsibility of the authors and does not necessarily represent the official views of the National Institutes of Health.

Please address correspondence to Steven W. Hetts, MD, Interventional Neuroradiology, 505 Parnassus Ave, L-352, San Francisco, CA 94143-0628; e-mail: steven.hetts@ucsf.edu

Indicates open access to non-subscribers at www.ajnr.org

Indicates article with supplemental on-line tables.

http://dx.doi.org/10.3174/ajnr.A3886

presentation as a continuous variable and dichotomizing the cohort into children and adult groups. The former is more relevant with respect to expected gradual biologic changes that occur with time and may affect AVM formation and symptom progression. The latter is a clinical convenience, because patients tend to be seen and treated by "pediatric" and "adult" groups, with varying degrees of overlap. Thus, we hope to provide information useful both to those interested in the underlying disease processes of brain vascular malformations and to those who take care of patients on the basis of somewhat arbitrary societal and administrative divisions of patient age.

MATERIALS AND METHODS

Data Acquisition

Under an approved human research protocol, the Brain AVM Data Base prospectively collects demographic, clinical, and radiologic data for all patients with vascular malformations treated at the University of California, San Francisco. Only patients with nidal AVMs treated between 2001 and 2013 were included for analysis ($n = 833$); those with a primary diagnoses of vein of Galen malformation, dural arteriovenous fistula, or non-Galenic pial arteriovenous fistula[8] were excluded. Children were defined as 18 years of age or younger at the time of the first angiogram on which the diagnosis of AVM was made. The earliest diagnostic angiogram available for each patient was evaluated by a neurointerventional radiologist, and a structured list of angioarchitectural features was scored by using methods recommended by the Joint Writing Group.[9] When available, the earliest MR imaging and CT examinations were also evaluated by a neurointerventional radiologist to confirm AVM nidus location and the presence or absence of current or prior intracranial hemorrhage.

Table 1: Demographic characteristics and mode of presentation (all ages)[a]

Characteristic	No. (%)	Median Dx Age (yr)	95% CI	*P* Value
Overall	833	33.8	(32.7–35.9)	NA
Sex				.937
Female	425 (51%)	33.4	(31.0–35.7)	
Male	408 (49%)	34.3	(31.5–37.7)	
Ethnicity				<.001
Asian/Pacific Islander	113 (14%)	29.9	(25.9–34.3)	
Black/African American	56 (5%)	46.5	(41.2–50.3)	
Hispanic	224 (27%)	27.0	(23.4–29.8)	
Native American	9 (1%)	37.1	(17.4–47.1)	
Non-Hispanic Caucasian	431 (52%)	38.7	(35.3–42.6)	
Hemorrhagic presentation				<.001
Yes	375 (45%)	28.7	(26.6–32.2)	
No	458 (55%)	37.6	(35.3–40.6)	
HHT diagnosis				.695
Yes	12 (1%)	38.3	(1.8–54.0)	
No	821 (99%)	33.7	(31.6–35.8)	

Note:—Dx indicates diagnosis; NA, not applicable; HHT, hereditary hemorrhagic telangiectasia syndrome.
[a] *P* values are from log-rank tests of survivor functions.

Table 2: Demographic characteristics and mode of presentation (children vs adults)[a]

Characteristic	All (*N* = 833)	Child (0–18 yr) (*n* = 203)	Adult (≥19 yr) (*n* = 630)	*P* Value
Age at diagnosis (yr)	35.1 ± 18.6	12.2 ± 4.7	42.6 ± 15.0	NA
Female sex	425 (51%)	101 (50%)	321 (51%)	.687
Ethnicity				.014
Asian/Pacific Islander	113 (14%)	31 (16%)	82 (13%)	
Black/African American	11 (5%)	11 (5%)	42 (7%)	
Hispanic	224 (27%)	71 (35%)	153 (24%)	
Native American	9 (1%)	1 (<1%)	8 (1%)	
Non-Hispanic Caucasian	431 (52%)	88 (43%)	343 (54%)	
Hemorrhagic presentation	375 (45%)	119 (59%)	256 (41%)	<.001
HHT diagnosis	12 (1%)	4 (2%)	8 (1%)	.500

Note:—NA indicates not applicable; HHT, hereditary hemorrhagic telangiectasia syndrome.
[a] Table entries are No. (%) or mean ± SD. *P* values are from the Fisher exact test.

Statistical Methods

Demographic, clinical, and angioarchitectural information for 833 patients with AVMs was analyzed by using the Kaplan-Meier survival analysis and log-rank tests. Our primary analysis assumed that the AVM was present from birth, starting survival time at the date of birth and ending at the date of AVM diagnosis with no censoring. We computed the median (p50) survival time to diagnosis (ie, age at diagnosis) for each characteristic with associated 95% confidence intervals to see whether characteristics were associated with younger or older patients. Secondary analysis compared angiographic characteristics of patients between children (18 years of age or younger) and adults (older than 18 years) by using the Fisher exact test for categoric variables.

We performed univariable and multivariable Cox regression survival analyses, calculating hazard ratios (HRs) and associated 95% CIs for the following predictors: AVM nidus size (centimeters), exclusively deep venous drainage, venous ectasia, central location, lobar location, posterior fossa location, and shunt-flow-related aneurysms (ie, aneurysms of arteries directly supplying the AVM or subjected to increased blood flow due to the AVM, such as the anterior communicating artery for frontal AVMs). These analyses were stratified by initial hemorrhagic presentation and ethnicity to allow the baseline hazard ratio to vary and, thus, better adhere to proportional hazard assumption of the Cox model.

We considered *P* values < .05 to be significant. All statistical analyses were performed by using STATA/SE 12.0 (StataCorp, College Station, Texas).[10]

RESULTS

Baseline Demographics and Clinical Presentation

Demographic and clinical data are listed in Tables 1 and 2, with the former considering age as a continuous variable (survival analysis) and the latter grouping patients into children versus adults. The median age at diagnosis for our sample was 33.8 years (95% CI, 32.7–35.9 years). Survival distributions did not significantly differ between men and women (log-rank $P = .937$); similarly, no sex difference was observed ($P = .687$) between children (50% female) and adults (51% female). However, we observed significant differences in median age at diagnosis by race/ethnicity (log-rank $P < .001$), with Asians and Hispanics having a younger median age at diagnosis (younger than 30 years) than other race/ethnicities. Hispanics composed 35% of the children in our cohort, but only 24% of the

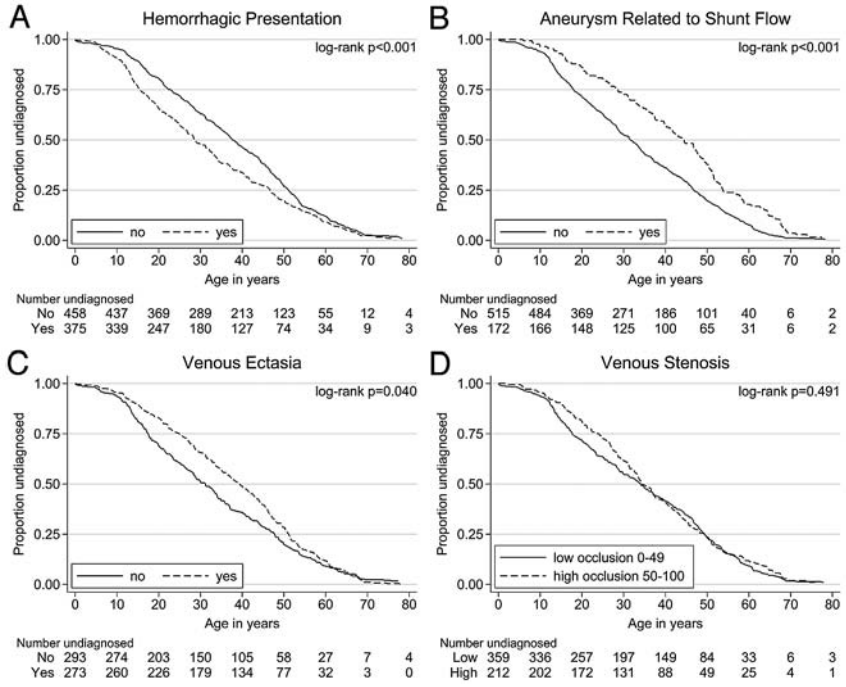

FIG 1. Age-related differences in AVM hemorrhagic presentation. Aneurysms related to shunt flow, draining venous ectasia, and draining venous stenosis. Hemorrhagic presentation (*A*) was more prevalent at younger patient ages than nonhemorrhagic presentation. Conversely, feeding artery aneurysms (*B*) and ectasia of draining veins (*C*) were more prevalent in older patients. There was not a significant difference in the prevalence of venous stenosis observed at presentation in older versus younger patients (*D*).

adults. An inverse trend was seen with non-Hispanic whites (43% of children and 54% of adults). The difference in diagnosis age between those who presented with a hemorrhage and those who did not was particularly pronounced (log-rank $P < .001$; Fig 1*A*). Those who presented with a hemorrhage had a median diagnosis age of 28.7 years (95% CI, 26.6–32.2 years), which is almost 9 years younger than those who did not (p50: 37.6; 95% CI, 35.3–40.6). Children were also more likely to present with AVM hemorrhage than adults (59% versus 41%, $P < .001$).

Nidus Morphology and Location

Angioarchitectural data are summarized in On-line Table 1, with age as a continuous variable; data are dichotomized into children versus adults in On-line Table 2. Larger AVMs (categorized as <3 cm, 3–6 cm, and >6 cm nidus size) were identified at younger ages than smaller AVMs (AVM > 6 cm p50: 26.8 years; 95% CI, 16.9–33.9 years versus AVM < 3 cm p50: 37.1 years; 95% CI, 34.1–40.2 years; log-rank $P = .009$). A comparison of AVM nidus size in children and adults was suggestive of an association but was not significant ($P = .069$). Most interesting, large AVMs (nidus of >6 cm) are twice as common in children (8%) as in adults (4%). The sharpness of the AVM border with adjacent brain on angiography, scored as "sharp" or "diffuse," did not differ by continuous age ($P = .707$) or between age groups (23% diffuse border in children versus 19% diffuse border in adults, $P = .218$).

When data were analyzed by using age at diagnosis as a continuous variable (On-line Table 1), AVMs found in lobar locations (as opposed to central locations) were marginally associated with older age (log-rank $P = .050$) and AVMs in the posterior fossa were observed in older patients (log-rank $P < .001$). No association with age based on either dural location (ie, dural arterial supply to a parenchymal AVM as opposed to a primary dural arteriovenous fistula, which would have been excluded from this cohort) or central location could be determined (log-rank $P = .518$ and log-rank $P = .617$, respectively).

Draining Veins

Venous drainage patterns varied significantly by age of diagnosis (log-rank $P = .040$). Patients with exclusively deep venous drainage had a median age at diagnosis of 26.8 years (95% CI, 21.9–32.2 years), while those with "superficial and deep" (p50, 31.5 years; 95% CI, 28.1–35.1 years) and "superficial" (p50, 37.8 years; 95% CI, 34.9–40.6 years) venous patterns were identified at older ages. Venous ectasia (Fig 1*C*) tended to be identified in older patients (log-rank $P = .040$). A dichotomized venous stenosis measure (Fig 1*D*) did not have an association with age at diagnosis (log-rank $P = .491$).

When age was dichotomized, the venous drainage of AVMs differed significantly between children and adults, but the location did not (On-line Table 2). Children were more likely to have exclusively deep venous drainage than adults (28% in children versus 14% in adults, $P < .001$). Venous ectasia was also more prevalent in adults than in children (35% in children versus 52% in adults, $P < .001$). There was a trend toward a central, deep location of AVMs in children compared with adults ($P = .075$), but this did not reach statistical significance.

Aneurysms

There was a significant difference between the presence and absence of flow-related feeding artery aneurysms (log-rank, $P < .001$; Fig 1*B*), because these aneurysms tended to appear in older patients. We do not have sufficient data to support an association for intranidal aneurysms (log-rank, $P = .143$) and aneurysms not related to shunt flow (log-rank, $P = .069$) with patient age. When age was dichotomized, feeding artery aneurysms related to flow were more prevalent in adults than in children (13% in children versus 29% in adults, $P < .001$). Intranidal aneurysms were similar in frequency in both age groups (17% in children versus 15% in adults, $P = .537$).

Regression Analysis

A multivariable Cox regression was performed on a subset of 550 patients (66%) in whom complete demographic, clinical, and angiographic information was available (Table 3). As with the Kaplan-Meier analysis, larger AVMs (HR, 1.13; $P < .001$) and centrally located AVMs (HR, 1.45; $P = .001$) were more likely to be diagnosed earlier independent of other characteristics. In con-

Table 3: Age at diagnosis: Cox survival analysis[a]

Predictor	Univariable (*n* = 550)			Multivariable (*n* = 550)		
	HR	95% CI	*P* Value	HR	95% CI	*P* Value
AVM nidus size (cm)	1.05	1.00–1.10	.065	1.13	1.07–1.20	<.001
Exclusively deep venous drainage	1.26	0.98–1.63	.077	1.27	0.95–1.69	.110
Venous ectasia	0.83	0.69–0.99	.034	0.75	0.62–0.91	.003
Central location	1.26	1.05–1.52	.014	1.45	1.16–1.81	.001
Lobar location	1.04	0.84–1.30	.716	1.10	0.75–1.61	.622
Posterior fossa location	0.76	0.59–0.98	.037	0.72	0.49–1.06	.099
Aneurysm related to shunt flow	0.59	0.48–0.71	<.001	0.53	0.43–0.65	<.001

[a] These are the results for Cox regression analyses using age at diagnosis as the survival time and stratifying by ethnicity and hemorrhagic presentation. The multivariable model includes all listed predictors.

trast, venous ectasia (HR, 0.75; $P = .003$) and shunt-flow-related aneurysms (HR, 0.53; $P < .001$) were significantly associated with later AVM diagnosis. Posterior fossa location and exclusively deep venous drainage were not significant in multivariable analysis, though there is a suggestion that these characteristics may also be associated with later or earlier diagnosis, respectively (Table 3).

DISCUSSION

Using a large institutional cohort of patients with brain AVMs, we were able to describe the angioarchitectural features in detail and also whether these features differ according to age at presentation or the demographic group. As expected, the method of data analysis affected the results of our study. When age was examined as a continuous variable, patient ethnicity, presentation with hemorrhage, nidus size, lobar location, location in the posterior fossa, eloquent location, venous drainage, venous ectasia, and feeding artery aneurysms all differed by age (Table 1 and On-line Table 1). When age was dichotomized into childhood and adult groups, only patient ethnicity, presentation with hemorrhage, venous drainage, number of draining veins, venous ectasia, and feeding artery aneurysms differed between children and adults (Table 2 and On-line Table 2). When a multivariable Cox regression analysis was conducted on the 550 patients with complete data (Table 3), only AVM nidus size, central (deep) AVM location, venous ectasia, and feeding artery aneurysms differed by age of presentation.

In previously reported studies, factors that have been associated with hemorrhage at presentation in patients of all ages with AVMs included the following: supply by perforating arteries, nidal aneurysms, multiple aneurysms, supply by the posterior circulation, basal ganglia location, deep venous drainage, venous reflux, and venous stenosis.[5,11] Specifically in children, a smaller AVM nidus, infratentorial nidus location, and exclusively deep venous drainage have previously been associated with increased risk of presentation with hemorrhage.[2] Although children with brain AVMs were more likely to present with an intracerebral hemorrhage,[3] high-risk features such as venous ectasia and feeding artery aneurysms were less frequent among the children in our cohort.

Brain AVMs are not static lesions; angioarchitectural features associated with hemorrhage can develop with time. It is reasonable to assume that venous stenosis, venous ectasia, and feeding artery aneurysms arise from chronic hemodynamic stresses, which may explain why they are under-represented in children, who have not had sufficient time to develop these features. In our cohort, only 1 feeding artery aneurysm was found in a patient younger than 8 years of age, and AVM flow-related feeding artery aneurysms have been reported rarely in young children.[12] Lack of specific time-dependent high-risk angioarchitectural features, similarly, may help explain why children with AVMs have been reported to have a lower risk of subsequent hemorrhage after initial presentation compared with adults in longitudinal studies,[3] despite the over-representation of AVMs in deep locations, which is typically a risk factor for increased incidence of subsequent hemorrhage.[4,13] The presence of venous ectasia and feeding artery aneurysms may be an indirect method of estimating how long an AVM has been present in a given patient and may potentially provide insight into the congenital-versus-acquired nature of such lesions. Selection of surgical tissue samples from patients with particular angioarchitectural features may permit direct evaluation of the age of a given AVM through techniques such as radiocarbon dating.[14]

AVMs and their draining veins were often located deep within the brain in children, raising the possibility that centrally located AVMs may arise earlier in development or may be more likely to come to clinical attention early in life than more peripherally located AVMs. Although angioarchitecturally distinct from nidal AVMs, vein of Galen malformations form early in embryonic development and are also centrally located in the brain. With the advent of fetal MR imaging and increasing use of MR imaging in children and adults, it may be possible to determine whether there is a continuous progression from centrally arising arteriovenous fistulas to peripherally located nidal AVMs in asymptomatic individuals.

A limitation of our study is its cross-sectional nature. Ultimately, longitudinal studies such as A Randomized Trial of Unruptured Brain AVMs will provide more detailed natural history data for brain AVMs.[15]

CONCLUSIONS

Although children with brain AVMs were more likely to come to clinical attention due to hemorrhage than adults, high-risk features such as venous stenosis and feeding artery aneurysms were under-represented in children. AVMs and their draining veins tended to be in deep locations in children compared with adults, raising the possibility that centrally located AVMs may arise earlier in development or be more likely to come to clinical attention early in life.

ACKNOWLEDGMENTS

We thank Nancy Quinnine, RN, Jeanne Scanlon, RN, Anne Federov, RN, Elizabeth Clain, and Diana Guo for their clinical support. We are deeply indebted to Bill Young, MD, for his guidance and mentorship in this project.

Disclosures: Steven W. Hetts—*RELATED*: *Grant*: National Institutes of Health- National Institute of Neurological Disorders and Stroke,* *UNRELATED*: *Consultancy*: Stryker Neurovascular, Silk Road Medical, Penumbra, *Grants/Grants Pending*: National Institutes of Health,* Stryker Neurovascular,* *Stock/Stock Options*: ChemoFilter. Jeffrey Nelson—*RELATED*: *Grant*: National Institutes of Health (R01 NS034949).* Michael T. Lawton—*UNRELATED*: *Consultancy*: Stryker, *Royalties*: Mizuho America Inc. Helen Kim—*RELATED*: *Grant*: National Institutes of Health (R01 NS034949). *Money paid to the institution.

REFERENCES

1. Lasjaunias P, Ter Brugge KG, Berenstein A. *Surgical Neuroangiography: Clinical and Interventional Aspects in Children.* 2nd ed. vol 3. Berlin: Springer-Verlag; 2006
2. Ellis MJ, Armstrong D, Vachhrajani S,et al. **Angioarchitectural features associated with hemorrhagic presentation in pediatric cerebral arteriovenous malformations.** *J Neurointerv Surg* 2013;5:191–95
3. Fullerton HJ, Achrol AS, Johnston SC, et al. **Long-term hemorrhage risk in children versus adults with brain arteriovenous malformations.** *Stroke* 2005;36:2099–104
4. Stapf C, Mast H, Sciacca RR, et al. **Predictors of hemorrhage in patients with untreated brain arteriovenous malformation.** *Neurology* 2006;66:1350–55
5. Turjman F, Massoud TF, Viñuela F, et al. **Correlation of the angioarchitectural features of cerebral arteriovenous malformations with clinical presentation of hemorrhage.** *Neurosurgery* 1995;37:856–60, discussion 860–62
6. Stefani MA, Porter PJ, terBrugge KG, et al. **Angioarchitectural factors present in brain arteriovenous malformations associated with hemorrhagic presentation.** *Stroke* 2002;33:920–24
7. Kim H, Sidney S, McCulloch CE, et al. **Racial/ethnic differences in longitudinal risk of intracranial hemorrhage in brain arteriovenous malformation patients.** *Stroke* 2007;38:2430–37
8. Hetts SW, Keenan K, Fullerton HJ, et al. **Pediatric intracranial nongalenic pial arteriovenous fistulas: clinical features, angioarchitecture, and outcomes.** *AJNR Am J Neuroradiol* 2012;33:1710–19
9. Atkinson RP, Awad IA, Batjer HH, et al, for the Joint Writing Group of the Technology Assessment Committee American Society of Interventional and Therapeutic Neuroradiology; Joint Section on Cerebrovascular Neurosurgery a Section of the American Association of Neurological Surgeons and Congress of Neurological Surgeons; Section of Stroke and the Section of Interventional Neurology of the American Academy of Neurology. **Reporting terminology for brain arteriovenous malformation clinical and radiographic features for use in clinical trials.** *Stroke* 2001;32:1430–42
10. StataCorp. *Stata Statistical Software: Release 12*. College Station, Texas: StataCorp LP; 2011
11. Nataf F, Meder JF, Roux FX, et al. **Angioarchitecture associated with haemorrhage in cerebral arteriovenous malformations: a prognostic statistical model.** *Neuroradiology* 1997;39:52–68
12. Ostergaard JR. **Association of intracranial aneurysm and arteriovenous malformation in childhood.** *Neurosurgery* 1984;14: 358–62
13. Stefani MA, Porter PJ, terBrugge KG, et al. **Large and deep brain arteriovenous malformations are associated with risk of future hemorrhage.** *Stroke* 2002;33:1220–24
14. Sarachine Falso MJ, Buchholz BA. **Bomb pulse biology.** *Nucl Instrum Methods Phys Res B* 2013;294:666–70
15. Stapf C. **The rationale behind "A Randomized Trial of Unruptured Brain AVMs" (ARUBA).** *Acta Neurochir Suppl* 2010;107:83–85

A Sonographic Quantitative Cutoff Value of Cerebral Venous Outflow in Neurologic Diseases: A Blinded Study of 115 Subjects

L. Monti, E. Menci, P. Piu, S. Leonini, U. Arrigucci, M. Bellini, A. Zandonella, P. Galluzzi, and A. Casasco

ABSTRACT

BACKGROUND AND PURPOSE: The autonomic nervous system maintains constant cerebral venous blood outflow in changing positions. Alterations in cerebral autoregulation can be revealed by postural changes at quantitative color Doppler sonography. The aim of this study was to reach an optimal cutoff value of the difference between the cerebral venous blood outflow in the supine and seated positions that can discriminate healthy controls from patients with multiple sclerosis and those with other neurologic diseases and to evaluate its specificity, sensitivity, and diagnostic accuracy.

MATERIALS AND METHODS: One hundred fifteen subjects (54 with MS, 31 healthy controls, 30 with other neurologic diseases) underwent a blinded quantitative color Doppler sonography evaluation of cerebral venous blood outflow in the supine and sitting positions. An optimal difference value between the supine and sitting positions of the cerebral venous blood outflow cutoff value was sought.

RESULTS: The difference value between supine and sitting positions of the cerebral venous blood outflow was ≤ 503.24 in 38/54 (70.37%) patients with MS, 9/31 (29.03%) healthy controls, and 13/30 (43.33%) subjects with other neurological diseases. A difference value between supine and sitting positions of the cerebral venous blood outflow at a 503.24 cutoff reached a sensitivity at 70.37%, a 70.96% specificity, a 80.85% positive predictive value, and a 57.89% negative predictive value; the quantitative color Doppler sonography parameters yielded significant differences. The difference value between supine and sitting positions of cerebral venous blood outflow ≤ 503.24 assessed the significant difference between MS versus other neurological diseases.

CONCLUSIONS: Alteration of cerebral venous blood outflow discriminated MS versus other neurologic diseases and MS versus healthy controls. The difference value between supine and sitting positions of cerebral venous blood outflow ≤ 503.24 was statistically associated with MS.

ABBREVIATIONS: AUC = area under the curve; CVF = cerebral venous blood outflow; ΔCVF = difference value between supine and sitting positions of the cerebral venous blood outflow; HC = healthy controls; OND = other neurologic diseases

Complete evaluation of the cerebral venous circulation is difficult due to its anatomic variability. In vivo study of this system began in the 1970s by venography.[1] Venography is still considered the criterion standard; however, only color Doppler sonography can evaluate dynamic aspects, including the efficiency of the jugular valves or flow characteristics in sitting and supine positions. MR venography can be a noninvasive imaging technique for the morphologic detection of extracranial venous anomalies in the internal jugular and vertebral veins in patients with multiple sclerosis, but it cannot give a dynamic evaluation.[2] Phase-contrast MR imaging was used to measure venous flow in the internal jugular and epidural veins but only in the supine position.[3] MR perfusion demonstrates a hypoperfusion of white and gray matter, and the parameters involved are cerebral blood volume, cerebral blood flow, and mean transit time, but not cerebral venous blood outflow (CVF).[4,5]

Disorders involving the cerebral venous system may result in CVF insufficiency, elevation of venous pressure, and an increase of intracranial pressure and may lead to parenchymal abnormalities. Compliance of the venous system depends on anatomic variants and the onset timing of venous pathologies. Multiple sclerosis is defined as an inflammatory demyelinating disease of the CNS, with presumed autoimmune etiology, which occurs in ge-

Received August 24, 2013; accepted after revision November 26.

From the Unit of Neuroimaging and Neurointervention (L.M., E.M., S.L., U.A., M.B., A.Z., P.G.), Department of Neurological and Sensorial Sciences, Azienda Ospedaliera Universitaria Senese, Santa Maria alle Scotte General Hospital, Siena, Italy; Department of Medicine, Surgery and Neuroscience (P.P.), University of Siena, Siena, Italy; and Unit of Endovascular and Percutaneous Therapy (A.C.), Clinica Nuestra Señora del Rosario, Madrid, Spain.

Please address correspondence to Lucia Monti, MD, Unit of Neuroimaging and Neurointervention, Department of Neurological and Sensorineural Sciences, Azienda Ospedaliera Universitaria Senese, "Santa Maria alle Scotte" General Hospital, Viale Bracci, 2-53100 Siena, Italy; e-mail: l.monti@ao-siena.toscana.it

http://dx.doi.org/10.3174/ajnr.A3864

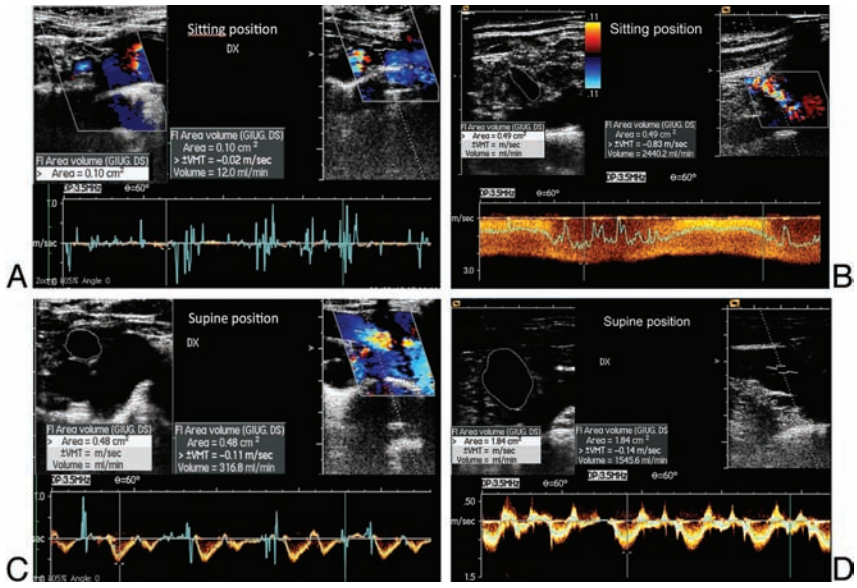

FIG 1. Quantitative evaluation of CVF in the supine and sitting positions in HC (*A* and *B*) and patients with MS (*C* and *D*). The ΔCVF was >503.24 in HC and <503.24 in patients with MS.

netically susceptible individuals. Recently, a causal relation between the cerebral venous system and MS has been suggested.[6-8] Accordingly, the term "chronic cerebrospinal venous insufficiency" has been coined to identify a chronic state of impaired venous drainage from the CNS as a putative causative factor responsible for MS. Stenosis of the internal jugular veins and intra- and extracranial reflux have been suggested as a cause of this impaired outflow. The hypothesis is that venous reflux may lead to the accumulation of iron in the CNS, triggering autoimmune events.[9,10]

Although chronic cerebrospinal venous insufficiency in MS has not been supported by recent studies,[11-14] it has forced research on possible vascular impairment in this complex multifactorial disease, including ischemic strokes, cerebral hypoperfusion, and venous blood drainage.[15,16] In the literature, there are controversial results on chronic cerebrospinal venous insufficiency. Notably, a phenomenon such as cerebral venous impairment can be studied by evaluating other sonographic parameters or factors. Thus, the difference value between the CVF in the supine position and the seated position (ΔCVF) has been proposed and evaluated in a previous scientific article,[17] in which MS and healthy controls (HC) groups were compared with a cutoff value of ΔCVF = 0. With that decision threshold, ΔCVF findings were mainly negative in patients with MS, an opposite result to that in healthy subjects.[18-20] A negative ΔCVF is consistent with a reduced venous outflow in the supine position, resulting from a reduced venous system compliance in patients with MS.

The aim of the present study was to identify the cutoff value of ΔCVF that maximizes the diagnostic accuracy of the model. Its specificity, sensitivity, and diagnostic accuracy in 3 different groups of patients, those with MS, those with other neurologic diseases (OND), and healthy controls, were evaluated.

MATERIALS AND METHODS

This study was approved by the Ethics Committee of our institution, and written informed consent was obtained from all subjects.

The sample included 115 consecutive subjects (81 women and 34 men; mean age, 42.25 ± 11.2526 years), including 54 (43 women and 11 men; mean age, 42.24 ± 9.66 years) patients with MS, 31 (19 women and 12 men; mean age, 36.64 ± 9.46 years) age-matched healthy controls, and 30 (19 women and 11 men; mean age, 48.93 ± 12.11 years) patients with OND, including patients with different defined neurologic diseases with autoimmune etiology, such as cerebral vasculitis ($n = 16$), neurosarcoidosis ($n = 2$), or chronic cerebral venous sinus thrombosis ($n = 2$); Parkinson disease ($n = 4$); and epilepsy ($n = 6$). The recruitment of those with nonoverlapping pathologies could test whether ΔCVF is strongly correlated to patients with MS.

Patients with MS were divided into 2 subgroups (ie, subgroup 1, including 40 with relapsing-remitting MS, and subgroup 2, including 14 with primary- and secondary-progressive MS ($n = 1$ and $n = 13$, respectively). No patients with clinically isolated syndromes were admitted; therefore, none were enrolled.

All patients underwent neurologic assessment before quantitative color Doppler sonography examination. The degree of disability was assessed by using the Expanded Disability Status Scale; arm/hand dexterity was tested by Nine Hole Peg Test; and leg function, by the timed 8-Meter Walk Test.

Quantitative color Doppler sonography was performed by 2 skilled neuroradiologists (E.M. and L.M.) with experience in the sonography field who were blinded to the patient history and clinical status.

A color-coded sonography system (Sequoia; Siemens, Erlangen, Germany), a 7- to 9-MHz linear probe, and a 2.5-MHz sector probe were used. The interobserver concordance was evaluated by the examination of 30 randomly selected subjects (ie, 10 subjects from each of the 3 groups) who had been examined separately by the 2 neuroradiologists, each one blinded to the results obtained by the other. Discrepancies were resolved through discussion to produce consensus assessments.

The ΔCVF was evaluated in all the subjects. The outflow of the internal jugular and vertebral veins was calculated from the time average velocity (TAV) and the cross-sectional area (CSA) of the vessel (CVF = CSA × TAV). The time average velocity was measured during a minimum of 3 cardiac cycles at the end of the expiratory phase.[21-23] The CVF of each vein was calculated in both clinostatism and the seated position. The sum of all the venous flows was then calculated in clinostatism and the seated position (Fig 1). The difference between the clinostatism and seated position is the ΔCVF value.[17]

A positive cutoff value of the ΔCVF between the different groups was sought, as well as its sensitivity, specificity, and diagnostic accuracy. The relationship among the values of ΔCVF and age, sex, and clinical status was considered.

Statistical Analysis

The reliability of the results obtained by 2 operators was calculated by using the Fleiss κ index. The frequency distributions of the ΔCVF cutoff value among the subjects in the MS, HC, and OND groups were displayed as contingency tables. The differences between the proportions of the outcomes of this diagnostic index over the MS, HC, and OND groups were assessed through the Marascuilo procedure, which enabled simultaneous testing of the differences of all pairs of proportions. The Kruskal-Wallis test was applied to compare the distributions of theΔCVF cutoff value among the groups and to evaluate the differences among the subclasses of MS disease. In either case, the post hoc tests were performed by the Dunn multiple comparison test.

All the statistical tests were 2-tailed, and the significance level was fixed at .05.

The errors of classification were reported in terms of sensitivity, specificity, negative predictive value, and positive predictive value (PPV), along with their 95% confidence intervals. The odds ratio was also provided, and its *P* value was determined by the Fisher exact test. The capability of the ΔCVF cutoff value to classify the MS forms (relapsing-versus-progressive) was reported as ORs.

The cutoff (ie, the threshold of the ΔCVF) had been initially set to zero—namely the negative values of ΔCVF were considered prognostic of pathologic status or "events," while the positive values of ΔCVF, as predictive "nonevents." By increasing the level of the threshold, we expected to decrease the number of the false-negative predicted cases because 68.52% of the patients with MS had a positive ΔCVF.

Performances of the models were assessed by the receiver operating characteristic analysis curve, which is reported to be the most opportune approach and a comprehensive description and measurement of diagnostic accuracy because it estimates all of the combinations of sensitivity and specificity that a diagnostic test can produce.[24,25] The range of the cutoff values from which selecting the optimal threshold was formed by the percentiles of the distribution of the ΔCVF in the HC group not only because the healthy condition is usually adopted as the reference standard in a diagnostic test, but also because the ΔCVF distributions of HC and OND groups were largely overlapping. Every percentile was, in turn, set as the "potential best threshold" (this implies, from time to time, establishing, a priori, the specificity of the test). Then, in correspondence with each percentile, the number of subjects (from MS, HC, OND) with a ΔCVF lower than the potential cutoff was counted as an "event" (ie, abnormal—this means, from time to time, determining the sensitivity of the test). Hence, by varying the percentile, it has been possible to trace the relationship between sensitivity and specificity to give rise to the receiver operating characteristic analysis curve.

The optimal positive cutoff threshold was determined in correspondence to the best compromise among sensitivity, specificity, and PPV.

We measured the area under the receiver operating characteristic analysis curve (AUC); and its statistical significance against the null hypothesis of AUC = 0.5 was assessed by means of the *Z*-test.[26] The area under the curve can take values between 0.5 and 1.0. The greater the area under the curve (ie, the more the curve approaches the vertex of the graph), the greater the discriminating power of the test will be. For the interpretation of the values of the area below the receiver operating characteristic analysis curve, we referred to the classification proposed by Swets[27]: AUC = 0.5, the test is not informative; $0.5 < \text{AUC} \leq 0.7$, the test is slightly accurate; $0.7 < \text{AUC} \leq 0.9$, the test is fairly accurate; $0.9 < \text{AUC} < 1.0$, the test is highly accurate; and AUC = 1 is a perfect test.

The robustness of the ΔCVF model was tested by using by an independent ("test") sample made of 52 subjects with MS and 27 HC. Thus, the AUC of the test set was evaluated, and in correspondence to the best threshold estimated from the "training" set (ie, the given sample), we traced the values of sensitivity, specificity, and accuracy for the test set.

An internal test set (ie, a cross-validation test) is used for getting an independent OND sample by iterating the leave-*n*-out algorithm 2000 times. A different subset of the data (10 records) was held out each time, so that the training sets included 20 subjects and the out-of-sample, 10 subjects. The medians of the classification errors obtained from each partition were calculated; then, the sensitivity, specificity, and diagnostic accuracy were assessed. Last, the AUCs measured from the training and testing samples were compared.

Logistic regression was applied to predict the realization of the variable ΔCVF dichotomized (according to the cutoff value), as a function of the demographic and clinical regressors—namely, age, sex and Expanded Disability Status Scale.

RESULTS

The Fleiss κ index, calculated on 30 subjects (10 with MS, 10 HC, 10 with OND), was 0.9333, and its confidence interval (95%) was 0.8402–1.0264. Therefore, the observed agreement between the 2 operators was not accidental ($z = 5.1117$, $P < .0001$).

An optimal cutoff value of the ΔCVF was reached at the 30th percentile (ie, ΔCVF = 503.24) of the HC data distribution. ΔCVF < 503.24 was present in 38/54 (70.37%) patients with MS, 9/31 (29.03%) HC, and 13/30 (43.33%) subjects with OND. The null hypothesis of equal proportions was rejected ($\chi^2 = 14.7584$, $P = .0006$, power = 0.9405).

By comparing MS versus HC groups with a cutoff of ΔCVF = 503.24, the sensitivity was 70.37%; the specificity, 70.97%; the PPV, 80.85%; and the negative predictive value, 57.89%; the OR calculated for ΔCVF < 503.24 was significant (5.81, $P = .00016$). Given OND versus HC, the sensitivity was 45%; the specificity, 70.97%; the PPV, 50%; the negative predictive value, 66.67%; and the OR was not significant (OR = 2, $P = .1091$). If one compared MS and OND, the sensitivity was 70.37%; the specificity, 55%; the PPV, 80.85%; the negative predictive value, 40.74%; and the OR was significant (2.90, $P = .0103$) (Table 1).

The Kruskal-Wallis test allowed rejecting the null hypothesis that the observed ΔCVF in subjects with MS, OND, and HC originated from the same distribution ($P = .0003$). The post hoc test indicated the significant difference ($P < .01$) between patients with MS and HC and between subjects with MS and OND. HC versus subjects with OND was not statistically different (Fig 2).

The Kruskal-Wallis test applied to compare HC and MS subgroups (relapsing-remitting, primary-progressive, and secondary-progressive) indicated a significant difference ($P = .0014$), which was determined by relapsing-remitting versus HC ($P < .01$) and primary-progressive/secondary-progressive versus HC ($P < .05$). No statistically significant difference was assessed between the relapsing and progressive forms (Fig 3).

Table 1: Analysis of classification errors: training sets[a]

	MS vs HC	MS vs OND	OND vs HC
Sen %	70.37	70.37	45
95% CI (Sen)	58.19–82.55	58.19–82.55	23.20–66.80
Spe %	70.97	55	70.97
95% CI (Spe)	54.99–86.95	33.20–76.80	54.99–86.95
FP %	29.03	45	29.03
95% CI (FP)	13.03–45.01	23.20–66.80	13.05–45.01
FN %	29.63	29.63	55
95% CI (FN)	17.45–41.81	17.45–41.81	33.20–76.80
PPV %	80.85	80.85	50
95% CI (PPV)	69.60–92.10	69.60–92.10	26.90–73.10
NPV %	57.89	40.74	67
95% CI (NPV)	42.20–73.59	22.21–59.27	50.58–82.75
OR	5.81	2.90	2
95% CI (OR)	2.20–15.33	1.01–8.34	0.62–6.47

Note—Sen indicates sensitivity; Spe, specificity; FP, false-positive; FN, false-negative; NPV, negative predictive value; PPV, positive predictive value.

[a] The columns refer to each comparison between the observed (ie, training) groups.

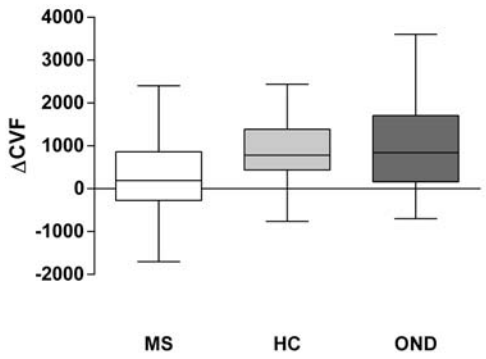

Kruskal-Wallis test
P value 0.0003
Kruskal-Wallis statistic 16.05

Dunn's multiple comparisons test	Mean rank diff.	Significant?	Summary	Adjusted P Value
MS vs. HC	-25.74	Yes	**	0.0018
MS vs. OND	-24.09	Yes	**	0.0045
HC vs. OND	1.649	No	ns	> 0.9999

FIG 2. The ΔCVF distribution among the 3 groups. If one applies the Kruskal-Wallis test, significant differences result between MS and HC and MS and OND, while HC versus OND is not statistically different.

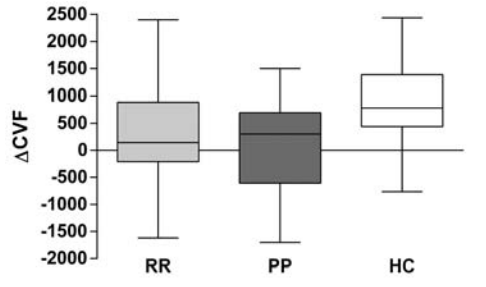

Kruskal-Wallis test
P value 0.0014
Kruskal-Wallis statistic 13.09

Dunn's multiple comparisons test	Mean rank diff.	Significant?	Summary	Adjusted P Value
RR vs. PP	0.9964	No	ns	> 0.9999
RR vs. HC	-19.85	Yes	**	0.0023
PP vs. HC	-20.85	Yes	*	0.0262

FIG 3. Boxplot ΔCVF and different subgroups of patients with MS. The Kruskal-Wallis test shows no significant difference among MS subgroups.

All the AUCs were different from one another—that is, the AUC was 0.7034 (standard error = 0.0564, $P = .00015$) in the comparison between MS and HC (ie, fairly accurate), 0.7306 (standard error = 0.0597, $P = .00001$) if the MS group was compared with OND (ie, fairly accurate), and 0.6323 (standard error = 0.0611, $P = .0152$) when comparing OND versus HC (ie, slightly accurate).

In the independent sample, ΔCVF < 503.24 was present in 41/52 patients with MS, 11/27 HC, and 4/10 subjects with OND (Table 2). Performance of the ΔCVF < 503.24 model was also assessed on the independent sample (test set) by the analysis of the receiver operating characteristic analysis curve. The AUC was 0.7877 (standard error = 0.0505, $z = 5.7018$, $P = .00015$) in the comparison between MS and HC; the AUC was 0.8260 (standard error = 0.0591, $z = 5.5162$, $P = 0$) if the MS group was compared with OND; and the AUC was 0.55 (standard error = 0.1092, $z = 0.4577$, $P = .3236$) when comparing OND versus HC. There was significant difference in the AUC values for MS versus HC ($z = 9.7015$, $P = 0$), MS versus OND ($z = -9.1021$, $P = 0$), and HC versus OND ($z = -3.7631$, $P = .000083$). The accuracy of the model was fair for the comparison between MS and HC and MS and OND, while it was not informative between OND and HC.

The criterion ΔCVF < 503.24 applied within the MS subgroups to assess their capability to classify relapsing forms versus progressive forms resulted in 29/40 for relapsing-remitting and 10/14 for primary-progressive and secondary-progressive, with OR = 1.0545, not significantly different from 1 ($P = .2674$).

The logistic regression was applied to predict the realization of the variable ΔCVF dichotomized according to the cut-off value, as a function of the demographic (age and sex) and clinical (Expanded Disability Status Scale; EDSS) regressors.

The implementation of the logistic model on the MS, HC, and OND groups did not result in the identification of significant effects of age, sex, and clinical status over the outcomes of ΔCVF. The *P* values corresponding to these considered variables for MS, HC, and OND were respectively: ($P_{age} = .81$; $P_{sex} = .79$; $P_{EDSS} = .75$), ($P_{age} = .77$; $P_{sex} = 0.56$), and ($P_{age} = .86$; $P_{sex} = .82$).

DISCUSSION

The cerebral venous system has very variable anatomic patterns,[28-31] to maintain an efficient and normal CVF. Qualitative (ie, jugular valves or flow characteristics) and quantitative (ie, flow rate and velocity) aspects of CVF are demonstrated by using quantitative

Table 2: Analysis of classification errors: out-of-sample sets[a]

	MS vs HC	MS vs OND	OND vs HC
Sen %	78.85	91.11	40
95% CI (Sen)	67.75–89.95	82.80–99.43	9.64–70.36
Spe %	59.26	35.29	59.26
95% CI (Spe)	40.73–77.79	12.58–58.01	40.73–77.79
FP %	40.74	64.71	40.74
95% CI (FP)	22.21–59.27	41.99–87.42	22.21–59.27
FN %	21.15	8.89	60
95% CI (FN)	10.05–32.25	0.57–17.20	29.64–90.36
PPV %	78.85	78.85	26.67
95% CI (PPV)	67.75–89.95	67.75–89.95	4.29–49.05
NPV %	59.26	60	72.73
95% CI (NPV)	40.73–77.79	29.64–90.36	54.12–91.34
OR	5.42	5.59	0.97
95% CI (OR)	1.95–14.97	1.34–23.34	0.22–4.26

Note:—Sen indicates sensitivity; Spe, specificity; FP, false-positive; FN, false-negative; NPV, negative predictive value; PPV, positive predictive value.

[a] The columns refer to each comparison between the groups in the independent samples.

color Doppler sonography in the same dynamic (ie, sitting and supine positions) examinations. On the other hand, MR venography, phase-contrast MR imaging, perfusion MR imaging, and the so-called criterion standard, venography, cannot provide jointly the qualitative and quantitative features of the venous system or CVF.

CVF has been demonstrated to change depending on different positions.[19,32] The major drainage in the supine position is usually by the internal jugular veins. Postural dependency of the CVF has been demonstrated in healthy subjects by quantitative color Doppler sonography.[17,18] A previous article[17] showed that the presence of negative ΔCVF is statistically correlated with a pathologic condition. The measurement of ΔCVF demonstrated a statistical difference between patients with MS and the HC group in the supine and sitting positions. The higher the blood volume difference is between the supine and sitting positions, the higher is the adaptability of the cerebral venous system. Therefore, healthy subjects with normal supine/orthostatic responses show a high blood volume difference. In patients with MS, this venous response is statistically reduced. The previous study was based only on 2 groups of subjects (ie, MS and HC) and was not blinded.

The analysis of the results reported here suggests the following considerations:

1) The ΔCVF cutoff value of 503.24 correctly diagnosed a larger number of patients with MS, despite the detriment of an increased number of false-positives.

2) ΔCVF $\leq$ 503.24 allowed differentiating MS versus HC and MS versus OND.

The distributions of the variable ΔCVF in the HC and OND groups largely overlapped. On the other hand, the difference between the ΔCVF in the OND and MS groups is statistically significant.

These data demonstrate that in some patients with MS, there is a hemodynamic alteration resulting in a reduced cerebral venous outflow in the supine position, most likely from decreased vertebral and internal jugular vein outflow.[17] The present study also confirmed that the reduced outflow was not correlated with stenosis and dynamic or morphologic leaflet alterations. Furthermore, the reduced CVF has been demonstrated in very young patients without any venous malformations. A possible explanation is that the active tension imparted by the smooth muscle layer of the veins is not sufficient to overcome transmural pressure. In the supine position, a lower venous wall tone is not sufficient to hold venous outflow, while in the sitting position, the physiologic collapse of the main drainage veins (ie, internal jugular veins) always overcomes the low vein wall tone. This deregulation might be due to a reduced responsiveness of the vessel wall because homeostasis might be lost in changing positions. Previous observations suggested that the autonomic nervous system may be intimately linked with the disordered immune regulation in MS. Vasoactive factors such as endothelin-1 and nitric oxide may play a role in the responsiveness of the vessel wall.[33-38]

Another possible explanation is that this abnormal venous response is secondary to white matter hypoperfusion, and its possible mechanisms and pathophysiology were reported by De Keyser et al.[39]

CONCLUSIONS

The present study showed that a cutoff of abnormal CVF could discriminate patients with MS from those with OND and HC.

ACKNOWLEDGMENTS

We thank Roberta Benvenuti, Roberta Baldi, Tiziana Caselli, Massimiliano Senesi, and Elena Spolaor for their technical assistance.

REFERENCES

1. Theron J, Moret J. *Spinal Phlebography. Lumbar and Cervical Techniques.* Berlin: Springer-Verlag; 1978
2. Zivadinov R, Karmon Y, Dolic K, et al. **Multimodal noninvasive and invasive imaging of extracranial venous abnormalities indicative of CCSVI: results of the PREMiSe pilot study.** *BMC Neurol* 2013;13:151
3. Macgowan CK, Chan KY, Laughlin S, et al. **Cerebral arterial and venous blood flow in adolescent multiple sclerosis patients and age-matched controls using phase contrast MRI.** *J Magn Reson Imaging* 2013 Sep 30. [Epub ahead of print]
4. Debernard L, Melzer TR, Van Stockum S, et al. **Reduced grey matter perfusion without volume loss in early relapsing-remitting multiple sclerosis.** *J Neurol Neurosurg Psychiatry* 2014;85:544–51
5. Varga AW, Johnson G, Babb JS, et al. **White matter hemodynamic abnormalities precede sub-cortical gray matter changes in multiple sclerosis.** *J Neurol Sci* 2009;282:28–33
6. Zamboni P, Consorti G, Galeotti R, et al. **Venous collateral circulation of the extracranial cerebrospinal outflow routes.** *Curr Neurovasc Res* 2009;6:204–12
7. Menegatti E, Zamboni P. **Doppler haemodynamics of cerebral venous return.** *Curr Neurovasc Res* 2008;5:260–65
8. Zamboni P, Galeotti R, Menegatti E, et al. **Chronic cerebrospinal venous insufficiency in patients with multiple sclerosis.** *J Neurol Neurosurg Psychiatry* 2009;80:392–99
9. Hojnacki D, Zamboni P, Lopez-Soriano A, el al. **Use of neck magnetic resonance venography, Doppler sonography and selective venography for diagnosis of chronic cerebrospinal venous insufficiency: a pilot study in multiple sclerosis patients and healthy controls.** *Int Angiol* 2010;29:127–39
10. Zamboni P, Galeotti R, Menegatti E, et al. **A prospective open-label study of endovascular treatment of chronic cerebrospinal venous insufficiency.** *J Vasc Surg* 2009:50:1348–58. Erratum in *J Vasc Surg* 2009;51:1079
11. Mayer CA, Pfeilschifter W, Lorenz MW, et al. **The perfect crime?**

CCSVI not leaving a trace in MS. *J Neurol Neurosurg Psychiatry* 2011;82:436–40
12. Baracchini C, Perini P, Calabrese M, et al. **No evidence of chronic cerebrospinal venous insufficiency at multiple sclerosis onset.** *Ann Neurol* 2011;69:90–99
13. Doepp F, Paul F, Valdueza JM, et al. **No cerebrocervical venous congestion in patients with multiple sclerosis.** *Ann Neurol* 2010;68:173–83
14. Khan O, Filippi M, Freedman MS, et al. **Chronic cerebrospinal venous insufficiency and multiple sclerosis.** *Ann Neurol* 2010;67:286–90
15. D'haeseleer M, Cambron M, Vanopdenbosch L, et al. **Vascular aspects of multiple sclerosis.** *Lancet Neurol* 2011;10:657–66
16. Mancini M, Morra VB, Di Donato O, et al. **Multiple sclerosis: cerebral circulation time.** *Radiology* 2012;262:947–55
17. Monti L, Menci E, Ulivelli M, et al. **Quantitative colour Doppler sonography evaluation of cerebral venous outflow: a comparative study between patients with multiple sclerosis and controls.** *PLoS One* 2011;6:e25012
18. Valdueza JM, Schmierer K, Mehraein S, et al. **Assessment of normal flow velocity in basal cerebral veins: a transcranial Doppler ultrasound study.** *Stroke* 1996;27:1221–25
19. Valdueza JM, von Münster T, Hoffman O, et al. **Postural dependency of the cerebral venous outflow.** *Lancet* 2000;355:200–01
20. Gisolf J, van Lieshout JJ, van Heusden K, et al. **Human cerebral venous outflow pathway depends on posture and central venous pressure.** *J Physiol* 2004;560:317–27
21. Wang DC, Klatzky R, Wu B, et al. **Fully automated common carotid artery and internal jugular vein identification and tracking using B-mode ultrasound.** *IEEE Trans Biomed Eng* 2009;56:1691–99
22. Dörfler P, Puls I, Schliesser M, et al. **Measurement of cerebral blood flow volume in extra cranial sonography.** *J Cereb Blood Flow Metab* 2000;20:269–71
23. Doepp F, Schreiber SJ, von Münster T, et al. **How does the blood leave the brain? A systematic ultrasound analysis of cerebral venous drainage patterns.** *Neuroradiology* 2004;46:565–70
24. Schäfer H. **Constructing a cut off point for a quantitative diagnostic test.** *Stat Med* 1989;8:1381–91
25. Metz CE. **Receiver operating characteristic analysis: a tool for the quantitative evaluation of observer performance and imaging systems.** *J Am Coll Radiol* 2006;3:413–22
26. Hanley JA, McNeil BJ. **The meaning and use of the area under a receiver operating characteristic (ROC) curve.** *Radiology* 1982;143:29–36
27. Swets JA. **Measuring the accuracy of diagnostic systems.** *Science* 1988;240:1285–93
28. Lepori D, Capasso P, Fournier D, et al. **High resolution ultrasound evaluation of internal jugular venous valves.** *Eur Radiol* 1999;9:1222–26
29. Schreiber SJ, Lurtzing F, Gotze R, et al. **Extrajugular pathways of human cerebral venous blood drainage assessed by duplex ultrasound.** *J Appl Physiol* 2003;94:1802–05
30. Chou CH, Chao AC, Hu HH. **Ultrasonographic evaluation of vertebral venous valves.** *AJNR Am J Neuroradiol* 2002;23:1418–20
31. Renard M, Masson JP, Lardé D. **Anatomo-radiological study of the spinal venous system of the lumbo-sacral junction** [in French]. *Bull Assoc Anat (Nancy)*1975;59:725–35
32. Alperin N, Hushek SG, Lee SH, et al. **MRI study of cerebral blood flow and CSF flow dynamics in an upright posture: the effect of posture on the intracranial compliance and pressure.** *Acta Neurochir Suppl* 2005;95:177–81
33. Pache M, Kaiser HJ, Akhalbedashvili N, et al. **Extraocular blood flow and endothelin-1 plasma levels in patients with multiple sclerosis.** *Eur Neurol* 2003;49:164–68
34. Flachenecker P, Reiners K, Krauser M, et al. **Cardiovascular autonomic dysfunction in multiple sclerosis: correlation with orthostatic intolerance.** *J Neurol* 1999;246:578–86
35. Olufsen MS, Ottesen JT, Tran HT, et al. **Blood pressure and blood flow variation during postural change from sitting to standing: model development and validation.** *J Appl Physiol* 2005;99:1523–37
36. Purkayastha S, Raven PB. **The functional role of the alpha-1 adrenergic receptors in cerebral blood flow regulation.** *Indian J Pharmacol* 2011;43:502–06
37. Sternberg Z. **Autonomic dysfunction: a unifying multiple sclerosis theory, linking chronic cerebrospinal venous insufficiency, vitamin D(3), and Epstein-Barr virus.** *Autoimmun Rev* 2012; 12:250–59
38. Capone C, Faraco G, Coleman C, et al. **Endothelin 1-dependent neurovascular dysfunction in chronic intermittent hypoxia.** *Hypertension* 2012;60:106–13
39. De Keyser J, Steen C, Mostert JP, et al. **Hypoperfusion of the cerebral white matter in multiple sclerosis: possible mechanisms and pathophysiological significance.** *J Cereb Blood Flow Metab* 2008;28:1645–51

Detection and Grading of Endolymphatic Hydrops in Menière Disease Using MR Imaging

K. Baráth, B. Schuknecht, A. Monge Naldi, T. Schrepfer, C.J. Bockisch, and S.C.A. Hegemann

ABSTRACT

BACKGROUND AND PURPOSE: Endolymphatic hydrops has been recognized as the underlying pathophysiology of Menière disease. We used 3T MR imaging to detect and grade endolymphatic hydrops in patients with Menière disease and to correlate MR imaging findings with the clinical severity.

MATERIALS AND METHODS: MR images of the inner ear acquired by a 3D inversion recovery sequence 4 hours after intravenous contrast administration were retrospectively analyzed by 2 neuroradiologists blinded to the clinical presentation. Endolymphatic hydrops was classified as none, grade I, or grade II. Interobserver agreement was analyzed, and the presence of endolymphatic hydrops was correlated with the clinical diagnosis and the clinical Menière disease score.

RESULTS: Of 53 patients, we identified endolymphatic hydrops in 90% on the clinically affected and in 22% on the clinically silent side. Interobserver agreement on detection and grading of endolymphatic hydrops was 0.97 for cochlear and 0.94 for vestibular hydrops. The average MR imaging grade of endolymphatic hydrops was 1.27 ± 0.66 for 55 clinically affected and 0.65 ± 0.58 for 10 clinically normal ears. The correlation between the presence of endolymphatic hydrops and Menière disease was 0.67. Endolymphatic hydrops was detected in 73% of ears with the clinical diagnosis of possible, 100% of probable, and 95% of definite Menière disease.

CONCLUSIONS: MR imaging supports endolymphatic hydrops as a pathophysiologic hallmark of Menière disease. High interobserver agreement on the detection and grading of endolymphatic hydrops and the correlation of MR imaging findings with the clinical score recommend MR imaging as a reliable in vivo technique in patients with Menière disease. The significance of MR imaging detection of endolymphatic hydrops in an additional 22% of asymptomatic ears requires further study.

ABBREVIATIONS: EH = endolymphatic hydrops, MD = Menière disease; 3D-IR = 3D real inversion recovery

According to the 1985 American Academy of Otolaryngology-Head and Neck Surgery Committee on Hearing and Equilibrium guidelines, Menière disease (MD) is defined by ≥2 definitive spontaneous episodes of vertigo 20 minutes or longer, audiometrically documented hearing loss on at least 1 occasion, and tinnitus or aural fullness.[1] In 1995, a clinical diagnostic scale was added with the categories possible, probable, definite, and certain,[2] with "certain" defined as definite disease plus histopathologic confirmation. It is universally agreed that the pathogenesis of MD consists of endolymphatic hydrops (EH), but a simple cause-effect relation between EH and clinical symptoms is not present. Moreover, EH appears to be an end point of different etiologies such as trauma,[2] viral infection and autoimmune processes,[3] electrolyte imbalance,[4] and cellular channelopathies.[5] Histopathology has provided evidence that not every individual with EH presents with symptoms of MD[6-8] and not every individual with the clinical diagnosis of MD has EH.[9-12] Only recently has MR imaging enabled depiction of EH,[13] opening a window for in vivo confirmation of EH. The purpose of our study was to assess the degree of EH in 53 patients with MD and to correlate the MR imaging findings obtained by a specific protocol with the certitude of clinical diagnosis.

Received August 30, 2013; accepted after revision November 20.

From the Medizinisches Radiologisches Institut (MRI Bethanien/Bahnhofplatz/Stadelhofen) Zurich (K.B., B.S.), Zurich, Switzerland; Department of Oto-Rhino-Laryngology (A.M.N., T.S.), University Hospital of Zurich, Zurich, Switzerland; and Departments of Neurology, Ophthalmology and Oto-Rhino-Laryngology (C.J.B.) and Oto-Rhino-Laryngology, Interdisciplinary Center for Vertigo and Balance Disorders (S.C.A.H.), University Hospital of Zurich, Zurich, Switzerland.

B. Schuknecht shared first authorship with K. Baráth.

Please address correspondence to Krisztina Baráth, Medizinisches Radiologisches Institut (MRI Bethanien/Bahnhofplatz/Stadelhofen) Zurich, Toblerstr 51, 8044 Zurich, Switzerland; e-mail: barath.krisztina@hin.ch

http://dx.doi.org/10.3174/ajnr.A3856

MATERIALS AND METHODS

From June 2012 until April 2013, sixty-three patients, 27–72 years of age, female/male = 21:42, with the clinical diagnosis of definite,

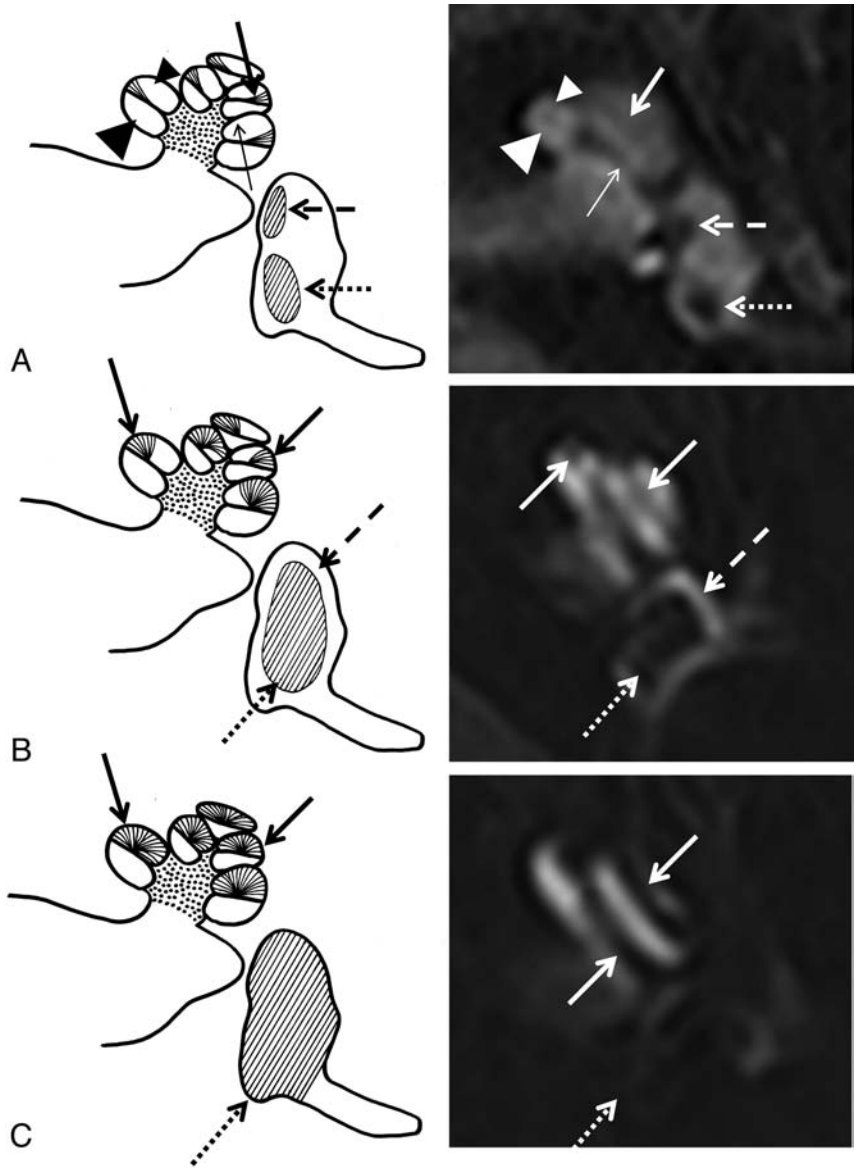

FIG 1. *A*, Normal labyrinth: interscalar septum (*thin arrow*), scala tympani (*large arrowhead*), osseous spiral lamina/cochlear duct (*thick arrow*), scala vestibuli (*small arrowhead*), saccule (*dashed arrow*), and utricle (*dotted arrow*). *B*, Cochlear hydrops grade I with irregular dilation and partial obstruction of the scala vestibuli (*arrows*). In vestibular hydrops grade I, dilation of the endolymphatic space (*dotted arrow*) encompasses >50% of the vestibulum. A circular perilymphatic space (*dashed arrow*) remains visible. *C*, Cochlear hydrops grade II with total obliteration of the scala vestibuli (*arrows*). In vestibular hydrops grade II, dilation of the endolymphatic space leads to effacement of the perilymphatic space (*dotted arrow*).

possible, or probable MD were referred for 3T MR imaging of the temporal bone to demonstrate EH and to exclude other causes of vertigo and hearing loss such as vestibular schwannoma. Nine patients with motion artifacts and 1 patient with the MR imaging diagnosis of hemorrhagic labyrinthitis were excluded from analysis. With institutional approval for the study and patient informed consent, the MR imaging data of the remaining 53 patients (106 ears) were retrospectively analyzed.

All patients underwent 3T MR imaging of the temporal bone by using a 32-channel phased array coil to rule out schwannoma or other causes of the symptoms. Following a delay of 4 hours after intravenous contrast administration (Gadovist; Bayer-Schering Pharma, Berlin, Germany; 1.0 mmol/mL at a dose of 0.2 mmol/kg), a 3D real inversion recovery (3D-IR) sequence[13] was performed with the following parameters: FOV, 190 mm; section thickness, 0.8 mm; TR, 6000 ms; TE, 177 ms; number of excitations, 1; TI, 2000 ms; flip angle, 180°; matrix, 384 × 384; bandwidth, 213 Hz/pixel; turbo factor, 27; scan time, 15 minutes.

The MR images were qualitatively analyzed by 2 experienced neuroradiologists (K.B. and B.S.) blinded to the side, uni- or bilaterality of symptoms and the clinical score of MD.

On the basis of previous histopathologic observations,[14] EH was categorized as none (Fig 1*A*), grade I (Fig 1*B*), and grade II (Fig 1*C*). Hydrops of the cochlea and vestibule was separately assessed by visual comparison of the relative areas of the nonenhanced endolymphatic space versus the contrast-enhanced perilymph space.

Statistical analysis for interobserver agreement on detecting and grading EH was performed by using the Cohen κ test. To test for independence of MR imaging and clinical results, we used the Pearson χ^2 test (when the clinical grading was simplified to normal and abnormal ears), and the Fisher exact test, when the clinical score was 4 levels (normal ears and ears with possible, probable, and definite MD). All tests were performed in R (Version 2.14.2; http://www.r-project.org/) and RStudio (Version 0.97; http://www.rstudio.com).

RESULTS

Normal MR Imaging Findings

On the delayed 3D-IR sequence, the normal cochlea displays the interscalar septum, scala tympani, osseous spiral lamina/cochlear duct, and scala vestibuli (Fig 1*A*). In the normal vestibule, the added surface areas of the saccule and utricle are less than half the area of the vestibule at the midmodiolar level (Fig 1*A*).

Grading of EH

Grade I cochlear hydrops was defined as mild dilation of the nonenhancing cochlear duct, sparing parts of the enhancing perilymph of the scala vestibuli (Fig 1*B*). Grade I vestibular hydrops presented as distention of the endolymph space of the saccule or utricle or both, with the perilymphatic space still visible along the periphery of the bony vestibule (Fig 1*B*).

In grade II cochlear hydrops, the scala vestibuli was uniformly obstructed by the maximally distended cochlear duct

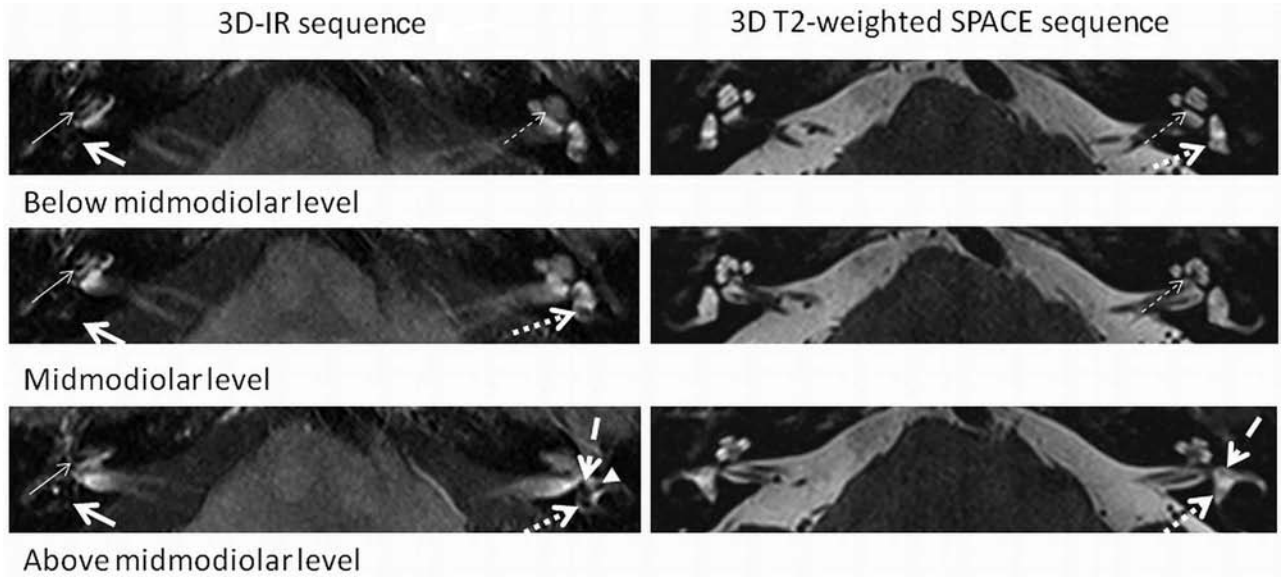

FIG 2. A 3D-IR sequence depicts cochlear EH grade II (*thin arrow*) and vestibular EH grade II (*thick arrow*) on the right. EH is not visible on the corresponding 3D T2-weighted spatial and chemical-shift encoded excitation (SPACE) sequence. No EH on the normal left side is seen. Normal anatomy is shown at different levels (below the midmodiolar, midmodiolar, and above the midmodiolar sections) on the 3D-IR (0.8 mm) and 3D heavily T2-weighted SPACE (0.4 mm) sequence: interscalar septum (*thin dashed arrow*), anterior ampulla (*thick dashed arrow*), utricle/common crus (*thick dotted arrow*), and the lateral ampulla (*arrowhead*).

(Figs 1*C* and 2). In grade II vestibular hydrops, the bony vestibule was entirely encompassed by the dilated endolymphatic spaces (Figs 1*C* and 2).

EH was not visible on the 3D heavily T2-weighted spatial and chemical-shift encoded excitation sequence obtained at a 0.4-mm section thickness (Fig 2).

MR Imaging Findings of EH

Cochlear hydrops was present in 53 ears (grade I in 35 and grade II in 18 cases), and vestibular hydrops was detected in 56 ears (grade I in 30 and grade II in 26 instances). Cohen κ test for interobserver agreement was 0.97 for cochlear findings and 0.94 for the vestibule (normal and abnormal). The average MR imaging grading of EH was 1.27 $\pm$ 0.66 for 55 clinically affected ears (55 cochleae and 55 vestibules) and 0.65 $\pm$ 0.581 for 10 clinically normal sides (10 cochleae and 10 vestibules).

Correlation of Imaging and Clinical Diagnosis

Ninety percent (55/61) of clinically diseased ears had EH on MR imaging, whereas 78% (35/45) of the clinically normal ears had no EH on MR imaging (Fig 3*A*). The results proved significantly different from chance (Pearson χ^2 test with the Yates continuity correction, $\chi^2 = 47.5754$, $df = 1$, $P < .001$). Conversely, 22% (10/45) of clinically normal ears showed EH on MR imaging, and 10% (6/61) of ears with a clinical diagnosis of MD did not show EH.

Of the 10 ears with asymptomatic unilateral EH, MR imaging in 9 ears (92%) depicted grade I EH in either the cochlea ($n = 3$), the vestibule ($n = 5$), or both ($n = 1$). Only in 1 case was grade II vestibular EH present in addition to a grade I cochlear EH.

The correlation between the presence of EH and the clinical score (normal ears and ears with possible, probable, and definite MD) was 0.67 (Spearman ρ, $P < .001$). EH was depicted in 73% (11/15) of ears with the clinical diagnosis of possible MD, in 100% (3/3) with probable MD, and in 95% (41/43) of sides with definite MD (Fig 3*B*). These percentages are significantly different from chance (Fisher Exact Test for Count Data, P value $< .001$).

DISCUSSION

MR Imaging Visualization of EH

Since the first publication of MR imaging visualization of EH in an animal study in 2001[15] and MR imaging demonstration of EH in patients with MD following intratympanic injection in 2007,[16] numerous studies have tried to visualize EH by using different routes of administration of contrast media, such as intratympanic[16] versus intravenous[17-20] and by altering intravenous dosage regimens (single,[13,17] double,[18] and triple[21] dose). Additional variations included technical parameters such as the number of receive channels of the head coil (8,[22] 12,[23] and 32,[17]) and a variable choice of sequences such as 3D-FLAIR,[23,24] heavily T2-weighted 3D-FLAIR,[24] and 3D-IR sequences.[13] On the basis of previous demonstration of the feasibility to separate the endo- and perilymphatic space 24 hours after intratympanic gadolinium injection by a 3D-IR sequence[13] and the observation that perilymphatic enhancement occurs 4 hours after intravenous contrast administration,[21,25] our protocol comprised a 3D-IR sequence obtained 4 hours following intravenous injection of contrast media.

The intravenous route of contrast administration is also less invasive and renders perilymph enhancement independent of the status of the round window membrane.[26,27] In a comparative study in patients with MD, however,[28] intratympanic contrast injection provided higher perilymphatic signal compared with intravenous administration. An additional advantage of the intravenous method is simultaneous examination of both labyrinths because provided the disease manifestation is unilateral, the nondiseased ear serves for comparison. A caveat to this, however, is

that asymptomatic EH had been observed by histopathology in 5%[7] and 26%[8] of postmortem examinations without documented MD. Finally, intravenous application of the contrast agent renders the function of the blood-perilymph barrier visible.

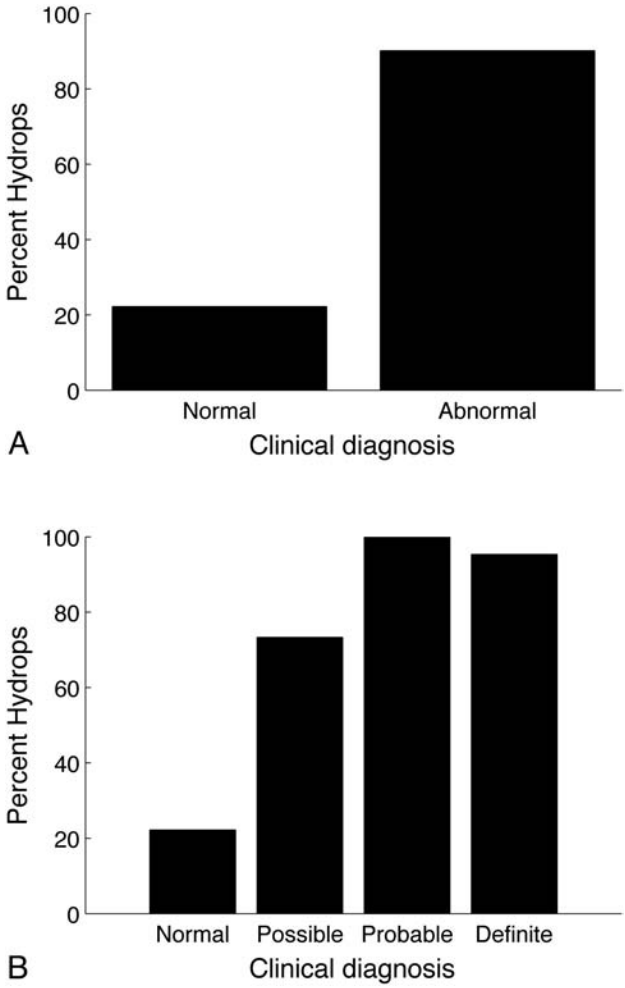

FIG 3. EH is present in 22% (10/45) of clinically normal ears and in 90% (55/61) of clinically diseased ears (irrespective of clinical score) (*A*) and in 73% of ears with possible (11/15), in 100% in ears with probable (3/3), and in 95% (41/43) of ears with definite MD (*B*).

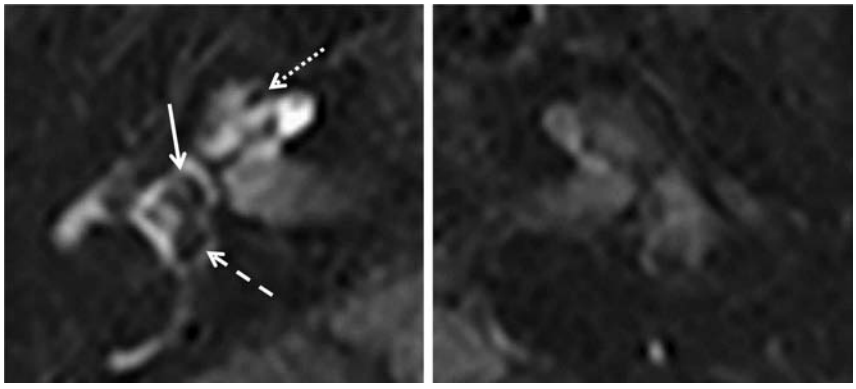

FIG 4. Predominant saccular dilation: 3D-IR sequence (right and left side of the same patient). The right side shows a dilated saccule (*arrow*) and a slightly distended utricle (*dashed arrow*) with grade I cochlear hydrops (*dotted arrow*). Note increased contrast enhancement of the perilymph on the symptomatic right side compared with the normal left labyrinth.

In accordance with others,[24,28] gadolinium uptake was more pronounced in symptomatic compared with asymptomatic ears in patients with unilateral EH in 90% of our cases (Fig 4).

Anatomic Considerations

In 1938, Hallpike and Cairns[29] described histopathologic changes that consisted of gross distention of the cochlear duct and predominant dilation of the saccule as opposed to the utricle. In most cases of our series, however, vestibular hydrops was not attributable to either the saccule or the utricle (Fig 1*B, -C*), and only rarely a preferential distention of the saccule (Fig 4) or the utricle (Fig 5) was observed. The saccule is located anteromedially in the pars inferior of the vestibule, while the utricle is posterior within the pars superior.[30] Because visual assessment was based on axial images at the widest part of the vestibule (Fig 2), dilation of the vertically oriented saccule may have been underestimated in comparison with the horizontally positioned utricle. Cochlear hydrops, an apical distention of the cochlear duct as a normal finding[31] and the interscalar septum (Fig 2), can be confidently identified at this level as well.

MR Imaging Grading of EH

MR imaging grading of EH is meant to assess the presence and degree of EH in patients with different clinical scores of MD.

In 20 healthy volunteers, Liu et al[32] found the endolymph to account for 8%–26% of the fluid space within the cochlea and 20%–41% in the vestibule. For the cochlea, Sperling et al[33] proposed a grading system of EH with the categories "slight, moderate, and profound," based on an increasing displacement of the Reissner membrane. Visualization of the perilymphatic space within the scala vestibuli in our study is an indirect measure to depict displacement of the Reissner membrane as well. Cochlear duct dilation was relatively uniform in grade II hydrops (Fig 1*C*) but commonly slightly nodular in grade I (Figs 1*B* and 4). Histopathologically, the existence of cochlear hydrops of varying severity in the same cochlea has been proved as well.[34]

The definition of a cutoff value of >50% required for vestibular hydrops grade I was derived from 41% of the total volume encompassed by the saccule and utricle.[33] Grade II was present when the entire vestibulum was occupied by the endolymph space. The MR imaging grading proposed by Nakashima et al[34] probably overestimates "mild hydrops" when defined as "one-third and a half ratio" of endo- to perilymphatic space.

Relationship between Clinical Diagnosis and MR Imaging Diagnosis of EH

Belal and Antunez[6] found an incidence of EH in 9% of 703 temporal bones, including normal ears and ears with various pathologies. By histopathology, Rauch et al[7] and Merchant et al[8] found EH in 5% and 26% of temporal bones in patients without previous symptoms of MD. The latter figure corresponds to an

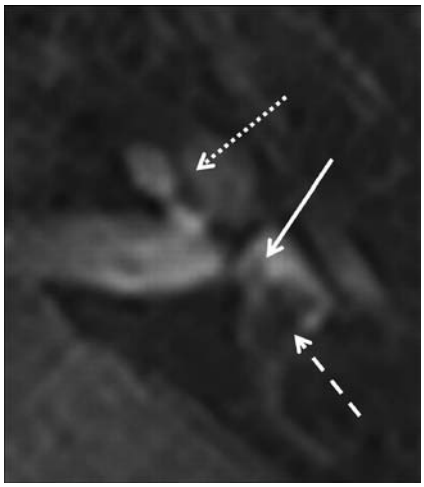

FIG 5. Predominant utricular dilation: 3D-IR sequence left side. Marked distention of the utricle (*dashed arrow*) and sparing of the normal-sized saccule (*arrow*) leave the perilymphatic space visible (grade I) with no cochlear hydrops. The interscalar septum (*dotted arrow*) should not be mistaken for a slight cochlear hydrops.

incidence of 22% in clinically "silent" ears in our series.

EH was found on the clinically affected side in 55/61 ears (90%). Histopathologically, Fraysse et al[12] described similar results in 93% of 21 affected ears.

The detection rate was 73% in ears with clinically possible MD (Fig 3), 100% in probable, and 95% in ears with definite MD in our series. The severity of hydrops was significantly more pronounced for 55 clinically affected ears, with an average grade of 1.27 ± 0.66 in comparison with an average grade of 0.65 ± 0.581 for 10 clinically normal sides. Accordingly, Sperling et al[33] found a tendency for more severe EH to occur in symptomatic cases and comparatively less EH in asymptomatic cases.

CONCLUSIONS

In patients with MD, a dedicated MR imaging protocol depicts cochlear and vestibular EH in vivo. In accordance with histopathologic data, 10% of patients did not have EH in the affected ear, while EH may be present in clinically silent ears of patients with MD. A high interobserver agreement on detecting and grading EH suggests that this MR imaging grading method is robust.

ACKNOWLEDGMENTS

The authors thank Irini Paschalis, Laura Kopácsi, Andreas Schiller, Kathleen Sullivan, and Stefanie Schuknecht for their support of this work.

Disclosures: Bernhard Schuknecht—*UNRELATED*: *Consultancy*: Antisense Pharmaceutical Company (Regensburg, Germany), *Comments*: TNF β treatment in gliomas. Stefan C.A. Hegemann—*UNRELATED*: *Expert Testimony*: SUVA, *Payment for Lectures (including service on Speakers Bureaus)*: As a lecturer at Zurich University, I get a small amount of money for my lectures and student courses. It has absolutely nothing to do with the submitted study, *Patents (planned, pending or issued)*: I have a patent pending (PCT/EP2013/052595), which also does not concern this study, and I still do not receive any money from it but, hopefully, will eventually, *Payment for Development of Educational Presentation and Travel/Accommodations/Meeting Expenses Unrelated to Activities Listed*: I sometimes give talks at conferences or courses that are supported by industrial sponsors, who also paid me some money (for my talk as well as traveling and accommodation). One sponsor I remember is Interacoustics (Drejervaenget 8, Assens, 5610. Denmark, www.interacoustics.com).

REFERENCES

1. Committee on Hearing and Equilibrium. **Meniere's disease: criteria for diagnosis and evaluation of therapy for reporting.** *AAO-HNS Bulletin* 1985;5:6–7
2. **Committee on Hearing and Equilibrium guidelines for the diagnosis and evaluation of therapy in Menière's disease: American Academy of Otolaryngology-Head and Neck Foundation, Inc.** *Otolaryngol Head Neck Surg* 1995;113:181–85
3. Greco A, Gallo A, Fusconi M, et al. **Meniere's disease might be an autoimmune condition?** *Autoimmun Rev* 2012;11:731–38
4. Lawrence M, McCabe BF. **Inner-ear mechanics and deafness: special consideration of Meniere's syndrome.** *J Am Med Assoc* 1959;171:1927–32
5. Gates P. **Hypothesis: could Meniere's disease be a channelopathy?** *Intern Med J* 2005;35:488–89
6. Belal A Jr, Antunez JC. **Pathology of endolymphatic hydrops.** *J Laryngol Otol* 1980;94:1231–40
7. Rauch SD, Merchant SN, Thedinger BA. **Meniere's syndrome and endolymphatic hydrops: double-blind temporal bone study.** *Ann Otol Rhinol Laryngol* 1989;98:873–83
8. Merchant SN, Adams JC, Nadol JB Jr. **Pathophysiology of Meniere's syndrome: are symptoms caused by endolymphatic hydrops?** *Otol Neurotol* 2005;26:74–81
9. Berggren S. **Histological investigation of three cases with Menière's syndrome.** *Arch Otolaryngol* 1949;37:30
10. Arnvig J. **Histological findings in a case of Menière's disease, with remarks on the pathologic-anatomical basis of this lesion.** *Acta Otolaryngol* 1947;35:453–66
11. Belal A Jr, Ylikoski J. **Pathologic significance of Meniere's symptom complex: a histopathologic and electron microscopic study.** *Am J Otolaryngol* 1980;1:275–84
12. Fraysse BG, Alonso A, House WF. **Menière's disease and endolymphatic hydrops: clinical-histopathological correlations.** *Ann Otol Rhinol Laryngol Suppl* 1980;89(6 pt 3):2–22
13. Naganawa S, Ishihara S, Iwano S, et al. **Three-dimensional (3D) visualization of endolymphatic hydrops after intratympanic injection of Gd-DTPA: optimization of a 3D-real inversion-recovery turbo spin-echo (TSE) sequence and application of a 32-channel head coil at 3T.** *J Magn Reson Imaging* 2010;31:210–14
14. Schuknecht HF. *Pathology of the Ear.* Cambridge, Massachusetts; Harvard University Press; 1974:88
15. Niyazov DM, Andrews JC, Strelioff D, et al. **Diagnosis of endolymphatic hydrops in vivo with magnetic resonance imaging.** *Otol Neurotol* 2001;22:813–17
16. Nakashima T, Naganawa S, Sugiura M, et al. **Visualization of endolymphatic hydrops in patients with Meniere's disease.** *Laryngoscope* 2007;117:415–20
17. Naganawa S, Yamazaki M, Kawai H, et al. **Visualization of endolymphatic hydrops in Menière's disease with single-dose intravenous gadolinium-based contrast media using heavily T(2)-weighted 3D-FLAIR.** *Magn Reson Med Sci* 2010;9:237–42
18. Tagaya M, Teranishi M, Naganawa S, et al. **3 Tesla magnetic resonance imaging obtained 4 hours after intravenous gadolinium injection in patients with sudden deafness.** *Acta Otolaryngol* 2010;130:665–69
19. Naganawa S, Yamazaki M, Kawai H, et al. **Imaging of Menière's disease after intravenous administration of single-dose gadodiamide: utility of subtraction images with different inversion time.** *Magn Reson Med Sci* 2012;11:213–19
20. Suzuki H, Teranishi M, Sone M, et al. **Contrast enhancement of the inner ear after intravenous administration of a standard or double dose of gadolinium contrast agents.** *Acta Otolaryngol* 2011;131:1025–31
21. Sano R, Teranishi M, Yamazaki M, et al. **Contrast enhancement of the inner ear in magnetic resonance images taken at 10 minutes or 4 hours after intravenous gadolinium injection.** *Acta Otolaryngol* 2012;132:241–46
22. Fukuoka H, Tsukada K, Miyagawa M, et al. **Semi-quantitative eval-**

uation of endolymphatic hydrops by bilateral intratympanic gadolinium-based contrast agent (GBCA) administration with MRI for Meniere's disease. *Acta Otolaryngol* 2010;130:10–16
23. Naganawa S, Sugiura M, Kawamura M, et al. **Imaging of endolymphatic and perilymphatic fluid at 3T after intratympanic administration of gadolinium-diethylene-triamine pentaacetic acid.** *AJNR Am J Neuroradiol* 2008;29:724–26
24. Tagaya M, Yamazaki M, Teranishi M, et al. **Endolymphatic hydrops and blood-labyrinth barrier in Menière's disease.** *Acta Otolaryngol* 2011;131:474–79
25. Carfrae MJ, Holtzman A, Eames F, et al. **3 Tesla delayed contrast magnetic resonance imaging evaluation of Menière's disease.** *Laryngoscope* 2008;118:501–05
26. Fiorino F, Pizzini FB, Beltramello A, et al. **Reliability of magnetic resonance imaging performed after intratympanic administration of gadolinium in the identification of endolymphatic hydrops in patients with Menière's disease.** *Otol Neurotol* 2011;32:472–77
27. Silverstein H, Rowan PT, Olds MJ, et at. **Inner ear perfusion and the role of round window patency.** *Am J Otol* 1997;18:586–89
28. Yamazaki M, Naganawa S, Tagaya M, et al. **Comparison of contrast effect on the cochlear perilymph after intratympanic and intravenous gadolinium injection.** *AJNR Am J Neuroradiol* 2012;33:773–78
29. Hallpike CS, Cairns H. **Observations on the pathology of Menière's syndrome.** *Proc R Soc Med* 1938;31:1317–36
30. Werner CF. *Das Gehörorgan der Wirbeltiere und des Menschen. Beispiel für eine vergleichende Morphologie der Lagebeziehungen.* Leipzig, Germany: Veb Georg Thieme; 1960:77–80
31. Yamashita T, Schuknecht HF. **Apical endolymphatic hydrops.** *Arch Otolaryngol* 1982;108:463–66
32. Liu F, Huang W, Meng X, et al. **Comparison of noninvasive evaluation of endolymphatic hydrops in Meniere's disease and endolymphatic space in healthy volunteers using magnetic resonance imaging.** *Acta Otolaryngol* 2012;132:234–40
33. Sperling NM, Paparella MM, Yoon TH, et al. **Symptomatic versus asymptomatic endolymphatic hydrops: a histopathologic comparison: review.** *Laryngoscope* 1993;103:277–85
34. Nakashima T, Naganawa S, Pyykko I, et al. **Grading of endolymphatic hydrops using magnetic resonance imaging.** *Acta Otolaryngol Suppl* 2009;560:5–8

Immunoglobulin G4–Related Disease of the Orbit: Imaging Features in 27 Patients

C.A. Tiegs-Heiden, L.J. Eckel, C.H. Hunt, F.E. Diehn, K.M. Schwartz, D.F. Kallmes, D.R. Salomão, T.E. Witzig, and J.A. Garrity

ABSTRACT

BACKGROUND AND PURPOSE: Immunoglobulin G4–related disease is a systemic fibroinflammatory process of unknown etiology, characterized by tissue infiltration by immunoglobulin G4 plasma cells. The purpose of this study was to retrospectively identify the spectrum of imaging features seen in immunoglobulin G4–related disease of the orbit.

MATERIALS AND METHODS: This study included 27 patients with biopsy-proved immunoglobulin G4–related disease of the orbit and either a CT or MR imaging of the orbits. These CT or MR imaging examinations were evaluated for the following: extraocular muscle size, extraocular muscle tendon enlargement, lacrimal gland enlargement, infiltrative process in the orbital fat (increased attenuation on CT or abnormal signal on MR imaging), infraorbital nerve enlargement, mucosal thickening in the paranasal sinuses, and extension of orbital findings intracranially.

RESULTS: Extraocular muscles were enlarged in 24 of 27 (89%) patients, 21 (88%) bilaterally. In 32 of 45 (71%) affected orbits, the lateral rectus was the most enlarged muscle. In 26 (96%) patients, the tendons of the extraocular muscles were spared. Nineteen (70%) patients had lacrimal gland enlargement. Twelve (44%) patients had an infiltrative process within the orbital fat. Infraorbital nerve enlargement was seen in 8 (30%) patients. Twenty-four (89%) patients had sinus disease. Cavernous sinus or Meckel cave extension was seen in 3 (11%) patients.

CONCLUSIONS: In patients with extraocular muscle enlargement, particularly when the tendons are spared and the lateral rectus is the most enlarged, and even more so when other noted findings are present, immunoglobulin G4–related disease should be a leading differential consideration, even over more commonly known etiologies of extraocular muscle enlargement.

ABBREVIATIONS: IgG4 = immunoglobulin G4

Immunoglobulin G4 (IgG4)-related disease is a systemic inflammatory process of unknown etiology, characterized by tissue infiltration by IgG4 plasma cells and sclerosing inflammation.[1-5] Although initially described in association with autoimmune pancreatitis, manifestations of IgG4-related disease are now reported in nearly every organ system.[1-3,5-10]

Multiple case reports and small case series of orbital manifestations of IgG4-related disease have noted involvement of the extraocular muscles, lacrimal glands, and infraorbital nerve,[1,2,4,7-19] but these small series do not allow evaluation of the typical patterns of imaging findings in IgG4-related disease. The purpose of this study was to retrospectively identify the spectrum of imaging features seen in IgG4-related disease of the orbit. Ideally, these characteristics will help clinicians and radiologists recognize IgG4-related orbital disease among a broad differential of orbital pathologies.

MATERIALS AND METHODS

Institutional review board approval was obtained for this Health Insurance Portability and Accountability Act–compliant retrospective research protocol, and the requirement for informed patient consent was waived. A pre-existing ophthalmology data base of all patients seen at our institution with biopsy-proved IgG4-related disease of the orbit was reviewed. Patients were seen in our Ophthalmology Department between January 1998 and April 2012. All patients in this data base who had undergone CT and/or MR imaging that included the orbits were included in this study. There were no exclusion criteria aside from lack of CT and/or MR

Received September 9, 2013; accepted after revision November 22.

From the Departments of Radiology (C.A.T.-H., L.J.E., C.H.H., F.E.D., K.M.S., D.F.K.), Pathology (D.R.S.), Hematology (T.E.W.), and Ophthalmology (D.R.S., J.A.G.), Mayo Clinic, Rochester, Minnesota.

Paper previously presented at: Annual Meeting of the American Society of Head and Neck Radiology, October 3–7, 2012; Miami Beach, Florida.

Please address correspondence to Laurence J. Eckel, MD, Department of Radiology, Mayo Clinic, 200 1st St SW, Rochester, Minnesota, 55905; e-mail: eckel.laurence@mayo.edu.

http://dx.doi.org/10.3174/ajnr.A3865

Summary of extraocular muscle findings

	Lateral Rectus	Inferior Rectus	Medial Rectus	Superior Rectus	Inferior Oblique	Superior Oblique
Average maximum diameter (mm)[a]	11.7	11.7	10.5	10.0	10.6	6.4
Average short-axis diameter (mm)[a]	6.4	6.4	5.2	5.5	3.0	3.3
Frequency of enlargement[b]	41 (76%)	19 (35%)	16 (30%)	11 (20%)	N/A	6 (11%)
Frequency of most enlarged[c]	32 (71%)	9 (20%)	3 (7%)	1 (2%)	N/A	0 (0%)

[a] Average diameters are based on measurements from all orbits ($n = 54$).
[b] Frequency of enlargement was determined by the number of times a muscle was enlarged of a possible 54 orbits.
[c] Frequency of most enlarged muscle was determined by the number of times a muscle was the most enlarged muscle in an eye of 45 affected orbits.

imaging. Twenty-seven patients were identified for inclusion in this study. There were 17 (63%) female patients. Mean age at the time of the initial imaging examination was 51 years (range, 30–71 years).

Orbital biopsies were performed at our or, less commonly, an outside institution between December 1997 and April 2012. All pathology was reviewed at our institution. Biopsies were performed of the lacrimal gland, extraocular muscle, orbital soft-tissue infiltrate, and/or infraorbital nerve. Similar to the report of Plaza et al,[7] diagnosis of IgG4 disease was made on the basis of the number of immunohistochemically identified IgG4-positive plasma cells per high-power field. For each specimen, 3 high-power fields with the highest attenuation of IgG4-positive plasma cells were selected, and an average number of IgG4-positive plasma cells per high-power field were calculated. Eleven or more IgG4 cells per high-power field were necessary to make the diagnosis of IgG4-related disease.

CT or MR imaging scans were obtained from January 1998 to December 2011. Twenty-two (81%) patients had CT as their initial imaging examination; 5 (19%) patients had MR imaging. CT scans were either contrast-enhanced (12, 55%) or unenhanced (10, 45%). Section thickness of the CT scans ranged from 1.25 to 5 mm, with most CT scans having a section thickness of 2–3 mm (17, 77%). All 5 of the MR imaging examinations were performed with and without IV gadolinium. Section thickness of the MR imaging scans ranged from 3 to 5 mm. Twenty-two (81%) patients had their first CT or MR imaging before their biopsy. The time between the first CT or MR imaging and biopsy was <1 month in 16 patients (59%), 1–2 months in 4 (15%), 2 months to 1 year in 2 (7%), 1–2 years in 3 patients (11%), and >2 years apart in 2 patients (7%).

For each patient, if more than 1 study was available, the earliest CT or MR imaging was evaluated by 2 neuroradiologists (12 and 8 years of imaging experience) and 1 Postgraduate Year 3 radiology resident in consensus. From the coronal imaging plane, each extraocular muscle was measured in 2 dimensions (millimeters): maximum diameter and maximum short axis. Short-axis extraocular muscle measurements were compared with normal values as described by Ozgen and Ariyurek[20] and Ozgen and Aydingöz.[21] Upper limits of normal used for each muscle were as follows: medial rectus, 5.0 mm; lateral rectus, 4.8 mm; inferior rectus, 6.5 mm; superior rectus, 6.1 mm; and superior oblique, 4.1 mm.[20,21] This reference does not provide a normal size for the inferior oblique muscle; however, this muscle was measured in a similar fashion. In addition, the examinations were subjectively evaluated for the presence or absence of extraocular muscle tendon involvement and lacrimal gland enlargement (including whether these distorted the globe or caused bony changes), the presence of an infiltrative process in the orbital fat (defined as increased attenuation on CT or abnormal signal on MR imaging in the intraconal or extraconal fat), the presence of infraorbital nerve enlargement (defined as enlargement of the infraorbital canal by CT and enlargement of the nerve by MR imaging), intracranial involvement (defined as a soft-tissue mass extending intracranially from the orbit), and incidental sinus disease (defined as fluid and/or mucosal thickening in any of the paranasal sinuses). Clinical and laboratory data, including age, sex, steroid use, serum IgG4 level (at our institution a normal IgG4 level is 2.4–121.0 mg/dL), clinical symptoms, duration of symptoms until the first imaging study, and any other areas of known disease involvement (both within and outside the head and neck), were identified by review of the electronic medical record.

RESULTS

Clinical Data

The most frequent presenting symptom was proptosis and/or periorbital swelling (26, 96%). Pain or discomfort was reported in 2 (7%) patients. Information regarding the duration of orbital symptoms was available by chart review in 24 (89%) patients. The duration of symptoms ranged from 0.5 to 228.0 months (average, 44.9 months). Four (15%) patients were taking oral steroids at the time of their initial imaging examination.

Seventeen (63%) patients had serum IgG4 levels measured during the course of their care, some on multiple occasions. Eight of 17 (47%) patients had an elevated serum IgG4 level recorded during this time. When we used only the earliest IgG4 level recorded, the average IgG4 level was 363 mg/dL, with a range from 13.3 to 3150 mg/dL. On the basis of this first available serum IgG4 level, 6 (35%) patients had elevated values and 11 (65%) had normal values. Serum IgG4 levels were not necessarily obtained at the time of either the initial diagnosis or initial imaging, however; in many cases, the first serum IgG4 level was not obtained until months or years after the diagnosis had been made, when the patient was already being treated.

Extraocular Muscle Involvement

The average maximal and the average short-axis diameters of each extraocular muscle (considering all 54 orbits) are shown in the Table. On the basis of an individual comparison of short-axis measurements with the aforementioned normal measurements, 24 of 27 (89%) patients and 45 of 54 (83%) orbits displayed extraocular muscle enlargement. Twenty-one of 24 (88%) patients with extraocular muscle involvement demonstrated bilateral enlargement. Examples of unilateral and bilateral extraocular muscle enlargement are shown in Fig 1. The tendons of the extraocular muscles were spared in 26 (96%) patients.

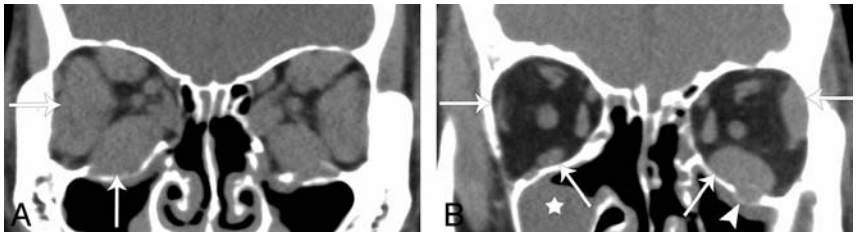

FIG 1. Noncontrast CT findings of IgG4-related ophthalmic disease. *A*, Bilaterally symmetric extraocular muscle enlargement in a 39-year-old man (*arrows*). Note that the lateral rectus is the most enlarged extraocular muscle bilaterally. *B*, Asymmetric left-more-than-right extraocular muscle enlargement in a 67-year-old man (*arrows*). Sinus disease (*star*) and infraorbital nerve enlargement (*arrowhead*) are also evident in this patient.

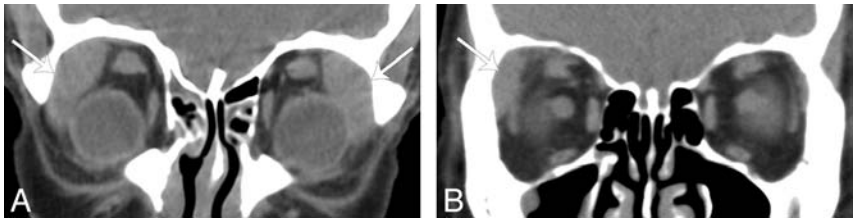

FIG 2. Lacrimal gland involvement in IgG4-related ophthalmic disease. *A*, Bilateral lacrimal gland enlargement in a 63-year-old woman (*arrows*). *B*, Unilateral lacrimal gland enlargement in a 59-year-old woman (*arrow*). This patient did not have extraocular muscle enlargement.

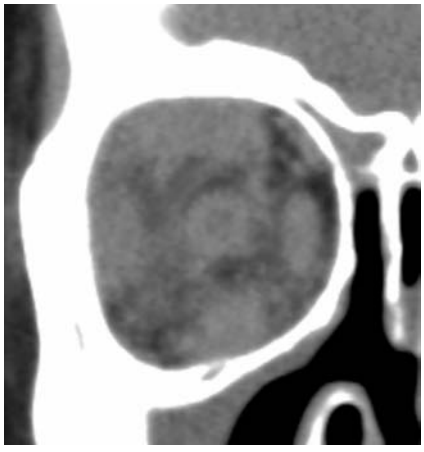

FIG 3. Infiltrative orbital process in a 42-year-old woman with IgG4-related ophthalmic disease.

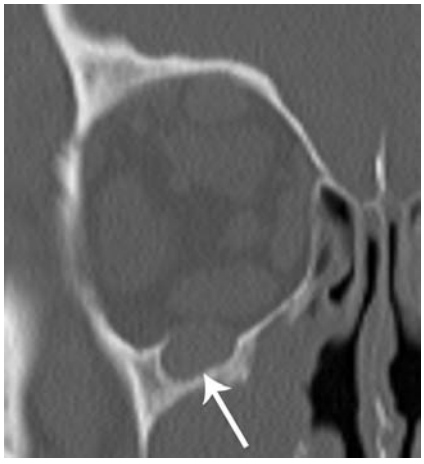

FIG 4. Infraorbital nerve enlargement in a 54-year-old man with IgG4-related ophthalmic disease (*arrow*).

The Table also lists how often each extraocular muscle was enlarged compared with normal values, as well as the frequency of each extraocular muscle being the most enlarged muscle on a per-orbit basis. The lateral rectus was enlarged most commonly, in 41 of 54 (76%) orbits. The lateral rectus was also most frequently the largest muscle in 32 of 45 (71%) orbits that had extraocular muscle enlargement.

Additional Imaging Features

Nineteen (70%) patients had lacrimal gland enlargement, 11 (58%) of whom had bilateral involvement. Examples of unilateral and bilateral lacrimal gland enlargement are shown in Fig 2. In all cases, lacrimal gland enlargement did not distort the globe, and there were no adjacent bony changes. Sixteen (60%) patients had both extraocular muscle enlargement and lacrimal gland enlargement. All 3 patients who did not have extraocular muscle enlargement demonstrated lacrimal gland involvement, 1 bilaterally and 2 with unilateral involvement.

Twelve (44%) patients were characterized as having an infiltrative process within the orbital fat (Fig 3). Eight (30%) patients had infraorbital nerve enlargement (Figs 1*B* and 4), 5 (63%) of which were bilateral. Three (11%) patients had intracranial IgG4 involvement, 1 bilateral and 2 unilateral (Fig 5). Both patients with unilateral involvement had unilateral soft-tissue masses within the cavernous sinus. The patient with bilateral involvement had soft-tissue masses within the cavernous sinuses and anterior Meckel cave. Fifteen (63%) patients had documented IgG4-related lesions outside the orbit, 11 (73%) of which were outside the head and neck. Other areas of involvement documented in the electronic medical record included lymph nodes (cervical, thoracic, and abdominal), parotid glands, autoimmune pancreatitis, and hepatic pseudotumor. Paranasal sinus mucosal thickening was seen in 24 (89%) patients, as demonstrated in Fig 1.

DISCUSSION

On the basis of this study of the imaging of 27 patients, typical imaging findings of IgG4-related disease of the orbit are evident. The most common orbital imaging finding in our patient population was extraocular muscle enlargement. The lateral rectus was the most commonly enlarged muscle and was typically enlarged to the greatest degree. Lacrimal gland enlargement was also a very common finding. Intraorbital inflammatory change, infraorbital nerve enlargement, and sinus disease are supportive findings in IgG4-related disease. While uncommon, a soft-tissue mass extending from the posterior orbit into the cavernous sinus and/or Meckel cave may also be noted. The combination of any primary (extraocular muscle enlargement or lacrimal gland enlargement)

and any of these other supportive findings is very suggestive of IgG4 disease (Fig 6).

The inflammatory mucosal thickening noted in the paranasal sinuses is an unknown association with IgG4-related disease of the orbit. Given that it was noted in 89% of our patients versus a prevalence of approximately 40% in the general population,[22] perhaps it reflects another manifestation of altered immune modulation in those patients with IgG4-related disease. As such, its presence may offer an additional clue when considering IgG4 of the orbit versus other etiologies.

The extraocular muscle enlargement seen in many patients in this series could be misinterpreted as being secondary to Graves ophthalmopathy. A useful distinguishing feature between these 2 entities is the pattern of extraocular muscle involvement. Graves ophthalmopathy tends to spare the lateral rectus until late in the disease course.[23,24] By contrast, in our study, the lateral rectus is the most commonly and most dramatically involved in IgG4-related disease. Additionally, findings of sinus disease and infraorbital nerve enlargement are also not usual features of Graves ophthalmopathy.[23]

Idiopathic inflammatory orbital pseudotumor could also be included in the differential diagnosis of IgG4-related disease of the orbit. Orbital pseudotumor can present with dacryoadenitis, myositis, apical, anterior, or diffuse disease.[25] Whereas IgG4 typically spares the tendinous insertions of the extraocular muscles, orbital myositis characteristically causes enlargement of the entire muscle, including the tendon.[25] Again, the pattern of extraocular muscle enlargement is an important differentiating feature. Orbital myositis most frequently affects the medial rectus, followed by the superior rectus and lateral rectus,[25] and is most often unilateral.[25] In contrast, IgG4 favors the lateral rectus and is most commonly bilateral. Unlike IgG4-related disease of the orbit, patients with orbital pseudotumor classically present with orbital pain.[25]

This case series is, to our knowledge, the largest to describe the pattern of imaging findings seen in IgG4-related disease of the orbit. A recent series of 9 cases also identified lacrimal gland enlargement, extraocular muscle thickening, orbital fat involvement, and perineural involvement as imaging features of IgG4-related disease.[19] While this series found all cases of extraocular muscle thickening to be unilateral, cases in our series were more often bilateral.[19] Several previous publications regarding IgG4-related disease of the head and neck have focused their attention within the orbit on lacrimal gland enlargement.[4,7,17,18] Although lacrimal gland enlargement was com-

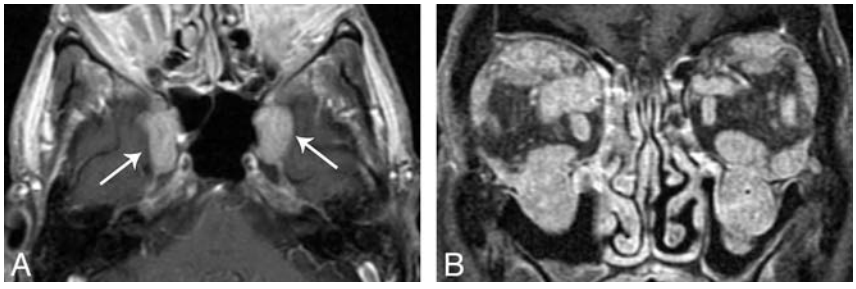

FIG 5. Intracranial disease in IgG4-related ophthalmic disease. *A*, Axial T1 postcontrast image in a 70-year-old man demonstrates enhancing soft-tissue masses extending bilaterally through the cavernous sinus to the anterior Meckel caves (*arrows*). *B*, Coronal T1 postcontrast image in the same patient demonstrates extraocular muscle enlargement, infraorbital nerve enlargement, and sinus disease.

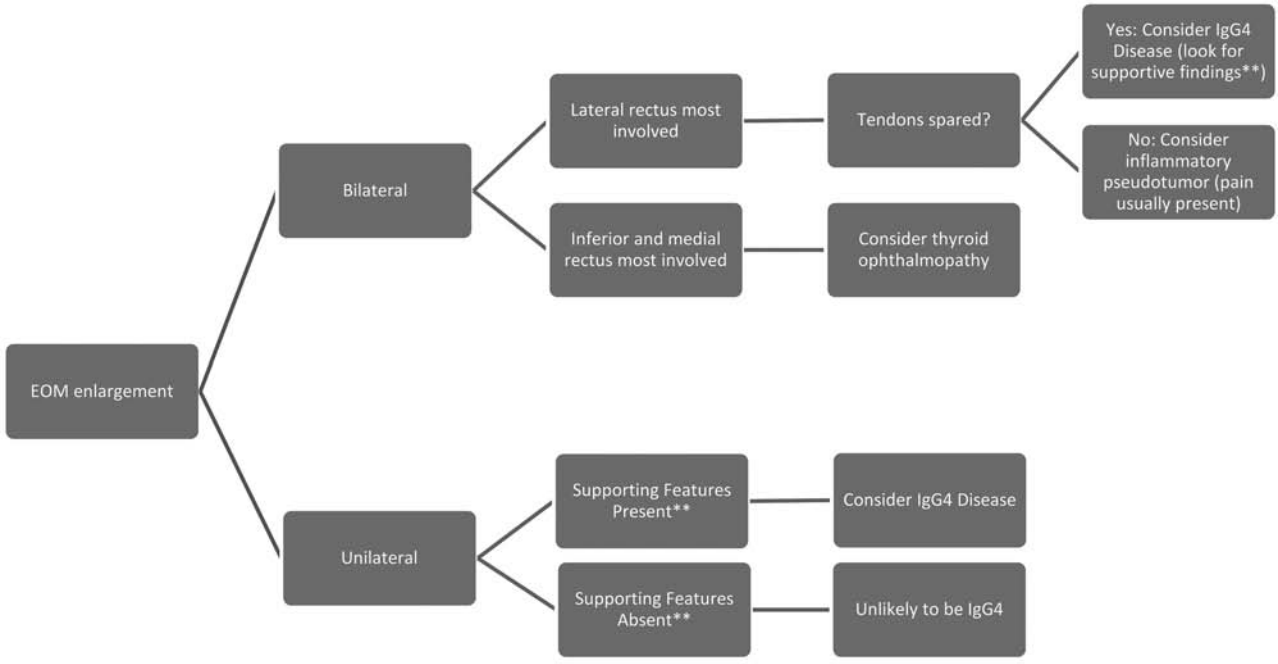

FIG 6. Decision tree for the differential diagnosis of extraocular muscle enlargement.

mon in this case series, extraocular muscle enlargement was the most common finding. Several authors have also reported the presence of perineural spread of IgG4-related disease, with expansion of the associated neural foramina.[4,8,9,17,18]

Limitations of our study include its retrospective nature. Additionally, the imaging-acquisition parameters were not consistent among all patients. The study used 2 different modalities, CT and MR imaging, because the initial examination technique differed among patients. Some scans were not dedicated orbital studies but were performed to assess the sinuses or entire head. This difference could potentially decrease the sensitivity of detection for some of the findings that were assessed.

Future research could include evaluation of imaging findings more closely coordinated to the date of systemic IgG4-level acquisition. We did not identify any published literature regarding serum IgG4 in relation to orbital manifestations. Additionally, further research to investigate changes in orbital imaging features with time would be helpful to document the suspected duration, natural course of presentation and suspected progression, and response to treatment.

CONCLUSIONS

In patients with proptosis or periorbital swelling who undergo CT or MR imaging, IgG4-related orbital disease can be strongly suspected when certain imaging features are also present. When extraocular muscle or lacrimal gland enlargement is noted, particularly when the lateral rectus is the most involved muscle, IgG4 should be a differential consideration. In these cases, if orbital inflammatory change, infraorbital nerve enlargement, or incidental sinus mucosal thickening, or all of these are also noted, IgG4-related orbital disease should be a leading consideration over other more commonly known etiologies of extraocular muscle and lacrimal gland enlargement.

Disclosures: David F. Kallmes—*UNRELATED*: *Consultancy*: ev3,* Codman,* Medtronic,* *Comments*: planning and implementing clinical trials, *Grants/Grants Pending*: MicroVention,* Codman,* ev3,* NeuroSigma,* Sequent Medical,* Benvenue Medical,* *Comments*: preclinical and clinical research, *Royalties*: University of Virginia Patent Foundation, *Comments*: Spine Fusion. *Money paid to the institution.

REFERENCES

1. Cheuk W, Chan JK. **IgG4-related sclerosing disease: a critical appraisal of an evolving clinicopathologic entity.** *Adv Anat Pathol* 2010;17:303–32
2. Wallace ZS, Khosroshahi A, Jakobiec FA, et al. **IgG4-related systemic disease as a cause of "idiopathic" orbital inflammation, including orbital myositis, and trigeminal nerve involvement.** *Surv Ophthalmol* 2012;57:26–33
3. Umehara H, Okazaki K, Masaki Y, et al. **Comprehensive diagnostic criteria for IgG4-related disease (IgG4-RD), 2011.** *Mod Rheumatol* 2012;22:21–30
4. Katsura M, Mori H, Kunimatsu A, et al. **Radiological features of IgG4-related disease in the head, neck, and brain.** *Neuroradiology* 2012;54:873–82
5. Zen Y, Nakanuma Y. **IgG4-related disease: a cross-sectional study of 114 cases.** *Am J Surg Pathol* 2010;34:1812–19
6. Fujinaga Y, Kadoya M, Hamano H, et al. **Radiologic findings of IgG4-related disease.** *Curr Immunol Rev* 2011;7:186–203
7. Plaza JA, Garrity JA, Dogan A, et al. **Orbital inflammation with IgG4-positive plasma cells: manifestation of IgG4 systemic disease.** *Arch Ophthalmol* 2011;129:421–28
8. Watanabe T, Fujinaga Y, Kawakami S, et al. **Infraorbital nerve swelling associated with autoimmune pancreatitis.** *Jpn J Radiol* 2011; 29:194–201
9. Inoue D, Zen Y, Sato Y, et al. **IgG4-related perineural disease.** *Int J Rheumatol* 2012;2012:401890
10. Masaki Y, Dong L, Kurose N, et al. **Proposal for a new clinical entity, IgG4-positive multiorgan lymphoproliferative syndrome: analysis of 64 cases of IgG4-related disorders.** *Ann Rheuma Dis* 2009;68: 1310–15
11. Katsura M, Morita A, Horiuchi H, et al. **IgG4-related inflammatory pseudotumor of the trigeminal nerve: another component of IgG4-related sclerosing disease?** *AJNR Am J Neuroradiol* 2011;32:E150–52
12. Kubota T, Moritani S, Katayama M, et al. **Ocular adnexal IgG4-related lymphoplasmacytic infiltrative disorder.** *Arch Ophthalmol* 2010;128:577–84
13. Takahira M, Ozawa Y, Kawano M, et al. **Clinical aspects of IgG4-related .orbital inflammation in a case series of ocular adnexal lymphoproliferative disorders.** *Int J Rheumatol* 2012;2012:635473
14. Cheuk W, Yuen HKL, Chan JKC. **Chronic sclerosing dacryoadenitis: part of the spectrum of IgG4-related sclerosing disease?** *Am J Surg Pathol* 2007;31:643–45
15. Higashiyama T, Nishida Y, Ugi S, et al. **A case of extraocular muscle swelling due to IgG4-related sclerosing disease.** *Jpn J Ophthalmol* 2011;55:315–17
16. Fonte R, Pirali B, Caramia V, et al. **Graves'-like orbitopathy in a patient with chronic autoimmune pancreatitis.** *Thyroid* 2011; 21:1389–92
17. Toyoda K, Oba H, Kutomi K, et al. **MR imaging of IgG4-related disease in the head and neck and brain.** *AJNR Am J Neuroradiol* 2012;33:2136–39
18. Fujita A, Sakai O, Chapman M, et al. **IgG4-related disease of the head and neck: CT and MR imaging manifestations.** *Radiographics* 2012;32:1945–58
19. Ginat DT, Freitag SK, Kieff D, et al. **Radiographic patterns of orbital involvement in IgG4-related disease.** *Ophthal Plast Reconstr Surg* 2013;29:261–66
20. Ozgen A, Ariyurek M. **Normative measurements of orbital structures using CT.** *AJR Am J Roentgenol* 1998;170:1093–96
21. Ozgen A, Aydingöz U. **Normative measurements of orbital structures using MRI.** *J Comput Assist Tomogr* 2000;24:493–96
22. Havas TE, Motbey JA, Gullane PJ. **Prevalence of incidental abnormalities on computed tomographic scans of the paranasal sinuses.** *Arch Otolaryngol Head Neck Surg* 1988;114:856–59
23. Kahaly GJ. **Imaging in thyroid-associated orbitopathy.** *Eur J Endocrinol* 2001;145:107–18
24. Kirsch E, Hammer B, von Arx G. **Graves' orbitopathy: current imaging procedures.** *Swiss Med Wkly* 2009;139:618–23
25. Ding ZX, Lip G, Chong V. **Idiopathic orbital pseudotumour.** *Clin Radiol* 2011;66:886–92

Role of Mastoid Pneumatization in Temporal Bone Fractures

A. Ilea, A. Butnaru, S.A. Sfrângeu, M. Hedeşiu, C.M. Dudescu, P. Berce, H. Chezan, L. Hurubeanu, V.E. Trombiţaş, R.S. Câmpian, and S. Albu

ABSTRACT

BACKGROUND AND PURPOSE: The mastoid portion of the temporal bone has multiple functional roles in the organism, including regulation of pressure in the middle ear and protection of the inner ear. We investigated whether mastoid pneumatization plays a role in the protection of vital structures in the temporal bone during direct lateral trauma.

MATERIAL AND METHODS: The study was performed on 20 human temporal bones isolated from cadavers. In the study group formed by 10 temporal bone samples, mastoid cells were removed and the resulting neocavities were filled. The mastoids were maintained intact in the control group. All samples were impacted at the same speed and kinetic energy. The resultant temporal bone fractures were evaluated by CT.

RESULTS: Temporal squama fractures were 2.88 times more frequent, and mastoid fractures were 2.76 times more frequent in the study group. Facial nerve canal fractures were 6 times more frequent in the study group and involved all the segments of the facial nerve. Carotid canal fractures and jugular foramen fractures were 2.33 and 2.5 times, respectively, more frequent in the study group.

CONCLUSIONS: The mastoid portion of the temporal bone plays a role in the absorption and dispersion of kinetic energy during direct lateral trauma to the temporal bone, reducing the incidence of fracture in the setting of direct trauma.

The mastoid portion of the temporal bone has a pneumatic structure similar to that of the paranasal sinuses. While pneumatized paranasal structures have developed phylogenetically because of multiple functional needs,[1] however, the functional roles of the mastoid are discussed less in the literature. Hill and Richtsmeier[2] designated pneumatic cells in the temporal bone as enigmatic structures. They showed that temporal bone pneumatization has diminished during the evolution of the human species, but little is known about the cause or effect of this process.[2] Mastoid cells are completely formed around 10 years of age and reach maturity between 15 and 20 years of age.[3,4] In the adult, there are no differences in the size of the mastoid between men and women.[5] Also, Han et al[6] found no statistically significant differences in mastoid pneumatization between the right and left side. The size of mastoid cells is not only determined genetically, but environmental factors are also involved. The volume of mastoid cells depends on the degree of impairment of the middle ear during childhood, such as recurrent acute otitis media or otitis media with effusion.[7] Turgut and Tos[8] found mastoid length to be significantly shorter in specimens with pathologic eardrum and middle ear adhesions. Pneumatization was also decreased in spec-

Received September 25, 2013; accepted after revision November 25.

From the Faculty of Dental Medicine, Department of Oral Rehabilitation, Oral Health and Dental Office Management (R.S.C., I.A.); Faculty of Medicine, Department of Radiology (A.B., S.A.S.); Faculty of Dental Medicine, Department of Dental Radiology (M.H.); Faculty of Dental Medicine, Department of Cervicofacial and Ear, Nose, and Throat Surgery (S.A., V.E.T.); and Faculty of Dental Medicine, Department of Oral and Maxillofacial Surgery (L.H.), "Iuliu Haţieganu" University of Medicine and Pharmacy Cluj-Napoca, Romania; and Faculty of Machine Building, Department of Manufacturing Engineering (P.B., H.C.) and Faculty of Mechanics, Department of Mechanical Engineering (C.M.D.), Technical University Cluj-Napoca, Romania.

Author Contributions: Aranka Ilea and Radu S. Câmpian: 1) substantial contributions to conception and design, acquisition of data, analysis and interpretation of data, 2) drafting the article and revising it critically for important intellectual content, 3) final approval of the version to be published; Anca Butnaru and Silviu A. Sfrângeu: 1) acquisition of data, analysis and interpretation of data; 2) revising the article critically for important intellectual content; 3) final approval of the version to be published; Mihaela Hedeşiu: 1) acquisition of data, analysis and interpretation of data; 2) revising the article critically for important intellectual content; 3) final approval of the version to be published; Cristian M. Dudescu: 1) substantial contributions to conception and design, acquisition of data, analysis and interpretation of data; 2) revising the article critically for important intellectual content; 3) final approval of the version to be published; Petru Berce and Horea Chezan: 1) acquisition of data; 2) revising the article critically for important intellectual content; 3) final approval of the version to be published; Lucia Hurubeanu: 1) substantial contributions to design; 2) revising the article critically for important intellectual content; 3) final approval of the version to be published; Silviu Albu and Veronica E. Trombiţaş 1) substantial contributions to conception and design, acquisition of data, analysis and interpretation of data; 2) drafting the article and revising it critically for important intellectual content; 3) final approval of the version to be published.

This work was supported by the POSDRU project 88/1.5/S/78702.

Please address correspondence to Aranka Ilea, MD, Victor Babeş, No 15, First Floor, Cluj-Napoca, Romania; e-mail: cseh.aranka@umfcluj.ro

http://dx.doi.org/10.3174/ajnr.A3887

FIG 1. The impacting system.

imens with a short length of the mastoid process. However, it is not clear whether reduced temporal bone pneumatization is the effect of middle ear infections or their cause.

Kellman and Schmidt[1] demonstrated the role of the paranasal sinuses in the protection of the eyeball. They showed that a direct blow on the eyeball causes fracture of the orbit floor, while the eyeball remains intact. In contrast, if the paranasal sinuses are filled with bone cement, direct eye trauma causes rupture of the eyeball, without orbit fractures.[1]

We hypothesize that mastoid pneumatization plays a role similar to that of the paranasal sinuses: to protect vital structures such as the facial nerve, blood vessels, and central nervous tissue, by dissipating energy.

MATERIALS AND METHODS

Study Samples

The study was performed on isolated temporal bones collected from human cadavers. After removal, the temporal bones were treated with formalin for preservation. The study was approved by the Ethics Board of the "Iuliu Haţieganu" University of Medicine and Pharmacy, Cluj-Napoca, No. 250/22. 02. 2011.

The study included 20 temporal bone samples that were randomly assigned to 2 groups. The study group consisted of 10 temporal bone samples (S1–S10) from which mastoid cells were removed by an external approach. The resulting cavity was filled with a mixture of calcium carbonate, white gypsum (semihydrated calcium sulfate), and hydroxyapatite in a proportion of 10:10:1. The other 10 temporal bone samples had their mastoid cells intact and represented the control group (M1–M10).

The Impacting System

Each of the 20 temporal bone samples was fixed on a metal support with an irreversible elastic material (sodium alginate, an irreversible hydrocolloid impression material). All samples were impacted at a mean speed of 3.35 ± 0.013 m/s and a mean kinetic energy of 50.50 ± 0.39 J generated by a rigid arm pendulum (Fig 1). There were no statistically significant differences in the impacting speed or kinetic energy between the 2 groups ($P = .17$). The weight of the impacting pendulum was 9 kg, the radius of the bob was 60 mm, and the length of the pendulum arm was 62 cm.

The impact to the temporal bone samples was performed at the same point on the exocranial surface of the temporal bone, in the region of the junction of the mastoid with the temporal squama, by using laser light guidance (Fig 2 or see impaction at the following link: https://vimeo.com/73047373).

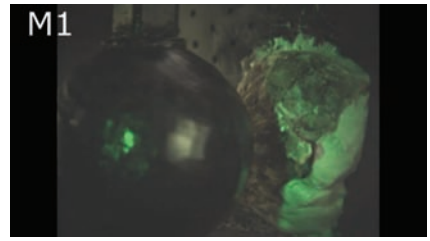

FIG 2. Impaction of sample M1 of the control group.

Imaging Examinations

All temporal bone samples were examined with CT, and images were analyzed by 3 radiologists. For the evaluation of fracture lines, the spiral acquisition mode with 350-mAs values was used (automatic modulation); 120 kV; collimation, 0.65; pitch, 0.8; reconstructed sections, 0.62–0.65 mm, with bone filter, by using a multidetector device with 64 detector rows (Optima CT660 128SL with ASiR; GE Healthcare, Milwaukee, Wisconsin).

CT images were evaluated by axial acquisitions of the impacted samples in the anatomic position of the right temporal bone. Temporal bone fractures were evaluated in the axial plane and in coronal and sagittal multiplanar reconstructions and in a 3D bone reconstruction volume-rendering technique.

Fractures were classified according to the anatomic segment of the temporal bone and the horizontal and vertical planes. The styloid process was not assessed because it was absent in some anatomic samples. Horizontal or transverse fractures were defined in the horizontal plane for the squamous and mastoid parts and as fractures coursing perpendicular to the petrous ridge for the petrous part. Vertical or longitudinal fractures were defined in the vertical plane for squamous and mastoid parts and as fractures running parallel to the petrous ridge for the petrous part. Oblique fractures were defined as fractures crossing the petrotympanic fissure, and coursing between the horizontal and vertical planes for the squamous and mastoid parts. The involvement of vital structures was defined by the presence of fracture lines on at least 1 of the walls surrounding that structure, regardless of the fracture plane. Comminuted fractures had multiple horizontal, longitudinal, and/or transverse components of the same parts of the temporal bone. Temporal bone fractures were defined as petrous fractures when the fracture lines were extending to the otic capsule or/and petrous apex. Nonpetrous fractures were defined as fractures that did not involve the otic capsule or petrous apex.[9]

For evaluation of temporal bone pneumatization, CT was performed in axial sections by using the spiral acquisition mode with values of 350 mAs (automatic modulation), 120 kV, with a 6-mm thickness of acquired and reconstructed sections, pitch of 0.5, by using a 20-row multidetector device, with an inner ear filter.

Temporal bone pneumatization was assessed after impaction. When evaluating the degree of temporal bone pneumatization, we monitored the extension of mastoid cells (in each axial section) in relation to the 3 parallel reference lines of the sigmoid

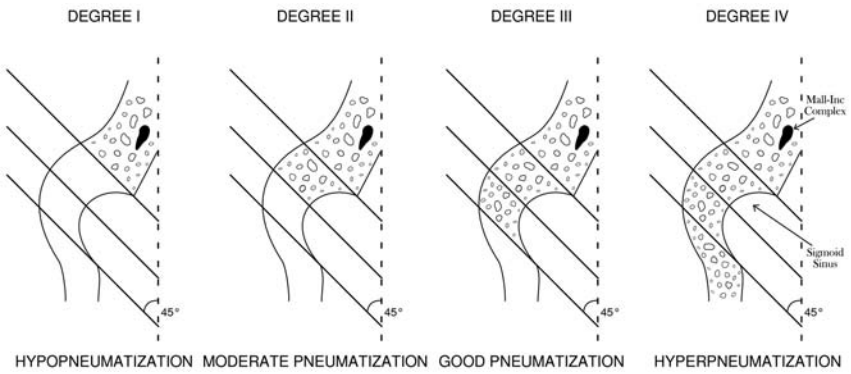

FIG 3. Degrees of mastoid pneumatization according to the descriptions of Han et al.[6]

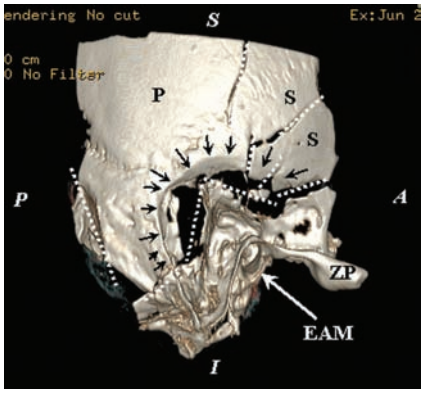

FIG 4. Temporal squama comminuted fracture: 3D reconstruction of the exocranial surface of the right temporal bone of sample S1 with a volume-rendering technique. Comminuted fracture of the mastoid with extension in the petrous bone and important depression. In the center of the image is highlighted the aspect of bone depression (*black arrows*) that keeps the ball contour impaction at the junction with the mastoid and temporal scales; the main fracture lines are marked by dashed white lines. The sample position is indicated by marginal marks with white letters: S indicates superior; I, inferior; A, anterior; and P, posterior; black letter marks: ZP, zygomatic process of the temporal bone; P, parietal portion; S, scaly portion of the temporal bone. EAM, the external acoustic meatus, is indicated by the white arrow.

sinus according to the study performed by Han et al[6]: through the anterior margin, through the maximal concavity opened medially, and through the posterior margin of the sigmoid sulcus. The lines maintained a 45° inclination in relation to the anteroposterior axis of the image. Han et al[6] showed that the degree of pneumatization of the entire mastoid can be estimated by evaluating the mastoid cells around the sigmoid sinus (Fig 3). Group I, with reduced pneumatization (hypopneumatization), is represented by mastoid cells positioned anteromedial to the most anterior line; group II, with moderate pneumatization, is represented by pneumatized cells extending between the first and second lines; group III, with good pneumatization, is represented by pneumatized cells between the middle and the last lines; and group IV, with hyperpneumatization, is represented by pneumatic cells situated posterolaterally to the last line.[6]

Statistical Data Processing

We used the following statistical tests: the Kolmogorov-Smirnov test for normal distribution and the Student *t* test for the comparison of the means in the case of 2 independent samples if the probability distribution was normal. If variables did not have a normal distribution, the Mann-Whitney test was used for the comparison of the ranks. The χ^2 test or the Fisher exact test was used in case of qualitative variables. For the linear relationship between 2 discrete quantitative variables, the Pearson correlation coefficient was used, and for the nonlinear relationship between 2 discrete quantitative variables, the Spearman correlation coefficient was used. The significance threshold for the tests used was $\alpha = .05$. Statistical calculations were performed by using the Statistical Package for the Social Sciences, Version 15.0 (IBM, Armonk, New York) and Excel applications (Microsoft, Redmond, Washington).

RESULTS

Temporal Squama Fractures

All temporal bone samples (M1–M10 and S1–S10) had temporal squama fractures (Fig 4). In the study group, horizontal, vertical, and oblique temporal squama fractures were present. In this group, horizontal and oblique fractures were predominant in equal proportions (36.53% horizontal fractures, 36.53% oblique fractures, 26.92% vertical fractures), and comminuted fractures represented 42.85% of all fractures. In the control group, there were also horizontal, vertical, and oblique fractures. Horizontal fractures were predominant, followed by oblique fractures (44.44% horizontal, 38.88% oblique, 16.66% vertical), and comminuted fractures represented 6.25% of all fractures. The number of temporal squama fracture lines was 2.88 times higher in the study group compared with the control group, and comminuted fractures were 12 times more frequent in the study group. Statistically significant differences were obtained between the 2 groups for horizontal ($P = .007$) and vertical fractures ($P = .03$).

Mastoid Fractures

All temporal bone samples (M1–M10 and S1–S10) had mastoid fractures. In both groups, horizontal, vertical, and oblique mastoid fractures were present. In both groups, oblique mastoid fractures were predominant, followed by horizontal fractures. In the study group, mastoid fractures were 2.76 times more frequent and comminuted fractures were 7 times more frequent compared with the control group. Statistically significant differences were obtained between the 2 groups for horizontal fractures ($P = .03$) and oblique fractures ($P = .001$).

Temporal Bone Fractures with the Involvement of the Facial Nerve Canal

The facial nerve canal was affected by fractures in 10% of the samples of the control group in the mastoid portion, compared with 60% in the study group. In the study group, facial nerve canal fractures were most frequently found in the mastoid portion (50%), followed by the tympanic area (20%) and the geniculate

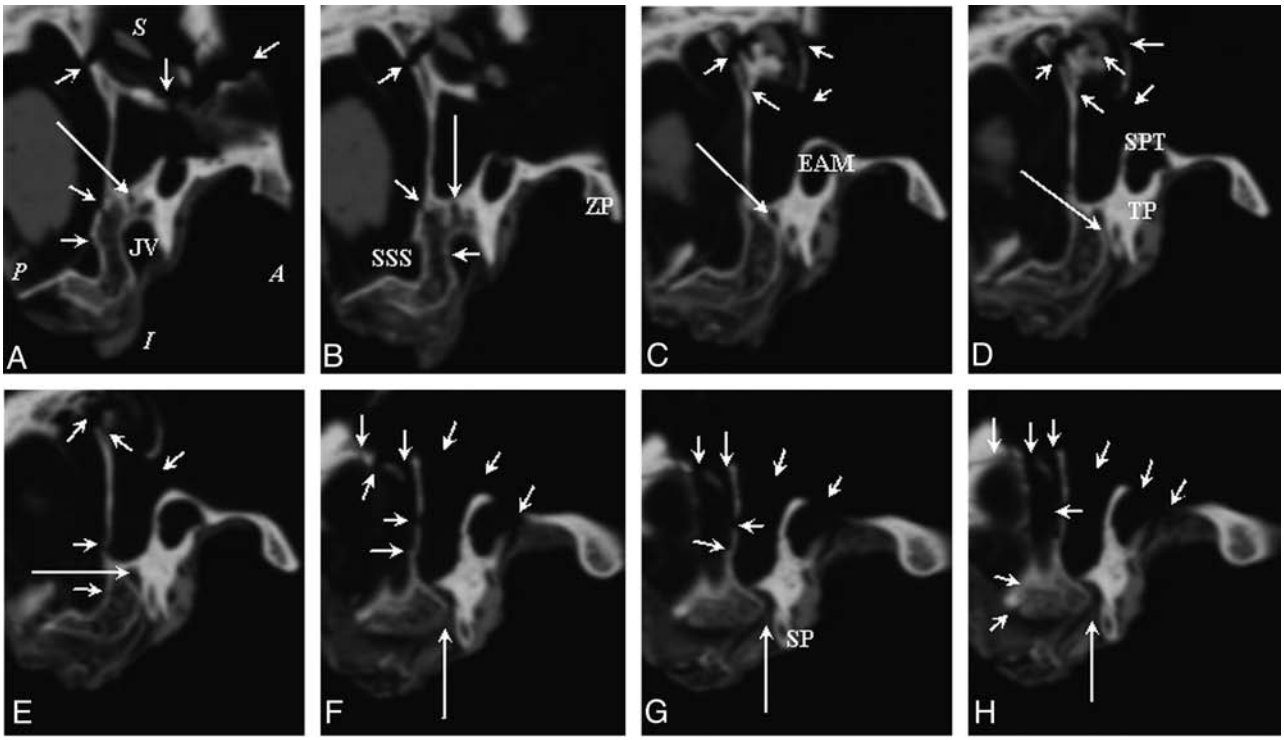

FIG 5. CT image of the mastoid segment of the facial nerve of sample S1 (*A–H*): successive CT sections reconstructed in the sagittal plane in the distal segment of the mastoid canal up to the stylomastoid foramen. In the first image (*A*), the position of the sample in the sagittal section is marked as follows: *A* indicates anterior; *P*, posterior; *S*, superior; *I*, inferior. The fracture lines are marked by short arrows; the facial nerve canal is marked by a long arrow. *A*, JV, jugular vein. *B*, SSS, sigmoid sinus sulcus; ZP, zygomatic process. *C*, EAM, external auditory meatus. *D* and *E*, The long arrow marks the descending segment of the facial nerve. *D*, TP, tympanic portion; SPT, squamous portion of the temporal bone (it forms the roof and the posterosuperior wall of the external auditory meatus). *F–H*, The long arrow indicates the stylomastoid foramen. *G*, SP, styloid process.

ganglion area (20%); in 10%, the internal auditory canal was affected (Fig 5).

Fractures of Temporal Bone Foramina and Canals

Fractures involving the carotid canal were found in 30% of the samples of the control group and in 70% of those of the study group. The stylomastoid foramen was affected by the fracture line in only 1 sample in the control group. The jugular foramen was affected in 20% of the samples of the control group and in 50% of the samples of the study group. The sigmoid sulcus was affected in 80% of the samples in the control group and 100% in the study group. These fractures can be seen in Fig 6.

Petrous and Nonpetrous Temporal Bone Fractures

Temporal bone fractures, summarized according to the Ishman and Friedland[9] classification (as petrous and nonpetrous), are shown in Table 1. The number of petrous fractures was 5.75 times more frequent in the study group than in the control group. The number of nonpetrous fractures was 3.18 times more frequent in the study group compared with the control group. In both groups, nonpetrous fractures were more frequent than petrous fractures.

Mastoid Pneumatization

In the control group, pneumatization type III was present in 30% of the samples, and pneumatization type IV, in 70% of the samples (Fig 7). Pneumatization types I and II, or sclerotic mastoids were not found in the control group. The samples with pneumatization type IV of the control group had more fracture lines with a higher severity than the samples with pneumatization type III, as can be seen in Table 2. By relating the number of fracture lines to the number of samples, one can see that the samples in the control group with pneumatization type IV had 1.8 times more fracture lines than the samples with pneumatization type III of the same group.

In the study group, pneumatization type IV was present in 30% of the samples. In the other temporal bone samples of this group, the degree of pneumatization could not be evaluated because multiple fragments were partially destroyed after impaction.

DISCUSSION

This study demonstrates that mastoid pneumatization and architecture play a role in the mechanical protection of the temporal bone structures during direct lateral trauma. The mastoid plays the role of absorbing and dispersing impacting kinetic energy. Trauma was applied to the temporal bone samples by using a weight with a radius of 60 mm. Rhee et al[10] showed, in a study on the biomechanics of zygomatic bone fractures on cadaver heads, that the severity of the fractures did not depend on the contact surface area or on the thickness of the soft tissue covering the bone. They showed that the impacting speed was best correlated with the severity of the fractures and its threshold was 3.5 m/s. In our study, the mean impacting speed of the temporal bone samples was 3.35 $\pm$ 0.013 m/s with an isolated and formalinized temporal bone.

By removing, in the study group, the external cortex of the mastoids and mastoid cells, a low-resistance area was created. In the study group, the fracture lines were, in fact, fracture surfaces and comminuted fractures were much more numerous. In addition, in the study group, the depressing effect of the impacting object was seen. All these results lead us to believe that the lesions of the brain tissue adjacent to the temporal bone would have been more severe in the study group.

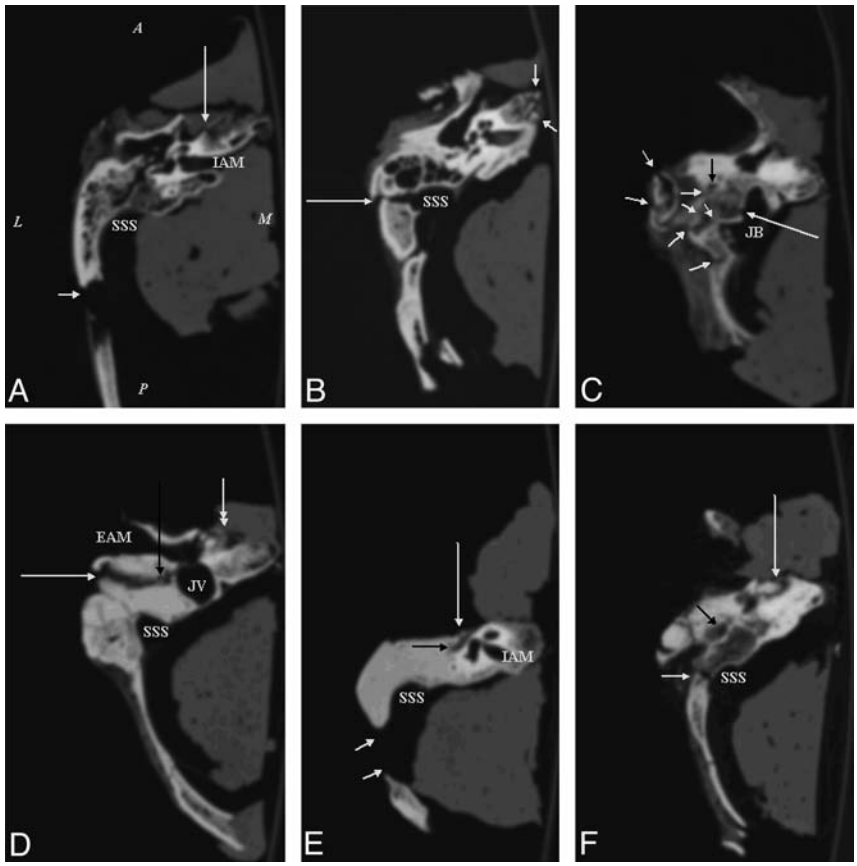

FIG 6. Axial CT sections involving vital structures of the temporal bone. The first images (*A–C*) belong to the control group, and the last images (*D–F*) belong to the study group. The position of the samples in the axial plane is marked as follows: *A* indicates anterior; *P*, posterior; *L*, lateral; *M*, medial on the first image. Short white arrows indicate fracture lines with different orientations in different parts of the temporal bone. Long white arrows indicate fractures of walls of vascular and nerve structures: carotid canal in images *A* and *D* (*double-tipped arrow*), and *F*; sigmoid sinus sulcus and jugular vein bulb in images *B* and *C*; the mastoid segment of facial nerve in the image *D*; the tympanic segment of the facial nerve in the image *E*; the stylomastoid foramen in the image *F*. The black arrows indicate the different portions of the facial nerve: the mastoid portion in *C* and *D*, tympanic in *E*, and the stylomastoid foramen in *F*. IAM indicates internal auditory meatus; SSS, sigmoid sinus sulcus; JB, jugular bulb; JV, jugular vein; EAM, external auditory meatus. *A*, M3 sample section at the level of the internal auditory meatus. The long white arrow indicates a fracture line at the medial wall of the carotid canal. *B*, M4 sample section at the level of epitympanic portion. The long white arrow indicates a longitudinal fracture line at the lateral wall of the sigmoid sulcus. The short white arrows indicate a comminuted fracture of the petrous apex. *C*, M8 sample section at the level of the jugular bulb: The long white arrow indicates a longitudinal fracture line at the lateral wall of the jugular bulb sulcus. The short white arrows indicate a comminuted fracture of the mastoid. *D*, S4 sample section at the level of the external auditory meatus. The long white arrow indicates a longitudinal fracture line involving the mastoid segment of the facial nerve; the white double-tipped arrow indicates a comminuted fracture of the lateral wall of the carotid canal. *E*, S6 sample section at the level of the tympanic portion of the facial nerve. The long white arrow indicates a fracture line involving the facial nerve. *F*, S5 sample section at the level of the stylomastoid foramen. The long white arrow indicates a bone fragment in the roof of the carotid canal.

The classic classification of temporal bone fractures (ie, transverse, longitudinal, and oblique) does not correlate with the clinical aspects of facial nerve dysfunction as well as the classification that categorizes fractures as petrous and nonpetrous.[9] Ishman and Friedland[9] showed that in petrous fractures, facial nerve lesions are 3 times more frequent and CSF leakage is 10 times more frequent. If fractures are nonpetrous and involve the mastoid portion of the facial nerve, facial nerve injuries are less likely to occur.[9] In our study, in the control group, the facial nerve canal fracture was in the mastoid portion, which is part of the nonpetrous temporal bone fracture, thus with fewer chances to induce facial nerve lesions. In contrast, in the study group, petrous fractures were 5.75 times more frequent, with higher chances to induce facial nerve lesions, considering that facial nerve canal fractures were 6 times more frequent.

Carotid canal fractures were 2.33 times more frequent in the study group. York et al[11] showed that carotid canal fractures had a 60% sensitivity and 67% specificity for the detection of internal carotid artery injuries in subjects with head trauma. In their study, the frequency of internal carotid injuries was twice as high in patients with carotid canal fractures as in those without carotid canal fractures. Internal carotid injuries were predominantly represented by dissection, and in 1 patient, by carotid cavernous fistula.[11]

The jugular foramen was affected by the fracture line 2.5 times more frequently in the study group, which increased the risk of sigmoid sinus thrombosis. Delgado Almandoz et al[12] showed

Table 1: Petrous and nonpetrous temporal bone fractures in the control and study groups

	M1–M10			S1–S10		
Type of Fracture	Transverse Fracture, No Fracture Lines	Longitudinal Fracture, No Fracture Lines	Oblique Fracture, No Fracture Lines	Transverse Fracture, No Fracture Lines	Longitudinal Fracture, No Fracture Lines	Oblique Fracture No, Fracture Lines
Petrous fracture	4	0	0	11	4	8
Non-petrous fracture	5	8	9	23	18	29

that patients with skull fractures in whom fractures were extended to the sigmoid sinus or/and jugular bulb had a 40.7% overall risk for thrombosis. They found a higher injury risk for the sigmoid sinus, transverse sinus, and jugular bulb in petrous temporal bone fractures.[12]

Given that mastoid pneumatization could not be evaluated in all samples in the study group (because some pieces were destroyed) and the small number of samples in the 2 groups, a statistical study between the degree of mastoid pneumatization and the severity of temporal bone fractures could not be performed. In the control group, however, samples with pneumatization type IV had more fracture lines than those with pneumatization type III. These results suggest that mastoids with hyperpneumatization have a higher susceptibility to fracture than mastoids with good pneumatization. By extrapolating the results obtained in the control group, it might be thought that a mastoid with a single large air cell would fracture more easily than one with the same air content but with bone septa. There might be an optimal ratio between the air volume of the mastoid and that of the bone walls of the mastoid air-cell system, which might provide the protection of vital structures in the temporal bone. Our study did not include acellular mastoids of developmental or secondary causes that could have provided additional information about the mechanical protection of the mastoid.

The limitations of the study are the small number of samples included. In addition, the study was not performed on fresh temporal bone samples, but on formalinized samples. The formalin used for conservation determined the dehydration of the samples and changes of bone structure proteins. All these aspects alter bone elasticity and the susceptibility of bone tissue to fracture.

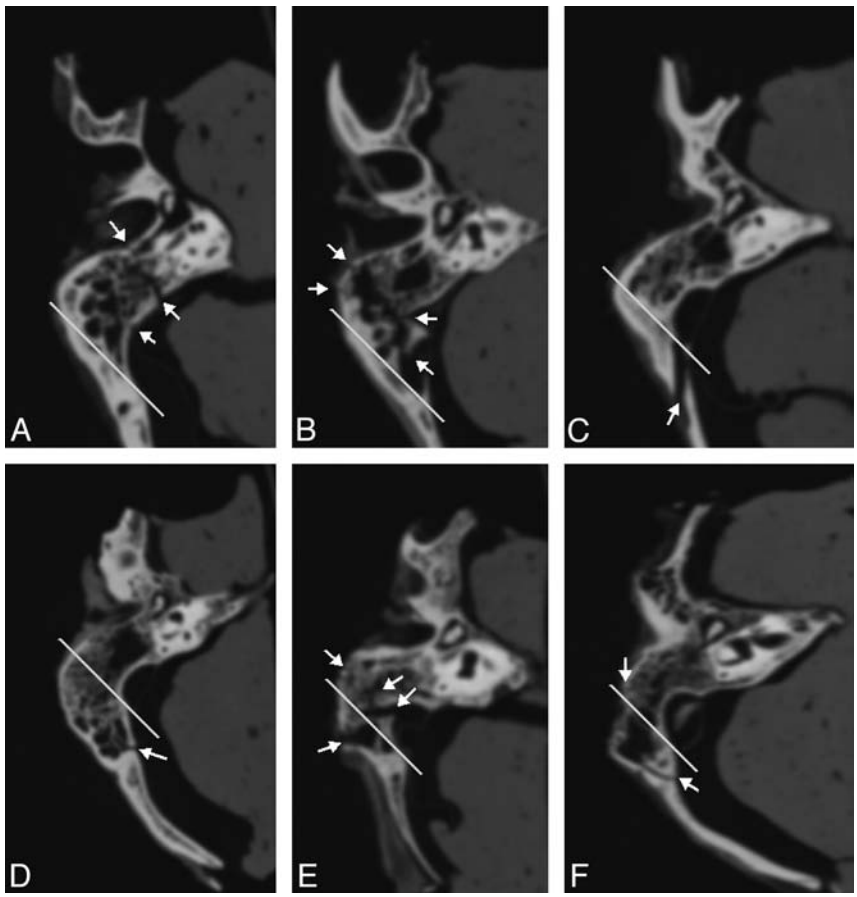

FIG 7. Axial CT section at the level of the sigmoid sinus and epitympanum in samples M1 (*A*), M5 (*B*), M6 (*C*), M7 (*D*), M8 (*E*), and M10 (*F*). The white line marks the separation between pneumatization degree III and IV. Samples from images *A*–*C* show pneumatization degree III, and the images *D*–*F* show pneumatization degree IV. Short white arrows mark the fracture lines highlighted in these sections.

CONCLUSIONS

In the setting of lateral trauma, mastoid architecture with air spaces appears to contribute to the absorption and dispersion of impacting kinetic energy and to the protection of vital structures in the temporal bone.

ACKNOWLEDGMENTS

The authors thank Remus Văidăhăzan for the beautiful illustration of the degrees of mastoid pneumatization.

Table 2: The degree of pneumatization and the type of fractures in the control group

Type of Fracture Samples M1–M10	Pneumatization Degree	Petrous Fracture			Nonpetrous Fracture		
		Transverse Fracture, No Fracture Lines	Longitudinal Fracture, No Fracture Lines	Oblique Fracture, No Fracture Lines	Transverse Fracture, No Fracture Lines	Longitudinal Fracture, No Fracture Lines	Oblique Fracture, No Fracture Lines
M1	IV	1	–	–	1	–	3
M2	III	–	–	–	–	1	1
M3	IV	–	–	–	–	–	1
M4	IV	1	–	–	1	1	–
M5	IV	1	–	–	3	1	1
M6	III	–	–	–	–	1	–
M7	IV	–	–	–	–	1	–
M8	IV	–	–	–	–	1	1
M9	III	1	–	–	–	1	–
M10	IV	–	–	–	–	1	2

Note:—indicates no fracture lines.

Disclosures: Aranka Ilea—*RELATED*: *Grant*: Sectorial Operational Programme for Human Resources Development (POSDRU) project 88/1.5/S/78702.* Lucia Hurubeanu—*UNRELATED*: *Grants/Grants Pending*: New Biocompatible Materials for Personalized Implants Made by Selective Laser Sintering and Selective Laser Melting (BIOMAPIM); Project CNCSIS (National Council of Scientific Research in Higher Education), PN-II-ID-PCCE-2008-1 (PN, National Plan; ID, Ideas; PCCE, Exploratory Complex Research Projects).* *Money paid to the institution.

REFERENCES

1. Kellman RM, Schmidt C. **The paranasal sinuses as a protective crumple zone for the orbit.** *Laryngoscope.* 2009;119:1682–90
2. Hill CA, Richtsmeier JT. **A quantitative method for the evaluation of three-dimensional structure of temporal bone pneumatization.** *J Hum Evol* 2008;55:682–90
3. Virapongse C, Sarwar M, Bhimani S, et al. **Computed tomography of temporal bone pneumatization: normal pattern and morphology.** *AJR Am J Roentgenol* 1985;145:473–81
4. Sadé J, Ar A. **Middle ear and auditory tube: middle ear clearance, gas exchange, and pressure regulation.** *Otolaryngol Head Neck Surg* 1997;116:499–524
5. Sadé J, Fuchs C. **Secretory otitis media in adults: I. The role of mastoid pneumatization as a risk factor.** *Ann Otol Rhinol Laryngol* 1996;105:643–47
6. Han SJ, Song MH, Kim J, et al. **Classification of temporal bone pneumatization based on sigmoid sinus using computed tomography.** *Clin Radiol* 2007;62:1110–08
7. Valtonen HJ, Dietz A, Qvarnberg YH, et al. **Development of mastoid air cell system in children treated with ventilation tubes for early-onset otitis media: a prospective radiographic 5-year follow-up study.** *Laryngoscope* 2005;115:268–73
8. Turgut S, Tos M. **Correlation between temporal bone pneumatization, location of lateral sinus and length of the mastoid process.** *J Laryngol Otol* 1992;106:485–89
9. Ishman SL, Friedland DR. **Temporal bone fractures: traditional classification and clinical relevance.** *Laryngoscope* 2004;114:1734–41
10. Rhee JS, Posey L, Yoganandan N, et al. **Experimental trauma to the malar eminence: fracture biomechanics and injury patterns.** *Otolaryngol Head Neck Surg* 2001;125:351–55
11. York G, Barboriak D, Petrella J, et al. **Association of internal carotid artery injury with carotid canal fractures in patients with head trauma.** *AJR Am J Roentgenol* 2005;184:1672–78
12. Delgado Almandoz JE, Kelly HR, Schaefer PW, et al. **Prevalence of traumatic dural venous sinus thrombosis in high-risk acute blunt head trauma patients evaluated with multidetector CT venography.** *Radiology* 2010;255:570–77

Osteoradionecrosis after Radiation Therapy for Head and Neck Cancer: Differentiation from Recurrent Disease with CT and PET/CT Imaging

L. Alhilali, A.R. Reynolds, and S. Fakhran

ABSTRACT

BACKGROUND AND PURPOSE: Our aim was to compare the CT and PET/CT imaging features of osteoradionecrosis with those of recurrent disease after treatment of head and neck malignancy.

MATERIALS AND METHODS: We retrospectively reviewed maxillofacial and neck CT scans obtained for suspected osteoradionecrosis or tumor recurrence for the presence of the following: 1) discrete solid mass, 2) cystic mass, 3) interruption of the bony cortex, 4) bony fragmentation, 5) bony trabecular loss, 6) intraosseous gas, and 7) bony sclerosis. Trabecular bone loss was further categorized as permeative (<75% loss of trabecula) or lucent (>75% loss). PET/CT studies performed for suspected osteoradionecrosis or tumor recurrence were evaluated for mean standard uptake value and maximum standard uptake value.

RESULTS: Ten maxillofacial CT, 53 neck CT, and 23 PET/CT studies were performed in 63 patients. Osteoradionecrosis was diagnosed by pathology or imaging stability in 46 patients, and tumor recurrence, in 17 patients. Bony sclerosis was found to be significantly more prevalent in osteoradionecrosis and was never seen with tumor recurrence ($P = .013$). Patients with tumor recurrence were more likely to have a solid ($P < .001$) or cystic mass ($P = .025$), which was rare in osteoradionecrosis. While patients with tumor recurrence had significantly higher mean standard uptake values and maximum standard uptake values, there was significant overlap in mean standard uptake values and maximum standard uptake values between the 2 groups.

CONCLUSIONS: There is significant overlap of standard uptake values in patients with osteoradionecrosis and tumor recurrence. CT findings provide more reliable diagnostic tools, with a solid or cystic mass strongly associated with tumor recurrence and bony sclerosis seen only with osteoradionecrosis.

ABBREVIATIONS: ORN = osteoradionecrosis; SUV = standard uptake value; SUV_{mean} = mean standard uptake value; SUV_{max} = maximum standard uptake value

Osteoradionecrosis (ORN), often with coexistent osteomyelitis, is a serious and often debilitating complication of radiation therapy for head and neck neoplasms. The mandible is the most common site of ORN due to its tenuous blood supply,[1-3] though ORN can be seen in almost any bone within a radiated field. The primary factor implicated in the pathogenesis of ORN is the amount of radiation given to the affected bone, with both early (<2 years from radiation) and late onset ORN (>2 years from radiation) seen.[4] There is a wide range of incidence of mandibular ORN reported, ranging from 5% to 22%, with more recent studies showing a decreased incidence, presumably attributable to increasing awareness and to improvements in preventive care and radiation techniques.[5-9]

Patients are often referred for imaging to evaluate the extent of clinically suspected ORN, and, at the same time, to assess potential tumor recurrence. Multiple previous reports have characterized the imaging findings of ORN,[10-14] namely soft-tissue thickening and enhancement, cortical bone erosion, trabecular disorganization, and bone fragmentation. All these findings can be seen in tumor recurrence, however, making the imaging differentiation of these 2 entities quite challenging.

We compared the relative frequency of CT and PET/CT findings of ORN and tumor recurrence to find patterns that might allow reliable differentiation of one entity from the other.

MATERIALS AND METHODS

Patient Selection and Image Acquisition

Our institutional review board approved this study, with a waiver of informed consent. All imaging examinations included in this

Received October 18, 2013; accepted after revision December 5.

From the Department of Radiology, University of Pittsburgh School of Medicine, Pittsburgh, Pennsylvania.

Please address correspondence to Saeed Fakhran, MD, 200 Lothrop St, Presby South Tower, 8th Floor, 8 North, Pittsburgh, PA 15213; e-mail: fakhrans@upmc.edu

http://dx.doi.org/10.3174/ajnr.A3879

study were performed as standard of care, and the results were retrospectively reviewed.

We searched our enterprise-wide electronic medical record encompassing 20 academic and community hospitals between January 1, 2008, and July 20, 2013, to identify patients in whom ORN was suspected on CT or PET/CT, or in whom a question of ORN versus recurrent tumor was raised. All neck and maxillofacial CT reports (including diagnostic neck CT studies performed as part of PET/CT) were searched by using the keywords "osteoradionecrosis," "ORN," "osteoradionecrosis versus tumor recurrence," "osteoradionecrosis or tumor recurrence," "osteoradionecrosis versus recurrent tumor," and "osteoradionecrosis or recurrent tumor." Patients were excluded if there was not pathologic confirmation of suspected tumor recurrence (1 patient) or if ORN could not be confirmed by either pathologic diagnosis or stability of >2 years on serial imaging (6 patients). A single patient was also excluded due to extensive artifacts from dental amalgam, which precluded accurate measurement of standard uptake value (SUV) values on PET/CT. The average time gap between imaging and pathologic confirmation of tumor recurrence or ORN was 14.3 days (range, 3–26 days) and 18.6 days (2–34 days), respectively. At our institution, all maxillofacial and neck CT examinations, as well as all PET/CT examinations performed for evaluation and/or follow-up of head and neck malignancy, are interpreted by fellowship-trained, Certificate of Added Qualification–certified neuroradiologists as part of a dedicated ear, nose, and throat imaging team. Demographic data collected included age and sex. Clinical data collected included location and type of primary neoplasm; initial imaging findings; follow-up imaging results, including any PET/CT results; time from completion of the last radiation therapy to the detection of the abnormality on imaging; and pathology results from either biopsy or operative intervention.

CT Examinations

CT examinations of the neck and maxillofacial bones were performed on 16- or 64-detector multidetector row CT scanners (LightSpeed VCT; GE Healthcare, Milwaukee, Wisconsin). CT acquisitions were obtained from the frontal sinuses to the thoracic inlet for the neck and from the top of the frontal sinuses through the mandible for the maxillofacial bones. Neck CT examinations were performed by using a pitch of 1.0, 2.5-mm collimation, 100 maximal mA, 120 kV(peak), 21.0-cm FOV, in bone and standard algorithms, with 2.0-mm sagittal and coronal reconstructions. Maxillofacial CT studies were performed by using pitch of 0.5, 1.25-mm collimation, 225 maximal mA, 125 kVp, 19.6-cm FOV, with bone and standard algorithms, with 1.0-mm sagittal and coronal reconstructions.

PET/CT Examinations

Patients fasted for at least 6 hours before the PET/CT examination with the exception of water intake. Intravenous access was established for both blood glucose measurement and radiopharmaceutical administration. If serum glucose was >200 mg/dL, the examination was cancelled and rescheduled. Patients received between 10 and 17 mCi of IV [^{18}F] FDG. Following radiopharmaceutical administration, the patients rested quietly during a standard 60-minute uptake period, after which imaging was performed.

The studies were performed on 16- to 64-section PET/CT scanners (Discovery; GE Healthcare). The CT scan parameters were 120–130 kVP, variable/smart milliampere, and 3.75-mm collimation. CT scanning commenced following a 30-second delay after the administration of IV contrast (125-mL iopamidol, Isovue-370; Bracco Diagnostics, Princeton, New Jersey) and was performed from the top of the skull through the abdomen or pelvis (based on ordering clinician's preference). Following CT, PET data were acquired by using a 4-minute bed position. The PET acquisition included an on-line delayed coincidence subtraction to correct for random coincidences as well as a dead-time correction. Two different PET/CT scanners were used in this study; one had a bismuth germanium oxide scintillation crystal, and the other had a lutetium oxyorthosilicate crystal. All PET acquisitions were uniform, using a 2D technique. The helical CT scan was reconstructed by filtered back-projection into 512 × 512 pixel images with a section thickness of 2.4 mm to match the PET scan. Images were reconstructed by using ordered-subset-expectation maximization with 2 full iterations of 8 subsets. Rescaled CT images were used to produce attenuation-correction values for the PET emission reconstruction.

Image Analysis

CT Examinations. All CT examinations were reviewed retrospectively in random order, separately by 2 Certificate of Added Qualification–certified neuroradiologists (L.A., S.F.), blinded to the clinical findings, the original study interpretation, and the final pathologic diagnosis. Reviewers were asked to comment on the presence or absence of the following imaging findings: 1) a solid measurable mass, 2) a cystic mass, 3) interruption of the cortical margin of the affected bone, 4) fragmentation of the affected bone, 5) loss of trabecula of the affected bone, 6) intraosseous gas in the affected bone, and 7) sclerosis of the affected bone. They were instructed that surrounding inflammatory change (ie, amorphous soft-tissue stranding or infiltration) and muscle or tissue thickening (Fig 1*A*, -*B*) did not qualify as a solid mass and that a discrete measurable mass (Fig 2) must be present. They were further asked to measure the size of any solid or cystic mass (Fig 2*E*, -*F*), and in those cases in which trabecular loss existed, they were asked to classify the pattern of trabecular loss as either permeative or lucent. They were instructed that a permeative pattern indicated multiple, independent focal lucent lesions, which, in sum, did not account for >75% loss of total bone trabecula (Fig 3*A*). A lucent pattern was defined as >75% loss of total bone trabecula in the area of abnormality (Fig 2*C*, -*D*). Radiologists were also asked to record the area or areas of the mandible affected, with choices being either the right or left mandibular condyle, coronoid process, ramus, angle, or body.

PET Examinations. In cases in which PET/CT was performed, the radiologists were asked to record both the mean (SUV_{mean}) and maximum (SUV_{max}) SUV values. All PET studies were analyzed quantitatively with a software platform capable of deformable registration of multimodal images in the sagittal, coronal, and axial planes (Mirada XD3; Mirada Medical, Denver, Colorado). On PET scans,

metabolic volumes were manually delineated at the most metabolically active site of suspected ORN or tumor recurrence.

The SUV was automatically calculated by using the following formula:

$$\mathrm{SUV} = C_{dc}/(d/w),$$

where d is the injected dose (in becquerels), w is the patient's body weight (in grams), and C_{dc} is the decay-corrected tracer tissue concentration (in becquerels per gram). SUV was measured as $\mathrm{SUV}_{\mathrm{mean}}$ and $\mathrm{SUV}_{\mathrm{max}}$. These parameters were obtained from a 2D region of interest placed onto the axial image containing the most metabolically active area of abnormality (based on visual inspection). The smallest possible region of interest was used that would capture the most metabolically active area of abnormality. $\mathrm{SUV}_{\mathrm{mean}}$ was defined as the average pixel value in the region of interest, while $\mathrm{SUV}_{\mathrm{max}}$ was defined as the highest pixel value in the region of interest.

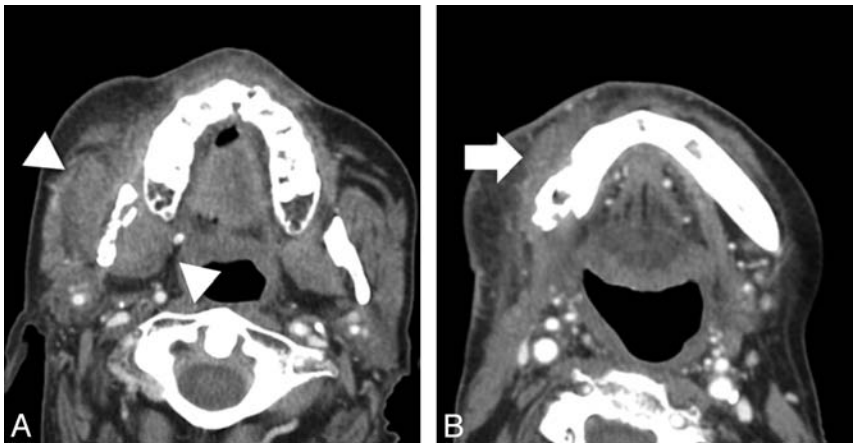

FIG 1. Images from 2 different patients with soft-tissue findings of osteoradionecrosis. *A*, Axial CT scan (soft-tissue window) shows enlargement and thickening of the musculature of the right masticator space (*white arrowheads*), without evidence of a distinct measurable mass, adjacent to an area of osteoradionecrosis. *B*, Axial CT scan (soft-tissue window) shows inflammatory thickening of soft tissues (*white arrow*) adjacent to an area of osteoradionecrosis involving the right mandibular body.

Statistical Analysis

Comparison of the demographic data between the 2 groups was performed by using a Fisher exact test for dichotomous variables and a 2-tailed, unpaired *t* test for continuous variables. The reproducibility of subjective imaging findings was tested between 2 fellowship-trained neuroradiologists on 50 randomly chosen cases from among patients with ORN and tumor, and a Cohen κ was calculated. Comparison of the prevalence of imaging findings between the 2 groups was performed with the Fisher exact test. Comparison of $\mathrm{SUV}_{\mathrm{mean}}$ and $\mathrm{SUV}_{\mathrm{max}}$ was performed between cases of osteoradionecrosis and tumor recurrence by using a 2-tailed, unpaired *t* test.

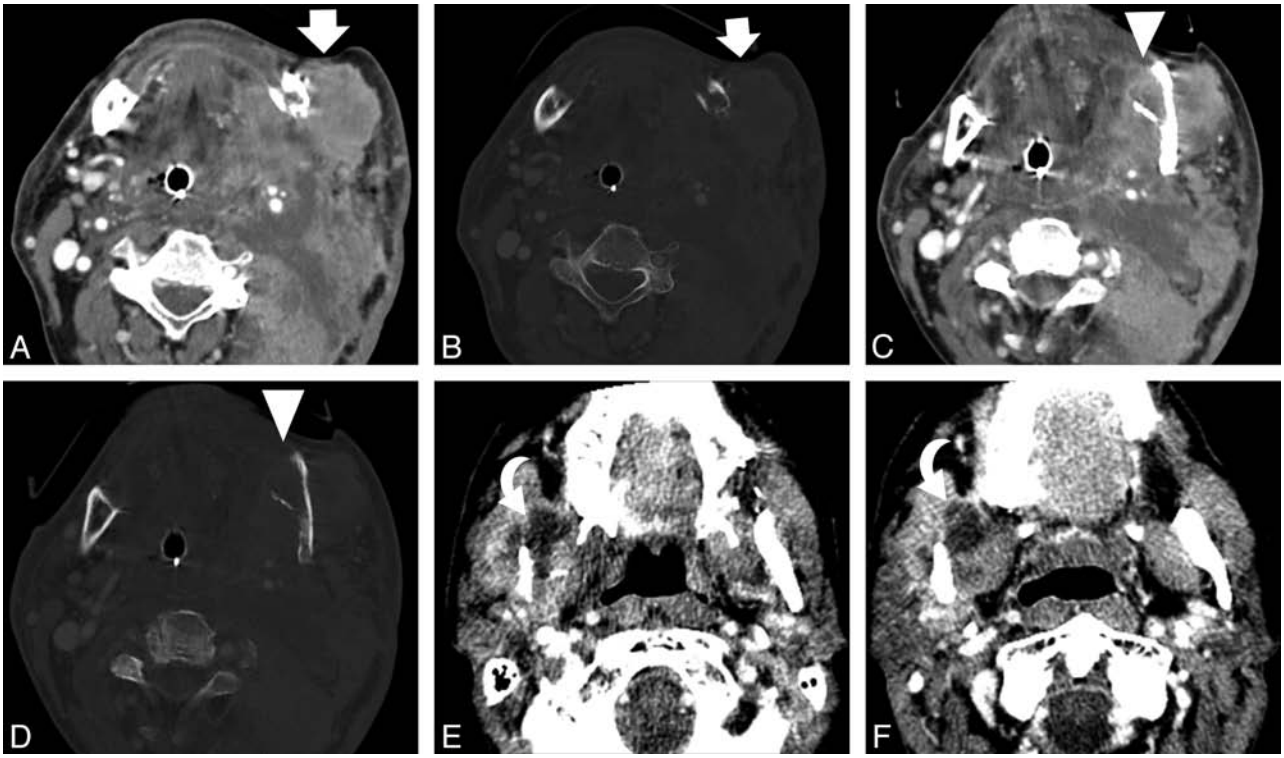

FIG 2. Images depicting soft-tissue findings of recurrent tumor. Axial CT scan from a 62-year-old man with recurrent oral cancer shows a large mass (*white arrows*) adjacent to the left mandibular angle in soft-tissue (*A*) and bone (*B*) algorithms. Axial CT scan at a different level shows an area of lucent trabecular loss involving the left mandibular angle (*white arrowheads*) in soft-tissue (*C*) and bone (*D*) algorithms. Axial CT images in an 83-year-old patient with recurrent oral cancer show another finding seen in recurrent tumor, a cystic mass (*curved arrows*), at 2 different levels (*E* and *F*).

$P < .05$ was considered indicative of a statistically significant difference.

RESULTS

Fifty-three neck CTs and 10 maxillofacial CTs were evaluated. Twenty-three patients had a PET/CT performed as well. Seventeen of these studies demonstrated findings of tumor recurrence, while 46 demonstrated findings of ORN. Of the subset of patients with a PET/CT, 14 demonstrated findings of ORN, while 9 demonstrated findings of tumor recurrence. No significant differences were found between the 2 groups with regard to age, sex, or the interval between the end of radiation therapy and the detection of an abnormality on imaging ($P = .11$, 1.00, and 0.19, respectively). Demographic and clinical data for the 2 groups are summarized in the Table.

Most cases of ORN primarily affected the mandible (43 patients, 93%), with 1 case involving the hard palate, and 2 cases involving the maxilla. Most cases of ORN involving the mandible affected either 1 or 2 subsites of the mandible ipsilateral to the site of primary tumor (31 patients, 72%), with the remaining cases affecting either 3 (6 patients, 14%) or >3 (6 patients, 14%) subsites of the mandible. The preponderance of ORN cases involving the mandible affected the lingual surface (20 patients, 47%), while the remainder affected either the buccal surface (13 patients, 30%) or involved both the lingual and buccal surfaces (10 patients, 23%). None of the patients received hyperbaric oxygen before detection of ORN.

Interpretation of the subjective imaging findings between observers was almost perfect, by using Cohen κ interpreted according to Landis and Koch,[15] with κ values as follows: 0.865 (95% CI, 0.683–1.00) for cortical disruption, 0.868 (95% CI, 0.724–1.00) for a pattern of trabecular loss, 0.891 (95% CI, 0.743–1.00) for the presence of a cystic mass, 0.940 (95% CI, 0.823–1.00) for the presence of a solid mass, 0.929 (95% CI, 0.792–1.00) for the presence of bony sclerosis, and 1.000 (95% CI, 1.00–1.00) for the presence of intraosseous gas.

CT Examinations

The CT imaging findings in both groups of patients are summarized in Fig 4. The presence of a measurable solid soft-tissue mass in the tumor-recurrence group was 59% (10 of 17 patients), which is significantly higher than that in the osteoradionecrosis group (1 of 46 patients, 2%, $P < .001$). Similarly, the presence of a cystic mass was also significantly higher in the recurrence group, 41% (7 of 17 patients), than in the osteoradionecrosis group (3 of 46 patients, 6.5%, $P = .025$).

Several osseous changes showed a significant difference between the 2 groups as well. A permeative pattern of trabecular loss was significantly higher in the ORN group, 80% (37 of 46 patients), than the tumor-recurrence group (4 of 24 patients, 16.7%, $P < .0001$). Bone sclerosis was also seen significantly more often in the setting of ORN, 28% (13 of 33 patients), than in tumor recurrence (0 of 17 patients, 0%, $P = .013$). While interruption of the cortical margin was seen significantly more often in the tumor-recurrence group (17 of 17 patients, 100%) than in the ORN group (33 of 46 patients, 71.7%, $P = .013$), it was noted to have a rather high prevalence in both groups.

PET Examinations

The SUV_{mean} was significantly higher in cases of tumor recurrence (SUV_{mean} range, 4.6–14.1; mean, 8.0) compared with ORN (SUV_{mean} range, 2.2–7.5; mean, 4.3), with a P value of .0021. Likewise, the SUV_{max} was significantly higher in cases of tumor recurrence (SUV_{max} range, 5.7–20.2; mean, 11.3) compared with ORN (SUV_{max} range, 1.7–9.2; mean, 5.3), with a P value of

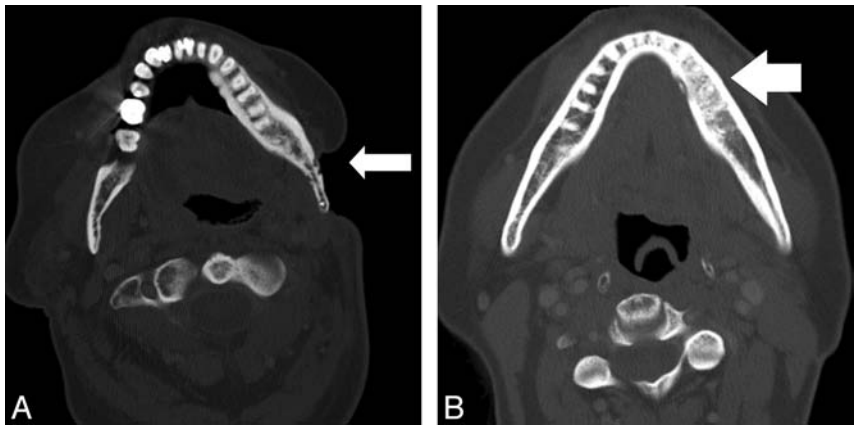

FIG 3. Images from 2 different patients with osseous findings of osteoradionecrosis. *A*, Axial CT scan (bone algorithm) shows ORN involving the mandibular angle with an adjacent soft-tissue defect. Areas of permeative trabecular loss (*white arrow*) are evident. *B*, Axial CT scan (bone algorithm) shows ORN involving the left mandibular body with bony sclerotic changes (*white arrow*) evident.

Patient demographics and clinical characteristics

	Patients Diagnosed with Osteoradionecrosis	Patients Diagnosed with Tumor Recurrence	*P* Value
No. of patients	46	17	NA
Average age (yr)	62	69	.11
Age range (yr)	33–93	53–85	
% Men (No.)	76.1 (35)	77.5 (13)	1.00
Primary malignancy site	Oral Cavity ($n = 27$), oropharynx ($n = 11$), parotid ($n = 5$), NPC ($n = 2$) unknown ($n = 1$)	Oral cavity ($n = 15$), oropharynx ($n = 1$), sinonasal ($n = 1$)	
Primary malignancy histology	Squamous cell ($n = 44$), adenoid cystic ($n = 2$)	Squamous cell ($n = 17$)	
Mean interval (range) between last RT and detection of abnormality (mo)	40.56 (6–110)	48.82 (5–98)	.19

Note:—NA indicates not applicable; NPC, nasopharyngeal cancer; RT, radiation therapy.

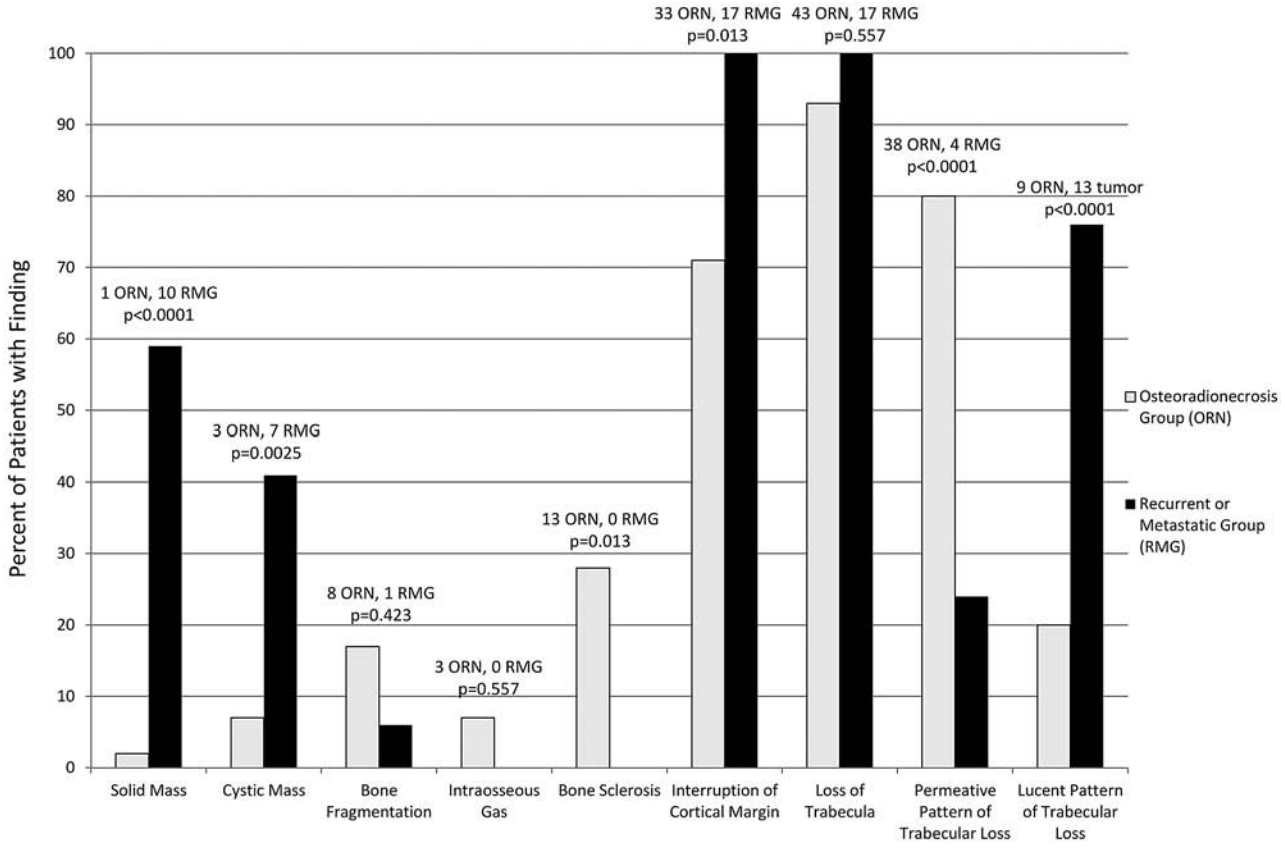

FIG 4. Prevalence of imaging findings of ORN and metastatic or recurrent lesions.

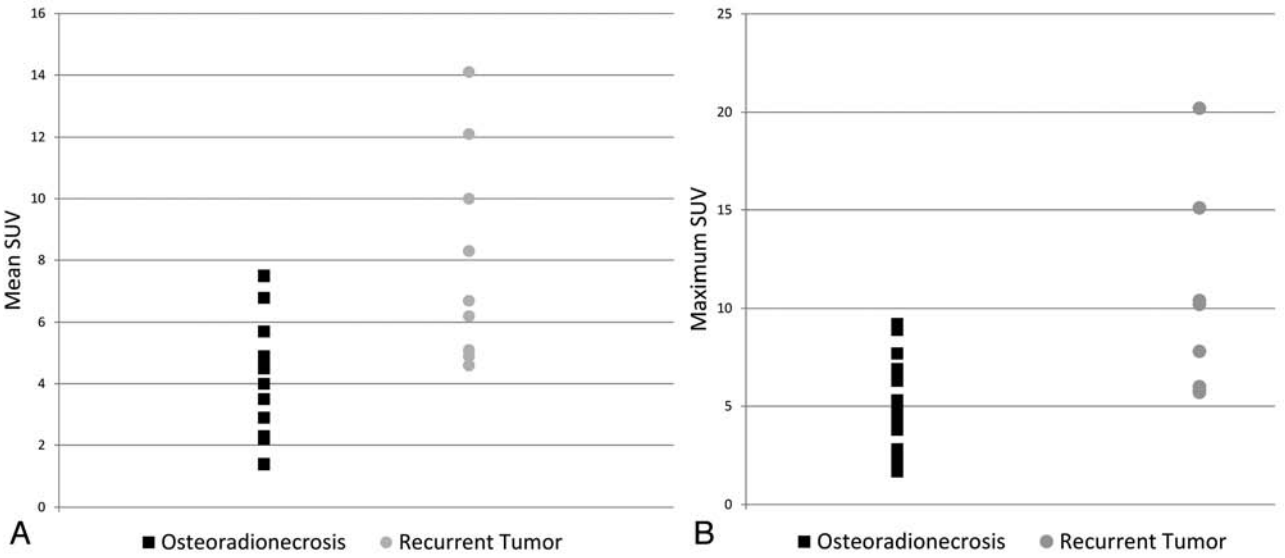

FIG 5. Scatterplots for SUV measurements for patients with ORN and those with tumor recurrence. *A*, Scatterplot for SUV_{mean} in patients with ORN and tumor recurrence demonstrates significant overlap between SUV values, despite a significant difference between their means. *B*, Scatterplot for SUV_{max} in patients with ORN and tumor recurrence also demonstrates significant overlap between maximum SUV values in the 2 groups.

.0023. There was, however, substantial overlap in both SUV_{mean} and SUV_{max} values between the 2 entities (Fig 5*A*, -*B*).

In the subset of patients with ORN who underwent histopathologic sampling, 20% (5 of 25 patients), had pathologic evidence of associated osteomyelitis. Unfortunately, only 1 of those patients also underwent a PET/CT examination; therefore, it is difficult to compare the relative SUV values of ORN with and without associated osteomyelitis.

DISCUSSION

The findings of a cystic or solid mass on imaging were significantly more prevalent in patients with tumor recurrence, being relatively

rare in patients with ORN. Conversely, the presence of bony sclerosis was not uncommon in patients with ORN but was never seen in tumor recurrence. Although the SUV values in tumor recurrence were significantly higher than in ORN, the substantial overlap in the SUV values for these 2 entities renders SUV measurements relatively impractical for differentiating ORN from tumor recurrence reliably in the clinical setting.

We attempted to evaluate the utility of various CT findings and PET/CT parameters in an effort to distinguish ORN from recurrent malignancy in the head and neck following irradiation for head and neck cancer. Multiple prior studies have also found the relative unreliability of an elevated SUV in differentiating recurrent tumor from ORN.[11,12,16-18] While recurrent tumor does, in general, demonstrate higher SUV_{mean} and SUV_{max} values compared with ORN, there is significant overlap, which makes differentiating the 2 entities on a case-by-case basis extremely unreliable. This overlap is presumably responsible for previous reports of false-positive results in PET scans attributed to osteoradionecrosis.[16]

Unlike SUV values, there were conventional imaging findings that were rather selective for differentiating ORN from tumor recurrence. In evaluating tumor recurrence, a discrete, associated mass provides a significant diagnostic indication for the presence of recurrent tumor. While ORN may be associated with inflammatory and edematous changes in the surrounding musculature and soft tissues,[10,19-21] an asymmetric, discrete solid mass was seen in more than half of the patients with recurrent malignancy, but it was exceedingly rare in ORN, seen in only 2% of patients with ORN. Similarly, a cystic mass was seen in nearly half of patients with recurrent tumor, but in <10% of patients with ORN. This indicates that the presence of a cystic component in a patient with suspected ORN should not be assumed to be an abscess from associated osteomyelitis but should instead prompt concern for possible recurrent neoplasm.

Osseous findings on CT can also be extremely helpful in differentiating ORN from tumor recurrence. Multiple prior studies have delineated the classic bony CT findings associated with ORN, namely cortical disruption, trabecular loss, bone fragmentation, bony sclerosis, and the presence of intraosseous gas.[1,10,11,13,21] However, we tested the value of these imaging findings for discriminating ORN and tumor recurrence. Traditionally, on the basis of known pathologic findings in ORN, it has been thought that a more permeative pattern of bone loss is seen in ORN as opposed to tumor recurrence. This was thought to be related to the fact that irradiation leads to a relatively hypoxic, hypocellular, and hypovascular substrate with an inconsistent ability to remodel tissue loss secondary to radiation-induced injury[22]; this, in turn, would lead to relatively less bony loss than would be seen when tissue is being actively destroyed and replaced by tumor. In our patients, the permeative pattern of bone loss, though significantly more common in ORN, was also seen in a significant minority of patients with tumor recurrence. This may be related to our patient population, which is actively surveyed both clinically and with imaging for tumor recurrence. This hypervigilance for tumor recurrence may lead to earlier detection of recurrent tumor, which may show less advanced bony replacement, mimicking the more restrained bone loss seen in ORN. Similarly, significant bone replacement producing a lucent pattern of trabecular loss, though common in tumor recurrence, was also seen in one-fifth of patients with ORN, presumably reflecting more advanced radiation injury or aggressive infection in this subset of patients.

Perhaps the most useful imaging feature in distinguishing ORN from tumor recurrence was the presence of bony sclerosis (Fig 3*B*). Seen in nearly one-third of patients with ORN, it was not seen in any of our patients with recurrent tumor. This finding may reflect the tendency of squamous cell carcinoma to induce bony destruction rather than sclerosis in contradistinction to the often chronic nature of ORN that may be associated with bony sclerosis.[13,23] Thus, while most patients with ORN may not have bony sclerosis, the presence of this finding on imaging should prompt a relatively confident diagnosis of ORN rather than tumor recurrence. Similarly, intraosseous gas, which has been suggested to be pathognomonic of superimposed osteomyelitis,[24] was not seen in any of our patients with tumor recurrence. This finding did not reach significance in our study, however, in part due to its overall rarity on imaging for either entity.

These imaging findings are readily incorporated into clinical practice and were highly reproducible among observers in our study. The near-perfect agreement indicated by the very high κ values for each of the imaging findings evaluated in this study suggests that interpretation of these imaging findings will be consistent when implemented clinically.

There were several limitations to our study. We purposefully geared our initial search to evaluate only lesions that were either thought to be ORN on imaging or for which the interpreting radiologist entertained the diagnosis of ORN versus tumor recurrence. While this search results in a selection bias toward cases in which the 2 entities look similar and results in a greater number of patients with ORN, we would argue that these "problem cases" are most relevant to everyday practice and the situation in which specific imaging findings may be the most useful. Additionally, not all patients in our study with ORN had pathologic correlation; in many cases, the clinician and patient preferred a noninvasive method of follow-up. As such, it is possible that undetected tumor recurrence occurred in the bed of ORN, confounding evaluation of imaging findings. However, we believe the chances of recurrent tumor remaining stable on imaging studies during a 2-year period are relatively low. Finally, clinical variables such as radiation dose and time from radiation were not considered in our analysis because we, instead, chose to focus on the imaging picture as it was presented to an interpreting radiologist.

CONCLUSIONS

The presence of a discrete solid or cystic mass is associated with tumor recurrence, while bony sclerosis, though not common, was seen exclusively in the setting of ORN in our study. Permeative rather than lucent trabecular loss was most often seen in the setting of ORN, but it may also be seen in a minority of patients with recurrent tumor. Finally, while an elevated SUV does suggest a diagnosis of tumor recurrence, the significant overlap of SUV values in patients with tumor recurrence and ORN renders SUV values relatively impractical for use on an individual clinical basis.

REFERENCES

1. Rabin BM, Meyer JR, Berlin JW, et al. **Radiation-induced changes in the central nervous system and head and neck.** *Radiographics* 1996;16:1055–72
2. Rayatt SS, Mureau MA, Hoffer SO. **Osteoradionecrosis of the mandible: etiology, prevention, diagnosis and treatment.** *Indian J Plast Surg* 2007;40:65–71
3. Bras J, de Jonge HK, van Merkesteyn JP. **Osteoradionecrosis of the mandible: pathogenesis.** *Am J Otolaryngol* 1990;11:244–50
4. Chopra S, Kamdar D, Ugur O, et al. **Factors predictive of the severity of osteoradionecrosis of the mandible.** *Head Neck* 2011;33:1600–05
5. Epstein JB, Wong FL, Stevenson-Moore P. **Osteoradionecrosis: clinical experience and a proposal for classification.** *J Oral Maxillofac Surg* 1987;45:104–10
6. Støre G, Boysen M. **Mandibular osteonecrosis: clinical behavior and diagnostic aspects.** *Clin Otolaryngol Allied Sci* 2000;25:378–84
7. Reuther T, Schuster T, Mende U, et al. **Osteoradionecrosis of the jaw as a side effect of radiotherapy of head and neck tumour patients: a report of a thirty year retrospective review.** *Int J Oral Maxillofac Surg* 2003;32:289–95
8. Jereczek-Fossa BA, Orrechia R. **Radiotherapy-induced mandibular bone complications.** *Cancer Treat Rev* 2002;28:65–74
9. Studer G, Grätz KW, Glanzmann C. **Osteoradionecrosis of the mandibula in patients treated with different fractionations.** *Stranhlenther Onkol* 2004;180:233–40
10. Chong J, Hinckley L, Ginsberg L. **Masticator space abnormalities associated with mandibular osteoradionecrosis: MR and CT findings in five patients.** *AJNR Am J Neuroradiol* 2000;21:175–78
11. Hamilton JD, Lai SY, Ginsberg LE. **Superimposed infection in mandibular osteoradionecrosis: diagnosis and outcome.** *J Comput Assist Tomogr* 2012;36:725–31
12. Yoo JS, Rosenthal DI, Mitchell K, et al. **Osteoradionecrosis of the hyoid bone: imaging findings.** *AJNR Am J Neuroradiol* 2010;31:761–66
13. Glastonbury CM, Parker EE, Hoang JK. **The postradiation neck: evaluating response to treatment and recognizing complications.** *AJR Am J Roentgenol* 2010;195:W164–71
14. Wu L, Liu J, Wang C, et al. **Osteoradionecrosis of the upper cervical spine after radiation therapy for head and neck cancer: differentiation from recurrent of metastatic disease with MR imaging.** *Radiology* 2012;264:136–45
15. Landis JR, Koch GG. **The measurement of observer agreement for categorical data.** *Biometrics* 1977;33:159–74
16. Liu S-H, Chang J, Ng SH, et al. **False positive fluorine-18 fluorodeoxy-D-glucose positron emission tomography finding caused by osteoradionecrosis in a nasopharyngeal carcinoma patient.** *Br J Radiol* 2004;77:257–60
17. Krabbe C, Pruim J, Dijkstra P, et al. **18F-FDG PET as a routine posttreatment surveillance tool in oral and oropharyngeal squamous cell carcinoma: a prospective study.** *J Nucl Med* 2009;50:1940–47
18. Abgral R, Querellou S, Potrad G, et al. **Does 18F-FDG PET/CT improve the detection of posttreatment recurrence of head and neck squamous cell carcinoma in patients negative for disease on clinical follow up?** *J Nucl Med* 2009;50:24–29
19. Ng SH, Liu MH, Ko SF, et al. **Post treatement imaging of the nasopharynx.** *Eur J Radiol* 2002;44:82–95
20. King AD, Griffith JF, Abrigo JM, et al. **Osteoradionecrosis of the upper cervical spine: MR imaging following radiotherapy for nasopharyngeal carcinoma.** *Eur J Radiol* 2010;73:629–35
21. Hermans R, Fossion E, Ioannides C, et al. **CT findings in osteoradionecrosis of the mandible.** *Skeletal Radiol* 1996;25:31–36
22. Marx RE. **Osteoradionecrosis: a new concept of its pathophysiology.** *J Oral Maxillofac Surg* 1983;41:283–88
23. Store G, Larheim TA. **Mandibular osteoradionecrosis: a comparison of computed tomography with panoramic radiography.** *Dentomaxillofac Radiol* 1999;28:295–300
24. Merine D, Fishman EK, Magid D. **CT detection of sacral osteomyelitis associated with pelvic abscesses.** *J Comput Assist Tomogr* 1988;12:118–21

Comparison of the T2 Relaxation Time of the Temporomandibular Joint Articular Disk between Patients with Temporomandibular Disorders and Asymptomatic Volunteers

N. Kakimoto, H. Shimamoto, J. Chindasombatjaroen, T. Tsujimoto, S. Tomita, Y. Hasegawa, S. Murakami, and S. Furukawa

ABSTRACT

BACKGROUND AND PURPOSE: T2 relaxation time is a quantitative MR imaging parameter used to detect degenerated cartilage in the knee and lumbar intervertebral disks. We measured the T2 relaxation time of the articular disk of the temporomandibular joint in patients with temporomandibular disorders and asymptomatic volunteers to demonstrate an association between T2 relaxation time and temporomandibular disorder MR imaging findings.

MATERIALS AND METHODS: One hundred forty-four patients with temporomandibular disorders and 17 volunteers were enrolled in this study. An 8-echo spin-echo sequence for measuring the T2 relaxation times was performed in the closed mouth position, and the T2 relaxation time of the entire articular disk was measured. Patients were classified according to the articular disk location and function, articular disk configuration, presence of joint effusion, osteoarthritis, and bone marrow abnormalities.

RESULTS: The T2 relaxation time of the entire articular disk was 29.3 ± 3.8 ms in the volunteer group and 30.7 ± 5.1 ms in the patient group ($P = .177$). When subgroups were analyzed, however, the T2 relaxation times of the entire articular disk in the anterior disk displacement without reduction group, the marked or extensive joint effusion group, the osteoarthritis-positive group, and the bone marrow abnormality–positive group were significantly longer than those in the volunteer group ($P < .05$).

CONCLUSIONS: The T2 relaxation times of the articular disk of the temporomandibular joint in patients with progressive temporomandibular disorders were longer than those of healthy volunteers.

ABBREVIATIONS: ADDWOR = anterior disk displacement without reduction; ADDWR = anterior disk displacement with reduction; PADDWOR = partial anterior disk displacement without reduction; PADDWR = partial anterior disk displacement with reduction; TMD = temporomandibular disorders; TMJ = temporomandibular joint

Disorders of the temporomandibular joint (TMJ) are characterized by intra-articular positional and/or structural abnormalities.[1] MR imaging is the preferred imaging technique for diagnosing temporomandibular disorders (TMD).[2] It has been reported that the diagnostic accuracy of MR imaging for the assessment of the articular disk position and articular disk formation is 95% and for the assessment of osseous changes is 93% in postmortem examinations.[3] Numerous studies of TMD by using MR imaging have reported qualitative and morphologic evaluations, because the most important subgroup of articular abnormalities in patients with TMD includes different forms of articular disk displacement and deformation of the articular disk, either with normal bony joint components or accompanied by degenerative joint diseases such as osteoarthritis.[4] Other MR imaging findings of TMD, including joint effusion and bone marrow abnormalities, have also been evaluated qualitatively and morphologically.[5,6]

The T2 relaxation time is a quantitative MR imaging parameter derived from multiecho spin-echo sequences. Measuring the T2 relaxation times by using MR imaging has been reported to detect degenerated cartilage in the knee and lumbar intervertebral disk.[7-11] The T2 relaxation time of the articular disk of the TMJ in healthy volunteers has been previously described by using a 3T MR imaging system,[12] but the T2 relaxation time of the articular disk of the TMJ in patients with TMD has not been reported, to our knowledge.

We hypothesized that the T2 relaxation time of the articular

Received October 23, 2013 accepted after revision December 11.

From the Department of Oral and Maxillofacial Radiology (N.K., H.S., T.T., S.T., S.M., S.F.), Osaka University Graduate School of Dentistry, Osaka, Japan; Department of Oral and Maxillofacial Radiology (J.C.), Faculty of Dentistry, Mahidol University, Bangkok, Thailand; and Department of Dentistry and Oral Surgery (Y.H.), Hyogo College of Medicine, Hyogo, Japan.

A part of this paper previously presented at: 18th International Congress of Dento-Maxillo-Facial Radiology, May 25-29, 2011; Hiroshima, Japan.

Please address correspondence to Naoya Kakimoto, DDS, PhD, Department of Oral and Maxillofacial Radiology, Osaka University Graduate School of Dentistry, 1-8 Yamadaoka, Suita, Osaka 5650871, Japan; e-mail: kakimoto@dent.osaka-u.ac.jp

http://dx.doi.org/10.3174/ajnr.A3880

disk of the TMJ correlates with the qualitative and morphologic variations in the pathology of the TMJ. The aims of this study were to measure the T2 relaxation time of the articular disk of the TMJ in patients with TMD and asymptomatic volunteers to demonstrate any association between T2 relaxation time and MR image findings of TMD.

MATERIALS AND METHODS

Institutional review board approval was obtained for this study, and all patients and volunteers provided their written informed consent after the nature of the procedure was fully explained.

Study Population

From 2009 to 2012, one hundred fifty patients with TMD referred for MR imaging due to facial or TMJ pain; mandibular dysfunction, such as clicking, crepitation, or locking; or suspected internal derangement were recruited for this study. Six patients were excluded from this study due to motion or metallic artifacts on MR images. After these exclusions, the remaining 144 patients (110 females, 34 males; median age, 36 years; age range, 11–80 years) were analyzed. In addition, 21 asymptomatic volunteers underwent MR imaging examinations. The MR images of the TMJ in 4 of these volunteers demonstrated abnormal findings such as anterior disk displacement; hence, data from these volunteers were excluded from this study. The remaining 17 asymptomatic healthy volunteers (5 women, 12 men; median age, 26 years; age range, 23–32 years) were considered to have normal TMJs.

MR Imaging

All subjects were examined by using a 1.5T MR imaging scanner (Signa HDxt 1.5T; GE Healthcare, Milwaukee, Wisconsin) equipped with a TMJ surface coil. The imaging protocol to diagnose TMD consisted of oblique sagittal and coronal fast spin-echo proton-attenuation-weighted sequences (TR/TE/echo-train length/NEX, 2500 ms/20 ms/8/2); fat-suppressed T2-weighted sequences (TR/TE/echo-train length/NEX, 2000 ms/85 ms/16/3) obtained perpendicular and parallel to the long axis of the mandibular condyle in a closed-mouth position; and sagittal spin-echo proton-attenuation-weighted sequences (TR/TE/echo-train length/NEX, 800 ms/24 ms/4/2) in closed- and open-mouth positions with the following parameters: 120 × 120 mm FOV; 256 × 160 matrix size; 3-mm section thickness; and 1-mm gap. In addition to these sequences, oblique sagittal 8-echo fast spin-echo sequences were obtained perpendicular to the long axis of the mandibular condyle in a closed-mouth position to measure the T2 relaxation times with the following parameters: TR/TE/NEX = 1000 ms/8.9, 17.8, 26.7, 35.6, 44.5, 53.4, 62.4, 71.3 ms/2; 120 × 120 mm FOV; 256 × 160 matrix size; 4-mm section thickness; and 1-mm gap. The total acquisition time for this T2 relaxation time–measuring sequence was 5 minutes 22 seconds for each joint.

MR Image Evaluation

All MR images were independently evaluated by 2 oral and maxillofacial radiologists (N.K. with 16 years of experience and H.S. with 8 years of experience). In cases of disagreement, the final diagnosis was made by consensus. We evaluated the following features: the articular disk position and function, the articular disk configuration, joint effusion, osteoarthritis, and bone marrow abnormalities.

The articular disk position and function were classified into 5 categories, as reported by Tasaki et al,[13] with some modifications: normal superior, partial anterior disk displacement with reduction (PADDWR), partial anterior disk displacement without reduction (PADDWOR), anterior disk displacement with reduction (ADDWR), or anterior disk displacement without reduction (ADDWOR) in closed- and open-mouth-position sagittal proton-attenuation-weighted MR images. The articular disk configuration was classified into 6 categories, as reported by Murakami et al,[14] with some modifications: biconcave, biplanar, hemiconvex, thickening of the posterior band, biconvex, or folded on closed-mouth-position oblique sagittal proton-attenuation-weighted MR images. Joint effusion was classified into 4 categories, as proposed by Larheim et al[5]: no or minimal fluid, moderate fluid, marked fluid, or extensive fluid on closed-mouth-position oblique sagittal fat-suppressed T2-weighted MR images. Osteoarthritis was classified into negative and positive, in which condylar osteophytes or erosion was observed, as reported by Kirk[15] on closed-mouth-position oblique sagittal proton-attenuation-weighted MR images. Bone marrow abnormalities of the mandibular condyle were classified into negative and positive on the basis of the presence of edema or osteonecrosis, as described by Larheim et al[16] on closed-mouth-position oblique sagittal proton-attenuation- and T2-weighted MR images.

Measurement of the T2 Relaxation Time

The 8-echo spin-echo image data were transferred to an independent workstation (Advantage Workstation, Version 4.4; GE Healthcare). ROIs for measuring the T2 relaxation time were manually placed by 2 observers independently (N.K. and H.S.) on the entire articular disk, the anterior band of the articular disk, and the posterior band of the articular disk (Fig 1). The T2 relaxation time of the articular disk was calculated by using a software program (Functool 4.4.5; GE Healthcare).

The average value measured by the 2 observers was defined as the T2 relaxation time. For the measurement of the intraobserver reproducibility, 1 observer (N.K.) placed ROIs on the entire articular disk in 17 healthy volunteers 10 times on different days.

Statistical Analysis

As mentioned above, the coefficient of variation of 10 datasets of the entire articular disk in healthy volunteers was calculated to evaluate the intraobserver reproducibility. To evaluate the interobserver reproducibility, the Pearson product moment correlation coefficient was calculated for the 2 observers' data for the T2 relaxation time of the entire articular disk in healthy volunteers and patients. In the healthy volunteers, a paired *t* test was used to compare the T2 relaxation times of the entire articular disk between the right and left TMJs and between the anterior and posterior bands of the articular disk. A P value $< .05$ was considered a significant difference. To compare the T2 relaxation times of the entire articular disk between healthy volunteers and patients, the Mann-Whitney *U* test or the Kruskal Wallis test was performed. A P value $< .05$ was considered a significant difference. A post hoc

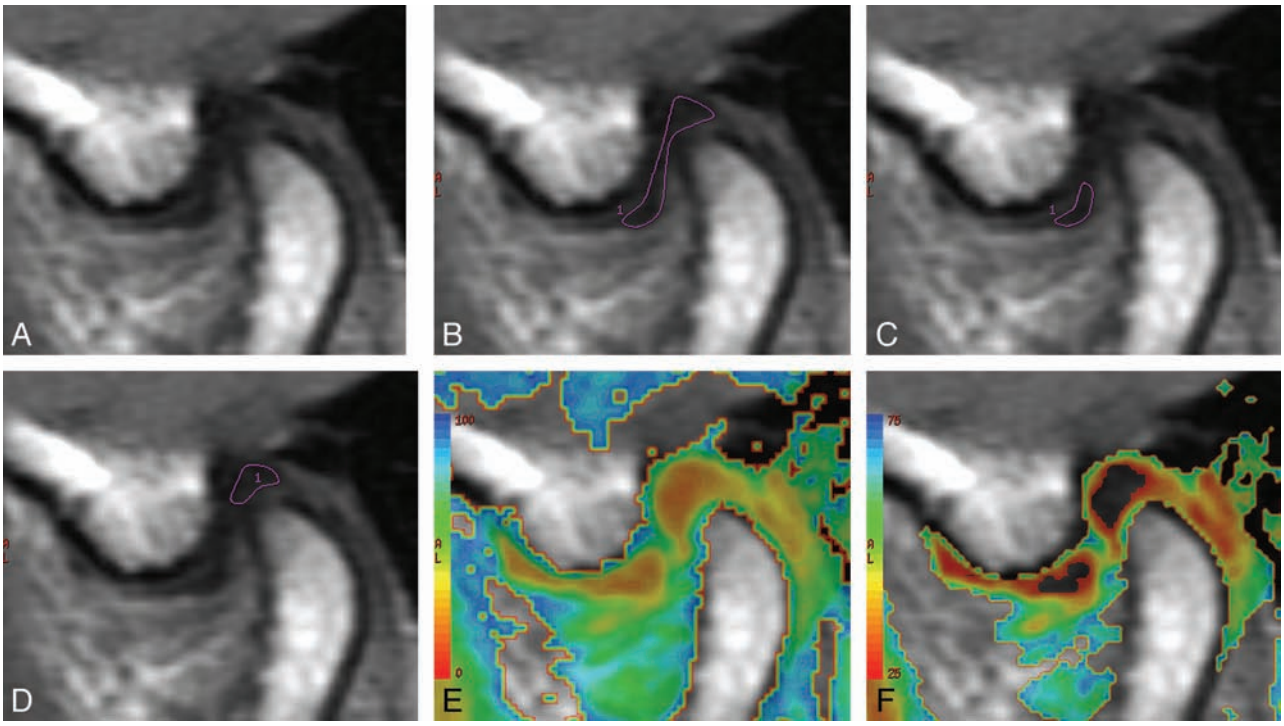

FIG 1. MR images of the articular disk of the TMJ, in a volunteer, used to measure the T2 relaxation time. *A*, The source MR image of the articular disk. The ROIs used for the measurement of the T2 relaxation time of the entire articular disk (*B*), the anterior band of the articular disk (*C*), and the posterior band of the articular disk (*D*). The T2 relaxation times on a color map ranging from 0 to 100 ms (*E*) and 25 to 75 ms (*F*).

pair-wise analysis was performed by using the Mann-Whitney *U* test with a Bonferroni correction, in which a *P* value of $< .05/5$ for the articular disk position and function and joint effusion, .05/7 for the articular disk configuration, and .05/3 for osteoarthritis and bone marrow abnormalities was considered a significant difference. Multiple-regression analyses with simultaneous entry were used to identify important predictor variables for the T2 relaxation time of the entire disk among the MR image interpretations, and the patient age and sex were used as confounding variables. All of the statistical analyses were performed by using a commercially available software package (Statistical Package for the Social Sciences, Version 16.0; IBM, Armonk, New York).

RESULTS

The MR imaging findings of TMJs in healthy volunteers and patients are summarized in Table 1. In the healthy volunteers, all joints showed normal articular disk position and function, and 32 biconcave and 2 biplanar disks were found. All joints were classified as having no or minimal fluid for joint effusion and were negative for both osteoarthritis and bone marrow abnormalities. In patients with TMD, most joints showed a normal articular disk position and function followed by anterior disk displacement without reduction, a biconcave disk, and no or minimal fluid for joint effusion and were negative for osteoarthritis and bone marrow abnormalities.

Intraobserver reproducibility by using the coefficient of variation of the T2 relaxation times of the entire articular disk in the healthy volunteers ranged from 1.1% to 4.7%. Interobserver reproducibilities, determined by using the Pearson product moment correlation coefficient for the 2 observers' data for the entire

Table 1: The patient and volunteer characteristics and MR imaging findings

	Volunteers	Patients
Cases	17	144
Male	12	34
Female	5	110
Age (yr)		
Range	23–32	11–80
Median	26	36
Articular disk position and function (joints)		
Normal superior	34	113
PADDWR	0	18
PADDWOR	0	2
ADDWR	0	48
ADDWOR	0	107
Articular disk configuration (joints)		
Biconcave	32	143
Biplanar	2	20
Hemiconvex	0	37
Thickening of the posterior band	0	36
Biconvex	0	7
Folded	0	45
Joint effusion (joints)		
None or minimal fluid	34	169
Moderate fluid	0	80
Marked fluid	0	24
Extensive fluid	0	15
Osteoarthritis (joints)		
Negative	34	237
Positive	0	51
Bone marrow abnormality (joints)		
Negative	34	260
Positive	0	28

Table 2: The T2 relaxation time of the articular disk

	T2 Relaxation Time (ms)	*P*
Volunteers		
Left TMJ	29.6 ± 3.9	
Right TMJ	28.9 ± 3.8	.585
All TMJs	29.3 ± 3.8	
Anterior band of all TMJs	29.0 ± 5.4	
Posterior band of all TMJs	26.5 ± 3.6	.007
Male	29.0 ± 3.6	
Female	29.8 ± 4.3	.620
Age ≤26 years	29.4 ± 3.9	
Age >26 years	29.1 ± 3.8	.814
Patients		
All TMJs	30.7 ± 5.1	.177[a]
Male	29.5 ± 4.0	
Female	31.1 ± 5.4	.890
Age ≤36 years	29.5 ± 4.4	
Age >36 years	31.9 ± 5.5	<.001

[a] The T2 relaxation time of all TMJs in patients was compared with that of all TMJs in volunteers.

articular disk T2 relaxation time, were 0.862 ($P < .001$) in the healthy volunteers and 0.891 ($P < .001$) in patients.

The mean T2 relaxation times of the entire articular disk are shown in Table 2. In healthy volunteers, there was no significant difference in the T2 relaxation times of the entire disk between the left and right TMJs (29.6 ± 3.9 versus 28.9 ± 3.8 ms, $P = .585$), whereas a significant difference between the T2 relaxation times of the anterior and posterior bands was observed (29.0 ± 5.4 versus 26.5 ± 3.6 ms, $P = .007$). Moreover, there were no significant differences in the T2 relaxation times of the entire articular disk between male and female groups (29.0 ± 3.6 versus 29.8 ± 4.3 ms, $P = .620$) and between younger and older age groups (29.4 ± 3.9 versus 29.1 ± 3.8 ms, $P = .814$). When healthy volunteers were compared with patients, the mean T2 relaxation times of the entire articular disk in healthy volunteers and patients with TMD were 29.3 ± 3.8 and 30.7 ± 5.1 ms, respectively. There were no significant differences in the mean T2 relaxation times of the entire articular disk between these 2 groups ($P = .177$). In patients with TMD, there was no significant difference in the T2 relaxation time of the entire articular disk between male and female groups (29.5 ± 4.0 versus 31.1 ± 5.4 ms, $P = .890$). However, there was a significant difference in the T2 relaxation times of the entire disk between younger and older age groups (29.5 ± 4.4 versus 3.19 ± 5.5 ms, $P < .001$).

With respect to the articular disk position and function, only 2 joints were classified as PADDWOR. The data from these 2 joints were excluded from further analyses of the articular disk position and function. The mean T2 relaxation times of the entire articular disk in the normal superior patients, the PADDWR, ADDWR, and ADDWOR groups were 29.4 ± 4.2, 28.9 ± 4.0, 30.5 ± 5.3, and 32.3 ± 5.7 ms, respectively. The mean T2 relaxation time of the entire articular disk in the ADDWOR group was significantly longer than that observed in the volunteer group ($P = .005$) and the normal superior patient group ($P < .001$) (Fig 2*A*).

With respect to the articular disk configuration, the mean T2 relaxation times of the entire articular disk in the biconcave, biplanar, hemiconvex, thickening of the posterior band, biconvex, and folded groups were 30.0 ± 4.6, 29.9 ± 4.8, 32.5 ± 6.6, 30.7 ± 3.9, 31.6 ± 6.9, and 31.6 ± 5.8 ms, respectively. There were no significant differences among these groups (Fig 2*B*).

With respect to joint effusion, the mean T2 relaxation times of the entire articular disk in the patient groups with no or minimal fluid, moderate fluid, marked fluid, and extensive fluid were 30.0 ± 4.7, 30.2 ± 4.5, 34.0 ± 6.3, and 36.2 ± 5.6 ms, respectively. The mean T2 relaxation time of the entire articular disk in the marked or extensive fluid group was significantly longer than that observed in the healthy volunteer group ($P = .002$ or $P < .001$), the patient group with no or minimal fluid ($P < .001$ or $P = .001$), and the moderate fluid group ($P = .002$ or $P < .001$) (Fig 2*C*).

With respect to osteoarthritis, the mean T2 relaxation times of the entire articular disk in patients with negative and positive findings were 29.9 ± 4.3 and 34.4 ± 6.7 ms, respectively. The mean T2 relaxation time of the entire articular disk in the osteoarthritis-positive group was significantly longer than that observed in the healthy volunteer group ($P < .001$) and the osteoarthritis-negative group ($P < .001$) (Fig 2*D*).

With respect to bone marrow abnormalities, the mean T2 relaxation times of the entire articular disk in the patients with negative and positive findings were 30.4 ± 5.0 and 33.6 ± 5.9 ms, respectively. The mean T2 relaxation time of the entire articular disk in the bone marrow abnormality–positive group was significantly longer than that observed in the healthy volunteer group ($P = .003$) and the bone marrow abnormality–negative in the group ($P = .002$) (Fig 2*E*).

According to the multiple-regression analysis, the important variables affecting the T2 relaxation time of the entire disk were identified as osteoarthritis ($P = .001$), joint effusion ($P = .003$), and bone marrow abnormalities ($P = .02$) (Table 3). The adjusted R^2 for the multiple regression analysis for the T2 relaxation time of the entire disk was 0.957 ($P < .001$).

DISCUSSION

Quantitative measurements of the T2 relaxation time are useful for characterizing knee osteoarthritis and degenerated intervertebral disks.[7-11] The immobilization of water protons in the cartilage by the collagen-proteoglycan matrix promotes T2 decay and renders the cartilage low in signal intensity on T2-weighted images, while mobile water protons in the synovial fluid retain their high signals. A loss of collagen and proteoglycan in degenerating cartilage increases the mobility of water, thus increasing its signal intensity on T2-weighted images.[17] The T2 relaxation times of the intervertebral disk anulus fibrosus and nucleus pulposus correlate strongly with the water content and weakly with the proteoglycan content.[18] It has been reported that the T2 relaxation times of the nucleus pulposus of the intervertebral disk in the lumbar spine exhibit significant differences in disks with herniation and anular tears compared with disks without these abnormalities,[10] and the T2 relaxation time in lumbar disks was reported to be correlated with the stage of disk degeneration and patient age.[11]

Measurement of the T2 relaxation time of the TMJ articular disk in normal joints has only been performed in 1 previous study.[12] In that study, the T2 relaxation time of the entire articular disk of the normal TMJ was 40.21 ± 2.95 ms, which was longer than the value measured in our study. They used a 3T MR imaging scanner to measure the T2 relaxation time of the articular disk,

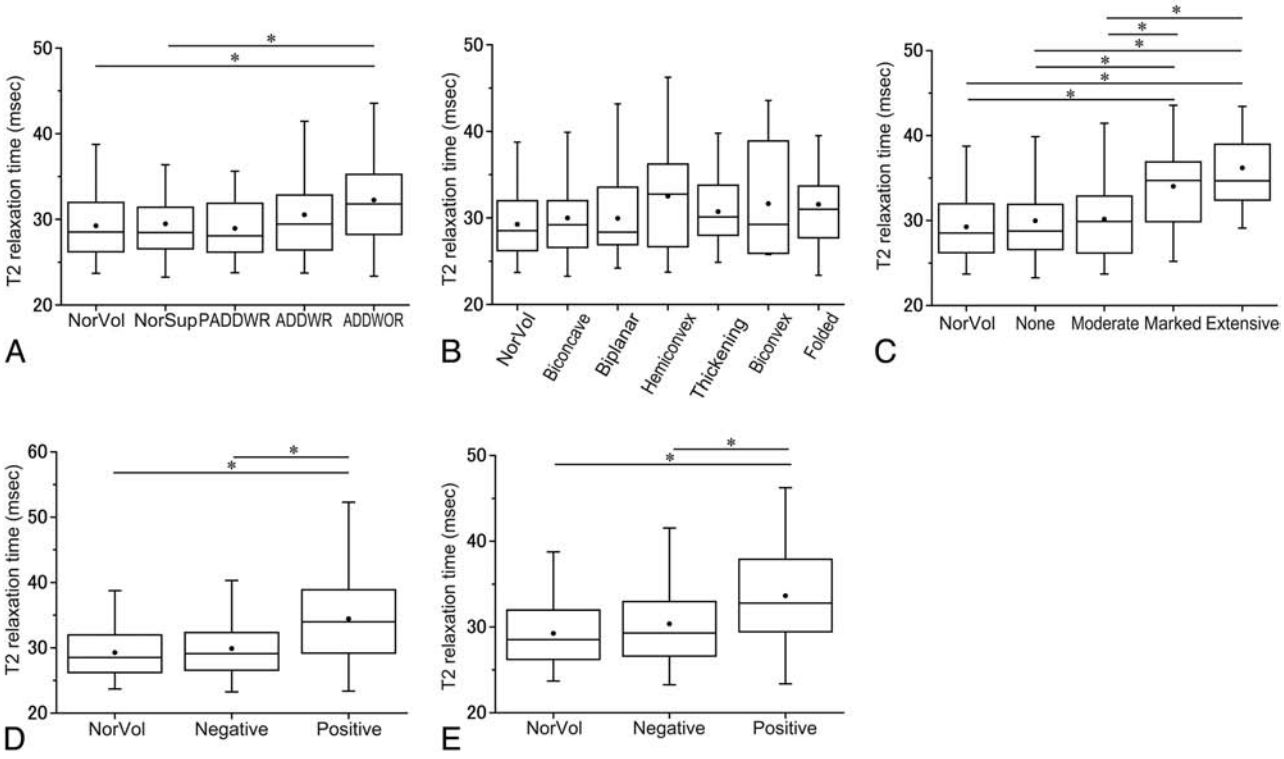

FIG 2. The T2 relaxation times according to the MR image interpretations. *A*, The T2 relaxation times according to the articular disk position and function categories. The asterisk indicates $P < .05/5$ in the Mann-Whitney test with a Bonferroni correction. *B*, The T2 relaxation times according to the articular disk configuration categories. "Thickening" indicates thickening of the posterior band. *C*, The T2 relaxation times according to the joint effusion categories. "None" indicates no or minimal fluid; "Moderate," moderate fluid; "Marked," marked fluid; and "Extensive," extensive fluid. The asterisk indicates $P < .05/5$ in the Mann-Whitney test with a Bonferroni correction. *D*, The T2 relaxation times according to the osteoarthritis categories. The asterisk indicates $P < .05/3$ in the Mann-Whitney test with a Bonferroni correction. *E*, The T2 relaxation times according to the bone marrow abnormality categories. The asterisk indicates $P < .05/3$ in the Mann-Whitney test with a Bonferroni correction. NorVol indicates healthy volunteers.

Table 3: The multiple regression model for T2 relaxation time of the entire disk

Variable	Unstandardized Coefficient (ß)	Unstandardized Coefficient (SE)	Standardized Coefficient (ß)	*T*	*P*	95% Confidence Interval	
Disk position and function	0.652	1.116	0.052	0.585	.559	−1.543	2.848
Disk configuration	−1.658	1.014	−0.12	−1.635	.103	−3.653	0.337
Joint effusion	2.467	0.838	0.188	2.944	.003	0.819	4.116
Osteoarthritis	3.986	1.221	0.273	3.264	.001	1.583	6.389
Bone marrow abnormalities	2.896	1.243	0.19	2.331	.02	0.451	5.341

but we used a 1.5T scanner. They also measured the T2 relaxation time at the anterior, middle, and posterior band and found that the middle zone of the articular disk showed longer T2 relaxation times than the anterior and posterior bands. In contrast to our study, there was no significant difference in the T2 relaxation times between the anterior and posterior bands. It has been reported that the elastic fiber attenuation of the anterior and posterior bands of the articular disk of the TMJ is significantly different.[19] Therefore, the T2 relaxation time of both bands may be different, as shown in our study. Further investigations might be necessary to confirm which findings are appropriate and whether there are population-based differences or scanner magnet-strength differences. Moreover, in patients with TMD, the T2 relaxation time of the entire articular disk in the older age group was significantly longer than that in the younger age group. Further investigations are needed for the correlation of age or duration of TMD and the T2 relaxation time.

The TMJ articular disk is composed of collagen fibers, proteoglycans, and tissue fluid.[20] It has been reported that the content of glycosaminoglycan, a polysaccharide attached to a core protein in proteoglycan, in the articular disk of the TMJ in patients with anterior disk displacement and those with chronic closed lock is considerably lower than that observed in normal disk tissue.[21,22] Therefore, the composition of the articular disk is thought to change under the above conditions. In this study, although patients and healthy volunteers showed no differences in the T2 relaxation time of the entire articular disk, the T2 relaxation times of the entire articular disk in the ADDWOR group, the severe joint effusion group, the osteoarthritis-positive group, and the bone marrow abnormality–positive group were significantly longer than that observed in the volunteer group. The multiple regression analyses showed that osteoarthritis, joint effusion, and bone marrow abnormalities were important variables affecting the T2 relaxation time of the entire disk. This finding means that

the T2 relaxation time of the articular disk is longer in patients with advanced TMD findings on MR imaging. Therefore, the T2 relaxation time of the articular disk of the TMJ may correlate with a progressive course of TMD.

It has been reported that the articular disk configuration changed from biconcave configuration to distorted configuration after disk displacement.[14] Then the T2 relaxation time of the distorted articular disk may show a value similar to that of the T2 relaxation time of the ADDWOR group. In our study, the T2 relaxation times of the hemiconvex, thickening of the posterior band, biconvex, and folded group were 32.5 ± 6.6, 30.7 ± 3.9, 31.6 ± 6.9, and 31.6 ± 5.8 ms, respectively, and that of ADDWOR group was 32.3 ± 5.7 ms. These T2 relaxation times were fairly similar. Although there were no significant differences among the T2 relaxation times of these disk-configuration groups, further study is needed.

There are some limitations associated with the present study. First, the T2 relaxation times were only measured on the central portion of the articular disk. The medial and lateral areas of the articular disk could not be evaluated because the section thickness of the MR images used to measure the T2 relaxation time was set to 4 mm with a 1-mm intersection gap, and this thickness led to a limited volume of the articular disk appearing on MR images. Second, there was no histopathologic correlation with the T2 relaxation time of the articular disk in this study. Almost all patients with TMD were treated conservatively with medication, splint therapy, or physical therapy, and due to the high diagnostic accuracy of MR imaging for assessing TMD,[3] the conditions of patients were not confirmed histopathologically. On the basis our study, the potential alterations in the T2 relaxation time of the articular disk may result from underlying pathologic conditions; thus, the T2 relaxation time can provide important information about TMD. Third, there was no clinical correlation such as pain scale with the T2 relaxation time of the articular disk in this study. Further studies with clinical correlation are needed to confirm the significance of the T2 relaxation time.

CONCLUSIONS

The T2 relaxation time of the entire articular disk was 29.3 ± 3.8 ms in healthy volunteers and 30.7 ± 5.1 ms in patients with TMD, and there was no significant difference between these groups. The T2 relaxation times of the entire articular disk in the ADDWOR group, the severe joint effusion group, the osteoarthritis-positive group, and the bone marrow abnormality–positive group were, however, significantly longer than those observed in the volunteer group; and the T2 relaxation times of the articular disk of the TMJ in patients with progressive TMD were longer than those of healthy volunteers. Hence, the T2 relaxation time of the TMJ articular disk may correlate with a progressive course of TMD.

REFERENCES

1. Tanaka E, Detamore MS, Mercuri LG. **Degenerative disorders of the temporomandibular joint: etiology, diagnosis, and treatment.** *J Dent Res* 2008;87:296–307
2. Larheim TA, Westesson PL. **TMJ imaging.** In: Laskin DM, Greene CS, Hylander WL, eds. *Temporomandibular Disorders An Evidence-Based Approach to Diagnosis and Treatment.* Chicago: Quintessence Publishing Co.; 2006:149–80
3. Tasaki MM, Westesson PL. **Temporomandibular joint: diagnostic accuracy with sagittal and coronal MR imaging.** *Radiology* 1993; 186:723–29
4. Larheim TA. **Current trends in temporomandibular joint imaging.** *Oral Surg Oral Med Oral Pathol Oral Radiol Endod* 1995;80:555–76
5. Larheim TA, Westesson PL, Sano T. **MR grading of temporomandibular joint fluid: association with disk displacement categories, condyle marrow abnormalities and pain.** *Int J Oral Maxillofac Surg* 2001;30:104–12
6. Sano T, Westesson PL, Larheim TA, et al. **The association of temporomandibular joint pain with abnormal bone marrow in the mandibular condyle.** *J Oral Maxillofac Surg* 2000;58:254–57, discussion 258–59
7. Dunn TC, Lu Y, Jin H, et al. **T2 relaxation time of cartilage at MR imaging: comparison with severity of knee osteoarthritis.** *Radiology* 2004;232:592–98
8. Koff MF, Amrami KK, Kaufman KR. **Clinical evaluation of T2 values of patellar cartilage in patients with osteoarthritis.** *Osteoarthritis Cartilage* 2007;15:198–204
9. Ludescher B, Effelsberg J, Martirosian P, et al. **T2- and diffusion-maps reveal diurnal changes of intervertebral disc composition: an in vivo MRI study at 1.5 Tesla.** *J Magn Reson Imaging* 2008;28:252–57
10. Trattnig S, Stelzeneder D, Goed S, et al. **Lumbar intervertebral disc abnormalities: comparison of quantitative T2 mapping with conventional MR at 3.0 T.** *Eur Radiol* 2010;20:2715–22
11. Marinelli NL, Haughton VM, Anderson PA. **T2 relaxation times correlated with stage of lumbar intervertebral disk degeneration and patient age.** *AJNR Am J Neuroradiol* 2010;31:1278–82
12. Cao Y, Xia C, Wang S, et al. **Application of magnetic resonance T2 mapping in the temporomandibular joints.** *Oral Surg Oral Med Oral Pathol Oral Radiol* 2012;114:644–49
13. Tasaki MM, Westesson PL, Isberg AM, et al. **Classification and prevalence of temporomandibular joint disk displacement in patients and symptom-free volunteers.** *Am J Orthod Dentofacial Orthop* 1996;109:249–62
14. Murakami S, Takahashi A, Nishiyama H, et al. **Magnetic resonance evaluation of the temporomandibular joint disc position and configuration.** *Dentomaxillofac Radiol* 1993;22:205–07
15. Kirk WS Jr. **Sagittal magnetic resonance image characteristics and surgical findings of mandibular condyle surface disease in staged internal derangements.** *J Oral Maxillofac Surg* 1994;52:64–68
16. Larheim TA, Westesson PL, Hicks DG, et al. **Osteonecrosis of the temporomandibular joint: correlation of magnetic resonance imaging and histology.** *J Oral Maxillofac Surg* 1999;57:888–98, discussion 899
17. Blumenkrantz G, Majumdar S. **Quantitative magnetic resonance imaging of articular cartilage in osteoarthritis.** *Eur Cell Mater* 2007;13:76–86
18. Marinelli NL, Haughton VM, Munoz A, et al. **T2 relaxation times of intervertebral disc tissue correlated with water content and proteoglycan content.** *Spine* 2009;34:520–24
19. Clément C, Bravetti P, Plenat F, et al. **Quantitative analysis of the elastic fibres in the human temporomandibular articular disc and its attachments.** *Int J Oral Maxillofac Surg* 2006;35:1120–26
20. Tanaka E, van Eijden T. **Biomechanical behavior of the temporomandibular joint disc.** *Crit Rev Oral Biol Med* 2003;14:138–50
21. Axelsson S, Holmlund A, Hjerpe A. **Glycosaminoglycans in normal and osteoarthrotic human temporomandibular joint disks.** *Acta Odontol Scand* 1992;50:113–19
22. Paegle DI, Holmlund AB, Hjerpe A. **Matrix glycosaminoglycans in the temporomandibular joint in patients with painful clicking and chronic closed lock.** *Int J Oral Maxillofac Surg* 2003;32:397–400

Correlation of Prenatal and Postnatal MRI Findings in Schizencephaly

S.A. Nabavizadeh, D. Zarnow, L.T. Bilaniuk, E.S. Schwartz, R.A. Zimmerman, and A. Vossough

ABSTRACT

BACKGROUND AND PURPOSE: Schizencephaly is a rare malformation of the brain characterized by a gray matter–lined defect extending from the pial surface to the lateral ventricles. The purpose of this study was to correlate imaging findings of schizencephaly and associated anomalies on fetal and postnatal MR imaging and assess possible changes that may occur from the prenatal-to-postnatal state.

MATERIALS AND METHODS: A retrospective review of subjects with schizencephaly who had both pre- and postnatal MR imaging was performed. Subject age, cleft type, number, location, and features of the defects and associated anomalies were recorded. Normalized dimensions of the defect and ipsilateral ventricle were measured and correlated to changes in the clefts between pre- and postnatal imaging.

RESULTS: Ten subjects with 18 clefts (8 bilateral) were included. Most defects (83%) were open on prenatal MR imaging, but 47% of those were found to have subsequently closed on postnatal imaging. Evidence of prior hemorrhage was seen in 83%. Prenatal MR imaging detected all cases of an absent septum pellucidum but detected a fraction of gross polymicrogyria and missed all cases of optic nerve hypoplasia. The normalized ipsilateral ventricular and inner and middle width dimensions of the defects were significantly decreased at postnatal imaging ($P < .05$). The widths of the defects, ventricular width, and presence of hemorrhage were not predictors of closure of prenatally diagnosed open defects ($P > .05$).

CONCLUSIONS: In our series, nearly half of prenatally open schizencephaly defects had closed on postnatal imaging. Prenatal MR imaging was only able to demonstrate some of the associated anomalies.

Schizencephaly is a rare malformation of the central nervous system characterized by a gray matter–lined defect extending from the pial surface to the lateral ventricles. The etiology of schizencephaly is poorly understood; however, it appears to be heterogeneous.[1-3] The presence of gray matter lining the defects, distinguishing schizencephaly from porencephaly, is usually ascribed to the damage to the radial glial cell fibers or to the molecules that promote neuronal migration and timing during pregnancy.[2,4] Despite early reports of the association of schizencephaly and mutations of the *EMX2* homeobox gene,[5] this association has not been verified in further studies.[6] The common pathophysiology of injury is frequently ascribed to a vascular disruption, hypoxia-ischemia, and/or prenatal infection at critical time points during neuronal development,[1-3] though there are some reports favoring schizencephaly as a developmental disorder.[7-9]

Classically, schizencephaly has been divided into "closed" or "closed-lip" defects, in which the walls appose one another within the defect, and "open" or "open-lip" defects, in which CSF fills the defect all the way from the lateral ventricle to the overlying subarachnoid space.[10] Open lesions have been further subclassified as small or large according to size of the defect.[10] These classifications have prognostic significance because it has been shown that a small, unilateral closed defect without involvement of the motor cortex can be associated with seizures but otherwise normal development.[10] The prognosis is poorer with open and bilateral defects.[2,10,11] Associated anomalies, such as optic nerve hypoplasia, absence of the septum pellucidum, and other migrational abnormalities, will also adversely affect the prognosis.[2,9,12,13]

MR imaging was reported to prenatally diagnose schizencephaly as early as 1989.[14] On the basis of the current literature, the

Received September 26, 2013; accepted after revision November 19.

From the Department of Radiology, Children's Hospital of Philadelphia, Philadelphia, Pennsylvania; and Department of Radiology, University of Pennsylvania, Philadelphia, Pennsylvania.

Please address correspondence to Arastoo Vossough, PhD, MD, Department of Radiology, Children's Hospital of Philadelphia, 324 S 34th St, Wood 2115, Philadelphia, PA 19104; e-mail: vossough@email.chop.edu

Indicates article with supplemental on-line table.

http://dx.doi.org/10.3174/ajnr.A3872

imaging appearance of schizencephaly on fetal MR imaging is considered identical to that in postnatal MR imaging.[2] The purpose of this study was to correlate imaging findings of schizencephaly and associated anomalies on fetal and postnatal MR imaging and to assess the possible changes that may occur from the prenatal-to-postnatal state on MR imaging.

MATERIALS AND METHODS

A retrospective review of fetal MRI at our institution was performed. A key word search of the PACS was done to find fetuses that were diagnosed with schizencephaly or porencephaly between 2000 and 2012. We included patients with the prenatal diagnosis of porencephaly in our primary search due to the potential difficulty of differentiating schizencephaly and porencephaly on prenatal MR imaging in some cases. Medical records were reviewed to determine which fetuses had postnatal brain MR imaging available to review. Medical records were also reviewed for subject sex and age at the time of prenatal and postnatal examinations. The study was performed with the approval of the institutional review board.

Retrospective search and chart review initially revealed 44 prenatal subjects. All patients had been referred from outside institutions for fetal MR imaging at our tertiary fetal diagnosis center. The MR imaging diagnosis among these patients included 23 with bilateral schizencephaly (52.2%), 9 with unilateral schizencephaly (20.4%), 8 with porencephaly (25%), 1 with agenesis of the corpus callosum with an interhemispheric cyst (2.2%), and 1 with transmantle cortical dysplasia (without heterotopia) confirmed postnatally (2.2%). In 2 patients, the distinction between schizencephaly and porencephaly could not be made on the basis of the available prenatal imaging (4.4%) and there was no postnatal follow-up. In the end, 10 subjects had both prenatal and postnatal MR imaging confirming schizencephaly and were, therefore, included in this study. The diagnosis of schizencephaly was further confirmed on postnatal MR imaging on the basis of the presence of a gray matter–lined defect extending from the brain surface to the ventricular system. The remaining fetal patients with a diagnosis of schizencephaly were not followed at our institution and were, therefore, excluded from this study. The outcome of the excluded subjects is not known to us.

MR Imaging Protocol

Prenatal MR imaging was performed on 1.5T magnets (Siemens, Erlangen, Germany). We used the following sequences: T2 HASTE in multiple orthogonal planes (TR = 1100 ms; 2 different sequences with TEs of 78 and 64 ms each, respectively; FOV = 280 mm^2; matrix = 56 × 192; section thickness = 3 mm) and 2 different echo-planar T2* sequences with different sensitivities to susceptibility (first with TR = 5290 ms, TE = 94 ms; second with TR = 4200 ms, TE = 42 ms, generalized autocalibrating partially parallel acquisition 2; and both with flip angle = 90°, FOV = 280 mm^2, matrix = 256 × 256, section thickness = 3 mm). Also T1 FLASH (TR = 202 ms, TE = 4.76 ms, FOV = 280 mm^2, flip angle = 60°, matrix = 256 × 166, section thickness = 4 mm) was available in patients who were imaged after 26 weeks' gestational age.

Postnatal MR imaging was performed on 1.5T or 3T magnets (Siemens). The MR imaging sequences varied among subjects, given the long timeframe in this retrospective study, but included sagittal and axial T1-weighted, axial and coronal T2-weighted, axial and coronal fluid-attenuation inversion recovery, axial diffusion-weighted imaging, and axial T2* gradient-echo or susceptibility-weighted imaging.

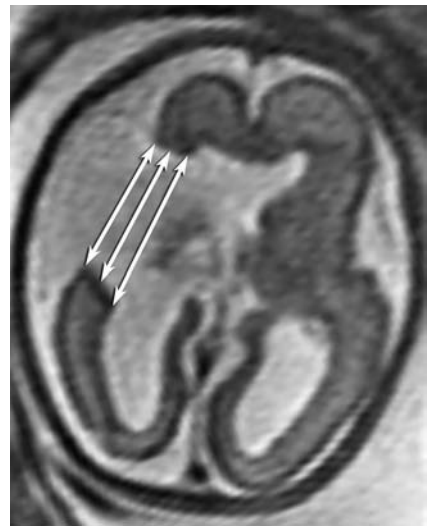

FIG 1. Measurement of the outer, middle, and inner widths of the schizencephalic cleft.

Imaging Review

All MR imaging studies of these subjects were reviewed by a pediatric neuroradiologist (with 8 years' fetal MR imaging experience) and a second-year neuroradiology fellow (with 1 year of fetal MR imaging experience) and were reported by consensus. For each scan, data on schizencephaly type, number of clefts, location of clefts, status of the cortex lining the defect, the presence or absence of a covering membrane (a thin linear membrane along the surface or depth of the cleft), the presence of signs of hemorrhage, and the presence of other anomalies were recorded. The schizencephalic clefts were considered open if CSF could be tracked through the defect from the lateral ventricle to the subarachnoid spaces. If there was complete apposition of the defect walls at any point or if the defect walls were only separated by intervening vessels in all 3 planes, the clefts were considered closed. Detection of hemorrhage was largely based on the presence of focal hypointensity on T2, hyperintensity on T1, and an excessive susceptibility effect on T2* gradient-echo or susceptibility-weighted images.

Quantitative measurements were made of the width of the schizencephalic cleft (outer, middle, and inner margins) and the width of the ipsilateral ventricle at the level of the atrium to assess a possible relationship between the size of the cleft or ventricle and changes in the appearance of the cleft between the prenatal and postnatal scans (Fig 1). Cleft-width measurements were done either on axial or coronal planes, based on the imaging plane that showed the clefts better for accurate measurement on prenatal imaging. However, they were performed consistently in the same plane between the prenatal and postnatal studies in each subject. In 2 clefts, the outer and midcleft width measurements could not be made because the clefts were large and it was difficult to deter-

mine the margins. Similarly, 2 ventricular width measurements could not be made because the cleft engulfed the region of the ventricular atrium. To account for the marked differences in head size in the various gestational and postnatal ages, we normalized all the measurements to the mean of the maximum anteroposterior and transverse inner diameters of the skull.

Statistical Analysis

Paired sample *t* tests were used to compare the absolute and normalized width of the ipsilateral ventricle and width (outer, middle, and inner) of the cleft between pre- and postnatal imaging. A χ^2 test was used to investigate the possible effect of hemorrhage between open defects that remained open and those that had closed on postnatal imaging. *T* tests were used to compare the prenatal absolute and normalized width of the ipsilateral ventricle at the level of the atrium and the width (outer, middle, and inner) of the defect between open defects that remained open and those that were closed on postnatal imaging.

RESULTS

Ten subjects with both prenatal and postnatal MR imaging were included in this study. The mean age of the subjects at the time of prenatal imaging was 27.6 ± 4.1 weeks (range, 25–35 weeks). The median age of the subjects at the time of postnatal imaging was 1.5 months (range, 1 day to 7 years) (On-line Table). The reasons for fetal MR imaging referral included sonographic suspicion or diagnosis of ventriculomegaly in 3 (30%), holoprosencephaly in 3 (30%), absence of the cavum septum pellucidum in 2 (20%), and detection of a cyst in the brain in 2 (20%), with one of the latter also diagnosed with agenesis of the corpus callosum by sonography. All patients had been referred from outside institutions for fetal MR imaging, so the actual experience of the sonography physician was not known.

Eight (80%) subjects had bilateral clefts, and 2 (20%) subjects had unilateral clefts, resulting in 18 clefts. Most (15 of 18, 83%) were open on prenatal MR imaging, but only 8 (53%) of those remained open on postnatal MR imaging, secondary to closing of the cleft in 7 (47%) (On-line Table and Figs 2 and 3). Only 3 (16%) clefts were closed on prenatal MR imaging compared with 10 (55%) on postnatal MR imaging. In all 18 clefts, there was at least partial visualization of the gray matter lining of the 2 margins (lips) of the cleft on prenatal imaging. In 67%, there was visualization of gray matter completely lining the cleft margins, and in 32%, there was only partial visualization of the gray matter lining a small portion of the cleft margins. A complete gray matter lining was visualized in all 18 clefts on postnatal imaging, confirming the diagnosis of schizencephaly. In schizencephaly, the clefts are anatomically lined with dysmorphic gray matter and polymicrogyria. Dysmorphic gray matter with polymicrogyria was grossly detectable along the cleft in only 3 of 18 (17%) subjects on prenatal imaging, with the remainder only showing an apparent smooth lining, within the resolution limits of prenatal MR imaging. Polymicrogyria separate from the defect was found in 3 subjects (17%) postnatally but was only detected in 2 of the 3 (66%) prenatally.

The septum pellucidum was absent in 9 subjects (complete in 8, partial in 1), and all were detected both prenatally and postnatally. Bilateral subependymal nodular heterotopia was also detected in 1 subject on postnatal MR imaging, which appeared to be only unilateral prenatally. Optic nerve hypoplasia was detected postnatally in 3 cases but could not be detected prenatally. A covering membrane was detected in 10 defects prenatally (Fig 4) but only persisted in 2 defects postnatally. Other associated anomalies included agenesis of the corpus callosum and coloboma in the same subject, detected both pre- and postnatally. Some evidence of prior hemorrhage was seen either on prenatal or postnatal imaging in 15 of 18 (83%) patients (Table 1).

When we compared the normalized pre- and postnatal ventricular and cleft width measurements, the normalized ipsilateral ventricular width (0.15 versus 0.12, $P = .003$), inner cleft width (0.14 versus 0.10, $P = .038$), and middle cleft width (0.15 versus 0.08, $P = .004$) were all significantly decreased postnatally compared with prenatal normalized widths. However, the normalized outer width of the defect did not significantly change between pre- and postnatal imaging (0.19 versus 0.13, $P = .09$). The χ^2 test revealed that there was no significant relationship in the prevalence of hemorrhage between open clefts that remained open postnatally and those that had closed on postnatal imaging (either pre- or postnatally detected hemorrhage, $P = .36$; prenatally detected only hemorrhage, $P = .33$; postnatally detected only hemorrhage, $P = .11$). Comparing open defects that remained open with those that closed demonstrated that although the outer, inner, and midwidths trended toward being smaller in the latter group, the differences were not statistically significant (Table 2). The normalized prenatal width of the ipsilateral lateral ventricle was also not different between defects that remained open compared with those that had closed (mean normalized width, 0.14 versus 0.16; $P = .24$; Table 2).

DISCUSSION

The results of this study suggest that most schizencephalic clefts are seen as open-lip defects in the prenatal period, and a large proportion (47%) will be seen as closed defects when imaged after birth. Most of our subjects demonstrated bilateral defects; this finding is higher than that reported in previous publications.[9,10,15,16] In previous studies of postnatal imaging of schizencephaly, open defects were the predominant pattern in some,[10,15] while closed defects were more common in another report.[9] None of these larger case series studies had serial imaging or had documented open defects converting to closed defects as we have shown in this study. Open defects were consistently the predominant pattern in prenatal imaging of schizencephaly in previous series,[3,17] which is consistent with our results.

The fine membrane that covers the roof or floor of the defect is likely a remnant of the pia mater or ependyma and is a rarely reported finding in schizencephaly.[15] In our series, the prevalence of detecting a membrane was much more common prenatally. Part of this may be due to closure of the defect in some cases; however, we had open defects with prenatally documented membranes that remained open after birth but a membrane could no longer be visualized. The reason the membrane is no longer seen postnatally is not clear, but it may be that chronic distention and tension on the membrane leads to its thinning and dissolution. A similar phenomenon is commonly observed in the septum pellucidum in patients with long-standing or severe hydrocephalus.

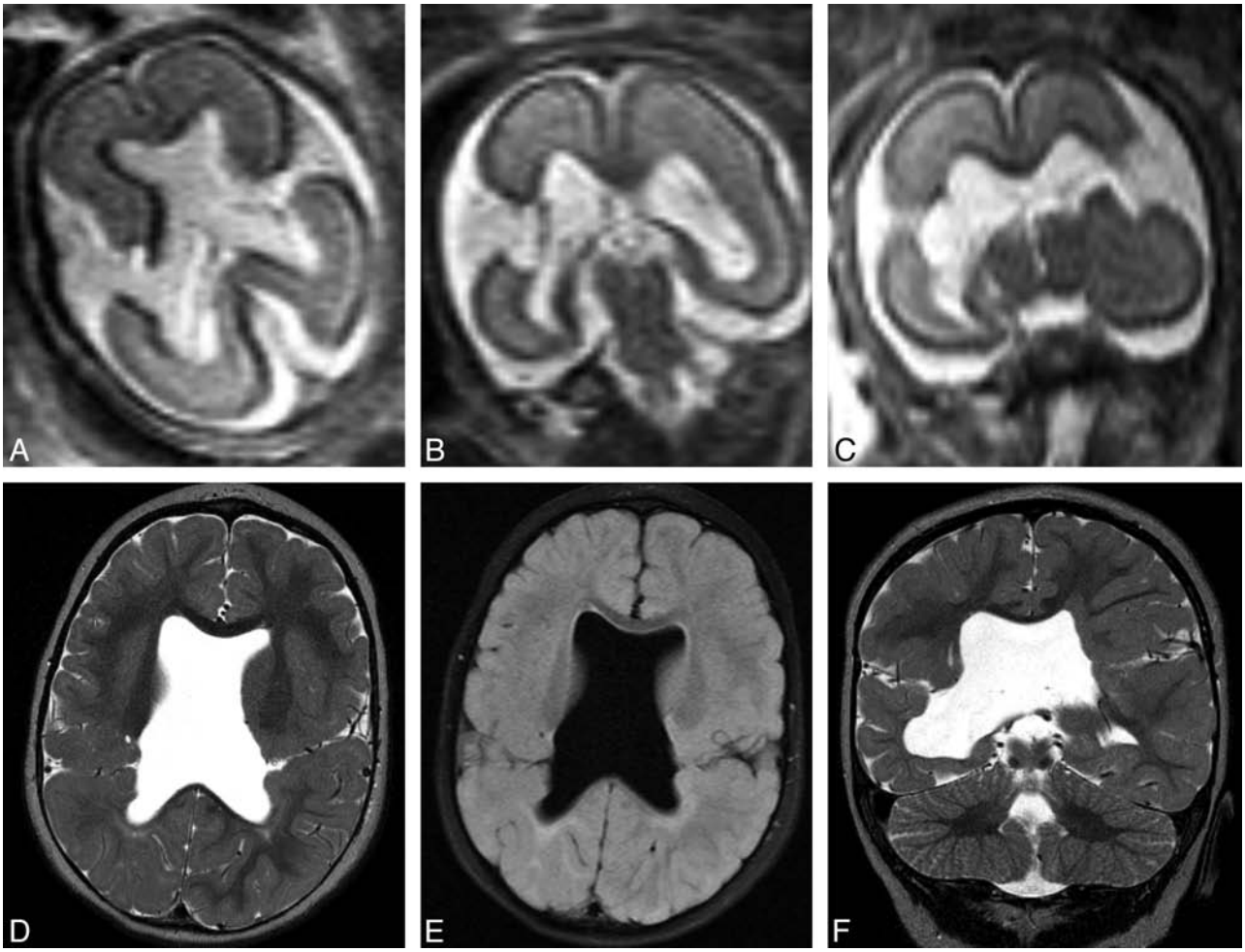

FIG 2. Prenatal imaging at 22 weeks' gestational age demonstrates bilateral wide-open clefts on axial (*A*) and coronal HASTE (*B* and *C*) imaging. Postnatal imaging at 15 months of age demonstrates interval closure of both defects, with apposed lips that contain intervening vessels. Note the complete absence of the septum pellucidum. Axial T2 (*D*), axial FLAIR (*D* and *E*), and coronal T2 (*F*) images are shown.

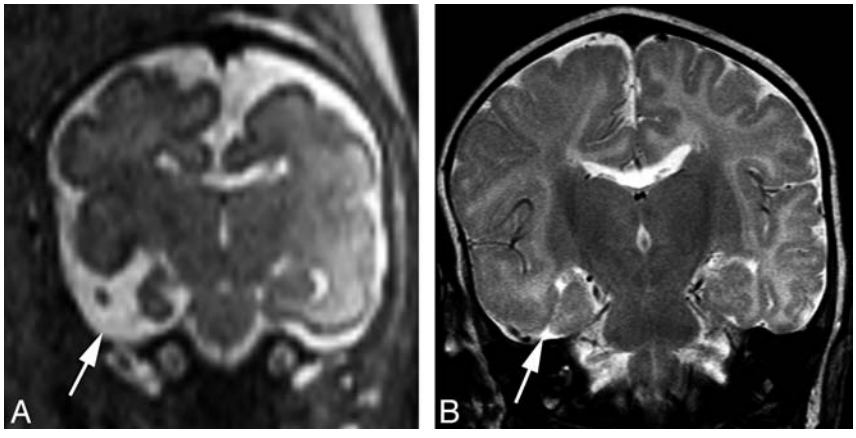

FIG 3. Prenatal coronal HASTE imaging at 26 weeks' gestational age demonstrating a right temporal open cleft communicating with the temporal horn (*arrow*), with a faint membrane covering (*A*). Postnatal coronal T2 imaging at 2 months of age demonstrates interval closure of defect lips, which are now apposed to each other and closed (*B*).

Although visualization of gray matter along the margin of the cleft was much better on postnatal imaging compared with prenatal MR imaging, there was at least partial visualization of gray matter in all cases to suggest the diagnosis of schizencephaly on prenatal MR imaging. A careful inspection for the gray matter lining is required on multiple planes to differentiate it from porencephaly because the gray matter lining may be small and appear incomplete in some cases and, therefore, difficult to identify.

Numerous associated anomalies have been reported with schizencephaly, including polymicrogyria (both adjacent to and remote from the defect)[15]; partial or complete absence of the septum pellucidum[3,9,12,18]; a thinned or absent corpus callosum; and gray matter heterotopia.[15] Fetal MR imaging did not detect a grossly dysmorphic appearance of the gray matter lining and polymicrogyria along the cleft in most patients. Fetal MR imaging also detected only some of the cases with polymicrogyria outside the defect and detected subependymal nodular heterotopia on only 1 side in a patient with bilateral heterotopia. The presence of optic

nerve hypoplasia was not identifiable on prenatal imaging in any of the 3 patients with this finding. These limitations are likely due to the resolution limits of fetal MR imaging.

The high number of subjects with absence of the septum pellucidum in our series is consistent with the findings in previous literature.[2,18,19] The high number of septal defects caused some authors to regard it as part of the definition of or in the same group[18,19] as schizencephaly. Raybaud et al,[9] in a retrospective study of 16 postnatal cases of schizencephaly, demonstrated a correlation between the absence of the septum pellucidum and the frontal location of the defect. We also found the same trend in our series (On-line Table), with all of our subjects with complete absence of the septum having frontal defects (unilateral or bilateral). We also had 1 case of partial absence of the septum (posterior septal defect) that had parietal and temporal defects, which is also consistent with the findings of Raybaud et al,[9] who noted a correlation of posterior septal defects with parietal schizencephalic defects. In our study, the absence of the septum pellucidum was detected by prenatal MR imaging in all cases, which was higher compared with the sonography series by Howe et al,[20] because they only detected the absence of the septum pellucidum in 6 of 8 cases.

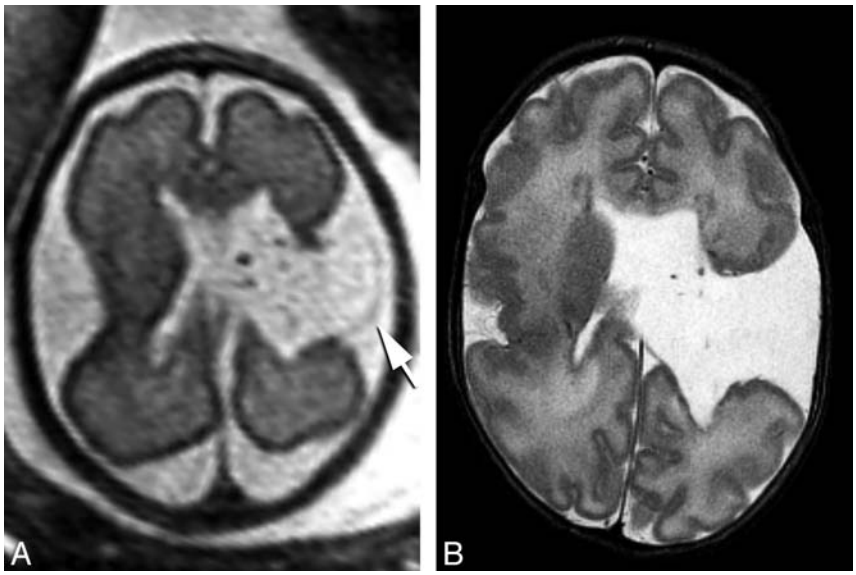

FIG 4. Prenatal imaging at 29 weeks' gestational age. Axial HASTE image (*A*) reveals an open cleft with a membrane along the roof of the cleft (*arrow*), which remained open in postnatal imaging 1 month after birth (*B*).

Clinical manifestations of schizencephaly are diverse but often include varying degrees of developmental delay, motor impairment, and seizures.[10,13,21] Bilaterality of the defect is the major poor prognostic factor.[10,13] While children with unilateral schizencephaly often present with hemiparesis and mild mental delay, those with bilateral defects may be tetraparetic with severe mental deficits.[16] Distinguishing porencephaly from schizencephaly can also be important. Defect size and location in the cortex are also important factors.[22] The presence of dysplasia and heterotopia can also contribute to a worse prognosis.[13] The prenatal diagnosis of schizencephaly and associated anomalies has an important role in prognostication and family counseling.[3] Usually subjects with open schizencephaly will be counseled about poor outcome, and a signif-

Table 1: Imaging characteristics of patients with schizencephaly

Subject	Clefts	Prenatal: Visualization of Cortex Lining the 2 Margins of the Cleft	Postnatal: Visualization of Cortex Lining the 2 Margins of the Cleft	Prenatal: Membrane along the Cleft	Postnatal: Membrane along the Cleft	Prenatal: Evidence of Hemorrhage	Postnatal: Evidence of Hemorrhage
1	R	Partial-partial	Complete-complete	Present	Absent	Bilateral ventricular hemosiderin staining	Absent
	L	Complete-partial	Complete-complete	Absent	Absent	Right choroid plexus hemorrhage	
2	L	Complete-partial	Complete-complete	Absent	Absent	Absent	Absent
	L	Complete-complete	Complete-complete	Absent	Absent		
3	R	Complete-partial	Complete-complete	Present	Absent	Absent	Absent
	L	Complete-complete	Complete-complete	Present	Absent		
4	R	Complete-partial	Complete-complete	Absent	Absent	Absent	Absent
	L	Complete-partial	Complete-complete	Absent	Absent		
5	R	Complete-complete	Complete-complete	Present	Absent	Left lateral ventricle and choroid plexus gross hemorrhage	Bilateral ventricular staining, left choroid plexus staining
	L	Complete-partial	Complete-complete	Present	Absent		
6	L	Complete-complete	Complete-complete	Absent	Absent	Hemosiderin staining in the cleft	Bilateral ventricular and cleft staining
7	R	Complete-partial	Complete-complete	Absent	Absent	Absent	Left choroid plexus hemorrhage
	L	Complete-partial	Complete-complete	Absent	Absent		
8	L	Complete-partial	Complete-complete	Present	Partial	Bilateral ventricular, choroid plexus, and cleft hemosiderin staining	Bilateral ventricular, choroid plexus, and cleft hemosiderin staining
9	R	Complete-partial	Complete-complete	Present	Absent	Bilateral ventricular hemosiderin staining	Bilateral ventricular hemosiderin staining
	L	Complete-partial	Complete-complete	Present	Absent		
10	R	Complete-complete	Complete-complete	Present	Absent	Bilateral ventricular hemosiderin staining	Bilateral ventricular hemosiderin staining
	R	Complete-complete	Complete-complete	Present	Present		

Note:—R indicates right; L, left.

Table 2: Comparison of the dimensions of the clefts and ipsilateral ventricle between different types of open clefts[a]

Measurement	Normalized Prenatal Diameters (Open Clefts That Closed)	Normalized Prenatal Diameters (Open Clefts That Remained Open)	*P* Value
Ipsilateral ventricle	Mean = 0.16 ± 0.045	Mean = 0.14 ± 0.039	.24
Cleft width (outer)	Mean = 0.17 ± 0.14	Mean = 0.27 ± 0.13	.11
Cleft width (inner)	Mean = 0.14 ± 0.88	Mean = 0.20 ± 0.12	.14
Cleft width (mid)	Mean = 0.12 ± 0.08	Mean = 0.23 ± 0.13	.06

[a] Measurements are all normalized to the mean of the maximum anteroposterior and transverse inner diameters of the skull.

icant proportion have terminated their pregnancies in previously published studies.[17,23] Awareness of the fact that open clefts can close may potentially affect prenatal counseling regarding postnatal prognosis.

Prenatal sonography has been used for diagnosis of schizencephaly,[3,24] though it has been reported that even sizeable open defects may be missed with second-trimester sonography scans[24] and it is more typically identified during the third-trimester sonography examinations.[3] Howe et al[20]studied 38 cases of schizencephaly by searching collected register data and revealed that only 18 of the 38 cases were identified prenatally. In their study, the main diagnostic technique was sonography, and MR imaging was used in only 6 of the 18 prenatally detected cases. Due to the limitations of sonography, MR imaging is considered the study of choice for the evaluation of suspected schizencephaly. The focus of our study was not a comparison of the accuracy of ultrasound versus MR imaging for the diagnosis of schizencephaly. There are only a few small studies evaluating the prenatal MR imaging of schizencephaly. The largest published series are those of Oh et al (6 cases)[3] and Denis et al (3 cases).[17] Both of these studies were limited to subjects with open-lip schizencephaly (unilateral or bilateral), and the pregnancy was terminated in all 3 subjects in the study of Denis et al. Recent work by Glenn et al[25] on a relatively large series of fetal MR imaging in subjects with malformations of cortical development included 3 subjects with schizencephaly. In their study, fetal MR imaging had 100% sensitivity and specificity for the prenatal diagnosis of schizencephaly in their 3 patients (both open and closed). We also demonstrated a perfect correlation on the number of defects between pre- and postnatal imaging; however, our methodology was different, having been based on retrospective selection of subjects with schizencephaly. Therefore, the sensitivity of prenatal MR imaging for the diagnosis of schizencephaly cannot be evaluated.

There are 2 single case reports in the literature that described unilateral schizencephaly changing from the open type prenatally to the closed type postnatally.[24,26] Our study of 18 clefts demonstrated closure of prenatally diagnosed open clefts in 47% of cases on postnatal imaging. We qualitatively and quantitatively assessed a number of parameters to determine whether we can predict closure of prenatally open clefts. These factors included cleft width at 3 measurement points, ventricular width, and the presence of hemorrhage, but none showed a statistically significant relationship to the closure of open defects. A smaller normalized width of the midportion of the cleft showed a strong trend ($P = .06$) in predicting closure of open clefts, but it did not reach statistical significance in our sample. The exact timing of the process of closure of the open schizencephalic clefts is not known. However, we believe that the closing occurs sometime in the later stages of prenatal life because some of our patients who were imaged in early postnatal life still showed closing of the clefts. The cause of closing of open schizencephalic clefts is also not known, but we hypothesize that it may be related to continued growth of the cortical plate or changes in CSF hemodynamics. While we could not statistically relate the closure of clefts to the presence of hemorrhage, the size of the clefts, or the size of the ventricles, future studies with larger numbers may be sufficiently powered to potentially demonstrate an association.

The major limitation of this study is the small sample size, despite being a rather large study of the condition, which is partly due to the rarity of the condition and lack of imaging follow-up, because most of our baseline subject pool was referred from other institutions only for their prenatal assessment. Prospective studies with larger numbers of subjects accompanied by short- and long-term clinical follow-up are needed to investigate the long-term clinical outcome between those subjects whose defects are closed after birth and those whose defects remain open. Larger studies may also elucidate factors that predict closure in a subset of open defects.

CONCLUSIONS

This study showed that nearly half of open schizencephaly defects seen on fetal imaging will be closed when evaluated on postnatal MR imaging. Prenatal MR imaging can only demonstrate some of the associated anomalies. More precise knowledge of the prenatal and postnatal imaging appearance of schizencephaly and associated anomalies may have important implications in counseling and management of these patients.

Disclosures: Robert A. Zimmerman—*UNRELATED*: *Expert Testimony*: various law firms.

REFERENCES

1. Curry CJ, Lammer EJ, Nelson V, et al. **Schizencephaly: heterogeneous etiologies in a population of 4 million California births.** *Am J Med Genet A* 2005;137:181–89
2. Barkovich AJ, Raybaud C. **Congenital malformations of the brain and skull.** In: Barkovich AJ, Raybaud C, eds. *Pediatric Neuroimaging*. 5th ed. Philadelphia: Lippincott Williams & Wilkins; 2012:367–568
3. Oh KY, Kennedy AM, Frias AE, et al. **Fetal schizencephaly: pre- and postnatal imaging with a review of the clinical manifestations.** *Radiographics* 2005;25:647–57
4. Squier W. **Pathology of fetal and neonatal brain damage: identifying the timing.** In: Squier W, ed. *Acquired Damage to the Developing Brain: Timing and Causation.* London, UK: Arnold; 2002:110–28
5. Granata T, Farina L, Faiella A, et al. **Familial schizencephaly associated with EMX2 mutation.** *Neurology* 1997;48:1403–06
6. Tietjen I, Bodell A, Apse K, et al. **Comprehensive EMX2 genotyping of a large schizencephaly case series.** *Am J Med Genet A* 2007;143A:1313–16

7. Brunelli S, Faiella A, Capra V, et al. **Germline mutations in the homeobox gene EMX2 in patients with severe schizencephaly.** *Nat Genet* 1996;12:94–96
8. Robinson RO. **Familial schizencephaly.** *Dev Med Child Neurol* 1991;33:1010–12
9. Raybaud C, Girard N, Levrier O, et al. **Schizencephaly: correlation between the lobar topography of the cleft(s) and absence of the septum pellucidum.** *Childs Nerv Syst* 2001;17: 217–22
10. Barkovich AJ, Kjos BO. **Schizencephaly: correlation of clinical findings with MR characteristics.** *AJNR Am J Neuroradiol* 1992;13:85–94
11. Battaglia G, Granata T. **Schizencephaly.** In: Barth PG, ed. *Disorders of Neuronal Migration*. London, UK: Mac Keith Press; 2003:127–34
12. Barkovich AJ, Fram EK, Norman D. **Septo-optic dysplasia: MR imaging.** *Radiology* 1989;171:189–92
13. Granata T, Battaglia G, D'Incerti L, et al. **Schizencephaly: neuroradiologic and epileptologic findings.** *Epilepsia* 1996;37:1185–93
14. Lituania M, Passamonti U, Cordone MS, et al. **Schizencephaly: prenatal diagnosis by computed sonography and magnetic resonance imaging.** *Prenat Diagn* 1989;9:649–55
15. Hayashi N, Tsutsumi Y, Barkovich AJ. **Morphological features and associated anomalies of schizencephaly in the clinical population: detailed analysis of MR images.** *Neuroradiology* 2002;44:418–27
16. Denis D, Chateil JF, Brun M, et al. **Schizencephaly: clinical and imaging features in 30 infantile cases.** *Brain Dev* 2000;22:475–83
17. Denis D, Maugey-Laulom B, Carles D, et al. **Prenatal diagnosis of schizencephaly by fetal magnetic resonance imaging.** *Fetal Diagn Ther* 2001;16:354–59
18. Kuban KC, Teele RL, Wallman J. **Septo-optic dysplasia-schizencephaly: radiographic and clinical features.** *Pediatr Radiol* 1989;19:145–50
19. Aicardi J, Goutieres F. **The syndrome of absence of the septum pellucidum with porencephalies and other developmental defects.** *Neuropediatrics* 1981;12:319–29
20. Howe DT, Rankin J, Draper ES. **Schizencephaly prevalence, prenatal diagnosis and clues to etiology: a register-based study.** *Ultrasound Obstet Gynecol* 2012;39:75–82
21. Guerrini R, Carrozzo R. **Epilepsy and genetic malformations of the cerebral cortex.** *Am J Med Genet* 2001;106:160–73
22. Packard AM, Miller VS, Delgado MR. **Schizencephaly: correlations of clinical and radiologic features.** *Neurology* 1997;48:1427–34
23. Gedikbasi A, Yildirim G, Saygi S, et al. **Prenatal diagnosis of schizencephaly with 2D–3D sonography and MRI.** *J Clin Ultrasound* 2009;37:467–70
24. Lee W, Comstock CH, Kazmierczak C, et al. **Prenatal diagnostic challenges and pitfalls for schizencephaly.** *J Ultrasound Med* 2009;28:1379–84
25. Glenn OA, Cuneo AA, Barkovich AJ, et al. **Malformations of cortical development: diagnostic accuracy of fetal MR imaging.** *Radiology* 2012;263:843–55
26. Fernández-Mayoralas DM, Fernández-Jaén A, Jiménez-De-la-Peña M, et al. **Schizencephaly: pre- and postnatal magnetic resonance imaging.** *J Child Neurol* 2010;25:1020–23

The Diagnostic Value of CT Myelography, MR Myelography, and Both in Neonatal Brachial Plexus Palsy

R. Tse, J.N. Nixon, R.S. Iyer, K.A. Kuhlman-Wood, and G.E. Ishak

ABSTRACT

BACKGROUND AND PURPOSE: Although most infants with brachial plexus palsy recover function spontaneously, approximately 10–30% benefit from surgical treatment. Pre-operative screening for nerve root avulsions is helpful in planning reconstruction. Our aim was to compare the diagnostic value of CT myelography, MR myelography, and both against a surgical criterion standard for detection of complete nerve root avulsions in birth brachial plexus palsy.

MATERIALS AND METHODS: Nineteen patients who underwent a preoperative CT and/or MR myelography and subsequent brachial plexus exploration were included. Imaging studies were analyzed for the presence of abnormalities potentially predictive of nerve root avulsion. Findings of nerve root avulsion on surgical exploration were used as the criterion standard to assess the predictive value of imaging findings.

RESULTS: Ninety-five root levels were examined. When the presence of any pseudomeningocele was used as a predictor, the sensitivity was 0.73 for CT and 0.68 for MR imaging and the specificity was 0.96 for CT and 0.97 for MR imaging. When presence of pseudomeningocele with absent rootlets was used as the predictor, the sensitivity was 0.68 for CT and 0.68 for MR imaging and the specificity was 0.96 for CT and 0.97 for MR imaging. The use of both CT and MR imaging did not increase diagnostic accuracy. Rootlet findings in the absence of pseudomeningocele were not helpful in predicting complete nerve root avulsion.

CONCLUSIONS: Findings of CT and MR myelography were highly correlated. Given the advantages of MR myelography, it is now the single technique for preoperative evaluation of nerve root avulsion at our institution.

Brachial plexus palsy occurs in approximately 1 in 1000 neonates.[1,2] Downward traction on the shoulder girdle produces stereotyped patterns of plexus injury.[3] Nerve lesions occur first at higher levels, with more severe traction resulting in progressive inferior extension.[3,4] More superior nerve injury is typically extraforaminal, at the level of the superior trunks, because a well-developed investing fascia protects the upper nerve roots from proximal traction. In contrast, inferior lesions are more often intraforaminal, manifesting as either partial or complete avulsion of the nerve root.[4]

Clinical manifestations and spontaneous recovery depend on the extent, location, and type of nerve lesions. The clinical presentation can generally be grouped into 1 of 4 patterns outlined by Narakas[5]: Type I involves C5 and C6 deficits (Erb-Duchenne type) with loss of shoulder abduction, shoulder external rotation, elbow flexion, and forearm supination. Type II involves C5 to C7/C8 deficits, resulting in a "waiter's tip" posture from additional loss of wrist extension. Type III involves C5 to C8/T1 deficits, resulting in an arm that is generally paralyzed. Type IV involves C5 to T1 and the sympathetic chain, resulting in a flail arm with Horner syndrome. Upward traction on the brachial plexus can result in isolated lower plexus deficits that manifest as paralysis of the hand only.[6,7] This pattern is known as Klumpke palsy.

The decision to proceed with surgical exploration and reconstruction is based on the clinical presentation and progression. While 70%–90% of infants are treated with therapy alone, 10%–30% have indications for surgical treatment.[8-11] Nerve injuries distal to the intervertebral foramen can be reconstructed by using nerve grafts, whereas intraforaminal nerve root avulsions require nerve transfer. While both partial and complete nerve root avulsions are described,[12,13] there is no clear consensus on the surgical approach to partial nerve root avulsions. Preoperative imaging capable of accurately identifying complete nerve root avulsions

Received October 17, 2013; accepted after revision December 16.

From the Department of Radiology (J.N.N., R.S.L., G.E.I.), and the Division of Plastic Surgery, Department of Surgery (R.T., K.A.K.-W.), the Seattle Children's Hospital, University of Washington, Seattle, Washington.

Paper previously presented at: XVIII International Symposium on Brachial Plexus Surgery, May 23-25, 2013; Montreux, Switzerland.

Please address correspondence to Raymond Tse, M/S OB.9.527, 4800 Sand Point Way NE, Seattle, WA 98105; e-mail: raymond.tse@seattlechildrens.org

http://dx.doi.org/10.3174/ajnr.A3878

and distinguishing them from extraforaminal nerve injuries is, therefore, critical for optimal surgical planning.

The current standard for preoperative assessment of nerve root avulsions in infants is CT myelography.[12,14-19] A pseudomeningocele is suggestive of nerve root avulsion, and the additional finding of absent rootlets traversing the pseudomeningocele greatly increases the specificity of this finding.[14] CT myelography requires a lumbar puncture for injection of intrathecal contrast, with attendant risks of infection and seizure.[20-22] Recent studies have also raised concern for malignancy with early exposure of children to radiation.[23,24] MR myelography can be performed without injection of contrast and is a promising alternative.[17,25] However, the performance of MR myelography for predicting nerve root avulsion is not yet established[26] in neonatal brachial plexus injury, and the diagnostic value of MR myelography has yet to be compared with CT myelography in this setting.

The purpose of this study was to determine the predictive value of CT myelography, MR myelography, and both CT and MR myelography for detecting complete nerve root avulsions in neonatal brachial plexus palsy, by using a surgical criterion standard.

MATERIALS AND METHODS

This study was approved by the institutional review board and was conducted in compliance with Health Insurance Portability and Accountability Act guidelines. Informed consent for participation was waived, given that evaluation was retrospective and data were pre-existing.

Subjects

All consecutive patients with neonatal brachial plexus palsy who underwent surgical exploration at our institution (from November 2009 to May 2013) and who had preoperative CT and/or MR myelography were included in this study. Indications for surgical treatment followed the protocol developed at the Toronto Hospital for Sick Children[9] and were based on clinical examination: flail arm and persistent Horner syndrome at 1 month of age; composite active movement scale score for elbow flexion, elbow extension, wrist extension, finger extensions, and thumb extension of <3.5/10 at 3 months of age; no clinical progression at 6 months of age; and failed "cookie test" (the child has to bring the hand to the mouth) at 9 months of age. One infant with isolated lower plexus palsy underwent exploration at 9 months of age because of lack of clinical recovery. Myelography was performed only on infants in whom a clinical decision to proceed with surgical exploration was made. Subject demographics were collected by retrospective chart review.

Imaging Studies

CT myelography was performed with a 64-detector LightSpeed CT scanner (GE Healthcare, Milwaukee, Wisconsin) following intrathecal injection of iopamidol iodinated contrast material (Isovue-M 200; General Injectables and Vaccines, Bastian, Virginia) under fluoroscopic guidance according to a weight-based protocol of 0.5 mL/kg with a maximum dose of 5 mL. Axial 0.625-mm sections were reconstructed from a volumetric acquisition extending from the skull base to T4 by using both standard and sharpening convolution kernels. A pitch of 0.53:1, reconstruction increment of 0.4 mm, beam width of 20 cm, focal spot size of 0.6 × 0.7 mm, matrix size of 512 × 512, and an FOV of 10 cm were used. Data were reconstructed into sagittal and curved coronal planes for optimal nerve root assessment. Kilovolt(peak) and milliampere values of 100 and 155 were used.

MR imaging examinations were performed on a 3T TrioTim MR imaging (Siemens, Erlangen, Germany) following a MR myelography protocol. Sequences included coronal and sagittal STIR, coronal and sagittal T1-weighted, and a fully-rewound coherent steady-state gradient-echo sequence with dual excitation (constructive interference in steady state on the Siemens platform) acquired at high resolution. Resolution of the steady-state sequence varied between 0.5 and 0.9 mm isotropic, and the time of the acquisition varied between 2 minutes 11 seconds and 7 minutes 38 seconds depending on plane, resolution, and coverage.

None of the imaging studies were excluded on the basis of study quality, so our results represented true clinical practice.

Table 1: Potential findings on myelography

	Finding	
Rating	Dura	Rootlets
A	Pseudomeningocele	Absent
B	Pseudomeningocele	Present
C	Normal	Absent
D	Normal	Thinned
E	Normal	Thickened
F	Normal	Normal

Blinded Myelogram Findings

CT and MR myelograms were de-identified, unlinked, randomized, and loaded onto a test PACS system. A subject key code was stored securely, and the participating radiologists were blinded to the identity of each scan and the results of surgical exploration. The side of the clinical deficit was provided, and the contralateral side was used for comparison.

Two pediatric radiologists (with 7 and 8 years' experience, respectively) independently evaluated each imaging study and rated each root level from C5 to T1 according to the system in Table 1. Discrepancies were resolved by consensus analysis. Findings A and B (Figs 1 and 2) have previously been used as predictors of nerve root avulsion in infants.[14] Finding C (Fig 3) has been described as a predictor in adults.[19] Findings D and E (Figs 4 and 5) have been suggested to indicate partial nerve root avulsion.[12]

To determine the subjective quality of each type of myelogram, each radiologist rated their confidence in their findings at each root level by using a 3-point scale: 1, absolutely sure; 2, likely; 3, unsure.

Surgical Findings

Brachial plexus exploration involved a supraclavicular approach with retroclavicular and infraclavicular exposures as needed. Each nerve root was dissected proximal to the intervertebral foramen for inspection. A nerve root was considered completely avulsed when we found any of the following:

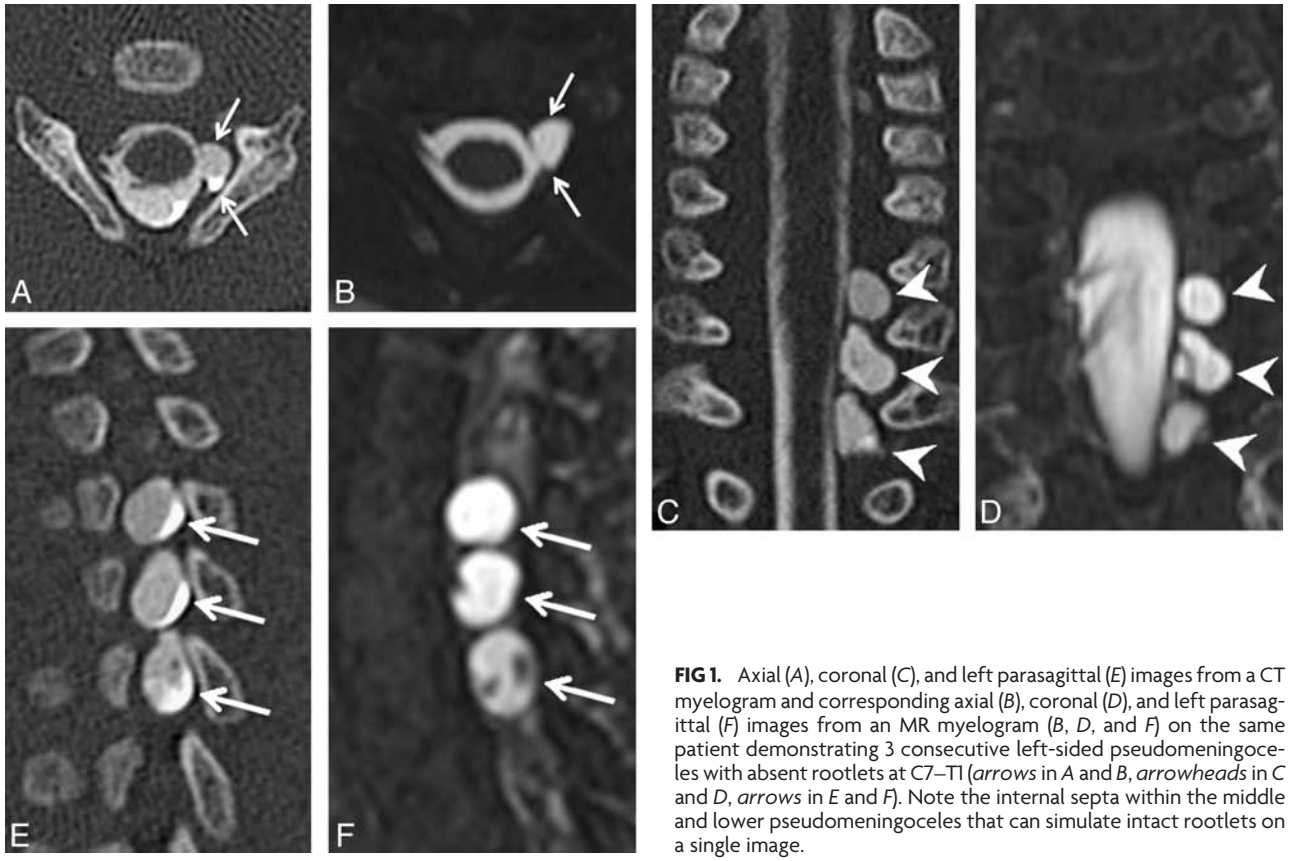

FIG 1. Axial (*A*), coronal (*C*), and left parasagittal (*E*) images from a CT myelogram and corresponding axial (*B*), coronal (*D*), and left parasagittal (*F*) images from an MR myelogram (*B*, *D*, and *F*) on the same patient demonstrating 3 consecutive left-sided pseudomeningoceles with absent rootlets at C7–T1 (*arrows* in *A* and *B*, *arrowheads* in *C* and *D*, *arrows* in *E* and *F*). Note the internal septa within the middle and lower pseudomeningoceles that can simulate intact rootlets on a single image.

1) The dorsal root ganglion was identified outside the intervertebral foramen.

2) The intervertebral foramen was empty.

3) There was a normal-appearing nerve with no response to electrical stimulation on exploration, no clinical function on preoperative examination, and no distal lesion identified.

We did not define partial nerve root avulsion based on surgical findings, given that this would require laminectomy for intraspinal exploration, and this is not performed for neonatal brachial plexus palsy.

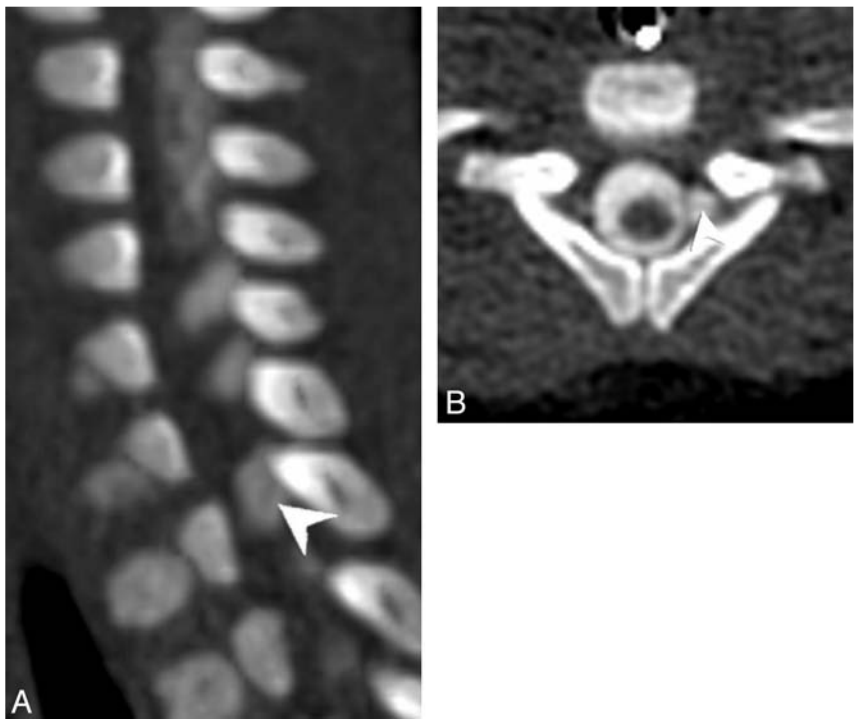

FIG 2. Left parasagittal (*A*) and axial (*B*) images from a CT myelogram demonstrating a left-sided pseudomeningocele at T1. A thin linear filling defect within the pseudomeningocele continued centrally to the cord and was interpreted as an intact nerve root.

Statistical Analysis

The radiologic findings on preoperative myelograms were compared with the surgical findings. The operative findings were considered the criterion standard. The diagnostic accuracy of each of the predictors identified on myelography was analyzed, and the sensitivity, specificity, positive predictive value, negative predictive value, and likelihood ratio for complete root avulsion of each were calculated.

Confidence ratings by each radiologist for each root level were compared for CT and MR myelography with a χ^2 test by using STATA (StataCorp, College Station, Texas). In contrast to other studies, which excluded imaging studies based on poor quality or technical error,[12,14] we included all

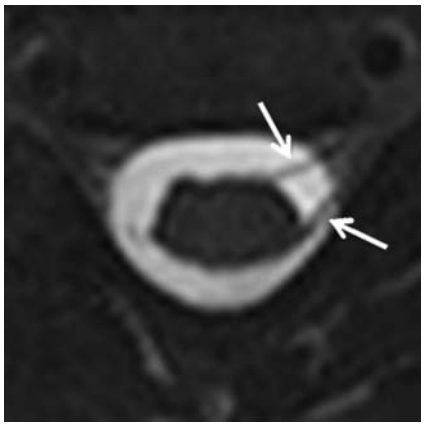

FIG 3. Axial minimum-intensity-projection image from an MR myelogram demonstrating only left-sided rootlets at C5 (*arrows*), with absent corresponding right-sided rootlets. The base resolution was 0.6-mm isotropic, with a 2-mm minimum-intensity-projection slab.

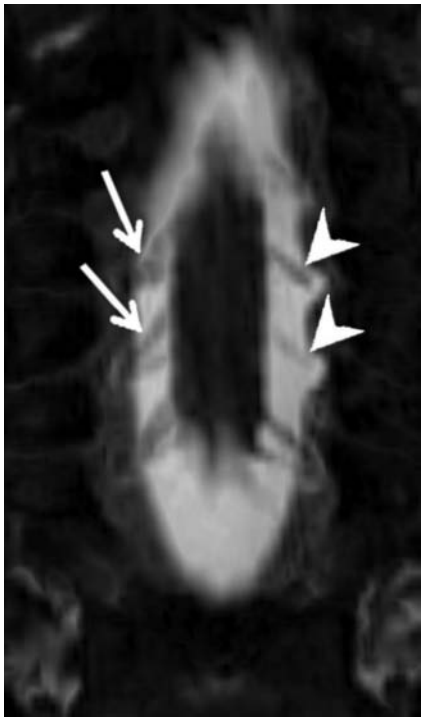

FIG 4. Coronal minimum-intensity-projection image from an MR myelogram demonstrating thinned left-sided ventral rootlets at C6 and C7 (*arrowheads*), relative to the normal fan-shaped right-sided ventral rootlets on the contralateral side at the same levels (*arrows*). Base resolution was 0.6-mm isotropic, with a 2-mm minimum-intensity-projection slab.

imaging studies to allow us to compare the 2 modalities in a practical clinical setting.

RESULTS

Subjects and Surgical Findings

During a 3.5-year period (between November 2009 and May 2013), 226 children presented to the Brachial Plexus Program at our institution. Of these new visits, 116 children were younger than 18 months of age at presentation. Nineteen of the 116 infants (16%) underwent surgical exploration, and all met the inclusion criteria for this study. Seventeen patients had both CT and MR myelography performed preoperatively. Two subjects underwent CT myelography alone without concomitant MR myelography. All imaging studies were included in this study.

The male/female ratio was 9:10. The mean gestational age was 39.5 weeks (range, 36–41 weeks), and the mean birth weight was 3978 g (range, 2580–4479 g). Seventeen infants (89%) presented in the cephalic position at vaginal delivery, and none presented breech. Two infants (11%) were born by cesarean delivery. Brachial plexus palsies were identified immediately after birth. Two infants had ischemic encephalopathy, 1 had a clavicle fracture, 2 had humerus fractures, and 6 had torticollis. Infants were followed clinically, and myelography was only performed if a decision was made to proceed with surgical exploration. The overall mean age at myelography was 25 weeks (range, 10–65 weeks). Incidence, age at myelography, and avulsions on surgical exploration according to clinical presentation are summarized in Table 2. Ten subjects (52%) had nerve root avulsions. There was an increasing incidence of root avulsion with increasing severity of injury according to the Narakas classification. Avulsions occurred more often in the lower roots.

Ninety-five root levels were examined (5 ipsilateral levels in 19 patients). There were no abnormalities detected on contralateral levels. Twenty-two avulsions were identified on surgical exploration, giving an overall incidence of 23%. The distribution of avulsions according to root level and palsy type is summarized in Table 2.

Predictive Value of Findings on Myelography

Table 3 summarizes the predictive values of CT myelography, MR myelography, and both CT and MR myelography for all root levels by using either pseudomeningocele with absent rootlets or all pseudomeningoceles as indicators of complete nerve root avulsion. No benefit of CT and MR myelography combined was found. The findings and predictive values of CT myelography compared with MR myelography were almost the same and were consistent with those previously reported in the literature.[12,14-16,18,19]

Other nerve root findings in the absence of pseudomeningocele were also analyzed (absent rootlets, thinned rootlets, and thickened rootlets). These findings did not improve the predictive values for CT, MR imaging, or both CT and MR myelography (Table 4). We found no association between the presence or type of additional findings and age at imaging.

Predictive Value According to Root Level

The predictive values of CT myelography alone, MR myelography alone, and both CT and MR myelography could not be determined according to root level by using quantitative methods, given the limited cohort size. For all clinical presentations, there were no avulsions of C5 and there were only 3 avulsions of C6 in 19 subjects (Table 5). Qualitative analysis revealed little variation in the predictive value according to root level.

Confidence Ratings

Confidence ratings (190 scores for CT and 170 scores for MR imaging) were pooled according to imaging technique. There was

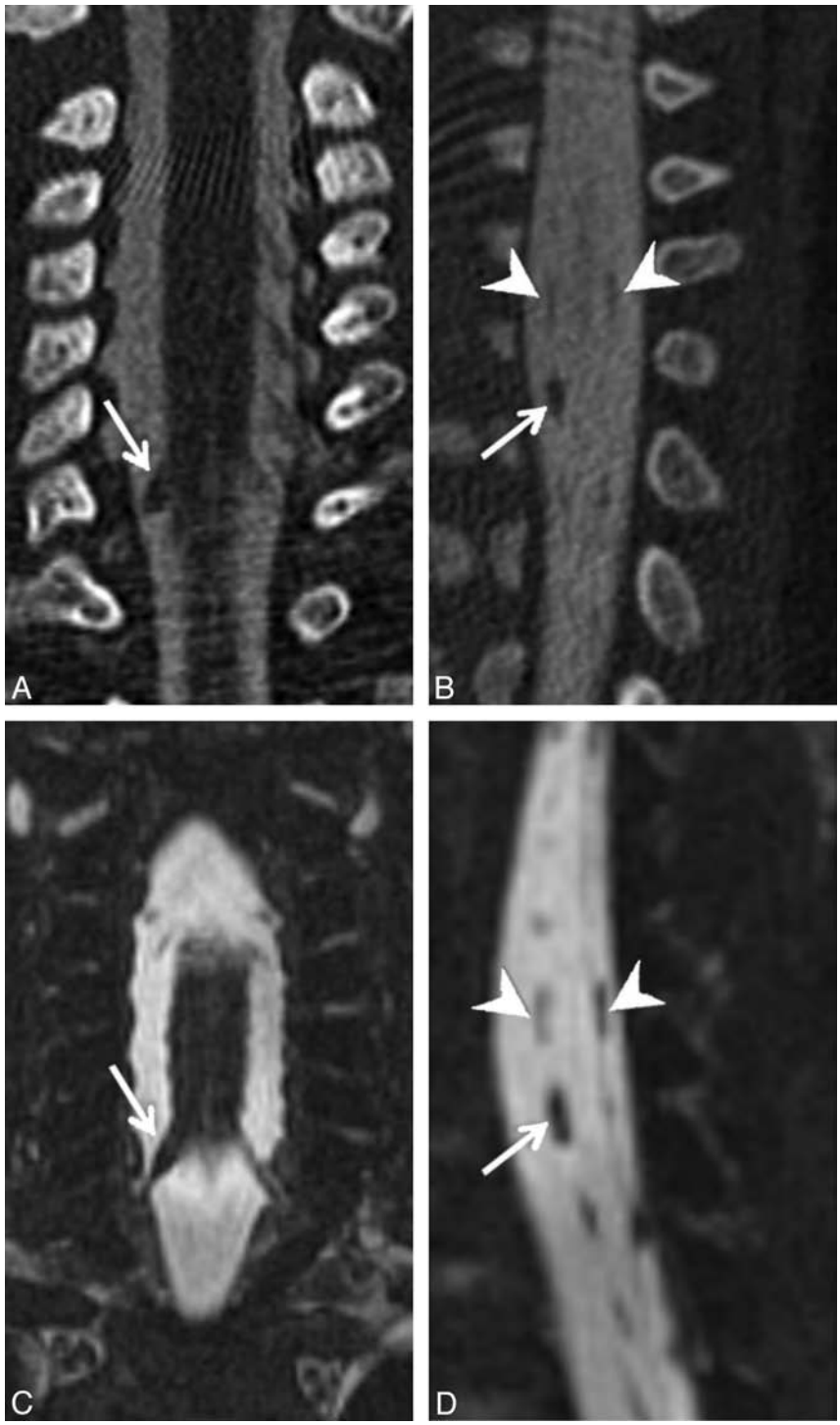

FIG 5. Coronal (*A*) and right parasagittal (*B*) images from a CT myelogram and the coronal (*C*) and right parasagittal (*D*) images from the corresponding MR myelogram demonstrating a thickened ventral rootlet at C8 on the right (*arrows* in *A* through *D*). Note that the dorsal rootlet at C8 is thinned. Normal caliber ventral and dorsal rootlets at C7 (*arrowheads* in *B* and *D*) are visible for comparison.

significantly better confidence on CT myelography compared with MR myelography ($P < .01$).

DISCUSSION

Preoperative assessment of nerve root avulsion is useful for surgical planning for brachial plexus palsy. Although CT myelography is the established standard in adults[13,18,19,26-28] and infants,[12,14,15,29] the risk of infection and seizure related to intrathecal contrast administration[20-22] and evidence that early exposure to radiation may increase later risks of malignancy[23,24] make identifying an alternative important.

MR myelography for brachial plexus palsy has evolved during the past decade.[30,31] Its predictive value for detecting nerve root avulsions has been evaluated[32-35] and has been found to have similar[36,37] or greater[38] value compared with CT myelography in adults. MR myelography has also been evaluated in neonatal brachial plexus palsy[25,39-44] but is yet to be widely adopted. Medina et al[43] demonstrated good sensitivity and specificity for the detection of extraforaminal neuromas by using an MR imaging–based technique, but sensitivity for the detection of findings reflecting proximal nerve root avulsions, particularly characterization of the nerve roots themselves, was poor. In addition, the predictive value of MR imaging for complete nerve root avulsion is yet to be compared in a side-by-side manner with CT, the current standard in infants.

Relative to previous studies, we used newer MR imaging technology. In our study, MR myelography was equal to and perhaps better than CT myelography for the prediction of complete nerve root avulsions on surgical exploration, and we found no benefit to the combined use of CT and MR imaging over MR myelography alone. This outcome supports the findings of several prior studies that evaluated the diagnostic performance of MR myelography alone[25,39-44] and is further evidence that with the current technique, MR myelography may be capable of replacing CT myelography in the preoperative assessment of infants with neonatal brachial plexus palsy. In addition, MR imaging has the advantage of evaluating the intrinsic signal intensity and integrity of the spinal cord in better detail compared with CT. Increased use of MR myelography will potentially allow a decrease in radiation exposure and morbidity associated with invasive myelography.

We evaluated specific predictors of nerve root avulsion (pseudomeningocele with or without visible rootlets) on both CT and MR imaging and found that the predictive value of these findings was similar to that in other published studies.[14]

Table 2: Subject demographics

Clinical Presentation	Subjects (No.)	Mean Age at Myelography (wk) (Range)	Nerve Root Avulsion on Surgical Exploration					Mean Avulsions per Subject (All Levels)
			C5	C6	C7	C8	T1	
Narakas I	4 (21%)	52 (46–65)	0%	0%	0%	0%	0%	0
Narakas II	4 (21%)	32 (16–49)	0%	25%	0%	0%	0%	0.25
Narakas III	3 (16%)	20 (14–27)	0%	33%	66%	33%	66%	2
Narakas IV	7 (37%)	14 (10–16)	0%	14%	57%	71%	71%	2.14
Klumpke	1 (5%)	14 (NA)	0%	0%	0%	0%	0%	0

Note:—NA indicates not applicable.

Table 3: Predictive value of CT versus MRI versus CT and MR myelography

	Pseudomeningoceles with Absent Rootlets			All Pseudomeningoceles		
	CT	MRI	CT and MRI	CT	MRI	CT and MRI
Sensitivity	0.68	0.68	0.68	0.73	0.68	0.68
Specificity	0.96	0.97	0.97	0.96	0.97	0.97
Positive predictive value	0.83	0.88	0.88	0.84	0.88	0.88
Negative predictive value	0.9	0.9	0.9	0.92	0.9	0.9
Likelihood ratio	17	22.7	22.7	18	22.7	22.7

Table 4: Likelihood ratios of detecting nerve root avulsions using different imaging predictors

Predictors of Nerve Root Avulsion	Findings on Imaging	Likelihood Ratio		
		CT	MRI	CT and MRI
Pseudomeningoceles with absent rootlets	A	17	22.7	22.7
Any pseudomeningocele	A and B	18	22.7	22.7
Any pseudomeningocele or any absent rootlets	A, B, and C	18	13.6	13.6
Any pseudomeningocele or any rootlet abnormality	A, B, C, D, and E	3.7	5.4	5.4

Table 5: Avulsions on surgical exploration according to root level

Root Level	Findings on Surgical Exploration	
	Avulsions (Roots Examined)	Prevalence of Avulsions
C5	0 (19)	0
C6	3 (19)	0.16
C7	6 (19)	0.32
C8	6 (19)	0.32
T1	7 (19)	0.37
All levels	22 (95)	0.23

Subtler isolated rootlet findings (ie, findings C, D, and E) did not improve the predictive value of either CT or MR myelography for complete nerve root avulsion. These findings, in the absence of pseudomeningoceles on imaging, may be indicators of proximal nerve insult that cannot be detected on surgical exploration (ie, partial nerve root avulsion). Further study to determine their relevance for surgical planning is necessary. Correlation with proximal nerve stump histopathology and results of nerve grafting may provide further insights.

Chow et al[14] previously reported that the additional finding of absent rootlets associated with a pseudomeningocele increased specificity from 0.85 to 0.98 for complete nerve root avulsion. We did not find this difference in our cohort because there were absent rootlets associated with 18 of 19 pseudomeningoceles on CT and with 17 of 17 pseudomeningoceles on MR imaging. The common finding of absent rootlets with pseudomeningoceles in our study may reflect the relatively high prevalence of severe injuries (ie, Narakas 3 and 4) in our cohort compared with that of Chow et al.[14] We identified avulsions in 23% of nerve roots examined, whereas Chow et al reported a rate of 14%. Similar to the study of Steens et al,[12] the number of patients with at least 1 avulsion was 52% in our cohort versus 56% in theirs. Steens et al also found pseudomeningoceles with intact rootlets to be rare, occurring in only 0.5% of root levels analyzed.

The lack of relevance of subtle nerve root findings for the prediction of complete avulsion, as well as the uncommon finding of pseudomeningoceles with present rootlets, may help explain the similar performance of CT and MR myelography in our study. One of the main advantages of CT myelography over MR imaging–based techniques is the higher spatial resolution that can be achieved in clinically acceptable scanning times. The effective spatial resolution of CT myelography by using the acquisition protocol at our institution was 0.4–0.5 mm isotropic. For MR myelography, the resolution ranged between 0.5 and 1.0 mm isotropic by using a fully rewound coherent gradient-echo sequence, depending on the required coverage and time constraints.

Because the more conspicuous imaging findings proved to be most predictive of complete nerve avulsion, the weakness of MR imaging in terms of spatial resolution was rendered less significant. In addition, improvements in MR imaging hardware and sequence design have allowed acquisition of progressively higher resolution imaging within acceptable scanning times. We were consistently able to assess the presence or absence of nerve roots in this study by using MR myelography, in contrast to prior studies.[43] As the impact of subtler nerve root findings on surgical planning and outcomes is elucidated, the relevance of high-resolution nerve root assessment may become clearer. Furthermore, nerve root status may prove more relevant in patient populations with less severe injury grades. For these reasons, continued ad-

vancement toward the acquisition of high-resolution MR myelographic images remains the ideal.

Confidence ratings were highly correlated between the 2 radiologists and were significantly better on CT myelography because of better spatial resolution compared with MR imaging (Fig 2). We found that MR myelography acquired with voxel sizes of 0.5–0.6 mm was sufficient for high-confidence evaluation commensurate with CT myelography; 0.7–0.8 mm voxel size yielded intermediate confidence ratings on average, while ≥0.9 mm voxel size led to severely diminished confidence ratings.

Similar to authors of other studies, we report predictive values by using sensitivity, specificity, and predictive values[14-16,18,19,35-37]; and we used clinical examination and/or findings on extradural surgical exploration as our reference standard for the detection of root avulsions.[14-16,18,19,35,37,45] Hemilaminectomy and opening of the dura mater would provide a more accurate reference standard and have been used to assess CT,[13,27] MR imaging,[32] and both CT and MR imaging[46] findings in adults. However, the procedure involves significant morbidity and is not performed in infants for neonatal brachial plexus palsy reconstruction.

Given that the decision for surgical treatment at our center is based on clinical examination, our imaging studies were designed to assist with surgical planning only and not to screen for injuries. Our myelography protocols are not optimized to detect more distal extraforaminal neuromas; thus, clinical and imaging findings could not be directly compared.

Accumulation of more CT and MR myelograms to compare diagnostic values would make our conclusions more robust. We had no subjects born breech (in which there is a higher likelihood of C5 and C6 avulsions), and our cohort size did not allow subgroup analysis according to nerve root level. However, this study was initiated as a quality improvement audit following a 3.5-year period during which we performed both CT and MR myelography preoperatively. While both CT and MR myelography are frequently used together and are thought to be complementary,[46-48] given the findings of this study, we can no longer justify routinely performing both CT and MR myelography in the evaluation of neonatal brachial plexus palsy at our institution.

CONCLUSIONS

The predictive values of CT and MR myelography are similar for the detection of complete nerve root avulsion in neonatal brachial plexus palsy, and we found no benefit to the combined use of CT and MR imaging over MR myelography alone. Although radiologists' confidence ratings were significantly better with CT myelography, findings on CT and MR myelography were highly correlated. Given the advantages of MR myelography, it is now the single technique for preoperative evaluation of nerve root avulsion at our institution.

ACKNOWLEDGMENTS

The authors thank Kathryn Whitlock, Center for Clinical and Transitional Research, Seattle Children's Hospital, for her guidance and assistance with statistical analysis.

REFERENCES

1. Pondaag W, Malessy MJ, van Dijk JG, et al. **Natural history of obstetric brachial plexus palsy: a systematic review.** *Dev Med Child Neurol* 2004;46:138–44
2. Hale HB, Bae DS, Waters PM. **Current concepts in the management of brachial plexus birth palsy.** *J Hand Surg* 2010;35A:322–31
3. Stevens JH. **Brachial plexus paralysis: By JH. Stevens, M.D., 1934.** *Clin Orthop Relat Res* 1988;237:4–8
4. Benjamin K. **Part 1. Injuries to the brachial plexus: mechanisms of injury and identification of risk factors.** *Adv Neonatal Care* 2005;5:181–89
5. Narakas AO. **Obstetrical brachial plexus injuries.** In: Lamb DW, ed. *The Paralyzed Hand.* Edinburgh, Scotland: Churchill Livingstone; 1987:116–35
6. Buchanan EP, Richardson R, Tse R. **Isolated lower brachial plexus (Klumpke) palsy with compound arm presentation: case report.** *J Hand Surg Am* 2013;38:1567–70
7. al-Qattan MM, Clarke HM, Curtis CG. **Klumpke's birth palsy: does it really exist?** *J Hand Surg Br* 1995;20:19–23
8. Hentz VR. **Congenital brachial plexus exploration.** *Tech Hand Up Extrem Surg* 2004;8:58–69
9. Borschel GH, Clarke HM. **Obstetrical brachial plexus palsy.** *Plast Reconstr Surg* 2009;124(suppl):144e–55e
10. Waters PM. **Comparison of the natural history, the outcome of microsurgical repair, and the outcome of operative reconstruction in brachial plexus birth palsy.** *J Bone Joint Surg Am* 1999;81:649–59
11. Malessy MJ, Pondaag W. **Obstetric brachial plexus injuries.** *Neurosurg Clin of N Am* 2009;20:1–14
12. Steens SC, Pondaag W, Malessy MJ, et al. **Obstetric brachial plexus lesions: CT myelography.** *Radiology* 2011;259:508–15
13. Carvalho GA, Nikkhah G, Matthies C, et al. **Diagnosis of root avulsions in traumatic brachial plexus injuries: value of computerized tomography myelography and magnetic resonance imaging.** *J Neurosurg* 1997;86:69–76
14. Chow BC, Blaser S, Clarke HM. **Predictive value of computed tomographic myelography in obstetrical brachial plexus palsy.** *Plast Reconstr Surg* 2000;106:971–77
15. Vanderhave KL, Bovid K, Alpert H, et al. **Utility of electrodiagnostic testing and computed tomography myelography in the preoperative evaluation of neonatal brachial plexus palsy.** *J Neurosurg Pediatr* 2012;9:283–89
16. Terzis JK, Novikov ML. **Radiological and electrophysiological detection of nerve roots avulsion in patients with birth-related brachial plexus paralysis.** *Semin Plast Surg* 2005;19:24
17. Van Ouwerkerk W. **Preoperative investigations in obstetric brachial plexus palsy.** *Semin Plast Surg* 2005;19:17
18. Bertelli JA, Ghizoni MF. **Use of clinical signs and computed tomography myelography findings in detecting and excluding nerve root avulsion in complete brachial plexus palsy.** *J Neurosurg* 2006;105:835–42
19. Yamazaki H, Doi K, Hattori Y, et al. **Computerized tomography myelography with coronal and oblique coronal view for diagnosis of nerve root avulsion in brachial plexus injury.** *J Brachial Plex Peripher Nerve Inj* 2007;2:16
20. Klein KM, Shiratori K, Knake S, et al. **Status epilepticus and seizures induced by iopamidol myelography.** *Seizure* 2004;13:196–99
21. Gelfand MS, Abolnik IZ. **Streptococcal meningitis complicating diagnostic myelography: three cases and review.** *Clin Infect Dis* 1995;20:582–87
22. Chitnis AS, Guh AY, Benowitz I, et al. **Outbreak of bacterial meningitis among patients undergoing myelography at an outpatient radiology clinic.** *J Am Coll Radiol* 2012;9:185–90
23. Pearce MS, Salotti JA, Little MP, et al. **Radiation exposure from CT scans in childhood and subsequent risk of leukaemia and brain tumours: a retrospective cohort study.** *Lancet* 2012;380:499–505
24. Mathews JD, Forsythe AV, Brady Z, et al. **Cancer risk in 680,000 people exposed to computed tomography scans in childhood or**

adolescence: data linkage study of 11 million Australians. *BMJ* 2013;346:f2360
25. van Ouwerkerk WJ, Strijers RL, Barkhof F, et al. **Detection of root avulsion in the dominant C7 obstetric brachial plexus lesion: experience with three-dimensional constructive interference in steady-state magnetic resonance imaging and electrophysiology.** *Neurosurgery* 2005;57:930–40
26. Yoshikawa T, Hayashi N, Yamamoto S, et al. **Brachial plexus injury: clinical manifestations, conventional imaging findings, and the latest imaging techniques.** *Radiographics* 2006;26(suppl 1):S133–43
27. Oberle J, Antoniadis G, Rath SA, et al. **Radiological investigations and intra-operative evoked potentials for the diagnosis of nerve root avulsion: evaluation of both modalities by intradural root inspection.** *Acta Neurochir (Wien)* 1998;140:527–31
28. O'Shea K, Feinberg JH, Wolfe SW. **Imaging and electrodiagnostic work-up of acute adult brachial plexus injuries.** *J Hand Surg Eur Vol* 2011;36:747–59
29. Terzis JK, Kostas I. **Outcomes with suprascapular nerve reconstruction in obstetrical brachial plexus patients.** *Plast Reconstr Surg* 2008;121:1267–78
30. Vargas MI, Viallon M, Nguyen D, **New approaches in imaging of the brachial plexus.** *Eur J Radiol* 2010;74:403–10
31. Amrami KK, Port JD. **Imaging the brachial plexus.** *Hand Clin* 2005;21:25–37
32. Tsai PY, Chuang TY, Cheng H, et al. **Concordance and discrepancy between electrodiagnosis and magnetic resonance imaging in cervical root avulsion injuries.** *J Neurotrauma* 2006;23:1274–81
33. Ochi M, Ikuta Y, Watanabe M, et al. **The diagnostic value of MRI in traumatic brachial plexus injury.** *J Hand Surg Br* 1994;19:55–59
34. Hems TE, Birch R, Carlstedt T. **The role of magnetic resonance imaging in the management of traction injuries to the adult brachial plexus.** *J Hand Surg Br* 1999;24:550–55
35. Abul-Kasim K, Backman C, Björkman A, et al. **Advanced radiological work-up as an adjunct to decision in early reconstructive surgery in brachial plexus injuries.** *J Brachial Plex Peripher Nerve Inj* 2010;5:14
36. Gasparotti R, Ferraresi S, Pinelli L, et al. et al. **Three-dimensional MR myelography of traumatic injuries of the brachial plexus.** *AJNR Am J Neuroradiol* 1997;18:1733–42
37. Doi K, Otsuka K, Okamoto Y, et al. **Cervical nerve root avulsion in brachial plexus injuries: magnetic resonance imaging classification and comparison with myelography and computerized tomography myelography.** *J Neurosurg* 2002;96:277–84
38. Nakamura T, Yabe Y, Horiuchi Y, et al. **Magnetic resonance myelography in brachial plexus injury.** *J Bone Joint Surg Br* 1997;79:764–69
39. Smith AB, Gupta N, Strober J, et al. **Magnetic resonance neurography in children with birth-related brachial plexus injury.** *Pediatr Radiol* 2007;38:159–63
40. Francel PC, Koby M, Park TS, et al. et al. **Fast spin-echo magnetic resonance imaging for radiological assessment of neonatal brachial plexus injury.** *J Neurosurg* 1995;83:461–66
41. Yilmaz K, Calişkan M, Oge E, et al. **Clinical assessment, MRI, and EMG in congenital brachial plexus palsy.** *Pediatr Neurol* 1999;21:705–10
42. Miller SF, Glasier CM, Griebel ML, et al. **Brachial plexopathy in infants after traumatic delivery: evaluation with MR imaging.** *Radiology* 1993;189:481–84
43. Medina LS, Yaylali I, Zurakowski D, et al. **Diagnostic performance of MRI and MR myelography in infants with a brachial plexus birth injury.** *Pediatr Radiol* 2006;36:1295–99
44. Gosk J, Hendrich B, Wiącek R, et al. **Assessment of the usefulness of X-ray myelography and magnetic resonance myelography, performed with an open low-field device, in diagnosing perinatal preganglionic injuries of the brachial plexus.** *Arch Med Sci* 2012;8:678–83
45. Malessy MJ, Pondaag W, van Dijk JG. **Electromyography, nerve action potential, and compound motor action potentials in obstetric brachial plexus lesions: validation in the absence of a "gold standard."** *Neurosurgery* 2009;65(4 suppl):A153–59
46. Penkert G, Carvalho GA, Nikkhah G, et al. **Diagnosis and surgery of brachial plexus injuries.** *J Reconstr Microsurg* 1999;15:3–8
47. Bowen BC, Seidenwurm DJ, for the Expert Panel on Neurologic Imaging. **Plexopathy.** *AJNR Am J Neuroradiol* 2008;29:400–02
48. Belzberg AJ, Dorsi MJ, Storm PB, et al. **Surgical repair of brachial plexus injury: a multinational survey of experienced peripheral nerve surgeons.** *J Neurosurg* 2004;101:365–76

Hydrocephalus Decreases Arterial Spin-Labeled Cerebral Perfusion

K.W. Yeom, R.M. Lober, A. Alexander, S.H. Cheshier, and M.S.B. Edwards

ABSTRACT

BACKGROUND AND PURPOSE: Reduced cerebral perfusion has been observed with elevated intracranial pressure. We hypothesized that arterial spin-labeled CBF can be used as a marker for symptomatic hydrocephalus.

MATERIALS AND METHODS: We compared baseline arterial spin-labeled CBF in 19 children (median age, 6.5 years; range, 1–17 years) with new posterior fossa brain tumors and clinical signs of intracranial hypertension with arterial spin-labeled CBF in 16 age-matched controls and 4 patients with posterior fossa tumors without ventriculomegaly or signs of intracranial hypertension. Measurements were recorded in the cerebrum at the vertex, deep gray nuclei, and periventricular white matter and were assessed for a relationship to ventricular size. In 16 symptomatic patients, we compared cerebral perfusion before and after alleviation of hydrocephalus.

RESULTS: Patients with uncompensated hydrocephalus had lower arterial spin-labeled CBF than healthy controls for all brain regions interrogated ($P < .001$). No perfusion difference was seen between asymptomatic patients with posterior fossa tumors and healthy controls ($P = 1.000$). The median arterial spin-labeled CBF increased after alleviation of obstructive hydrocephalus ($P < .002$). The distance between the frontal horns inversely correlated with arterial spin-labeled CBF of the cerebrum ($P = .036$) but not the putamen ($P = .156$), thalamus ($P = .111$), or periventricular white matter ($P = .121$).

CONCLUSIONS: Arterial spin-labeled–CBF was reduced in children with uncompensated hydrocephalus and restored after its alleviation. Arterial spin-labeled–CBF perfusion MR imaging may serve a future role in the neurosurgical evaluation of hydrocephalus, as a potential noninvasive method to follow changes of intracranial pressure with time.

ABBREVIATIONS: ASL = arterial spin-labeled; ICP = intracranial pressure; PF = posterior fossa

Hydrocephalus is a common neurosurgical condition in children and adults, accounting for approximately 69,000 annual hospital admissions and 39,000 shunt procedures in the United States.[1,2] While concepts of hydrocephalus remain complex, including pathophysiology, diagnostic and therapeutic approaches,[3-5] and outcome,[6,7] it is generally accepted that hydrocephalus reflects pathologic dynamics among brain, spinal cord, blood, and CSF within a confined environment.[8-10] In clinical practice, imaging is often used to work-up hydrocephalus in search of obstructing lesions or the presence of ventriculomegaly. However, ventricular size, a frequently used imaging feature, does not always correlate with underlying CSF pressures or resorptive capacity for CSF[11-16] and, therefore, may not reliably identify compensated hydrocephalus without signs of raised intracranial pressure (ICP) and progressive hydrocephalus with raised ICP.

Prior studies have shown reduced CBF with elevated ICP in various animal models of hydrocephalus.[17-20] Reduced CBF has also been reported in small case series of children with either congenital hydrocephalus or acute hydrocephalus from brain tumors by using ^{15}O-PET[21] or SPECT.[22] Recently, 2D phase-contrast MRA has shown that carotid and basilar arterial flow rates are reduced in infants with hydrocephalus.[23] However, 2D phase-contrast MRA does not directly measure CBF at the tissue level and may be hampered by long scanning times and flow-sensitive technical challenges.[24,25]

In contrast, arterial spin-labeled (ASL) MR imaging perfusion directly measures tissue perfusion without requiring long scanning times, contrast, or radioisotope injection.[26] It is also

Received October 22, 2013; accepted after revision November 13.

From the Departments of Radiology (K.W.Y.) and Neurosurgery (R.M.L., A.A., S.H.C., M.S.B.E.) and Division of Pediatric Neurosurgery (S.H.C., M.S.B.E.), Lucile Packard Children's Hospital at Stanford University, Palo Alto, California.

Paper was previously presented in part in abstract form at: Meeting of American Association of Neurological Surgeons, April 14–18, 2012, Miami, Florida; and Annual Meeting of the Society for Pediatric Radiology, April 16–17, 2012; San Francisco, California.

Please address correspondence to Kristen W. Yeom, MD, Department of Radiology, Lucile Packard Children's Hospital, Stanford University, Pediatric MRI & CT, Room 0511, 725 Welch Rd, Palo Alto, CA 94304; e-mail: kyeom@stanford.edu


Indicates article with supplemental on-line figures.

http://dx.doi.org/10.3174/ajnr.A3891

uniquely advantageous in children with high labeling efficiency and SNR and can be repeated in the event of patient motion or after CSF diversion without the risk of radiation exposure.[27] While ASL perfusion has increasingly become clinically available, no studies have investigated its role for evaluating hydrocephalus. We hypothesized that ASL-CBF is reduced in uncompensated hydrocephalus and improved after its alleviation and, therefore, can be used as a marker for symptomatic hydrocephalus.

MATERIALS AND METHODS

Patients with Symptomatic Hydrocephalus

All patients presenting with a posterior fossa (PF) brain tumor at our children's hospital from 2010 to August 2013 were retrospectively reviewed after approval by the institutional board (protocol 28674). The study cohort was identified by using the following inclusion criteria: The patients underwent a baseline ASL perfusion MR imaging at 3T, presented acutely with clinical signs of elevated ICP that required neurosurgical intervention (tumor resection or CSF diversion) within 7 days of a baseline ASL scan, had ventriculomegaly, and received no prior medical/radiation therapy or neurosurgical intervention, including CSF diversion.

One of the important pathogenic factors in hydrocephalus is increase in resistance to outflow of CSF, which has been correlated with elevated CSF pressure.[11,14] Children acutely presenting with uncompensated hydrocephalus from a new PF tumor that required symptom alleviation were selected as our study cohort, given that this group represented a relatively uniform cohort with similar obstructive mechanisms and could be distinguished from those with chronic compensated or uncompensated hydrocephalus.

Patients with underlying cardiac disease, epilepsy, migraines, hemorrhage, vascular lesions (aneurysm, AVM, fistula, or stenoocclusive disease), prior strokes, concomitant supratentorial tumors or leptomeningeal seeding, and prior history of radiation or chemotherapy were excluded, given their potential impact on cerebral perfusion.

Asymptomatic Patients

Patients with an incidentally discovered PF tumor but without signs of elevated ICP based on neurosurgical assessment and without ventriculomegaly or interstitial periventricular edema on MR imaging were also included for comparison if they had undergone a treatment-naïve ASL perfusion MR imaging at 3T.

Controls

Healthy controls who underwent ASL perfusion at 3T as part of routine brain MR imaging were randomly selected from our data base and matched for age and sedation status of the study subjects. The control group consisted of children with no underlying neurologic diseases and normal brain MR imaging findings. Examples of clinical reasons for undergoing MR imaging were isolated headaches, cholesteatoma of the middle ear, isolated facial lesions (eg, hemangioma, dermoid), scalp nevus, inflammatory nasal obstruction, short stature, and family history of aneurysms. Children with neurocutaneous syndromes; ataxia; gaze abnormality; developmental delay; endocrinopathies; psychiatric diseases; migraines; and any chronic diseases, including epilepsy, cancer, and previously treated neurologic diseases; and prior or ongoing medical therapy were excluded.

Clinical Assessment

Neurosurgical documentation regarding patient symptoms at baseline and after neurosurgical intervention was reviewed, including the patient's clinical status at follow-up ASL perfusion and, if present, the functional status of the shunt or ventriculostomy.

Imaging Methods

All subjects underwent brain MR imaging at 3T (Discovery 750; GE Healthcare, Milwaukee, Wisconsin), by using an 8-channel head coil. The technique used to perform perfusion ASL MR imaging has been described in detail elsewhere.[28] Briefly, our vendor-supplied ASL was performed by using a pseudocontinuous labeling period of 1500 ms, followed by a 1500-ms postlabel delay. Whole-brain images were acquired with a 3D background-suppressed fast spin-echo stack-of-spirals method, with a TR of approximately 5 seconds. Multiarm spiral imaging was used, with 8 arms and 512 points acquired on each arm (bandwidth, 62.5 kHz), yielding in-plane and through-plane spatial resolutions of 3 and 4 mm, respectively. A high level of background suppression was achieved by 4 separate inversion pulses spaced around the pseudocontinuous labeling pulse. The sequence required 5 minutes to acquire, which included proton-attenuation images required for CBF quantitation. For graphic prescription of the ASL, the sagittal image following the 3-plane localizer was used for alignment. Postprocessing was performed by using an automated reconstruction script that returned CBF images directly to the scanner console within 1 minute, by using the microsphere methodology described by Buxton et al.[29] Other ASL MR imaging parameters were TR/TE, 4632/10.5 ms; FOV, 24 cm; matrix, 512 × 8; and NEX, 3.

Imaging Analysis

ASL Perfusion. Quantitative mean cerebral CBF was measured and averaged at 3 consecutive axial images just above the centrum semiovale near the vertex by using region-of-interest analysis (size, 6500 mm^2). The axial planes near the vertex were selected, given a higher proportion of gray matter in this region, and because higher SNR is seen in the gray matter compared with white matter.[30,31] Also, a large region-of-interest size was chosen in this region for a more global CBF assessment that is easy to perform in a clinical setting by a radiologist or a neurosurgeon. In addition, more specific anatomic regions were interrogated by using region of interest (size, 85 mm^2) at the bilateral basal ganglia (at the level of putamina), thalami, and periventricular white matter. Examples are shown in Fig 1. The ROIs were independently performed by 2 neurosurgeons (A.A., R.M.L.) blinded to clinical information, including the status of hydrocephalus and follow-up clinical management. A blinded pediatric neuroradiologist (K.W.Y.) with a Certificate of Added Qualification in neuroradiology (7 years of experience) confirmed the proper region-of-interest placement.

For comparison between CBF at baseline and after neurosurgical intervention, the last follow-up ASL perfusion scan at 3T before initiation of any medical/radiation therapy was used so

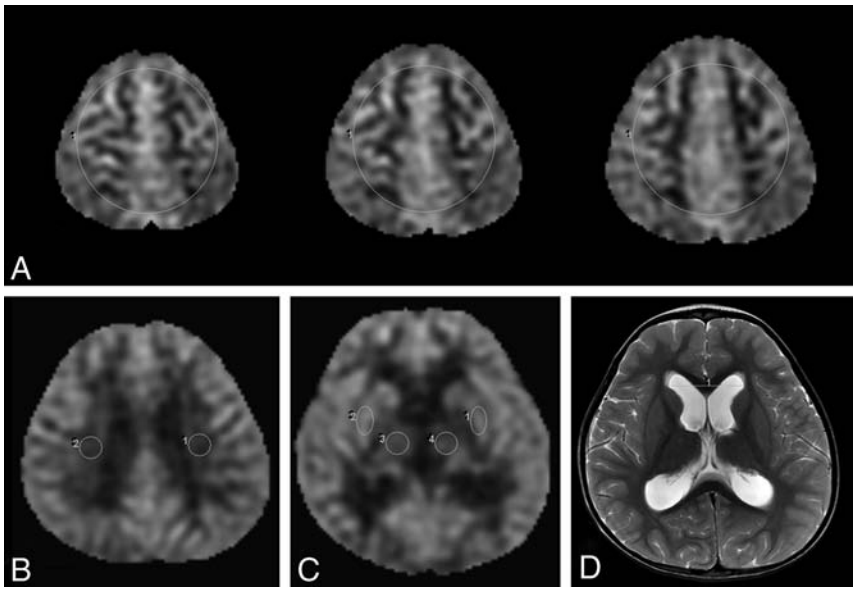

FIG 1. Brain region-of-interest placement and ventricular measurement. *A*, ROIs were placed in the 3 axial levels of the cerebrum near the vertex and just above the centrum semiovale. *B* and *C*. Additional ROIs were placed in bilateral periventricular white matter, and the deep gray matter, including the bilateral thalami and putamina. *D*, Ventricular measurement of the bilateral frontal horns was performed at the level of the caudate heads.

Table 1: Patient characteristics ($n = 23$)

Characteristic	
Age at initial diagnosis (yr)	
Median	6.2
Range	0.9–18
Sex	
Male	17 (74%)
Female	6 (26%)
Diagnosis (in order of frequency)	
Medulloblastoma	8 (35%)
Pilocytic astrocytoma	5 (22%)
Ependymoma	5 (22%)
Choroid plexus papilloma	2 (9%)
Tectal astrocytoma	2 (9%)
Diffuse intrinsic pontine glioma	1 (5%)
Hydrocephalus at presentation	19 (83%)

that no therapy other than tumor decompression or CSF diversion occurred in the interval between the baseline and the follow-up MR imaging.

Ventricular Size and Edema

The bifrontal diameter at the level of the caudate heads and underlying perfusion were measured in each patient at baseline and serial follow-up MR imaging by a neuroradiologist (K.W.Y.) blinded to patient clinical status (symptomatic versus asymptomatic with regard to hydrocephalus) at the time of imaging. The presence or lack of periventricular interstitial edema was noted based on T2-weighted images.

Statistical Analysis

All statistical analyses were performed with the Statistical Package for the Social Sciences, Version 20.0 (IBM, Armonk, New York) with an a priori significance level of $\alpha = .05$. Associations of perfusion at various sites (eg, thalamus, putamen, and white matter) with age and diameter between the frontal ventricular horns were tested by using the 2-tailed Pearson correlation. Comparisons of perfusion between sexes and between patients with and without interstitial edema were made by using the Mann-Whitney *U* test for independent samples. Comparisons of perfusion between healthy controls and asymptomatic patients with tumor and those symptomatic from obstructive hydrocephalus, based on tumor type, were made by using the Kruskal-Wallis test for independent samples with pair-wise comparisons. Differences between perfusion before and after relief of obstructive hydrocephalus were evaluated with the Wilcoxon signed rank test for related samples.

RESULTS

Clinical Findings

Twenty-three patients, median age, 6.2 years (range, 0.9–18 years), were included in the study. Patient demographics and clinical data are shown in Table 1. The control group matched by age and sedation status consisted of 16 children (7 boys and 9 girls; median age, 8.2 years; range, 1–18 years).

Patients with Symptomatic Hydrocephalus

Nineteen patients with PF tumor presented with symptomatic obstructive hydrocephalus, 16 of whom underwent at least partial resection. In 6 of these patients, CSF diversion in the form of an extraventricular drain or ventriculoperitoneal shunt was performed at the time of the surgery or subsequent to tumor resection. Three patients with unresectable brainstem tumors also underwent CSF diversion: ventriculoperitoneal shunt placement in 1 case of diffuse intrinsic pontine glioma and endoscopic third ventriculostomy in 2 cases of tectal astrocytoma.

Seventeen patients demonstrated symptomatic improvement after removal of the obstructing mass and/or CSF diversion. Two patients continued to demonstrate intractable hydrocephalus after tumor resection either from shunt complications or extraventricular drain malfunction that required further surgery.

Asymptomatic Patients

Four patients with PF tumor were asymptomatic for hydrocephalus at presentation. These patients underwent MR imaging for neurofibromatosis type 1, whole-body fever work-up, possible Bell palsy, and chronic headaches. Three of these patients electively underwent surgical resection of the tumor and 1 underwent focal CyberKnife.

Sedation Status

Sedation status was matched for all patients and their respective age-matched controls. For all patients with symptomatic hydrocephalus who underwent follow-up ASL perfusion, the sedation

Table 2: Cerebral blood flow in healthy controls ($n = 16$) and patients with PF Tumor ($n = 23$)

	Median Cerebral Blood Flow (mL/100 g/min) (Range)			
	Cerebrum	Basal Ganglia	Thalamus	White Matter
Healthy control	62.3 (50.4–68.9)	57.3 (44.6–70.8)	56.4 (45.4–67.8)	37.3 (26–43.4)
PF tumor without hydrocephalus	56.7 (46.4–63.1)	57.4 (49.7–60.0)	59.7 (53.2–65.4)	32.3 (20.8–35.8)
PF tumor with hydrocephalus	34.3 (8.6–59.0)	39.8 (12.5–59.6)	32.4 (8.1–50.5)	17.7 (6.0–28.1)

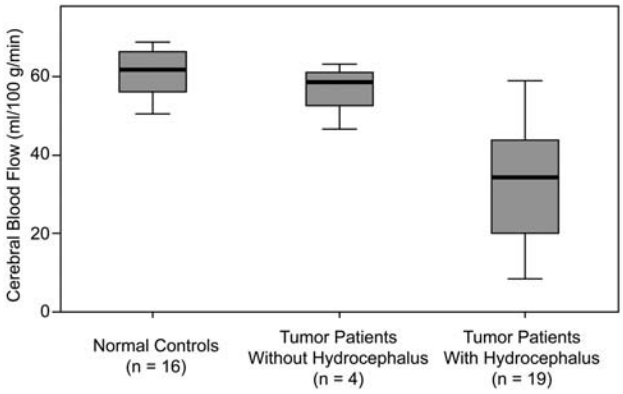

FIG 2. Comparison of ASL-CBF among controls, asymptomatic patients, and patients with hydrocephalus.

status was also identical for both baseline and follow-up MR imaging.

Cerebral Blood Flow

Controls. For the 16 age-matched and sedation-matched healthy controls, there was no correlation between age and CBF of the cerebrum at the vertex ($P = .884$). Similarly, there were no correlations between age and perfusion at more specific sites—that is, the putamen ($P = .920$), thalamus ($P = .244$), or periventricular white matter ($P = .297$).

Baseline CBF. CBF for all interrogated cerebral regions is summarized in Table 2. Patients with symptomatic hydrocephalus had lower CBF than healthy controls for all brain regions interrogated ($P < .001$) (Fig 2). No perfusion difference was seen between asymptomatic patients with PF tumor and healthy controls ($P = 1.000$).

Baseline and Follow-Up Comparison

Of 17 patients who showed symptomatic relief after neurosurgical intervention, 16 had both baseline and follow-up ASL perfusion. The median time between intervention and follow-up MR imaging used in the comparison analysis was 27 days (range, 1 day to 7 months). The median CBF increased after alleviation of obstructive hydrocephalus ($P < .002$) (Table 3 and Fig 3). Examples are shown in Figs 4 and 5.

Two patients continued to demonstrate elevated ICP after tumor resection due to ventriculoperitoneal shunt complications (peritoneal contamination from gastrostomy) and extraventricular drain malfunction that required a new shunt placement or revision. Therefore, these patients were only included in the preintervention CBF analysis. For these 2 patients, CBF values were low during elevated ICP. For example, the patient with elevated ICP due to shunt complications from peritoneal contamination showed further decrease in perfusion with CBF values of 10, 15, 12, and 6 mL/100 g/min at the cerebral vertex, putamen, thalamus, and periventricular white matter, respectively. MR imaging performed several hours after shunt revision showed mild improvement with CBF of 21, 33, 33, and 13 mL/100 g/min in the respective brain regions. The other patient also showed low CBF during extraventricular drain malfunction with improvement after a new shunt placement (Fig 6).

Ventricular Size and Other Parameters

The bifrontal ventricle size ranged from 35 to 65 mm in our patients with hydrocephalus at presentation. CBF at each site did not correlate with sex ($P > .082$) or tumor type ($P > .203$). Among the patients with tumor, the distance between the frontal horns inversely correlated with CBF of the cerebrum ($P = .036$), but not the putamen ($P = .156$), thalamus ($P = .111$), or periventricular white matter ($P = .121$).

Among patients with clinical improvement following relief of symptomatic hydrocephalus, ventricular size showed a small but statistically significant decrease, with a median change of 0.8 mm (range, 0.4–13.3 mm) ($P = .002$).

DISCUSSION

Reduced ASL-CBF was seen in children presenting with acute hydrocephalus from PF tumors compared with controls, with restoration of CBF close to the normal range after alleviation of hydrocephalus. Prior studies have shown that when ICP increases, disturbance in autoregulatory vasomotor capacity can reduce cerebral perfusion pressure, where a pronounced decrease in CBF can result at cerebral perfusion pressure below 40–50 mm Hg.[17,18] Because CBF was not significantly reduced in patients with PF tumors but without signs of raised ICP, CBF changes in our study were likely driven primarily by ICP effects rather than the presence of a mass lesion.

Infants and young children with hydrocephalus often present with nonspecific symptoms[32]; therefore, the distinction between ventriculomegaly and hydrocephalus with increased ICP is critically important. Given that many different etiologies for ventriculomegaly (underdevelopment, atrophy, metabolic diseases, and others) exist and ventricular size does not reliably identify symptomatic hydrocephalus,[11-14,16] a method that reflects alterations in cerebral hydrohemodynamics is desired. To our knowledge, this is the first study to report the use of ASL perfusion as a marker for symptomatic hydrocephalus. In contrast to nuclear medicine, CT and MR imaging contrast perfusion, or 2D phase-contrast MRA methods, ASL perfusion does not require contrast or radiation, provides quantitative CBF measurements directly at the tissue level, and is technically easy to acquire at a relatively short scan time.

The CBF of our hydrocephalus cohort (34.3 ± 14.9 mL/100 g/min) is consistent with a prior report by Hayashi et al,[33] which

Table 3: Cerebral blood flow before and after alleviation of obstructive hydrocephalus ($n = 16$)[a]

	Median Cerebral Blood Flow (mL/100 mg/min) (Range)			
	Cerebrum	Basal Ganglia	Thalamus	White Matter
Before alleviation of hydrocephalus	35.8 (8.6–59)	38.0 (12.5–59.6)	29.9 (8.1–50.3)	17.5 (6.0–28.1)
After alleviation of hydrocephalus	52.6 (29.8–69.7)	53.9 (40.2–68.8)	55.3 (29.1–63.3)	31 (23.4–45.4)

[a] For each site, CBF was increased following alleviation of hydrocephalus (Wilcoxon signed rank test for related samples, $P < .002$).

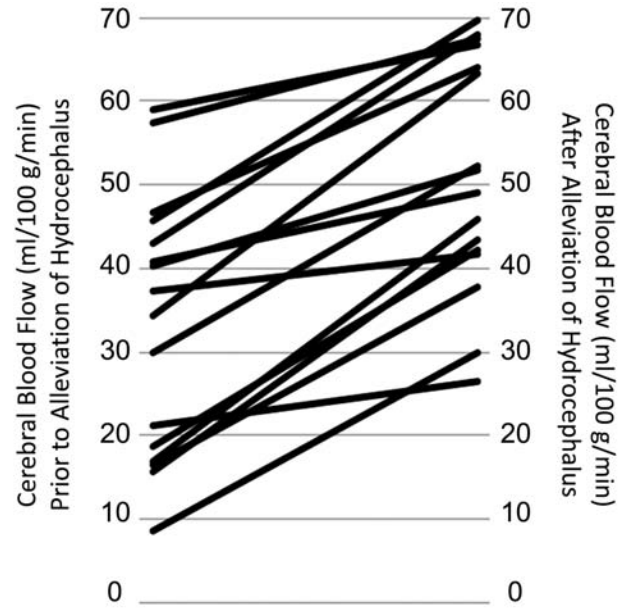

FIG 3. ASL-CBF values before and after alleviation of obstructive hydrocephalus.

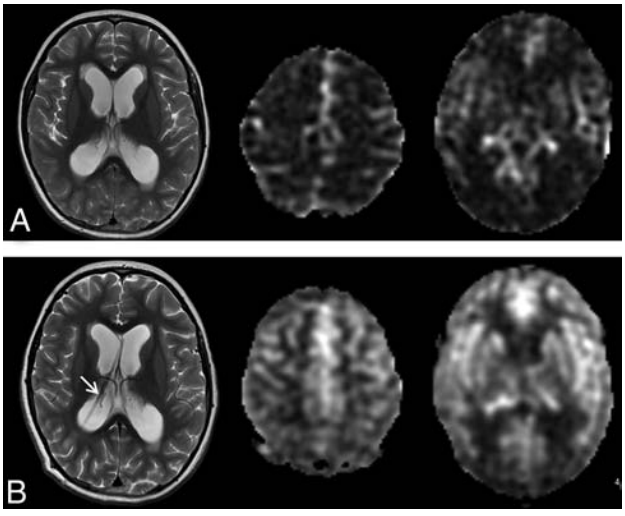

FIG 4. ASL perfusion of a 6-year-old girl presenting with hydrocephalus from a diffuse intrinsic pontine glioma. *A*, The patient presented with acute symptoms, including headache, nausea/vomiting, and somnolence. Enlarged ventricles and periventricular edema were noted and low CBF of 9, 13, 8, and 6 mL/100 g/min at the cerebral vertex, putamina, thalami, and periventricular white matter, respectively. A shunt was placed a day after the MR imaging. *B*, Improved CBF (30, 40, 36, 27 mL/100 g/min) and resolution of acute symptoms were noted in the respective brain regions a month later. Note the shunt catheter in place (*arrow*) and residual ventricular enlargement and edema.

showed low hemispheric CBF (32 ± 6 mL/100 g/min) by using ^{133}Xe CT in adults who presented with hydrocephalus after aneurysm rupture and correlative high ICP levels (36 ± 6 mm Hg).

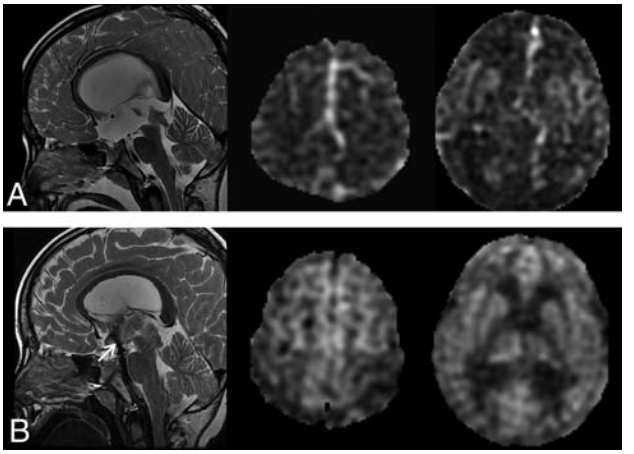

FIG 5. ASL perfusion of a 5-year-old boy presenting with acute hydrocephalus due to aqueduct obstruction from a tectal glioma. *A*, The patient presented with acute gait abnormality, nausea/vomiting, and somnolence. Enlarged ventricles and low global CBF of 16, 20, 17, and 8 mL/100 g/mL were seen at the cerebral vertex, putamina, thalami, and periventricular white matter, respectively. The patient underwent third ventriculostomy a day later and subsequently showed symptomatic relief. *B*, Two months later, improved CBF was seen, with CBF of 43, 58, 50, and 32 mL/100 g/min in the respective brain regions. Note a CSF jet at the patent third ventriculostomy site (*arrow*).

Leliefeld et al[23] also reported low CBF (25 ± 11 mL/100 g/min) calculated from carotid and basilar artery flow rates by using 2D phase-contrast MRA in children with hydrocephalus. The lower CBF estimated in that study may be attributed to some combination of the younger age (range, 1 day to 7 months) of their cohort that might have had less robust autoregulatory mechanisms or more compressible parenchymal vessels within an immature brain, low signal due to a 2D phase-contrast MRA technique, and variable etiologies of hydrocephalus (intraventricular hemorrhage, arachnoid cyst, mucopolysaccharidosis, and various obstructive lesions). Of note, CBF of our healthy pediatric controls (62.3 ± 6 mL/min/100 g) is consistent with a normal mean CBF range of 53–71 mL/min/100 g in children 2–19 years of age measured by ^{133}Xe SPECT[34] but higher than ^{133}Xe CT–based mean CBF of 50 mL/min/100 g reported for healthy adults.[33]

CBF was reduced for all brain regions in patients presenting with symptomatic hydrocephalus. Studies have shown that ventriculomegaly may directly decrease CBF via mechanical distortion and reduced vessel caliber.[35,36] Alternatively, reduced brain compliance and, thereby, narrow-capacitance vessels, induced by ventricular enlargement, may decrease CBV and CBF, similar to a hydrodynamic mechanism proposed by Greitz.[37,38] However, it is noteworthy that ventricular size inversely correlated with CBF of the cerebrum at the vertex, but not in the other brain regions. It is possible that deep gray and periventricular regions are more vulnerable to mechanical effects with pronounced CBF changes, even with mild ventriculomegaly. This finding unlikely reflects under-

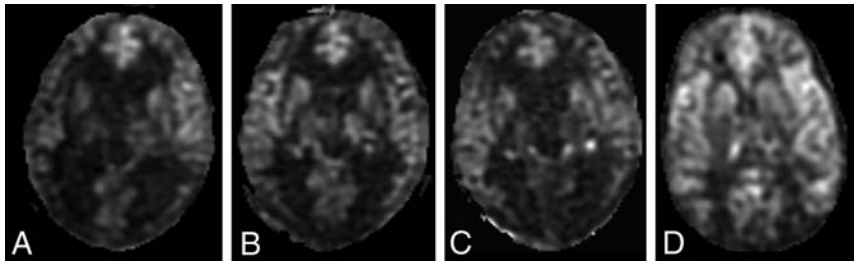

FIG 6. Serial ASL perfusion of a 10-year-old boy with hydrocephalus from medulloblastoma. *A*, The patient presented acutely with headaches and nausea/vomiting. Relatively low CBF of 29, 50, 45, 20 mL/100 g/min, compared with controls, was noted in the cerebral vertex, putamina, thalami, and periventricular white matter. The patient underwent PF tumor resection and extraventricular drain placement 2 days later. *B*, One day after the surgery, the patient continued to have high ICP despite extraventricular drain placement and showed low CBF of 22, 34, 30, and 12 mL/100 g/min in the respective brain regions. *C*, The symptoms continued to worsen with high ICP and further decrease in CBF of 17, 31, 18, and 10 mL/100 g/min 2 days later. Due to extraventricular drain malfunction, a new ventriculoperitoneal shunt was subsequently placed. *D*, Several months later, the patient presented for routine surveillance of medulloblastoma with a functioning ventriculoperitoneal shunt and decreased ventricular size and was clinically asymptomatic at this time. While some perfusion alteration may be expected from interval chemotherapy and radiation, it has, nevertheless, improved, with a CBF of 36, 44, 34, 21 mL/100 g/min in the respective brain regions.

lying regional pressure differences because no evidence for transmantle pressure gradient has been shown in hydrocephalus due to viscoelasticity of the brain substance.[8,39]

Concepts of hydrocephalus are complex and continue to evolve.[8,9,37,38] They include the following: the conventional major CSF pathway, including the original work of Dandy and Blackfan[40] on bulk flow theory and distinction of obstructive and communicating hydrocephalus; and a minor CSF pathway that describes interactions of brain compliance, CSF and arteriole pulsations, vascular capacitance/pulse pressures, and capillary absorption.[8,9,37,40-42] Given the complex pathophysiology, understanding the physiology of hydrocephalus remains a challenging neurosurgical problem.

While ventricular size remains important for the work-up of hydrocephalus, prior studies have shown that it may not reliably identify abnormal ICP[11-13,15] or resorptive capacity for CSF,[11] particularly in cases of chronic hydrocephalus or shunt failure in which brain compliance may be altered from injury, periventricular gliosis, and other reactive changes.[12] Our results suggest that ASL perfusion identifies changes in underlying tissue physiology and may, therefore, be a useful adjunct to conventional MR imaging without the need for contrast or radiation exposure.

There are a few limitations of this study. Direct CSF pressure recordings that correspond to CBF changes would be desirable; however, pressure measurements are not routinely obtained during resection of PF tumors or at the time of MR imaging and, therefore, were not feasible. While ASL-CBF was altered in the uncompensated state and was restored after CSF symptomatic relief in this population of pediatric patients with PF tumors, baseline perfusion metrics and deficit patterns may vary to some degree in other models of hydrocephalus, such as normal-pressure hydrocephalus of older adults; chronic, compensated, or nonprogressive hydrocephalus; and various conditions of hydrocephalus associated with prior hemorrhage/injury, brain malformations, and metabolic disorders and congenital chromosomal disorders. However, CBF changes across time intervals, nevertheless, could help identify altered physiologic conditions that relate to ICP status and other challenging cases of ventriculomegaly (On-line Figs 1–3). Finally, general effects of sedation on childhood cerebral perfusion and metabolism are relatively unknown[27]; however, this lack of knowledge is unlikely to have impacted our study, given that the sedation status was matched for baseline and follow-up ASL scans, and for the patient and control groups.

CONCLUSIONS

ASL-CBF was reduced in patients with symptomatic hydrocephalus and restored after surgically mediated alleviation. ASL perfusion MR imaging may serve a future role in the evaluation of hydrocephalus, as a potential noninvasive method to follow changes in ICP.

REFERENCES

1. Bondurant CP, Jimenez DF. **Epidemiology of cerebrospinal fluid shunting.** *Pediatr Neurosurg* 1995;23:254–58, discussion 259
2. Simon TD, Riva-Cambrin J, Srivastava R, et al. **Hospital care for children with hydrocephalus in the United States: utilization, charges, comorbidities, and deaths.** *J Neurosurg Pediatr* 2008;1:131–37
3. Eklund A, Smielewski P, Chambers I, et al. **Assessment of cerebrospinal fluid outflow resistance.** *Med Biol Eng Comput* 2007;45:719–35
4. Sundström N, Andersson K, Marmarou A, et al. **Comparison between 3 infusion methods to measure cerebrospinal fluid outflow conductance.** *J Neurosurg* 2010;113:1294–303
5. Walker CT, Stone JJ, Jacobson M, et al. **Indications for pediatric external ventricular drain placement and risk factors for conversion to ventriculoperitoneal shunt.** *Pediatr Neurosurg* 2012;48:342–47
6. Stone JJ, Walker CT, Jacobson M, et al. **Revision rate of pediatric ventriculoperitoneal shunts after 15 years.** *J Neurosurg Pediatr* 2013;11:15–19
7. Vinchon M, Rekate H, Kulkarni AV. **Pediatric hydrocephalus outcomes: a review.** *Fluids Barriers CNS* 2012;9:18
8. Rekate HL. **A consensus on the classification of hydrocephalus: its utility in the assessment of abnormalities of cerebrospinal fluid dynamics.** *Childs Nerv Syst* 2011;27:1535–41
9. Symss NP, Oi S. **Theories of cerebrospinal fluid dynamics and hydrocephalus: historical trend.** *J Neurosurg Pediatr* 2013;11:170–77
10. Preuss M, Hoffmann KT, Reiss-Zimmermann M, et al. **Updated physiology and pathophysiology of CSF circulation—the pulsatile vector theory.** *Childs Nerv Syst* 2013;29:1811–25
11. Børgesen SE, Gjerris F. **Relationship between intracranial pressure, ventricular size, and resistance to CSF outflow.** *J Neurosurg* 1987;67:535–39
12. Dahlerup B, Gierris F, Harmsen A, et al. **Severe headache as the only symptom on long-standing shunt dysfunction in hydrocephalic children with normal or slit ventricles revealed by computed tomography.** *Childs Nerv Syst* 1985;1:49–52
13. Ashley WW Jr, McKinstry RC, Leonard JR, et al. **Use of rapid-se-**

quence magnetic resonance imaging for evaluation of hydrocephalus in children. *J Neurosurg* 2005;103(2 suppl):124–30
14. Tans JT, Poortvliet DC. **Relationship between compliance and resistance to outflow CSF in adult hydrocephalus.** *J Neurosurg* 1989;71:59–62
15. Brawanski A, Soerensen N. **Increased ICP without ventriculomegaly. Diagnostic and therapeutic problems in a 1-year old boy.** *Childs Nerv Syst* 1985;1:66–68
16. Johnston I, Paterson A. **Benign intracranial hypertension. II. CSF pressure and circulation.** *Brain* 1974;97:301–12
17. Grubb RL, Raichle ME, Phelps ME, et al. **Effects of increased intracranial pressure on cerebral blood volume, blood flow, and oxygen utilization in monkeys.** *J Neurosurg* 1975;43:385–98
18. Häggendal E, Lofgren J, Nilsson NJ, et al. **Effects of varied cerebrospinal fluid pressure on cerebral blood flow in dogs.** *Acta Physiol Scand* 1970;79:262–71
19. Jones HC, Richards HK, Bucknall RM, et al. **Local cerebral blood flow in rats with congenital hydrocephalus.** *J Cereb Blood Flow Metab* 1993;13:531–34
20. da Silva MC, Michowicz S, Drake JM, et al. **Reduced local cerebral blood flow in periventricular white matter in experimental neonatal hydrocephalus-restoration with CSF shunting.** *J Cereb Blood Flow Metab* 1995;15:1057–65
21. Shirane R, Sato S, Satao K, et al. **Cerebral blood flow and oxygen metabolism in infants with hydrocephalus.** *Childs Nerv Syst* 1992;8:118–23
22. Shinoda M, Yamaguchi T, Tanaka Y, et al. **Single photon emission computerized tomography in childhood hydrocephalus.** *Childs Nerv Syst* 1992;8:219–21
23. Leliefeld PH, Gooskens R HJM, Vincken KL, et al. **Magnetic resonance imaging for quantitative flow measurements in infants with hydrocephalus: a prospective study.** *J Neurosurg Pediatr* 2008;2:163–70
24. Wheaton AJ, Miyazaki M. **Non-contrast enhanced MR angiography: physical principles.** *J Magn Reson Imaging* 2012;36:286–304
25. Ozsarlak O, Van Goethem JW, Maes M, et al. **MR angiography of the intracranial vessels: technical aspects and clinical applications.** *Neuroradiology* 2004;46:955–72
26. Wang J, Licht DJ, Jahng GH, et al. **Pediatric perfusion imaging using pulsed arterial spin labeling.** *J Magn Reson Imaging* 2003;18:404–13
27. Wang J, Licht DJ. **Pediatric perfusion MR imaging using arterial spin labeling.** *Neuroimaging Clin Am* 2006;16:149–67, ix
28. Dai W, Garcia D, Bazelaire C, et al. **Continuous flow-driven inversion for arterial spin labeling using pulsed radio frequency and gradient fields.** *Magn Reson Med* 2008;60:1488–97
29. Buxton RB, Frank LR, Wong EC, et al. **A general kinetic model for quantitative perfusion imaging with arterial spin labeling.** *Magn Reson Med* 1998;40:383–96
30. van Gelderen P, de Awart JA, Duyn JH. **Pitfalls of MRI measurements of white matter perfusion based on arterial spin labeling.** *Magn Reson Med* 2008;59:788–95
31. Ye FQ, Berman KF, Ellmore T, et al. **H2 15O PET validation of steady-state arterial spin tagging cerebral blood flow measurements in humans.** *Magn Reson Med* 2000;44:450–56
32. Kirkpatrick M, Engleman H, Minns RA. **Symptoms and signs of progressive hydrocephalus.** *Arch Dis Child* 1989;64:124–28
33. Hayashi M, Kobayashi H, Kawano H, et al. **Cerebral blood flow and ICP patterns in patients with communicating hydrocephalus after aneurysm rupture.** *J Neurosurg* 1984;61:30–36
34. Chiron C, Raynaud C, Maziere B, et al. **Changes in regional cerebral blood flow during brain maturation in children and adolescents.** *J Nucl Med* 1992;33:696–703
35. Wozniak M, McLone DG, Raimondi AJ. **Micro- and macrovascular changes as the direct cause of parenchymal destruction in congenital murine hydrocephalus.** *J Neurosurg* 1975;43:535–45
36. Del Bigio MR. **Neuropathological changes caused by hydrocephalus.** *Acta Neuropathol* 1993;85:573–85
37. Greitz D. **Radiological assessment of hydrocephalus: new theories and implications for therapy.** *Neurosurg Rev* 2004;27:145–65, discussion 166–67
38. Greitz D. **Paradigm shift in hydrocephalus research in legacy of Dandy's pioneering work: rationale for third ventriculostomy in communicating hydrocephalus.** *Childs Nerv Syst* 2007;23:487–89
39. Stephensen H, Tisell M, Wikkelsö C. **There is no transmantle pressure gradient in communicating or noncommunicating hydrocephalus.** *Neurosurgery* 2002;50:763–71, discussion 771–73
40. Dandy WE, Blackfan KD. **Internal hydrocephalus: an experimental, clinical, and pathological study.** *Am J Dis Child* 1914;8:406–82
41. Oi S, Di Rocco C. **Proposal of "evolution theory in cerebrospinal fluid dynamics" and minor pathway hydrocephalus in immature brain**. *Childs Nerv Syst* 2006;22:662–69
42. Dandy WE. **Where is cerebrospinal fluid absorbed?** *JAMA* 1929;92:2012–14

Risk Factors of Hematomyelia Recurrence and Clinical Outcome in Children with Intradural Spinal Cord Arteriovenous Malformations

G. Saliou, A. Tej, M. Theaudin, M. Tardieu, A. Ozanne, M. Sachet, D. Ducreux, and K. Deiva

ABSTRACT

BACKGROUND AND PURPOSE: Few published data are available concerning the risk of re-bleeding of spinal cord AVM after an hematomyelia and concerning the long-term clinical outcome. Our aim was to assess the risk of recurrence and long-term clinical outcome after hematomyelia in children with spinal cord AVMs.

MATERIALS AND METHODS: This single-center retrospective study reviewed the clinical and radiologic data of 28 children younger than 18 years of age with arteriovenous malformation who had experienced at least 1 episode of hematomyelia between 1988 and 2012. Long-term clinical outcome was assessed by the American Spinal Injury Association Impairment Scale, and radiologic review included MR imaging and angioarchitecture on angiography (blinded to clinical information) before treatment and at recurrence.

RESULTS: Sixteen children (57%) experienced 1 episode of hematomyelia, while 12 children (43%) experienced recurrence. Girls and boys were equally affected (sex ratio, 1:1), and mean clinical follow-up was 5.7 ± 4.4 years. The risk of recurrence was higher for AVMs of the cervical and upper thoracic spine, 12 (100%) versus 11 (69%) ($P = .01$). A high American Spinal Injury Association scale score at last follow-up was reported for 11 children (39%), and the risk of recurrence tended to be associated with poorer functional prognosis (7 [64%] versus 5 [29%], $P = .07$). At the time of recurrence, perimedullary venous drainage was the main factor associated with recurrence ($P = .002$). Occlusion rate ≥50% was associated with a decreased risk of recurrence ($P = .047$).

CONCLUSIONS: In the present series, cervical and upper thoracic spinal cord AVMs and microarchitecture were predictive of the risk of hematomyelia recurrence. Perimedullary venous drainage was one of the main parameters associated with recurrence. Functional prognosis was better in patients with a single episode of hematomyelia.

ABBREVIATION: ASIA = American Spinal Injury Association

Spinal cord vascular malformations, particularly arteriovenous malformations, are the most common causes of nontraumatic intraspinal bleeding, called "hematomyelia."[1] Spinal cord AVMs may present with acute neurologic symptoms or deterioration of pre-existing neurologic deficits after hematomyelia.[1] MR imaging is a useful tool for the diagnosis of hematomyelia and defining the type of vascular injury but may not be sufficient to accurately define the type of injury, the site of the shunt, and the angioarchitecture of the lesion. Angiography is therefore the reference tool for diagnosis, detailed analysis of the angioarchitecture of spinal vascular malformations, and defining the treatment strategy.[2] Due to the fragility of vascular lesions and their eloquent localization in the spinal cord, partial and targeted treatment can be proposed to avoid deterioration of the neurologic deficit because endovascular treatment is often technically challenging, especially when no specific vascular target is identified. Although a number of angioarchitectural factors associated with an increased risk of bleeding in cerebral AVMs have been described,[3-7] few published data are available concerning the risk of bleeding of spinal AVMs, particularly predictive factors of intraspinal rebleeding after a first

Received October 1, 2013; accepted after revision December 10.

From the Service de Neuroradiologie (G.S., M.S., D.D., A.O.), Service de Neurologie Pédiatrique (A.T., M. Tardieu, K.D.), and Service de Neurologie (M. Theaudin), Centre Hospitalier Universitaire Bicêtre, National Referral Center for Neurovascular Malformations in Children, Le Kremlin Bicêtre Cedex, France.

Contribution of the authors: Guillaume Saliou: conception and design, acquisition of data and drafting the article, analysis and interpretation of data. Amel Tej: acquisition of data and drafting the article, analysis and interpretation of data. Marie Theaudin: acquisition of data and drafting the article, analysis and interpretation of data. Marc Tardieu: conception and design, drafting the article, analysis and interpretation of data. Augustin Ozanne: acquisition of data and drafting the article, analysis and interpretation of data. Marina Sachet: acquisition of data and drafting the article, analysis and interpretation of data. Denis Ducreux: acquisition of data and drafting the article, analysis and interpretation of data. Kumaran Deiva: acquisition of data and drafting the article, analysis and interpretation of data, statistical analysis.

Paper previously presented in part at: Annual Meeting of the World Federation of Interventional and Therapeutic Neuroradiology, January 15–20, 2012; Cape Town, South Africa.

Please address correspondence to Guillaume Salio, MD-PhD, Service de Neuroradiologie, CHU Bicêtre, 78 rue du General Leclerc, 94275 Le Kremlin Bicêtre Cedex, France; e-mail: guillaume.saliou@bct.aphp.fr

http://dx.doi.org/10.3174/ajnr.A3888

episode of hematomyelia and predictive factors of long-term clinical outcome. Moreover, endovascular embolization is considered a good option to prevent rebleeding.[2,8] The primary objective of this study was, therefore, to identify clinical, radiologic, and angiographic factors associated with recurrent hematomyelia in a series of children with hematomyelia. Treatment decisions and targets in the AVM management strategy could be facilitated when only partial removal was acceptable in terms of the risks of treatment, to prevent further bleeding. The secondary objective was to determine the clinical, radiologic, and angiographic factors of clinical severity after a first or subsequent episodes of hematomyelia.

MATERIALS AND METHODS

Patient Inclusion

The patient cohort was extracted from a single-center data base comprising 235 patients with spinal cord AVMs. Among them, 43 patients had a hemorrhage related to a spinal cord AVM. Patients older than 18 years of age (5 patients), patients without MR imaging or without clinical or imaging follow-up (3 patients), or patients with isolated subarachnoid hemorrhage secondary to their malformation (7 patients) were excluded from this study. A total of 28 patients younger than 18 years of age with an arteriovenous malformation and at least 1 episode of hematomyelia, followed jointly by the National Referral Center for Neurovascular Diseases in Children and the Pediatric Neurology Department, Hôpitaux Universitaires Paris-Sud, Hôpital Bicêtre, were included in a retrospective study from January 1, 1988, to December 31, 2012. We retrospectively reviewed the following clinical data: date of birth, sex, time of first episode of hematomyelia, date of discovery of the AVM, type of clinical symptoms at onset, date of recurrence, date of last follow-up, and the American Spinal Injury Association (ASIA) Impairment Scale score at onset, at first recurrence, and at last follow-up. We used the following ASIA Impairment Scale: A, complete neurologic deficit with no motor or sensory function; B, incomplete neurologic deficit with sensory but not motor function preserved below the neurologic level; C, incomplete neurologic deficit with motor function preserved below the neurologic level, muscle grade <3; D, incomplete neurologic deficit with motor function preserved below the neurologic level, muscle grade ≥ 3; and E, normal motor and sensory function.[9] The ASIA scale was assessed retrospectively on the basis of the neurologic reports in the patient charts. A severe ASIA score at onset or at last follow-up was defined by an ASIA Impairment Scale of A, B, or C, while ASIA Impairment Scale D or E was considered not severe.

Most patients were referred to our center for further management of the AVM, and initial management at the acute phase of hematomyelia was therefore performed according to the primary physician's decision. Consequently, surgical decompression of the spinal cord was performed for 6 patients before referral in an effort to improve neurologic recovery. Two patients were treated by laminectomy alone, 2 patients underwent hematoma evacuation, and 2 patients underwent hematoma evacuation and partial nidus excision. One of these last patients experienced worsening of his previous neurologic status, and the other remained stable. First-line management of the malformation was always embolization. Only 1 patient was subsequently referred to another center for surgical excision following failure of AVM catheterization. This patient was lost to clinical follow-up.

When the mass effect resolved after hematomyelia, AVM treatment was always considered as soon as possible to avoid recurrence. All patients were treated by *n*-butyl 2-cyanoacrylate embolization under general anesthesia. The aim of endovascular management was to at least target angioarchitectural weaknesses such as intranidal aneurysms or pseudoaneurysms and to decrease the size of the malformation without inducing glue fragmentation and distal venous embolism. All procedures were performed with the patient under general anesthesia, and no specific monitoring or xylocaine test was used. No anticoagulation was used during endovascular treatment. Embolization was performed in 1 or several sessions in an attempt to cure the disease but was not successful in every case due to safety issues because the benefit/risk balance to cure the patient was sometimes considered unacceptable and only partial embolization was then performed.

Radiologic Assessments

Imaging review included conventional MR imaging sequences and macro- and microarchitecture on angiography before and after partial or complete treatment. All imaging examinations were reviewed by 2 experienced neurovascular specialists blinded to the diagnosis (G.S. and P. Lasjaunias or M.S.). All except 1 of the patients were assessed by MR imaging at clinical onset of symptoms. For 27 patients, acute hematomyelia was diagnosed in the context of a sudden episode of spinal cord neurologic deficit associated with focal changes on MR imaging: increased diameter of the cord with intraspinal hypointensity on T2* and hyperintensity on T1-weighted sequences surrounded by hyperintense edema on T2-weighted sequences. For 1 patient, hematomyelia was diagnosed on the basis of identical clinical features associated with hyperattenuation in the spinal cord on CT. Spinal cord MR images were analyzed for the size of the ASIA scale lesion on sagittal T2-weighted sequences: T2 hypersignal involving >3 vertebrae on sagittal MR imaging and T1 hyposignal corresponding to a signal identical to that of CSF on T1-weighted sequences.

We studied the following angioarchitectural features: type of arteriovenous malformation (ie, fistula or nidus), number (1, 2, or 3 versus >3) and type of arterial feeders (radiculomedullary feeders for arteries that feed the anterior spinal artery in the midline or radiculopial feeders for arteries that feed the ipsilateral posterior spinal cord artery), venous drainage (perimedullary venous drainage, radicular venous drainage, anterior spinal vein drainage, and draining vein stenosis $>50\%$), vascular intranidal dilation (pseudoaneurysm corresponding to the site of vascular rupture, intranidal or draining vein aneurysm or ectasia), treatment (ie, endovascular embolization, surgery, both), and occlusion rate. Because it could not be determined whether the AVM perimedullary venous drainage traveled in a physiologic direction or corresponded to venous reflux, it was called "perimedullary venous drainage" and not "perimedullary venous reflux." All angioarchitectural features were assessed on angiography.

Perimedullary AVM venous drainage was defined as a dilated network around the spinal cord separated from the nidus itself and corresponding to direct drainage of the vascular malformation. A pseudoaneurysm was defined as vascular intranidal dila-

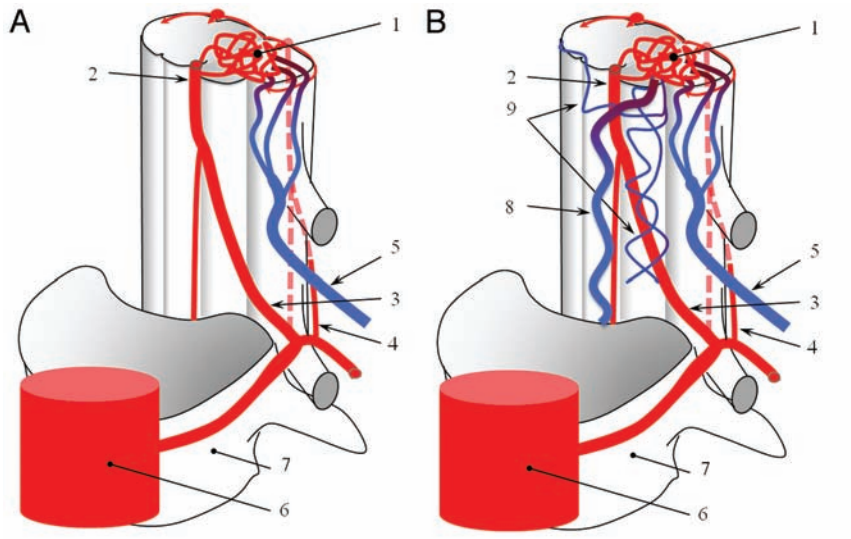

FIG 1. Diagrams of a spinal cord arteriovenous malformation with various venous drainage pathways. *A*, Nidus AVM drained by a single radicular vein. *B*, Nidus AVM with additional drainage via the anterior spinal vein and perimedullary veins: 1) nidus, 2) anterior spinal artery, 3) radiculomedullary artery, 4) radiculopial artery, 5) radicular vein, 6) aorta, 7) vertebral body, 8) anterior spinal vein, 9) perimedullary venous drainage.

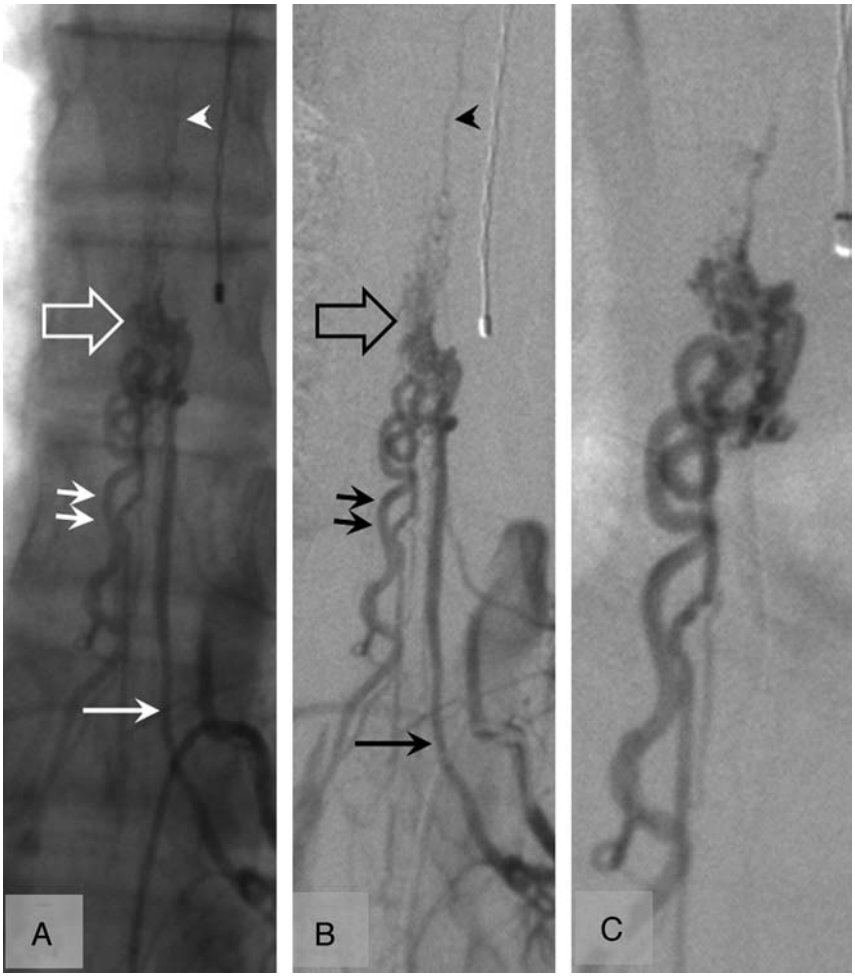

FIG 2. Spinal angiogram without (*A*) and with (*B*) digital subtraction and selective injection (*C*) in a 16-year-old boy with a lower thoracic spinal cord AVM at the time of control after a single episode of hematomyelia (39 months' follow-up). The AVM (*open arrow*) is fed by a radiculopial artery (*single arrow*). The AVM is drained by 2 radicular veins (*double arrows*) and the anterior spinal vein (*arrowhead*) with no perimedullary venous drainage.

tion (either arterial or venous) without a true wall and representing the nonthrombotic portion of the hematoma with a certain degree of contrast pooling on angiography. Anterior spinal vein drainage was assessed on angiography and checked on MR imaging because a single posterior midline longitudinal venous drainage can sometimes be incorrectly interpreted on angiography. Radicular vein drainage was defined as venous drainage through the intervertebral foramina. The various pathways of venous drainage are illustrated in Fig 1, with angiographic findings in Fig 2 and Fig 3. Draining vein stenosis of ≥50% corresponded to a focal decrease in vein diameter by at least one-half. The nidus occlusion rate was assessed by measuring the decrease in the mean radius [(height + width)/2]. Angiographic cure was defined as the disappearance of the nidus with no persistent arteriovenous shunts. The site of the AVM was classified into 3 groups comprising equal numbers of vertebrae: cervical (C1 to C7), upper thoracic (T1 to T7), and lower thoracic (T8 to conus medullaris), as previously proposed.[10]

Statistical Analysis

Statistical analysis was performed with the Statistical Package for the Social Sciences software for Windows (Version 17; IBM, Armonk, New York). Descriptive data were compared by using the χ^2 test or Fisher exact test for proportions and a Mann-Whitney test for continuous measurements. Differences were considered significant for P values $< .05$. Three angiographies were analyzed for each patient: the angiography performed at the time of the first or only episode of hematomyelia (Table 1); the angiography performed at the time of recurrence (last episode if several recurrences of hematomyelia) or any angiography performed close to the mean time of angiography performed for children with recurrence and for routine follow-up in children without recurrence (Table 2); and the last angiography performed. Statistical analysis of angiographic findings at the end of follow-up compared the results of the last angiography with the ASIA Impairment Scale (Table 3).

Ethical Issues

This was a retrospective noninterventional study. No blood tests or clinical investigations

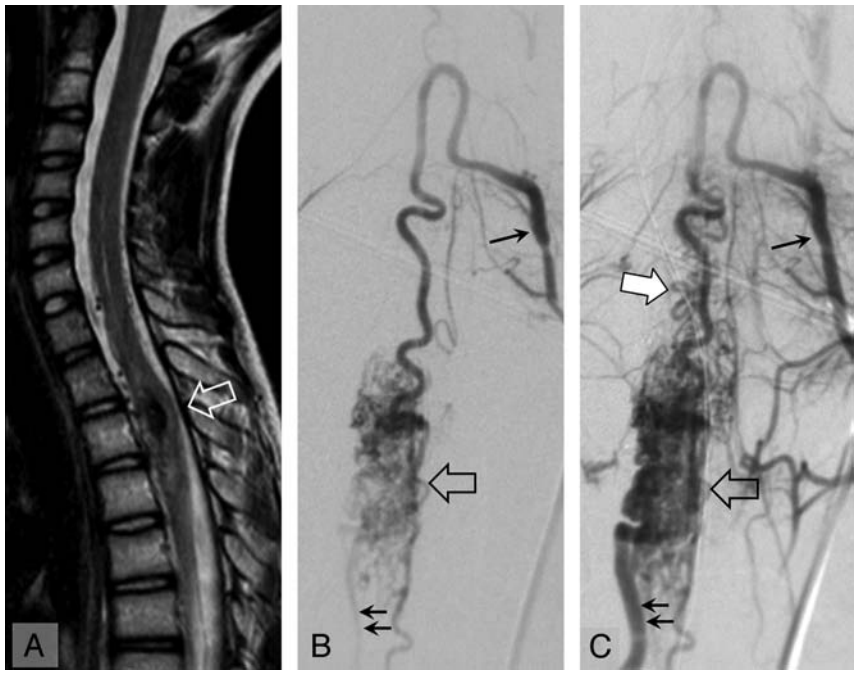

FIG 3. Spinal cord MR imaging (*A*, sagittal T2 TSE) and angiography, anteroposterior view, early (*B*) and late (*C*) arterial phase in a 15-year-old girl with an upper thoracic spinal cord AVM at the time of recurrence of hematomyelia (29 months' follow-up). On MR imaging, the hematomyelia and AVM are located at T2 (*open arrow*). On angiography, the AVM (*open arrow*) is fed by a radiculomedullary artery (*single arrow*). The AVM is drained inferiorly by a radicular vein (*double arrows*) and superiorly by perimedullary veins (*white arrow*).

were required in addition to standard care of these patients. The study was performed in accordance with French ethical guidelines.

RESULTS

All 28 malformations were intradural and were classified according to a previous classification[11] as follows: 18 intramedullary AVMs, 3 juvenile metameric AVMs, 6 intradural dorsal AVFs, and 1 intradural ventral AVF.

Risk of Recurrence of Hematomyelia

The main initial clinical and radiologic findings are summarized in Table 1. The mean clinical follow-up for the 28 patients was 5.7 ± 4.4 years. One or more recurrences were observed in 12 children (43%), with a mean follow-up of 3.3 years (median, 2.6 years; SD, 2.6 years; minimum, 0.1 year; maximum, 8.9 years) (date of last hematomyelia when > 1 recurrence). Children with recurrent episodes were older than those without recurrence, but the difference was not statistically significant. At the end of follow-up, 1 patient had experienced 3 episodes of hematomyelia, and 1 patient had experienced 2 episodes of hematomyelia and 1 episode of isolated subarachnoid hemorrhage. Similarly, boys tended to experience more recurrent episodes than girls, but no significant differences were observed in terms of clinical and MR imaging characteristics.

The frequency of spinal cord localization of the AVM was as follows: cervical ($n = 16$, 57%) followed by upper thoracic ($n = 7$; 25%) and lower thoracic ($n = 5$; 18%). No recurrences were observed among patients with a lower thoracic AVM ($P = .01$), while cervical and upper thoracic AVMs were frequently associated with recurrent hematomyelia ($P = .01$). Twenty-five patients (89%) had a single spinal AVM, and 3 patients (11%) had multiple AVMs (spinal cord, $n = 1$, or cerebral, $n = 2$). Assessment of AVM angioarchitecture showed that fistulas tend to be rare in children with recurrent hematomyelia (28% of fistulas), while a similar percentage of nidus AVMs was observed in the 2 groups. Microarchitectural analysis demonstrated that radiculomedullary arterial feeder ($P = .03$) and intranidal or draining vein ectasia ($P = .03$) were observed more frequently in patients with recurrence.

At the time of recurrence (Table 2), perimedullary venous drainage was the main factor associated with recurrence ($P = .002$). An occlusion rate of ≥50% was associated with a decreased risk of recurrence ($P = .047$), and no recurrence was observed when the occlusion rate was ≥70%.

Finally, at the end of treatment, the overall percentage embolization rate was similar for patients with 1 episode of hematomyelia and patients with recurrent episodes (mean/median/±SD/minimum-maximum: 77%/90%/±32/0%-100% and 72%/85/±32/0%-100%, respectively).

Functional Prognosis

Complications related to endovascular treatment with temporary clinical deterioration were observed in 5 patients. No early hemorrhage (subarachnoid hemorrhage or hematomyelia) related to embolization was observed. Good recovery within 1 month was observed in all of these patients. No permanent deterioration directly related to endovascular embolization was observed.

At last follow-up (Table 3), 11 children (39%) had a severe ASIA score. Apart from tetraplegia at onset ($P = .03$), which was significantly more frequent in children with a severe ASIA score at last follow-up, no other clinical or MR imaging characteristics were noted. In angiographic studies, macroarchitecture was unremarkable, but recurrent hematomyelia ($P = .07$) tended to be associated with a more severe clinical outcome. Endovascular arterial embolization was the treatment of choice for most patients in this population, and endovascular embolization was not performed in only 1 patient (refusal of treatment). A ≥90% decrease of the nidus or angiographic cure was not associated with better clinical outcome, and surgical decompression did not tend to improve clinical outcome.

DISCUSSION

This study presents the usual limitations of retrospective studies. The main patient recruitment of our institution via our referral center for CNS vascular diseases in children explains the predominant pediatric recruitment and probably explains the different modalities of management compared with series mainly including adults. The mean clinical follow-up was relatively short for the pediatric population, which confers a significant disadvantage in terms of determining the risk of a new episode of bleeding or

Table 1: Clinical and angiographic characteristics at onset

	All Children	Children with Recurrent Episodes	Children with Single Episode	
	(*n* = 28)	(*n* = 12) (43)	(*n* = 16) (57)	*P*
Mean age (yr)	9.9 ± 5.2	10.1 ± 5.1	9.7 ± 5.4	NS
Male/female	14:14	8:4	6:10	NS
Mean follow-up (yr)	5.7 ± 4.4	5.9 ± 3.2	5.6 ± 5.3	NS
Clinical evaluation				
Back pain	18 (64)	7 (58)	11 (69)	NS
Tetraplegia	7 (25)	5 (42)	2 (13)	NS
Paraplegia	3 (11)	1 (33)	2 (13)	NS
Sensory deficit	19 (68)	10 (83)	9 (56)	NS
Respiratory distress	4 (15)	3 (25)	1 (7)	NS
Sphincter dysfunction	18 (64)	9 (75)	9 (56)	NS
Severe ASIA score at onset (<D)	20 (71)	7 (58)	13 (81)	NS
Severe ASIA score at last follow-up	11 (39)	7 (58)	4 (25)	NS
MRI characteristics at onset (*n* = 22)				
Size of lesions >3 vertebrae (*n* = 20)	14 (70)	4 (57)	10 (77)	NS
T1 hyposignal (*n* = 15)	6 (40)	3 (43)	3 (38)	NS
Angiographic evaluation at onset				
Macroarchitecture				
Fistula	7 (25)	2 (17)	5 (31)	NS
Nidus	21 (75)	10 (83)	11 (69)	NS
Site				
Cervical	16 (57)	8 (67)	8 (50)	NS
Upper thoracic (T1–T7)	7 (25)	4 (33)	3 (19)	NS
Lower thoracic (T8–conus)	5 (18)	0	5 (31)	.01
Cervical and upper thoracic	23 (82)	12 (100)	11 (69)	.01
Microarchitecture				
Perimedullary venous drainage	27 (96)	12 (100)	15 (94)	NS
Radiculomedullary arterial feeder	20 (71)	11 (92)	9 (56)	.03
Anterior spinal vein drainage	9 (33)	5 (42)	4 (27)	NS
No. of arterial feeders >3 (*n* = 26)	15 (58)	8 (73)	7 (47)	NS
Draining vein stenosis ≥50% (*n* = 26)	3 (12)	1/11 (9)	2/15 (13)	NS
Pseudoaneurysm (*n* = 23)	9 (39)	4/9 (44)	5/14 (36)	1
Intranidal or draining vein ectasia (*n* = 24)	14 (58)	9/10 (90)	5/14 (36)	0.03
Radicular vein drainage	23 (82)	9 (75)	14 (88)	NS
Treatment				
Angiographic cure (*n* = 27)	5 (19)	0/12	5/15 (33)	0.01
Surgical decompression	6 (21)	2 (17)	4 (25)	0.6

Note:—NS indicates not significant.

disability. In the present study, no significant difference in mean age was observed between patients with recurrence and patients without recurrence. Although the risk of bleeding at presentation has been previously described to be lower in adults than in children[1,8,12-14] due to the peak incidence at the growth spurt, the risk of recurrence does not appear to be different in a pediatric population.

The main result of this study is that the risk of recurrence of hematomyelia was increased in a particular condition: malformative perimedullary venous drainage ($P = .002$). All patients who had a recurrence had perimedullary venous drainage compared with 33% of patients with a single episode of hematomyelia. This increased risk can be explained by a hypothesis based on mechanical considerations. Perimedullary venous drainage involves relatively small veins, while radicular venous drainage involves larger veins. However, venous drainage involving small veins may reflect higher upstream blood pressure inside the nidus. Because the outlet is smaller, it could interfere with venous outflow and could be responsible for higher blood pressure inside the AVM. Higher pressure inside the AVM would therefore be associated with a higher risk of bleeding.

A high occlusion rate was correlated with a lower risk of recurrence. An occlusion rate ≥50% was associated with a lower recurrence rate ($P = .047$). We can hypothesize that a nidus whose size was decreased by treatment was associated with lower blood pressure inside it and a lower risk of recurrent hematomyelia. When venous drainage is preserved during treatment, a decrease in the size of the nidus would proportionally decrease the pressure. In a 2007 study, Corkill et al[15] obtained a high occlusion rate with injection of Onyx (Covidien, Irvine, California). Although the occlusion rate was not specified, embolization achieved total or subtotal obliteration in 69% of cases with this liquid embolic system. A significant reduction of the flow load was obtained in the remaining patients, though a substantial part of the nidus remained patent. In their series, no recurrence of hematomyelia was reported with a mean follow-up of 24.3 months. The shorter follow-up in that study probably cannot explain this discrepancy in terms of recurrence rate compared with our series because the mean time to recurrence in our series was 3.7 ± 2.7 years. The absence of recurrence of hematomyelia could also be explained by the high mean obliteration rate achieved by Onyx injection. However, it seems difficult to transpose this technique to our population, which was mainly children, while the study by Corkill et al mainly concerned adults.

A high rebleeding rate (43%) was observed in this study. Although few data are available in the literature concerning the real frequency of hematomyelia and recurrence, the risk of recurrence was higher than that reported after similar treatment (a similar acrylic agent such as *n*-butyl 2-cyanoacrylate or Glubran Tiss [Aspide Medical, La Talaudière, France]; 18%, 2/11 patients)[1] in an exclusively pediatric population, while no recurrences were observed after the use of Onyx.[15] Several explanations can be proposed for the high recurrence rate observed in our series: In 50% of cases (6 patients), rebleeding occurred before the first treatment session (failure of embolization [$n = 1$]) or while the patient was waiting for transfer to our institution for embolization ($n = 5$); these scenarios could explain why recurrence occurred and why the risk of rebleeding of spinal cord AVMs appears to be higher in the absence of treatment. Partial treatment was initiated for the remaining 6 patients who rebled: Three were treated surgically with partial removal of the hematoma and resection of the malfor-

Table 2: Angiographic characteristics at recurrence or in children with a single episode of hematomyelia on angiography performed close to the mean time of the angiography performed in children with recurrence

Microachitecture	Children with Recurrent Episodes (*n* = 12) (44)	Children with Single Episode (*n* = 15) (56)	*P*
Follow-up (yr)			
Median	2.8 (0.10–9.3)	1.3 (0.4–4.8)	NS
Mean	3.7 ± 2.7	1.8 ± 1.3	NS
Cure	0	5 (33)	
Radiculomedullary feeder alone	3 (25)	1 (7)	NS
Radiculopial feeders alone	8 (67)	5 (33)	NS
Combination of both feeders	1 (8)	5 (33)	NS
Anterior spinal vein drainage	4 (33)	0	NS
Radicular vein drainage	7 (58)	8[a] (53)	NS
Anterior spinal and radicular vein drainage	1 (8)	2[a] (13)	NS
Perimedullary vein drainage	12 (100)	5 (33)	.002
Intranidal ectasia	6 (50)	2 (15)	.01
Draining vein stenosis ≥50% (*n* = 26)	1/11 (9)	2 (13)	NS
Pseudoaneurysm (*n* = 23)	2 (17)	0	NS
Occlusion rate ≥50%	4 (33)	10 (66)	.047
Occlusion rate ≥70%	0	10 (66)	

Note:—NS indicates not significant.

[a] For children with a single episode, radicular vein, or a combination of radicular and anterior spinal veins, drainage was associated with perimedullary vein drainage in 50% of cases.

Table 3: Clinical and angiographic characteristics according to the ASIA scale at last follow-up[a]

Characteristics	Severe ASIA Scale (*n* = 11) (39)	Nonsevere ASIA Scale (*n* = 17) (61)	*P*
Mean age at onset (yr)	9.2 ± 6.4	10.4 ± 4.3	NS
Male/female	6:5	8:9	NS
Mean follow-up (yr)	6.0 ± 4.5	5.5 ± 4.5	NS
Clinical evaluation			
Back pain	6 (55)	12 (71)	NS
Tetraplegia	6 (55)	1 (6)	.03
Paraplegia	1 (9)	2 (12)	NS
Sensory deficit	9 (82)	10 (59)	NS
Respiratory distress	2 (20)	2 (12)	NS
Sphincter dysfunction	9 (82)	9 (53)	NS
Severe ASIA score at onset (<D)	9 (82)	11 (65)	NS
Recurrence of hematomyelia	7 (64)	5 (29)	.07
MRI characteristics at onset (*n* = 22)			
T2 hyperintensity <3 vertebrae (*n* = 20)	6 (75)	8 (67)	NS
T1 hypointensity (*n* =15)	4 (67)	2 (22)	NS
Angiographic evaluation			
Macroarchitecture			
Fistula	2 (18)	5 (29)	NS
Nidus	9 (82)	12 (71)	NS
Site			
Cervical	7 (64)	9 (53)	NS
Upper thoracic (T1–T7)	2 (18)	5 (29)	NS
Lower thoracic (T8–conus)	2 (18)	3 (18)	NS
Cervical and upper thoracic	9 (82)	14 (82)	NS
Surgical decompression at onset	2 (18)	4 (24)	NS
Angiographic cure (≥90%)	7 (64)	8 (50)	NS

Note:—NS indicates not significant.

[a] Percentages are shown in parentheses.

mation and 3 were treated by partial embolization. Only a small percentage of malformations were removed (mean percentage of treatment, 38%); this finding could also help to explain recurrence.

Cervical AVM has been reported as associated with a higher risk of hematomyelia.[1] This appeared to be the case in our series because 57% of AVMs were cervical (16 patients), which was much more frequent, though not significantly, than upper thoracic (25%; 7 patients) and lower thoracic sites (18%; 5 patients). Although the risk of recurrence was not significantly higher for cervical AVMs, a lower risk of recurrence was observed in the lower thoracic spine ($P = .01$), in which no recurrences were observed. In lesions situated more caudally in the spinal canal, the Adamkiewicz artery may be frequently involved in the malformation. These AVM sites were considered very eloquent lesions, as in 3 of the 5 cases in this study. This lower recurrence rate can be explained by the high mean occlusion rate (95%) in this group of lower thoracic AVMs. The high mean occlusion rate can probably be explained by angioarchitectural findings because fistulas were more frequently observed in this site (63%, 3/5 patients) than in cervical (19%, 3/16 patients) or upper thoracic sites (28%, 2/7 patients). This angioarchitecture is usually easier to treat due to the presence of a smaller number of feeders usually presenting a good caliber that are easier to catheterize than in nidus AVMs with multiple small feeders.

Intranidal aneurysms have been more frequently described in the spinal cord with bleeding on presentation,[1] as in our cases of recurrence ($P = .01$). When possible, intranidal aneurysms should therefore be a target of choice during embolization, especially when only a small part of the malformation is removed.

The present study was based on patients with one or several episodes of hematomyelia, and the results cannot be extrapolated to patients with spinal cord AVMs that never bleed. However, because of the rarity of these malformations, it would be difficult to conduct a prospective study in patients with nonbleeding spinal cord AVMs to assess the angiographic criteria associated with an increased risk of bleeding. When endovascular treatment is required, at least a 50% reduction of the AVM and especially obliteration of the perimedullary venous drainage could be considered as a treatment option when cure of the lesion is not associated with an acceptable benefit/risk balance. Moreover, a >90% decrease or anatomic cure was not associated with a better clinical outcome. Although this study was based on a small population, it supports the hypothesis that cure of malformations situated in high eloquent areas is not required to improve clinical outcome and prevent recurrence of hematomyelia.

Finally, regarding the late clinical outcome, it is not surprising that recurrences were associated, though not significantly, with poorer outcome, because 64% of patients with recurrence had a severe ASIA score (ie, A, B, or C), while a severe outcome was observed in only 29% of patients without recurrence. These results suggest that treatment should be performed to prevent recurrence, which certainly constitutes one of the main parameters responsible for poorer outcome.

In this study, no clinical symptoms were associated with an increased risk of recurrence or severe ASIA score. In other my-

elopathies, particularly inflammatory myelopathies in children, younger age at onset and the presence of sphincter involvement were associated with a poorer clinical prognosis.[16,17] Imaging studies revealed that T1 hyposignal and extensive lesions could be MR imaging signs predictive of poorer outcome. In our study, we did not observe any clinical or MR imaging criteria able to distinguish recurrence or more severe ASIA scale apart from younger age, though not significant, suggesting that these factors are less important in hematomyelia in contrast to inflammatory myelopathies.

CONCLUSIONS

The treatment of spinal cord AVM while avoiding neurologic sequelae is challenging. In the presence of hematomyelia, treatment must prevent recurrence that can worsen the clinical status. When cure of the malformation is not associated with an acceptable benefit/risk balance, a 50% decrease of the malformation can constitute a good option to prevent further recurrence. Disappearance of perimedullary venous drainage appears to be 1 primary target of treatment to avoid recurrences.

ACKNOWLEDGMENTS

We thank Professor Pierre Lasjaunias for his contribution in the collection of the clinical and imaging data as well as his overall contribution to our understanding of spinal cord AVMs.

Disclosures: Marie Theaudin—*UNRELATED*: *Travel/Accommodations/Meeting Expenses Unrelated to Activities Listed*: Biogen Idec, Novartis, Merck Serono, Bayer, LFB Biomedicaments. Marina Sachet—*UNRELATED*: *Travel/Accommodations/Meeting Expenses Unrelated to Activities Listed*: Covidien, *Other*: Covidien,* Balt,* MicroVention,* *Comments*: fees for participation in review activities such as data-monitoring boards, statistical analysis, endpoint committees, and the like. Kumaran Deiva—*UNRELATED*: *Travel/Accommodations/Meeting Expenses Unrelated to Activities Listed*: Merck Serono, Biogen Idec, *Comments*: travel grants for meetings, but no money received directly (accommodations booked directly by companies), Principal Investigator for Merck Serono. *Money paid to the institution.

REFERENCES

1. Rodesch G, Hurth M, Alvarez H, et al. **Angio-architecture of spinal cord arteriovenous shunts at presentation: clinical correlations in adults and children—the Bicêtre experience on 155 consecutive patients seen between 1981–1999.** *Acta Neurochir (Wien)* 2004;146:217–26, discussion 226–27
2. Rodesch G, Lasjaunias P. **Spinal cord arteriovenous shunts: from imaging to management.** *Eur J Radiol* 2003;46:221–32
3. Hernesniemi JA, Dashti R, Juvela S, et al. **Natural history of brain arteriovenous malformations: a long-term follow-up study of risk of hemorrhage in 238 patients.** *Neurosurgery* 2008;63:823–29, discussion 829–31
4. Halim AX, Johnston SC, Singh V, et al. **Longitudinal risk of intracranial hemorrhage in patients with arteriovenous malformation of the brain within a defined population.** *Stroke* 2004;35:1697–702
5. Mast H, Young WL, Koennecke HC, et al. **Risk of spontaneous haemorrhage after diagnosis of cerebral arteriovenous malformation.** *Lancet* 1997;350:1065–68
6. Stapf C, Mast H, Sciacca RR, et al. **Predictors of hemorrhage in patients with untreated brain arteriovenous malformation.** *Neurology* 2006;66:1350–55
7. Stefani MA, Porter PJ, terBrugge KG, et al. **Angioarchitectural factors present in brain arteriovenous malformations associated with hemorrhagic presentation.** *Stroke* 2002;33:920–24
8. Rodesch G, Pongpech S, Alvarez H, et al. **Spinal cord arteriovenous malformations in a pediatric population children below 15 years of age: the place of endovascular management.** *Interv Neuroradiol* 1995;1:29–42
9. Maynard FM Jr, Bracken MB, Creasey G, et al. **International Standards for Neurological and Functional Classification of Spinal Cord Injury: American Spinal Injury Association.** *Spinal Cord* 1997;35:266–74
10. Du J, Ling F, Chen M, et al. **Clinical characteristic of spinal vascular malformation in pediatric patients.** *Childs Nerv Syst* 2009;25:473–78
11. Kim LJ, Spetzler RF. **Classification and surgical management of spinal arteriovenous lesions: arteriovenous fistulae and arteriovenous malformations.** *Neurosurgery* 2006;59(5 suppl 3):S195–201, discussion S3–13
12. Emery DJ, Willinsky RA, Burrows PE, et al. **Paediatric spinal arteriovenous malformations: angioarchitecture and endovascular treatment.** *Interv Neuroradiol* 1998;4:127–39
13. Scarff TB, Reigel DH. **Arteriovenous malformations of the spinal cord in children.** *Childs Brain* 1979;5:341–51
14. Cullen S, Alvarez H, Rodesch G, et al. **Spinal arteriovenous shunts presenting before 2 years of age: analysis of 13 cases.** *Childs Nerv Syst* 2006;22:1103–10
15. Corkill RA, Mitsos AP, Molyneux AJ. **Embolization of spinal intramedullary arteriovenous malformations using the liquid embolic agent, Onyx: a single-center experience in a series of 17 patients.** *J Neurosurg Spine* 2007;7:478–85
16. Pidcock FS, Krishnan C, Crawford TO, et al. **Acute transverse myelitis in childhood: center-based analysis of 47 cases.** *Neurology* 2007;68:1474–80
17. Thomas T, Branson HM, Verhey LH, et al. **The demographic, clinical, and magnetic resonance imaging (MRI) features of transverse myelitis in children.** *J Child Neurol* 2012;27:11–21

Target® Detachable Coil

See package insert for complete indications, contraindications, warnings and instructions for use.

INTENDED USE / INDICATIONS FOR USE
Target Detachable Coils are intended to endovascularly obstruct or occlude blood flow in vascular abnormalities of the neurovascular and peripheral vessels.

Target Detachable Coils are indicated for endovascular embolization of:
- Intracranial aneurysms
- Other neurovascular abnormalities such as arteriovenous malformations and arteriovenous fistulae
- Arterial and venous embolizations in the peripheral vasculature

CONTRAINDICATIONS
None known.

POTENTIAL ADVERSE EVENTS
Potential complications include, but are not limited to: allergic reaction, aneurysm perforation and rupture, arrhythmia, death, edema, embolus, headache, hemorrhage, infection, ischemia, neurological/intracranial sequelae, post-embolization syndrome (fever, increased white blood cell count, discomfort), TIA/stroke, vasospasm, vessel occlusion or closure, vessel perforation, dissection, trauma or damage, vessel rupture, vessel thrombosis. Other procedural complications including but not limited to: anesthetic and contrast media risks, hypotension, hypertension, access site complications.

WARNINGS
- Contents supplied STERILE using an ethylene oxide (EO) process. Do not use if sterile barrier is damaged. If damage is found, call your Stryker Neurovascular representative.
- For single use only. Do not reuse, reprocess or resterilize. Reuse, reprocessing or resterilization may compromise the structural integrity of the device and/or lead to device failure which, in turn, may result in patient injury, illness or death. Reuse, reprocessing or resterilization may also create a risk of contamination of the device and/or cause patient infection or cross-infection, including, but not limited to, the transmission of infectious disease(s) from one patient to another. Contamination of the device may lead to injury, illness or death of the patient.
- After use, dispose of product and packaging in accordance with hospital, administrative and/or local government policy.
- **This device should only be used by physicians who have received appropriate training in interventional neuroradiology or interventional radiology and preclinical training on the use of this device as established by Stryker Neurovascular.**
- Patients with hypersensitivity to 316LVM stainless steel may suffer an allergic reaction to this implant.
- MR temperature testing was not conducted in peripheral vasculature, arteriovenous malformations or fistulae models.
- The safety and performance characteristics of the Target Detachable Coil System (Target Detachable Coils, InZone Detachment Systems, delivery systems and accessories) have not been demonstrated with other manufacturer's devices (whether coils, coil delivery devices, coil detachment systems, catheters, guidewires, and/or other accessories). Due to the potential incompatibility of non Stryker Neurovascular devices with the Target Detachable Coil System, the use of other manufacturer's device(s) with the Target Detachable Coil System is not recommended.
- To reduce risk of coil migration, the diameter of the first and second coil should never be less than the width of the ostium.
- In order to achieve optimal performance of the Target Detachable Coil System and to reduce the risk of thromboembolic complications, it is critical that a continuous infusion of appropriate flush solution be maintained between a) the femoral sheath and guiding catheter, b) the 2-tip microcatheter and guiding catheters, and c) the 2-tip microcatheter and Stryker Neurovascular guidewire and delivery wire. Continuous flush also reduces the potential for thrombus formation on, and crystallization of infusate around, the detachment zone of the Target Detachable Coil.
- Do not use the product after the "Use By" date specified on the package.
- Reuse of the flush port/dispenser coil or use with any coil other than the original coil may result in contamination of, or damage to, the coil.
- Utilization of damaged coils may affect coil delivery to, and stability inside, the vessel or aneurysm, possibly resulting in coil migration and/or stretching.
- The fluoro-saver marker is designed for use with a Rotating Hemostatic Valve (RHV). If used without an RHV, the distal end of the coil may be beyond the alignment marker when the fluoro-saver marker reaches the microcatheter hub.
- If the fluoro-saver marker is not visible, do not advance the coil without fluoroscopy.
- Do not rotate delivery wire during or after delivery of the coil. Rotating the Target Detachable Coil delivery wire may result in a stretched coil or premature detachment of the coil from the delivery wire, which could result in coil migration.
- Verify there is no coil loop protrusion into the parent vessel after coil placement and prior to coil detachment. Coil loop protrusion after coil placement may result in thromboembolic events if the coil is detached.
- Verify there is no movement of the coil after coil placement and prior to coil detachment. Movement of the coil after coil placement may indicate that the coil could migrate once it is detached.
- Failure to properly close the RHV compression fitting over the delivery wire before attaching the InZone® Detachment System could result in coil movement, aneurysm rupture or vessel perforation.
- Verify repeatedly that the distal shaft of the catheter is not under stress before detaching the Target Detachable Coil. Axial compression or tension forces could be stored in the 2-tip microcatheter causing the tip to move during coil delivery. Microcatheter tip movement could cause the aneurysm or vessel to rupture.
- Advancing the delivery wire beyond the microcatheter tip once the coil has been detached involves risk of aneurysm or vessel perforation.
- The long term effect of this product on extravascular tissues has not been established so care should be taken to retain this device in the intravascular space.

Damaged delivery wires may cause detachment failures, vessel injury or unpredictable distal tip response during coil deployment. If a delivery wire is damaged at any point during the procedure, do not attempt to straighten or otherwise repair it. Do not proceed with deployment or detachment. Remove the entire coil and replace with undamaged product.

- After use, dispose of product and packaging in accordance with hospital, administrative and/or local government policy.

CAUTIONS / PRECAUTIONS
- Federal Law (USA) restricts this device to sale by or on the order of a physician.
- Besides the number of InZone Detachment System units needed to complete the case, there must be an extra InZone Detachment System unit as back up.
- Removing the delivery wire without grasping the introducer sheath and delivery wire together may result in the detachable coil sliding out of the introducer sheath.
- Failure to remove the introducer sheath after inserting the delivery wire into the RHV of the microcatheter will interrupt normal infusion of flush solution and allow back flow of blood into the microcatheter.
- Some low level overhead light near or adjacent to the patient is required to visualize the fluoro-saver marker; monitor light alone will not allow sufficient visualization of the fluoro-saver marker.
- Advance and retract the Target Detachable Coil carefully and smoothly without excessive force. If unusual friction is noticed, slowly withdraw the Target Detachable Coil and examine for damage. If damage is present, remove and use a new Target Detachable Coil. If friction or resistance is still noted, carefully remove the Target Detachable Coil and microcatheter and examine the microcatheter for damage.
- If it is necessary to reposition the Target Detachable Coil, verify under fluoroscopy that the coil moves with a one-to-one motion. If the coil does not move with a one-to-one motion or movement is difficult, the coil may have stretched and could possibly migrate or break. Gently remove both the coil and microcatheter and replace with new devices.
- Increased detachment times may occur when:
  - Other embolic agents are present.
  - Delivery wire and microcatheter markers are not properly aligned.
  - Thrombus is present on the coil detachment zone.
- Do not use detachment systems other than the InZone Detachment System.
- Increased detachment times may occur when delivery wire and microcatheter markers are not properly aligned.
- Do not use detachment systems other than the InZone Detachment System.

Stryker Neurovascular
47900 Bayside Parkway
Fremont, CA 94538-6515

stryker.com/neurovascular

Date of Release: JUN/2014

EX_EN_US

Trevo® XP ProVue Retrievers

See package insert for complete indications, complications, warnings, and instructions for use.

INDICATIONS FOR USE
The Trevo Retriever is intended to restore blood flow in the neurovasculature by removing thrombus in patients experiencing ischemic stroke within 8 hours of symptom onset. Patients who are ineligible for intravenous tissue plasminogen activator (IV t-PA) or who fail IV t-PA therapy are candidates for treatment.

COMPLICATIONS
Procedures requiring percutaneous catheter introduction should not be attempted by physicians unfamiliar with possible complications which may occur during or after the procedure. Possible complications include, but are not limited to, the following: air embolism; hematoma or hemorrhage at puncture site; infection; distal embolization; pain/headache; vessel spasm, thrombosis, dissection, or perforation; emboli; acute occlusion; ischemia; intracranial hemorrhage; false aneurysm formation; neurological deficits including stroke; and death.

COMPATIBILITY
3x20 mm retrievers are compatible with Trevo® Pro 14 Microcatheters (REF 90231) and Trevo® Pro 18 Microcatheters (REF 90238). 4x20 mm retrievers are compatible with Trevo® Pro 18 Microcatheters (REF 90238). Compatibility of the Retriever with other microcatheters has not been established. Performance of the Retriever device may be impacted if a different microcatheter is used. The Merci® Balloon Guide Catheters are recommended for use during thrombus removal procedures. Retrievers are compatible with the Abbott Vascular DOC® Guide Wire Extension (REF 22260).

WARNINGS
- Contents supplied STERILE, using an ethylene oxide (EO) process. Nonpyrogenic.
- To reduce risk of vessel damage, adhere to the following recommendations:
  - Take care to appropriately size Retriever to vessel diameter at intended site of deployment.
  - Do not perform more than six (6) retrieval attempts in same vessel using Retriever devices.
  - Maintain Retriever position in vessel when removing or exchanging Microcatheter.
- To reduce risk of kinking/fracture, adhere to the following recommendations:
  - Immediately after unsheathing Retriever, position Microcatheter tip marker just proximal to shaped section. Maintain Microcatheter tip marker just proximal to shaped section of Retriever during manipulation and withdrawal.
  - Do not rotate or torque Retriever.
  - Use caution when passing Retriever through stented arteries.
- Do not resterilize and reuse. Structural integrity and/or function may be impaired by reuse or cleaning.
- The Retriever is a delicate instrument and should be handled carefully. Before use and when possible during procedure, inspect device carefully for damage. Do not use a device that shows signs of damage. Damage may prevent device from functioning and may cause complications.
- Do not advance or withdraw Retriever against resistance or significant vasospasm. Moving or torquing device against resistance or significant vasospasm may result in damage to vessel or device. Assess cause of resistance using fluoroscopy and if needed resheath the device to withdraw.
- If Retriever is difficult to withdraw from the vessel, do not torque Retriever. Advance Microcatheter distally, gently pull Retriever back into Microcatheter, and remove Retriever and Microcatheter as a unit. If undue resistance is met when withdrawing the Retriever into the Microcatheter, consider extending the Retriever using the Abbott Vascular DOC guidewire extension (REF 22260) so that the Microcatheter can be exchanged for a larger diameter catheter such as a DAC® catheter. Gently withdraw the Retriever into the larger diameter catheter.
- Administer anti-coagulation and anti-platelet medications per standard institutional guidelines.

PRECAUTIONS
- Prescription only – device restricted to use by or on order of a physician.
- Store in cool, dry, dark place.
- Do not use open or damaged packages.
- Use by "Use By" date.
- Exposure to temperatures above 54°C (130°F) may damage device and accessories. Do not autoclave.
- Do not expose Retriever to solvents.
- Use Retriever in conjunction with fluoroscopic visualization and proper anti-coagulation agents.
- To prevent thrombus formation and contrast media crystal formation, maintain a constant infusion of appropriate flush solution between guide catheter and Microcatheter and between Microcatheter and Retriever or guidewire.
- Do not attach a torque device to the shaped proximal end of DOC® Compatible Retriever. Damage may occur, preventing ability to attach DOC® Guide Wire Extension.

Concentric Medical
301 East Evelyn
Mountain View, CA 94041

EC REP

EMERGO Europe
Molenstraat 15
2513 BH, The Hague
The Netherlands

CE 0459

Stryker Neurovascular
47900 Bayside Parkway
Fremont, CA 94538-6515

stryker.com/neurovascular
stryker.com/emea/neurovascular

Date of Release: JUN/2014

EX_EN_GL

Beyond Soft

The softest coil technology* available, combined with Target Coil's consistently smooth deployment and exceptional microcatheter stability, results in an experience that is beyond soft. Designed to treat small spaces, the Target Nano Coil's incredible softness delivers increased conformability and shape adjustment.

Target Nano Coils–**Smooth and Stable** has never been so soft.

For more information, please visit www.strykerneurovascular.com/Target

stryker® Neurovascular

*Testing performed by Stryker Neurovascular. n=3. Data are on file at Stryker Neurovascular and will be made available upon request. Bench test results may not necessarily be indicative of clinical performance.

Stroke: *Our Only Focus. Our Ongoing Promise.*